School of Civil and Mechanical Engineering

Interfacial Bond Behaviour between FRP Sheet and Concrete under Static and Dynamic Loads

Cheng Yuan

This thesis is presented for the Degree of
Doctor of Philosophy
of
Curtin University

Feb 2020

Declaration

To the best of my knowledge and belief this thesis contains no material previously published by any other person except where due acknowledgment has been made.

This thesis contains no material which has been accepted for the award of any other degree or diploma in any university.

Signature: 

Date: 2/6/2020

Abstract

Fibre-reinforced polymer (FRP), as an effective strengthening composite material with high strength to weight ratio and excellent corrosion resistance, has been widely used to strengthen existing reinforced-concrete (RC) structures. The interfacial bond between FRP and the strengthened element is often the governing factor in determining the strengthening efficiency. The existing studies on the interfacial bond strength focus on the static loading conditions. Mechanical properties of concrete, FRP, and adhesive resin are identified as the main factors affecting the interfacial bond capacity between FRP and strengthened element. On the other hand, it is believed that the interfacial bond performance also depends on other factors such as hybrid FRPs (carbon and basalt fibre composite), coarse aggregate sizes, and characteristics of steel fibre reinforced concrete, which have not been investigated. Furthermore, it is believed that the interfacial bond performances between FRP and concrete would be different under static and dynamic loading conditions, but only very limited studies on the dynamic bond behaviour of FRP-to-concrete interface under low strain rate have been reported. Since the strain rate under impact and blast loads can reach up to 100 s^{-1} or even higher, it is necessary to investigate the dynamic interfacial bond performance of FRP-to-concrete interface under a higher strain rate.

To investigate the effects of FRP configurations (sole BFRP, sole CFRP and BFRP/CFRP hybrid FRPs), concrete substrate characteristics (coarse aggregate sizes, concrete strength and steel fibre reinforcement), and strain rate on the interfacial bond behaviour between FRP and concrete, two series of single-lap shear tests (SST) are conducted under various loading speeds of $8.33E^{-6}$ m/s, 0.1 m/s, 1 m/s, 3 m/s, 5 m/s, and 8 m/s by using Shimadzu and Instron VHS machines to achieve the strain rate up to 175 s^{-1}. Digital image correlation (DIC) technique is employed to measure the fields of displacement. Experimental results including failure mode, strain distributions, and

bond-slip response are reported and discussed to reveal the effects of FRP configurations and concrete substrate characteristics on the quasi-static and dynamic interfacial bond behaviours. The new semi-empirical bond strength models and interfacial bond-slip models are proposed by incorporating these effects. In addition, to study the strain rate effect, dynamic testing results are compared with the quasi-static testing results, such as failure modes, strain distribution, interfacial shear stress, fracture energy, and bond strength. The difference is found remarkable between dynamic and quasi-static testing results. The empirical bond-slip models incorporating the strain rate effect are established for the predictions of dynamic bond behaviours.

Numerical study is also conducted to predict the dynamic interfacial bond behaviour under different loading rates. A three-dimensional (3D) numerical model is established in LS-DYNA and validated with experimental results, such as strain distributions, load-slip curves, and bond-slip curves. Comparisons between numerical and testing results show that the numerical model is capable of capturing the debonding load, FRP strain distributions, and interfacial bond-slip responses under different loading rates. The numerical results are also compared with the predictions by the analytical models proposed in this study. The validated numerical model of interfacial bonding can be used to yield a more accurate prediction of the dynamic response of FRP strengthened structure.

To enhance the interfacial bond between FRP sheets and concrete, a new anchorage system called epoxy anchor is proposed in this study. Epoxy anchors are formed by drilling holes into the concrete substrate before applying epoxy resin. It is found that the proposed epoxy anchors remarkably enhance the shear resistance while the progressive FRP debonding is significantly postponed. Using epoxy anchors yields 77.49% increment in bond strength, 86.71% increment in the utilization of BFRP sheet, and 78.10% increase in the peak shear stress on average. Accordingly, a new bond strength model by incorporating the effects of strain energy and bonding area of epoxy

resin is proposed to predict the effect of anchorage on the bonding behaviour. The predicted debonding load shows good agreement with the testing data.

Furthermore, to monitor the interface damage caused by FRP debonding, a stress-wave based sensing approach is used to quantitatively monitor the entire debonding process by using surface mounted piezoceramic-based transducers (also called as smart aggregates SAs). The debonding level and the assessment of interface condition can be well quantified by the wavelet-based damage index. The proposed method can provide an alternative solution for fast detection and real-time monitoring of FRP-concrete interfacial debonding in engineering practice.

List of Publications

This thesis is assembled by the accepted and submitted papers, which form the individual chapters and are listed below.

Chapter 3

Yuan C, Chen W, Pham TM, Hao H. Bond Behaviour between Hybrid Fibre Reinforced Polymer Sheets and Concrete. Construction and Building Materials. 2019; 210:93-110.

Chapter 4

Yuan C, Chen W, Pham TM, Hao H. Effect of Aggregate Size on Bond Behaviour between Basalt Fibre Reinforced Polymer Sheets and Concrete. Composites Part B: Engineering. 2019; 158:459-74.

Yuan C, Chen W, Pham TM, Hao H. Bond Behaviour between Basalt Fibres Reinforced Polymer Sheets and Steel Fibres Reinforced Concrete. Engineering structures. 2018; 176:812-24.

Chapter 5

Yuan C, Chen W, Pham TM, Hao H, Cui J, Shi Y. Dynamic Interfacial Bond Behaviour between Basalt Fibre Reinforced Polymer Sheets and Concrete. International Journal of Solid and Structures. (Under review)

Yuan C, Chen W, Pham TM, Hao H, Jian C, Shi Y. Dynamic Interfacial Bond Behaviour between Hybrid Fibre Reinforced Polymer Sheets and Concrete. International Journal of Adhesion and Adhesive. 2020; 99: 102569.

Chapter 6

Yuan C, Chen W, Pham TM, Chen L, Cui J, Shi Y, Hao H. Effect of Aggregate Size on the Dynamic Interfacial Bond Behaviour between Basalt Fibre Reinforced Polymer Sheets and Concrete. Construction and Building Materials. 2019; 227:116584.

Yuan C, Chen W, Pham TM, Hao H, Cui J, Shi Y. Influence of Concrete Strength on Dynamic Interfacial Fracture Behaviour between Fibre Reinforced Polymer Sheets and Concrete. Engineering Fracture Mechanics. 2020:106934.

Yuan C, Chen W, Pham TM, Hao H, Cui J, Shi Y. Strain Rate Effect on Interfacial Bond Behaviour between BFRP Sheets and Steel Fibre Reinforced Concrete. Composites Part B: Engineering. 2019:107032.

Chapter 7

Yuan C, Chen W, Pham TM, Li H, Hao H. Finite element modelling of dynamic bonding behaviours between fibre reinforced polymer sheet and concrete. Construction and Building Materials. 2020; 255:118939.

Chapter 8

Yuan C, Chen W, Pham TM, Hao H, Chen L, Zhang M. New epoxy anchor for better bonding between FRP sheets and concrete. Construction and Building Materials. 2020; 248:118628.

Chapter 9

Yuan C, Kong Q, Chen W, Jiang J, Hao H. Interfacial Debonding Detection in Externally Bonded BFRP Reinforced Concrete Using Stress Wave-based Sensing Approach. Smart Materials and Structures. 2020; 29: 035039.

Acknowledgement

I would like to express my deepest gratitude to my supervisors Prof. Hong Hao and Dr. Wensu Chen for their valuable advice, enlightening guidance, patience and kindness throughout my PhD journey. Their generous support and invaluable comments helped to improve and shape this thesis.

I would also like to express my sincere thanks to Dr. Thong Pham for his exemplary guidance, assistance and encouragement during my study. Many thanks are also expressed to Prof. Li Chen, Prof. Yanchao Shi, Dr. Qingzhao Kong, Dr. Jiafei Jiang, Dr. Jian Cui, Mr. Huawei Li, Dr. Zhejian Li, Dr. Tin Van Do, Dr. Haoran Zuo, Mr. Tung Thanh Tran, Mr. Ruisheng Ma, Mr. Tuan Tang Ngo and research colleagues in Centre for Infrastructure Monitoring and Protection (CIMP) for their great friendship and help during my PhD study.

Last but not least, I would like to express my profound gratitude to my wife Ms Ting He whose love, encouragement and understanding made this thesis possible.

Statement of Contribution of Others

The work presented in this thesis was primarily designed, experimentally executed, analytically evaluated, numerically simulated, analysed and written by the first author (Cheng Yuan) of the individual manuscripts. Contributions by others are described as follows. The signed contribution forms are attached in the appendix.

Chapter 3 to Chapter 4

Prof. Hong Hao, Dr. Wensu Chen and Dr. Thong M. Pham revised and edited the manuscript, provided intellectual input towards data processing, analysis, and discussion of the results. Civil and Mechanical Engineering Lab helped machining and manufacturing specimens and set-ups. The financial support was provided by Australian Research Council (ARC LP150100259).

Chapter 5 to Chapter 6

Prof. Hong Hao, Dr. Wensu Chen, Dr. Thong M. Pham and Prof. Li Chen revised and edited the manuscript, provided intellectual input towards data processing, analysis, and discussion of the results. Dr. Jian Cui and Prof. Yanchao Shi from Tianjin University assisted with the dynamic testing set-up, data recording, and analysis. The financial support was provided by Australian Research Council (ARC LP150100259).

Chapter 7

Prof. Hong Hao, Dr. Wensu Chen and Dr. Thong M. Pham revised and edited the manuscript, provided intellectual input towards data processing, analysis, and discussion of the results. Mr. Huawei Li helped with the numerical modelling. The financial support was provided by Australian Research Council (ARC LP150100259).

Chapter 8

Prof. Hong Hao, Dr. Wensu Chen, Dr. Thong M. Pham and Prof. Li Chen revised and edited the manuscript, provided intellectual input towards data processing, analysis, and discussion of the results. Ms. Mi Zhang helped with the experiments. The financial support was provided by Australian Research Council (ARC LP150100259).

Chapter 9

Prof. Hong Hao, Dr. Wensu Chen, Dr. Qingzhao Kong and Dr. Jiafei Jiang revised and edited the manuscript, provided intellectual input towards data processing, analysis, and discussion of the results. The financial support was provided by Australian Research Council Linkage Project (ARC LP150100259) and Chinese State Key Laboratory of High Performance Civil Engineering Materials (2018CEM003).

Table of Contents

1. Introduction

1.1 Background

Fibre-reinforced polymer (FRP), as an effective strengthening composite material with high strength to weight ratio and excellent corrosion resistance, has been widely used to strengthen existing reinforced-concrete (RC) structures. The interfacial bond between FRP and the strengthened element is a governing factor in determining the strengthening efficiency. The existing studies with respect to the interfacial bond focus on the static loading conditions. Mechanical properties of concrete, FRP, and adhesive resin are identified as the main factors affecting the interfacial bond capacity between FRP and strengthened element. Besides these factors, it is believed properties of hybrid FRPs (carbon and basalt fibre composite), coarse aggregate sizes, steel fibres in fibre reinforced concrete also affect the interfacial bonding behaviour between FRP and concrete, which, however, have not been investigated. Furthermore, only limited studies on the dynamic bond behaviour of FRP-to-concrete interface under low strain rate have been reported. Since the strain rate under impact and blast can reach up to 100 s^{-1} or even higher, it is necessary to investigate the dynamic interfacial bond performance of FRP-to-concrete interface under a wider range of strain rates.

1.2 Objectives

The objective of this study is to reveal the effects of FRP configurations (sole BFRP, sole CFRP and BFRP/CFRP hybrid FRPs), concrete substrate characteristics (coarse aggregate sizes, concrete strength and steel fibres in fibre reinforced concrete) and strain rate on the interfacial bond behaviour between FRP and concrete, two series of single-lap shear tests (SST) are conducted under various loading speeds of $8.33E^{-6}$ m/s, 0.1 m/s, 1 m/s, 3 m/s, 5 m/s, and 8 m/s by using Shimadzu and Instron VHS machines to achieve the strain rate up to 175 s^{-1}. Digital image correlation (DIC) technique is employed to measure the fields of displacement. Experimental results including failure

mode, strain distributions, and bond-slip response are reported and discussed to reveal the effects of FRP configurations and concrete substrate characteristics on the quasi-static and dynamic interfacial bond behaviours. The semi-empirical bond strength models and interfacial bond-slip models are proposed by incorporating these effects. In addition, to study the strain rate effect, dynamic testing results are compared with the quasi-static testing results, such as failure modes, strain distribution, interfacial shear stress, fracture energy, and bond strength.

Numerical study is also conducted to predict the dynamic interfacial bond behaviour under different loading rates. A three-dimensional (3D) numerical model is built up in LS-DYNA and validated with experimental results, in terms of the strain distributions, load-slip curves, and bond-slip curves. The numerical results are also compared with the predictions by the analytical models proposed in this study.

To enhance the interfacial bond between FRP sheets and concrete, a new anchorage system called epoxy anchor is proposed in this study. Epoxy anchors are formed by drilling holes into the concrete substrate before applying epoxy resin. Additionally, a new bond strength model by incorporating the effects of strain energy and bonding area of epoxy resin is proposed to analyse the effect of anchorage on the bonding behaviour.

Furthermore, to monitor the interface damage caused by FRP debonding, a stress-wave based sensing approach is used to quantitatively monitor the entire debonding process by using surface mounted piezoceramic-based transducers (also called as smart aggregates SAs). The debonding level and the assessment of interface condition can be well quantified by the wavelet-based damage index. The proposed method can provide an alternative solution for fast detection and real-time monitoring of FRP-concrete interfacial debonding in engineering practice.

1.3 Research outline

This thesis comprises ten chapters. The contents of seven chapters following the introduction and literature review are presented as follows:

Chapter 3 presents an experimental and analytical analysis of static interfacial bond behaviour between hybrid FRPs (BFRP+CFRP) and concrete. The aim of this chapter is to investigate the effect of hybrid FRPs with different elastic modulus and thickness and FRP stacking sequence on the bonding performance under static loading.

Chapter 4 presents an experimental and analytical analysis of static interfacial bond behaviour between FRP and concrete affected by the coarse aggregate size and additional steel fibres. The effect of aggregate sizes (i.e. 5-10 mm, 10-15 mm, and 15-20 mm) on the debonding load, maximum bond stress, effective bond length, local slip at peak shear stress, as well as the bond-slip relationship between the BFRP sheets and concrete are presented and discussed. Short steel fibres with four volume fractions (i.e. V_f =0%, 0.25%, 0.50% and 1.0%) are used to improve the interfacial bond behaviour of BFRP-concrete as the mechanical properties of the concrete substrate (i.e. compressive strength and tensile strength) can be improved by adding steel fibres.

Chapter 5 presents the experimental and analytical analysis of dynamic interfacial bond behaviour between sole FRP / hybrid FRPs and concrete under high loading velocities (i.e., 8.33E-6, 1.0, 3.0, and 8.0 m/s). The single-lap shear specimens are evaluated with different stacking sequences of FRP sheets (i.e., CFRP and BFRP) bonded to the concrete substrates. Experimental results including debonding failure modes, ultimate debonding strain, debonding load, interfacial fracture energy, and bond-slip response are discussed and evaluated.

Chapter 6 presents experimental and analytical analysis of dynamic interfacial bond behaviour between FRP and concrete affected by the concrete strength (i.e. C20, C30,

and C40), coarse aggregate size (i.e. 5-10 mm, 10-15 mm, and 15-20 mm) and additional steel fibres (i.e. V_f = 0.5%, 1.0%, and 1.5%) under various loading speeds (i.e. 8.33E-6, 0.1, 1.0, 3.0, 5.0, and 8.0 m/s). The semi-empirical dynamic bond-slip models by incorporating these parameters are proposed accordingly.

Chapter 7 presents a numerical analysis of dynamic interfacial bond behaviour of FRP-to-concrete interface. A three-dimensional (3D) finite element (FE) model is built and a bond-slip model is incorporated into the simulation of the interfacial bond between FRP and concrete. The debonding load and shear slip responses, FRP strain distributions, and interfacial bond-slip responses are compared between the numerical and experimental results.

Chapter 8 presents an experimental and analytical analysis of the enhanced interfacial bond by using a new proposed epoxy anchor. Epoxy anchors are formed by drilling holes into the concrete substrate before applying epoxy resin. The depth and diameter of epoxy anchors are designed to enhance the cohesive strength of the interface. A bond strength model by incorporating the effects of strain energy and bonding area of epoxy resin is proposed to analyse the effect of anchorage.

Chapter 9 presents a stress-wave based sensing approach to monitor the interfacial damage caused by FRP debonding. The scanning wave signals in swept-frequency mode and single frequency mode are utilized in experimental and numerical methods, respectively. The proposed method has the potential for fast determination or real-time monitoring of FRP-concrete interfacial debonding for both research and field applications.

Chapter 10 summarizes the main findings from this study, as well as some future works.

2. Literature review

2.1 Overview

This chapter presents a literature review of static and dynamic interfacial bond behaviour between FRP and concrete. The literature review includes four parts: 1. Debonding phenomenon of FRP-strengthened RC structures; 2. Debonding mechanism under static and dynamic loads; 3. Existing anchorage systems to improve bond performance; 4. Debonding damage monitoring.

2.2 Debonding phenomenon of FRP-strengthened RC structures

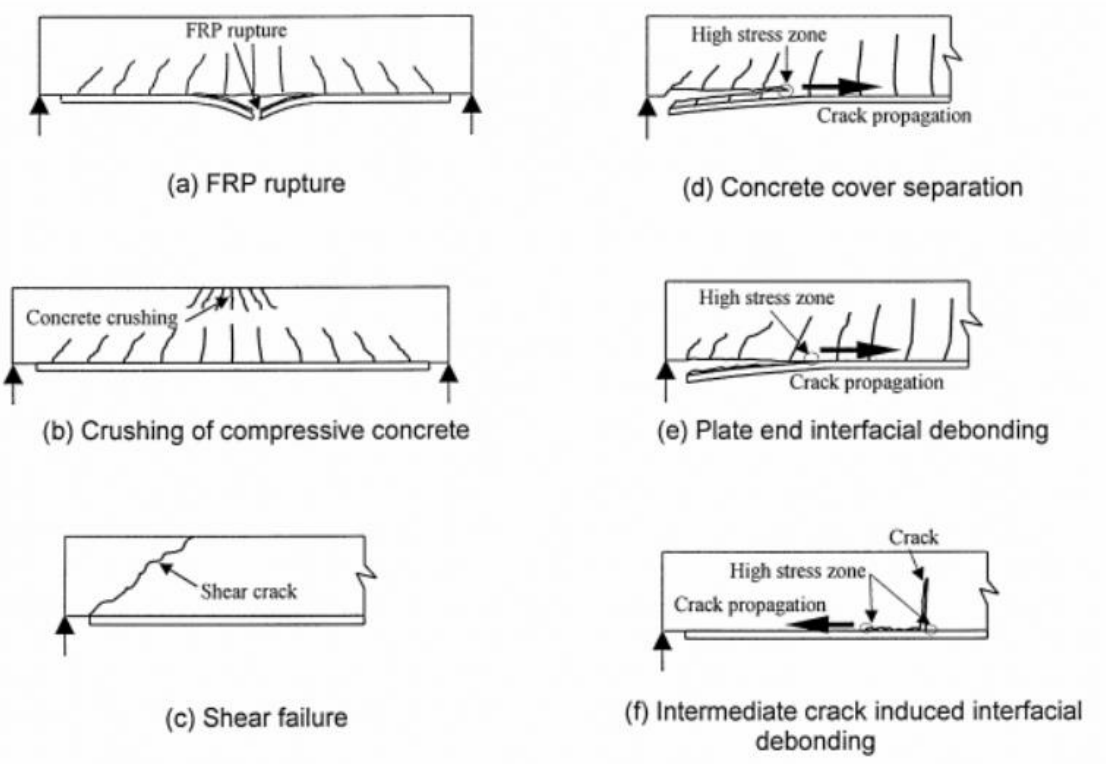

Figure 2-1. Failure modes of FRP-strengthened RC beams (1)

FRP strengthening has become increasingly popular in construction and retrofit applications (2, 3), specifically in aging, damaged or overloaded reinforced concrete (RC) structures (4, 5). The use of fibre reinforced polymer (FRP) sheet is an effective

strengthening method due to its superior properties, such as high strength to weight ratio and excellent corrosion resistance. Glass fibre (GFRP) and carbon fibre (CFRP) are the common FRP composites used in the industry. Compared to GFRP and CFRP, Basalt fibre (BFRP) has been increasingly used owing to its superior characteristics such as high strength to weight ratio and cost-effectiveness (6, 7). Externally bonded (EB) FRP to concrete structures and near-surface mounted (NSM) FRP to concrete elements are two common practices in the FRP applications. The present study focuses on the bond performance of EB FRP sheets to concrete elements.

The strengthening performance of the EB method mainly depends on the interfacial bond behaviour between FRP and concrete (8). The interfacial bond behaviour is primarily determined by the substrate properties, FRP sheet stiffness, adhesive types and thickness, environmental conditions, and loading types, etc. As reported, FRP debonding from the concrete substrates is the primary failure mode at the interface between FRP and concrete due to high-stress concentrations (9-11). Premature debonding failure decreases the utilization rate of FRP (12). To understand the debonding mechanism between FRP and RC structures, numerous investigations have been carried out and the corresponding failure modes have been reported. The behaviour of structures strengthened with FRP under static loads has been intensively investigated and presented in the literature, especially for flexural strengthening of RC beams (1, 13, 14). The strengthening of RC elements by using FRP composites on the tension side has shown notable enhancement of stiffness and load-carrying capacity (15). A total of six typical failure modes have been identified as shown in Figure 2-1: (a) flexural failure by FRP rupture, (b) crushing of compressive concrete, (c) shear failure of concrete, (d) concrete cover separation, (e) interfacial debonding at the plate end, and (f) intermediate crack caused interfacial debonding. In general, these failure modes have been classified into two types: (a) plate end (PE) debonding; and (b)

intermediate crack (IC) debonding, which are identified as the commonly observed failure modes (16-18).

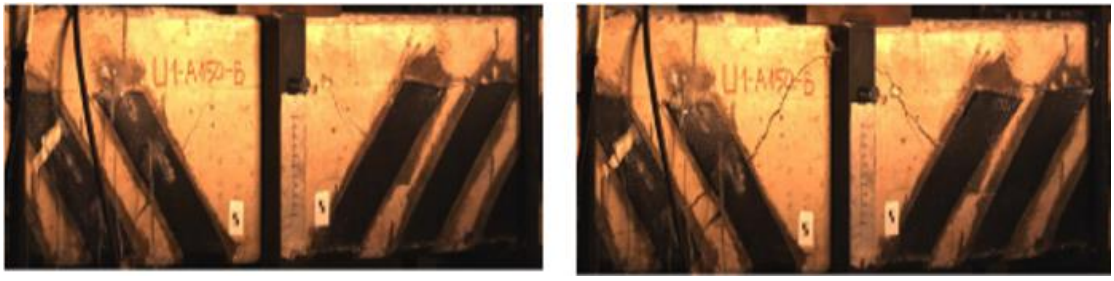

(a) Debonding under impact loads (19)

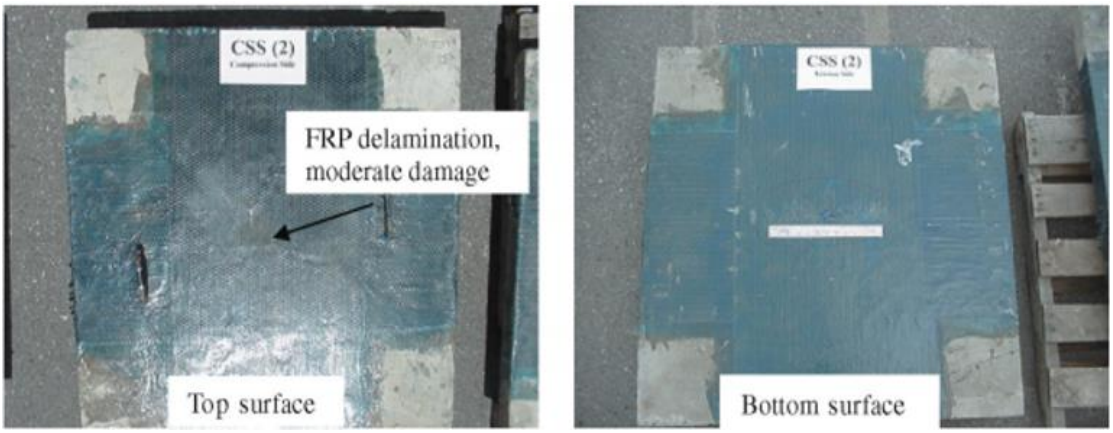

(b) Debonding under blast loads (20)

Figure 2-2. Failure modes under impact and blast loads

During service life, RC structures might be subjected to extreme loads such as impact and blast loads and FRP strengthening is popularly used to enhance the strength, stiffness, and load-carrying capacity of RC structures (21). The impact loads can be generated from vehicle impact, ship impact, rock fall impact, windborne debris or missile impact. Pham and Hao (22) presented a review of concrete structures strengthened with FRP against impact loads. FRP debonding was reported as very common failure mode of FRP strengthened RC beams under impact loads (19, 23-27). As specified in ACI 440.2R-08 (28), cover delamination or FRP debonding occurs when FRP cannot be sustained by the substrate. As reported in (29), the peeling stress developed at the edges of FRP on the FRP strengthened RC beams under impulsive loads, and the bonding between FRP and concrete experienced high shear stress. The debonding of FRP sheets under impact loads is shown in Figure 2-2 (a). Furthermore,

numerous studies have been conducted to investigate the performance of RC structures in resisting blast loads (30, 31). It was reported that FRP strengthening was effective in enhancing blast-resistant capacities of RC elements (32). Buchan and Chen (33) conducted a review on blast resistance of FRP strengthened concrete and masonry structures. The strain rate can reach up to 1000 s^{-1} under blast loads. The debonding or delamination of FRP was observed for the FRP strengthened RC slabs under blast loads (20), as shown in Figure 2-2 (b). It was reported that bonding behaviour between FRP and concrete under dynamic loads was a bit different from that under static loads (32). The interfacial bond behaviour between FRP and concrete under static loads has been intensively investigated. However, very limited studies have been conducted to investigate the effect of strain rate on the interfacial bonding behaviour between FRP and concrete.

2.3 Debonding mechanism under static and dynamic loads

2.3.1 Testing methods of FRP debonding

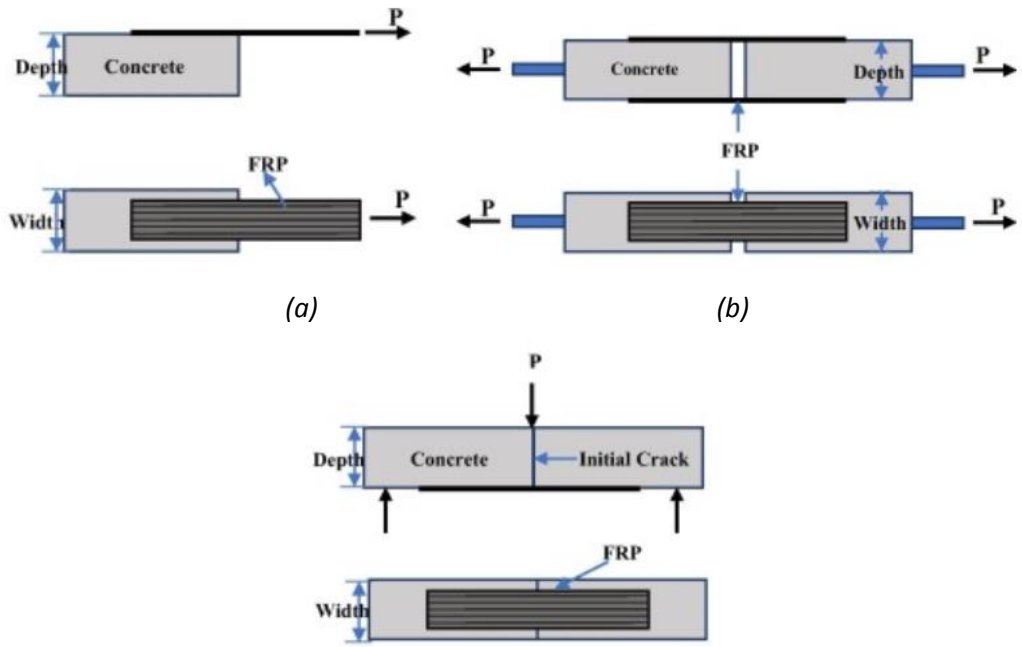

Figure 2-3. Testing methods of debonding: (a) single-lap shear test; (b) double-lap shear test; and (c) beam bending test (34)

To quantify the interfacial bond strength and shear resistance between FRP and concrete substrate, there are three main testing setups to replicate the debonding process: (a) Single-lap shear test (35-39); (b) Double-lap shear test (3, 40-42), and (c) Beam bending type test (43-46), as shown in Figure 2-3. Single/double lap shear test directly applies tensile force on the FRP sheets, which have been popularly used in the literature. For the beam bending test, a concrete prism is strengthened with FRP sheets at its bottom face and applied with an axial load that causes bending, which indirectly reflects the bonding behaviour.

2.3.2 Factors affecting interfacial bond behaviour

Numerous studies have been conducted on the FRP-concrete interfacial bond behaviour through pull-off shear tests to derive the models for debonding predictions. It was found that the interfacial bond performance was mainly determined by several factors including concrete mechanical properties (47), the FRP sheet stiffness, adhesive types and thickness (48), environmental conditions (49), and loading types (50).

Bonding behaviour was found greatly affected by the tensile strength of concrete and the content of coarse aggregate (51). Pan et al. (8, 52) conducted an experimental study on the effect of aggregate content ranging from 0.030 to 0.119 (the ratio of bonding area to area of coarse aggregates) on the FRP/concrete bonding behaviour. The results showed that the ultimate bond strength increased with the aggregate content. The initial debonding strength, the residual shear strength, and the maximum slippage between FRP and concrete were affected by the content of coarse aggregate. In addition, the interfacial fracture energy was affected by the interfacial shear interlocking and softening, which were sensitive to the content of coarse aggregate. It should be noted that no study has been carried out to investigate the effect of aggregate size on the interfacial bond behaviour of FRP-concrete.

In order to improve the utilization and the ductility of FRP composites, hybrid FRPs have been used to strengthen concrete structures. Grace et al. (53) developed a uniaxial ductile hybrid FRP fabric composed of two types of carbon fibres and one type of glass fibre. An experimental study on eight concrete beams strengthened by the hybrid FRPs was carried out. It was found that the beams strengthened with hybrid fabric could obtain higher ultimate strength and ductility as compared to those beams strengthened with sole CFRP systems. Grace et al. (53) also developed a new pseudo-ductile FRP fabric composed of CFRP and GFRP with three different angles (0°, 45°, and -45°). A ductile plateau in load-displacement curves similar to steel reinforcement was observed. Li et al. (54) numerically simulated the debonding process between carbon fibre sheet and glass fibre sheet (CFRP-GFRP) as well as CFRP-CFRP and GFRP-GFRP. The numerical results showed that it was an effective method for CFRP-GFRP hybrid sheets to strengthen concrete substrates due to the fact that hybrid FRPs can effectively reduce interfacial shear stresses of FRP sheets. Choi et al. (55) conducted experimental and analytical studies on the debonding of hybrid FRPs for strengthening reinforced concrete (RC) beams. The experimental results showed that the beams strengthened with stiffer FRP had higher debonding strength than the beams strengthened with less stiff FRP; and the beam strengthened with thinner FRP had higher debonding strength than the beam strengthened with thicker FRP. Hawileh et al. (56) experimentally and analytically studied the flexural performance of RC beams with different combinations of CFRP and GFRP sheets. The hybrid FRPs combining the GFRP sheets of lower stiffness with the CFRP sheets of higher stiffness were used to provide improved strength and ductility in beams. The beams strengthened with GFRP sheets and hybrid FRP sheets were more ductile than that strengthened with sole CFRP sheets. Therefore, hybrid FRPs can effectively improve the utilization of FRP composites on strengthening concrete structures However, no study has been carried out to investigate the effect of hybrid FRPs on the interfacial bond behaviour of FRP-concrete.

Plain concrete (PC) is brittle because of its low tensile strength and strain capacity (57). Adding fibre reinforcement to concrete is one of the effective methods to improve its tensile strength. Steel fibre reinforced concrete (SFRC) has superior resistance to cracking and crack propagation due to the fact that steel fibre composites possess the increased ductility and tensile strength, both at pre-cracking and post-cracking stage (58). Therefore, SFRC material is relatively more ductile as compared with plain concrete, which can also increase energy absorption capacity to withstand seismic, impact and blast loads. In the literature, numerous studies have investigated the flexural and shear behaviours of FRP strengthened RC beams (19, 59, 60). Some studies have been conducted on FRP strengthened fibre reinforced concrete (FRC) beams (61-63). Guo et al. (62) conducted experimental study on hybrid FRP strengthened FRC beams. CFRP and GFRP sheets were used to improve the average rupture strain energy of the FRC beams. Short steel fibres with 0.9% and polymeric fibres with 0.1% volume fraction were used in the concrete mixture. Three types of concrete beams were tested, which included plain concrete beams, polypropylene fibre (PF) concrete beams and PF/SF (steel fibre) hybrid reinforced concrete beams. The hybrid FRC beams strengthened with hybrid FRPs exhibited higher bending stiffness and the crack propagation can be suppressed more effectively. Ibrahim et al. (61) investigated short-steel fibre (1.0% volume fraction) reinforced concrete (SFRC) beams retrofitted with GFRP laminates. The GFRP laminates retrofitted SFRC beams exhibited smaller crack spacing and the maximum increase of the ultimate load was found to be 130% as compared to GFRP laminates retrofitted RC beam. They also found that GFRP strengthened SFRC beams only exhibited FRP debonding induced by flexural cracks and none of the beams experienced delamination. In addition, the retrofitted SFRC beams exhibited higher ductility as compared to the retrofitted RC beams. Yin and Wu (63) conducted experimental and numerical studies on the structural performances of short SFRC beams with externally bonded FRP sheets. Four cases with different volume fractions of short steel fibres (0, 0.25%, 0.5%, and 1.0%) were mixed in the

concrete beams. The concrete toughness was greatly improved by mixing short steel fibres. The failure mode of FRP-strengthened SFRC beams changed from the interfacial debonding to FRP rupture with a significant increase of load-bearing capacity. It should be noted that the study on the interfacial bond behaviour of FRP-SFRC concrete is deemed necessary since FRP strengthened SFRC structures have been increasingly used.

Besides the concrete properties and FRP types, the interfacial bond is also affected by adhesive properties. To properly bond the FRP laminates to substrates, many types of adhesives with high tensile strength and ductility have been used. In general, two typical types of adhesive can be found in the literature, i.e. stiff adhesives with elastic modulus larger than 4.0 GPa and soft adhesives with elastic modulus less than 2.0 GPa (64). Stiff adhesives are superior to soft adhesives in terms of the efficiency of shear stress transmission through the FRP-to-concrete interface. In contrast, soft adhesives have better advantages in delaying debonding and enhancing the debonding resistance. Harries et al. (65) studied the load-carrying capacity of FRP-strengthened RC beams with two types of adhesives and found that the adhesive with lower elastic modulus but higher rupture strain extended the debonding process. The disadvantage of applying soft adhesive is the lower glass transition temperature (64). To balance the enhancement of bond capacity and the reduction of the glass transition temperature, numerous methods have been proposed to modify the soft adhesive by using liquid rubber or other solutions (66). Some studies have demonstrated that the structural performance of FRP-strengthened RC beams with liquid rubber-modified adhesive was remarkably improved (67). Shi et al. (64) conducted numerical studies on the effect of adhesive properties on the interfacial bond behaviour by considering different thickness and elastic modulus of adhesive. Based on the results of 128 bonded joints, a bond-slip model was proposed and the prediction showed high accuracy for the FRP-to-concrete joints with different adhesives.

The design guides, such as ACI 440.2R (21), HB 305 (68), fib Bulletin 14 (69), and CNR-DT200 (70), provide design procedures for engineering practice. However, most of the available models are proposed based on the quasi-static loading condition. Since the interfacial bond characteristics between FRP and concrete under dynamic loads are different from those under quasi-static loads (71), understanding the bond performance under dynamic loading conditions is important. Some experimental investigations have been carried out to unveil the interfacial bond behaviour between FRP and concrete subjected to dynamic loads. The experimental study by Shi et al. (72) reported that the interfacial bond was strain rate dependent and the interfacial fracture energy and peak shear stress increased with strain rate. The peak strain rate in the tests by Shi et al. (72), however, was only around $0.1s^{-1}$. To evaluate the dynamic bonding behaviour, a finite-element model based on high-order theory method with the consideration of nonlinearity of bonding, the presence of irregular point and cracking of mortar joints was proposed for an FRP-strengthened RC wall. Shen et al. (41) carried out experimental studies on the strain rate effect on the bond performance with the strain rate up to 0.63 s^{-1} and reported that the effective bond length decreased with the increase of strain rate and the corresponding model for predicting the effective bond length was established. Based on Shen et al.'s testing results (41), Antonio et al. (73) proposed a modified Duvant-Lions zero-thickness interface model to simulate the strain rate effect on the interfacial bond. Huo et al. (74) found that the interface was sensitive to strain rate through impact tests on CFRP-strengthened RC beams and the corresponding strain rate was up to 4.90 s^{-1}. Salimian et al. (75) conducted debonding tests to exam the loading rate effect on the interfacial bond capacities between CFRP and concrete and reported that the specimens with lower concrete strength showed more sensitivity to loading rate. To sum up, the strain rate in the literature regarding bonding behaviour study is up to 4.90 s^{-1} and the testing results are insufficient to reflect the strain rate effect for the blast and impact scenarios, which have the corresponding strain rate up to hundreds per second.

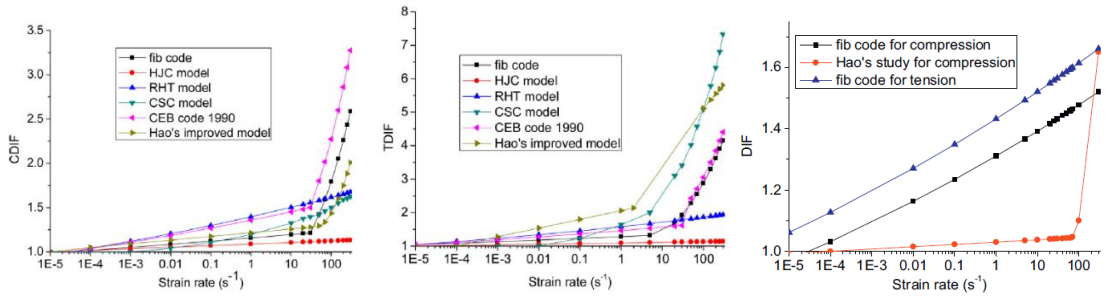

(a) *(b)* *(c)*

Figure 2-4. DIF for (a) compressive strength, (b)tensile strength, and (c) Young' modulus(76)

The interfacial bond behaviour is affected by strain rate. The interfacial shear stress distributes at the interface between the concrete substrate and epoxy resin, where the shear stress penetrates into the concrete layer (75, 77). As shear stress is transformed into tensile and compressive stress at the angles of 45^{o}, consequently the tensile strength of concrete is the main factor to determine the interfacial bond performance (75, 78). It is well-known that concrete exhibits sensitivity to high loading rates since it is a strain rate dependent material with respect to the compressive strength, tensile strength, and Young's modulus. The corresponding dynamic increase factor (DIF) has been quantified for concrete material when subjected to dynamic loadings, as shown in Figure 2-4. The strain rate effect of concrete is induced by the viscoelastic behaviour and time-dependent microcrack growth of the cement paste (76). Furthermore, the interfacial fracture path of the FRP-to-concrete interface under high loading rates differs from that under static loads (74, 75). This is because the propagation of microcracking in the concrete layer under relatively low loading rates has enough time to penetrate along the weak interface between the mortar and the aggregate. However, under high loading rates there is not enough time for cracks to propagate along the weak path and the fracture path may shift to the coarse aggregates, which is of higher strength than the interface between mortar and aggregates. Consequently, the surface tensile strength of concrete substrates could be enhanced under high loading rates (79). Salimian and Mostofinejad (75) reported that the aggregate to mortar ratio of the

concrete mixture might affect the fracture path as well. With higher aggregate contents, the fracture path is more likely to propagate through the aggregate instead of the interface between mortar and aggregate.

To study the deteriorated behaviour of adhesively bonded joint, numerous investigations have been conducted to determine the interfacial bond performance under different environmental conditions, e.g. water immersion, humidity, and temperature (80-82). Yun and Wu (83) experimentally investigated the effects of water immersion and temperature on the interfacial bond and found that the presence of water molecules enhanced the deleterious effects of the freeze-thaw cycles. An 82% reduction in the interfacial fracture energy was reached after 50 freeze-thaw cycles in water. It is demonstrated that the deterioration of the interface between FRP and concrete is more severe when subjected to freeze-thaw cycles in water. This is because the tensile strength or surface tensile strength of concrete is sensitive to water immersion and temperature.

2.3.3 Analytical study of FRP debonding

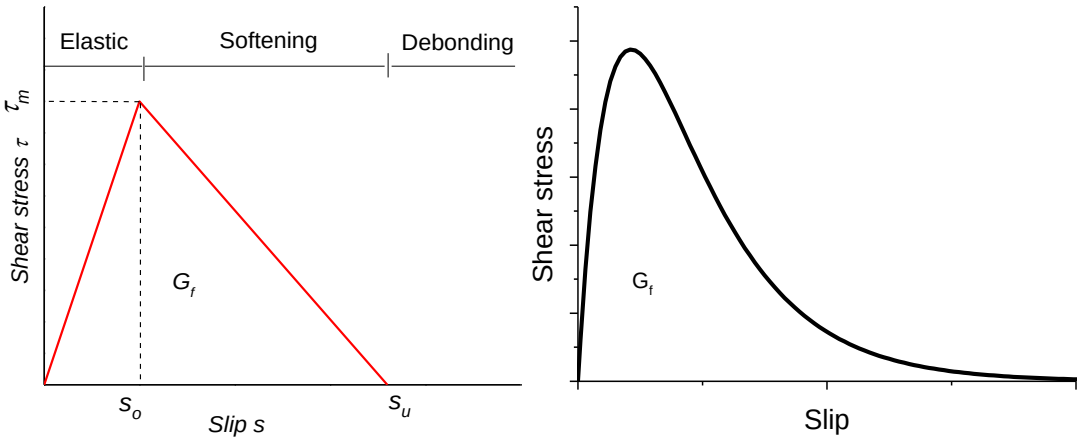

Figure 2-5. Bond-slip curve: (a) bilinear; (b) nonlinear

In addition to experimental studies, the bond characteristics of the FRP-to-concrete interface have been investigated analytically (37, 84-91). The interface model called

Linear Elastic Brittle Interface Model (LEBIM) is an efficient modelling tool to simulate the interfacial fracture when the overall stiffness of the system (adherents and adhesives) is essentially ruled by the adherent stiffness (92). Furthermore, the Cohesive Zone Model (CZM) proposed by Hillerborg et al. (93) is used to simulate fracture in concrete structures. The CZM model has been widely used to predict the damage propagation in concrete, especially for modelling of FRP-to-concrete interface, which provides accurate predictions of debonding propagation due to the cohesive softening functions (94). Single-curve models with an ascending branch have been proposed for simplicity of predictions but the descending branch has been unrealistically neglected, which is not consistent with the experimental results (91). To improve the accuracy of prediction, exponential-curve models have been proposed (35, 95, 96). With the consideration of the proposed exponential-curve, models may compromise the estimation, consequently, bilinear models consisting of an ascending branch and a descending branch have been proposed and they are easier to be used in analytical predictions (88, 89). In general, the common way to present the FRP-to-concrete bonding behaviour is to construct a bond-slip curve, as shown in Figure 2-5. The enclosed area of the bond-slip curve is defined as the interfacial fracture energy (G_f), which is also used to quantify the released energy of the interface between FRP and concrete during the debonding process. The peak value refers to the maximum shear stress with the corresponding shear slip. At the final debonding stage, the shear stress is zero and the corresponding slip refers to the ultimate slip.

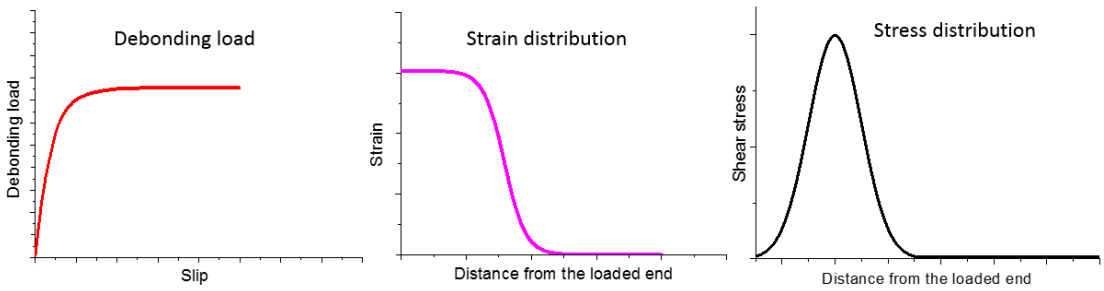

Figure 2-6. The curves of debonding load, strain distribution and stress distribution

Table 2-1. Existing bond-slip models (96)

References	Bond-slip models
Neubauer and Rostasy (1997)	$\tau = \begin{cases} \tau_{max} s/s_0 \text{ if } s \leqslant s_0 \\ 0 \text{ if } s > s_0 \end{cases}$, $\tau_{max} = 1.8\kappa_w f_t, s_0 = 0.202\kappa_w$, $\kappa_w = \sqrt{1.125\frac{2-b_f/b_c}{1+b_f/400}}$
Monti et al. (2003)	$\tau = \begin{cases} \frac{s}{s_0}\tau_{max} \text{ if } s \leqslant s_0 \\ \frac{s_f - s}{s_f - s_0}\tau_{max} \text{ if } s > s_0 \end{cases}$, $\tau_{max} = 1.8\kappa_w f_t$, $s_0 = 2.5\tau_{max}\left(\frac{t_a}{E_a} + \frac{50}{E_c}\right)$, $s_f = 0.33\kappa_w$, $\kappa_w = \sqrt{1.125\frac{2-b_f/b_c}{1+b_f/400}}$
Nakaba et al. (2001)	$\tau = \tau_{max}\frac{s}{s_0}\frac{3}{2+(s/s_0)^3}$, $\tau_{max} = 3.5f_c^{0.19}$, $s_0 = 0.051$
Savoia et al. (2003)	$\tau = \tau_{max}\frac{s}{s_0}\frac{2.86}{2.86+(s/s_0)^{2.86}}$, $\tau_{max} = 3.5f_c^{0.19}$, $s_0 = 0.051$
Dai and Ueda (2003)	$\tau = \begin{cases} \tau_{max} \times \left(\frac{s}{s_0}\right)^{0.575} \text{ if } s \leqslant s_0 \\ \tau_{max} e^{-\beta(s-s_0)} \text{ if } s > s_0 \end{cases}$, $\tau_{max} = \frac{-1.575\alpha K_\alpha + \sqrt{2.481\alpha^2 K_\alpha^2 + 6.3\alpha\beta^2 K_\alpha G_f}}{2\beta} s_0 = \frac{\tau_{max}}{\alpha K_\alpha}$, $\alpha = 0.028(E_f t_f)^{0.254}$, $\beta = 0.0035K_\alpha(E_f t_f)^{0.34}$, $K_\alpha = \frac{G_a}{t_a}G_f = 7.554K_\alpha^{-0.449}f_c^{0.343}$
Ueda et al. (2003)	$\tau = 2BG_f(e^{-Bs} - e^{-2Bs})$, $B = 6.846(E_f t_f)^{0.108}(G_a/t_a)^{0.833}$, $G_f = 0.446(E_f t_f)^{0.023}(G_a/t_a)^{-0.352}f_{co}^{0.236}$
Lu et al. (2005)	$\tau = \begin{cases} \tau_{max} \times \left(\frac{s}{s_0}\right)^{0.5} \text{ if } s \leqslant s_0 \\ \tau_{max} e^{-\alpha(s/s_0 - 1)} \text{ if } s > s_0 \end{cases}$, $\alpha = \left(\frac{G_f}{\tau_{max}s_0} - \frac{2}{3}\right)^{-1}$, $G_f = 0.308\kappa_w^2\sqrt{f_t}$, $\kappa_w = \sqrt{\frac{2.25-b_f/b_c}{1.25+b_f/b_c}}$
Wu and Jiang (2013)	$\tau = \frac{E_f t_f \alpha}{\beta^2}e^{-s/\alpha}(1 - e^{-s/\alpha})$, $\alpha = 0.094f_{co}^{0.026}$, $\beta = \frac{0.134\sqrt{E_f t_f}}{\kappa_w f_{co}^{0.082}}$, $\kappa_w = 1 + 0.222f_{co}^{0.304}(1 - b_f/b_c)$
Pan and Wu (2014)	$\tau = \begin{cases} ks \text{ if } s \leqslant s_0 \\ \tau_{max} e^{-\beta(s-s_0)} \text{ if } s > s_0 \end{cases}$, $\tau_{max} = 0.131\kappa_w^2 f_{co}^{0.19}$, $\kappa_w = 1 + 0.222f_{co}^{0.304}(1 - b_f/b_c)$ $\beta = 5.304f_{co}^{-0.026}$, $\rho = \frac{A_f}{A_c}$, $k = \frac{G(1+\rho')A_f \tanh(\alpha L)}{\alpha t_f h}$, $\alpha = \sqrt{\frac{G}{ht_p}\frac{E_c - \rho E_f}{E_f E_c}}$
Wu and He (2019)	$\tau = \frac{E_f t_f \alpha}{\beta^2}e^{-s/\alpha}(1 - e^{-s/\alpha})$, $\alpha = 0.124f_{co}^{-0.103}$, $\beta = 0.174f_{co}^{-0.205}(E_f t_f)^{0.5}$

Analytical bond-slip models have been widely used to describe and predict the full-range debonding process. Yuan et al. (86) proposed an analytical solution to provide a theoretical basis for understanding the full-range debonding process by using a realistic bi-linear local bond-slip model. Wu and Jiang (35) proposed an analytical bond-slip model with two parameters, i.e. α and β. By extracting these two parameters from experimental data, the width factor and the corresponding bond-slip response could be quantified accordingly. In general, based on the quantified bond-slip relationship, the debonding load, the interfacial fracture energy, the ultimate debonding strain, the strain distributions and the peak shear stress can be obtained accordingly, as shown in Figure 2-6. The peak shear stress and the corresponding slip could be obtained by the function of the width ratio factor and the concrete tensile strength. The existing models simply assume that the width factor is a function of concrete width and FRP width, which cannot yield accurate predication on debonding. Therefore, Wu and He (96) proposed a comprehensive width factor model by incorporating the effect of concrete strength and FRP stiffness and the predictions showed very accurate results. To obtain the shear slip, the interfacial fracture energy is also an important factor, while it is widely

accepted that the interfacial fracture energy and the peak shear stress are not related to FRP stiffness (90, 97). Wu and He (96) stated that the effect of width effect should be considered in modelling the fracture energy of the debonding because the interfacial fracture is similar to the size effect in fracture mechanics. With the consideration of these critical parameters, numerous bond-slip models have been proposed for accurate predictions of FRP-strengthened RC elements. The existing bond-slip models are presented in Table 2-1, which are based on static loads without considering strain rate effect.

2.3.4 Numerical modelling of FRP debonding

Beside experimental and analytical studies, the interfacial bond of FRP-to-concrete interface has been investigated numerically (98-104). There are two approaches to simulate the bonding behaviours of FRP-to-concrete interface (100, 102, 105, 106): (a) indirect approach to simulate debonding by introducing a layer of cohesive element zone, in which an appropriate bond-slip model for the interface elements is required for accurate modelling (107); and (b) direct approach to simulate debonding by tying FRP to concrete, in which the debonding is assumed to occur inside the concrete substrate adjacent to FRP sheets (108). To simulate concrete cracking, two approaches including smeared crack models and discrete crack models are adopted in FE analysis, as shown in Figure 2-7. The interface with an appropriate bond-slip model is commonly adopted for simulating the interface between FRP and concrete in the indirect modelling approach. The FRP-to-concrete interface is usually modelled by zero thickness interface elements and a constitutive law for the zero thickness elements should be appropriately selected (100, 101). In the direct modelling approach, concrete element size varying from 0.5 mm to 2 mm is commonly adopted to model the concrete substrate underneath the FRP so that the bond-slip response can be obtained. Pham and Al-Mahaidi (99) adopted smeared concrete cracking model with rotating angle to simulate the debonding and found that the effect of thickness of the fine layer with element size

varying from 2 mm to 10 mm was marginal but it could be remarkable when the simulated concrete cracks propagated into both fine layer and coarse layer. A rotation angle crack model with the consideration of a user-defined constitutive model for concrete was adopted in the study by Lu et al. (102) and found that the predictions were sensitive to the shear retention model. To model accurate concrete cracking in the direct modelling approach, an appropriate concrete constitutive law should be prepared and the mechanical properties of concrete including tensile strength and size effect fracture energy need to be determined experimentally (103, 104, 109). However, the numerical studies on the dynamic interfacial bond behaviour are very limited in the literature. A two-dimensional (2D) FE model was built by Li et al (108), in which a direct modelling approach was adopted to predict the static and dynamic bonding performance and the maximum loading rate considered in the study was 100 mm/s. In the study by Caggiano et al. (73), the loading rate-dependent bonding mechanisms were simulated by incorporating an overstress viscoplastic approach. The numerical predictions were validated by the experimental results from Shen et al. (41) and the loading rate ranged from 0.007 mm/s to 70 mm/s.

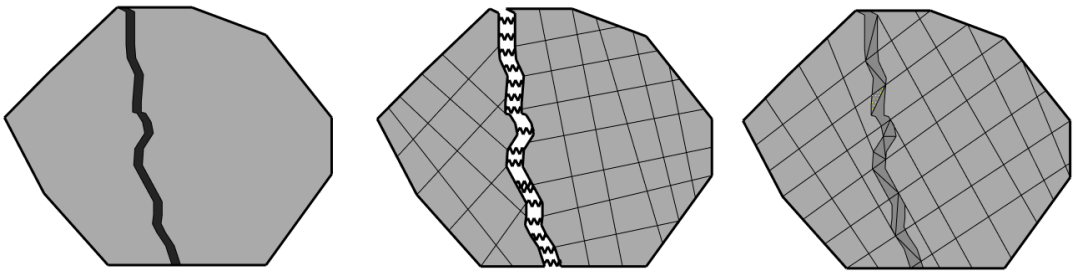

Figure 2-7. Concrete cracking models: (a) real crack body; (b) discrete crack model; and (c) smeared crack model

2.4 Anchorage systems to improve bond performance

To maximize the utilization of FRP sheets and postpone the debonding process, different anchorage systems have been developed, such as FRP anchors (11, 110-112), FRP U-jacket anchors (14, 60), and mechanical anchors (i.e., anchor bolts) (36, 113,

114), as shown in Figure 2-8. Smith et al. (1) experimentally tested the FRP-strengthened RC slabs with FRP spike anchors and found that the increments of 30% in the load-carrying capacity and 110% in the flexural capacity were achieved by using FRP spike anchors as compared to the control slab. Zhang et al. (11, 110) experimentally investigated the effect of FRP anchor position and number of anchors on the interfacial bond performance and found that the bond performance was significantly affected by anchor position and anchor numbers. Wu and Huang (113) experimentally investigated the effect of steel bolts anchorage system on the interfacial bond capacities. The testing results showed the bond strength of the strengthened concrete beam with anchorage was approximately eight times the bond strength of the specimen without anchorage. Chen et al. (14) experimentally tested the FRP-strengthened RC beams with U-anchors and found that the flexural capacity was significantly enhanced, as shown in Figure 2-8. Generally, the anchorage system was designed to (a) enhance the cracking-resistance of the concrete substrate; (b) eliminate or delay the interfacial cracking; and (c) increase the effective interfacial shear stress transfer length.

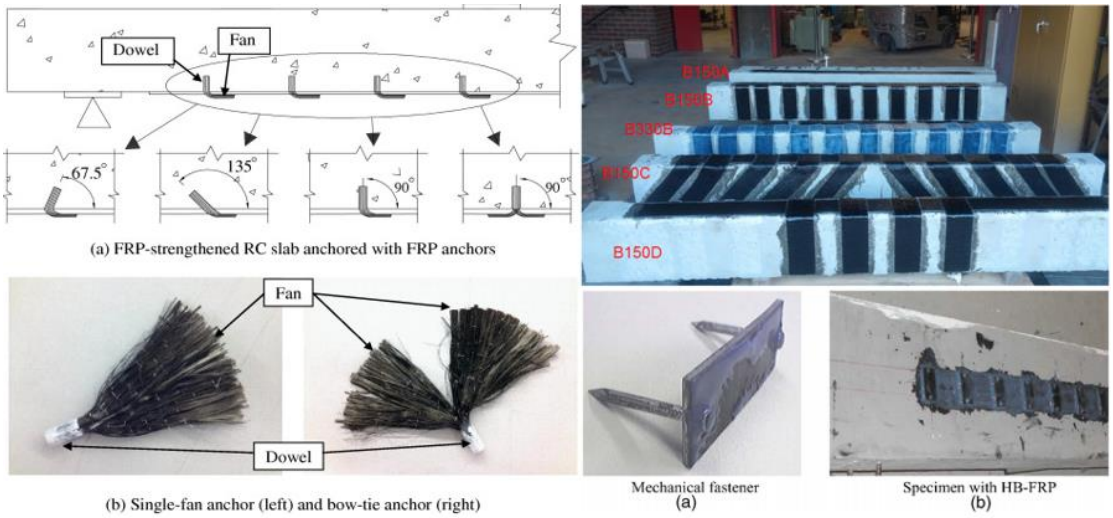

Figure 2-8. Anchorage systems (14) and (113)

Various indirect anchorage methods have been also developed to enhance the interfacial shear resistance (47, 115-118). Near-surface mounted (NSM) method was an indirect way to anchor the FRP composites by increasing the adhesive area between FRP and concrete (119-121), as shown in Figure 2-9. The concrete grooving method (GM), as a simplified version of NSM, has been recommended by ACI (122) due to its significant enhancement on concrete surface roughness. By grooving the concrete substrates before applying the epoxy resin, the interfacial bond strength can be remarkably enhanced with the adhesive area between FRP and concrete (12, 123). Numerous studies investigated the effect of transverse, diagonal, and longitudinal grooves on EB FRP-strengthened RC beams and found that the bond stiffness was remarkably enhanced and the shear slip was significantly reduced with the increasing width of the longitudinal grooves. However, there was slight difference with the increase of groove depth. Deeper grooves were found to work more effectively than wider ones for transverse grooves and the recommended depth was 10 mm (124). It was also found that the application of grooves to enhance the shear strength of RC beams showed an enhancement of 10-15% on bond strength and delayed FRP debonding (125). In general, the grooving method (GM) was determined by two factors, i.e. groove width and groove depth. However, the preparation of concrete surface grooves greatly increased construction works and it was also difficult to control the quality of grooving (126).

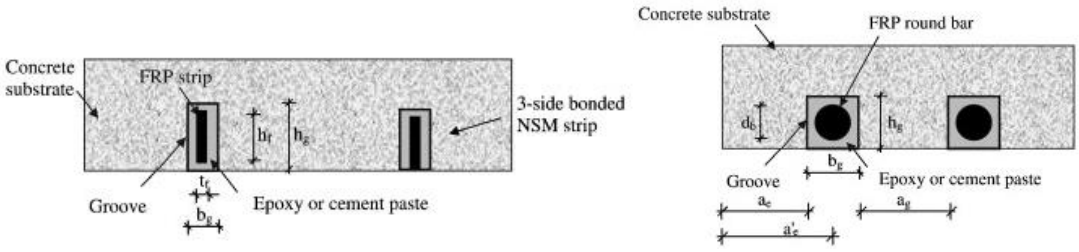

Figure 2-9. Near-surface mounted FRP anchorage (119)

2.5 Debonding damage detection for FRP-strengthened RC structures

The methods of debonding detection are available to quantify the interfacial damage caused by the local cracks in concrete and local bond-slip between FRP and concrete. For the interfacial debonding detection, the existing techniques mainly include strain gauge measurement and imaging technology (126, 127). Externally mounted strain gauge measurement is a conventional way to obtain the strain development on FRP surface. However, strain gauges might be easily damaged during operating, and the measured results could be affected by the workmanship. Furthermore, mounted strain gauges cannot be removed or reused, which results in the increased cost for laboratory research and field applications. Alternatively, the digital image correlation (DIC) technique, as a contactless measurement method, has shown potentials to replace the conventional contact-measuring method. Successive digital images can be recorded, and the full-field displacement and strain can be analysed from surface speckles tracked by the DIC system (71). It has been demonstrated that the DIC technique exhibits great accuracy with an acceptable cost (128, 129). However, the DIC technique is not suitable for long-term measurement due to large amounts of data to be stored.

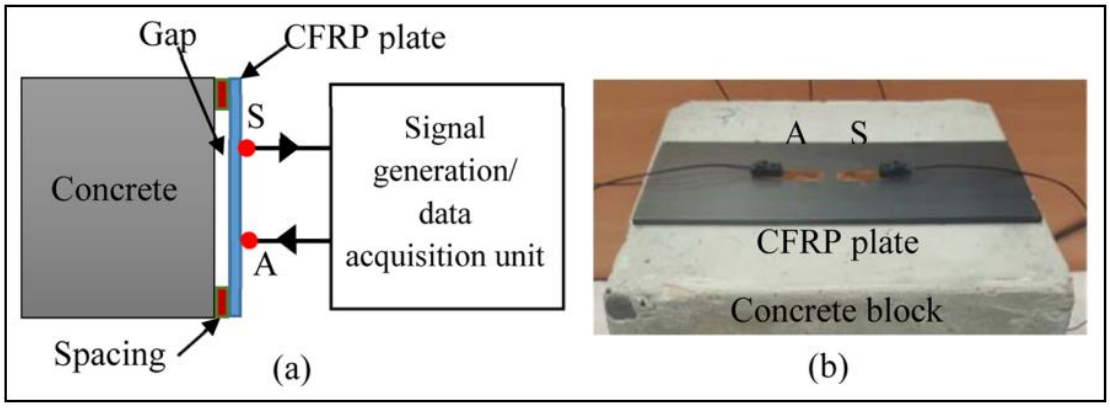

Figure 2-10. Detection and monitoring of the gap between FRP plate and concrete (130)

On the other hand, wave-based methods have been widely used for target detection, classification, localization, and prediction in engineering practice (131), as shown in Figure 2-10. Ong et al. (132) proposed a technique for detecting lap joints based on lamb wave technology and found that the proposed method had the potential to identify the presence of debonding in an adhesive-bonded joint. In recent years, there is an increasing use of acoustic wave as a non-invasive tool for health monitoring and condition assessment of engineering structures (133). It has been demonstrated that the acoustic-based (active or passive) damage detection technique is an effective way to detect cracks and holes of composite enclosures, and measure the vibroacoustic flexibility matrix of damaged surface of aluminium enclosures (134, 135).

2.6 Summary

This chapter presents a literature review on debonding of FRP-strengthened RC structures under static and dynamic loads, existing anchorage systems of FRP-strengthened RC structures and debonding damage detection techniques. The research gaps are identified as follows.

1. The interfacial bond behaviour is primarily determined by the concrete properties, FRP sheet stiffness, adhesive types and thickness, and loading types. Intensive studies have been carried out to investigate the effect of FRP types (i.e. AFRP, CFRP, and BFRP), adhesive types, and concrete strength on the interfacial bond between FRP and concrete under static loads. However, the effects of some important factors such as hybrid FRPs (carbon and basalt fibre composite), coarse aggregate sizes, steel fibre characteristic in SFRC on the interfacial bonding behaviour between FRP and concrete have not been investigated under static and dynamic loads, which are deemed necessary to be investigated in this study.

2. Various anchorage systems have been proposed to enhance the interfacial bonding. The preparation and installation of these anchors significantly increase the complication

of implementation and the requirement of workmanship. To simplify the construction process and reduce the cost, an epoxy anchor is proposed in this study to enhance the interfacial bond between BFRP and concrete that can be easily applied in engineering practice.

3. A few methods of debonding detection have been proposed to quantify the interfacial damage caused by the local cracks in concrete and local bond-slip between FRP and concrete. For the interfacial debonding detection, the existing techniques mainly include strain gauge measurement and imaging technology. However, strain gauges might be easily damaged during operating, and the measured results could be affected by the workmanship. Furthermore, the DIC technique is not suitable for long-term measurement due to large amounts of data to be stored. Therefore, a stress wave-based sensing approach is developed in this study to detect the interfacial debonding of the BFRP-concrete interface in real-time.

Chapter 3. Effect of FRP configurations on static bond behaviour

3.1 Introduction

In this chapter, an experimental investigation is conducted to investigate the bonding behaviour between hybrid FRPs and concrete blocks by using the method of single-lap shear tests. The effects of FRP stacking order and the mechanical properties of FRP on the bond behaviour are evaluated. The experimental results show that the FRP stacking order has obvious influences on the debonding load and the bond-slip relationship. The effect of FRP stacking order on the fracture energy is also examined. The bond-slip relationships of hybrid FRPs are obtained from strain distributions during loading processes. Meanwhile, a fitting procedure is proposed and verified to obtain the bond-slip curves. Simplified bond-slip curves for hybrid FRP-to-concrete are proposed in this chapter and compared with the bond-slip curves predicted by two existing bond-slip models.

The related work in this chapter has been published in Construction and Building Materials.

Yuan C, Chen W, Pham TM, Hao H. Bond Behaviour between Hybrid Fibre Reinforced Polymer Sheets and Concrete. Construction and Building Materials. 2019; 210:93-110. DOI: doi.org/10.1016/j.conbuildmat.2019.03.082

3.2. Experimental program

3.2.1 Material properties

Concrete blocks with a length of 350 mm, the width of 150 mm and the height of 150 mm were prepared as substrates. Coarse aggregates with the size of 5~20 mm and fine aggregates of silica-based river sand were used in preparing the concrete blocks. The concrete blocks were demolded 24 hours after casting and then cured in water tank for

28 days. The average compressive strength of three concrete cylinders was f_c = 39.68 MPa.

The polymer matrix used to saturate the fibre was a mixture of epoxy resin (West System 105) and hardener at a ratio of 5:1. The epoxy resin had a tensile strength of 50.5 MPa, the tensile modulus of 2.8 GPa and rupture tensile strain of 4.5% (6, 136). Unidirectional basalt fibre and carbon fiber had the same unit weight of 300 g/m^2. The material tests of CFRP and BFRP were conducted according to ASTM D3039 (137) and the material properties are listed in Table 3-1.

Table 3-1. *Mechanical properties of FRP materials*

Material	Tensile strength (MPa)	Young's modulus (GPa)	Rupture strain (%)	Nominal thickness (mm)
CFRP	1990	191	1.04	0.167
BFRP	1333	71	1.70	0.120

3.2.2 Specimens preparation

A total of 24 specimens were prepared for this experiment. Figure 3-1 shows the details of the specimens. To investigate the effect of the FRP type, FRP stacking order and FRP stiffness on the bonding behaviour, different layers of FRP (CFRP and BFRP) with the bonded width of 40 mm and the bonded length of 200 mm were prepared with epoxy resin on one side of the concrete blocks along the axial direction. The concrete surface was prepared with a needle scaler to remove the vulnerable mortar and expose the aggregates. After removing dust, FRP sheets of different layers were bonded onto the concrete blocks. The specimens are divided into three groups as defined in Table 3-2. The first group was designed to study the effect of FRP types on bonding behaviour. The second and third groups were designed to examine the effects of stacking order and FRP stiffness on the bonding behaviour, respectively. The name of the specimens includes three parts, the first part is the order of the group, and the second and third parts indicate the number of CFRP and/or BFRP layers, respectively. For example,

G3_1C4B represents that the specimen belongs to group 3, and has one layer of CFRP (named 1C) attached to the concrete block and four layers of BFRP (named 4B). To reduce the uncertainties, at least three specimens (i.e. 1, 2, 3) were prepared for each configuration.

3.2.3 Prediction of elastic modulus of hybrid FRPs

The modulus of elasticity of the hybrid FRP sheets (i.e. 1C1B, 1B1C, 1C4B and 4B1C) can be measured in the testing using Equation (3-1) and also predicted from the rule of mixtures using Equation (3-2) (138, 139):

$$E_H = \frac{f_{HF}}{\varepsilon_{HF}} \tag{3-1}$$

$$E_H = \frac{E_B t_B + E_C t_C}{t_B + t_C} \tag{3-2}$$

where E_H = elastic modulus of hybrid FRPs, f_{HF} is the experimental tensile stress of hybrid FRPs, ε_{HF} is the experimental rupture strain of hybrid FRPs, E_B = elastic modulus of BFRP sheet, E_C = elastic modulus of CFRP sheet, t_B = thickness of BFRP sheet, and t_C = thickness of CFRP sheet. These two equations, however, do not necessarily give the same estimations of the hybrid FRP sheet. For example, the elastic modulus of G2_1B1C is predicted by Equation (3-2) as 141 MPa, which is however different from the results of the coupon tests (121 MPa). The cause of this discrepancy is explained below. When the hybrid carbon-basalt FRP sheet was subjected to loads, the CFRP layer of relatively higher elastic modulus and lower ultimate strain ruptured first followed by the rupture of BFRP layer, as shown in Figure 3-2. It is found that the rupture strain of hybrid specimen is enhanced due to the hybrid effect, which is consistent with the findings in the literature (139, 140). Manders and Bader (139) reported that the rupture strain of laminated hybrid carbon-glass FRPs was about 50% higher than that of single CFRP. Aveston and Sillwood (140) found that the strain of

hybrid carbon-glass composites at CFRP rupture increased by 30%. In this chapter, the rupture of hybrid sheet 1C1B and 1C4B both initiated at CFRP layer and the rupture strain of CFRP layer is 1.36% and 1.50%, respectively, which is higher than the rupture strain of 1.04% for single sheet 1C, as shown in Figure 3-2. If Equation (3-2) is used to calculate the elastic modulus, it leads to over prediction because the actual rupture strain for hybrid sheet ε_{HF} is higher than that of the single sheet ε_C.

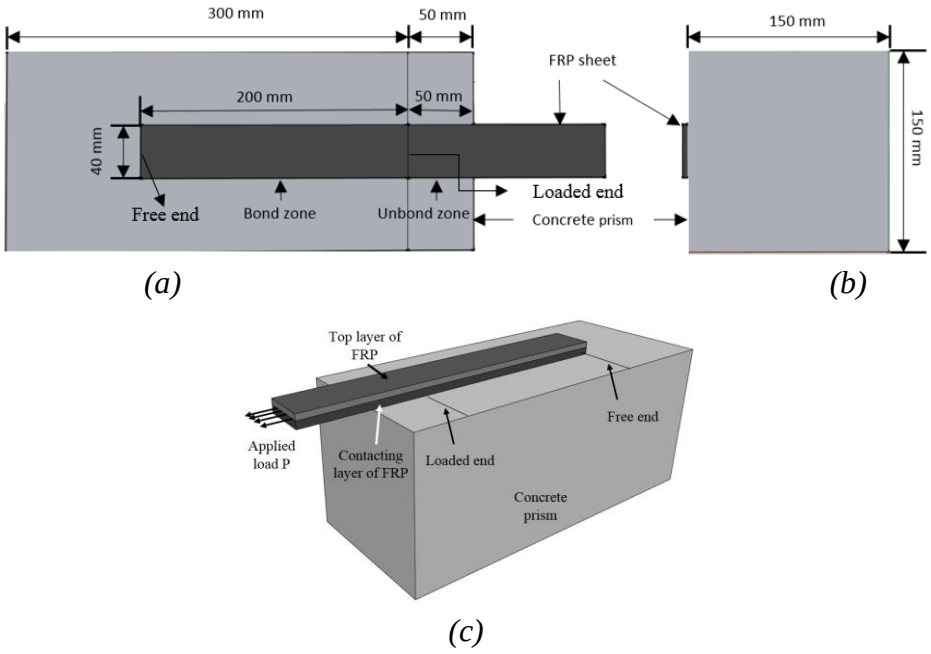

Figure 3-1. Scheme of single-lap shear specimen (a) front view; (b) side view; (c) 3D view

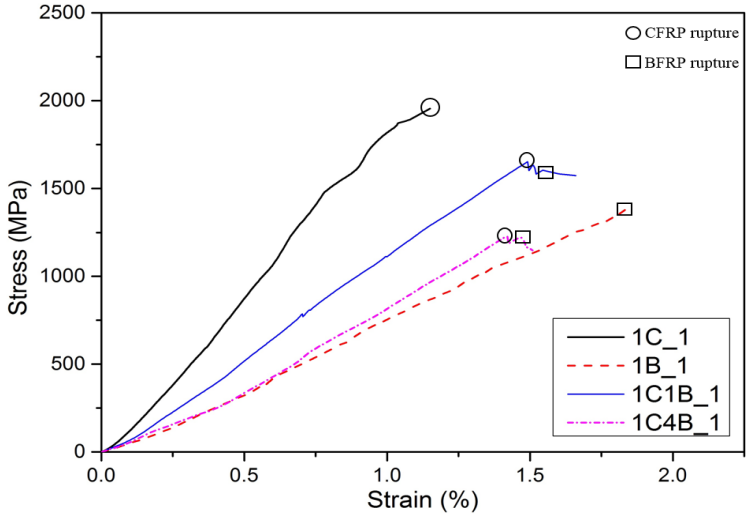

Figure 3-2. Experimental stress and strain of FRP sheet

Table 3-2. Testing scheme and specimen parameters

Specimen	Nominal thickness (mm)	Tensile strength (MPa)	Rupture strain (%)	Elastic modulus (GPa)	FRP stiffness (N/mm)	Predicted elastic modulus (MPa)
			Group one			
G1_1B_1, 2, 3	0.120	1333	1.71	71	8.52	N/A
G1_1C_1, 2, 3	0.167	1990	1.04	191	31.90	N/A
			Group two			
G2_1B1C_1, 2, 3	0.287	1644	1.36	121	34.73	141
G2_1C1B_1, 2, 3	0.287	1644	1.36	121	34.73	141
G2_1B1B_1, 2, 3	0.240	1459	1.81	80	19.20	71
G2_1C1C_1, 2, 3	0.334	1908	1.19	160	49.43	179
			Group three			
G3_1C4B_1, 2, 3	0.647	1277	1.50	85	54.99	102
G3_4B1C_1, 2, 3	0.647	1277	1.50	85	54.99	102

Note: The data are averaged from three specimens.

3.2.4 Testing setup

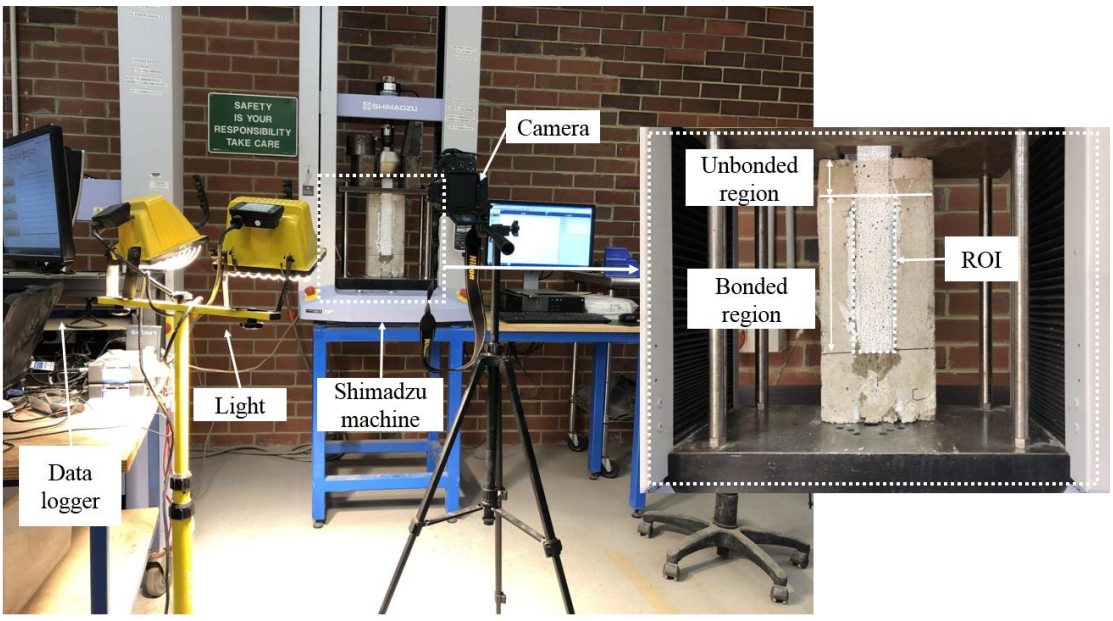

Figure 3-3. Shimadzu AGS-X 50KN testing machine (L) Setup; (R) Schematic diagram

The single-lap shear tests were carried out using the Shimadzu AGS-X 50KN Series universal testing machine as shown in Figure 3-3. All the specimens were tested in displacement control at a loading rate of 0.3 mm/min (110). The machine was equipped with an inbuilt load cell to measure the load during the tests. Two strain gauges with 5 mm gauge length were mounted onto the surface of FRP sheets to measure the strain.

3.3 Experimental results and discussion

3.3.1 Failure mode

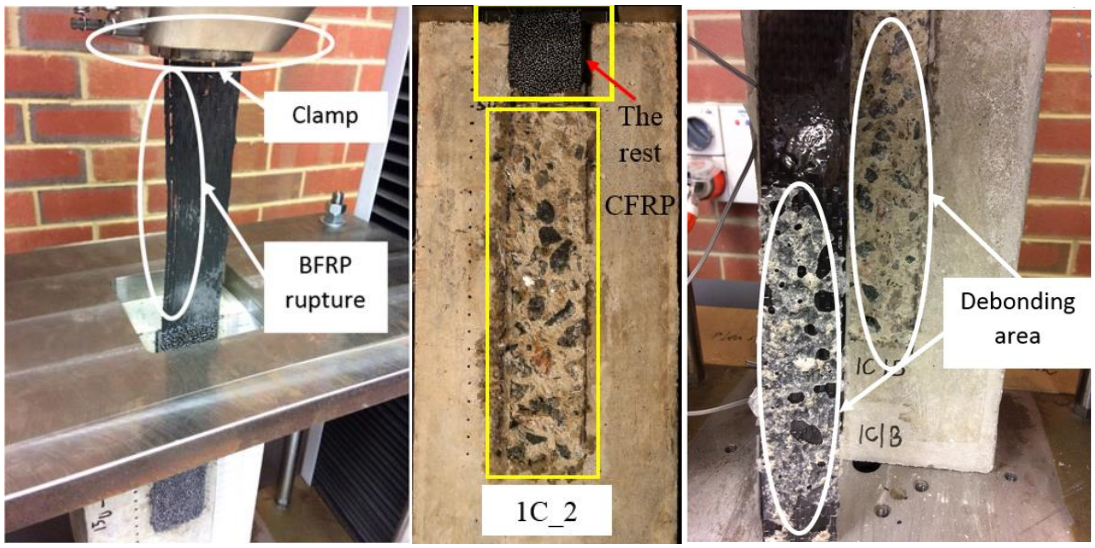

(a) FRP rupture *(b) FRP debonding*

Figure 3-4. Failure modes of specimens

Two typical failure modes were observed in this chapter: debonding failure within a thin layer of concrete and FRP rupture. The specimens G1_1B_2, G1_1B_3, and G1_1C_2 experienced FRP rupture failure. As shown in Figure 3-4 (a), the rupture failure occurred near the clamp area of the loading machine. For the specimens 1B and 1C, the ultimate bonding strength between FRP and concrete is close to the tensile strength of FRP, which could result in either debonding failure or FRP rupture. For instance, the rupture strength of one layer of BFRP sheet 1B is calculated as 6.3 kN, which is close to the ultimate bonding strength of 5 kN. For the one-layer-CFRP 1C, the rupture strength is calculated as 13.2 kN which is close to the ultimate bonding strength of 12 kN. Except the specimens G1_1B_2, G1_1B_3, and G1_1C_2, the rest

of the specimens experienced debonding failure, and all the debonding initiated at the loaded end for all the specimens, which is consistent with the results in the previous studies (39, 45, 141). The photographs of rupture failure of specimen G1_1B_2 and debonding failure of specimen G2_1C1B_2 after the tests are shown in Figure 3-4. The variations in stiffness and stacking order of hybrid FRPs have no effect on the failure modes of hybrid FRPs-concrete interface.

3.3.2 Load and displacement

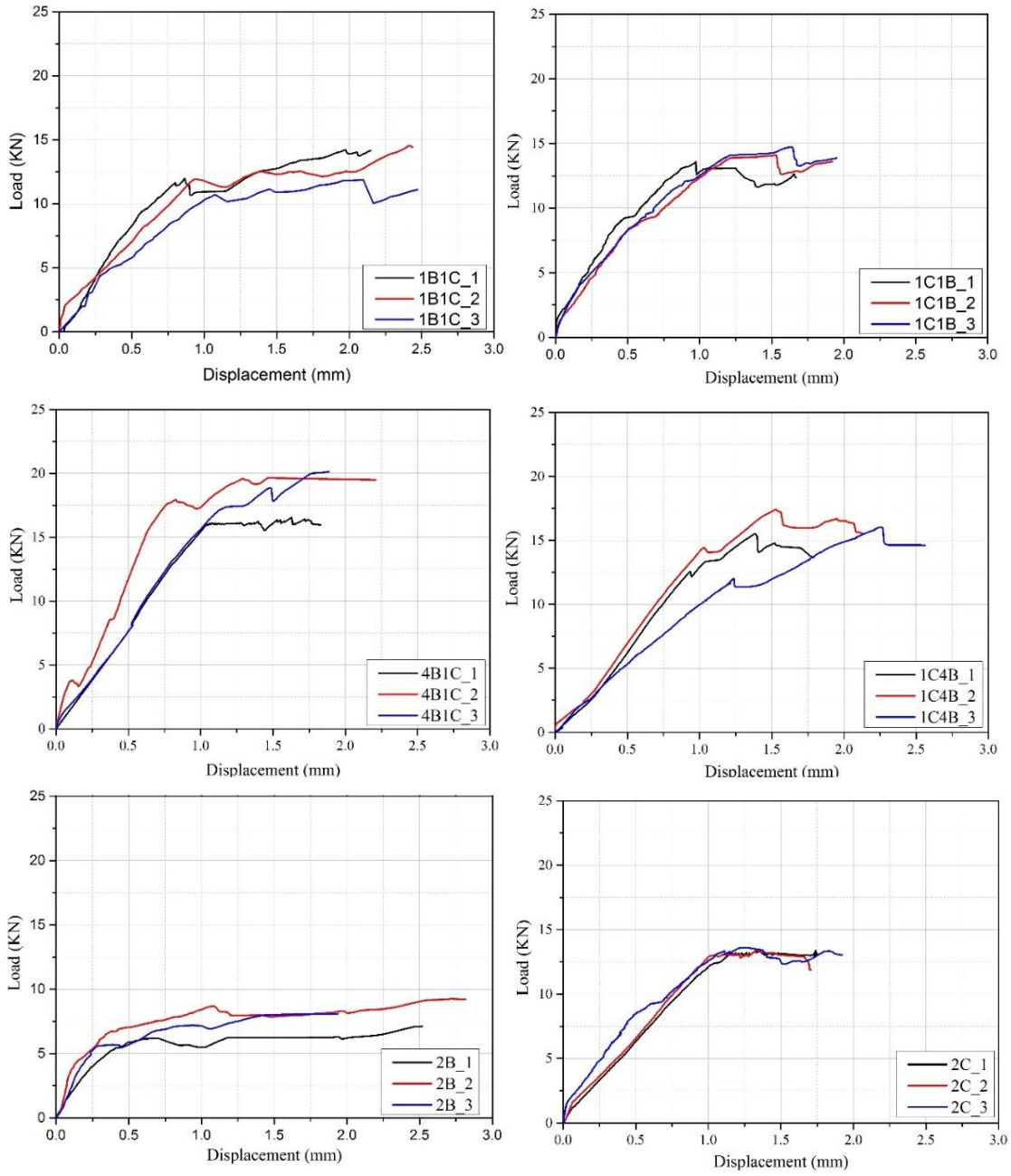

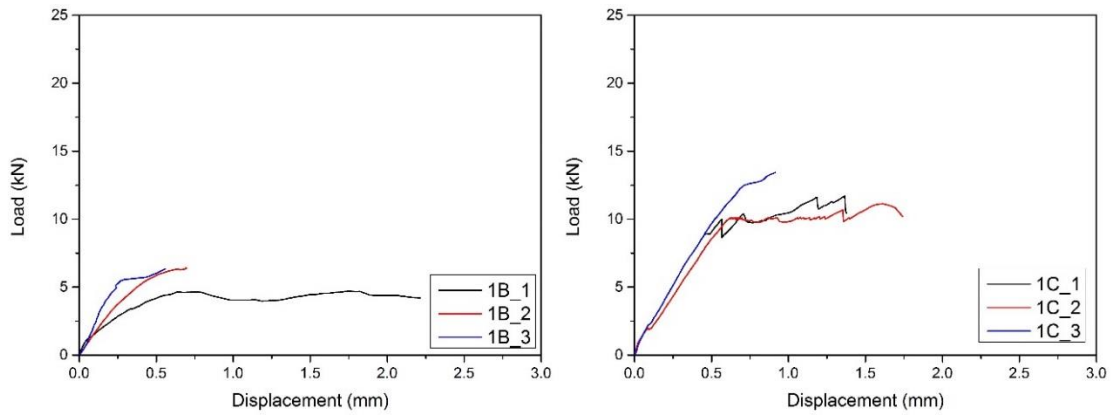

Figure 3-5. Load-displacement curves

Figure 3-5 shows the experimental results of load-displacement graphs. Most of the testing results are consistent for each configuration. The measured displacement includes the shear slip of the bonded part and the elongation of the unbonded part of FRP sheets similar to the testing presented in the previous study (39). The load-displacement curves of the specimens G1_1B_2, G1_1B_3, and G1_1C_2 experiencing FRP rupture failure were also plotted herein for completeness. As observed, the bonding strength is greatly affected by the FRP stiffness and stacking order. The average bonding strength of the specimens G1_1B, G2_2B, G1_1C, G2_1B1C, G2_1C1B, G2_2C, G3_1C4B, and G3_4B1C is 4.61, 7.17, 9.00, 11.91, 13.10, 13.85, 13.96, and 17.53 kN, respectively. As shown in Figure 3-6, the bonding strength increases with the stiffness of FRP sheet, which is also consistent with the previous studies (4, 89). For the specimens G2_1C1B/G2_1B1C with the same stiffness of FRP but different stacking order, the bonding strength are different and the variation may be resulted from the difference in the stiffness of the contacting layer.

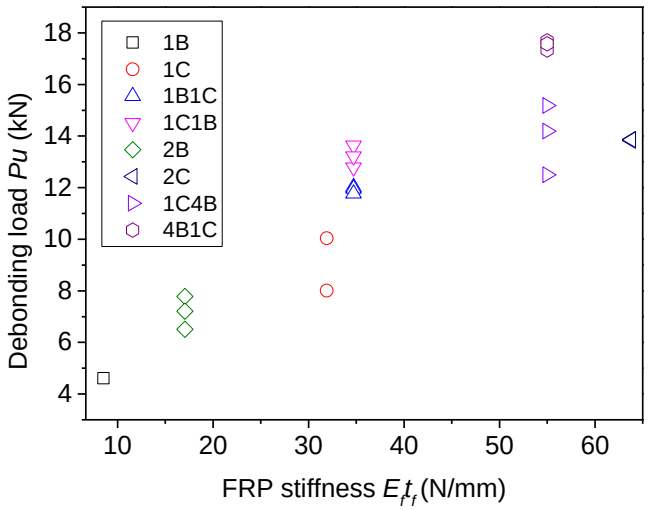

Figure 3-6. Relationship between FRP stiffness and bonding strength

Figure 3-7 shows the typical load-displacement curve for the specimen G2_1C1B_2. Theoretically, three stages exist in the load and displacement curves, i.e. elastic stage, softening stage, and debonding stage. After the elastic stage, interfacial softening induced by microcracking at adhesive-concrete interface initiates along with the loss of shear stress as the increase of the interfacial shear slip (142). Debonding initiated at the loaded end when reaching the debonding load shown in the red mark, followed by debonding plateau. In this chapter, all the specimens were prepared with 200 mm bond length, which was longer than the corresponding effective lengths and enough to develop the debonding plateau.

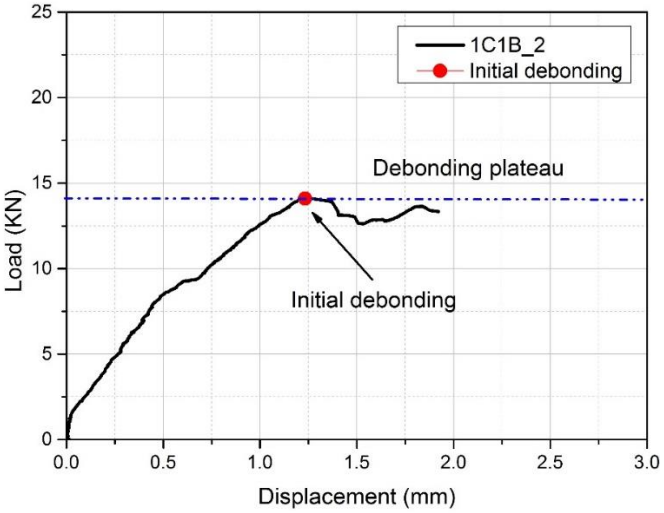

Figure 3-7. Debonding load and typical load-displacement curve (G2_1C1B_2)

3.3.3 Strain distribution of hybrid FRPs

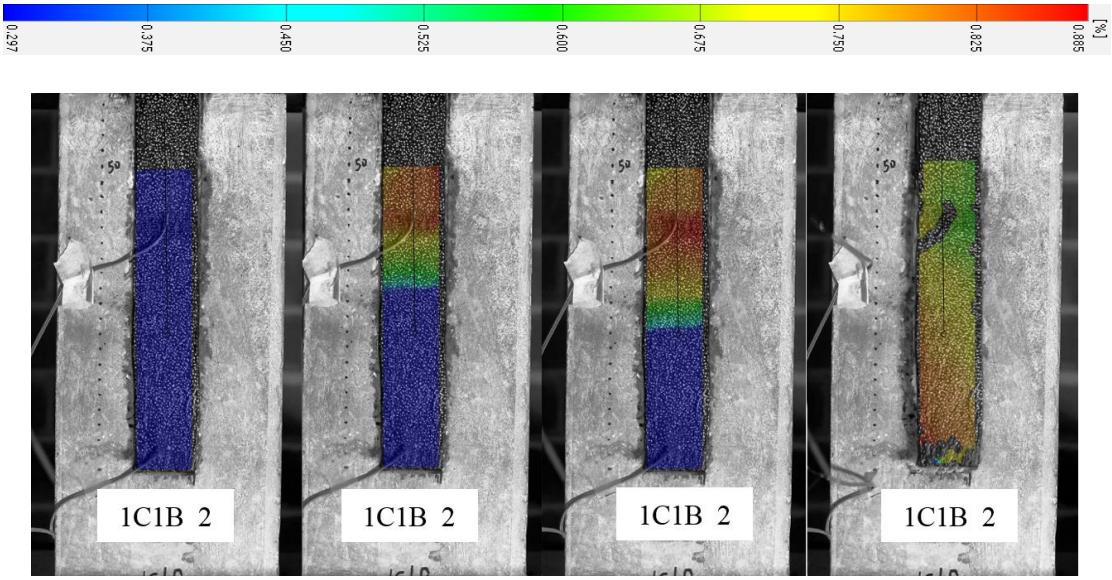

(a) *(b)* *(c)* *(d)*

Figure 3-8. Distribution and propagation of FRP strain of G2_1C1B_2 at different loading stages *(a) 0 kN; (b) 13.28 kN (Debonding load); (c) 13.64 kN; (d) Completed debonding*

DIC images of strain fields (ε) in the anchorage area along the loading direction at different loading levels for the specimen G2_1C1B_2 are shown in Figure 3-8. When the applied load increased before reaching the debonding load, the FRP strain also increased and redistributed within the anchorage area. It should be noted that the strain can only develop within a certain region, which is called the effective bond length (9, 80, 143, 144). After reaching the debonding load, the FRP strain redistributed along the anchorage area and propagated toward the free end until the completed debonding of the FRP sheet. The development of strain fields implies the progress of interfacial damage of the FRP-to-concrete interface.

3.3.3.1 Smoothen method

The fluctuation of FRP strain was observed, which was caused by the ambient noise during tests and the local material variation in the FRP laminate (145). To reduce the fluctuation, two methods (i.e. averaging spatial filter method and median spatial filter

method) (146) were used in this chapter. The graphs of the specimens filtered by these two methods are shown in Figure 3-9 (a). The smoothened strain by the median filtering method is closer to the measured strain traced from strain gauge SG1. Therefore, the median filtering method is used for strain smoothening. Figure 3-9 (b) shows the comparison between the DIC results and the smoothened results. The distribution of strain exhibits a descending tendency. The local strain fluctuation, especially for the DIC strain at 13.28 kN, is due to the stress concentration caused by the aggregates embedded between the FRP sheet and concrete block. Curve fitting procedure is conducted to eliminate the fluctuations of strain distribution. In brief, the DIC technique and the filtering method yield reliable strain as verified by the experimental measures from the strain gauge so that they were utilized to monitor the FRP strain and its distribution.

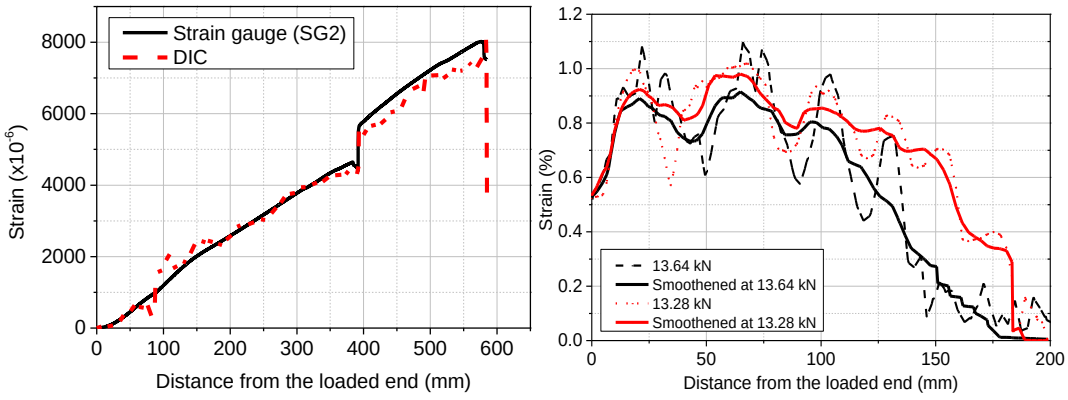

(a) *(b)*

Figure 3-9. (a) Strain comparisons by using average filtering and median filtering methods for G2_1C1B_2; (b) Strain distribution of G2_1C1B_2 at different loading levels

3.3.3.2 Fitting procedure for strain

A non-linear formula expressed by Equation (3-3) (145) is adopted for the fitting procedure. It is found that the expression can simulate the strain distribution along the anchorage length, as follows:

$$\varepsilon(x) = a + \frac{b}{1 + \exp(\frac{x_o - x}{\beta})^c} \quad (3\text{-}3)$$

where a, b, c, β and x_o are determined by using non-linear regression analysis of the smoothened strain and x is the distance from the loaded end. Figure 3-10 shows the strain distribution of specimen G2_1C1B_2 at the debonding load of 13.28 kN. The ultimate strain was approximately 0.9% when the debonding load P_d was reached. After reaching the debonding load P_d, the load and strain stopped increasing, which indicated the forming of effective bond length. The effective bond length is the bond length beyond which no further increase in ultimate load can be achieved (9).

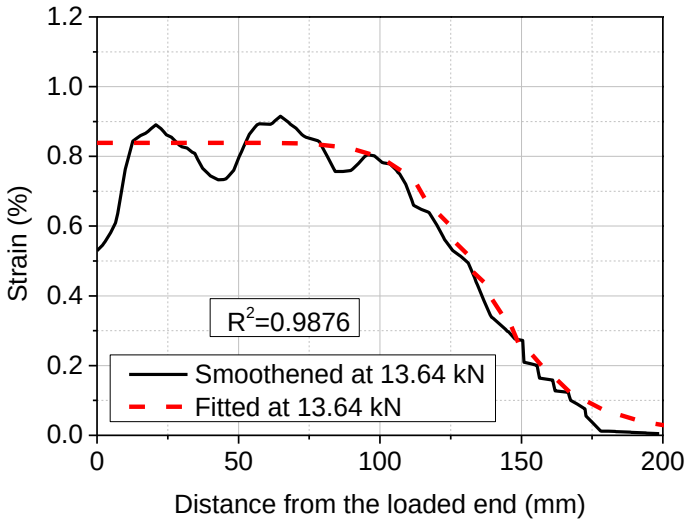

Figure 3-10. Strain distribution of G2_1C1B_2 at debonding load

3.3.3.3 Effective bond length

Figure 3-11 illustrates the strain field of the effective bond length for specimen G2_1C1B_2 at the debonding load of 13.28 kN. The black points at the left edge of the concrete substrate were marked every 10 mm to measure the effective bond length. The total bonded length was 200 mm. The 50 mm un-bonded region is to eliminate the edge effect of the concrete blocks. The effective bond length can be determined by the strain contour. The effective bond length is defined as the bond length over which the strain

decreases from the peak value to zero (9). Therefore, the effective bond length of specimen G2_1C1B_2 was 78 mm at the debonding load of 13.28 KN as can be seen in Figure 3-11.

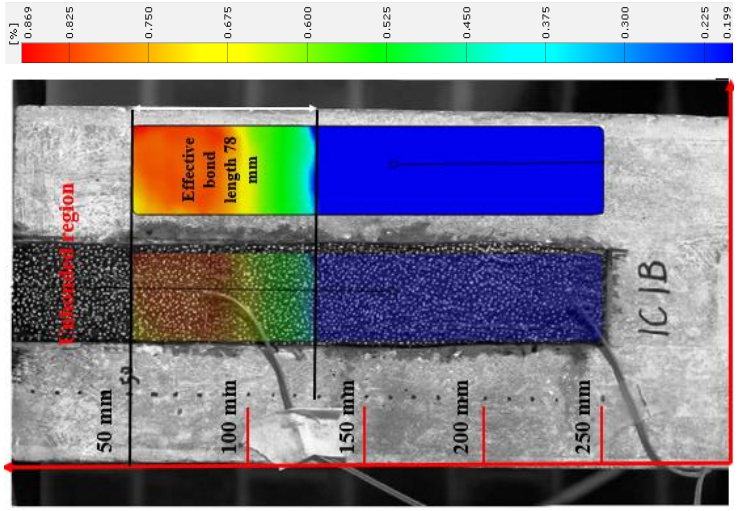

Figure 3-11. The effective bond length of specimen G2_1C1B_2 at debonding load of 13.28 kN

3.4 Bond stress and local slip calculation

The bond-slip relationship in the longitudinal direction can be obtained from the smoothened strain by Equations (3-4) and (3-5). The interfacial bond stress distribution within the bonded length can be evaluated by imposing the equilibrium condition of an FRP sheet with a length *dx* as follows:

$$\tau(x) = t_f E_f \frac{\mathrm{d}\varepsilon_f}{\mathrm{d}x} \tag{3-4}$$

where $\tau(x)$ is the interfacial bond stress, $\frac{d\varepsilon_f}{dx}$ is the gradient of FRP strain along the bonded length, t_f is the FRP thickness, and E_f is the FRP elastic modulus. In addition, the local slip $s(x)$ between FRP plate and concrete at distance x from the free end of the specimen can be calculated by assuming a zero slip in the free end as (147):

$$s(x) = \int_0^{\infty} \varepsilon_f dx \tag{3-5}$$

3.4.1 Bond stress distribution

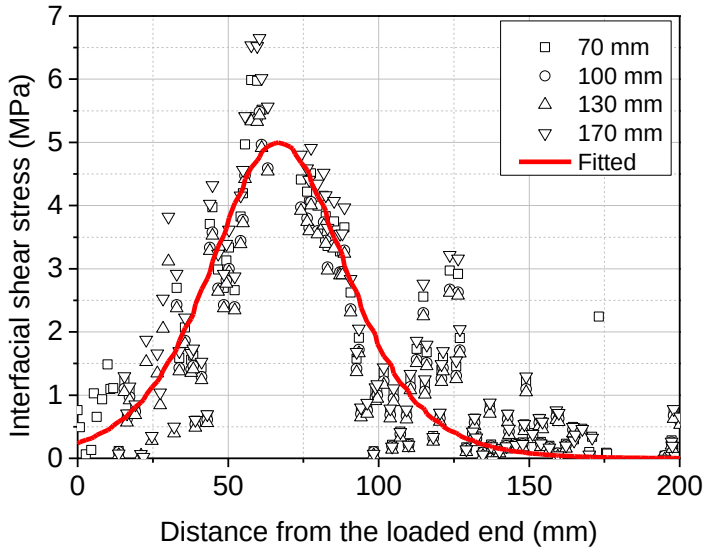

Figure 3-12. Bond stress distribution along the bonded length of specimen G2_1C1B_2

Figure 3-12 shows the interfacial bond stress for G2_1C1B_2 at 13.28 kN (debonding load) and 13.65 kN based on the smoothened strain profile by Equation (3-3). It can be seen that the plotted graph can well present the development of interfacial bond stress. The interfacial shear stress initially rises with the applied load. After reaching its peak value, the shear stress starts to decrease until the debonding of the FRP sheet is completed. The bond stress obtained from the fitted strain matches well the smoothened result, and the fluctuation of the bond stress can be eliminated by the fitting strain. With the increase in applied load, the peak bond stress propagates from the loaded end along the length of the FRP sheet, which implies the debonding propagation.

3.4.2 Local slip distribution

Figure 3-13 shows the local slip distribution for G2_1C1B_2 at the debonding load of 13.28 kN along the bonded length based on the smoothened strain profile by Equation (3-3). The local slip between the FRP plate and concrete shows an increasing trend from the free end during the loading process. After reaching the debonding load, the local slip increases sharply, which indicates the debonding occurrence.

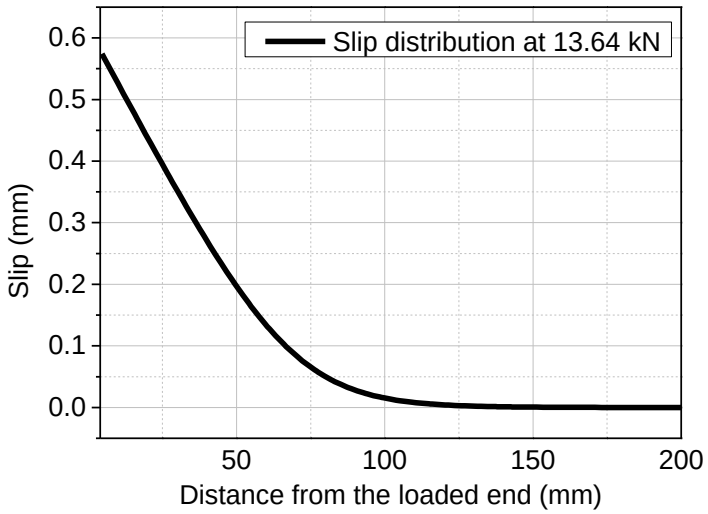

Figure 3-13. Local slip distribution calculated from smoothened strain at the debonding load of 13.28 kN for G2_1C1B_2

3.4.3 Bond-slip relationship

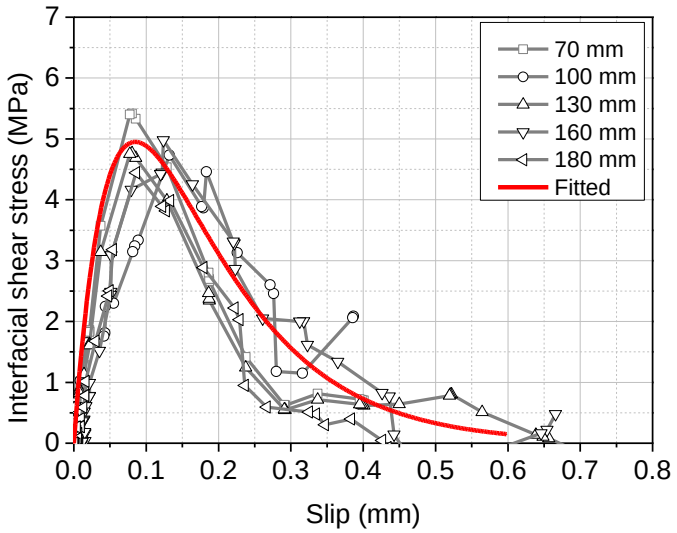

Figure 3-14. Bond-slip curve for G2_1C1B_2

Figure 3-14 shows the bond-slip curve of Specimen G2_1C1B_2 at 13.28 kN based on the smoothened strain and the fitted strain profile. The bond-slip curve estimated from the fitted strain is close to the smoothened result. The interfacial shear stress increases sharply with the increasing applied loads, and then drops gradually after reaching the peak shear stress until full debonding. It is obvious that the bond-slip constitutive relation exhibits softening behaviour. It is approximately linear up to 40% of the maximum shear stress, after which it increases nonlinearly up to the peak stress. The

results agreed well with those in the previous study (148). From the experimental results, the maximum bond stress τ_{max} and the corresponding slip s_o of the specimen G2_1C1B_2 were 5.11 MPa and 0.099 mm, respectively. After reaching the peak stress, a nonlinear softening behaviour is observed due to the slip. Therefore, the non-linear bond-slip curves contain an ascending branch ($0 < s \leq s_o$) and a descending branch ($s > s_o$). The area under the bond-slip curve represents the interfacial fracture energy G_f, defined as:

$$G_f = \int \tau ds \tag{3-6}$$

The fitted results of the maximum bond stress τ_{max}, slip s_o at the maximum bond stress, and fracture energy G_f are summarized in Table 3-3.

Table 3-3. Test results of debonding loads, bond stress, slip, fracture energy and parameter c

Specimen	**Debonding load (kN)**	**Fitting parameter (*c*)**	**Fracture energy G_f (N/mm)**	**Parameters for the developed model**			**Failure mode**
				τ_{max} (MPa)	**s_o (mm)**	**s_u (mm)**	
G1_1B_1	4.61	0.54	0.71	2.36	0.110	0.550	D
G1_1B_2	N/A	N/A	N/A	N/A	N/A	N/A	R
G1_1B_3	N/A	N/A	N/A	N/A	N/A	N/A	R
G1_1C_1	10.04	0.51	0.68	4.53	0.051	0.290	D
G1_1C_2	N/A	N/A	N/A	N/A	N/A	N/A	R
G1_1C_3	8.01	0.50	0.67	5.01	0.049	0.271	D
G2_1B1C_1	12.02	0.55	1.80	6.50	0.089	0.440	D
G2_1B1C_2	11.95	0.54	1.78	6.07	0.087	0.460	D
G2_1B1C_3	11.77	0.56	1.79	5.99	0.078	0.450	D
G2_1C1B_1	12.79	0.51	1.39	5.11	0.099	0.505	D
G2_1C1B_2	13.28	0.55	1.43	5.20	0.093	0.500	D
G2_1C1B_3	13.22	0.52	1.41	5.16	0.089	0.530	D
G2_2B_1	6.51	0.53	0.81	5.77	0.091	0.460	D
G2_2B_2	7.78	0.54	0.72	5.68	0.093	0.440	D
G2_2B_3	7.21	0.53	0.71	5.59	0.096	0.410	D
G2_2C_1	13.87	0.56	0.95	5.21	0.058	0.280	D
G2_2C_2	13.83	0.54	0.99	5.23	0.057	0.310	D

G2_2C_3	13.85	0.52	0.93	5.60	0.049	0.340	D
G3_1C4B_1	15.18	0.52	1.90	5.67	0.119	0.610	D
G3_1C4B_2	14.19	0.50	1.95	5.70	0.110	0.613	D
G3_1C4B_3	12.50	0.55	1.78	6.11	0.114	0.630	D
G3_4B1C _1	17.33	0.54	1.10	6.39	0.064	0.290	D
G3_4B1C _2	17.69	0.55	1.09	6.48	0.061	0.310	D
G3_4B1C _3	17.58	0.50	1.04	7.11	0.059	0.330	D

Note: R - Rupture of FRP sheet. D - Debonding of FRP sheet.

3.4.4 Simplified bond-slip relationship

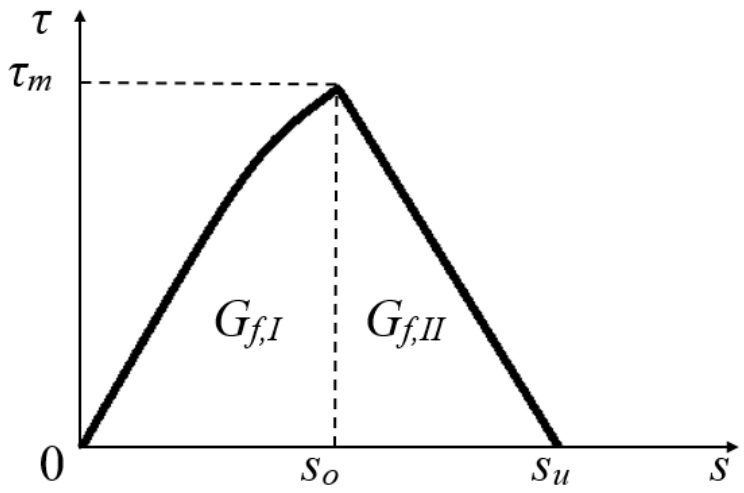

Figure 3-15. Typical bond-slip relationship

The bond-slip model is important for analyzing the behaviour of FRP-strengthened concrete structures because it describes the relationship between the local interfacial shear stress and the local slip (149). To describe the interfacial bond properties, the shape of the bond-slip model should be chosen first. The CEB-FIP model (CIB 1993) (150) is used to simplify the bond-slip relationship due to its simplicity and a good match with the experimental results. The bond-slip relationship is determined by four parameters, i.e. the maximum shear stress τ_{max}, the slip s_o at the maximum shear stress, the ultimate slip s_u, and c, which is the fitting parameter from the experimental data. Four key parameters extracted from the non-linear bond-slip curves are listed in Table 3-3. It can be seen that the bond-slip curves cover an ascending branch and a descending

branch as shown in Figure 3-15. The nonlinear ascending part can be expressed as a hyperbolic equation. The descending branch can be depicted by a linear equation. The bond-slip relationship is proposed by using the following formulae:

$$\tau(s) = \tau_{max}\left(\frac{s}{s_o}\right)^c,\ 0 \le s \le s_o \tag{3-7}$$

$$\tau(s) = \tau_{\max}\frac{s_u - s}{s_u - s_o},\ 0 \le s \le s_o \tag{3-8}$$

$$\tau(s) = 0,\ s_u \le s \tag{3-9}$$

For all the specimens, the nonlinear descending branch can be converted into a linear part in order to compare with the current bilinear bond-slip models. The conversion process always maintains the same interfacial fracture energy for the curves before and after converting. The interfacial fracture energy is used to determine the ultimate slip s_u. For the simplified bond-slip, the interfacial fracture energy G_f can be obtained by integrating the bond stress with respect to the slip:

$$G_{f,s} = G_{f,I} + G_{f,\mathrm{II}} = \int_0^{S_O} \tau_{\max}\left(\frac{s}{s_o}\right)^c ds + \frac{1}{2}\tau_{\max}\left(s_u - s_o\right) \tag{3-10}$$

For the non-linear bond-slip, $G_{f,I}$ and $G_{f,II}$ can be obtained by integrating the bond stress with respect to the slip to figure out the interfacial fracture energy $G_{f,n}$, as shown in Equation (3-11). The key parameters c and ultimate slip s_u can be obtained for all the specimens and are listed in Table 3-3.

$$G_{f,n} = G_{f,I} + G_{f,\mathrm{II}} = \int_0^{s_o} \tau(s)\,ds + \int_{s_o}^{\infty} \tau(s)ds \tag{3-11}$$

3.5 Effect of FRP stacking order

3.5.1 Debonding load

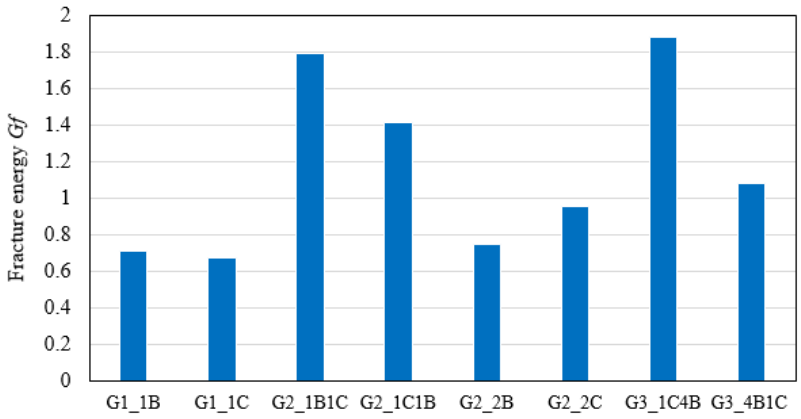

Figure 3-16. Averaged interfacial fracture energy

The debonding loads (P_d) of the tested specimens are given in Table 3-4. As can be seen that the debonding loads of two specimens with the same combination but different stacking orders were significantly different. For example, the debonding load of G2_1B1C (i.e. P_d=11.91 kN) is lower than that of G2_1C1B (i.e. P_d=13.09 kN). These specimens were made of the same type and number of FRP layers but they were bonded to the concrete blocks by different sequences. These experimental results have shown that the stiffness and thickness of the first layer of the hybrid FRP sheets affected the bonding behaviour. Although both hybrid FRPs (i.e. G2_1B1C and G2_1C1B) have the same stiffness ($E_f t_f$), the higher debonding strength was observed when the CFRP layer (i.e. G1_1C1B) is attached to the concrete block. For specimens G2_1C1C and G3_4B1C, four layers of BFRP sheets have a thickness of 0.48 mm, which is much thicker than that of one layer of CFRP sheet (i.e. 0.167 mm). When one layer of CFRP was attached to the concrete, the lower debonding load was achieved as the specimen G2_1C1C experienced a lower debonding load (P_d=13.85 kN) than the specimen G3_4B1C (P_d=17.54 kN). It was observed that for the similar stiffness of the contacting layer of FRP, the higher debonding strength can be achieved when the thicker FRP sheets (G3_4B1C) are attached to the concrete. This is because the thicker FRP resulted in higher interfacial fracture energy (G_f). As shown in Figure 3-16, the average value of fracture energy of the specimen G2_1C1C and G3_4B1C is 0.96 and 1.08 N/mm,

respectively. The bond strength is proportional to the fracture energy (89, 95). It is noted that the stiffness of the contacting layer of 1C is approximately similar to that of 4B.

Table 3-4. Effect of FRP stacking order on the debonding load and the effective bond length

Specimen	G1_1B	G1_1C	G2_1B1C	G2_1C1B	G3_4B1C	G2_1C1C	G3_1C4B
Average debonding load (kN)	4.61	9.00	11.91	13.09	17.54	13.85	14.00
Average effective bond length (mm)	31	59	67	78	81	90	92

Note: The data are averaged from three specimens

3.5.2 Effective bond length

Table 3-4 also shows the effect of FRP stacking order on the effective bond length. It was observed that the first layer of FRP attached to the concrete surface had a great influence on the effective bond length. When one ply of the CFRP sheet is attached to the concrete surface prior to one ply of the BFRP sheet, a larger effective bond length can be achieved, which means that a larger area of stress distribution can be obtained. There is a 14.10% difference caused by the stacking order effect as the effective bond length for G2_1C1B and G2_1B1C is 78 mm and 67 mm, respectively. Theoretically, the effective bond length of G3_1C4B and G3_4B1C should be the same due to the similar stiffness (i.e. the stiffness of 1C4B is similar to that of 4B1C) according to the previous effective bond length models (4, 144). This is because the effective bond length is proportional to the FRP stiffness ($E_f t_f$), and a stiffer FRP sheet can achieve a longer effective bond length, which is consistent with the literature (35). However, the effective bond length of G3_1C4B is 92 mm which is larger than that of G3_4B1C (i.e. L_e = 81 mm). The 11.96% difference should be caused by the FRP stacking order and the relative slips within the internal layers between FRP sheets and the contacting layer between FRP and concrete, as shown in Figure 3-17. It should be noted that multilayer

BFRP sheets have been bonded together to increase the hybrid stiffness (i.e. 4B). The shear redistribution induces the variations in effective bond length. The shear redistribution in multilayered FRPs has been also specified in the literature (142).

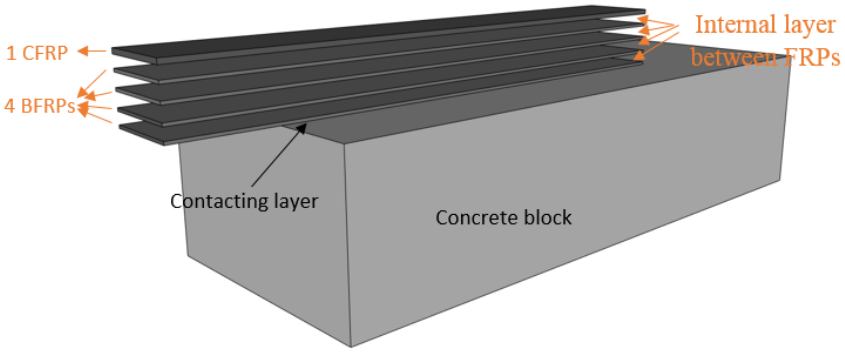

Figure 3-17. Internal layers between FRPs and contacting layer of FRP-concrete

3.5.3 Bond stress and the local slip

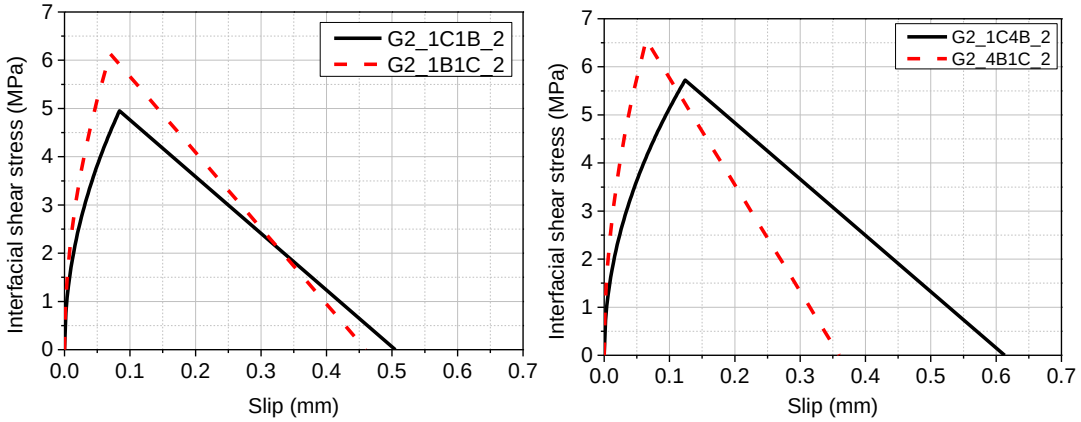

(a) *(b)*

Figure 3-18. Bond-slip curves for (a) hybrid FRPs (G2_1C1B_2 and G2_1B1C_2); (b) hybrid FRPs with four-ply of BFRP and one ply of CFRP (G3_1C4B_2 and G3_4B1C_2)

For specimens G2_1C1B_2 and G2_1B1C_2, the bond-slip relationships are shown in Figure 3-18. It can be seen that the FRP stacking order had a significant influence on the bond-slip relationship. The maximum bond stress (τ_{max}) for G2_1B1C_2 is 6.07 MPa and G2_1C1B_2 is 5.20 MPa which meant that the peak bond stress was reduced when the stiffer FRP plate was used as the contacting layer. The peak bond stresses of

these two cases varied by 16.73%. However, the ultimate slip improved when a stiffer FRP sheet was used. The fracture energy (G_f) for specimens G2_1B1C_2B and G2_1C1B_2 were 1.78 N/mm and 1.43 N/mm, respectively, which meant the specimen G2_1B1C_2B had a greater ability to absorb energy. Both the specimens G2_1C4B_2 and G2_4B1C_2 consisted of 1C and 4B, which had similar stiffness. However, the maximum shear stress and slip values were quite different as there was a 13.68% difference in the peak bond stress and 49.43% in the ultimate slip, as shown in Figure 3-18. When the contacting layer was CFRP sheet (1C), the maximum shear stress was lower than that of BFRP sheets (4B), which meant that the interfacial shear stress was reduced if the stiffer FRP plate was placed as a contacting layer. However, the ultimate slip could be greatly improved when the CFRP was placed as a contacting layer as compared to BFRP. Specimen G2_1C4B_2 possessed a higher capacity for energy absorption than that of Specimen G2_4B1C_2 as there was a 44.10% difference in the test results of fracture energy, as given in Table 3-3. Compared with the sole FRP strengthened concrete, the strain distribution is more complicated as the shear stress redistribution occurred in the internal layers between FRP. This is caused by the different strain capacities of the FRP composite. The full-fields strain was obtained from the surface rather than the internal layers. The obtained shear stress and slip were calculated based on the surface strain in this chapter. This should be a possible reason that the obtained shear stress and slip are quite different from each other (i.e. 1C1B and 1B1C or 1C4B and 4B1C).

3.6 Comparison of experimental results with theoretical predictions

3.6.1 Bond strength model

Two bond strength models i.e. Lu et al. (89) and Chen and Teng (4) were adopted for the bond strength prediction of a single type of FRP sheet. Table 3-5 lists the experimental and predicted debonding loads for all the specimens. Among the

specimens of group 1B, one specimen experienced debonding and the other two ruptured. Among the specimens of group 1C, two specimens experienced debonding and the other one ruptured. For the specimens 1B and 1C, the bonding strength is close to the tensile strength of FRP, which leads to either debonding failure or FRP rupture. The rest of the specimens experienced debonding failure. As given in Table 3-5, the bond strength of hybrid FRPs cannot be well predicted by the models by Lu et al. (89) and Chen and Teng (4). These two models predict the same debonding loads for the specimens G2_1C1B and G2_1B1C or G3_1C4B and G3_4B1C, respectively. However, the experimental results show different results, e.g. 11.91 kN for G2_1B1C and 13.09 kN for G2_1C1B even though these specimens had the same stiffness. The significant variation between the predicted versus the experimental results may be resulted from the difference in the stiffness of the contacting layer. When using Equation (3-2) to predict the stiffness, it causes a variation of 9.7% and 14.1% for 1B1C/1C1B and 1C4B/4B1C as compared to the measured stiffness, respectively, as given in Table 3-2. Therefore, the test result of elastic modulus rather than the predicted elastic modulus should yield better prediction of the debonding load. Figure 3-19 shows the errors of the predicted effective bond length and there are considerable differences between the experimental and analytical results, especially for the hybrid specimens. It should be noted that the stiffness used in calculations was the measured results.

Chen and Teng (4) bond strength model is given as:

$$P_u = 0.427\beta_1\beta_w b_f L_e \sqrt{f_{co}} \tag{3-12}$$

where $\beta_1 = \begin{cases} 1, & L \geq L_e \\ \sin\dfrac{\pi L}{2L_e}, & L < L_e \end{cases}$, $\beta_w = \sqrt{\dfrac{2 - b_f / b_c}{1 + b_f / b_c}}$, and $L_e = \sqrt{\dfrac{E_f t_f}{\sqrt{f_{co}}}}$.

Lu et al. (89) bond strength model is given by:

$$P_u = b_p \beta_1 \sqrt{2 E_f t_f G_f} \tag{3-13}$$

where $\beta_1 = \begin{cases} 1, & L \geq L_e \\ \left(2 - \dfrac{L}{L_e}\right)\dfrac{L}{L_e}, & L < L_e \end{cases}$, $\beta_w = \sqrt{\dfrac{2.25 - b_f / b_c}{1.25 + b_f / b_c}}$, and $G_f = 0.308 \beta_w^{\,2} \sqrt{f_t}$

Table 3-5. Experimental and predicted debonding loads

Specimen	$P_{u,exp}$ **(kN)**	**Lu et al. Model (89)**		**Chen and Teng model (4)**	
		$P_{u,pre}$ **(kN)**	$P_{u,pre}/P_{u,exp}$	$P_{u,pre}$ **(kN)**	$P_{u,pre}/P_{u,exp}$
		Sole FRP			
G1_1B	4.61	4.80	1.04	5.68	1.23
G1_1C	9.00	8.37	0.93	9.91	1.10
G2_2B	7.17	6.88	0.96	8.15	1.13
G2_2C	13.85	11.83	0.85	14.02	1.01
Mean value			0.95		1.12
		Hybrid FRP			
G2_1B1C	11.91	9.25	0.77	10.96	0.92
G2_1C1B	13.09	9.25	0.71	10.96	0.83
G3_1C4B	14.00	11.65	0.83	13.79	0.98
G3_4B1C	17.54	11.65	0.66	13.79	0.79
Mean value			0.74		0.88

Note: The data is averaged from three specimens

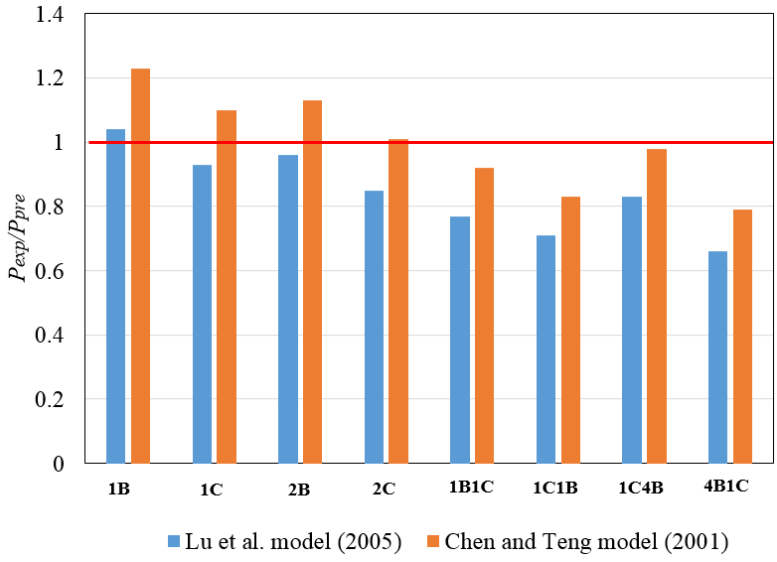

Figure 3-19. Comparisons of the predicted debonding loads with the test results

3.6.2 Effective bond length model

Table 3-6 lists the experimental and predicted effective bond length L_e for all the specimens. Two effective bond length models by Chen and Teng (4) and Lu (151) are employed to make comparisons. The errors of the predicted effective bond length for hybrid FRPs are given in Figure 3-20. These two models can give accurate predictions for a single type of FRP sheet with low variations. However, the effective bond length of hybrid FRP sheets, i.e. specimen 1C1B and 4B1C, cannot be well predicted due to the effects of FRP stacking order.

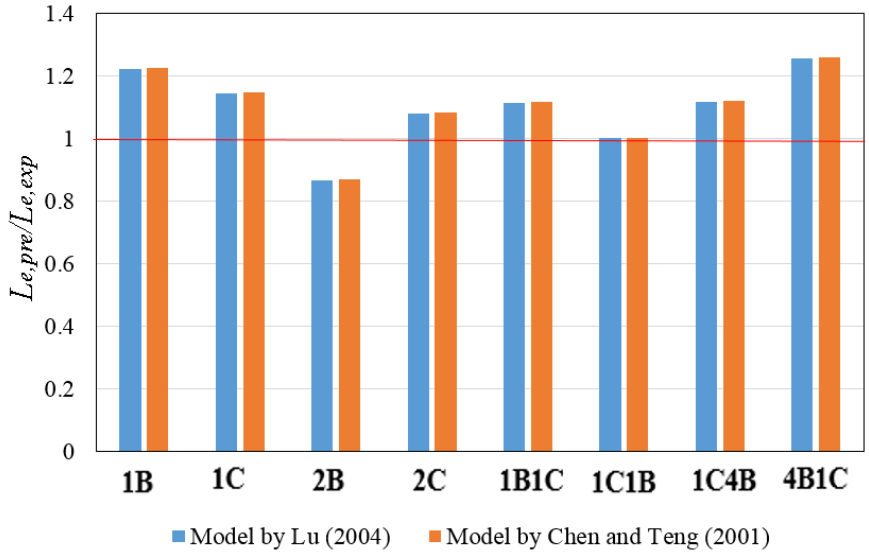

Figure 3-20. Comparisons of the predicted and tested effective bond length

Chen and Teng (4) effective bond length model is given as:

$$L_e = \sqrt{\frac{E_f t_f}{\sqrt{f_{co}}}} \tag{3-14}$$

where $E_f t_f$ is the stiffness of FRP, and f_{co} is the concrete compressive strength.

Lu (151) effective bond length model is given as:

$$L_e = 1.33\frac{\sqrt{E_f t_f}}{f_t} \tag{3-15}$$

where $E_f t_f$ is the stiffness of FRP, and f_t is the concrete tensile strength.

Table 3-6. Experimental and predicted results of the effective bond length L_e

Specimen	$L_{e,exp}$ (mm)	Lu model (151)		Chen and Teng model (4)	
		$L_{e,pre}$ (mm)	$L_{e,pre}/L_{e,exp}$	$L_{e,pre}$ (mm)	$L_{e,pre}/L_{e,exp}$
Sole FRP					
G1_1B	31	36.78	1.19	36.65	1.18
G1_1C	59	68.89	1.17	68.64	1.16
G2_2B	60	52.01	0.87	51.83	0.86
G2_2C	90	97.42	1.08	97.07	1.08
Mean value			1.08		1.07
Hybrid FRP					
G2_1B1C	67	78.10	1.17	77.81	1.16
G2_1C1B	78	78.10	1.00	77.81	1.00
G3_1C4B	92	100.78	1.10	100.42	1.09
G3_4B1C	81	100.78	1.24	100.42	1.24
Mean value			1.13		1.12

Note: The data are averaged from three specimens.

3.6.3 Bond-slip model

Two bond-slip models by Lu et al. (89) and Sun et al. (142) are employed and their predictions are compared to the experimental results. Lu et al. (89) proposed a bilinear model based on the experimental results in the literature. The maximum interfacial shear stress τ_{max}, the elastic slip $s_{o,}$ the interfacial fracture energy G_f, and the ultimate slip s_u are given as:

$$\tau(s) = \tau_{max}(\frac{s}{s_o}),\ 0 \le s \le s_o \tag{3-16}$$

$$\tau(s) = \tau_{max}(\frac{s_o - s}{s_u - s_o}),\ s_o \le s \le s_u \tag{3-17}$$

where $\tau_{max} = 1.5\beta_w f_t$, , , $G_f = 0.308\beta_w^2\sqrt{f_t}$, $\alpha = \frac{1}{\frac{G_f}{\tau_{max}s_o} - \frac{2}{3}}$, $\beta_w = \sqrt{\frac{2.25 - b_f/b_c}{1.25 + b_f/b_c}}$,

and b_f and b_c are the width of FRP and concrete blocks, respectively. Another bilinear bond-slip model proposed by Sun et al. (142) was employed for comparison. The

expressions of the bilinear model are the same as Lu et al. model (145), as shown in Equation (3-16) and Equation (3-17). Figure 3-21 (a-e) shows the predicted and experimental results. It can be seen that Sun et al. (142) model underestimates the maximum shear stress not only for the sole type of FRP (1C and 2C) but also for hybrid FRPs. For the model proposed by Lu et al. (89), the predicted interfacial shear stresses are higher than the testing results of the specimens G2_1C1B and G3_1C4B but lower than those of the specimens G3_4B1C and G2_1B1C.

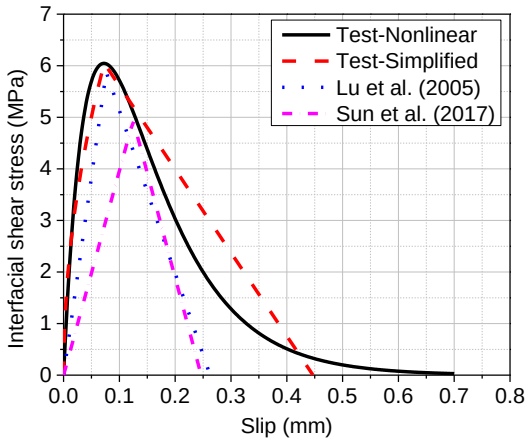

(a) G1_2B_2

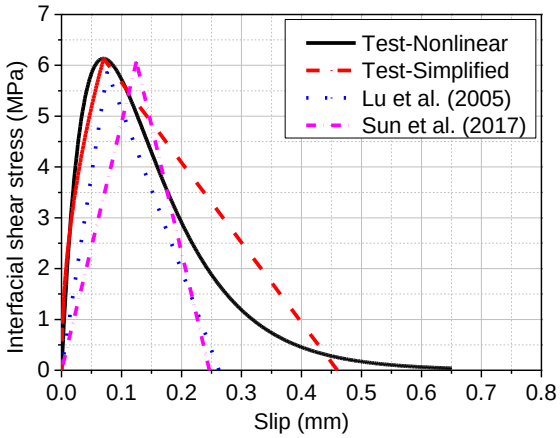

(b) G2_1B1C_2

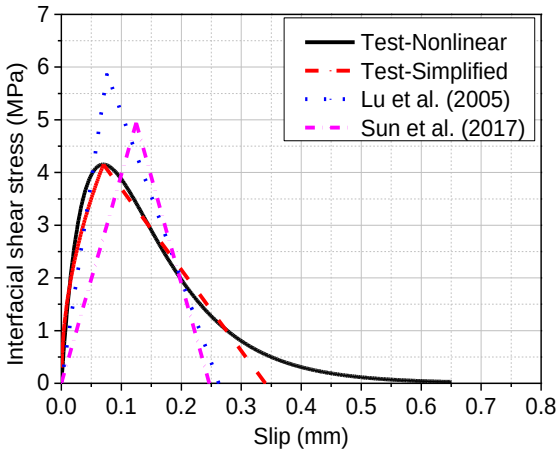

(c) G1_1C_1

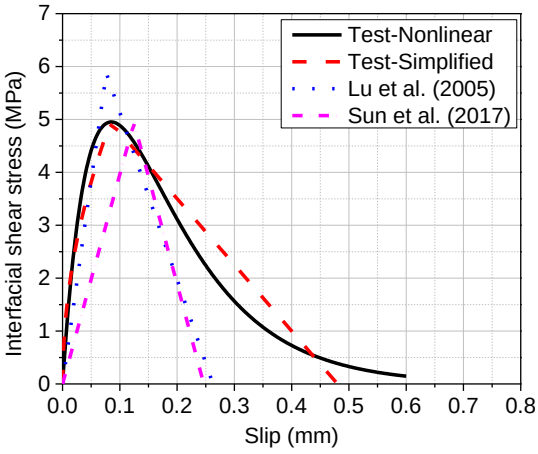

(d) G2_1C1B_2

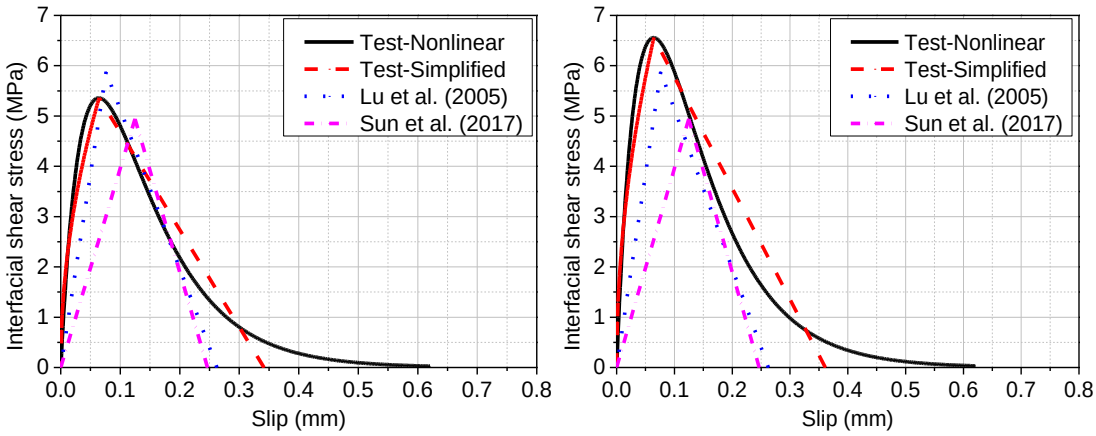

(e) G2_2C_2 *(f) G2_4B1C_2*

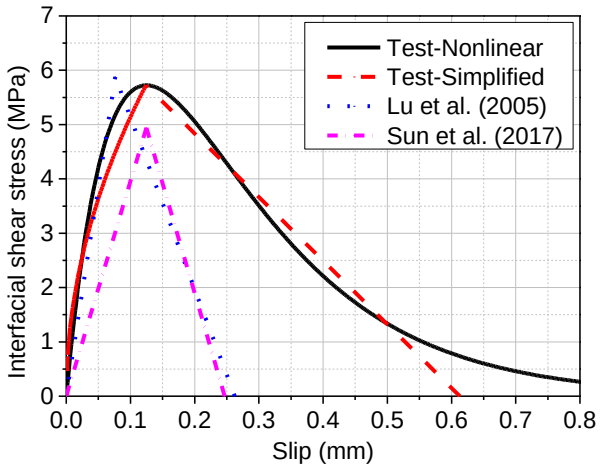

(g) G2_1C4B_2

Figure 3-21. Comparisons of the predicted and experimental bond-slip curves

3.7 Proposed model for hybrid FRPs

As can be seen from the discussions above, the existing models cannot predict well the bond behaviour of hybrid FRPs. The primary reason is due to the actual stiffness of hybrid FRP sheets in which the current models could not well predict. This chapter, thus, proposes new models based on the existing ones and considers the actual stiffness of hybrid FRPs.

3.7.1 Elastic modulus of hybrid FRPs

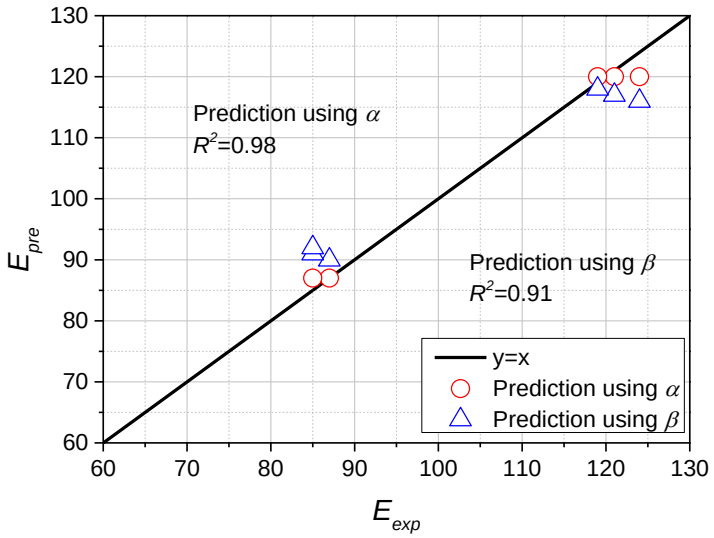

Figure 3-22. Experimental versus predicted elastic modulus of hybrid FRPs

The experimental elastic modulus of hybrid FRPs was determined from flat coupon tests. The predicted values are higher than the experimental results, which can be found in Table 3-7. Based on the rule of mixtures (139), the tensile stress of hybrid FRPs (f_{HF}) can be determined by the following formula:

$$f_{HF} = [E_C \frac{A_C}{A_{HF}} + E_B \frac{A_B}{A_{HF}}]\varepsilon_{HF}, \ \varepsilon_{HF} \le \varepsilon_C \tag{3-18}$$

As FRP is a heterogeneous material and hybrid FRPs consist of multilayered FRP sheets prepared manually by wet lay-up process, the fibres tend to be twisted and poor alignment of the fibres can lead to the reduction in modulus. Therefore, two reduction factors i.e. α and β are introduced to model the modulus reductions. The elastic modulus of hybrid FRPs (E_H) can be expressed as:

$$E_H = \frac{f_{HF}}{\varepsilon_{HF}} = \alpha[\frac{E_C t_C + E_B t_B}{t_C + t_B}] = \frac{f_{HF}}{\beta \varepsilon_C} \tag{3-19}$$

where E_H is the elastic modulus of hybrid FRPs, E_C and E_B are the elastic modulus of CFRP and BFRP, respectively, f_{HF} is the tensile stress of hybrid FRPs, ε_{HF} is the first rupture strain of hybrid FRPs, ε_C is the rupture strain of one layer of CFRP sheet, α is

the reduction factor induced by workmanship, β is the reduction factor caused by the increase of rupture strain in hybrid FRPs, and t_C and t_B are the thickness of CFRP and BFRP layers, respectively. After regression analysis, the reduction factors α = 0.853 and β = 0.742 are determined. As given in Table 3-7, the elastic modulus of hybrid FRPs is predicted with the mean values of 1.004 (the standard variation SD=0.020) and 1.014 (SD=0.059) by using the Equation (3-19) with the factor α and β, respectively. The equation with the reduction factor α yields a more accurate result with a higher correlation coefficient ($R^2 = 0.9875$), as shown in Figure 3-22.

Table 3-7. Comparisons between experimental and predicted elastic modulus

Hybrid FRPs	$E_{,\exp}$ **(GPa)**	**Tensile stress (MPa)**	**Rupture strain ε (mm/mm)**	$\frac{f_{HF}}{\varepsilon_C}$	$\frac{f_{HF}}{\varepsilon_{HF}}$	$\frac{E_C t_C + E_B t_B}{t_C + t_B}$	**Prediction using α**	$\frac{E_{,\text{pre}}}{E_{,\exp}}$	**Prediction using β**	$\frac{E_{,\text{pre}}}{E_{,\exp}}$
1C_1	188	1994	0.0106	N/A	N/A	N/A	N/A	N/A	N/A	N/A
1C_2	191	1990	0.0104	N/A	N/A	N/A	N/A	N/A	N/A	N/A
1C_3	193	1986	0.0103	N/A	N/A	N/A	N/A	N/A	N/A	N/A
1C1B_1	124	1649	0.0133	156	124	141	120	0.970	116	0.934
1C1B_2	121	1644	0.0136	158	121	141	120	0.994	117	0.970
1C1B_3	119	1639	0.0138	159	119	141	120	1.011	118	0.992
1C4B_1	87	1281	0.0148	121	87	102	87	1.000	90	1.033
1C4B_2	85	1277	0.0150	123	85	102	87	1.024	91	1.075
1C4B_3	85	1273	0.0149	124	85	102	87	1.024	92	1.083
Average								1.004		1.014
SD								0.020		0.059

3.7.2 Bond strength model for hybrid FRPs

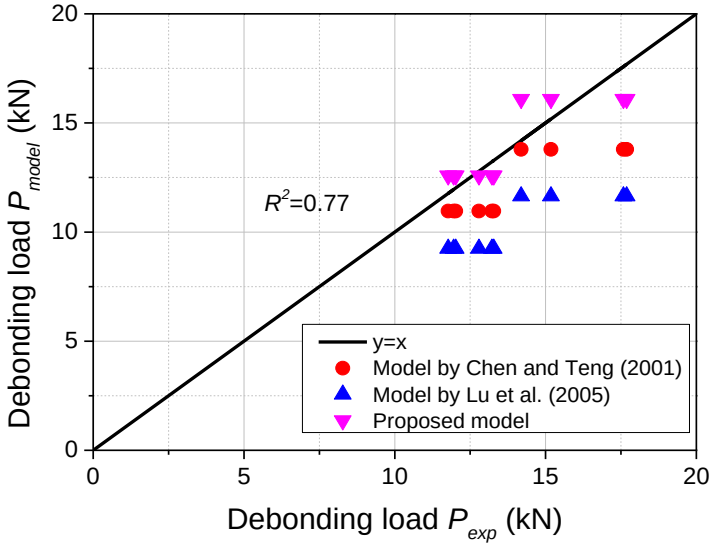

Figure 3-23. Experimental versus calculated debonding loads for hybrid FRPs

As previously presented, the previous models by Lu et al. (89) and Chen and Teng (4) cannot provide accurate predictions of bond strength for hybrid FRPs. Their capability to predict debonding loads were plotted in Figure 3-23. It should be noted that the points (i.e. blue and red) which are located above the baseline ($y = x$) represent conservative predictions. Therefore, a more accurate bond strength model for hybrid FRPs should be proposed as bond strength is an important factor controlling debonding failures in FRP-strengthened members (39).

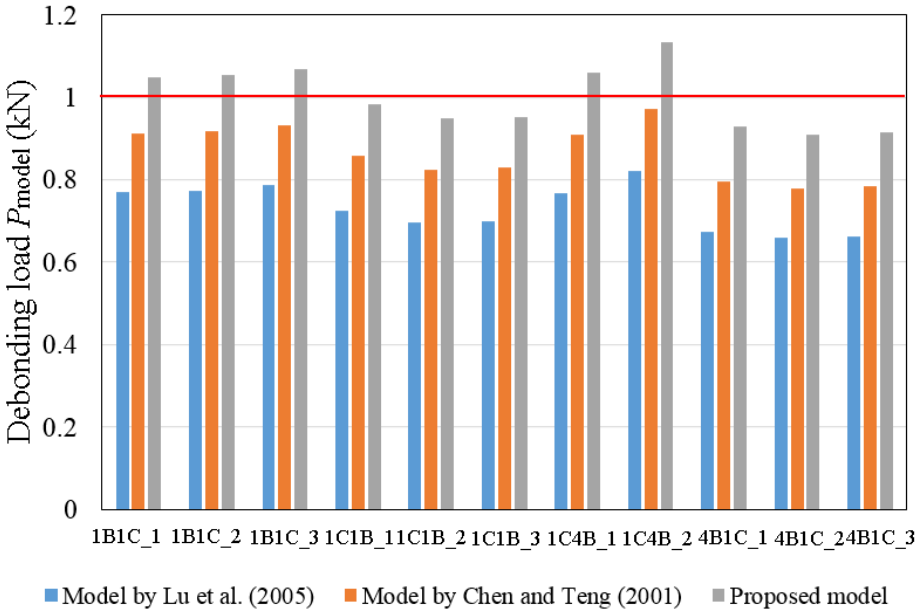

Figure 3-24. The errors of the predicted debonding loads

The model by Chen and Teng (4) was used as the basis in modifying the model for hybrid FRP sheets in this chapter as it was proposed based on the effective bond length and gave relatively better predictions. The effective bond length of hybrid FRPs can be predicted by Chen and Teng (4) with high accuracy (i.e. mean value is 1.11). One calibration factor α was proposed in their bond strength model and $\alpha = 0.427$ suggested by Yao et al. (39) using 72 single shear specimens. However, this model underestimates the debonding loads of the hybrid FRP in this chapter. Consequently, the calibration factor $\alpha = 0.576$ is introduced to Equation (3-12) to better predict the debonding loads, as given in Equation (3-20). It should be noted that the specimen G3_1C4B_3 was not

considered in the analysis as well as in the calibration process because a malfunction happened during testing, leading to unreliable results. Figure 3-24 gives the errors of the debonding loads predicted by the proposed bond strength model. The proposed bond strength model provides more accurate predictions with a mean value of 1.0001 and standard variation 0.075 for the ratio of the tested and predicted bonding strengths. The mean values and the corresponding standard variations of the models by Lu et al. (89) and Chen and Teng (4) are 0.73 and 0.056, and 0.86 and 0.066, respectively.

$$P_u = 0.576\beta_l\beta_w b_f L_e\sqrt{f_{co}} \tag{3-20}$$

3.7.3 Bond stress model for hybrid FRPs

Based on the comparisons between the predicted and experimental results, the models proposed by Lu et al. (89) and Sun et al. (142) cannot well predict the interfacial shear stress for hybrid FRPs as the predicted bond stresses are constant values for different hybrid specimens, which are different from the experimental results. The parameters β_w and f_t were considered in their models. The experimental results, however, show that the stiffness $E_f t_f$ of FRP should be a key parameter governing the interfacial bond stress, especially for hybrid FRPs. Pellegrino et al. (45) considered the term $\left(n_f E_f t_f\right)^{0.32}$ in their model. Consequently, the interfacial shear stress can be described by the function of $\left(E_f t_f\right)^{0.32}$ (45) and $\beta_w f_t$ (89). Based on the test results, this chapter proposes the calibration factor α = 0.395 in Equation (3-21) to be used for hybrid FRP. Figure 3-25 shows the errors of the predicted bond stress. As shown the proposed model provides more accurate results than other models due to its mean value of 1.0001 and standard variation 0.093. The mean values and the corresponding standard variations of the models by Lu et al. (89) and Sun et al. (142) are 1.153, 0.101 and 0.848, 0.074, respectively.

$$\tau_m = \alpha\left(E_f t_f\right)^{0.32}\beta_w f_t \tag{3-21}$$

where τ_m is the peak interfacial shear stress, $E_f t_f$ is the stiffness of FRP, β_w is the width ratio of FRP-concrete, and f_t is the tensile strength of concrete.

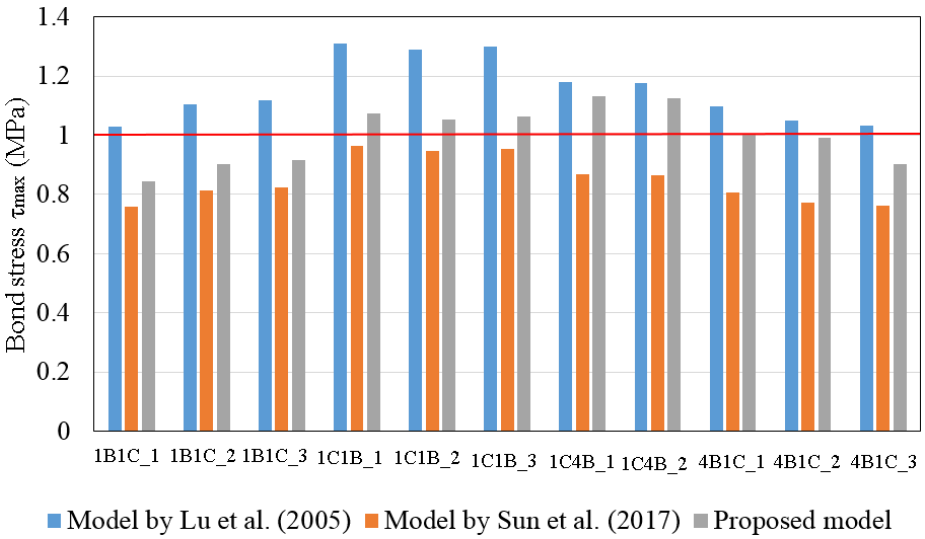

Figure 3-25. The errors of the predicted interfacial shear stress

3.8 Summary

This chapter investigates the static bond behaviour between hybrid FRPs and concrete. The 2D-DIC technique is employed to monitor the fields of displacement and strain. A fitting process is used to obtain bond-slip curves from the fields of strain distributions. The following conclusions can be drawn:

1. The debonding mode of hybrid FRPs is similar to that of sole type of FRP sheets in the single-lap shear tests.
2. The stacking order of hybrid FRPs influences the debonding strength, and the higher debonding strengths can be achieved when a layer of CFRP is attached to the concrete prior to a BFRP layer.
3. FRP stacking order affects the effective bond length because the contacting layer of FRP sheets affects the development of effective bond length. A stiffer FRP sheet can be used as the contacting layer to obtain a longer effective bond length.

4. FRP stacking order has significant effects on the bond-slip relationship. The maximum shear stress reduces if the contacting layer is stuck with a stiffer FRP plate. However, the ultimate slip improves when a stiffer FRP sheet is used.
5. Current bond-slip models in the literature do not well predict the debonding loads and interfacial shear stress for hybrid FRPs. The proposed models in this chapter based on experimental test results give better predictions of the bond strength and the interfacial shear stress between hybrid FRP sheets and concrete.

Chapter 4. Effect of concrete substrate characteristics on static bond behaviour

In this chapter, the effect of concrete substrate characteristics on the static bond behaviour is investigated, including the effect of coarse aggregate size in section 4.1 and the effect of adding short steel fibres in section 4.2.

4.1 Effect of aggregate size

In this section, the effect of aggregate sizes (i.e. 5-10 mm, 10-15 mm, and 15-20 mm) on the debonding load, maximum bond stress, effective bond length, local slip at peak shear stress, as well as the bond-slip relationship between the BFRP sheets and concrete are presented and discussed. The relative slip between BFRP and concrete at the peak bond stress increases with the aggregate size. Existing models regarding the bond strength and interfacial bond-slip are adopted and recalibrated versus the experimental results in which the size effect of aggregates is incorporated.

The related work in this section has been published in Composites Part B: Engineering.

Yuan C, Chen W, Pham TM, Hao H. Effect of Aggregate Size on Bond Behaviour between Basalt Fibre Reinforced Polymer Sheets and Concrete. Composites Part B: Engineering. 2019; 158:459-74. DOI: doi.org/10.1016/j.compositesb.2018.09.089

4.1.1 Experimental program

4.1.1.1 Material properties

The effect of coarse aggregate size on the bonding behaviour was investigated in the test program and the coarse aggregate sizes (d_n) with three ranges from 5-10 mm, 10-15 mm to 15-20 mm were used as shown in Figure 4-1. In addition, the concrete mix design was based on 5-10 mm coarse aggregate size and two different concrete mixes

with a grade of 40 MPa and 60 MPa were used in this experiment. The details of the concrete mix design are summarized in Table 4-1.

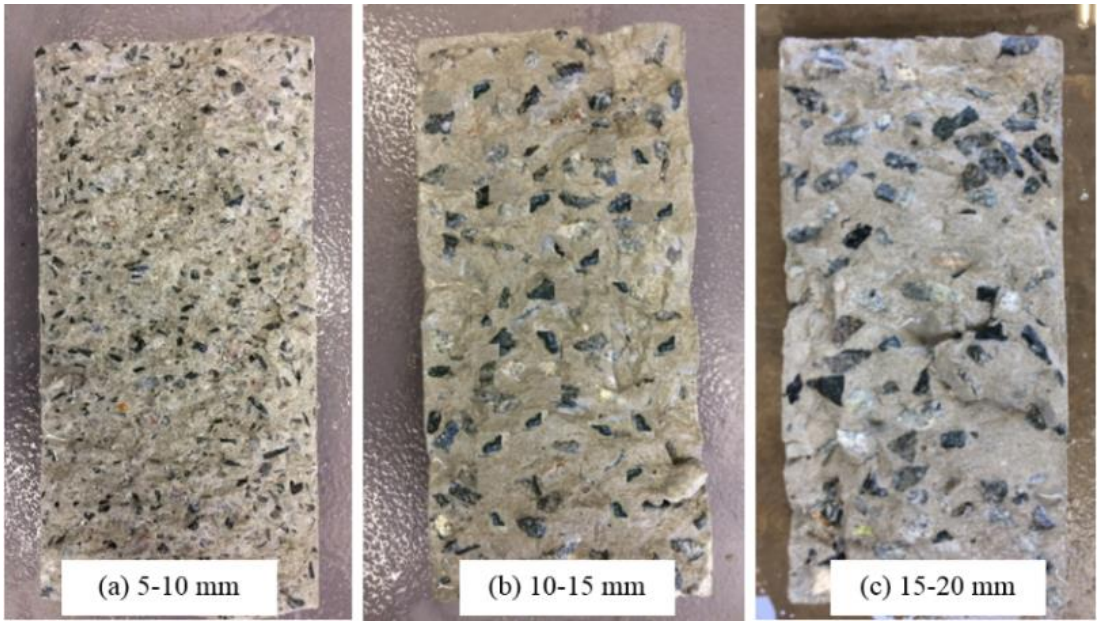

Figure 4-1. Concrete specimens with different coarse aggregate sizes after splitting tensile tests (a) 5-10 mm; (b) 10-15 mm; (c) 15-20 mm

***Table 4-1**. Concrete mix design*

Mix ID	Water/Cement (%)	Sand/Aggregate (%)	Unit weight (kg/m^3)				
			Water	Cement	Sand	Coarse aggregate	Superplasticizer
C40	50	50.4	204	408	876	863	2.04
C60	39.2	61.3	164	418	710	1158	2.04

In the tests, concrete prisms with 350 (*L*) x 150 (*H*) x 150 (*W*) mm as substrate were demolded 24 hours after casting and then cured in water tanks at room temperature for 28 days. The mechanical properties of concrete with different coarse aggregate sizes, including compressive strength f_c' and splitting tensile strength f_t were measured to study the effect of aggregate size on the bond behaviour. Three concrete cylinders with a diameter of 100 mm and a height of 200 mm from each batch were tested to obtain the compressive strength according to ASTM C39 (152). Three concrete cylinders with a diameter of 150 mm and a height of 300 mm were tested for the splitting tensile test according to ASTM C496 (153). The testing setups are shown in Figure 4-2 and the

mechanical properties of four groups of concrete specimens are summarized in Table 4-2. For material properties of BFRP sheet and epoxy resin, please refer to Chapter 3.2.1.

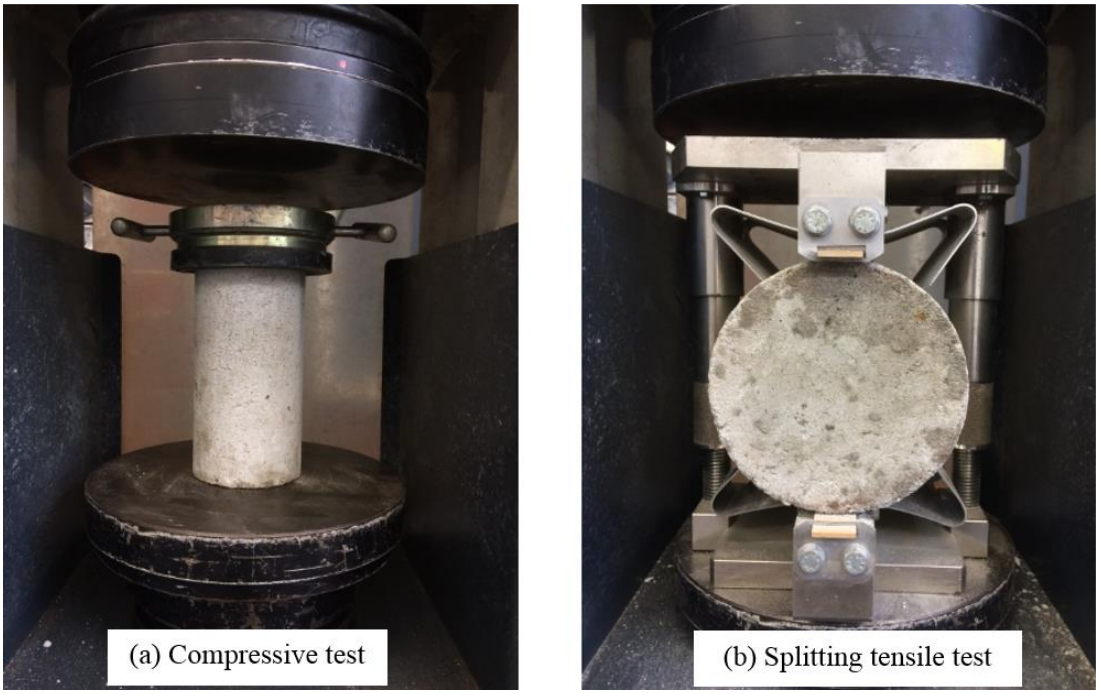

Figure 4-2. Test set-up for (a) compressive test; (b) splitting tensile test

Table 4-2. Mechanical properties of concrete substrates

Group ID	**Specimen ID**	**Aggregate size d_n (mm)**	**f_c' (MPa) Average**	**f_t (MPa) Average**
G1	C40_5-10 _1	5-10	39.68	4.64
	C40_5-10 _2		40.41	4.75
	C40_5-10 _3		40.01	4.89
G2	C40_10-15_1	10-15	44.00	4.23
	C40_10-15_2		43.04	4.19
	C40_10-15_3		43.09	4.31
G3	C40_15-20_1	15-20	45.06	3.49
	C40_15-20_2		45.66	3.63
	C40_15-20_3		46.01	3.58
G4	C60_5-10_1	5-10	50.60	4.98
	C60_5-10_2		50.98	5.07
	C60_5-10_3		50.79	5.10

4.1.1.2 Specimens details

A total of 12 specimens were tested in this section. The surface of all the specimens was roughened by a needle scaler to expose coarse aggregates. A manual lay-up procedure was conducted to bond the BFRP sheets onto the surface of concrete substrates. Two layers of BFRP sheets with a width of 40 mm were bonded with adhesive on one side of the concrete prism along the axial direction. All specimens had a bonded length of 200 mm, which was longer than the effective bond length estimated from the previous model (42). An unbonded length of 50 mm was reserved to eliminate the effect of the concrete edge during the loading process (154). The specimens were cured for 7 days in order to ensure the full hardening of epoxy.

Table 4-3. Summary of testing specimens and experimental results

Specimen ID	**Aggregate size d_n (mm)**	**Debonding load P_d (KN)**	**Peak bond stress τ_m (MPa)**	**Slip at peak bond stress s_o (mm)**	**Interfacial fracture energy G_f (N/mm)**
G1_C40_5-10_1		11.51	6.22	0.112	1.70
G1_C40_5-10_2	5-10	11.89	6.45	0.103	1.76
G1_C40_5-10_3		11.83	6.02	0.121	1.64
Mean		11.75	6.23	0.112	1.70
S.D.		0.208	0.215	0.009	0.060
G2_C40_10-15_1		11.27	5.41	0.118	1.69
G2_C40_10-15_2	10-15	11.02	4.78	0.131	1.49
G2_C40_10-15_3		10.65	5.06	0.125	1.58
Mean		10.98	5.08	0.125	1.59
S.D.		0.312	0.316	0.007	0.100
G3_C40_15-20_1		10.87	4.21	0.139	1.41
G3_C40_15-20_2	15-20	10.73	4.07	0.136	1.36
G3_C40_15-20_3		10.12	4.10	0.135	1.37
Mean		10.57	4.13	0.136	1.38
S.D.		0.398	0.446	0.006	0.140
G4_C60_5-10_1		12.96	6.65	0.091	1.64
G4_C60_5-10_2	5-10	12.85	6.61	0.086	1.62
G4_C60_5-10_3		12.80	6.51	0.107	1.65
Mean		12.87	6.59	0.094	1.64
S.D.		0.082	0.072	0.011	0.015

Table 4-3 gives the details and testing results of the 12 specimens. The specimen ID was assigned to each specimen as “GX_CY_d_n”. “GX” means the testing group from

G1 to G4, a totally of four testing groups in this section. “CY” refers to the grade of concrete, and C40 and C60 represent the concrete prisms with the compressive strength of 40 MPa and 60 MPa, respectively. The letter “d” refers to the size of coarse aggregate (e.g. d_n (5-10) means the aggregate size ranging 5-10 mm). The letter “*n*” represents the specimen number from 1 to 3 (three identical specimens for each configuration).

4.1.1.3 Testing setup

A camera together with a digital image correlation (DIC) technique was used to monitor the strain distribution of the BFRP sheets for all the tests. Three specimens were tested for each configuration to reduce the uncertainties of experimental results. For static testing machine and test set-up, please refer to Chapter 3.2.4.

4.1.2 Test results and discussions

4.1.2.1 Failure mode

Failure mode determines the performance and efficiency of the bonding between BFRP sheets and concrete. There was only one failure mode in this section, i.e. debonding failure in the concrete substrate, where a thin layer of concrete was attached to the BFRP sheets after debonding. In addition, the debonding failure initiated at the loaded end for all the specimens, which was consistent with the previous studies (39, 86). The typical debonding failure mode of the specimens after testing is shown in Figure 4-3. It was observed that the aggregate size had a limited effect on the failure for all the specimens. To examine the distribution of aggregates, the method of image thresholding was employed and the black area and the white region represent the aggregates and the mortar, respectively. It was observed that the small aggregate size (i.e. 5-10 mm) resulted in more uniform and denser distribution than that of large aggregate sizes. As shown in Figure 4-4 (a), small aggregates shown in black were attached to FRP after debonding. The pull-out of the small aggregates from the concrete matrix can be seen for specimen G1_C40_5-10_1. In contrast, more mortar is attached with BFRP sheets

for the specimen G3_C40_15-20_1 after debonding, as shown in Figure 4-4 (c). It was also observed that the specimens G3_C40_15-20 with the largest aggregates in the adhesive-concrete layer experienced a fracture of mortar with small amounts of aggregates.

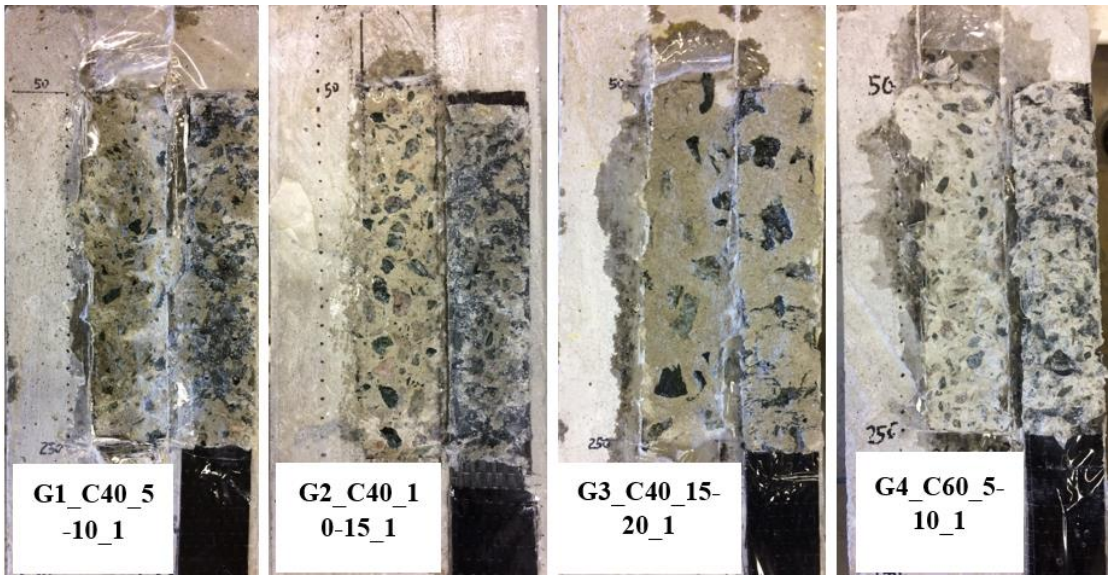

(a) G1_C40_5-10_1 (b) G2_C40_10-15_1 (c) G3_C40_15-20_1 (d)G4_C60_5-10_1

Figure 4-3. Failure modes of the specimens

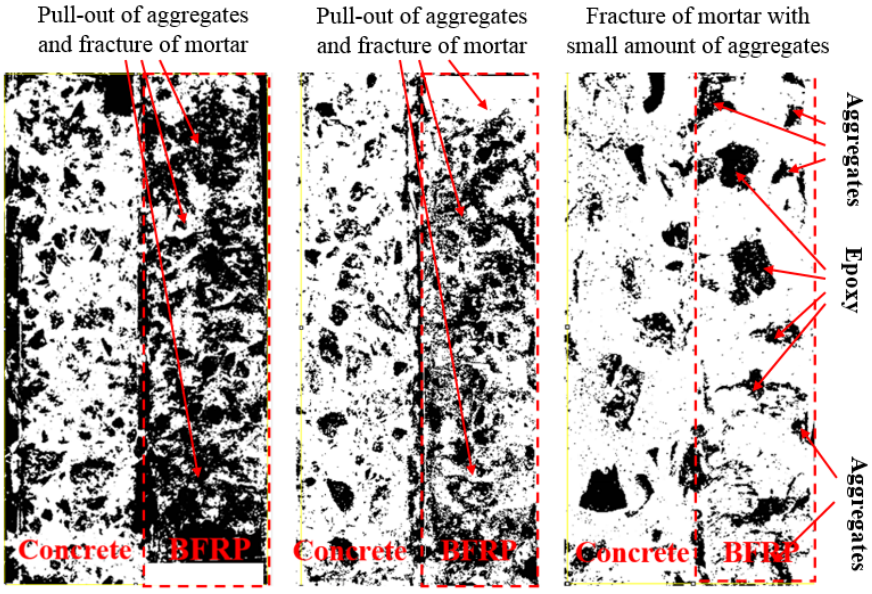

(a) d_n (5-10 mm) (b) d_n (10-15 mm) (c) d_n (15-20 mm)

Figure 4-4. Aggregate distributions (processed by image thresholding)

4.1.2.2 Load and displacement

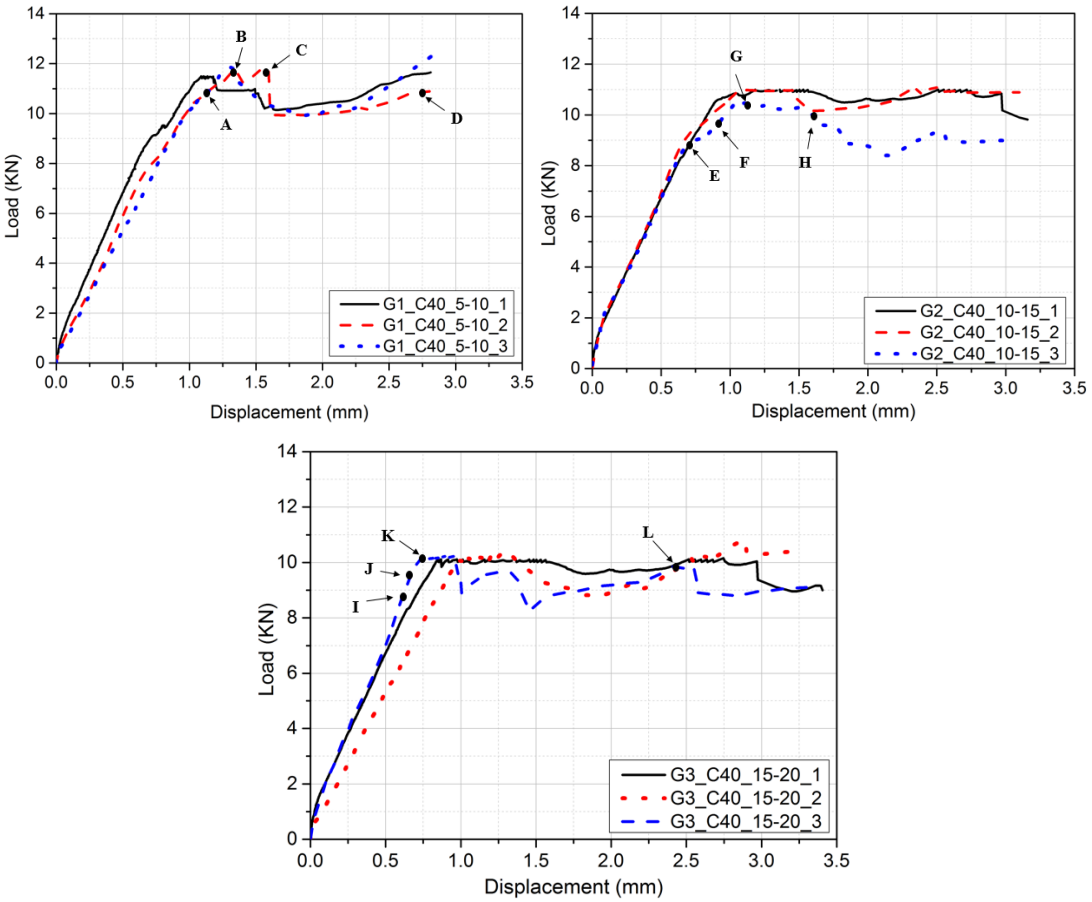

Figure 4-5. Debonding loads of concrete specimens (C40) with different coarse aggregate sizes (G1/G2/G3)

For the specimens with the same concrete mix but different coarse aggregate sizes, the load and displacement curves are plotted in Figure 4-5. It can be seen that the debonding loads reduced with the increase of the aggregate size. In addition, two different concrete grades of C40 and C60 with the same aggregate size 5-10 mm were prepared in this section. Figure 4-6 shows the testing results of the specimens with the same aggregate size but different concrete grades. The debonding load increased with the tensile strength, which is consistent with the previous studies (89, 155). The measured displacement includes the shear slip of the bonded part and the elongation of the unbonded part of the BFRP sheets (39). The average debonding loads for specimens G1_C40_5-10, G2_C40_10-15, and G3_C40_15-20 were 11.7 kN, 10.9 kN, and 10.3 kN, respectively. The debonding loads decreased slightly with the rising maximum

aggregate size, which indicates the aggregate size has effects on the interfacial bond strength. In addition, four different points were highlighted in the load-displacement curves for the specimens G1_C40_5-10_2, G2_C40_10-15_3, and G3_C40_15-20_3 in order to track the strain distributions and the interfacial shear stress distributions at different loading stages.

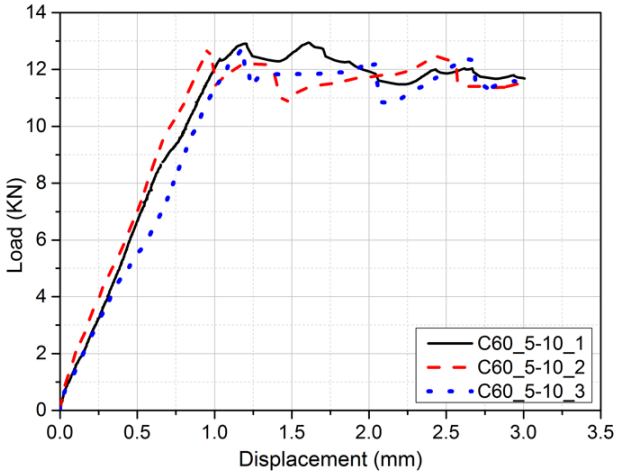

Figure 4-6. Debonding load of concrete specimens (C60) with aggregate sizes (5-10 mm)

In this section, the mass ratio of coarse aggregates over total weight was kept the same at approximately 40%. Figure 4-7 shows the relationship between the aggregate size and the aggregate interlocking action. For the specimens with smaller size aggregates, the spacing between each aggregate is small due to the fact that the small aggregates are distributed close to each other, which results in strong interlocking action. Meanwhile, for the specimens with larger aggregate size, more spaces between each aggregate result in relatively weak interlocking action. The interfacial shear interlocking is a major factor affecting the debonding failure of FRP as the aggregate interlocking action is very sensitive to the aggregate as reported in the previous study (52). Stronger interlocking action results in higher interfacial bond strength between FRP and concrete as higher fracture energy is required to develop cracks and pull-out of the coarse aggregates. In addition, the tensile strength of concrete is a key factor determining the interfacial bond strength of FRP-concrete as increasing aggregate size

leads to a lower tensile strength. This is because the increased surface area of large size aggregate results in an increased stress concentration and micro-cracks in the vicinity of the aggregates (156). The lower tensile strength of concrete results in weaker interfacial bond strength of FRP-concrete as the bond strength is proportional to the tensile strength of concrete (155).

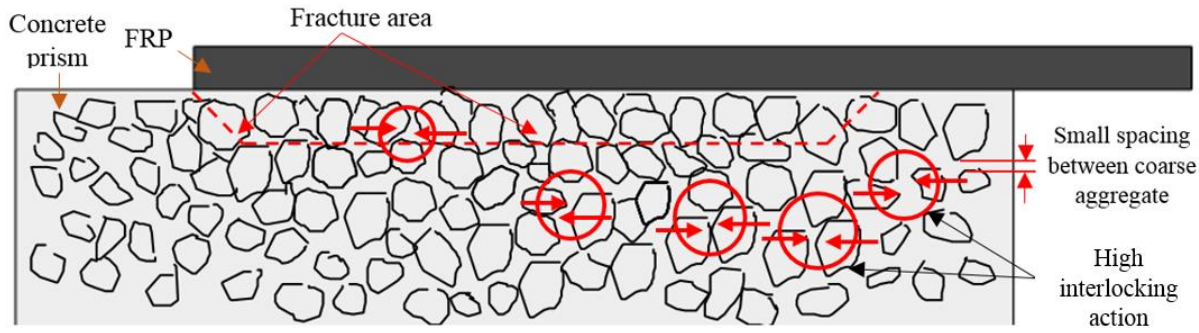

(a) Small aggregate size

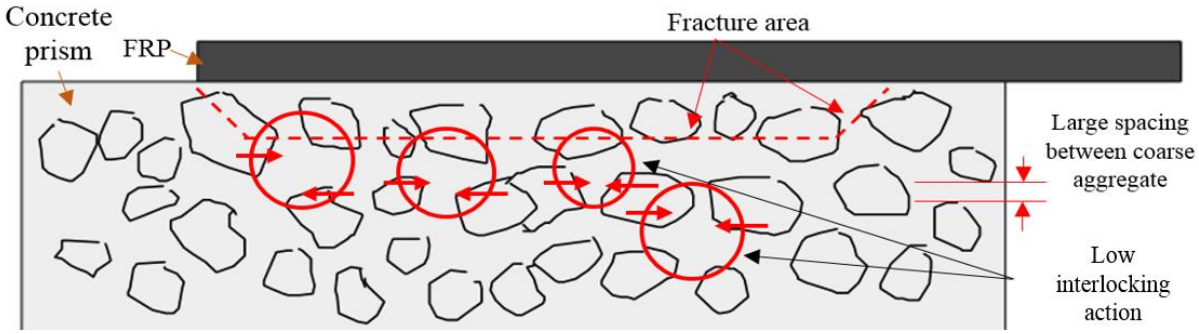

(b) Large aggregate size

Figure 4-7. Relationship between aggregate size and aggregate interlocking action

Figure 4-8 plots the typical load-displacement curve for shear bond tests. Theoretically, three stages exist before the complete debonding, i.e. elastic stage, softening stage, and debonding plateau. After reaching the elastic stage, microcracks initiate at the adhesive-concrete interface with the increase of shear slip (137). Debonding initiates at the loaded end when approaching the end of the softening stage. Then a plateau can be seen with the growth of the displacement, illustrating the gradual debonding process. The debonding plateau stage is mainly dominated by the bond length of the BFRP sheets, a longer debonding plateau can be found when using a longer bond length of FRP as

reported in the previous study (86). In this section, a bond length of 200 mm was used and it is long enough to develop the debonding plateau (41).

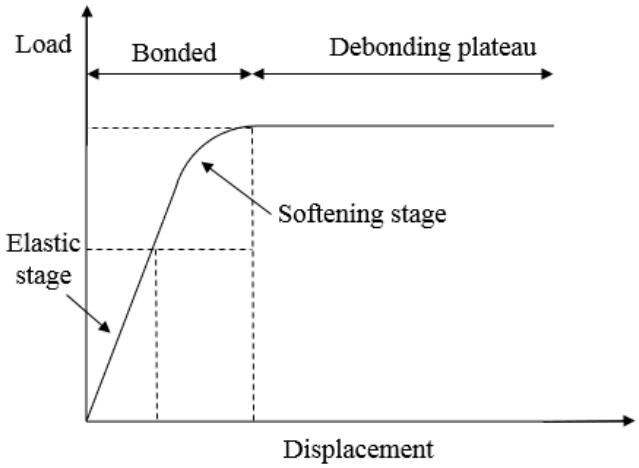

Figure 4-8. Typical load versus displacement curve with enough bond length (142)

4.1.2.3 Strain distribution

The strain distributions of all the specimens are shown in Figure 4-9. The strain derived from DIC has been compared with the results from strain gauges. It can be observed that there was a significant spatial variation in the axial strain along the surface of BFRP sheets. The fluctuations in the measured surface strain were induced by the local material variations and the material in-homogeneities due to the non-uniform distributions of resin and the varied thickness of FRP sheets (145, 148, 157). To eliminate the influence of the local material variations, a nonlinear regression analysis can be performed by using Equation (4-1) (148) to fit the strain:

$$\varepsilon(x) = a + \frac{b}{1+(\frac{x}{x_o})^c} \quad (4\text{-}1)$$

where a, b, c, and x_o are the coefficients to be obtained from testing results and x is the distance from the loaded end. The original DIC strain distributions and the fitted strain distributions are shown in Figure 4-9. It is noted that FRP strain derived from the DIC technique was verified against those directly measured by strain gauges with very high

accuracy and this technique was also successfully used in the previous studies (145, 148, 158). Each curve refers to the strain distribution along with the FRP sheets at a particular load stage. The strain distribution presents a descending curve from the loaded end toward the free end of the BFRP sheet as indicated in Figure 4-9. The strain firstly increased with the rising applied load. After the initiation of debonding at the loaded end, a strain plateau can be found in the graphs, illustrating the stress transfer zone (145, 157).

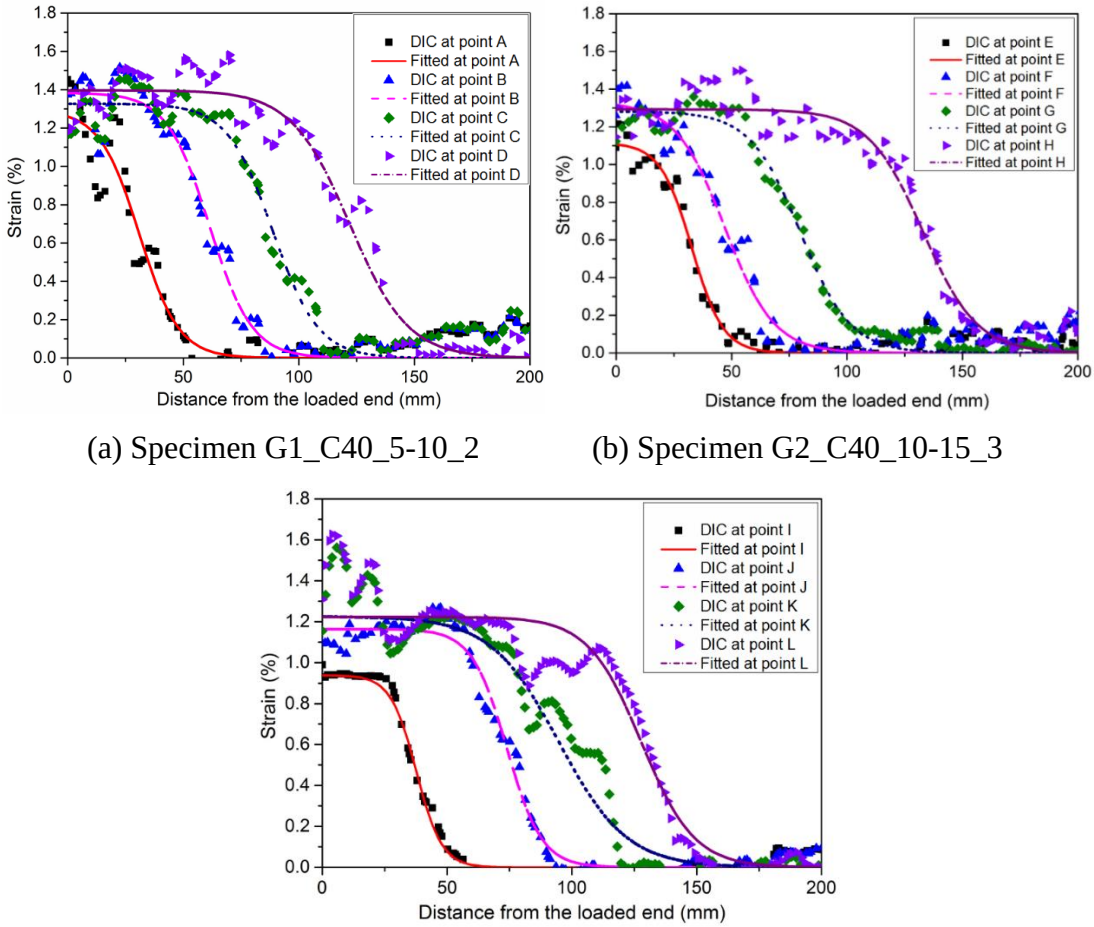

(a) Specimen G1_C40_5-10_2 (b) Specimen G2_C40_10-15_3

(c) Specimen G3_C40_15-20_3

Figure 4-9. Strain distributions at different loading stages

Figure 4-9 shows that the peak strain decreases with the increase of the aggregate size. The ultimate strain for specimens G1_C40_5-10_2, G2_C40_10-15_2, and G3_C40_15-20_3 were 1.40%, 1.29%, and 1.22%, respectively. This meant that the

aggregate size had a significant effect on the BFRP strain within the bonded region. After the softening stage, more micro-cracks were accumulated to form a destruction crack within the layer of adhesive-concrete. Due to the action of aggregate interlocking, the BFRP sheets continued to resist the shear force. The specimens with smaller aggregate sizes possessed higher fracture energy due to the stronger interlocking action. The specimens G1_C40_5-10 had the largest strain among the three groups. It is because the larger shear force resulted in larger deformation of the BFRP sheets with the same stiffness.

4.1.2.4 Bond stress and local slip calculation

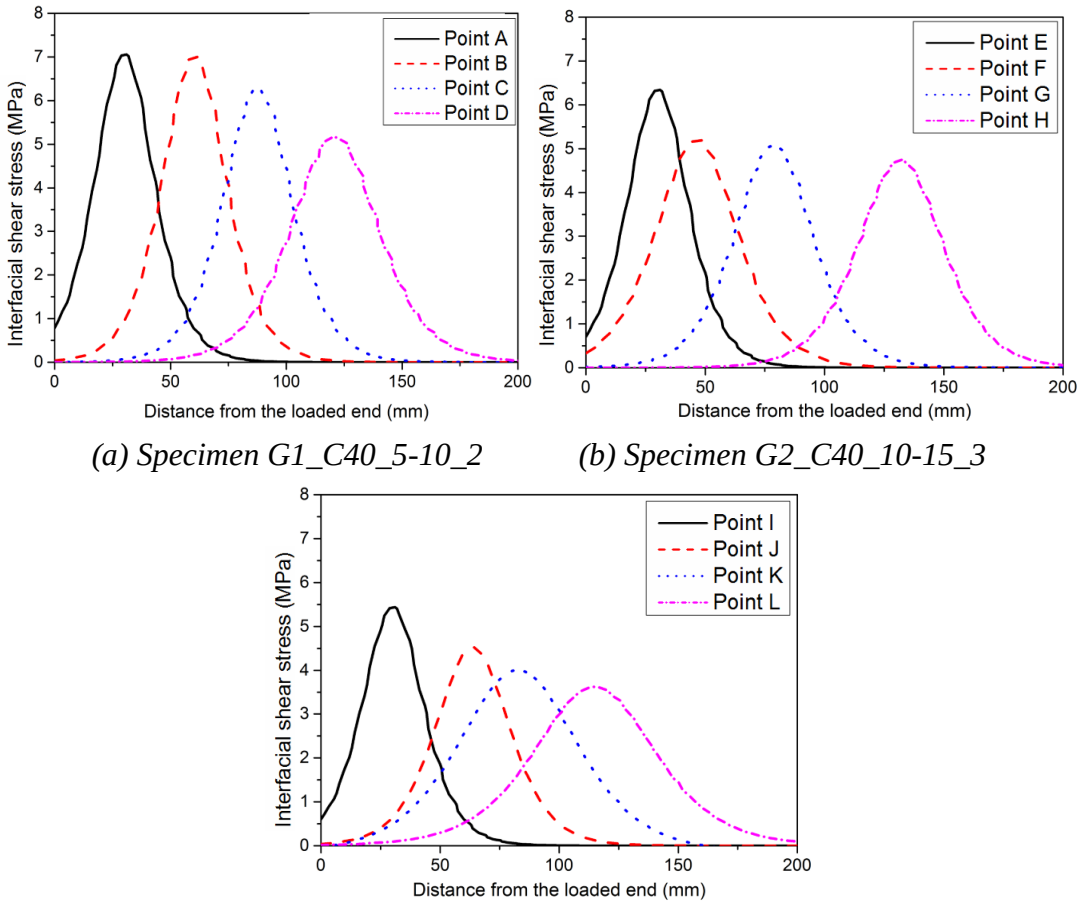

(a) Specimen G1_C40_5-10_2 *(b) Specimen G2_C40_10-15_3*

(c) Specimen G3_C40_15-20_3

Figure 4-10. Interfacial shear stress distribution at different loading stages

The interfacial shear stress distribution along the bonded length reflects the stress development and stress transfer in the interface between BFRP sheets and concrete. The

bond-slip laws in the longitudinal direction can be obtained from the FRP strain by using Equation (4-2). The interfacial shear stress distribution within the bond length can be evaluated by imposing the equilibrium condition of an FRP sheet with a length *dx* bonded to concrete (147, 159), as:

$$\tau(x) = t_f E_f \frac{d\varepsilon_f}{dx} \tag{4-2}$$

where τ is the interfacial shear stress, $\frac{d\varepsilon_f}{dx}$ is the gradient of FRP strain along the bonded length, t_f is the FRP thickness, and E_f is the FRP elastic modulus.

In addition, the local slip between FRP sheet and concrete at distance *x* from the free end of the specimen can be calculated by assuming a zero slip at the free end as (147):

$$s(x) = \int_0^{\infty} \varepsilon_f dx \tag{4-3}$$

The fitted strain distribution measured from the DIC technique can provide consecutive values, which can reduce the data intervals. This is beneficial for the accuracy of the interfacial shear stress and local slip. Figure 4-10 shows the interfacial shear stress distributions along the length of the BFRP sheets at different loading stages. The interfacial shear stress distributions for all the specimens were similar to the specimens with different sizes of aggregates exhibited the same shapes. As the applied load increased, the maximum interfacial shear stress moved along the BFRP sheets from the loaded end, which implied debonding crack propagation. Theoretically, the interfacial shear stress should be constant during the loading process while the experimental results presented stress fluctuations, as also observed by previous studies (40, 86). The possible reason is that the length of the interfacial shear stress transfer zone increased during the loading process, which can be evidenced by the interfacial shear stress distributions in Figure 4-10. It should be noted that the transfer zone of interfacial shear stress can be defined from the interfacial shear stress distributions (41).

The peak shear stress (τ_m) for all the specimens is summarized in Table 4-3. The results indicate that the aggregate size has significant influences on the interfacial shear stress. The shear stress decreased with the increasing aggregate size. For the specimens G1_C40_5-10, G2_C40_10-15, and G3_C40_15-20, the average values of the shear stress were 6.23 MPa, 5.08 MPa, and 4.77 MPa, respectively. These shear stresses of specimens G2_C40_10-15 and G3_C40_15-20 result in a reduction of 18% and 23% when respectively compared to specimens G1_C40_5-10. The tensile strength of concrete should be a key factor governing the interfacial bond of the FRP-concrete interface as debonding occurred inside the concrete layer in this section. The tensile strength of the concrete substrates decreases with increasing the aggregate size (156). As can be seen that increasing the aggregate size leads to a reduction in the interfacial shear stress. This observation is reasonable since using larger aggregates leads to a reduction in the tensile concrete strength and thus the interfacial shear stress.

4.1.2.5 Effective bond length

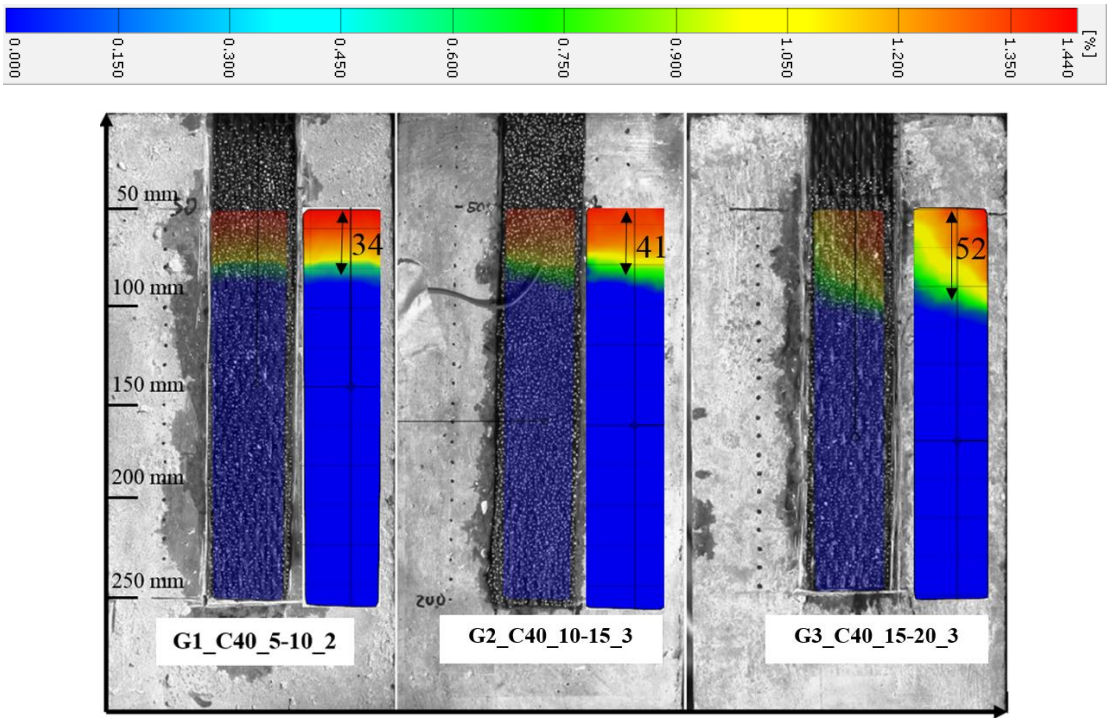

Figure 4-11. Effective bond length derived from DIC strain distributions

Effective bond length is the bond length beyond which no further increase in the ultimate load can be achieved (9). This can be evidenced by the load and displacement curves as well as the debonding plateau after the initial debonding load. An active bond zone exists at any stage of loading and over which interfacial shear stresses are transferred from the fibre sheet to the concrete, which is consistent with the finding in the previous studies (144, 160). In this section, the effective bond length can be extracted from the strain distributions as it is defined through the strain distributions where the effective bond length is the length required for the strain to vanish (144, 161).

The length of the active zone at debonding loads can be evaluated using longitudinal strain fields of the BFRP sheets obtained from the DIC analysis as shown in Figure 4-11. Successive digital images were captured and analysed using the DIC technique, and a longitudinal strain field corresponding to each load level was derived. As can be seen from the figure that the effective bond length increased with the aggregate size. The effective bond lengths for specimens G1_C40_5-10_2, G2_C40_10-15_3, and G3_C40_15-20_3 were 34 mm, 41 mm, and 52 mm, respectively. The average effective bond length for groups G1_C40_5-10, G2_C40_10-15, and G3_C40_15-20 was 37 mm, 45 mm, and 54 mm, respectively. The effective bond length increased with the aggregate size while it is inversely proportional to the tensile strength of concrete (89). This statement is reasonable because using larger aggregates leads to a reduction of the tensile strength of concrete and thus results in longer effective bond length. In addition, as observed from the strain contours of Figure 4-11, the strain distribution of the specimen G3_C40_15-20_3 was not uniform as compared with G1_C40_5-10_2. This is because the large aggregates in the adhesive-concrete layer are not placed uniformly and closely with each other as compared with the small aggregates. In addition, the interfacial shear stress for the interface of FRP-aggregate and FRP-mortar is different, which results in non-uniform strain distributions in the bonded area. This variation

became more prominent with specimens G3_C40_15-20 with 15-20 mm large aggregates.

4.1.3 Theoretical predictions and proposed models

4.1.3.1 Mechanical properties of concrete with various aggregate sizes

To investigate the bond behaviour between FRP and concrete, the tensile strength of concrete considering the aggregate size effect needs to be determined. In addition, the tensile strength of concrete can be estimated from its compressive strength. As a result, this section proposes new empirical equations to predict the compressive and tensile strengths of concrete in which the effect of the aggregate size is taken into consideration. As shown in Figure 4-12, the compressive strength increases while the tensile strength decreases with increasing the aggregate size. The results are consistent with the previous study (156). This is because larger aggregates result in an increased interfacial transition zone (ITZ) and increases of micro-cracks in the vicinity of the aggregate. In addition, larger aggregates result in poor bond zone inside concrete due to internal bleeding (156, 162). Based on Bazant's law of size effect (163) and the calibrated model by Kim et al. (164), Jiang and Wu (51) proposed a model to predict the unconfined concrete uniaxial strength by considering the aggregate size effect:

$$f_c = f_c^{'} \cdot \delta(d_{max}, h, {d_a}^{\mathrm{m}}) \tag{4-4}$$

$$\delta(d_{max}, h, {d_a}^{\mathrm{m}}) = \alpha + \frac{B}{\sqrt{1 + \frac{d_{max}}{\lambda_o {d_a}^m}(h/d - \beta)}} \tag{4-5}$$

Where $f_c^{'}$ is the strength of concrete specimen of standard size, f_c is the actual strength of concrete specimen considering the size effect, h and d are the height and diameter of specimens, respectively, d_{max} is the maximum aggregate size of concrete, ${d_a}^m \approx 1$based on the regression results of Kim et al. (164), α, B, λ_o, m, and β are the coefficients which can be determined by the regression of testing results. It should be noted that the height

and diameter of the concrete cylinder in this section are h = 200 mm and d = 100 mm, respectively. The compressive strength of concrete considering the aggregate size can be expressed as follows:

$$f_c = \alpha f_c' + \frac{B f_c'}{\sqrt{1 + \frac{d_{max}}{\lambda_o}(\frac{h}{d} - \beta)}} \quad (4\text{-}6)$$

Based on the standards ACI 318-08 (21) and CEB-FIB (165), the splitting tensile strength of concrete can be correlated with compressive strength by the following equation:

$$f_t = \varphi(f_c)^c \quad (4\text{-}7)$$

where f_t (MPa) is the predicted splitting tensile strength of concrete, f_c (MPa) is the predicted compressive strength of concrete, f_c' is the designed compressive strength that was 40 MPa in this section, and d_{max} (mm) is the maximum aggregate size. With the regression analysis, coefficients α = 1.568, B = -1.136, λ_o = 1.933, and β = 1.415 can be obtained in this section.

Equations (4-8) and (4-9) can be used to describe the relationship between the concrete strength and the maximum aggregate size. As shown in Figure 4-12, the predicted compressive strength and splitting tensile strength show good agreement with the experimental results.

$$f_c = 1.568 f_c' - \frac{1.136 f_c'}{\sqrt{1 + \frac{d_{max}}{1.933}(\frac{h}{d} - 1.415)}} \quad (4\text{-}8)$$

$$f_t = 7845(f_c)^{-2.006} \quad (4\text{-}9)$$

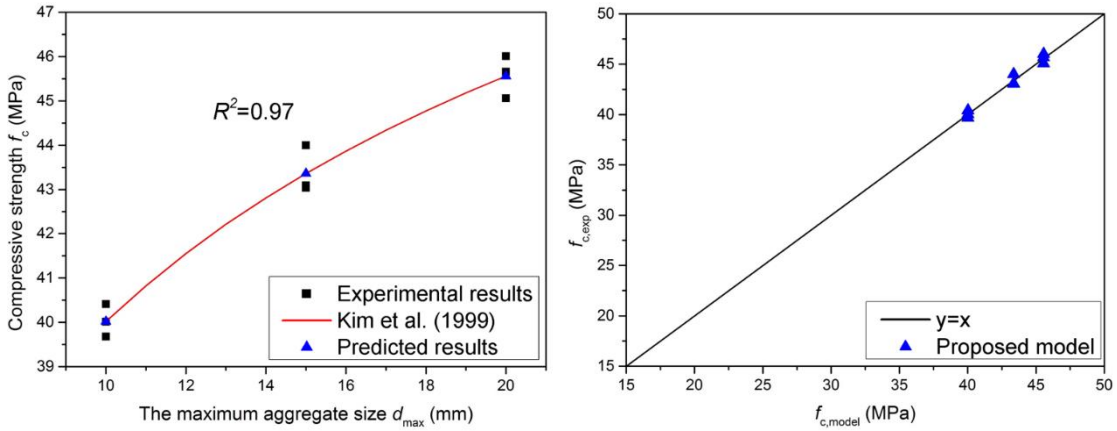

(a) Compressive strength

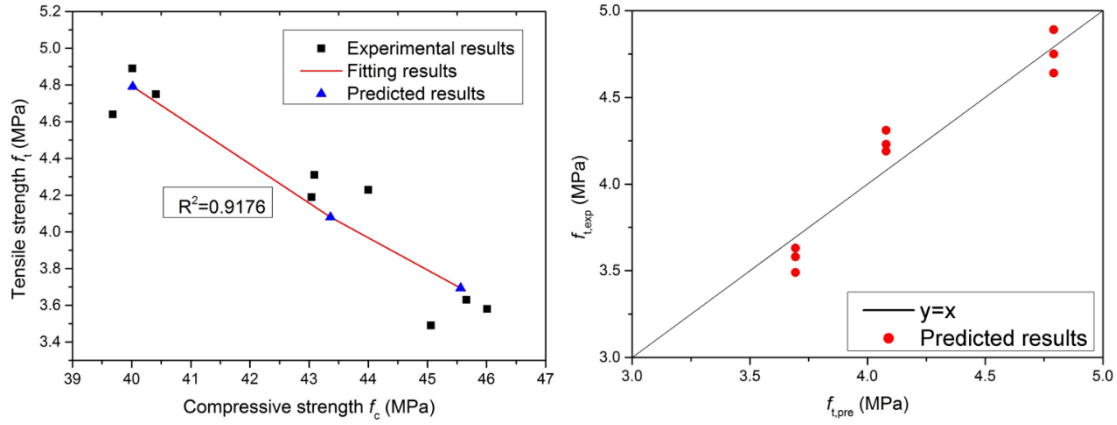

(b) Splitting tensile strength

Figure 4-12. Predicted and experimental results of (a) compressive strength; (b) splitting tensile strength

4.1.3.2 Interfacial bond strength

In order to predict the ultimate debonding load between FRP and concrete, numerous studies have been conducted to develop bond strength models based on empirical data and the theory of fracture mechanics. The bond strength can be calculated from the FRP stiffness and interfacial fracture energy. As the same BFRP sheet has been used in this section, the bond strength is mainly dominated by interfacial fracture energy. In this section, the bond length of BFRP sheets was 200 mm, which was long enough to develop the effective bond length (41). This is evident by the debonding plateau in the load versus displacement curves. Based on the fracture mechanics, two models from CNR DT-200 (150) and Lu et al. (89) are employed to predict the interfacial fracture

energy and the predicted results are presented in Table 4-4. CNR DT-200 (150) presented a formula to calculate the fracture energy of the FRP-concrete interface, which can be described as:

$$G_f = k_G k_b \sqrt{f_c' f_t} \tag{4-10}$$

where G_f (N/mm) is the interfacial fracture energy, f_c' is the cylinder axial compressive strength of concrete, f_t is the tensile strength of concrete, k_G is the fracture energy coefficient with an average value of 0.064, and k_b is a geometrical factor, which can be expressed as,

$$k_b = \sqrt{\frac{2 - b_f / b_c}{1 + b_f / b_c}} \tag{4-11}$$

Lu et al. (89) also provided the following formula for calculating the interfacial fracture energy, as:

$$G_f = 0.308 \beta_w^{\ 2} \sqrt{f_t} \tag{4-12}$$

$$\beta_w = \sqrt{\frac{2.25 - b_f / b_c}{1.25 + b_f / b_c}} \tag{4-13}$$

where f_t is the tensile strength of concrete, b_f and b_c are the width of FRP and concrete, respectively, and β_w is the width ratio between FRP and concrete.

As can be seen from Table 4-4, the two models above cannot predict well the interfacial fracture energy of concrete with varying aggregate sizes. This is because the aggregate size is not a parameter in both the models and different factors, such as workmanship and different materials utilized in the testing, affect the testing results. Both models provided a general prediction on the interfacial fracture energy for FRP-strengthened concrete. Due to the limited testing data, this section mainly uses these empirical models to achieve more accurate prediction results. In this section, the debonding loads

decreased with rising the maximum aggregate size. The CNR DT-200 (150) model considers both compressive strength and tensile strength of concrete. The calculated interfacial fracture energy underestimates the experimental results. Therefore, CNR DT-200 (150) model cannot accurately predict the interfacial fracture energy. Based on the existing interfacial fracture energy models in the literature, it can be found that the interfacial fracture energy (G_f) correlates well with the tensile strength (f_t) of concrete and the width ratio (β_w) between FRP and concrete. In this section, Lu et al. (89) model was recalibrated to predict the experimental results. The interfacial fracture energy can be described by the function of f_t^d and β_w^2 (89), as given in Equation (4-14). Two coefficients γ and d can be obtained through a fitting procedure based on the testing data.

$$G_f = \gamma \beta_w^{\,2} f_t^{\,d} \tag{4-14}$$

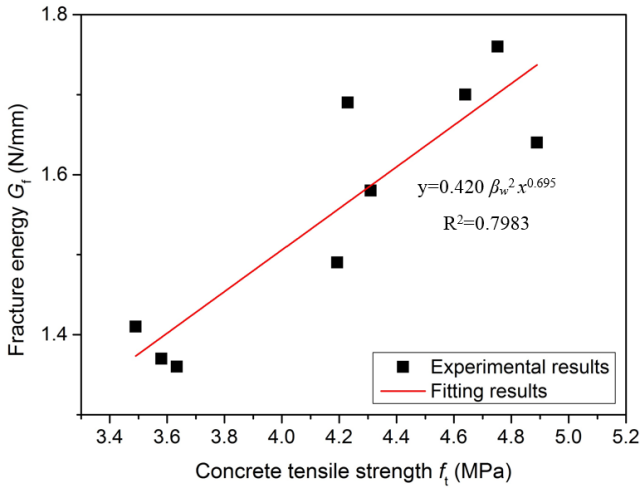

Figure 4-13. Fitted results of coefficient γ and d

After fitting analysis of the testing results, two coefficients γ and d are determined as 0.420 and 0.695, respectively, as shown in Figure 4-13. β_w is the width ratio between FRP and concrete which can be calculated by Equation (4-13). In addition, Equation (4-15) can be used to predict the interfacial fracture energy in consideration of the

maximum aggregate size. Also, the mean value of the predictions based on the proposed model provides acceptable accuracy, as given in Table 4-4.

$$G_f = 0.420\beta_w{}^2 f_t^{0.695} \tag{4-15}$$

Table 4-4. Comparison of the predicted fracture energy

Specimen ID	**Aggregate size d_n (mm)**	**Fracture energy $G_{f,\exp}$ (N/mm)**	**Predicted fracture energy**		**Proposed model Eq. (4-15)**	
			Eq. (4-10)	**Eq. (4-12)**	$G_{f,pre}$	$\frac{G_{f,pre}}{G_{f,\exp}}$
G1_C40_5-10_1		1.70	1.016	0.785		0.985
G1_C40_5-10_2	5-10	1.76	1.038	0.794	1.675	0.952
G1_C40_5-10_3		1.64	1.047	0.806		1.021
G2_C40_10-15_1		1.69	1.021	0.750		0.911
G2_C40_10-15_2	10-15	1.49	1.006	0.746	1.539	1.033
G2_C40_10-15_3		1.58	1.020	0.757		0.974
G3_C40_15-20_1		1.41	0.939	0.681		0.992
G3_C40_15-20_2	15-20	1.36	0.964	0.695	1.398	1.028
G3_C40_15-20_3		1.37	0.961	0.690		1.021
Mean						0.991
S.D.						0.041

Note: $G_{f,exp}$ is the experimental fracture energy; $G_{f,pre}$ is the predicted fracture energy.

The calibrated bond strength model is employed to calculate the debonding loads. Fracture energy obtained by Equation (4-15) was substituted into Equation (4-16) to predict the debonding loads, as given in Table 4-5. A calibration factor η = 1.212 was introduced herein to consider the effect of the maximum aggregate size.

$$P = \eta b_f \sqrt{2E_f t_f G_f} \tag{4-16}$$

Table 4-5. Comparison of theoretical and experimental debonding load (P)

Specimen ID	$G_{f,pre}$ **(N/mm)**	P_{exp} **(kN)**	P_{pre} **(kN)**	P_{pre}/P_{exp}
G1_C40_5-10_1		11.51		1.006
G1_C40_5-10_2	1.675	11.90	11.58	0.973
G1_C40_5-10_3		11.83		0.979
G2_C40_10-15_1		11.27		0.985
G2_C40_10-15_2	1.539	11.02	11.10	1.008
G2_C40_10-15_3		10.65		1.043
G3_C40_15-20_1		10.87		0.974
G3_C40_15-20_2	1.398	10.73	10.58	0.986
G3_C40_15-20_3		10.12		1.046
Mean				1.001
S.D.				0.028

Note: P_{exp} is the experimental debonding load; P_{pre} is the predicted debonding load.

Figure 4-14 shows the experimental and predicted debonding loads. The points (i.e. red, blue, and pink) located above the baseline ($y=x$) indicate the under-predictions of the debonding load. The proposed model fits very well with the experimental results as the correlation coefficient R^2 is 0.891 and the mean value P_{pre}/P_{exp} is 1.001 (S.D. = 0.028).

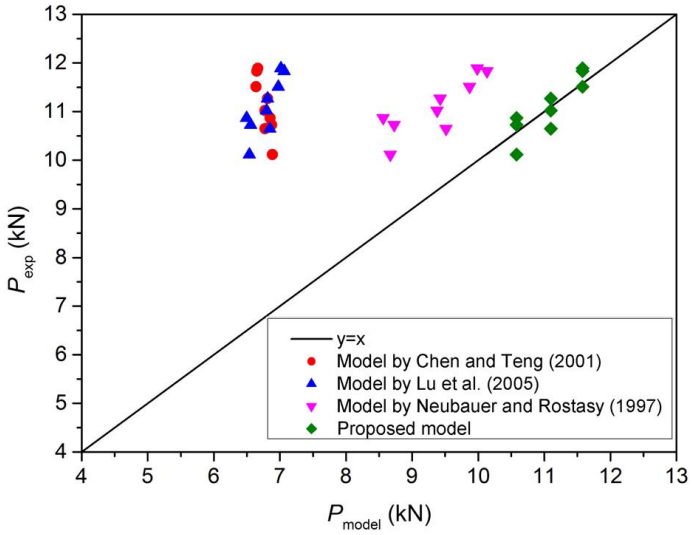

Figure 4-14. Experimental versus predicted debonding loads

4.1.3.3 Peak interfacial shear stress

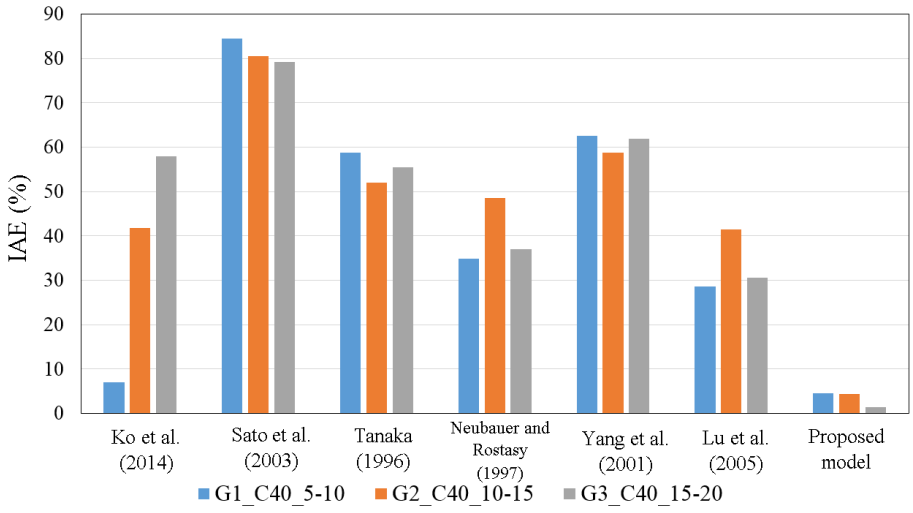

Figure 4-15. IAE of the peak shear stress

Many analytical models have been developed to predict the interfacial shear stress between FRP and concrete. Six interfacial shear stress models are considered in this section to compare their predictions with the experimental data, as shown in Figure 4-15. The integral absolute error (IAE), which has been often used for model assessments, is employed herein to evaluate the accuracy of the existing models of peak interfacial shear stress, as presented in Equation (4-17) (35, 41, 166).

$$IAE = \sum \frac{|Expe. - Theo.|}{|Expe.|} \tag{4-17}$$

where *Expe*. and *Theo*. are the experimental and theoretical results, respectively.

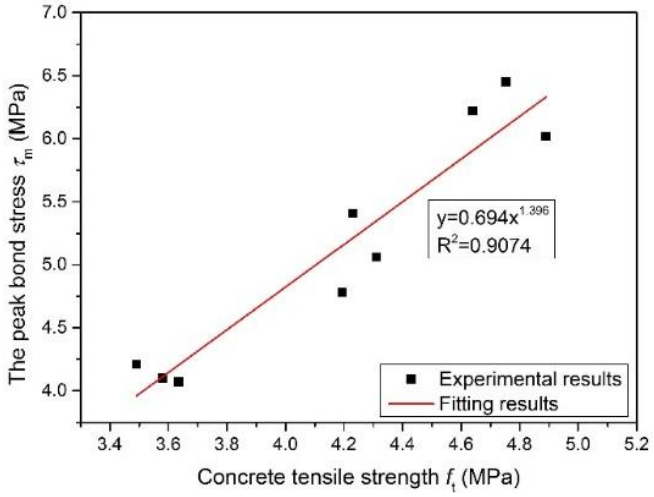

Figure 4-16. Fitted results of coefficient k and e

The higher IAE value indicates that the theoretical model cannot well predict the interfacial shear stress. The predicted results obtained by Ko et al. (167) and Sato et al. (168) are based on the compressive strength of concrete with higher IAEs. The predicted results obtained by Tanaka (169), Neubauer and Rostasy (170), Yang et al. (171), and Lu et al. (89) are based on the tensile strength of concrete. Among these models, the model by Lu et al. (89) can generate the most accurate predictions due to the lowest mean value of IAE. Based on the existing bond stress models, the interfacial shear stress can be described by the function of β_w and f_t^c (89), as given in Equation

(4-18). The coefficients *k* and *e* determined from the fitting analysis are 0.694 and 1.396, respectively, as shown in Figure 4-16.

$$\tau_m = \kappa \beta_w f_t^e \tag{4-18}$$

The predicted peak shear stress obtained from Equation (4-19) matches well with the experimental results as its mean value is 0.982 (S.D. = 0.042), as given in Table 4-6. The predicted interfacial shear stress decreases with the increase of the maximum aggregate size, which is evidenced by the experimental results.

$$\tau_m = 0.606 \beta_w f_t^{1.396} \tag{4-19}$$

Table 4-6. Comparison of theoretical and experimental peak bond stress (τ_m)

Specimen ID	**Maximum aggregate size d_{max} (mm)**	**Peak bond stress $\tau_{m,exp}$ (MPa)**	**Calibrated model**	
			τ_{mprep}	$\frac{\tau_{m,pre}}{\tau_{m,\exp}}$
G1_C40_5-10_1		6.22		0.955
G1_C40_5-10_2	10	6.45	5.94	0.921
G1_C40_5-10_3		6.02		0.987
G2_C40_10-15_1		5.41		0.927
G2_C40_10-15_2	15	4.78	5.01	1.049
G2_C40_10-15_3		5.06		0.991
G3_C40_15-20_1		4.21		0.982
G3_C40_15-20_2	20	4.07	4.13	1.016
G3_C40_15-20_3		4.10		1.008
Mean				0.982
S.D.				0.042

Note: $\tau_{m,exp}$ is the experimental peak shear stress; $\tau_{m,pre}$ is the predicted peak shear stress.

4.1.3.4 Slip at peak shear stress

The slip s_o is the relative displacement between FRP sheet and concrete at the peak interfacial shear stress, which is an important parameter for analyzing shear softening in the debonded zone. Numerous bond-slip models have been developed in the literature (35, 89, 90, 142). There are two branches existing in these models, namely the ascending branch and the descending branch, respectively. During the elastic stage and softening stage, the stress keeps increasing to peak stress (τ_m). Debonding stage initiates

in the concrete layer with increasing the shear slip. In the existing bond-slip models, the slip s_o can be predicted by the equations in Table 4-7.

Table 4-7. The slip at the peak interfacial shear stress (s_o) and its IAE

References	Equation	Factors	Theoretical results (MPa)	IAE (%)
Nakaba et al. (91)	0.065	N/A	G1: 0.065	41.71
			G2: 0.065	47.77
			G3: 0.065	52.43
Mean				47.30
Neubauer and Rostasy (170)	$s_o = 0.202\beta_w$	β_w	G1: 0.269	141.17
			G2: 0.269	116.13
			G3: 0.269	96.82
Mean				118.04
Lu et al. (89)	$s_o = 0.0195\beta_w f_t$	f_t , β_w	G1: 0.104	6.19
			G2: 0.093	22.19
			G3: 0.081	40.43
Mean				22.93
Sun et al. (142)	$s_o = 0.016 - 0.0046\beta_w f_t + 0.11\beta_w$	f_t , β_w	G1: 0.121	8.65
			G2: 0.123	4.02
			G3: 0.126	7.26
Mean				6.64

Note: β_w is the width ratio factor between FRP and concrete; f_t is the axial tensile strength of concrete.

The accuracy of each analytical model is evaluated by comparing the experimental results with the predicted results. The predicted slip by using the previous models by Nakaba et al. (91) and Neubauer and Rostasy (170) is a constant value, which is different from the testing results. The model proposed by Lu et al. (89) shows a higher IAE as compared with the model by Sun et al. (142). The model developed by Sun et al. (142) is the most accurate due to its lowest IAE. Based on the analytical models and the experimental results, the slip s_o is affected by the width ratio factor (β_w) and the tensile strength of concrete (f_t). Calibration is conducted to predict the slip at the peak bond stress based on the model developed by Sun et al. (142).

$$s_o = \omega - \zeta\beta_w f_t + \theta\beta_w \tag{4-20}$$

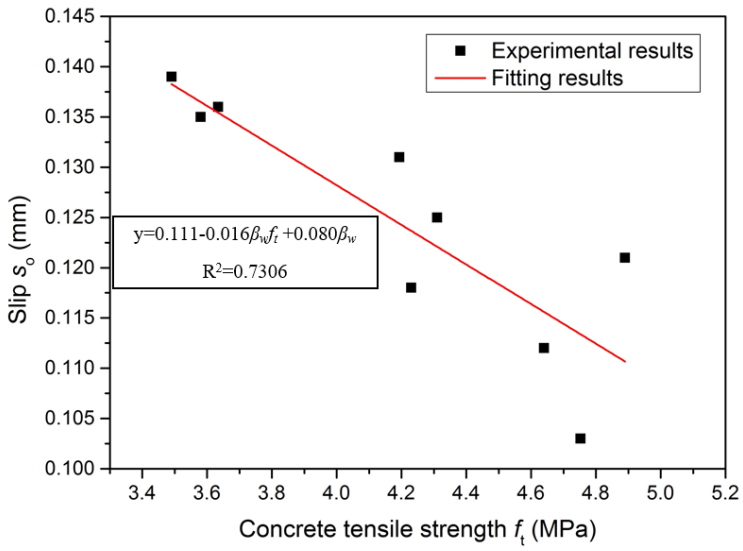

Figure 4-17. Fitting results of coefficients

As can be seen from Figure 4-17, the coefficients ω, ξ and θ can be obtained by the regression analysis. Based on Equation (4-21), the analytical slip at the peak shear stress presents good matches with the experimental results by giving the mean value of 1.029 (S.D. = 0.055), as given in Table 4-8.

$$s_o = 0.111 - 0.016\beta_w f_t + 0.080\beta_w \quad (4\text{-}21)$$

Table 4-8. Comparisons of the predicted slip at the peak bond stress

Specimen ID	**Maximum aggregate size d_{max} (mm)**	**Slip at peak bond stress s_o (mm) Exp.**	**Calibrated model** $S_{o,pre}$	$\frac{S_{o,pre}}{S_{o,\exp}}$
G1_C40_5-10_1		0.112		1.049
G1_C40_5-10_2	10	0.103	0.118	1.141
G1_C40_5-10_3		0.121		0.971
G2_C40_10-15_1		0.118		1.082
G2_C40_10-15_2	15	0.131	0.128	0.974
G2_C40_10-15_3		0.125		1.021
G3_C40_15-20_1		0.139		0.991
G3_C40_15-20_2	20	0.136	0.138	1.013
G3_C40_15-20_3		0.135		1.020
Mean				1.029
S.D.				0.055

4.1.3.5 Interfacial bond-slip relationship

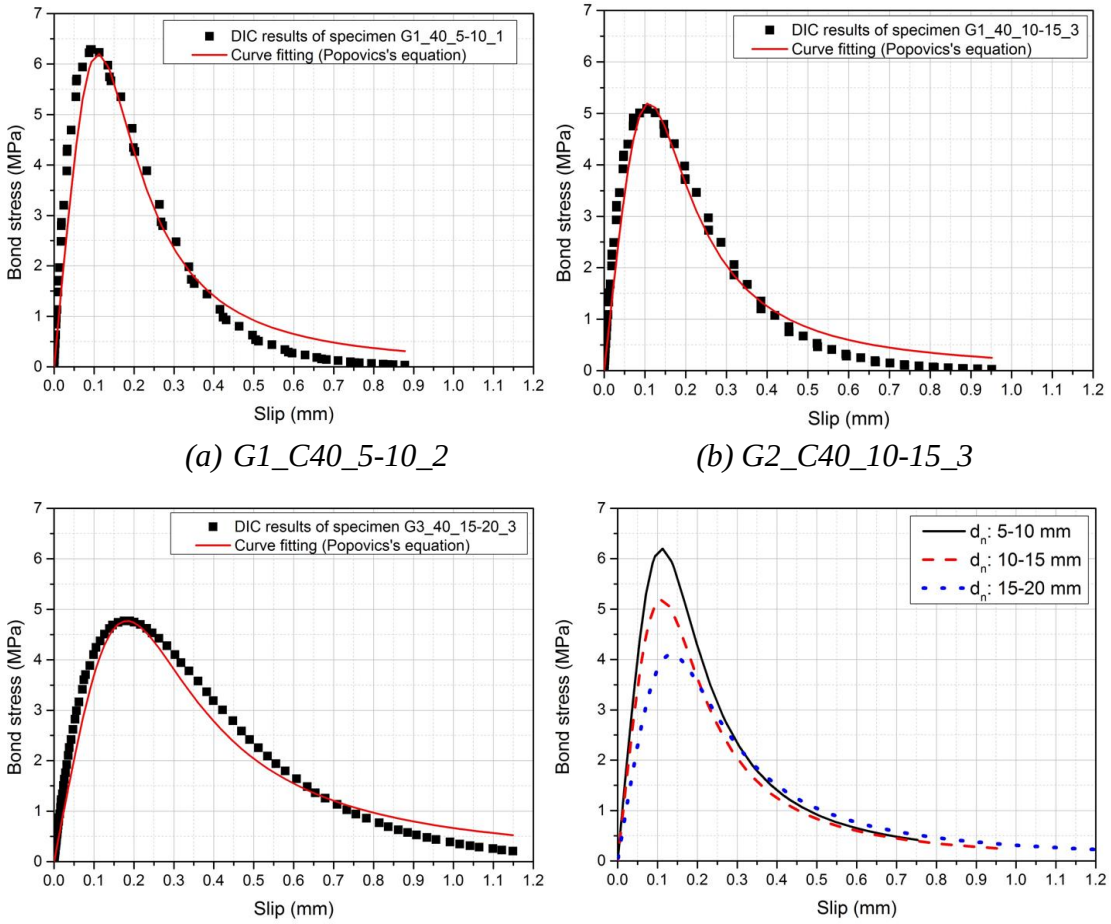

(a) G1_C40_5-10_2 *(b) G2_C40_10-15_3*

(c) G3_C40_15-20_3 *(d) Comparisons of the predictions*

Figure 4-18. Relationship between interfacial shear stress and slip

An interfacial bond-slip relationship is of fundamental importance in modelling FRP-strengthened RC structures. In this section, the interfacial shear stress and slip are obtained by analyzing the surface strain in the BFRP sheets from the DIC technique at the centreline of the stress-transfer length (172, 173). The bond stress can be obtained from the measured strain. The relative slip between BFRP and concrete can be obtained by integrating the strain profile. The previous studies (91, 147) stated that the assumptions should be made to define the slip distribution along the FRP sheets: (a) zero slip between concrete and BFRP at the free end of the BFRP sheet; (b) deformation of concrete specimen far from the external cover is negligible with respect to its BFRP counterpart; and (c) linear variation of strain in BFRP sheet. Non-linear bond-slip

curves with an ascending branch and a descending branch based on the measured data can be obtained, as shown in Figure 4-18.

Popovics's equation (174) is used to predict the relationship between the interfacial shear stress and slip, as:

$$\tau = \tau_{\max}[\frac{s}{s_o}\frac{n}{(n-1)+(s/s_o)^{\mathrm{n}}}] \quad (4\text{-}22)$$

where τ is the interfacial shear stress, s is the local slip, τ_{max} is the peak interfacial shear stress, s_o is the slip at the peak shear stress, and n is a coefficient related to the concrete compressive strength, which causes the slope of both ascending and descending branches (174). Coefficient n was proposed as a constant in some studies (91, 175). However, the correlation between the coefficient n and the aggregate size can be found in this section as the compressive strength of the concrete substrates increases with the aggregate size. Table 4-9 gives the regression coefficient n and the corresponding correlation coefficient. Equation (4-23) developed by Popovics (174) is used to establish the relationship between n and the maximum aggregate size through the compressive strength of concrete. Equation (4-24) is proposed based on the experimental results to predict the coefficient n and the coefficient of correlation R^2 is 0.822. The prediction by Equation (4-24) shows a low mean value of 0.997 (S.D. = 0.011).

Table 4-9. Experimental results and fitted results of interfacial bond-slip relationship

ID	**Maximum aggregate size d_{max} (mm)**	τ_{max} **(MPa)**	s_o **(mm)**	**Regression coefficient,** n	**Correlation coefficient,** R^2
G1_40_5-10_1		6.22	0.112	2.966	0.946
G1_40_5-10_2	10	6.45	0.103	2.957	0.937
G1_40_5-10_3		6.02	0.121	2.961	0.935
G2_40_10-15_1		5.41	0.118	2.908	0.954
G2_40_10-15_2	15	4.78	0.131	2.899	0.945
G2_40_10-15_3		5.08	0.125	2.897	0.960
G3_40_15-20_1		5.11	0.128	2.754	0.968
G3_40_15-20_2	20	4.22	0.139	2.699	0.971
G3_40_15-20_3		4.77	0.135	2.744	0.970

$$n = \alpha + \beta f_c \tag{4-23}$$

$$n = 4.52 - 0.038 f_c \tag{4-24}$$

Figure 4-18 shows the shear stress versus shear slip response for the interface between BFRP and concrete, in which the predictions match the experimental results well. There are three stages for the bond-slip curves. After linear elastic response at around 40% of the maximum shear stress, it is non-linear up to the peak stress with the increase of shear slip. In the descending branch after reaching τ_{max}, a softening stage induced by microcracks can be observed where increasing shear slip results in decreasing shear stress. The shear stress gradually drops to zero with the increase of shear slip.

Similar shapes of the interfacial shear stress versus slip curves and the bond-slip curves were observed. The peak interfacial shear stress decreases with the increasing maximum aggregate size. In addition, the slope of the ascending branch decreases as the maximum aggregate size increases due to the decreased interfacial fracture energy. It should be noted that the area of the bond-slip is defined as the interfacial fracture energy. Popovics's equation can be used to predict the shear stress versus slip relationship of the BFRP-concrete interface by considering the coarse aggregate of different sizes as the prediction fit well with the experimental results.

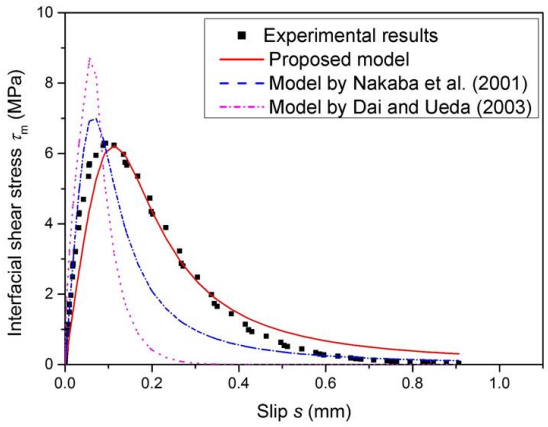

(a) G1_C40_5-10_2

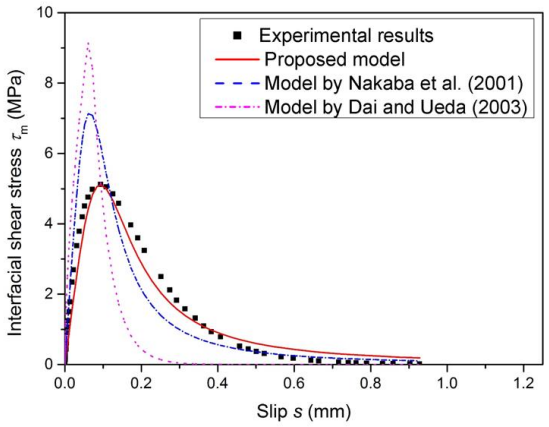

(b) G2_C40_10-15_3

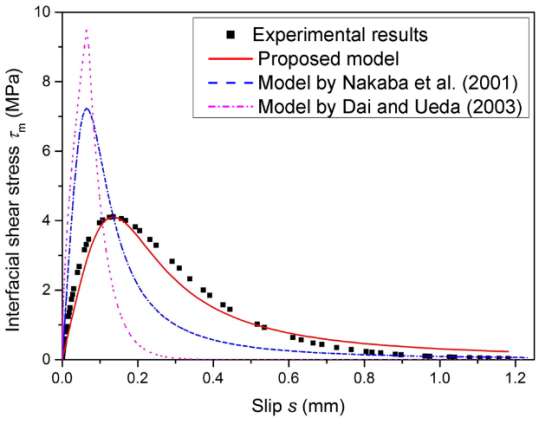

(c) G3_C40_15-20_3

Figure 4-19. Predicted and experimental interfacial shear stress versus slip

As shown in Figure 4-19, the proposed model yields better prediction than the two existing models with higher accuracy and the correlation coefficient R^2 predicted by the proposed model are larger than 0.9 for all the specimens, as given in Table 4-9. It is because the effect of aggregate size is incorporated into the proposed model. Two existing bond-slip models by Nakaba et al. (91) and Dai and Ueda (176) cannot provide accurate predictions as compared with the experimental results, as shown in Figure 4-19.

4.1.4 Section summary

This section investigates the effect of aggregate size on the bond behaviour between BFRP and concrete, including the debonding load, maximum interfacial shear stress, and bond-slip relationship. The following conclusions can be drawn:

1. Debonding of all the tested specimens occurs because of the failure of the concrete substrate. The pull-out of small aggregates from the concrete matrix is observed on the debonded BFRP sheets.
2. The debonding loads decreases with the increasing coarse aggregate size. Compared to the specimens with the aggregate size of 5–10 mm, a reduction of 6.55% and 10.04% for the specimens with the aggregate size of 10–15 mm and 15–20 mm can be found, respectively. The debonding loads could be predicted by considering the interfacial fracture energy and the maximum aggregate size.

3. The testing results show that the effective bond length increases with the aggregate size. Compared to the specimens with the aggregate size of 5–10 mm, a growth of 21.62% and 45.95% for the specimens with the size of 10–15 mm and 15–20 mm are observed, respectively.
4. Findings from the present tests show that the specimens with the aggregate size of 10–15 mm and 15–20 mm experience a significant decrease in the peak shear stress up to 18.46% and 33.71% compared to the specimens with the size of 5–10 mm. The local slip at peak shear stress experiences a significant increase with the aggregate size. An increase of 11.61% and 21.43% for the specimens with the aggregate size of 10–15 mm and 15–20 mm are found as compared to the specimens with the aggregate size of 5–10 mm.
5. The proposed empirical model for the interfacial bond-slip relationship by incorporating the effect of aggregate size can well predict the bond-slip behaviours.

4.2 Effect of adding steel fibres

Steel fibre reinforced concrete (SFRC) has been increasingly used and has superior resistance to cracking and crack propagation due to the fact that steel fibre composites possess increased extensibility and tensile strength at both pre-cracking and post-cracking stage. In this section, the interfacial bond behaviour between basalt fibre reinforced polymer sheet (BFRP) and steel fibre reinforced concrete (SFRC) is investigated by conducting single-lap shear tests. Short steel fibres with four-volume fractions (i.e. V_f =0%, 0.25%, 0.50%, and 1.0%) are used to improve the interfacial bond of BFRP-concrete as the mechanical properties of the concrete substrate (i.e. compressive strength and tensile strength) are improved by adding steel fibres. The effect of volume fraction on bond strength, effective bond length, local slip at peak shear stress, and interfacial bond-slip relationship are evaluated and discussed.

The related work in this section has been published in Engineering Structures.

Yuan C, Chen W, Pham TM, Hao H. Bond Behaviour between Basalt Fibres Reinforced Polymer Sheets and Steel Fibres Reinforced Concrete. Engineering structures. 2018; 176:812-24. DOI: doi.org/10.1016/j.engstruct.2018.09.052

4.2.1 Experimental program

4.2.1.1 Material properties

Concrete prisms with a length of 350 mm, the width of 150 mm and a height of 150 mm were prepared as concrete substrates. Coarse aggregates size of 5-10 mm was used in the test program. The short steel fibres with a length of 25 mm and a diameter of 0.30 mm (i.e. aspect ratio of 83.33) were used in the testing program, as shown in Figure 4-20. Four different volume fractions of short steel fibers, i.e. 0%, 0.25%, 0.5% and 1.0%, were used for the concrete with grade of 40 MPa. The Young's modulus, tensile strength, and density of the short steel fibers are 200 GPa, 2.5 GPa, and 7,800 kg/m^3.

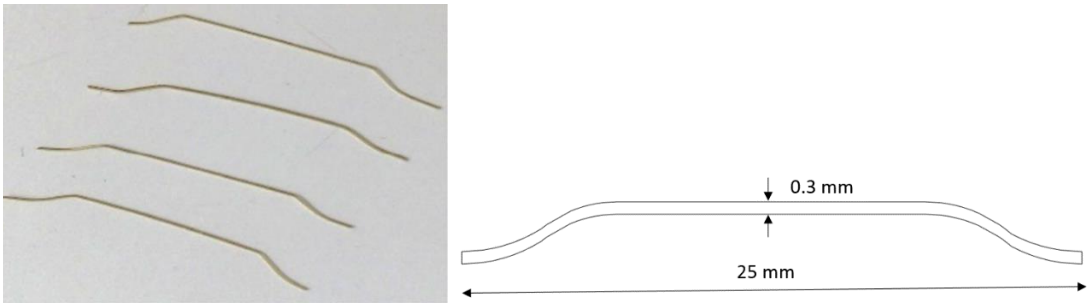

Figure 4-20. Short steel fibres

Mechanical properties of PC and SFRC, including compressive strength and splitting tensile strength, were measured to investigate the correlations between the concrete material properties and the interfacial bond behaviour. Three concrete cylinders with 100 x 200 mm from each batch of PC and SFRC were tested to obtain the axial compressive strength according to ASTM C39 (177) and another three larger concrete cylinders with 150 x 300 mm were tested based on ASTM C496 (178) for the splitting

tension test after 28 days of curing. The obtained concrete material properties are summarized in Table 4-10.

Table 4-10. Mechanical properties of concrete

Group ID	Specimen ID	Volume fraction V_f (%)	Fiber reinforcing index RI ($V_f L_f / \phi_f$)	Compressive strength f_c' (MPa)	Splitting tensile strength f_t (MPa)
G1	PC_1	0	0	40.09	3.98
	PC_2			39.87	4.05
	PC_3			41.05	3.89
Mean				40.34	3.97
G2	SFRC_0.25_1	0.25	0.208	41.83	4.44
	SFRC_0.25_2			41.05	4.29
	SFRC_0.25_3			40.90	4.16
				41.26	4.30
G3	SFRC_0.5_1	0.50	0.417	42.59	5.53
	SFRC_0.5_2			44.07	5.28
	SFRC_0.5_3			43.56	5.01
Mean				43.41	5.27
G4	SFRC_1.0_1	1.00	0.833	43.82	5.93
	SFRC_1.0_2			44.24	5.96
	SFRC_1.0_3			41.32	5.87
Mean				43.13	5.92

Table 4-10 gives the details of 12 specimens. The specimen ID was assigned to each specimen as "GX_PC/SFRCY_n_m". "GX" refers to the group from G1 to G4, and there are four groups in this section. "PC/SFRC" refers to the type of concrete, i.e. plain concrete (PC) and steel fiber reinforced concrete (SFRC). The letter "*n*" refers to the volume fraction of steel fibres. The letter "*d*" means the specimen number from 1 to 3 (three specimens for each configuration). For the material properties of the epoxy resin and BFRP sheet, please refer to chapter 3.2.1.

4.2.1.2 Specimen preparations

The concrete prisms were demolded 24 hours after casting and then cured in a water tank at Curtin University for 28 days. At least 12 concrete prisms including 3 PCs and 9 SFRCs were prepared in this section. The details of the specimens and testing results are given in Table 4-11. All specimens were cut in half in order to obtain the surface with a more uniform distribution of steel fibres. The cutting surface of all specimens

was roughened by a needle scaler to expose coarse aggregates. To prevent the effect of the protruding steel fibers on the bond capacity, the bulge was cut off. A manual lay-up procedure was conducted to bond the BFRP sheets onto the roughed surface of concrete substrates. The bond length of BFRP sheets was 200 mm for all specimens in this section.

Table 4-11. Experimental results

Specimens ID	**Volume fraction V_f (%)**	**Debonding load P_d (kN)**	**Peak shear stress τ_m (MPa)**	**Slip at peak shear stress s_o (mm)**	**Interfacial fracture energy G_f (N/mm)**	**Effective bond length L_e (mm) DIC**	
G1_PC_1		8.27	3.01	0.052	0.461	65	71
G1_PC_2	0	8.66	3.49	0.049	0.465	66	77
G1_PC_3		8.56	2.91	0.051	0.429	73	72
Mean		8.50	3.21	0.051	0.452	68	73
G2_SFRC_0.25_1		9.30	4.15	0.057	0.586	71	66
G2_SFRC_0.25_2	0.25	8.95	4.09	0.067	0.556	65	60
G2_SFRC_0.25_3		9.45	4.38	0.063	0.563	61	63
Mean		9.23	4.21	0.062	0.568	66	63
G3_SFRC_0.5_1		10.16	5.12	0.093	1.297	57	59
G3_SFRC_0.5_2	0.50	9.97	4.91	0.102	1.251	60	61
G3_SFRC_0.5_3		9.95	4.72	0.107	1.276	53	54
Mean		10.03	4.92	0.100	1.275	57	59
G4_SFRC_1.0_1		11.11	5.96	0.116	1.811	52	55
G4_SFRC_1.0_2	1.00	11.44	5.51	0.123	1.656	59	61
G4_SFRC_1.0_3		10.56	5.49	0.127	1.817	55	59
Mean		11.04	5.65	0.122	1.761	55	58

4.2.1.3 Testing setup

For static testing machine and testing set-up, please refer to Chapter 3.2.4.

4.2.2 Experimental results and discussions

4.2.2.1 Failure mode

Failure mode reflects the performance and efficiency of the interfacial bonding (40). Only one failure mode was observed in this section, i.e. debonding failure in the concrete prisms, where a thin layer of concrete with some steel fibers was attached to the BFRP sheet after debonding for the SFRC specimens. The debonding failure initiated at the loaded end for all specimens, which was the same as the previous studies (39, 45). The typical debonding failure photographs of the specimens after testing are shown in Figure 4-21 (a). Although the added short steel fibers had little effect on the failure mode, the debonding process between BFRP and SFRC was more ductile than the interface of BFRP-to-PC joints due to the pull-out behavior of fibers, which was shown in Figure 4-21 (b). This is because the bond strength between steel fibers and concrete is lower than the bond strength between steel fibers and epoxy. With the increase of the volume fraction, more and more steel fibers were pulled out of the SFRC substrates.

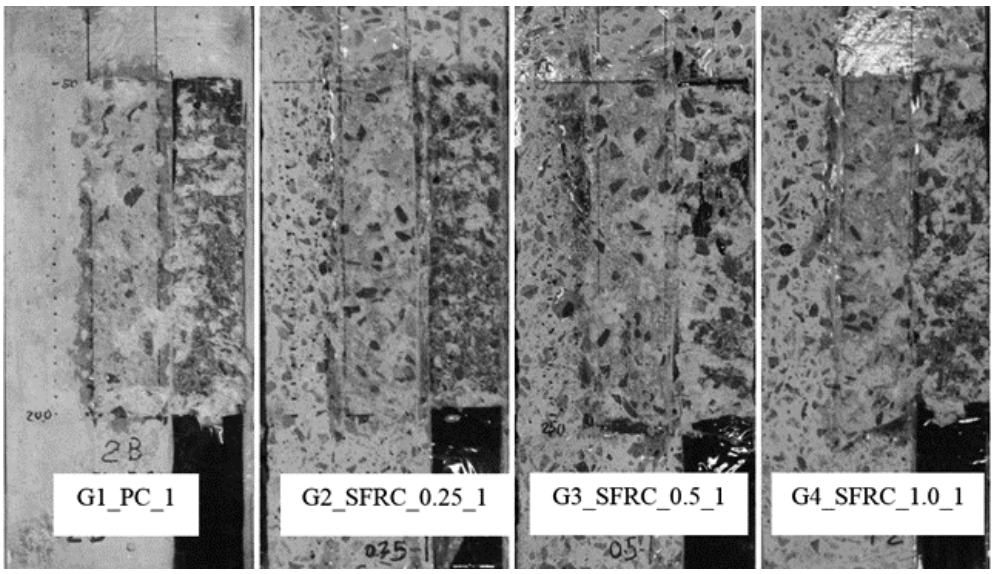

(a) Debonding failure

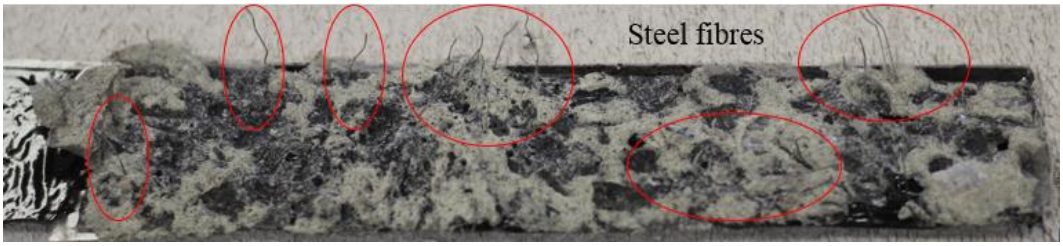

BFRP sheets (After debonding)

Bonded area of SFRC substrate (After debonding)
(b) Pull-out of steel fibers for G3_SFRC_0.5_1 (after debonding)

Figure 4-21. Failure modes of specimens

4.2.2.2 Load-displacement curve

As reported in the previous studies, there are three stages existing in the load-displacement curves, which are elastic stage, softening stage and debonding plateau stage (142), as shown in Figure 4-22 (a). After the elastic stage, microcracks develop in the concrete layer with the increasing shear slip. Figure 4-22 (b-e) shows the testing results of load and displacement. The measured displacement consists of the shear slip of the bonded part and the elongation of the unbonded part of the BFRP sheets (39). The average debonding loads for specimens G1_PC, G2_SFRC_0.25, G3_SFRC_0.50, and G4_SFRC_1.0 were 8.50 kN, 9.23 kN, 10.03 kN, and 11.04 kN, respectively. The debonding loads increased with the rising volume fraction of steel fibres, which indicates that the bond strength between BFRP and concrete is improved by adding short steel fibres. In addition, the debonding process is more ductile as the softening stage and debonding plateau stage are extended with the increasing fibre volume fraction.

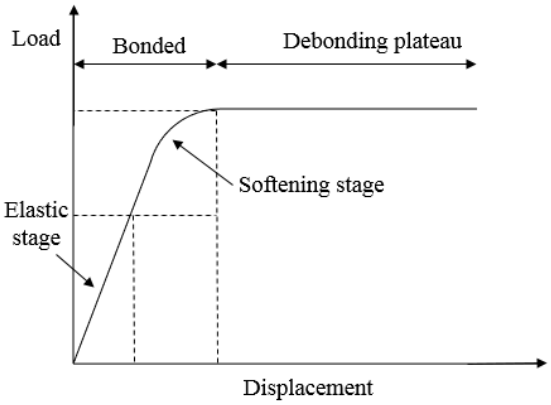

(a) Typical load-displacement curve with enough effective bond length (142)

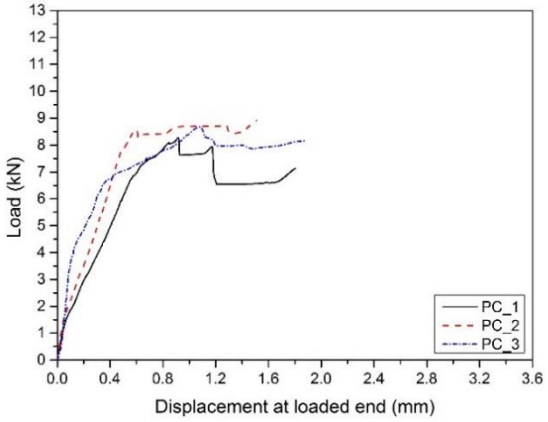

(b) G1_PC

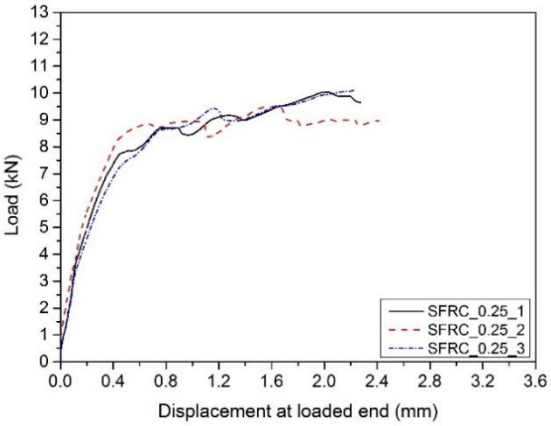

(c) G2_SFRC_0.25

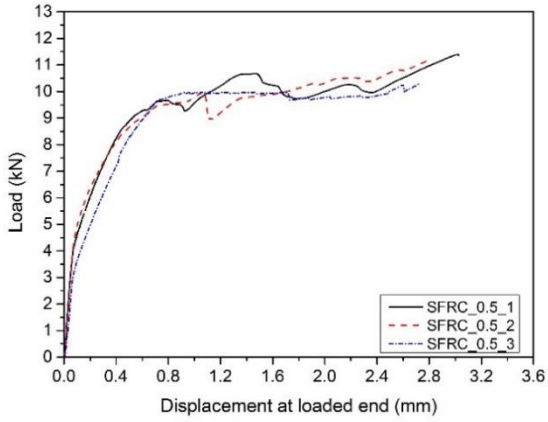

(d) G3_SFRC_0.5

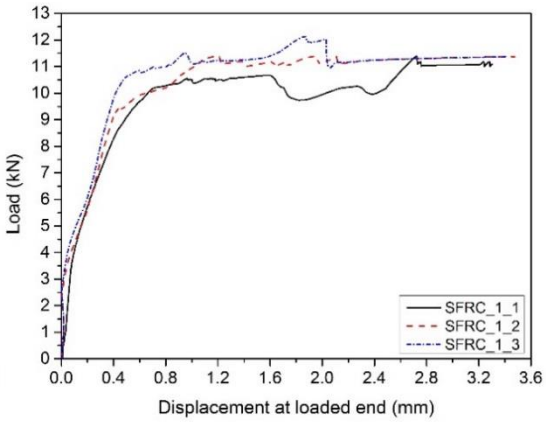

(e) G4_SFRC_1.0

Figure 4-22. Load-displacement curves

There are fluctuations in load-displacement curves due to the randomly distributed steel fibres and embedded aggregates in the adhesive-concrete layer. For the ease of comparison, a fitting procedure is conducted to smoothen the load and displacement curves based on Equation (4-25) (90). This formula provides very accurate

smoothening as the coefficient correlation R^2 for all the specimens is higher than 0.95. As given in Figure 4-23 (a), the coefficient correlation R^2 of the specimen G4_SFRC_1.0_2 is 0.9608.

$$P = E_f t_f b_f (\frac{a}{b})(1 - e^{-\frac{s}{a}}) \quad (4\text{-}25)$$

where P is the bond strength, E_f is the elastic modulus of FRP, t_f is the thickness of FRP, b_f is the width of FRP, a and b are coefficients, and s is the displacement.

The fitted load-displacement curves of BFRP-to-PC and BFRP-to-SFRC interfaces are plotted and compared in the same graph, as shown in Figure 4-23 (b). It can be seen that the interfacial bond strength increases with the rising steel fibre volume. This is because the tensile strength of concrete increases with the rising steel fibre volume. The testing results indicate that splitting the tensile strength of SFRCs is higher than the PCs by around 8-37%. For the specimens G4_SFRC_1.0, the specimen with 1.0% fibre volume has the highest split tensile strength, which is consistent with previous studies (179, 180). In addition, some existing interfacial bond strength models indicate that the bond strength between FRP and concrete correlates well with the tensile strength of concrete (89, 142). In this section, the tensile strength is used to correlate with the interfacial bond behaviour. The added steel fibres also tend to increase the toughness of the concrete (i.e. area under the stress-strain curve), which results in higher fracture energy. In this section, pulling out of steel fibres from the concrete matrix can be observed when debonding occurs, which can be seen in Figure 4-21 (b). Higher bond strength is needed to debond and pull out the fibres from the concrete matrix. Also, the slope of the initial elastic stage of the load-displacement curves increases with the volume fraction of steel fibres. This is because both normal stiffness and tangential stiffness of the SFRC are improved by adding steel fibres (181).

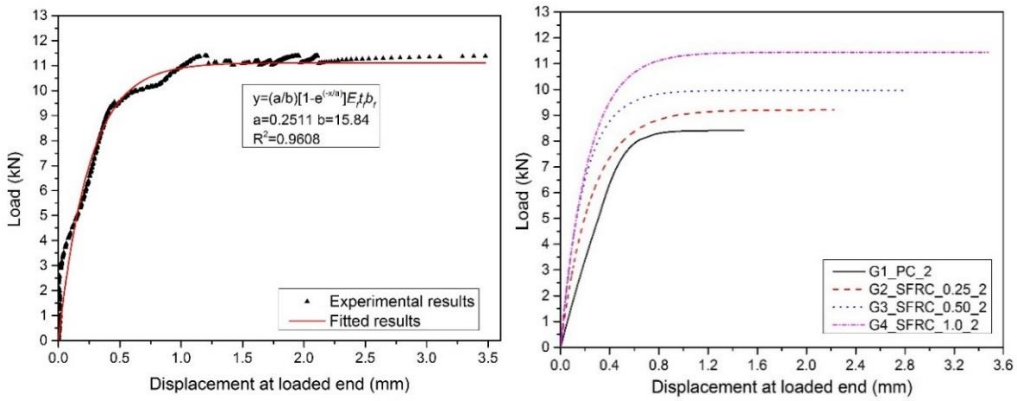

(a) Curve fitting of G4_SFRC_1.0_2 (b) Comparison of the fitted load-displacement curves

Figure 4-23. Curve fitting of experimental load-displacement curves

In addition, the debonding plateau is significantly extended due to the increment of displacement, which is evidenced in Figure 4-23 (b). The testing results indicate that the displacement of SFRCs is higher than the PCs by about 66-133%. This is because the softening stage of the concrete layer has been improved by adding steel fibres. The extension and propagation of microcracks in the softening stage are improved by the stress transferring capability of the added steel fibres.

4.2.2.3 Strain distribution

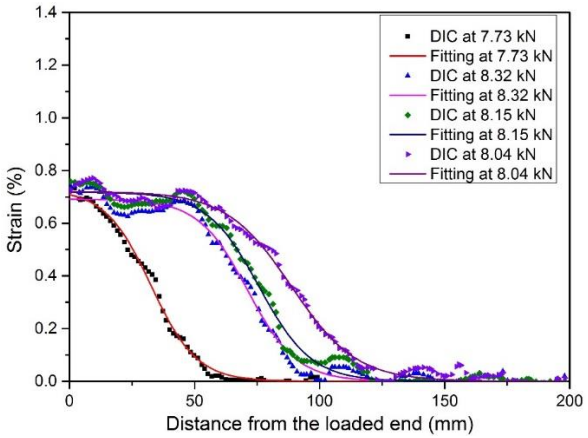

Figure 4-24. Strain distributions of G1_PC_1 along with the FRP sheets at different loading stages

Figure 4-24 shows the strain distributions along the loading direction at different loading stages. The fluctuations of the original strain curves extracted from the digital

images can be observed due to the variations of the BFRP sheets (145) and the embedded aggregate in the adhesive-concrete layer (182). The fluctuations derived from the DIC measurements in the interfaces of FRP-concrete, FRP-masonry, and FRP-steel were also overserved in the literature (35, 148, 157, 183). In this section, the strain distributions of all the specimens are similar and show a zigzag curve after debonding. Prior to the initial debonding, the strain at the loaded end increased with the applied load.

To eliminate the fluctuations of the strain profiles, a non-linear curve fitting method was employed in this section, which can be expressed by Equation (4-26) (90). A comparison of the strain distributions before and after curve fitting is presented in Figure 4-24. It can be observed that the expression can suitably simulate the strain distributions along the bonded length, as:

$$\varepsilon_{yy} = (a/b)/(1+e^{\frac{x-x_o}{b}}) \quad (4\text{-}26)$$

where ε_{yy} is the strain along the loading direction, a, b, and x_o are coefficients, and x is the distance from the loaded end. The ultimate strain for specimens G1_PC_1, G2_SFRC_0.25_2, G3_SFRC_0.50_1, and G4_SFRC_1.0_1 were 0.76%, 0.80%, 1.15%, and 1.37%, respectively, illustrating that the ultimate strain increased with the rising fiber volume. This is because the crack toughness and crack resistance of the concrete substrate was enhanced by adding steel fibers. The specimens with higher fiber volume possessed higher fracture energy due to the enhanced concrete properties. The calculated interfacial fracture energy for all the specimens is given in Table 4-11. The average values of the interfacial fracture energy for G1_PC, G2_SFRC_0.25, G3_SFRC_0.50, and G4_SFRC_1.0 were 0.452 N/mm, 0.568 N/mm, 1.275 N/mm, and 1.761 N/mm, respectively. The added short steel fibers had a significant effect on the interfacial fracture energy. This is because as the fiber volume increases, higher fracture energy is needed to debond and pull out steel fibers from the concrete matrix. The larger

shear force results in larger deformation of BFRP sheets of the same stiffness, which is the reason why the specimens G4_SFRC_1.0 have the largest ultimate strain among the four groups.

4.2.2.4 Interfacial shear stress and local slip calculation

The bond-slip relationship in the longitudinal direction can be obtained from the smoothened strain using Equation (4-27). The interfacial shear stress distribution within the bonded length can be evaluated by imposing the equilibrium condition of an FRP sheet with a length *dx* bonded to concrete, as:

$$\tau(x) = t_f E_f \frac{d\varepsilon_f}{dx} \tag{4-27}$$

Where *τ(x)* is the shear stress at distance *x* from the free end of the specimen, $\frac{d\varepsilon_f}{dx}$ is the gradient of FRP strain along the bonded length, t_f is the FRP thickness, and E_f is the FRP elastic modulus. In addition, the local slip between FRP plate and concrete at distance *x* from the free end of the specimen can be calculated assuming a zero slip at the free end as:

$$s(x) = \int_0^{\infty} \varepsilon_f dx \tag{4-28}$$

The smoothened strain distributions measured from DIC can provide continuous strain, which can reduce the data intervals. This is beneficial for the accuracy of the interfacial shear stress and local slip. Figure 4-25 shows the typical interfacial shear stress distributions along with the BFRP sheets at different loading stages for specimens G1_PC_1, G2_SFRC_0.25_2, G3_SFRC_0.50_1, and G4_SFRC_1.0_1. The interfacial shear stress distributions for all the specimens are similar due to the same shapes of shear stress distributions. After reaching the peak shear stress, the shear stress gradually decreased toward the free end with the increasing applied load. The

propagation of debonding occurred when the shear stress reduced to zero. The shear stress maintaining its shape shifted from the loaded end to the free end of the BFRP sheets along with the propagation of the debonding. Theoretically, the peak shear stress should be a constant, while the experimental peak shear stress decreased from the loaded end to the free end of the BFRP sheets. The possible reason is that the length of the interfacial shear stress transfer zone increased during the loading process, which can be evidenced by the interfacial shear stress distributions in Figure 4-25. It should be noted that the transfer zone of interfacial shear stress can be defined from the interfacial shear stress distributions (41).

The results of the peak interfacial shear stress of all the specimens with different volume fractions of steel fiber are given in Table 4-11, which indicates that the steel fiber volume has significant influences on the peak shear stress due to the fact that the peak interfacial shear stress increases with the rising fiber volume. The average peak shear stress of specimens G1_PC, G2_SFRC_0.25, G3_SFRC_0.50, and G4_SFRC_1.0 were 3.21 MPa, 4.21 MPa, 4.92 MPa, and 5.65 MPa, respectively. Compared with the control group G1_PC, a growth of 31%, 53%, and 76% for group G2_SFRC_0.25, G3_SFRC_0.50, and G4_SFRC_1.0 in terms of the peak interfacial shear stress can be obtained, respectively. In addition, the slip at the peak shear stress also increased with the rising fiber volume. The average slips of specimens G1_PC, G2_SFRC_0.25, G3_SFRC_0.50, and G4_SFRC_1.0 were 0.051 mm, 0.062 mm, 0.100 mm, and 0.122 mm, respectively. Based on the existing models of interfacial shear stress of FRP-to-concrete (89), the interfacial shear stress is proportional to the tensile strength of concrete. As given in Table 4-10, the tensile strength of concrete increases with the fiber volume because more fibers are active in arresting cracks (184). Also, the measured strain increases with the fiber volumes, as shown in Figure 4-24. Because of the linear behavior of BFRP material, the shear stress developed in the BFRP sheets is proportional to the strain, indicating that the peak interfacial shear stress increases with

the rising fiber volume. Meanwhile, the shear slip is also proportional to the strain as the shear slip is the integration of the strain, indicating that the shear slip also increases with the rising fiber volume. This means that the interfacial shear stress and the corresponding shear slip are sensitive to the added short steel fibers.

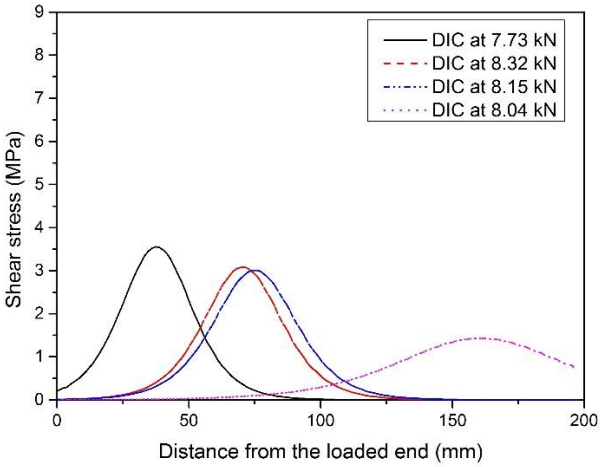

Figure 4-25. Typical interfacial shear stress distribution of G1_PC_1

Figure 4-26 shows the experimental and predicted bond-slip curves. It can be observed that the bond-slip curves for the specimens with or without steel fibres exhibit the same trend: a non-linear ascending branch and a non-linear descending branch, which is consistent with the previous study (154). The shear stress linearly increased to 40% of the maximum shear stress (145), after which it increased non-linearly and reached the peak shear stress. After the peak shear stress, a softening branch was observed where increasing the shear slip resulted in the reduction of shear stress. In addition, two existing bond-slip models proposed by Nakaba et al. (91) and Lu et al. (89) are used to compare with the experimental results. It can be observed that both the models cannot provide accurate predictions for the BFRP-to-SFRC interfaces due to the fact that the fibre-reinforcing index ($V_f L_f/\phi_f$) is not a parameter in the two bond-slip models. The prediction on the peak shear stress by Nakaba et al. (91) increases less significantly with the increasing fibre volume as compared with the model proposed by Lu et al. (89). This is because the compressive strength of concrete is considered in the model

proposed by Nakaba et al. (91) and the tensile strength of concrete is considered in the model proposed by Lu et al.(89). Adding fibre volume increases the tensile strength of concrete but has very limited effect on the compressive strength. In addition, adding steel fibres affects the interfacial fracture energy (i.e. the area under the bond-slip curve). The higher interfacial fracture energy the SFRC has, the higher shear stress of FRP sheets can be obtained. This is consistent with the findings by Yin and Wu (63). Both models by Nakaba et al. (91) and Lu et al. (89) overestimate the peak shear stress of BFRP-SFRC. It is because the calibration factors used in both models are for plain concrete. The calibration factors need be adjusted for the accurate predication of BFRP-SFRC. Thus, an accurate model needs to be proposed based on existing bond-slip models for FRP-to-SFRC joints.

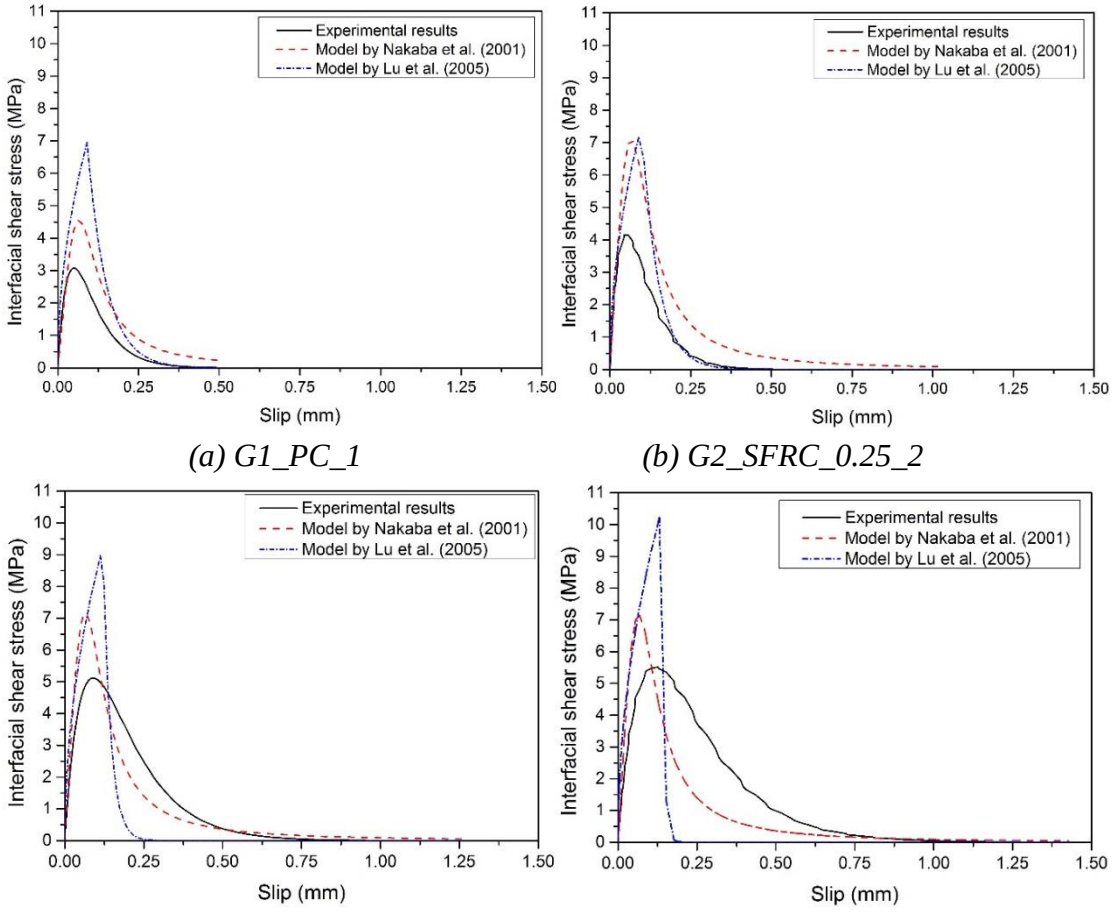

(a) G1_PC_1 *(b) G2_SFRC_0.25_2*

(c) G3_SFRC_0.50_1 *(d) G4_SFRC_1.0_1*

Figure 4-26. Bond-slip relationship

As shown in Figure 4-26, the bond-slip relationship is sensitive to the added steel fibres as the peak interfacial shear stress and the corresponding shear slip increased with the fibre volume. Compared with the group G1_PC, a growth of 22%, 96%, and 139% for group G2_SFRC_0.25, G3_SFRC_0.50, and G4_SFRC_1.0 in the shear slip at the peak interfacial shear stress can be obtained, respectively. The increased local slip at the peak shear stress indicates that the elastic stage of the load and displacement relationship is improved by the added steel fibres. Also, the ultimate slip increases by the added steel fibres and the ultimate slip for specimens G1_PC_3, G2_SFRC_0.25_2, G3_SFRC_0.50_1, and G4_SFRC_1.0_1 were 0.49 mm, 0.78 mm, 0.94 mm, and 1.21 mm, respectively. The extended ultimate slip indicates that the softening stage of the load and displacement relationship is improved by the added steel fibers. This is because the steel fibres improve the microcracking and crack propagation of the concrete substrates at pre-cracking and post-cracking stages. SFRC is more ductile than plain concrete. The ductility would also increase the energy absorption capacity, which is evidenced by the interfacial fracture energy of BFRP-SFRC. The experimental results of fracture energy obtained from Equation (4-29) are summarized in Table 4-11.

$$G_f = \int \tau ds \tag{4-29}$$

4.2.2.5 Effective bond length

Effective bond length (*EBL*) is the active bonding zone along which most of the interfacial shear stress is transmitted to the concrete (144). The extra bonded length has no effect on the ultimate debonding load, which can be evidenced by the load and displacement curves as well as the debonding plateau after the initial debonding load (173). The distance of the active bonding zone at debonding loads can be evaluated by using longitudinal strain fields of the BFRP sheets from DIC analysis, as shown in Figure 4-27 (a). Successive digital images were analysed by using the DIC method, and the longitudinal strain field corresponding to each loading stage was derived (7, 143).

Also, the EBL can be defined through strain distributions. At the ultimate debonding load, the obtained strain distribution can be divided into three zones: (a) the fully debonded zone near the loaded end; (b) the stress transfer zone (the effective bond zone); and (c) the unstressed zone near the free end, as shown in Figure 4-27 (b). Dai et al. (90) proposed an equation to calculate the effective bond length, as:

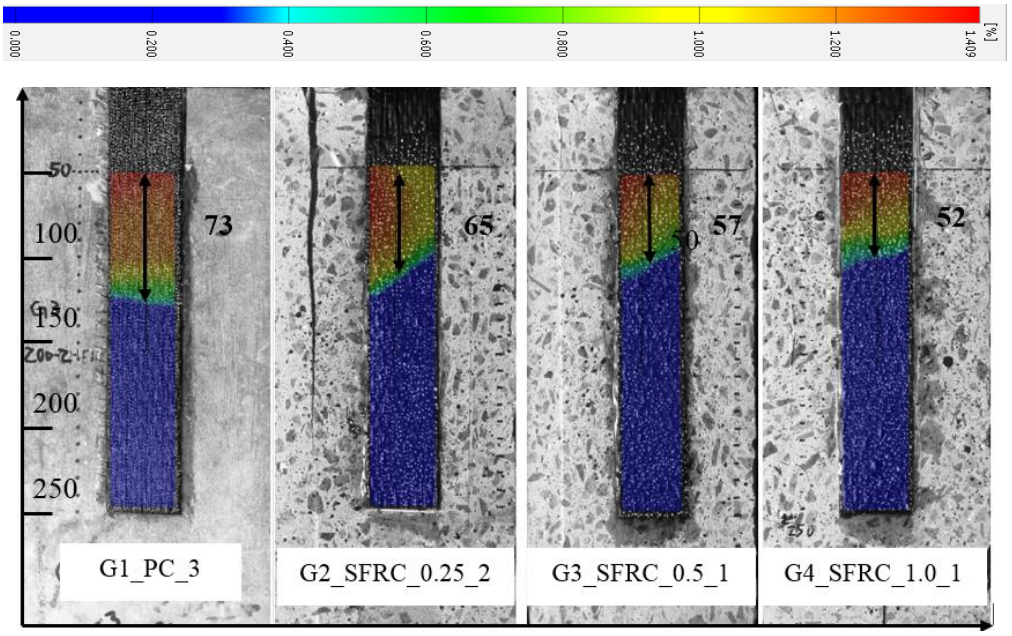

(a) Effective bond length obtained from DIC (unit: mm)

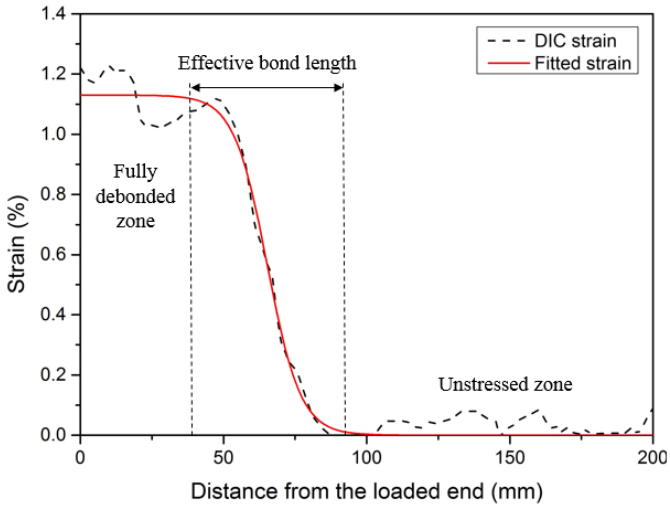

(b) Effective bond length obtained from the fitted strain profile (G3_SFRC_0.5_1)

Figure 4-27. Effective bond length

$$L_e = 2bLn(\frac{1+\alpha}{1-\alpha}) \quad (4\text{-}30)$$

where L_e is the effective bond length, b is the coefficient obtained from Equation (4-26), and α is equal to 0.96.

Table 4-11 gives the effective bond length obtained from the DIC method and Equation (4-30). The average EBLs obtained from the DIC analysis for specimens G1_PC, G2_SFRC_0.25, G3_SFRC_0.50, and G4_SFRC_1.0 were 68 mm, 66 mm, 57 mm, and 55 mm, respectively. The average EBLs derived from Equation (4-30) for specimens G1_PC, G2_SFRC_0.25, G3_SFRC_0.50, and G4_SFRC_1.0 were 73 mm, 63 mm, 59 mm, and 58 mm, respectively. There is a maximum of 7.27% difference in the results by using these two methods, which is an acceptable difference. Thus, both methods can be used to obtain the EBL of the BFRP-to-SFRC interface. The results indicate that the EBL decreases with the increase of steel fibre volume. This is because EBL is inversely proportional to the tensile strength of concrete (89). Also, the strain distribution gradient of the BFRP-to-SFRC interface is steeper than that of the BFRP-to-PC interface, as shown in Figure 4-24. This indicates that the EBL decreases with the increasing fibre volume as higher shear stress concentrates on the short stress transfer zone. In addition, similar patterns of strain contour development can be observed for all the specimens in Figure 4-27 (a). The shear strain contour in colours of red, yellow, and green refers to the shear stress distribution along the loading direction. A relative uniform distribution of strain can be observed from the specimens G1_PC_1 and G4_SFRC_1.0_1, however, the specimens G2_SFRC_0.25_2 and G3_SFRC_0.5_1 exhibited non-uniform strain fields, which was due to the random distributions of steel fibres in the concrete substrates.

4.2.3 Theoretical verification and proposed models

4.2.3.1 Tensile strength of SFRC

For the specimens with the fibre aspect ratio of 83.3, the tensile strength of concrete increased with the volume fraction of fibres, as given in Table 4-10. Meanwhile, the

added short steel fibres had minimal effects on the compressive strength of the concrete substrates in this study. The average compressive strength slightly decreased from 43.41 MPa (i.e. the volume fraction of 0.5%) to 43.13 MPa (i.e. the volume fraction of 1.0%).

The tensile strength of SFRC from splitting tensile tests is given in Table 4-10. It can be seen that the splitting tensile strength increases with the steel fibre volume, which is consistent with the previous study (185). The increase of the fibre volume fraction from 0% to 1.0% results in an increase of 48.99% in the splitting tensile strength. Thus, the tensile strength of concrete will be correlated with the interfacial bond behaviour in this study. Thomas and Ramaswamy (186) proposed a formula to predict the tensile strength of SFRC concrete as follows:

$$f_{SFRC} = A(f_{cu}')^{\alpha 1} + B(f_{cu}')^{\alpha 2}(RI) + C(RI) \quad (4\text{-}31)$$

where f_{SFRC} is the tensile strength of SFRC concrete, f_{cu}' is the standard cube compressive strength of the plain concrete and it is equal to 33.62 MPa. It should be noted that a factor of 1.2 is used to convert the cylinder strength to cube strength for plain concrete in this study (187). In this study, *A*, *B*, and *C* are regression coefficients, both $\alpha 1$ and $\alpha 2$ are equal to 0.5, and *RI* is the fibre-reinforcing index ($\frac{V_f L_f}{\phi_f}$). After regression analysis, the coefficients (R^2=0.92) can be expressed as follows:

$$f_t = 0.628(f_{cu}')^{0.5} + 0.165(f_{cu}')^{0.5}(\frac{V_f L_f}{\phi_f}) + 1.404(\frac{V_f L_f}{\phi_f}) \quad (4\text{-}32)$$

4.2.3.2 Interfacial bond strength

A number of analytical models of bond strength have been proposed to predict the ultimate debonding strength between FRP and concrete. The analytical models by Lu et al. (89) and Dai et al. (188) are adopted in this study to predict the ultimate bonding

strength as the both models considered interfacial fracture energy, which increased with the rising volume fraction of the steel fibres. The specimens with steel fibres of 0.25%, 0.50% and 1.0% experienced significant increase in the interfacial fracture energy up to 20%, 64%, and 74% over the control specimen without steel fibres, respectively. As compared to the model by Dai et al. (188), the model by Lu et al. (89) considering the tensile strength of concrete yield more accurate results in this study since the tensile strength of concrete instead of the compressive strength is the main factor determining the bond strength.

The model proposed by Lu et al. (89) is presented as follows:

$$P_{db} = \beta_l b_f \sqrt{2E_f t_f G_f} \tag{4-33}$$

$$G_f = 0.308\beta_w^{\,2}\sqrt{f_t} \tag{4-34}$$

$$\beta_w = \sqrt{\frac{2 - b_f / b_c}{1 + b_f / b_c}} \tag{4-35}$$

The model proposed by Dai et al. (188) is presented as follows:

$$P_{max} = (b_f + 7.4)\sqrt{2E_f t_f G_f} \tag{4-36}$$

$$G_f = 0.514\, f_{co}^{\,0.236} \tag{4-37}$$

where P_{max} is debonding load, β_l is the bond length factor ($\beta_l = 1$ when $L \geq L_e$), b_f is the width of FRP, b_c is the width of concrete, t_f is the thickness of FRP, E_f is the elastic modulus of FRP, G_f is the interfacial fracture energy, β_w is the width ratio of FRP-concrete, and f_{co} is the compressive strength and f_t is the tensile strength of concrete.

For FRP-to-PC joints, an equation can be presented to predict the interfacial fracture energy based on the model proposed by Lu et al. (89). A calibration factor of 0.165 was determined from the testing results as follows:

$$G_{f(PC)} = 0.165\beta_w{}^2\sqrt{f_t} \quad (4\text{-}38)$$

The volume fraction of steel fibres has a significant effect on the interfacial fracture energy for SFRC. Therefore, the fibre-reinforcing index ($\frac{V_f L_f}{\phi_f}$) should be a factor determining the interfacial fracture energy. The comparison between the experimental and predicted interfacial fracture energy is presented in Figure 4-28. After regression analysis, the relationship between the interfacial fracture energy of FRP-SFRC and the fibre-reinforcing index is presented as follows (R^2=0.93):

$$G_{f(SFRC)} = 4.533\left(\frac{V_f t_f}{\phi_f}\right)^{0.691} G_{f(PC)} \quad (4\text{-}39)$$

Based on the bond strength models of Lu et al. (89) and , the debonding loads of FRP-to-PC joints are determined by the interfacial fracture energy (G_f) and FRP stiffness ($E_f t_f$). A calibration factor of 1.68 obtained from the experimental results was introduced into the following equation:

$$P_{(PC)} = 1.68 b_f \sqrt{2E_f t_f G_{f(PC)}}$$

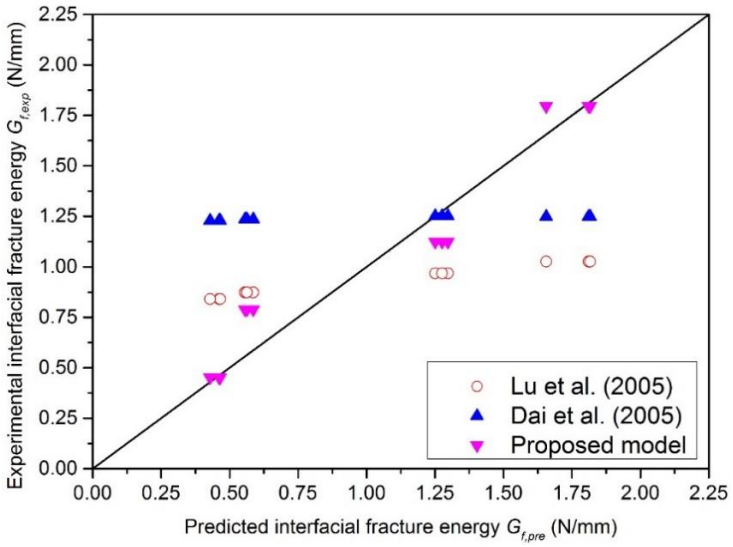

Figure 4-28. Comparison of the interfacial fracture energy (experimental vs. predicted)

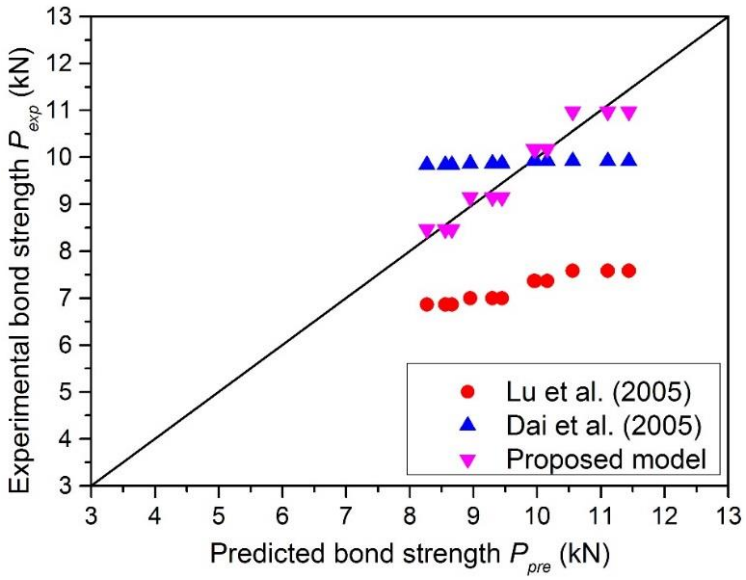

Figure 4-29. Comparison of the experimental and predicted bond strength

The bond strength between FRP and SFRC increased with the rising fibre volume due to the improved interfacial fracture energy. Two factors mainly affect the debonding loads, i.e. interfacial fracture energy and FRP stiffness, and the comparison of the predicted results is shown in Figure 4-29. By substituting the fibre-reinforcing index ($\frac{V_f L_f}{\phi_f}$) and the interfacial fracture energy (G_f) of the FRP-to-SFRC into Equation (4-39), the debonding force can be expressed as follows (R^2=0.93):

$$P_{(\mathrm{SFRC})} = (1.47 - 0.452\frac{V_f L_f}{\phi_f}) b_f \sqrt{2E_f t_f G_{f(\mathrm{SFRC})}} \quad (0 \le \frac{V_f L_f}{\phi_f} \le 3.25) \quad (4\text{-}40)$$

4.2.3.3 Peak interfacial shear stress and slip

Theoretical models have been developed to predict the maximum interfacial shear stress (τ_{max}) and the corresponding slip (s_o). The peak shear stress and the corresponding slip are important factors determining the bond-slip relationship. For bilinear bond-slip models, it can be characterized by three factors, including the peak shear stress, the maximum slip at the peak shear stress, and the ultimate slip, which can be extracted from the non-linear bond-slip curves. Some bond-slip models have been developed and

stated that the maximum shear stress is independent of FRP stiffness $E_f t_f$ (35, 95). Wu and Jiang (35) proposed an accurate bond stress model $\tau_{max} = 1.31 k_w^2 (f_{co})^{0.19}$ by considering the compressive strength of concrete (f_{co}) and width ratio (k_w). Similar to the model by Nakaba et al. (91), Dai et al. (90) considers the compressive strength in the model. Therefore, the model by Dai et al. (90) is not suitable to predict the bonding behaviour of BFRP-SFRC for this study. Similar to the model by Lu et al. (89), Sun et al. (142) considers both width ratio of FRP-to-concrete and the tensile strength in the model. However, the model by Sun et al. (142) is more complicated than the model by Lu et al. (89) and the calibration factors are difficult to be determined.

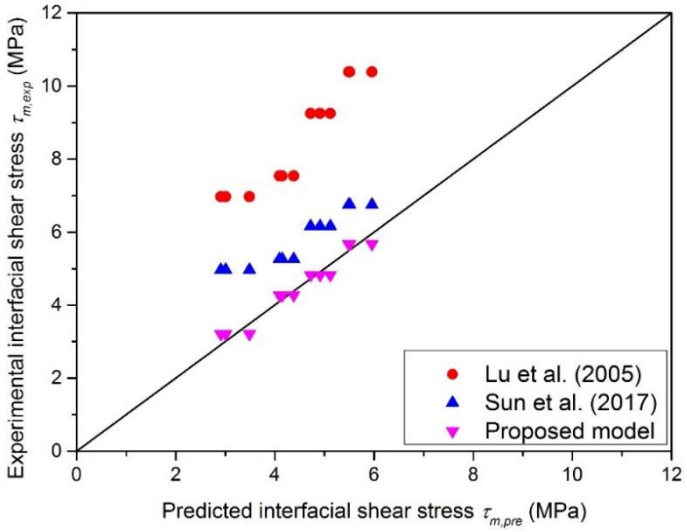

Figure 4-30. Comparison of the experimental and predicted peak shear stress

The model proposed by Lu et al. (89) is presented below:

$$\tau_{\max} = 1.5 \beta_w f_t \tag{4-41}$$

$$s_o = 0.0195 \beta_w f_t \tag{4-42}$$

The model proposed by Sun et al. (142)

$$\tau_{\max} = 1.35 + 0.25 \beta_w f_t + 0.62 f_t \tag{4-43}$$

$$s_o = 0.016 - 0.0046\beta_w f_t + 0.11\beta_w \quad (4\text{-}44)$$

where τ_{max} is the peak shear stress, s_o is the slip at the peak shear stress, β_w is width ratio of FRP-concrete, and f_t is the tensile strength of concrete.

The comparison of peak shear stress is made between the predictions and the experimental results, as presented in Figure 4-30. For FRP-to-PC joints, the interfacial shear stress is determined by the width ratio (β_w) between FRP and concrete and the tensile strength of concrete (f_t). An equation was proposed based on the model developed by Lu et al. (89). The peak interfacial shear stress can be written as:

$$\tau_{m(PC)} = 0.69\beta_w f_t \quad (4\text{-}45)$$

Due to the effect of the volume fraction (V_f) of steel fibres, the fibre-reinforcing index $(\frac{V_f L_f}{\phi_f})$ is introduced into the following equation as follows (R^2=0.92):

$$\tau_{m(\mathrm{SFRC})} = 1.836(\frac{V_f L_f}{\phi_f})^{0.212}\tau_{m(PC)} \quad (4\text{-}46)$$

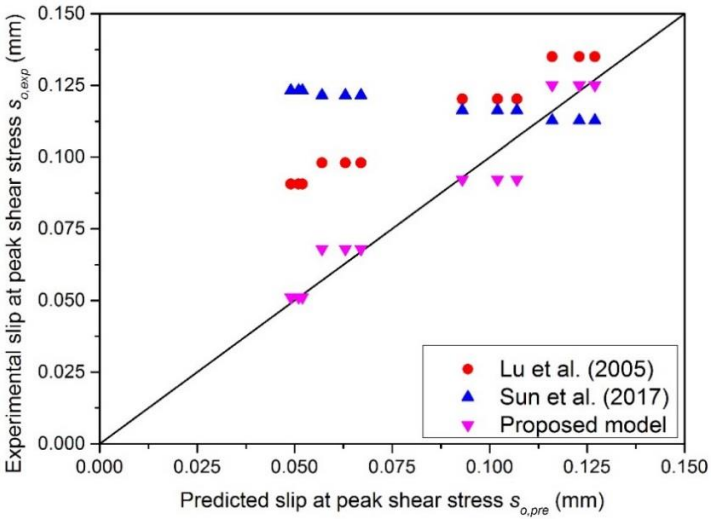

Figure 4-31. Comparison of the slip at peak shear stress (experimental vs. predicted)

The comparison is made between the slip at the predicted peak shear stress and the experimental results, as presented in Figure 4-31. Based on the bond-slip model proposed by Lu et al. (89), the width ratio (β_w) of FRP-to-concrete and the tensile strength of concrete (f_t) are the two main factors influencing the slip at the peak shear stress. For FRP-to-PC joints, the slip at the peak shear stress can be expressed as follows:

$$s_{o(PC)} = 0.011\beta_w f_t \quad (4\text{-}47)$$

The fibre volume has a significant effect on the slip at the peak shear stress for SFRC as the slip increased with the fibre volume. Thus, the fibre-reinforcing index ($\frac{V_f L_f}{\phi_f}$) is considered when predicting the slip. An equation is proposed based on the regression analysis as follows (R^2=0.90):

$$s_{o(SFRC)} = 2.651\left(\frac{V_f t_f}{\phi_f}\right)^{0.439} s_{o(PC)} \quad (4\text{-}48)$$

4.2.3.4 Interfacial bond-slip relationship

The interfacial bond-slip curve presents the relationship between the local interfacial shear stress and the local slip, which can be used to analyse the bond performance of FRP-strengthened concrete structures using analytical and numerical methods. In this section, the nonlinear bond-slip curves can be experimentally obtained by using the DIC method. Figure 4-32 shows the experimental bond-slip relationship for all specimens. Two distinctive branches can be identified, i.e. ascending branch and descending branch. The shear stress increases up to the peak shear stress (τ_{max}) with the increasing shear slip. After reaching the peak stress, the interfacial shear stress decreases with the increase of the shear slip. Popovics' equation (174) can be used to predict the interfacial bond-slip as follows:

$$\tau(s) = \tau_{max}[\frac{s}{s_o}\frac{n}{(n-1)+(s/s_o)^n}] \quad (4\text{-}49)$$

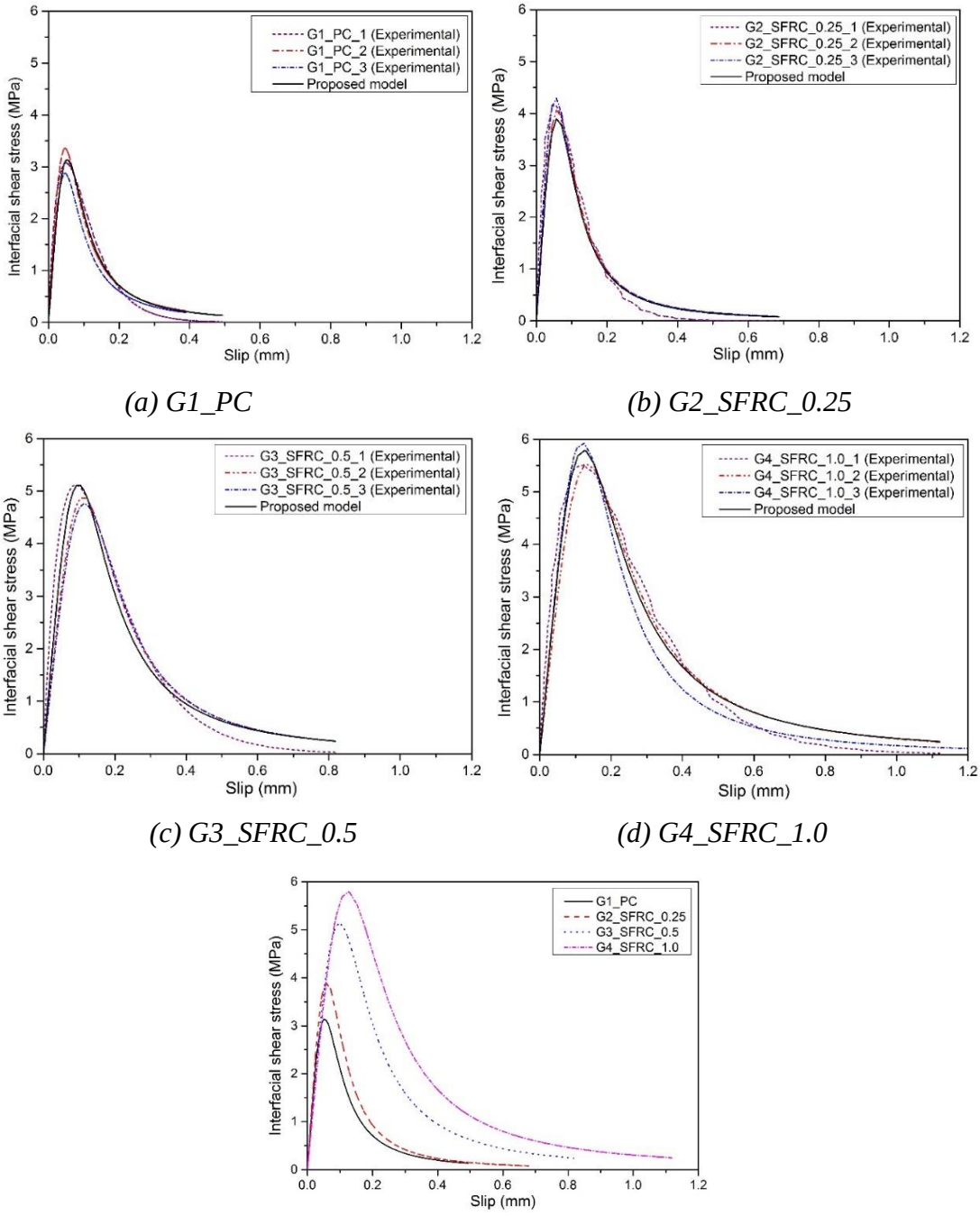

(a) G1_PC *(b) G2_SFRC_0.25*

(c) G3_SFRC_0.5 *(d) G4_SFRC_1.0*

(e) Comparison of the predicted bond-slip curves

Figure 4-32. Experimental and predicted bond-slip relationships

where $\tau(s)$ is the local shear stress, s is the local slip, τ_{max} is the peak local shear stress, s_o is the slip at the peak shear stress, and n is the parameter in terms of concrete

compressive strength which determines the slope of both ascending and descending branches (174). The analytical results of the peak shear stress (τ_{max}) and the corresponding slip (s_o) can be obtained by Equations (4-44) and (4-46). The interfacial bond-slip relationship between PC and SFRC is similar to the specimens with different fibre volumes exhibit similar shapes. The slopes of the ascending branch and the descending branch of all the specimens are almost the same. Therefore, the coefficient (*n)* should be constant in this section. Based on the experimental results, the constant (*n*) ranges from 2.827 to 2.926. The average value of *n* is 2.888 in this section. In addition, the interfacial fracture energy (G_f) increases with the increasing volume fraction of steel fibres as the peak shear stress and the corresponding shear slip increase with the rising volume fraction of steel fibres, which is shown in Figure 4-32 (e). The interfacial fracture energy represented as the enclosed area of the bond-slip curve is summarized in Table 4-11.

4.2.4 Section summary

This section investigates the effect of adding short steel fibres on the interfacial bond behaviour, i.e. the bond strength, the peak shear stress, the corresponding slip and the bond-slip relationship between BFRP and concrete. The following conclusions can be drawn:

1. Adding short steel fibres has no effect on the failure mode as debonding occurred in the concrete layer for all specimens. Pull-out of steel fibres from the concrete matrix was observed when debonding occurred;
2. Bond strength increases with the rising volume fraction of short steel fibres. A calibrated bond strength model is proposed for BFRP-to-SFRC bonding behaviour, which fits very well with the experimental results;
3. The effective bond length can be obtained by using either the longitudinal strain fields or the strain distribution gradient of the BFRP sheets, which yields similar results. The effective bond length decreases with the increasing fibre volume;

4. The interfacial shear stress and the corresponding slip at peak shear stress increase with the increase of the fibre volume. The calibrated models of peak shear stress and the corresponding slip are proposed by incorporating the effect of short steel fibres, which matches well with the experimental results;
5. The bond-slip model of BFRP and SFRC is proposed based on Popovics' equation, which matches well with the experimental results by using rational coefficient correlation values.

4.3 Summary

This chapter investigates the effect of aggregate size (section 4.1) and adding short steel fibre (section 4.2) on the bond behaviour between BFRP and concrete, including the debonding load, maximum interfacial shear stress, and bond-slip response. It is found that the debonding loads decrease with the increasing coarse aggregate size. Compared to the specimens with the aggregate size of 5–10 mm, a reduction of 6.55% and 10.04% for the specimens with the aggregate size of 10–15 mm and 15–20 mm can be found, respectively. Additionally, bond strength increases with the rising volume fraction of short steel fibres. An enhancement up to 20%, 64%, and 74% for specimens with steel fibres of 0.25%, 0.50% and 1.0% over the control specimen without fibres can be achieved, respectively. The empirical bond-slip models by incorporating the effect of coarse aggregate size and fibre volume can give more accurate predictions.

Chapter 5. Effect of strain rate and FRP configurations on dynamic bond behaviour

In Chapter 3, it is found FRP configurations (i.e. sole FRP and hybrid FRPs) have significant effects on the static interfacial bond behaviour. In this chapter, the effect of strain rate on the dynamic bond behaviour is investigated in section 5.1 and the effect of FRP configurations (i.e. hybrid FRPs) on the dynamic bond behaviour is studied in section 5.2.

5.1 Effect of strain rate

In this section, to investigate the effect of strain rate, an experimental investigation on the dynamic interfacial bond behaviour between basalt fibre (BFRP) sheets and concrete under different loading speeds (i.e. 8.33E-6 m/s, 0.1 m/s, 1 m/s, 3 m/s, 5 m/s, and 8 m/s) by using single-lap shear tests is carried out. Experimental results including bond strength, strain time histories, strain distributions in the bonding areas, interfacial fracture energy, and bond-slip curves are evaluated and discussed. An empirical bond-slip model including the strain rate effect is established for the predictions of bond properties between BFRP sheets and concrete under dynamic loadings.

The related work in this section is under review in International Journal of Solid and Structures.

Dynamic Interfacial Bond Behaviour between Basalt Fibre Reinforced Polymer Sheets and Concrete. International Journal of Solid and Structures. (Under review)

5.1.1 Experimental program

5.1.1.1 Material properties

The dimensions of concrete blocks were given as follows: the length was 150 mm, the width was 150 mm and the height was 300 mm, as shown in Figure 5-1. Concrete blocks

with 30.14 MPa compressive strength and 2.89 MPa tensile strength were prepared in this section. The maximum coarse aggregate size of 10 mm was used in the concrete preparation. For the material properties of the BFRP sheet and epoxy resin, please refer to Chapter 3.2.1.

5.1.1.2 Dynamic test setup

The single-lap shear tests (SST) were carried out by using Instron VHS 160-20 high-speed servo-hydraulic testing machine. This machine is able to provide constant velocity in the range of 0.1 m/s to 25 m/s. Figure 5-1 illustrates the specimen details and Figure 5-2 shows the testing machine and experimental setup. Twenty-seven specimens were tested with three specimens for each configuration in total. Table 5-1 summarizes the details of the specimens and the testing data. It should be noted that n_f refers to the number of BFRP layers, L represents the bonding length of BFRP sheets, b_f refers to the bond width of BFRP sheets, s^{-1} is the measured strain rate, P_u represents the debonding loads, τ_m refers to the peak shear stress (PSS), s_o refers to the slip at the peak shear stress, G_f is the interfacial fracture energy (IFE), and L_e refers to the effective bond length (EBL).

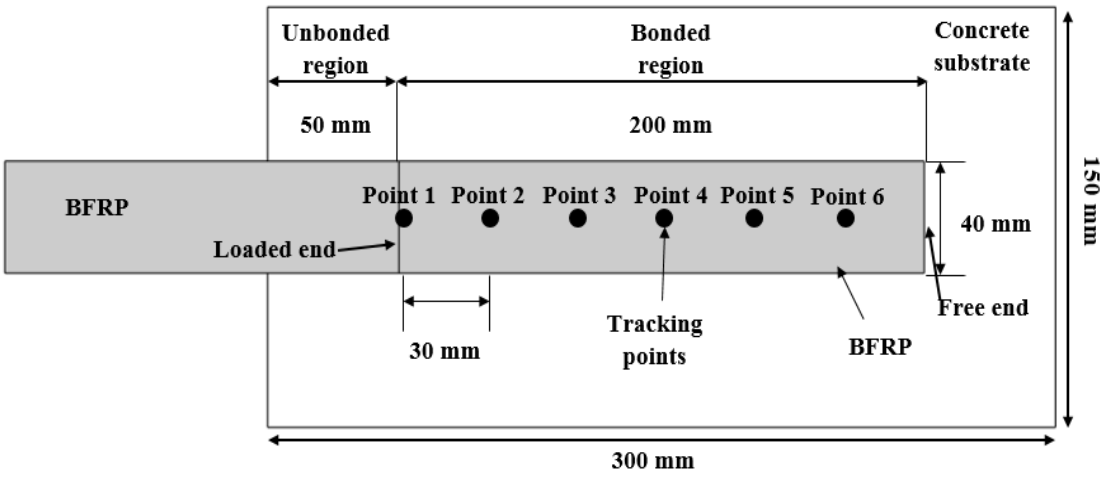

Figure 5-1. Specimen detail

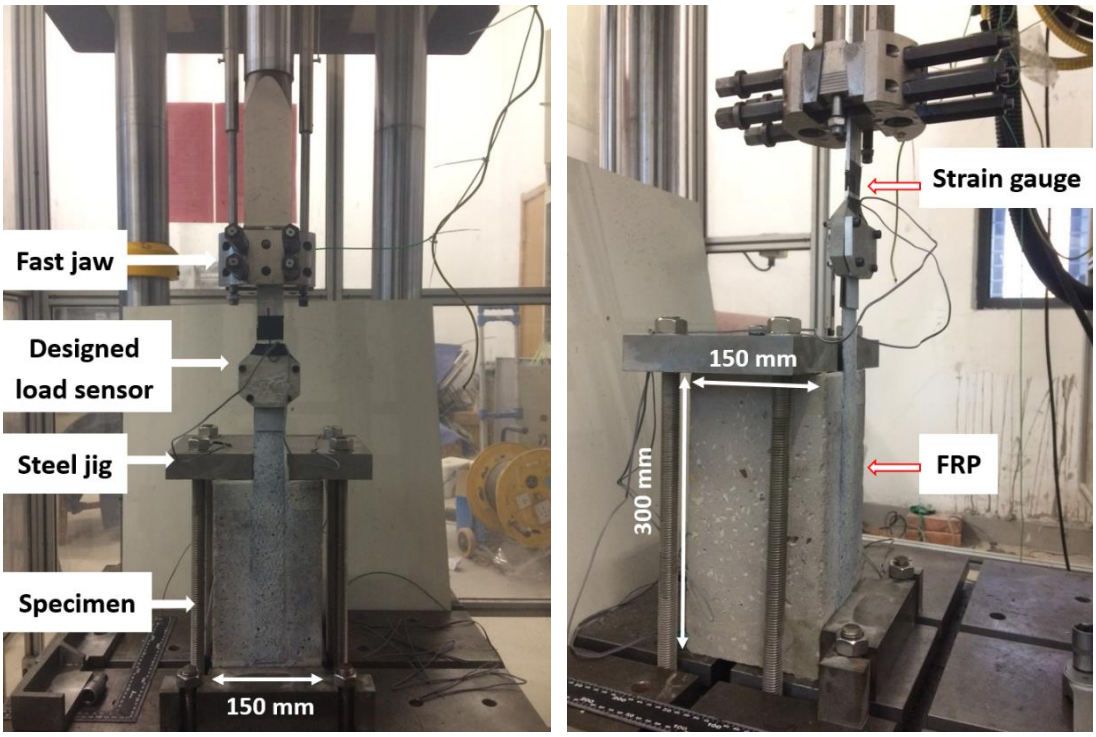

(a) SST: (L) Front view; (R) Side view

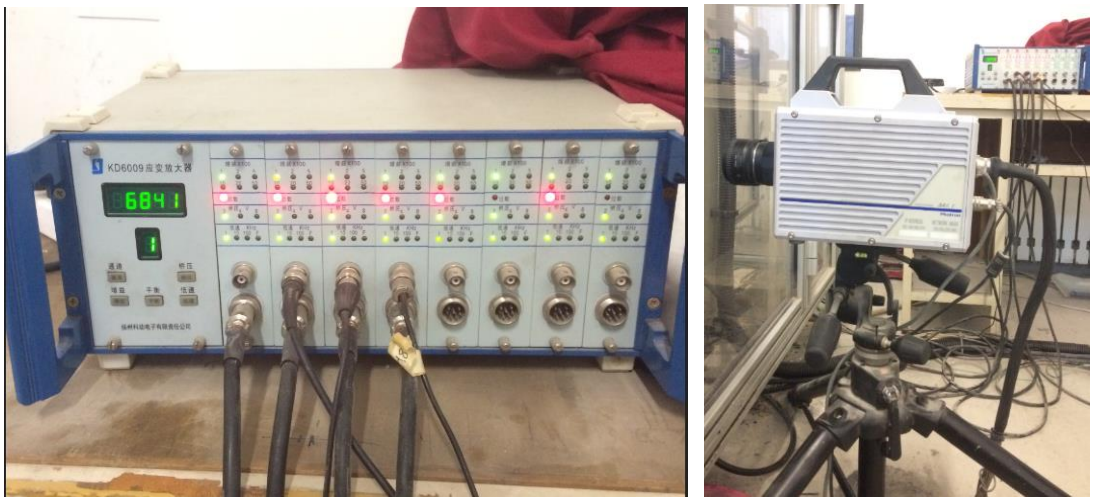

(b) Test instruments: (L) Strain amplifier; (R) High-speed camera

Figure 5-2. Test setup and instruments

Table 5-1. Details of the specimens and main results for the static and dynamic tests

Specimen ID	n_f	L (mm)	b_f (mm)	Loading speed (m/s)	s^{-1}	P_u (kN)	τ_m (MPa)	s_o (mm)	G_f (N/mm)	A (%)	B (mm^{-1})	Le (mm)	$f_{t,DIF}$ (MPa)	Failure mode
QS_1	2	200	40	8.33E-6	2.50E-5	6.93	2.11	0.146	0.89	1.009	4.737	96	/	C
QS_2	2	200	40	8.33E-6	2.50E-5	7.87	2.20	0.131	0.70	0.897	4.897	89	/	C
QS_3	4	200	40	8.33E-6	2.50E-5	9.04	2.72	0.125	0.98	0.746	5.534	105	/	C
QS_4	4	200	40	8.33E-6	2.50E-5	8.65	2.80	0.133	1.07	0.780	5.210	96	/	C
QS_5	2	200	25	8.33E-6	2.50E-5	4.12	2.21	0.109	0.88	1.002	6.368	85	/	C
QS_6	2	200	25	8.33E-6	2.50E-5	3.69	1.97	0.138	0.78	0.946	5.021	80	/	C
D1_0.1MPS_1	2	200	40	0.1	4.50	7.00	2.95	0.131	1.11	1.128	5.295	94	3.27	C
D1_0.1MPS_2	2	200	40	0.1	4.20	7.80	2.67	0.129	0.99	1.066	5.372	87	3.21	C
D1_0.1MPS_3	2	200	40	0.1	4.11	8.08	2.65	0.139	1.06	1.103	4.978	92	3.19	C
D2_1MPS_1	2	200	40	1.0	25.80	8.01	5.34	0.130	2.00	1.512	5.331	66	5.20	C
D2_1MPS_2	2	200	40	1.0	33.20	8.02	4.89	0.131	1.84	1.452	5.297	55	5.53	C
D2_1MPS_3	2	200	40	1.0	29.40	8.40	4.85	0.125	1.75	1.415	5.541	78	5.37	C
D3_3MPS_1	2	200	40	3.0	46.60	9.91	7.03	0.119	2.41	1.661	5.815	59	6.00	C
D3_3MPS_2	2	200	40	3.0	53.50	9.50	6.85	0.127	2.51	1.694	5.457	65	6.20	C/CE
D3_3MPS_3	2	200	40	3.0	54.30	10.01	7.25	0.109	2.29	1.620	6.312	66	6.22	C/CE
D4_5MPS_1	2	200	40	5.0	103.10	12.00	8.66	0.099	2.49	1.688	6.947	48	7.19	C/CE
D4_5MPS_2	2	200	40	5.0	104.80	9.01	7.65	0.110	2.44	1.670	6.265	55	7.22	C/CE
D4_5MPS_3	2	200	40	5.0	101.60	13.12	8.64	0.101	2.51	1.693	6.879	50	7.17	C/CE
D5_8MPS_1	2	200	40	8.0	155.10	15.03	9.55	0.100	2.85	1.781	6.875	45	7.85	C/CE
D5_8MPS_2	2	200	40	8.0	150.10	12.95	9.05	0.099	2.60	1.726	6.939	48	7.80	C/CE
D5_8MPS_3	2	200	40	8.0	130.40	11.02	9.82	0.097	2.75	1.774	7.125	50	7.57	C/CE
D6_5MPS_1	4	200	40	5.0	98.70	15.62	8.47	0.101	2.47	1.182	6.860	42	7.12	C/CE
D6_5MPS_2	4	200	40	5.0	94.50	14.59	9.24	0.102	2.73	1.241	6.786	40	7.05	C/CE
D6_5MPS_3	4	200	40	5.0	92.70	13.72	9.23	0.114	3.03	1.310	6.087	46	7.02	C/CE
D7_5MPS_1	2	200	25	5.0	98.57	8.29	6.53	0.128	2.43	1.665	5.378	61	7.12	C/CE
D7_5MPS_2	2	200	25	5.0	104.51	7.33	7.60	0.139	3.05	1.866	4.984	57	7.21	C/CE
D7_5MPS_3	2	200	25	5.0	108.72	7.24	6.01	0.133	2.67	1.745	5.198	75	7.27	C/CE

Note: *C* refers to debonding due to concrete failure, *CE* refers to debonding in the interface of concrete-epoxy, *A* is the ultimate strain derived from the regression analysis, *B* refers to the stiffness index obtained from the regression analysis, and $f_{t,DIF}$ refers to the estimated dynamic tensile strength of concrete.

5.1.2 Experimental results and discussions

5.1.2.1 Failure mode

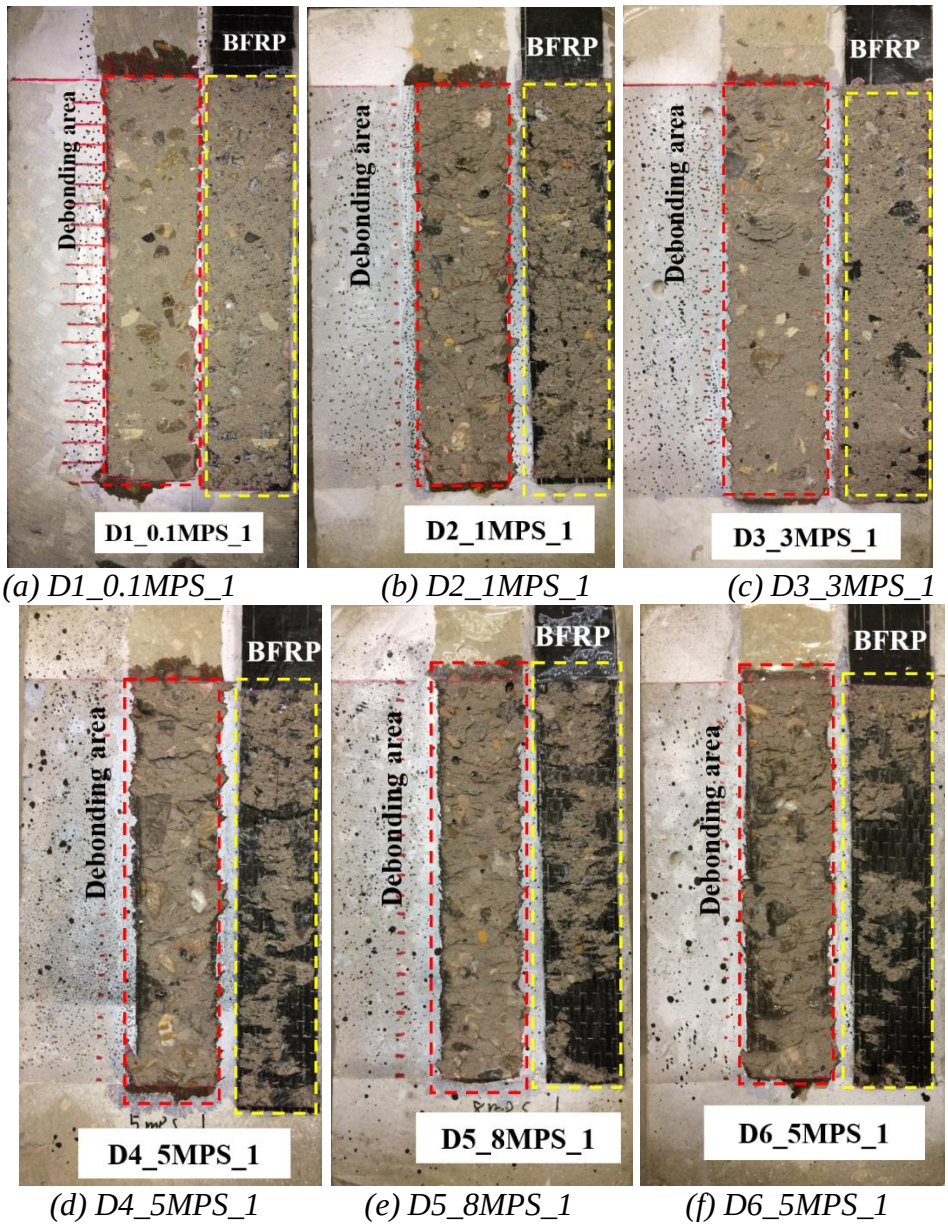

(a) D1_0.1MPS_1 *(b) D2_1MPS_1* *(c) D3_3MPS_1*

(d) D4_5MPS_1 *(e) D5_8MPS_1* *(f) D6_5MPS_1*

Figure 5-3. Failure modes under different loading speeds

The failure modes under different loading speeds are shown in Figure 5-3. For the specimens under quasi-static loading and the dynamic loading speeds of 0.1 m/s, 1 m/s and 3 m/s, debonding occurred owing to the failure of concrete substrates and a thin layer of concrete was peeled off. In addition, the fracture path always penetrated through the aggregate-to-mortar interface, where it is the interfacial transition zone (ITZ). However, under the higher loading speeds of 5 m/s and 8 m/s, the failure mode changed, as shown in Figure 5-3 (d), (e) and (f). The peel-off failure of the concrete substrate is no longer uniform. The more concrete detachment was observed near the loaded end. A small amount of adhesive layer, which is not very clear in the photos, was found on the detached concrete substrates

close to the free end. These results show that the debonding failure not only occurred because of the concrete failure but also because of the failure of the concrete-epoxy interface, and the failure was not uniform along the bonded area. This indicates that the debonding failure was sensitive to the loading speed. This might be due to the interfacial transition zone between aggregate and mortar is strong enough under higher strain rate because of the enhanced concrete tensile strength. In general, high-speed loading leads to two possible debonding failure modes: (1) concrete failure (C) and (2) concrete-epoxy (CE) interface failure. The cracking resistance of concrete and rupture resistance of epoxy is enhanced under dynamic loads. The debonding initiated from the weaker layer of two interfaces (i.e. C and CE).

5.1.2.2 Load-slip relationship

Digital image correlation (DIC) technique was used to measure the fields of displacement and strain of the Region of Interest (ROI), which is shown in Figure 5-4. The reliability of the DIC technique is verified against actual reading from strain gauges as proven in the previous study by Yuan et al. (127). Due to the ringing effect, severe oscillation may be observed in the measured load-time curves. The system ringing in dynamic tests is a common phenomenon and cannot be eliminated if the contact measurement method is adopted (189, 190). Therefore, DIC as the non-contact measurement method was used to mitigate the vibration effect. The ROI consists of two parts, one is the unbonded part which is reserved to eliminate the edge effect of concrete, and the other region is the bonded part with a bond length of 200 mm.

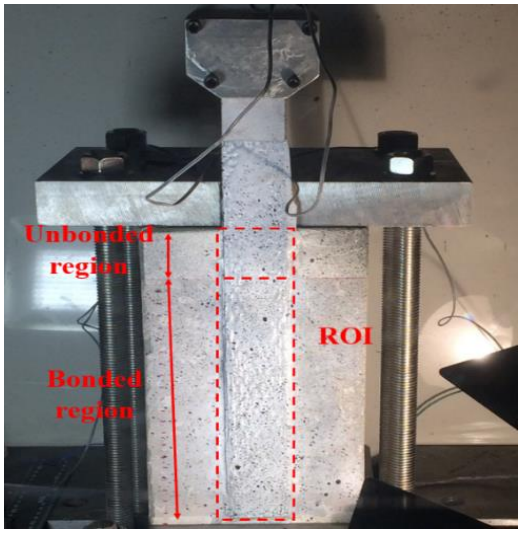

Figure 5-4. Region of interest (ROI)

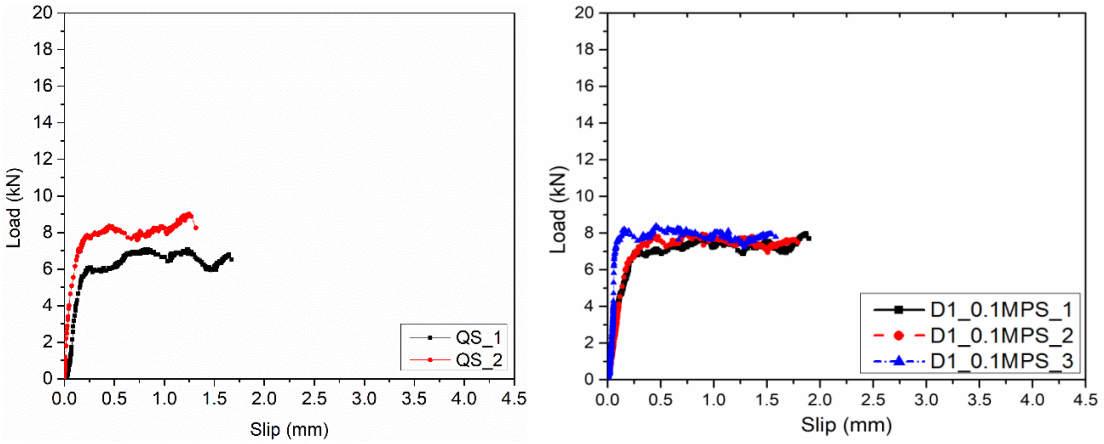

(a) QS_1 and 2

(b) D1_0.1MPS

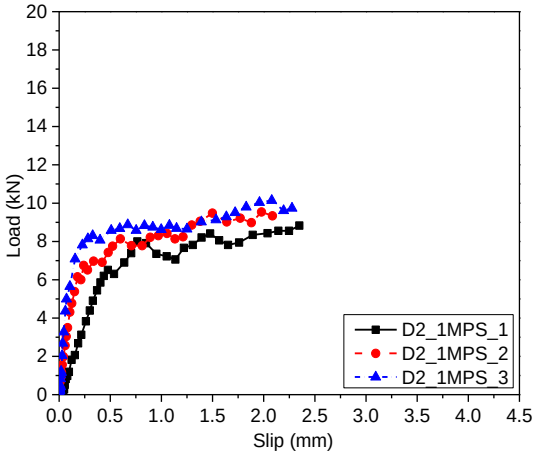

(c) D2_1MPS

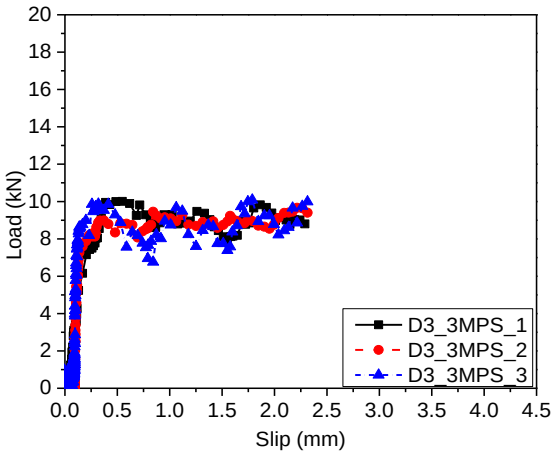

(d) D3_3MPS

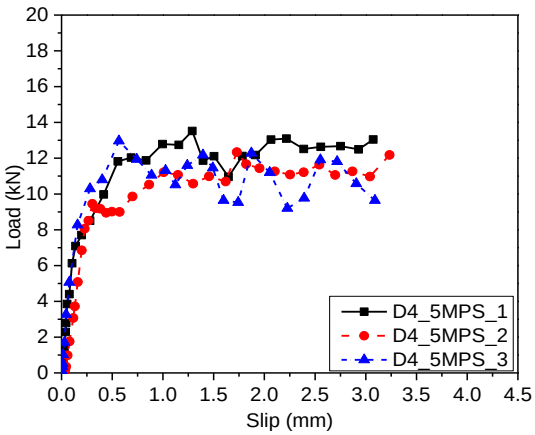

(e) D4_5MPS

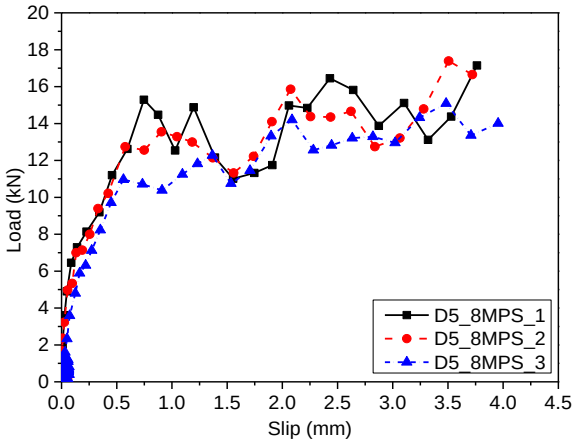

(f) D5_8MPS

Figure 5-5. Load and slip curves

Figure 5-5 illustrates the load-slip curves for all the tested specimens. As can be seen, the pattern of the load-slip curves has not been affected by the strain rate as the elastic stage and debonding plateau under dynamic loadings are similar to those under quasi-static loads. The debonding load and ultimate slip increased with the loading velocity. As listed in Table 5-1, the average debonding loads of the specimens QS (i.e. QS_1 and QS_2), D1_0.1MPS, D2_1MPS, D3_3MPS, D4_5MPS, and D5_8MPS were 7.63 kN, 8.14 kN, 9.81 kN, 11.38 kN, 13.00 kN, and 14.64 kN, respectively. With the increasing

strain rate from 2.59E-5 s^{-1} to 4.27 s^{-1}, 29.47 s^{-1}, 51.47 s^{-1}, 103.17 s^{-1}, and 155.10 s^{-1}, the dynamic debonding loads increased by 3.06%, 10.05%, 32.52%, 53.74%, and 97.88%, respectively. This indicates that the interfacial bond strength is enhanced due to the increased cracking resistance of concrete substrates under dynamic loads. In addition, the ultimate slip increased as well with the rising strain rate, indicating that the debonding process under dynamic loads is more ductile than that under quasi-static loads. Up to the loading velocity of 3 m/s, the slip at debonding load was approximately 0.25 mm while the corresponding values for the cases of 5 m/s and 8 m/s were about 0.5 mm and 0.6 mm, respectively. This is because the BFRP sheets can experience more deformation during the microcracking stage and debonding process to overcome the enhanced interfacial bond strength under dynamic loads. The increased debonding load and slip indicate that the ductility of the single-lap shear specimens increases with the strain rate. It should be noted that only two specimens were tested under quasi-static tests.

5.1.2.3 Strain distribution

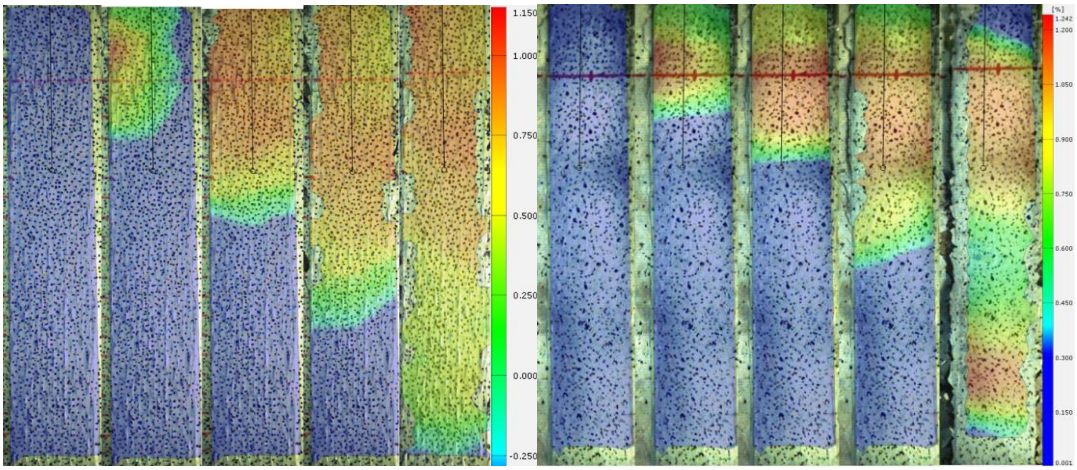

(a) QS_1 (b) D1_0.1MPS_1

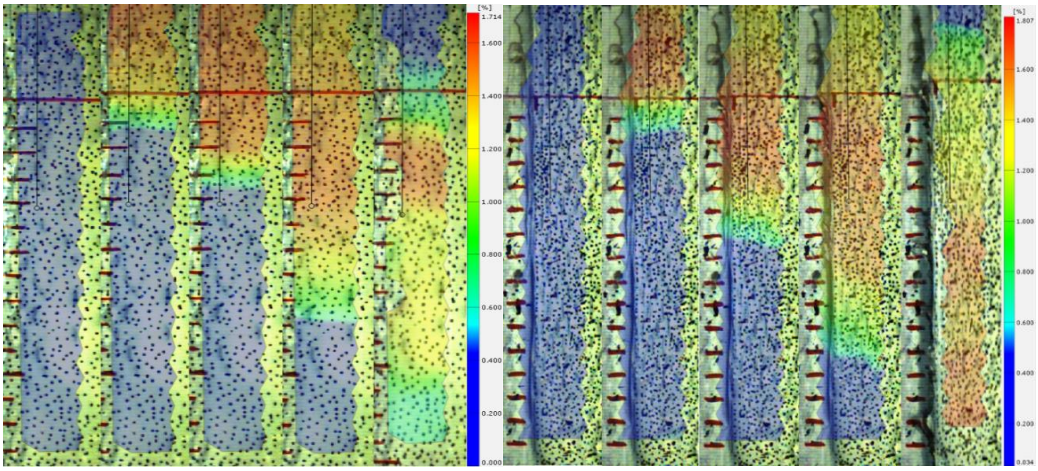

(c) D3_3MPS_1 (d) D5_8MPS_1

Figure 5-6. Strain contours under different loading instants

FRP strain profile of each specimen under different loading stages was derived by the DIC technique. Figure 5-6 illustrates the strain contours in different colours. Red and blue colours represent the maximum and minimum strain. The strain contours also provide the strain value and strain transfer length of BFRP sheets. Overall, similar patterns of strain distribution along the loading direction were observed. It seems that the pattern of strain fields was not affected by the strain rate. With the increasing loading speed, more uniform strain distribution was observed in the ROI. For the specimens under the loading speeds of 8.33E-6 m/s and 0.1 m/s, non-uniform strain concentration was observed around the loaded end of the BFRP sheets at the beginning of loading, as shown in Figure 5-6 (a and b), indicating that the strain profile was marginally impacted by the strain rate because the cracking in the concrete layer had enough time to penetrate from the weak parts of the concrete under relatively lower loading speed (e.g. less than 0.1 m/s). The localization of strain indicates the concentration of shear stress in the red colour. The colours of yellow, green and light blue refer to the shear stress transition zone. The dark blue represents the non-stress transfer zone.

Figure 5-7 plots the strain time histories of BFRP sheets at the selected six points indicated in Figure 5-1. The debonding initiated from Point 1 (closer to the loaded end) to Point 6 (closer to the free end), which is similar to the results under quasi-static loadings as reported by Baky et al. (191). With the increase of loading speed, significantly higher ultimate debonding strain and shorter duration of loading time were obtained. As compared to the case of low loading speeds, the BFRP strain of specimens associated with high loading speeds raised much more rapidly. The FRP debonding strain raised with strain, indicating that the shear resistance of the BFRP-to-concrete interface was enhanced with the strain rate. In addition, changing the BFRP sheets from two layers (Figure 5-7 d) to four layers (Figure 5-7 f) resulted in the decrease of the strain under the same loading velocity of 5 m/s, indicating that the increased thickness of BFRP sheets reduced the strain development under dynamic loading.

To obtain dynamic stress equilibrium, at least three reverberations of the loading wave in the specimen are required for a uniaxial tensile test (192, 193). To estimate the velocity of the stress wave, the equation $c = \sqrt{\frac{E}{\rho}}$ can be employed. However, the stress wave velocity of the FRP-to-concrete joints is not easy to estimate due to the two interfaces including BFRP-to-epoxy and epoxy-to-concrete in the FRP-to-concrete joints. The elastic modulus E and the density ρ cannot be confirmed due to the multiple interfaces. Thus, six points were selected from the BFRP sheets to compare the strain distributions at different instants of time, as shown in Figure 5-1 (194, 195). As can be observed in Figure 5-7, once the strain of the first five selected points reaches the maximum value it remains

almost a constant leading to a uniform strain distribution along with the specimen, demonstrating that the dynamic SST satisfies the dynamic stress equilibrium. The reason for the different strain distribution of point 6 from the other points including the shape and value is because the point closer to the free end of FRP cannot develop the full debonding process due to the brittle behaviour.

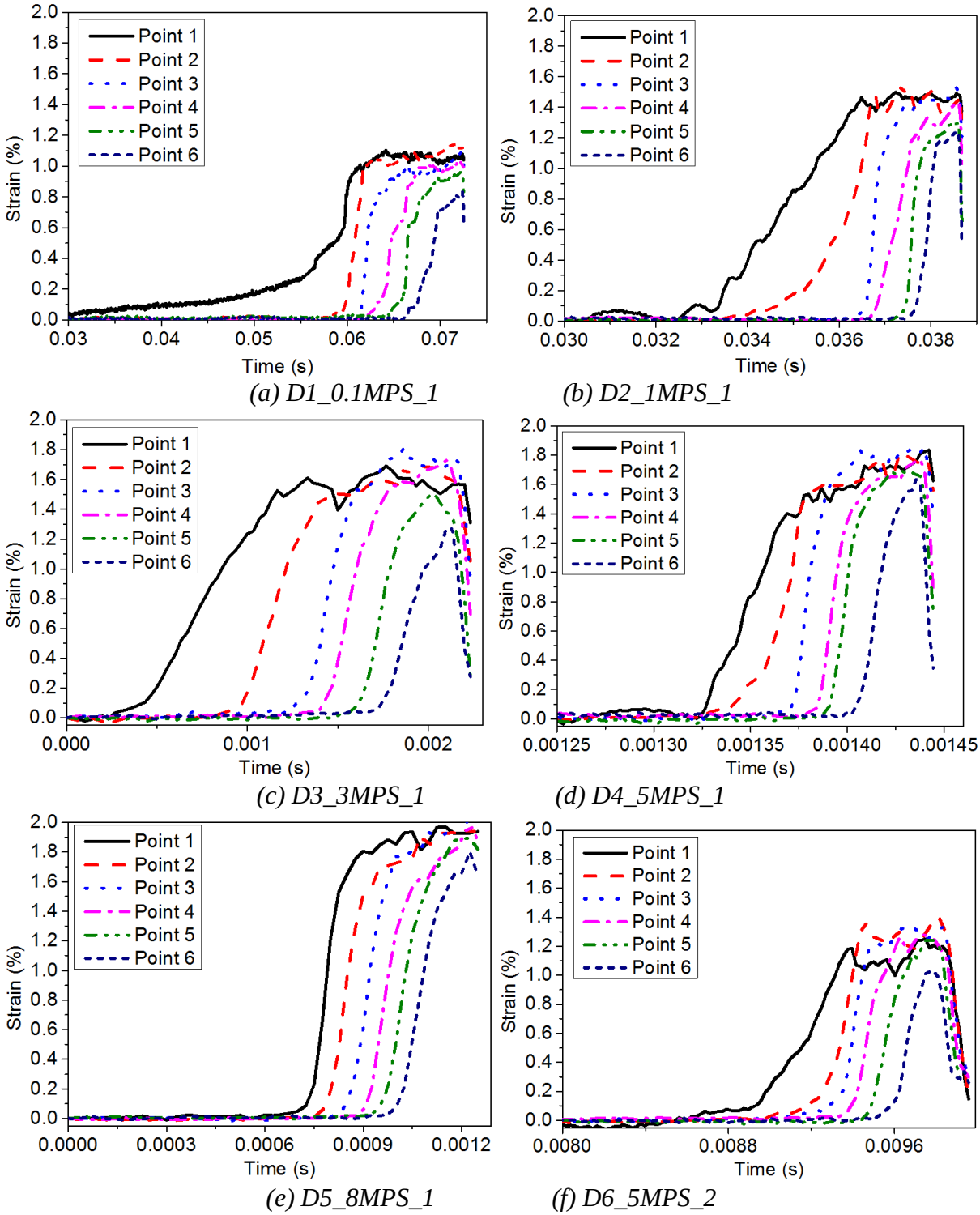

(a) D1_0.1MPS_1 *(b) D2_1MPS_1*

(c) D3_3MPS_1 *(d) D4_5MPS_1*

(e) D5_8MPS_1 *(f) D6_5MPS_2*

Figure 5-7. Strain-time histories

Figure 5-8 shows the strain distributions along the bond length of BFRP sheets at different loading levels. For all the specimens, the strain firstly increased with the applied loads. As the applied load

reached the initial debonding stage (P_u), there was nearly no further increment of the strain. The strain distribution remained the "*Z*" profile to develop the debonding process. As shown in Figure 5-8, the FRP debonding strain significantly raised with the rising loading rate, and the larger shear stress transfer region can be observed when the ultimate load was achieved. In addition, the BFRP strain profile under higher loading speeds is steeper than that obtained with lower loading speeds, indicating that the enhanced shear resistance is obtained for BFRP-strengthened concrete joints under higher speed loadings. Figure 5-8 (d) and (f) shows the strain distributions by changing two layers of BFRP sheets to four layers under the same loading speed of 5 m/s. The measured results demonstrated that increasing BFRP stiffness significantly enhanced the shear resistance under dynamic loads. However, the loading speeds had a marginal effect on the strain distribution gradient. The profile of the strain distribution subjected to dynamic loadings is similar to that under static tests, which has been also reported by Huo et al. (196).

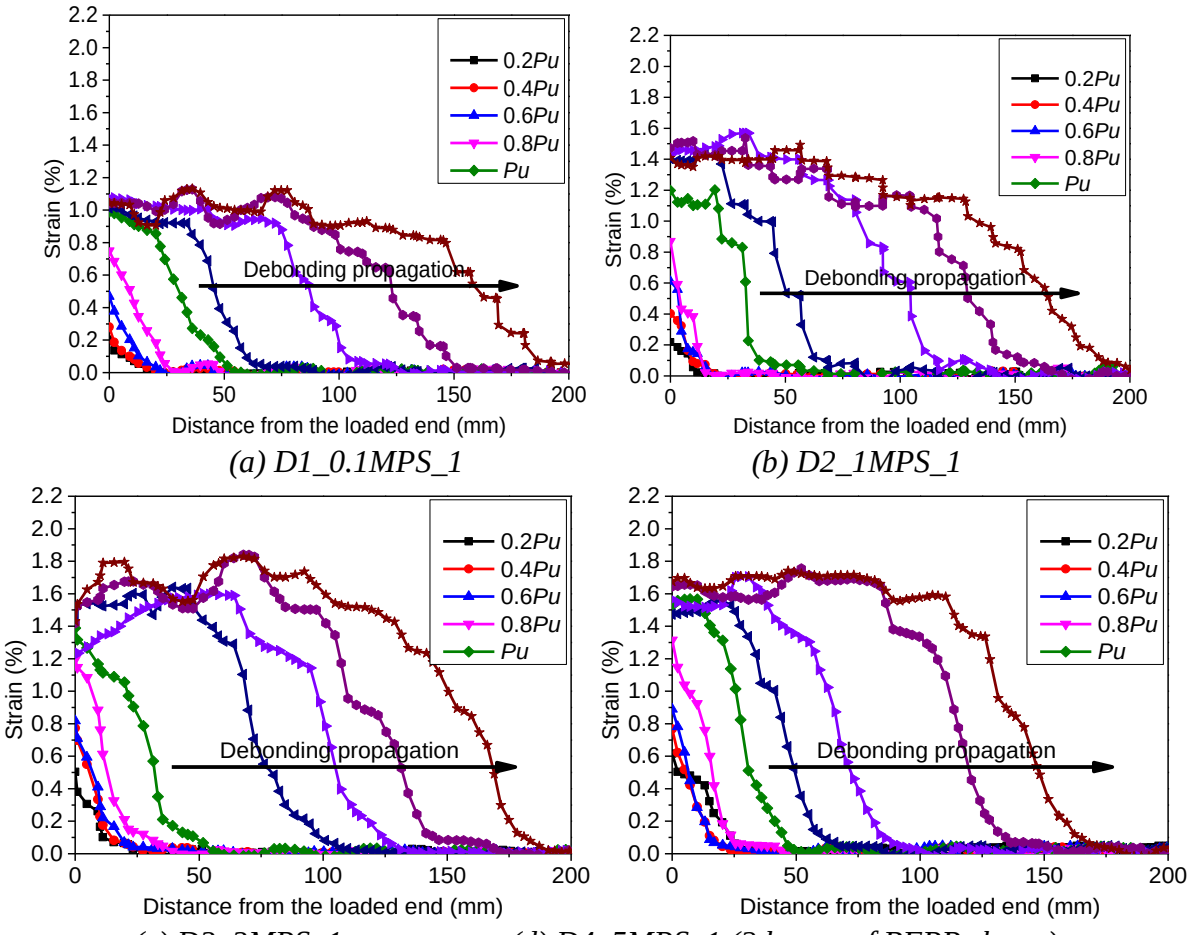

(a) D1_0.1MPS_1 *(b) D2_1MPS_1*

(c) D3_3MPS_1 *(d) D4_5MPS_1 (2 layers of BFRP sheets)*

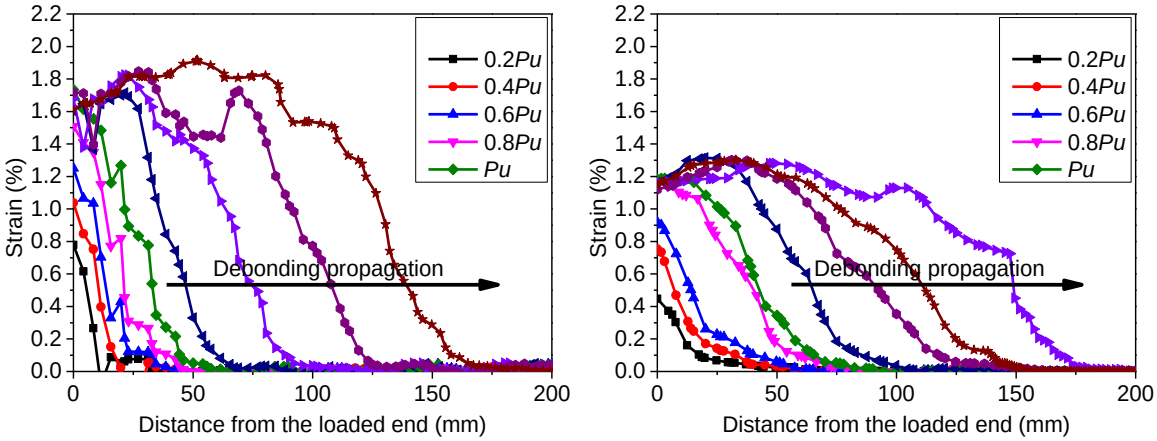

(e) D5_8MPS_1 *(f) D6_5MPS_2 (4 layers of BFRP sheets)*

Figure 5-8. Strain distributions under different loading speeds

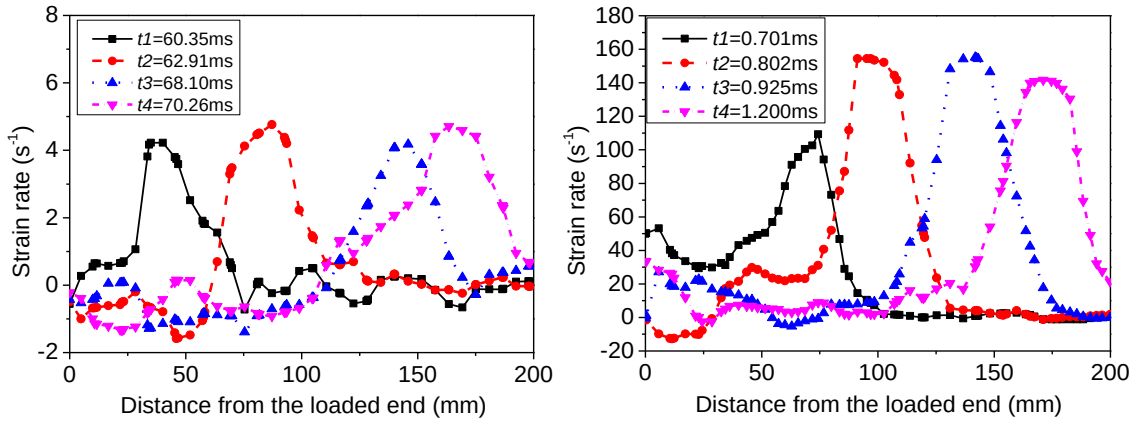

(a) D1_0.1MPS_1 (b) D5_8MPS_1

Figure 5-9. Strain rate distributions at different time instants

Table 5-1 gives the maximum strain rate for all the tested specimens. The determination of the strain rate in this section was based on the differentiation of strain time history, as given in Equation (5-1). In general, the peak strain rate increased with the loading speed. Figure 5-9 illustrates the relationship between the strain rate and the location at different time instants. The strain rates varied with time reaching the maximum strain rate and maintained its bell shape to propagate along the bonded length of BFRP sheets. The maximum strain rate was approximately 155.10 s^{-1} at the loading speed of 8 m/s while the strain rate was around 4 s^{-1} at the loading speed of 0.1 m/s.

$$\dot{\varepsilon} = \frac{d\varepsilon}{dt} \tag{5-1}$$

5.1.2.4 Strain-slip relationship

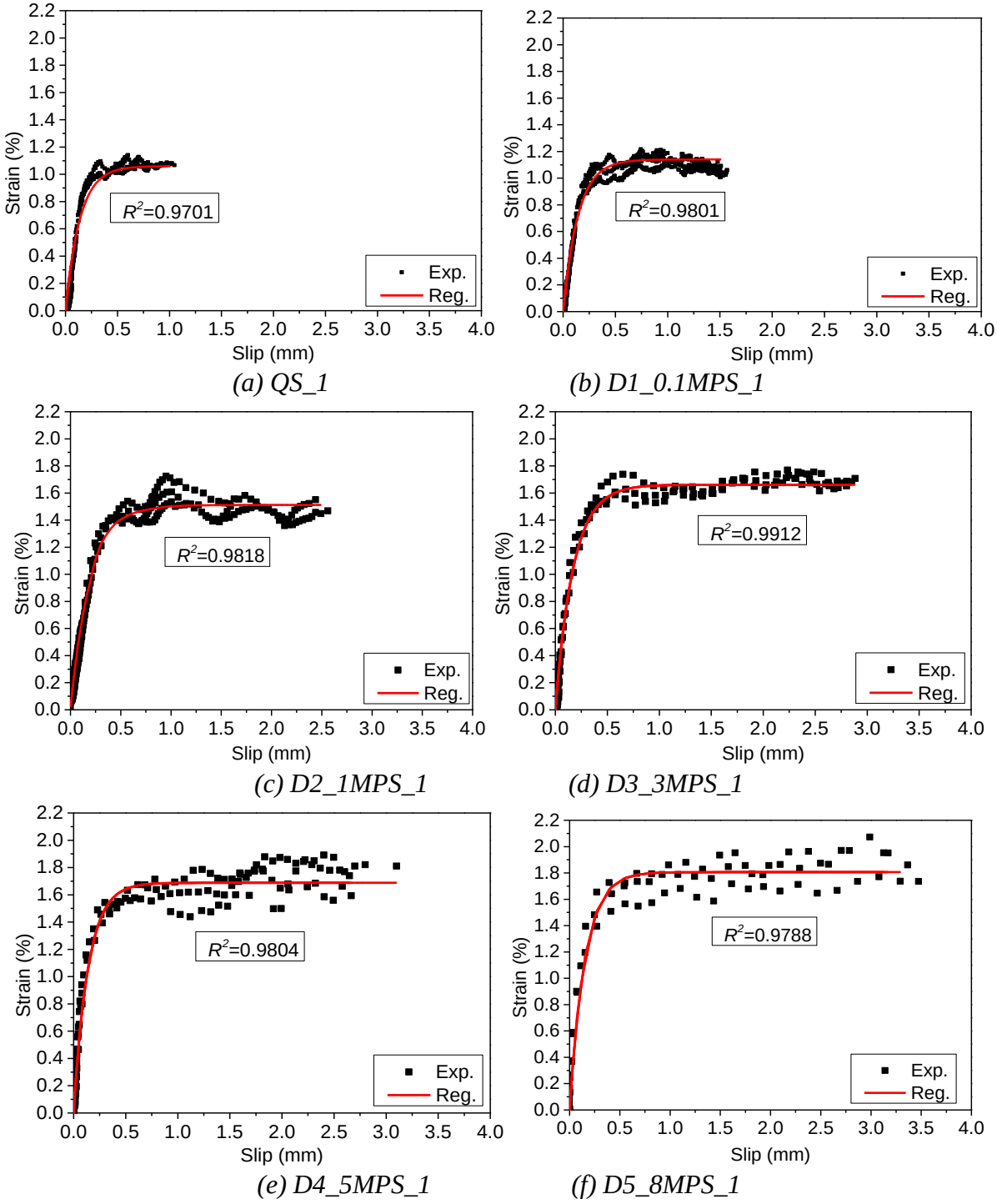

Figure 5-10. Strain-slip curves from the experimental results

To obtain the interfacial bond-slip relationships between FRP and concrete, a non-linear fitting equation proposed by Dai et al. (90) was employed herein. Three sets of strain-slip curves corresponding to each specimen were adopted for regression analysis. Three points (i.e. Point 1, Point 2, and Point 3 as shown in Figure 5-1) near the loaded end of BFRP sheets were selected from the DIC, as shown in Figure 5-10. The points close to the free end were not selected because the points

near the free end cannot represent the debonding behaviour of the points close to the loaded end due to the brittle debonding of the BFRP-to-concrete interface. As proposed by Dai et al. (188), the relationship between strain and slip can be expressed as follows (37, 90):

$$\varepsilon = f(s) = A\left(1 - e^{-Bs}\right) \tag{5-2}$$

where *A* and *B* are the coefficients obtained from the fitted *ε*-*s* curves of experimental results, *A* is the ultimate debonding strain of the FRP with enough bond length, *B* refers to the stiffness index, which dominates the shape of the bond-slip curves (90).

The selected three points measured in these tests had a similar strain-slip relationship, and the tested and regressed strain-slip curves show non-linear behaviour because of concrete cracking (197). Figure 5-11 illustrates the relationship between the bond-slip curve (R) and the strain-slip curve (L). After regression analysis of the strain-slip curves, two parts can be obtained including part 1 (red colour) and part 2 (black colour). A nonlinear exponential function can be employed to describe the bond-slip curve due to the cracking of the concrete layer during the debonding process (90).

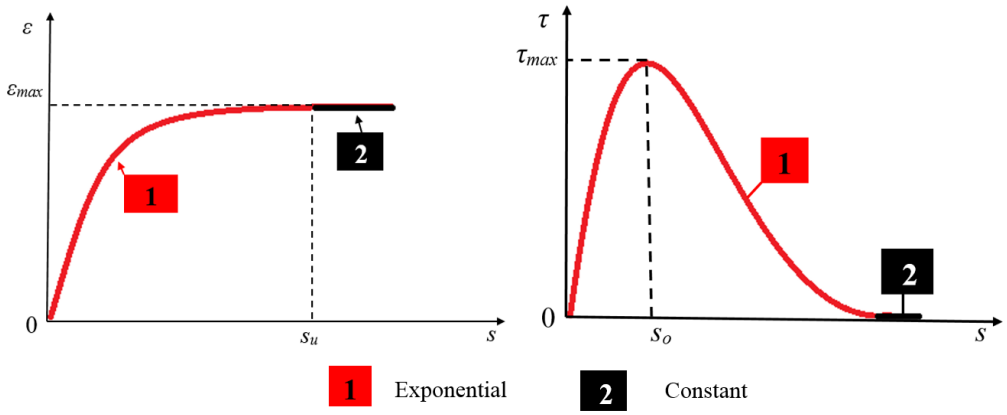

Figure 5-11. (L) Strain-slip curve; (R) Bond-slip curve

The coefficients *A* and *B* from regression analysis are listed in Table 5-1. The comparison of the best-fitted strain-slip curves is plotted in Figure 5-12 (L). With the rising loading rate, the BFRP strain and the ultimate slip raised significantly. The average ultimate debonding strains (i.e. *A*) of the specimens D1_0.1MPS, D2_1MPS, D3_3MPS, D4_5MPS, and D5_8MPS were 1.099%, 1.459%, 1.658%, 1.683%, and 1.760%, respectively. With the increasing strain rate from 2.50E-5 s^{-1} to 4.27 s^{-1}, 29.47 s^{-1}, 51.47 s^{-1}, 103.17 s^{-1}, and 155.10 s^{-1}, the dynamic debonding strains increased by 15.32%, 53.17%, 74.01%, 76.67%, and 84.12%, respectively, and the stiffness index *B* increased by 7.63%, 10.63%, 17.81%, 28.07%, and 30.99%, respectively. For the specimens subjected to dynamic loads, a slight change in the initial interface stiffness can be observed in Figure 5-12. The improved initial stiffness indicates that the effect of strain rate on the interface was significant. The improved interfacial

stiffness should be affected by the stiffness of the concrete layer, the adhesive layer, and the FRP layer. Additionally, the bonding width of BFRP sheets has a limited effect on the interfacial stiffness except for the ultimate debonding strain under dynamic loading of 5 m/s by changing the BFRP width from 25 mm to 40 mm, as given in Table 5-1 and as shown in Figure 5-12 (R). By increasing the BFRP layers from 2 to 4, the interfacial stiffness is slightly improved due to the increased average value of B but the ultimate debonding strain drops significantly in the tests. This indicates that the increased BFRP stiffness ($E_f t_f$) enhances the shear resistance of the BFRP-to-concrete interface under dynamic loads, which is consistent with the results under static loads as reported by Subramaniam et al. (198). The interfacial stiffness K can be expressed as follows (199):

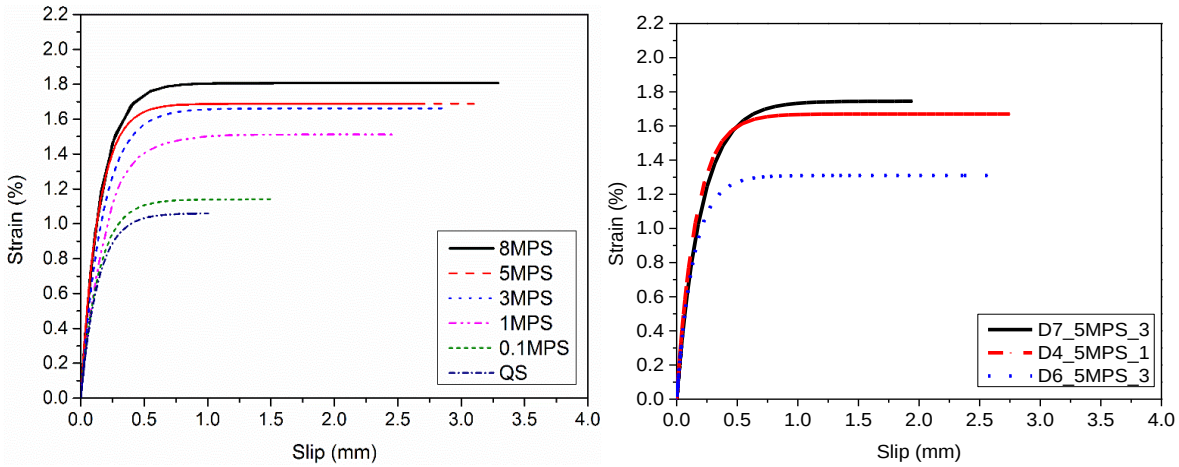

Figure 5-12. Strain-slip curves for the specimens under different loading speeds

$$K = \frac{1}{\frac{t_c}{G_c} + \frac{t_a}{G_a} + \frac{t_s}{G_s}} \tag{5-3}$$

$$G_i = \frac{E_i}{2(1+\nu_i)} \tag{5-4}$$

where G_c, G_a, and G_s are the shear modulus of concrete, adhesive, and FRP layer, respectively; t_c, t_a, and t_s are the thickness of the concrete, adhesive, and FRP layer, respectively; G_i is the shear modulus, and ν_i is Poisson's ratio (200). The interfacial stiffness improved significantly because Young's modulus of concrete is strain rate dependent (76, 201, 202). Hao and Hao (202) proposed equations to define the strain rate effect on the Young's modulus of concrete. Chen et al. (203) proposed equations to describe the relationship between strain rate and elastic modulus of BFRP sheets. Liao et al. (201) demonstrated the effect of strain rate on the tensile strength of epoxy. The interfacial stiffness K increased with the increase in G_c, G_a, and G_s according to Equations (5-3) and (5-4). It

should be noted that the thickness of the concrete, adhesive, and FRP were assumed as a constant in this section.

5.1.2.5 Strain profile and effective bond length

EBL is the distance of the stress transfer zone along which most of the bond shear stress is transmitted into the concrete (9). Three regions can be observed in the measured strain distribution: (1) fully debonded stage near the loaded end; (2) bond shear stress transferring stage; and (3) unstressed stage near the free end. In addition, EBL can be obtained through the strain distribution derived from the DIC technique (127).

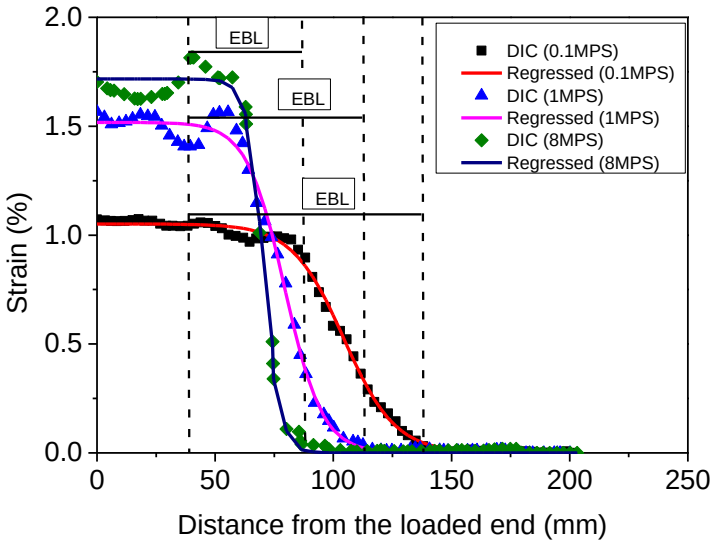

Figure 5-13. EBL under different loading speeds

As shown in Figure 5-13, successive digital images were prepared and analyzed using DIC and the longitudinal strain profile at each loading level was obtained. The averaged EBL at 8 m/s was 47.7 mm which is lower than 91 mm at 0.1 m/s. This indicates that the EBL decreased with the raising strain rate, which is evident with the steeper strain distribution gradient in Figure 5-13. The steeper strain distribution gradient indicates the shorter distance of the shear stress transferring zone. Table 5-1 gives the EBLs for all the tested specimens. The averaged EBLs for specimens QS, D1_0.1MPS, D2_1MPS, D3_3MPS, D4_5MPS, and D5_8MPS are 92.5 mm, 91 mm, 66.3 mm, 63.3 mm, 51 mm, and 47.7mm, respectively. As the strain rate raised from 2.59E-5 s^{-1} to 4.27 s^{-1}, 29.47 s^{-1}, 51.47 s^{-1}, 103.17 s^{-1}, and 155.10 s^{-1}, the dynamic EBL decreased by 1.62%, 28.29%, 31.53%, 44.86%, and 48.46%, respectively. In addition, changing the BFRP sheets from two layers to four layers resulted in the increasing effective bond length under static loads due to the increased BFRP stiffness ($E_f t_f$). For the specimens with four layers of BFRP sheets, the EBL decreased with the strain rate, which is the same as the specimens with two BFRP layers under dynamic loads. The test results show that the

descent rate after the loading speed of 3 m/s is slow indicating that the strain rate effect has a certain range of influence on the EBL, which agrees with the conclusions by Shen et al. (41) and Huo et al. (74).

5.1.2.6 Interfacial bond stress-slip relationship

The shear stress and the slip can be obtained by imposing the equilibrium condition of FRP sheets with the infinite length. The shear stress and slip can be obtained by the following equations:

$$\tau = E_f t_f \frac{df(s)}{ds} f(s) \tag{5-5}$$

where *f(s)* is the function of slip (*s*).

$$\frac{df(s)}{ds} = ABe^{-Bs} \tag{5-6}$$

By substituting Equation (5-6) into Equation (5-5), the interfacial bond-slip relationship can be expressed as a function of *A* and *B* as follows (90):

$$\tau = A^2 BE_f t_f (\mathrm{e}^{-Bs} - \mathrm{e}^{-2Bs}) \tag{5-7}$$

The IFE G_f is defined as follows:

$$G_f = \int_0^\infty \tau ds \tag{5-8}$$

By substituting Equation (5-7) into Equation (5-8), G_f can be yielded:

$$G_f = \frac{1}{2} A^2 E_f t_f \tag{5-9}$$

The coefficients *A* and *B* can be obtained by fitting the strains-slip curves in section 3.3. Figure 5-14 shows the fitted interfacial bond stress-slip curves at various loading rates. Table 5-1 gives the experimental results of PSS and the corresponding slip. It is obvious that the PSS raised remarkably with the strain rate. The average PSS of specimens D1_0.1MPS, D2_1MPS, D3_3MPS, D4_5MPS, and D5_8MPS are 2.76 MPa, 5.03 MPa, 7.04 MPa, 8.32 MPa, and 9.47 MPa, respectively. It can be observed that the IFE increases with the strain rate as well, which is defined as the enclosed area of the bond-slip curve. The average IFE of specimens of D1_0.1MPS, D2_1MPS, D3_3MPS, D4_5MPS, and D5_8MPS are 1.05 N/mm, 1.86 N/mm, 2.40 N/mm, 2.48 N/mm, and 2.73 N/mm, respectively. The reason for the increment of the IFE is because the shear modulus of concrete, adhesive and FRP increased with the strain rate and the interfacial stiffness *K* increases with the shear modulus according to Equations (5-2) and (5-3). The increase of PSS is mainly due to the increment of IFE.

To verify the dynamic interfacial shear stress of the BFRP-to-concrete interface, the dynamic tensile strength of concrete corresponding to the strain rate was estimated to compare with the interfacial shear stress because of stripping of the concrete layers. There was no normal stress applied in the single-lap shear test, shear stress penetrated into the concrete with a 45^{o} angle and consequently, the debonding always initiated on the tensile side of the concrete substrate. The dynamic increase factor (DIF) of the concrete was employed herein to obtain the dynamic tensile strength of the concrete substrates ($f_{t,DIF}$) (204), as summarized in Table 5-1. It can be observed that the estimated dynamic tensile strength of the concrete substrates is close to the interfacial shear stress of the BFRP-to-concrete interfaces, indicating that the obtained PSS is reasonable and consistent with the tensile strength increment of concrete material with strain rate.

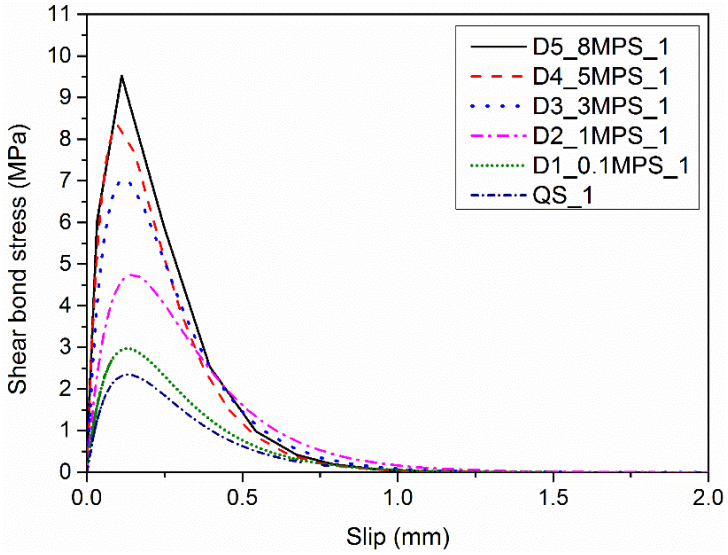

Figure 5-14. Fitted bond-slip curves under different loading speeds

5.1.3 Theoretical predictions and proposed models

5.1.3.1 Effect of strain rate on IFE

Figure 5-15 shows the relationship of the IFE against the strain rate. As the IFE increases with the strain rate, the relationship between $G_{f,d}$ and $G_{f,s}$ can be established by incorporating strain rate effect. Yen and Caiazzo (205) proposed logarithmic functions to define the strain rate effects on the mechanical properties of composites. Shen et al. (40) also used logarithmic functions to describe the relationship between strain rate and bond properties of the BFRP-to-concrete interface. Thus, the non-linear logarithmic function is employed herein to describe the impact of strain rate on the interfacial bond properties. After regression analysis, empirical equations incorporating strain rate effect are given below:

$$\frac{G_{f,d}}{G_{f,s}} = 1 + 3.354\times10^{-5}\left(\log(\frac{\dot{\varepsilon}_d}{\dot{\varepsilon}_s})\right)^{5.881} \quad \text{when } 2.5\times10^{-5} \le \dot{\varepsilon} \le 155.10 \qquad (5\text{-}10)$$

where $G_{f,d}$ and $G_{f,s}$ refer to the dynamic and static interfacial fracture energy, respectively; $\dot{\varepsilon}_d$ and $\dot{\varepsilon}_s$ refer to the dynamic and static strain rate, respectively.

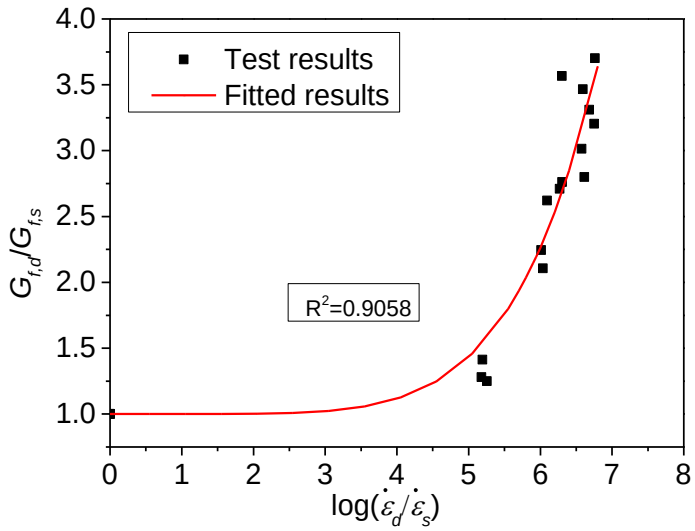

Figure 5-15. Relationship between IFE and strain rate

Dai et al. (90) proposed an equation to predict the $G_{f,s}$ considering the concrete compressive strength (f_c'), FRP stiffness (E_ft_f), and interfacial stiffness (G_a/t_a). As the shear modulus of concrete, adhesive, and BFRP (i.e. G_c, G_a, and G_F) together determine the interfacial stiffness, these factors (i.e. G_c, G_a, and G_F) are incorporated into the interfacial stiffness (K) and consequently the static interfacial fracture energy ($G_{f,s}$). Then the effect of strain rate is incorporated into the proposed static model to obtain the dynamic interfacial fracture energy. The proposed model is given below:

$$G_{f,s} = \varphi\left(E_f t_f\right)^{\theta} K^{C} \qquad (5\text{-}11)$$

$$K = \frac{\frac{G_c}{t_c}\frac{G_a}{t_a}\frac{G_F}{t_f}}{\frac{G_c}{t_c}\frac{G_a}{t_a} + \frac{G_a}{t_a}\frac{G_F}{t_F} + \frac{G_F}{t_F}\frac{G_c}{t_c}} \qquad (5\text{-}12)$$

where φ, θ, and C are coefficients determined from the data collection (35). After regression analysis according to the testing data, the coefficients are determined, and the static IFE is given as:

$$G_{f,s} = 0.345\left(E_f t_f\right)^{0.029} K^{-0.986} \qquad (5\text{-}13)$$

By substituting Equations (5-11), (5-12) and (5-13) into Equation (5-10), the dynamic interfacial fracture energy $G_{f,d}$ can be predicted by incorporating strain rate effect. It should be noted that the thickness of concrete t_c = 20 mm was selected according to (199). The thickness of concrete should be 2 or 3 times the aggregate size (147). E_c was determined by using $E_c = 4700\sqrt{f_c'}$ (21).

5.1.3.2 Effect of strain rate on bond strength

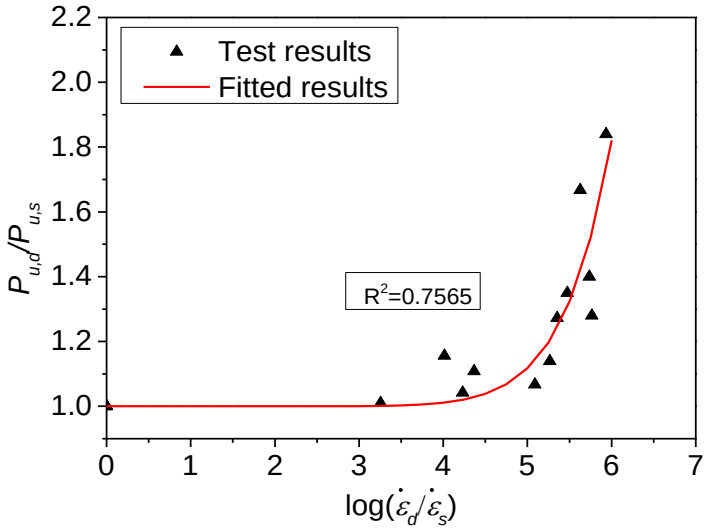

Figure 5-16. DIF of debonding load

Figure 5-16 shows the relationship of the debonding load P_u against strain rate. As the debonding load increases with the strain rate, the relation between dynamic and static debonding loads ($P_{u,d}$ and $P_{u.s}$) can be established by incorporating the effects of strain rate. After regression analysis, empirical equation incorporating the strain rate effect is given below:

$$\frac{P_{u,d}}{P_{u,s}} = 1 + 1.444\times10^{-10}\left(\log\left(\frac{\dot{\varepsilon}_d}{\dot{\varepsilon}_s}\right)\right)^{11.74} \quad \text{when } 2.5\times10^{-5} \le \dot{\varepsilon} \le 155.10 \tag{5-14}$$

The debonding load can be expressed by considering the IFE, which has been widely applied in estimating the interfacial debonding loads (35, 197, 200). The $G_{f,s}$ can be expressed by Equation (5-13) and the static debonding load ($P_{u.s}$) is given as:

$$P_{u,s} = b_f\sqrt{2E_f t_f G_{f,s}} \tag{5-15}$$

By substituting Equations (5-10) and (5-15) into Equation (5-14), the dynamic debonding load ($P_{u,d}$) can be obtained.

5.1.3.3 Effect of strain rate on interfacial shear stress and slip

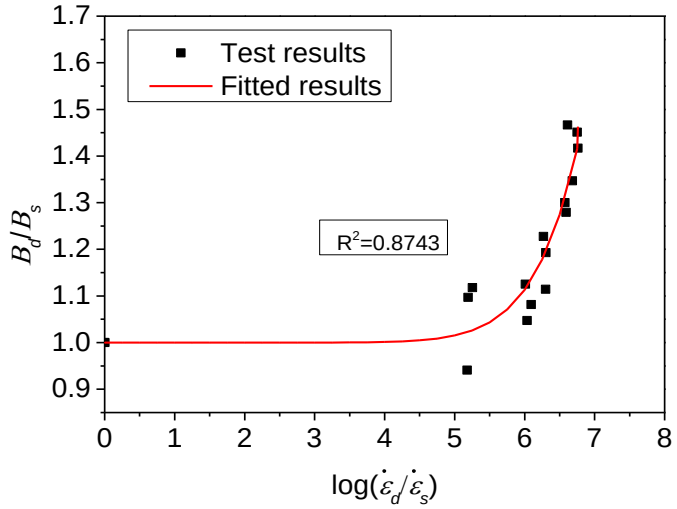

Figure 5-17. Relationship between stiffness index and strain rate

As discussed in section 5.3.4, two coefficients (i.e. G_f and B) can be obtained from the fitted strain-slip relationship, as shown in Figure 5-17. According to the previous model (90), both the interfacial fracture energy and the stiffness index B determine the bond stress-slip relationship.

$$\tau = 2BG_f\left(e^{-Bs} - e^{-2Bs}\right) \tag{5-16}$$

$$\tau_{\max} = \frac{1}{2}BG_f \tag{5-17}$$

$$s_o = \frac{In2}{B} = \frac{0.693}{B} \tag{5-18}$$

As the stiffness index B increases with the strain rate, and using the testing results given in Table 5-1, the dynamic stiffness index B_d by incorporating strain rate can be expressed by Equation (5-20). The relationship between the static stiffness index (B_s) and the mechanical properties of FRP, epoxy, and concrete can be expressed by Equation (5-19). After regression analysis, the stiffness index model is proposed as Equation (5-20).

$$B_s = 5.908\left(E_f t_f\right)^{0.108} K^{0.833} \tag{5-19}$$

$$\frac{B_d}{B_s} = 1 + 2.963\times10^{-10}\left(\log(\frac{\dot{\varepsilon}_d}{\dot{\varepsilon}_s})\right)^{11.03} \quad \text{when } 2.5\times10^{-5} \le \dot{\varepsilon} \le 155.10 \tag{5-20}$$

The PSS τ_m and the corresponding slip s_o are two critical factors determining the bond-slip response. The test results showed that the PSS increased while the corresponding slip decreased with the rising strain rate, as shown in Figure 5-18. After regression analysis, the τ_m and s_o can be obtained by the following equations:

$$\frac{\tau_{m,d}}{\tau_{m,s}} = 1 + 1.328\times10^{-6}\left(\log(\frac{\dot{\varepsilon}_d}{\dot{\varepsilon}_s})\right)^{7.795} \quad \text{when} \quad 2.5\times10^{-5} \le \dot{\varepsilon} \le 155.10 \tag{5-21}$$

$$\frac{s_{o,d}}{s_{o,s}} = 1 - 6.618\times10^{-9}\left(\log(\frac{\dot{\varepsilon}_d}{\dot{\varepsilon}_s})\right)^{9.226} \quad \text{when} \quad 2.5\times10^{-5} \le \dot{\varepsilon} \le 155.10 \tag{5-22}$$

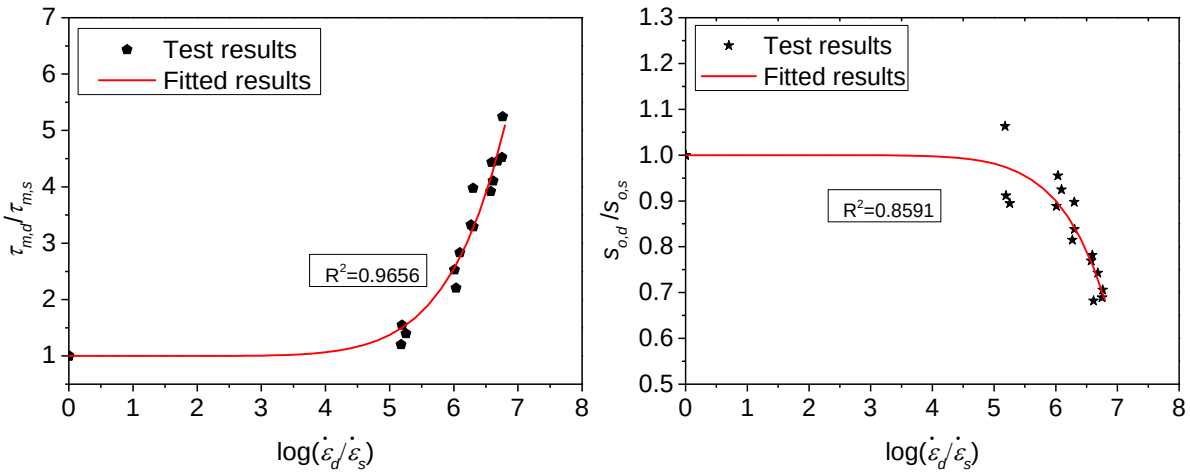

(a) PSS *(b) Slip at PSS*

Figure 5-18. Relationship between (a) peak shear stress vs. strain rate; (b) slip vs. strain rate

By substituting Equations (5-10) and (5-20) into Equation (5-17) and substituting Equations (5-19) and (5-20) into Equation (5-18), the dynamic peak shear stress $\tau_{m,d,}$ and the corresponding slip $s_{o,d}$ can be obtained. Additionally, the dynamic bond-slip relationships can be determined by substituting Equations (5-10), (5-17), (5-18) and (5-20) into Equation(5-16). Figure 5-19 plots the comparison of the predicted and tested bond-slip curves. It should be noted that all the proposed models in this section are applicable for the strain rate ranging between 2.5x10^{-5} s^{-1} and 155.10 s^{-1}.

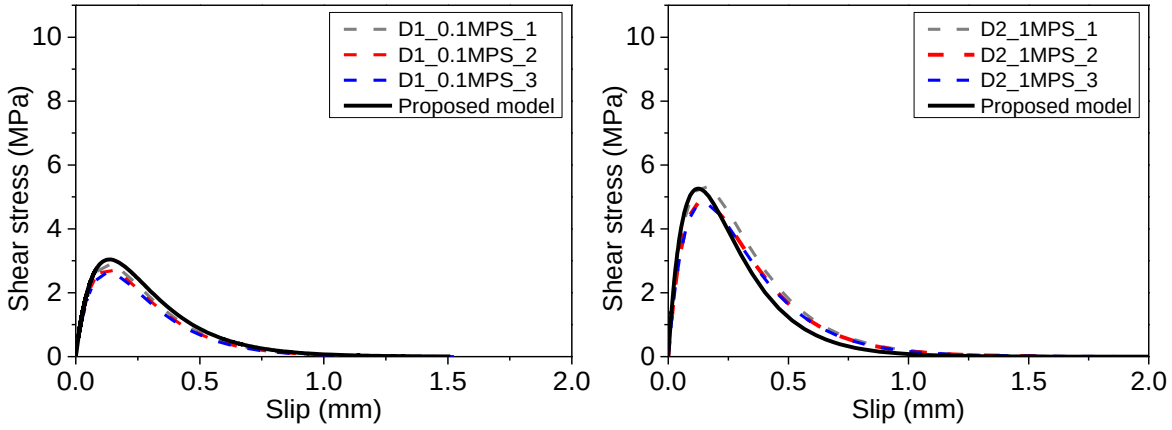

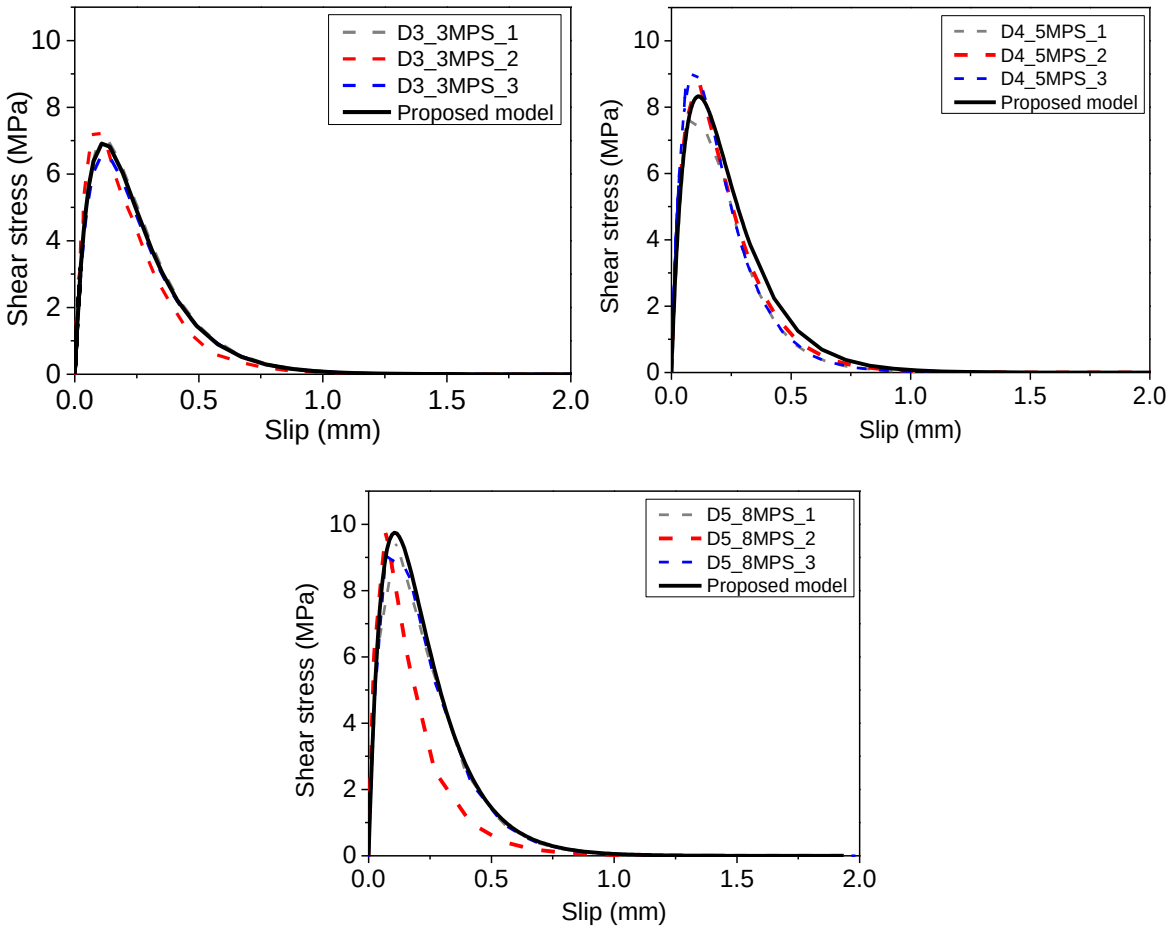

Figure 5-19. Predicted vs. tested bond-slip curves

5.1.3.4 Validation of the proposed dynamic models

The proposed dynamic bond-slip model can be used to determine the debonding load, the PSS, the BFRP strain distribution and the bond-slip curve. Testing results can directly provide the debonding load and FRP strain distribution. In this section, the present and previous testing data were collected to compare with the predicted results. As there were limited experimental studies in the literature regarding the dynamic interfacial bond of FRP-to-concrete interface, two studies by Huo et al. (74) and Shen et al. (41) are selected to validate the predictions. Figure 5-20 shows the comparisons of the predicted and tested results. The experimental results from the present study and the study of Shen et al. (41) match well with the predicted results. However, the experimental results by Huo et al. (74) are overestimated by the proposed model. The discrepancies might be due to different testing methods. Huo et al. (74) used the testing method of three-point impact tests on beams bonded by FRP for dynamic bonding test and consequently the additional bending moment and normal stress complicated the debonding process. However, Shen et al. (41) employed a double-lap shear test method and the present section used a single-lap shear test method to investigate dynamic bonding behaviours.

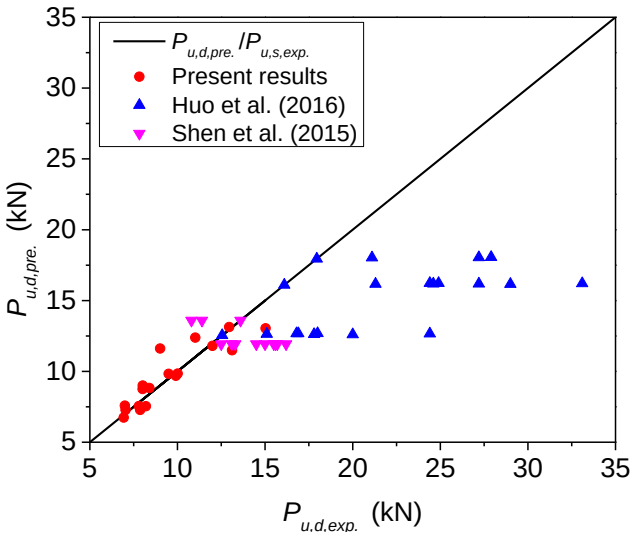

Figure 5-20. Experimental results vs. predicted results

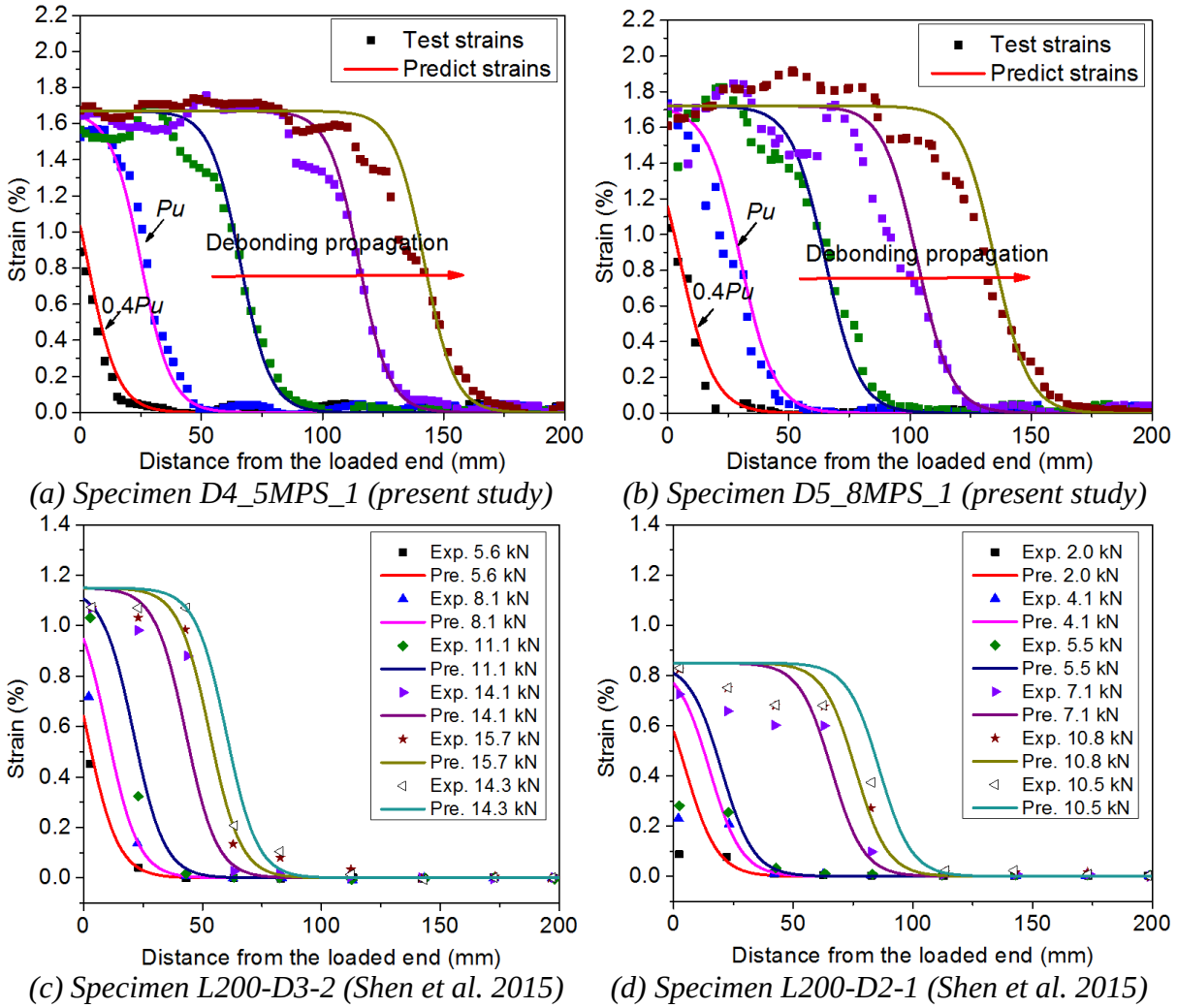

(a) Specimen D4_5MPS_1 (present study) *(b) Specimen D5_8MPS_1 (present study)*

(c) Specimen L200-D3-2 (Shen et al. 2015) *(d) Specimen L200-D2-1 (Shen et al. 2015)*

Figure 5-21. Comparison between the tested and predicted strain distributions

The FRP strain distributions along the bonded length can be obtained by the proposed bond-slip model based on the studies from Zhou et al. (37) and Yuan et al. (86). Analytical studies were carried

out by Zhou et al. (37) and Yuan et al. (86) on the full debonding process of FRP-to-concrete joints, and consequently, the strain distributions at various loading levels were predicted based on the proposed models. Figure 5-21 illustrates the comparison between the tested and predicted FRP strain distributions of four specimens. The Specimen D4_5MPS_1 and D5_8MPS_1) are selected from the present section, and it is noted that the BFRP strains were measured by the DIC method. The other two specimens (i.e. L200-D3-2 and L200-D2-1) were tested by Shen et al. (41), and the BFRP strains were measured by the strain gauges. Comparisons show that the predicted strain distributions match well with the tested results at different dynamic loading stages. The proposed model can properly predict the pre-debonding stage and post-debonding stage, and the predicted strain profile remained the same shape to propagate the debonding process. The experimental strain distributions of Huo et al. (74) were not compared herein due to different testing methods and different FRP materials.

5.1.4 Section summary

This section investigates the strain rate effect on the failure modes, strain distributions, interfacial fracture energy, strain-slip response, debonding load, and bond-slip response. The following conclusions can be drawn:

1. Strain rate changes the failure modes of the BFRP-to-concrete interface. Two debonding failure modes of the BFRP-to-concrete interface under dynamic loadings can be observed, i.e. debonding in concrete failure (C) and debonding in the interface of concrete-epoxy (CE).
2. The single-lap shear specimens under dynamic loadings exhibit more ductile behaviour due to the increased ultimate slip. The shear slip increases by 13.89%, 32.61%, 34.97%, 52.06%, and 58.48% with the rising strain rate from $2.5x10^{-5}$ s^{-1} to 4.27 s^{-1}, 29.47 s^{-1}, 51.47 s^{-1}, 103.17 s^{-1}, and 155.10 s^{-1}, respectively. The increased slippages at the interface improves the interfacial fracture energy and consequently the bond strength of the interface.

3. The strain distributions in BFRP sheets are significantly affected by the dynamic loads. The strain distribution gradient in the BFRP sheets under higher loading speeds is steeper than those obtained with lower loading speed. By changing the BFRP sheets from two layers to four layers, the debonding strain of BFRP sheets reduces due to the increased FRP thickness. Reducing the bonding width of BFRP sheets from 40 mm to 25 mm has little effect on the interfacial stiffness while the ultimate debonding strain increases under dynamic loads.

4. The dynamic effective bond length (EBL) decreases with the increasing strain rate, but the effect of strain rate on the EBL becomes less prominent when subjects to a relatively higher loading rate, such as 5 m/s and 8 m/s.

5. By comparing the predicted results with the testing data, the validated proposed dynamic bond-slip model by incorporating the strain rate can accurately predict the dynamic bond behaviour of the BFRP-to-concrete interface.

5.2 Effect of hybrid FRPs

In this section, to investigate the effect of hybrid FRPs, an experimental investigation on the dynamic interfacial bond behaviours between hybrid carbon/basalt fibre reinforced polymer (FRP) sheets and concrete under high loading velocities (i.e., 8.33E-6, 1.0, 3.0, and 8.0 m/s) is carried out. The single-lap shear specimens are evaluated with different stacking sequences of FRP sheets (i.e., CFRP and BFRP) bonded to the concrete substrates. Experimental results including debonding failure modes, ultimate debonding strain, debonding load, interfacial fracture energy, and bond-slip response are discussed and evaluated. Empirical formulae are proposed based on the test data to predict the dynamic interfacial bonding strength and shear stress between sole or hybrid FRP sheets and concrete at various strain rates.

The related work in this section has been published in International Journal of Adhesion and Adhesive.

Yuan C, Chen W, Pham TM, Hao H, Cui J, Shi Y. Dynamic Interfacial Bond Behaviour between Hybrid Fibre Reinforced Polymer Sheets and Concrete. International Journal of Adhesion and Adhesive. 2020; 99: 102569.

5.2.1 Experimental program

5.2.1.1 Material properties

Forty-four FRP-to-concrete specimens were prepared in total. The concrete substrate had 30.14 MPa compressive strength and 3.12 MPa tensile strength. The dimension of the concrete block was 150 mm x 150 mm x 300 mm, and the dimension of the carbon fibre (CFRP), basalt fibre (BFRP), and hybrid composites (HCB) were 40 mm x 400 mm. The nominal thickness of the CFRP and BFRP sheet was 0.167 mm and 0.12 mm, respectively. The bond area was 40 mm x 200 mm with a 50 mm unbonded region reserved at the loaded end to eliminate the concrete edge effect. Details of the specimens are shown in Figure 5-22. The specimen with stacking order of 1C1B denotes one non-attaching layer of CFRP (1C) and one attaching layer of BFRP (1B) to the concrete substrate, as shown in Figure 5-22. The measured mechanical properties of FRPs (CFRP, BFRP, and HCB) were summarized in Table 5-2.

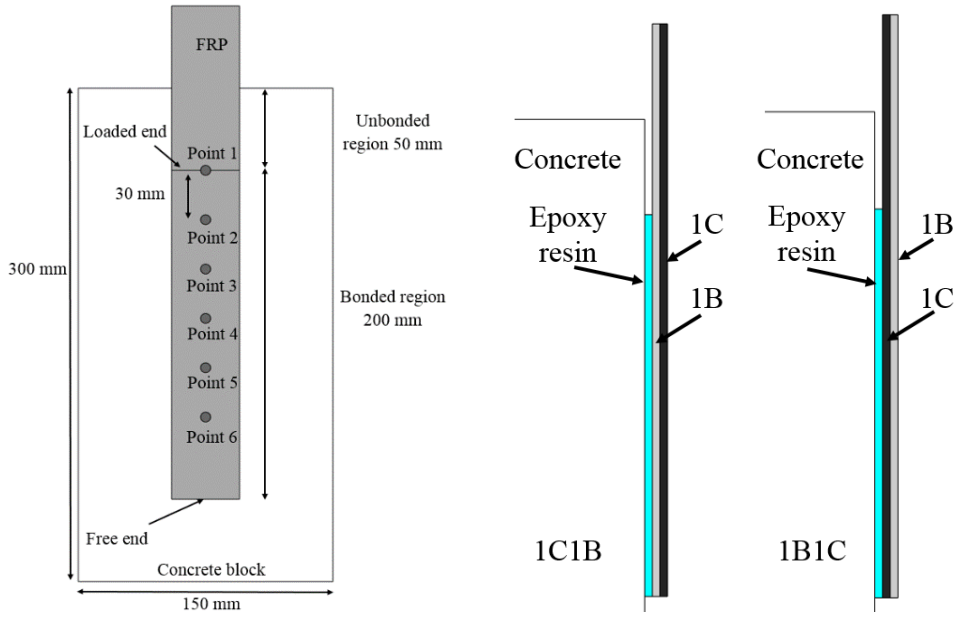

Figure 5-22. Specimen details (L) and stacking sequence of FRP sheets (R)

Table 5-2. Mechanical properties of FRP sheets

Material	Elastic modulus (GPa)	Rupture strain (%)	Tensile strength (MPa)	Nominal thickness (mm)	Stiffness $E_f t_f$ (N/mm)
CFRP (1C)	210	1.21	2450	0.167	35.07
BFRP (1B)	73	1.85	1400	0.120	8.76
1C1B/1B1C	147	1.36	2050	0.287	42.20

5.2.1.2 Test setup

For dynamic testing machine and test set-up, please refer to Chapter 5.1.1.2

5.2.2 Experimental results and discussions

Dynamic single-lap shear testing results are valid only when the dynamic stress equilibrium is achieved. Therefore, validation of stress equilibrium is conducted first, the details are presented in Section 5.1.2.3 by comparing the FRP surface strain derived from the DIC technique. The measurement accuracy was verified by matching the readings from strain gauges and those from the DIC technique.

5.2.2.1 Failure mode and bond strength

Under dynamic loadings, some debris consisting of mortar and coarse aggregates were stripped off with the detachment of the FRP sheet, indicating that the dynamic debonding process should release greater fracture energy. The typical failure modes after testing are shown in Figure 5-23. After the

detachment of FRP sheets, a flake layer of concrete beneath the FRP was observed under quasi-static loading, indicating that the shear stress penetrated the weakest part of the concrete layer. Since there was no normal stress applied in the single-lap shear test, shear stress changed into tensile stress along 45^{o} plane and consequently fracture initiated on the tensile side of the concrete substrate (78). However, with the increased loading rate, a combined failure was observed as the debonding location was shifted from concrete to concrete-epoxy interface. The changed pattern of the debonding mode indicates that the interfacial shear resistance of the FRP-concrete interface was enhanced with strain rate, which was caused by the improved concrete tensile strength. When subjected to a relatively low loading rate, the microcracks initiate and propagate along the interfacial transition zone (ITZ) since it is the weakest part in strength as compared to aggregates and mortar. However, there is not enough time for the cracks to initiate and propagate along the weakest part due to the short loading duration under high loading rates. Therefore, the debonding interface shifted from the enhanced concrete layer to the concrete-epoxy interface with the rising strain rate. Fracture of adhesive can be observed in some cases with the strain rate over 30 s^{-1}. As the adhesive has a stronger tensile strength than concrete, fracture in the adhesive layer resulted in a higher debonding load. Additionally, the hybrid composites (i.e., 1C1B or 1B1C) showed similar debonding failure modes as the sole composite (i.e., 1C or 1B). A similar observation is also reported in a previous study (206). For easier presentations, notations are introduced to denote quasi-static and dynamic tests. The specimen identification "*QSCB-m*" refers to the quasi-static test of 1C1B, and *m* represents the specimen number. The specimen identification "*DCB-n-m*" represents the dynamic test of 1C1B, the letter *n* represents the loading speed, and the letter *m* represents the specimen number.

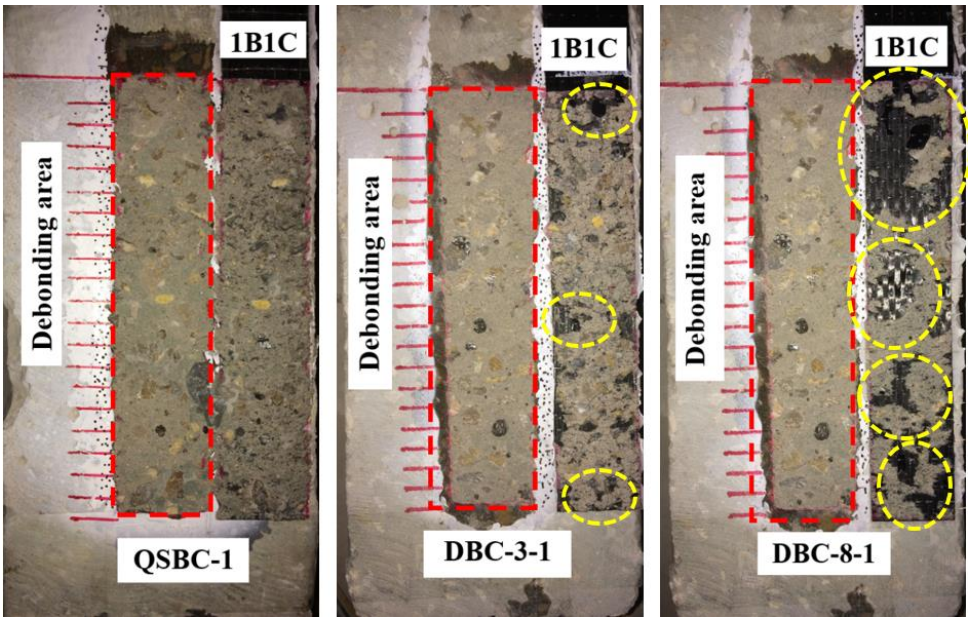

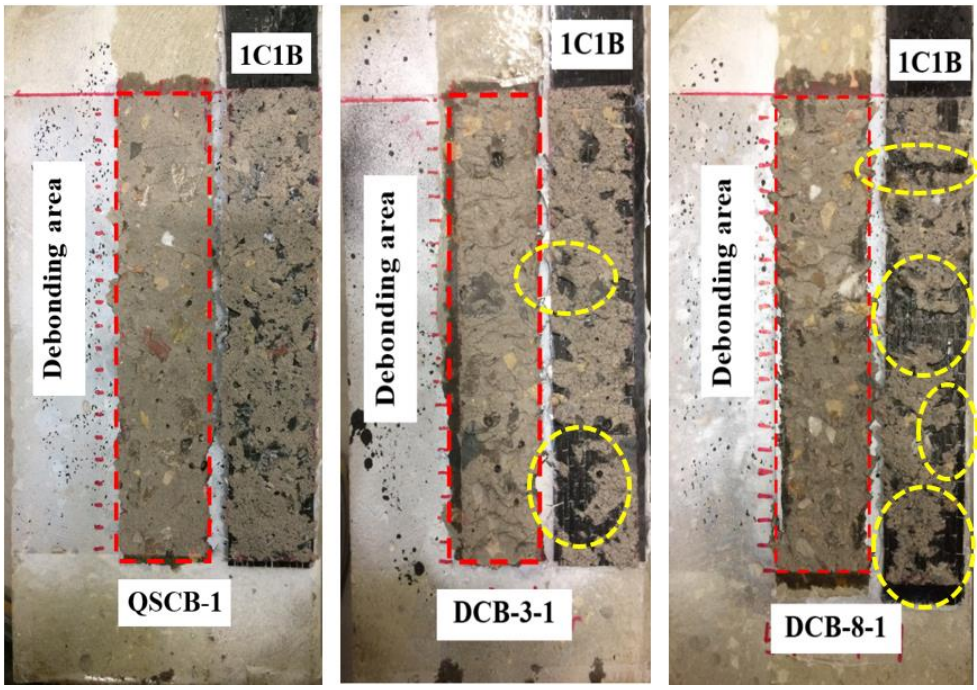

Figure 5-23. Typical failure modes of specimens from quasi-static and dynamic tests

Figure 5-24 illustrates the typical load-slip curves corresponding to different loading velocities. In general, the debonding load and the shear slip raised significantly with the rising strain rate for all the tested specimens, indicating that the debonding plateau under dynamic loading is longer than the case under quasi-static loads. According to the previous study, the load-slip curves can be separated into three regions during the debonding process (35), as shown in Figure 5-25. Region one refers to the linear-elastic stage, where the interfacial bond experiences minor shear slips with the high interfacial stiffness. Region two is the softening stage caused by microcracks of concrete, where the interfacial bond stiffness decreases with large shear slips. Region three is the debonding stage, where the bond deteriorates with increasing slips till the final debonding of FRP sheets. Irrespective of the quasi-static or dynamic loading condition, both the sole FRP sheets and hybrid composites exhibited three regions in the load-slip curves, indicating that hybrid composite has no effect on load and slip response mode.

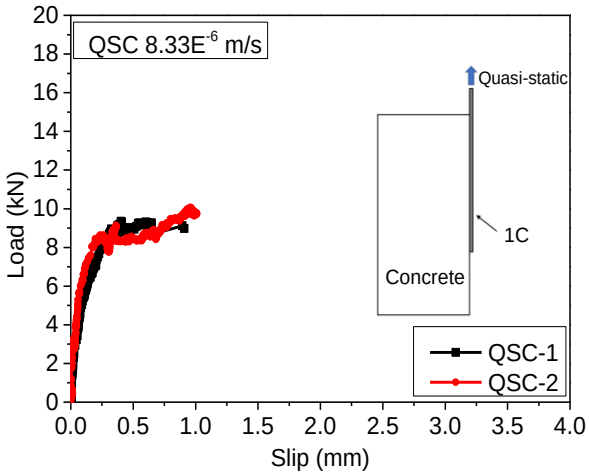
QSC 8.33E-6 m/s
Quasi-static
1C
Concrete
QSC-1
QSC-2
Load (kN)
Slip (mm)

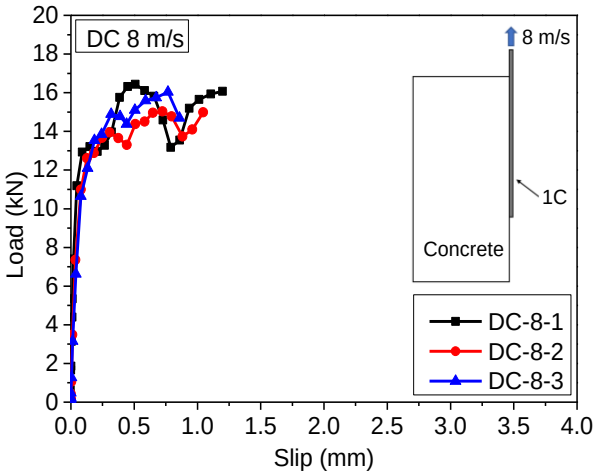
DC 8 m/s
8 m/s
1C
Concrete
DC-8-1
DC-8-2
DC-8-3
Load (kN)
Slip (mm)

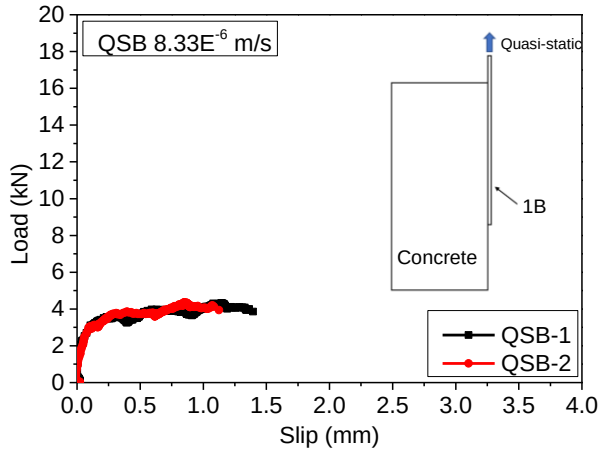
QSB 8.33E-6 m/s
Quasi-static
1B
Concrete
QSB-1
QSB-2
Load (kN)
Slip (mm)

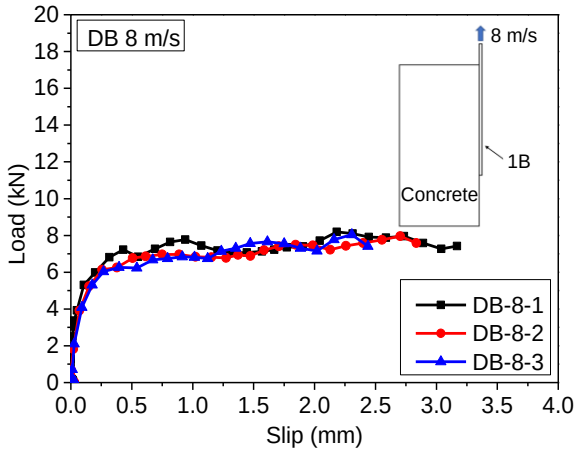
DB 8 m/s
8 m/s
1B
Concrete
DB-8-1
DB-8-2
DB-8-3
Load (kN)
Slip (mm)

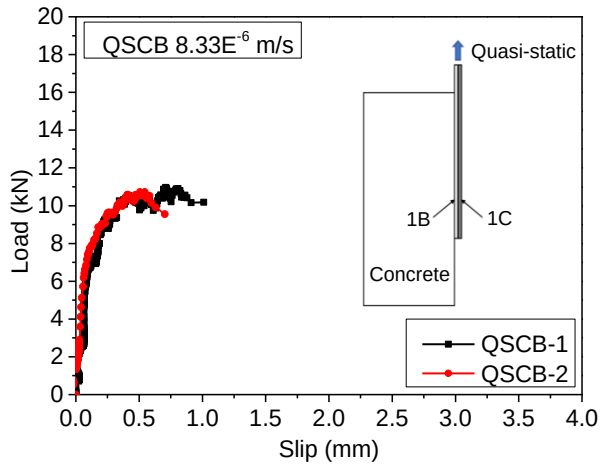
QSCB 8.33E-6 m/s
Quasi-static
1B
1C
Concrete
QSCB-1
QSCB-2
Load (kN)
Slip (mm)

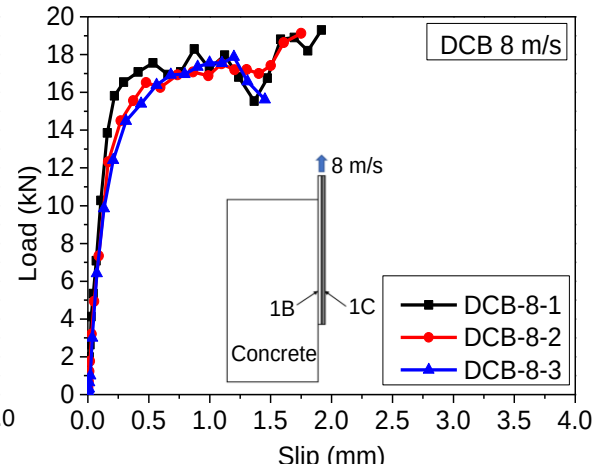
DCB 8 m/s
8 m/s
1B
1C
Concrete
DCB-8-1
DCB-8-2
DCB-8-3
Load (kN)
Slip (mm)

Table 5-3. Test results

Specimen ID	Testing data							Post-processing data					
	FRP	FRP stiffness (N/mm)	Loading velocity (m/s)	Strain rate (s^{-1})	Pu (kN)	ε_u (%)	Failure mode	τ_m (MPa)	s_o (mm)	G_f (N/mm)	$f_{t,DIF}$ (MPa)	A (mm)	B (mm)
QSC-1	CFRP	35.07	8.33E-6	2.50E-5	9.31	0.664	C	3.98	0.98	0.77	2.89	10.81	16.09
QSC-2	CFRP	35.07	8.33E-6	2.50E-5	8.99	0.641	C	3.92	0.94	0.72	2.89	10.64	16.28
QSB-1	BFRP	8.76	8.33E-6	2.50E-5	3.98	1.136	C	2.04	1.34	0.57	2.89	6.56	6.61
QSB-2	BFRP	8.76	8.33E-6	2.50E-5	3.73	1.064	C	1.98	1.24	0.50	2.89	6.72	6.43
QSCB-1	1C1B	42.20	8.33E-6	2.50E-5	10.52	0.663	C	4.71	1.35	0.93	2.89	7.11	13.49
QSCB-2	1C1B	42.20	8.33E-6	2.50E-5	10.58	0.651	C	4.89	1.41	0.89	2.89	7.49	12.98
QSBC-1	1B1C	42.20	8.33E-6	2.50E-5	10.98	0.613	C	4.51	1.25	0.79	2.89	7.94	11.97
QSBC-2	1B1C	42.20	8.33E-6	2.50E-5	11.09	0.639	C	4.72	1.19	0.86	2.89	7.89	12.45
DC-1-1	CFRP	35.07	1.0	14.98	11.31	0.806	C	6.49	1.02	1.14	5.06	9.57	11.13
DC-1-2	CFRP	35.07	1.0	20.03	10.86	0.774	C	6.57	0.92	1.05	5.11	9.74	12.01
DC-1-3	CFRP	35.07	1.0	19.75	11.29	0.805	C	6.41	0.94	1.14	5.11	10.38	11.37
DC-3-1	CFRP	35.07	3.0	49.75	13.05	0.930	C/CE	7.25	1.05	1.52	6.19	11.18	9.31
DC-3-2	CFRP	35.07	3.0	47.20	13.31	0.949	C/CE	7.84	1.10	1.58	6.08	10.78	9.12
DC-3-3	CFRP	35.07	3.0	39.90	13.59	0.969	C	7.63	1.07	1.65	5.75	11.22	9.26
DC-8-1	CFRP	35.07	8.0	116.33	14.31	1.020	C/CE	11.31	0.96	1.82	8.21	11.87	11.19
DC-8-2	CFRP	35.07	8.0	126.36	13.95	0.994	C/CE	11.19	0.94	1.73	8.44	10.97	12.36
DC-8-3	CFRP	35.07	8.0	127.97	14.90	1.062	C/CE	12.04	1.04	1.98	8.48	10.78	13.02
DB-1-1	BFRP	8.76	1.0	25.80	4.09	1.167	C	4.11	1.21	0.60	5.16	16.60	11.79
DB-1-2	BFRP	8.76	1.0	33.20	5.43	1.550	C	4.26	1.23	1.05	5.21	10.66	7.70
DB-1-3	BFRP	8.76	1.0	29.40	4.62	1.318	C	4.09	1.18	0.76	5.18	10.12	9.81
DB-3-1	BFRP	8.76	3.0	46.60	6.28	1.792	C/CE	5.12	1.20	1.41	6.05	19.89	11.20
DB-3-2	BFRP	8.76	3.0	53.50	5.74	1.638	C/CE	4.79	1.17	1.18	6.34	20.88	12.18
DB-3-3	BFRP	8.76	3.0	54.30	5.17	1.475	C/CE	5.56	1.15	0.95	6.37	18.21	10.09
DB-8-1	BFRP	8.76	8.0	155.10	7.23	1.918	C/CE	6.56	1.06	1.61	9.04	14.35	8.61
DB-8-2	BFRP	8.76	8.0	150.10	7.02	2.003	C/CE	6.29	1.13	1.76	8.94	19.98	13.12
DB-8-3	BFRP	8.76	8.0	130.40	6.80	1.852	C/CE	6.82	1.09	1.50	8.53	21.12	13.67
DCB-1-1	1C1B	42.20	1.0	16.89	13.03	0.772	C	5.78	1.21	1.26	5.08	8.63	11.25
DCB-1-2	1C1B	42.20	1.0	12.40	12.93	0.766	C	5.92	1.18	1.24	5.02	8.72	11.92
DCB-1-3	1C1B	42.20	1.0	13.66	12.33	0.731	C	6.02	1.14	1.13	5.04	9.32	14.11
DCB-3-1	1C1B	42.20	3.0	46.96	14.08	0.834	C/CE	8.08	1.16	1.47	6.07	7.64	9.58
DCB-3-2	1C1B	42.20	3.0	50.26	14.89	0.882	C/CE	7.79	1.09	1.64	6.21	8.78	11.05
DCB-3-3	1C1B	42.20	3.0	39.46	14.35	0.850	C/CE	7.67	1.03	1.52	5.73	9.11	10.54
DCB-8-1	1C1B	42.20	8.0	98.21	17.55	1.006	C/CE	11.10	1.04	2.13	7.76	15.23	14.24
DCB-8-2	1C1B	42.20	8.0	95.95	17.08	0.928	C/CE	11.89	1.01	1.82	7.70	16.21	12.49
DCB-8-2	1C1B	42.20	8.0	87.46	16.81	0.996	C/CE	12.08	1.05	2.09	7.47	17.19	13.24
DBC-1-1	1B1C	42.20	1.0	14.37	11.97	0.709	C	6.69	1.19	1.06	5.05	10.98	17.21
DBC-1-2	1B1C	42.20	1.0	15.12	13.22	0.783	C	7.51	1.11	1.29	5.06	12.99	16.19
DBC-1-3	1B1C	42.20	1.0	14.68	13.25	0.785	C	6.34	1.09	1.30	5.05	12.96	15.64
DBC-3-1	1B1C	42.20	3.0	44.54	14.74	0.873	C	8.18	1.11	1.61	5.96	13.51	13.49
DBC-3-2	1B1C	42.20	3.0	50.58	13.99	0.829	C/CE	9.16	1.06	1.45	6.22	14.13	12.76
DBC-3-3	1B1C	42.20	3.0	44.95	15.17	0.899	C/CE	8.79	1.12	1.70	5.98	15.12	11.29
DBC-8-1	1B1C	42.20	8.0	114.11	17.66	1.004	C/CE	11.57	1.02	2.13	8.16	14.92	15.26
DBC-8-2	1B1C	42.20	8.0	107.85	17.07	1.012	C/CE	12.13	1.11	2.16	8.01	15.38	14.68
DBC-8-3	1B1C	42.20	8.0	118.96	16.91	0.942	C/CE	11.95	1.03	1.87	8.27	17.11	11.47

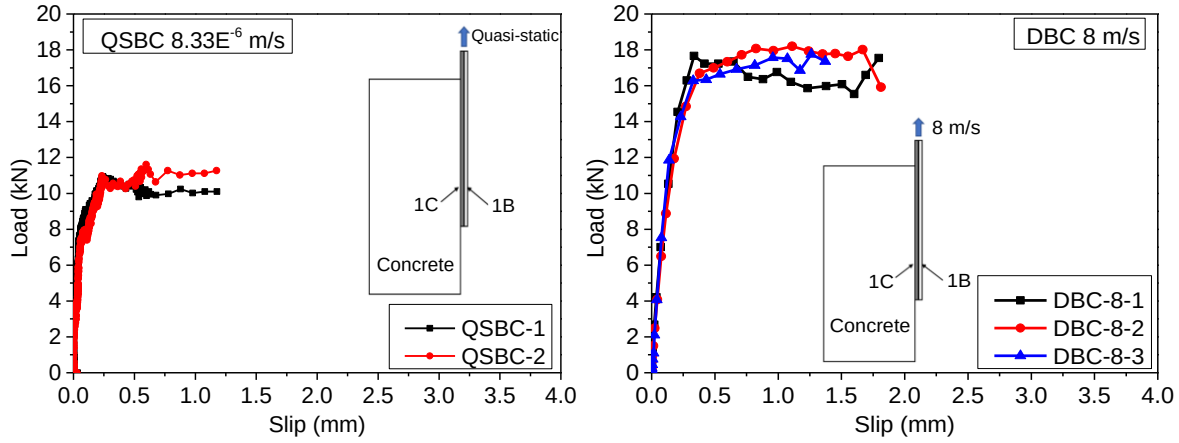

Figure 5-24. Load-slip responses

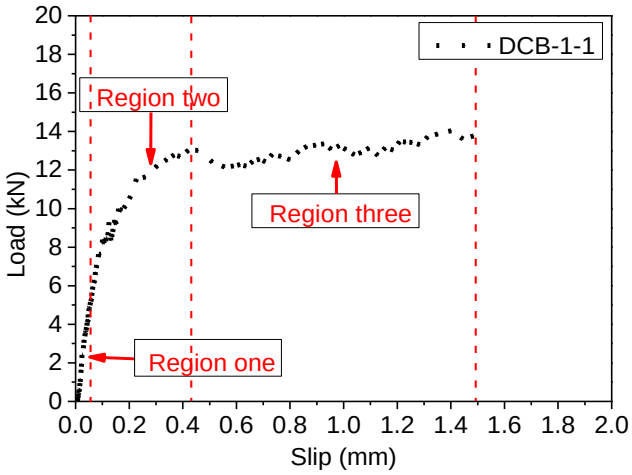

Figure 5-25. Three regions of a typical bond-slip curve

Figure 5-26 compares the average debonding load of all the tested specimens. The increment of debonding load and shear slip indicates that the bonding behaviour of the FRP-concrete interface is strain rate dependent. These observations agree well with findings from the previous study (77). As compared with the specimen of the 1B-concrete interface, the 1C-concrete interface showed a relatively higher debonding load at each loading rate due to the greater stiffness of the CFRP plate. However, the debonding process of the specimen 1B-concrete was more ductile than 1C-concrete with higher shear slip at the loaded end. Given the same FRP stiffness but different FRP stacking sequence, the debonding load of specimen 1B1C-concrete was higher than that of specimen 1C1B-concrete under quasi-static loads while the specimen 1C1B and 1B1C showed similar results of debonding loads under dynamic loadings. Under quasi-static loads, the higher bond strength resulted from the relatively higher stiffness of CFRP sheets which were directly bonded to concrete substrates. There was a consistent finding that the bond strength correlates well with FRP stiffness as well as concrete

tensile strength, consequently, the bond strength is mainly determined by the FRP layer which is directly attached to the concrete substrate (143). The influence of the FRP stacking sequence on the bond strength should be resulted from the shear stress redistribution within the FRP interlayers. Under quasi-static loads, the average debonding load of Specimen QBC was 11.04 kN while its counterpart (i.e., QCB) was 10.55 kN. However, the impact of the FRP stacking sequence on the bond strength is marginal when the loading speed is over 1 m/s, which indicates that effect of strain rate on the bond strength is more prominent than the FRP stacking sequence under dynamic loads. This is due to the enhanced tensile strengths of concrete and epoxy under dynamic loading which results in the increment of interfacial bond strength.

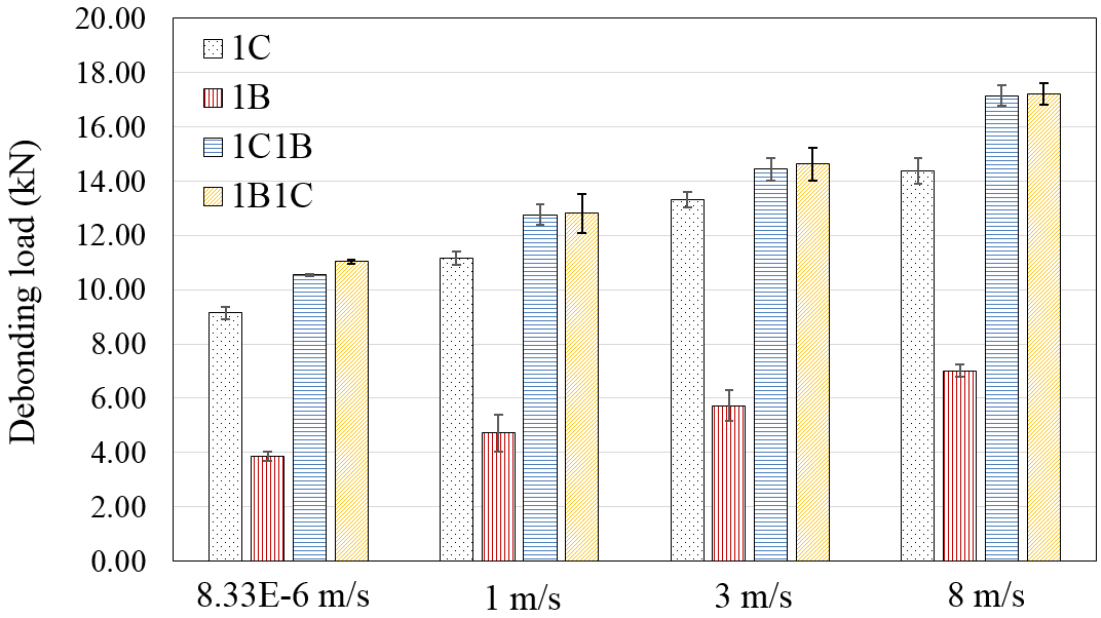

Figure 5-26. Comparison of debonding load

5.2.2.2 Strain time history and stress equilibrium

The strain contours of the tested specimens at the loading rate of 1 m/s are plotted in Figure 5-27, which consists of different colours (i.e., red, yellow, green, light blue, and dark blue) showing the strain distributions at different loading levels. With the increase of the applied load, the strain gradient in red colour continued to develop and propagate along with the FRP sheets. The region with the colours of yellow, green and light blue represents the shear stress transfer zone and the dark blue represents the non-stress transfer zone. At the initial debonding stage (i.e., *P*), a large local strain gradient shown in red colour was observed close to the loaded end. As compared with the sole FRP (i.e., 1C and 1B), the hybrid composites (i.e., 1C1B and 1B1C) show a larger range of shear stress transfer zone at the initial debonding stage (i.e., *P*),

indicating that the relative slippage occurred between CFRP and BFRP sheets due to their different stiffness.

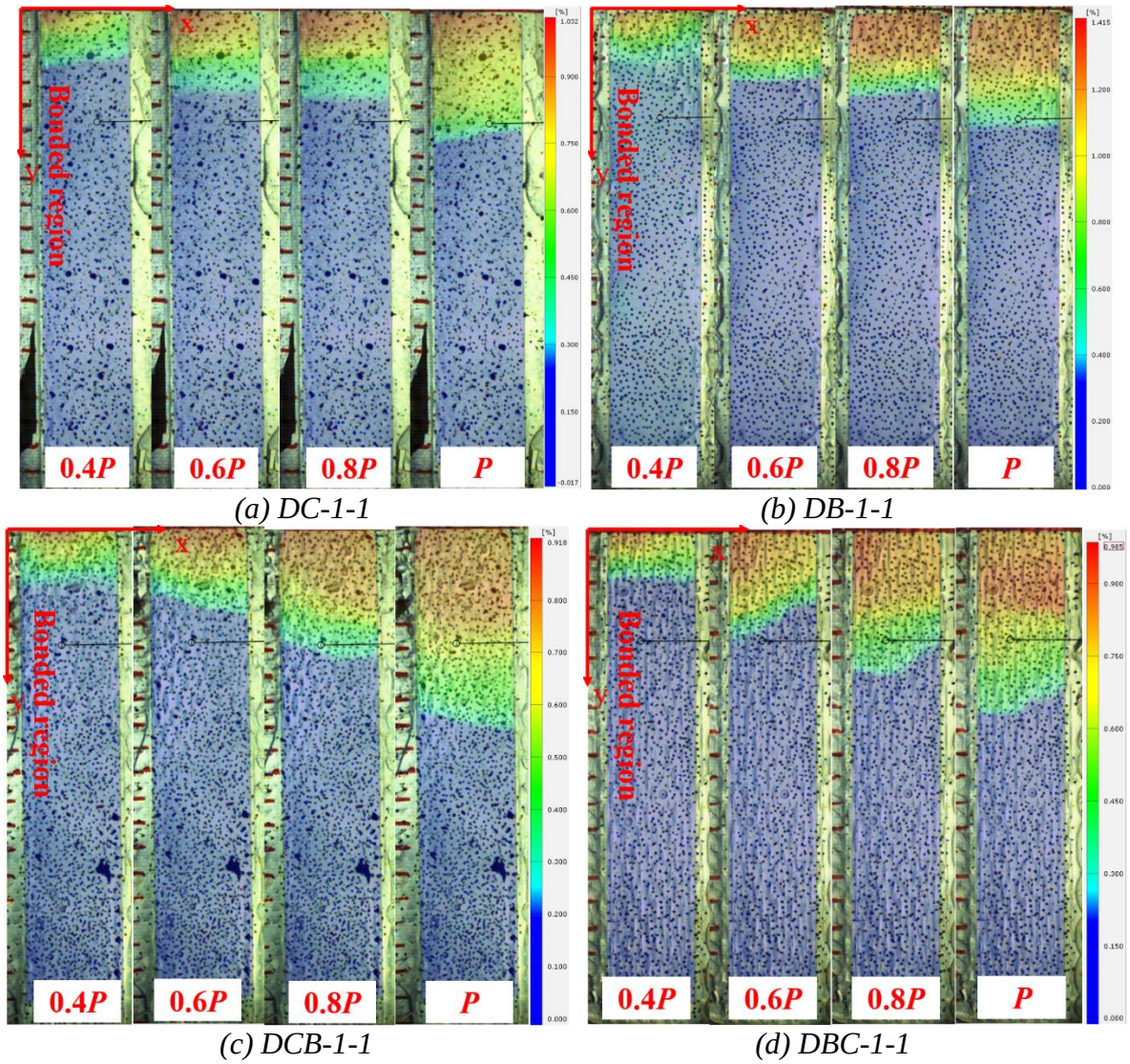

(a) DC-1-1 *(b) DB-1-1*

(c) DCB-1-1 *(d) DBC-1-1*

Figure 5-27. Strain contours of the tested specimens

Figure 5-28 plots the strain time-history curves at different loading speeds. The average values of all the testing results are shown in Figure 5-29. The general trend of the testing results shows that the ultimate debonding strain increased with the rising strain rate. Due to the high loading rate and short-time loading, the strain time-history curves under high loading speed become steeper as compared to those under low loading velocity. Compared with the 1C-concrete interface, the interface of 1B-concrete is more sensitive to strain rate due to the significant increment of the ultimate debonding strain. The ultimate debonding strain of the 1B-concrete interface increased by 84% from 0.98% at the strain rate of 2.5E-5 s^{-1} to 1.80% at the strain rate of 155 s^{-1} while the ultimate debonding strain of the 1C-concrete interface increased by 35% from 0.78% to 1.05% when the strain rate increased from 2.5E-5 s^{-1} to 128 s^{-1}, respectively.

It can be concluded that the 1C-concrete interface is less sensitive to strain rate as the stiffer CFRP lacks of strain rate sensitivity as also observed in the previous study (207).

For the hybrid composites (i.e., 1C1B and 1B1C), the ultimate debonding strain decreased significantly as compared to the 1B-concrete interface under all the corresponding loading velocities, indicating that an addition of a CFRP sheet resulted in the decreased debonding strain. This observation under a high loading rate agrees well with the well-known behaviour under quasi-static loads, where the thicker FRP sheets show a lower debonding strain (206). The reduction of the ultimate debonding strain indicates that the enhancement of shear resistance between FRP and concrete caused by the increased FRP stiffness ($E_f t_f$). Additionally, the stacking sequence of FRP sheets resulted in the different ultimate strain at the quasi-static loads while the effect of stacking sequence on the ultimate debonding strain was marginal under dynamic loads. The 1C1B-concrete interface resulted in a relatively higher ultimate strain than its counterpart (1B1C-concrete interface) at the quasi-static loads, as shown in Figure 5-29. However, the FRP stacking sequence had a marginal effect on the ultimate debonding strain under dynamic loads, which is shown in Figure 5-29. The possible reason is that there is not enough time for the shear stress to be redistributed in the FRP interlayers under dynamic loading.

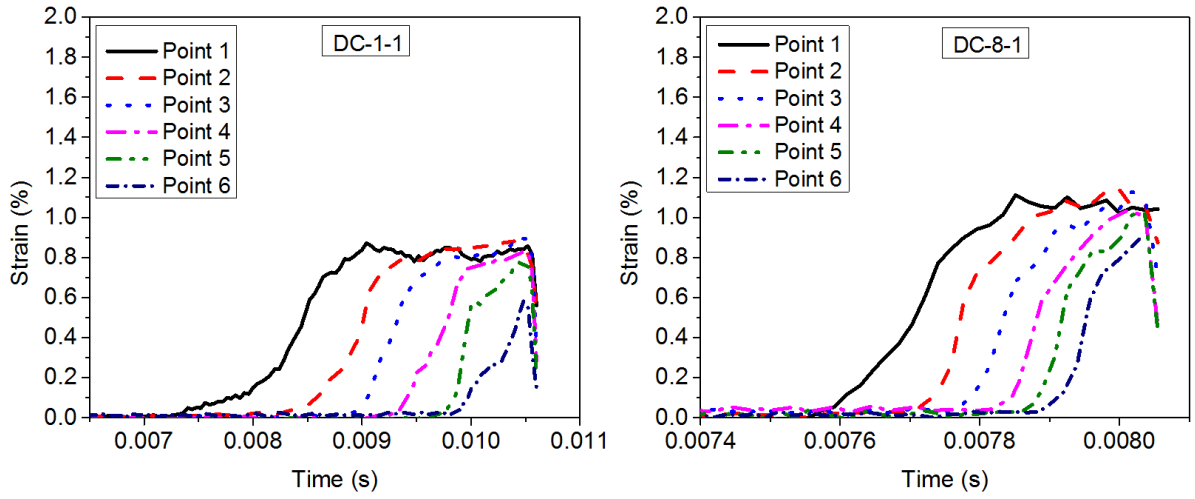

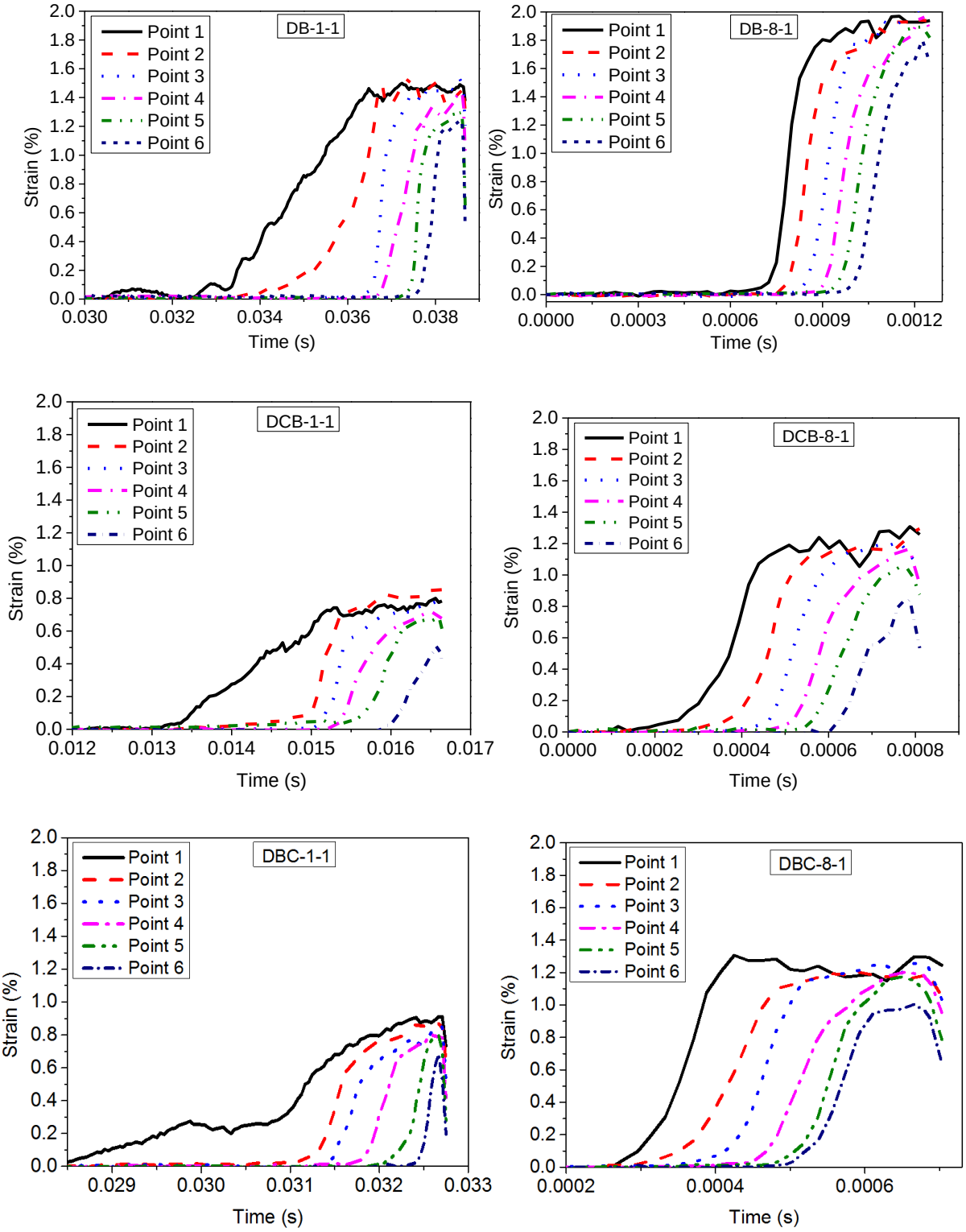

Figure 5-28. Strain time history at different loading rates

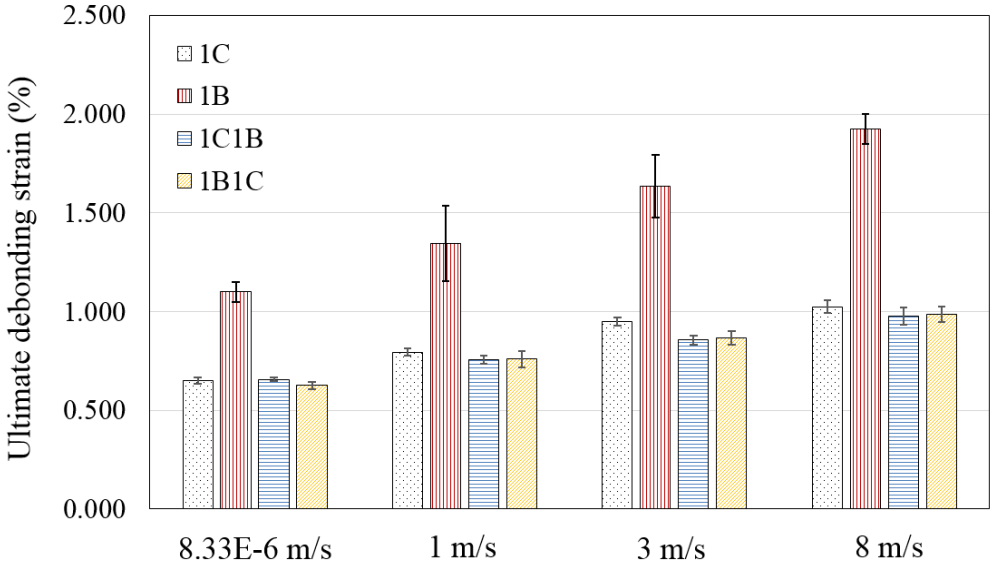

Figure 5-29. Comparison of ultimate debonding strain

Please refer to Section 5.1.2.3 for the validation of dynamic stress equilibrium. Figure 5-30 plots the strain rate distributions along with the FRP sheet at different time instants. All the tested specimens exhibited a similar pattern of propagation from the loaded end to the free end. The peak strain rate increases with the rising loading rate and the peak strain rate for DCB-1-1 and DCB-8-1 is 16.89 s^{-1} and 98.21 s^{-1}, respectively. The peak strain rate of each specimen is summarized in Table 5-3.

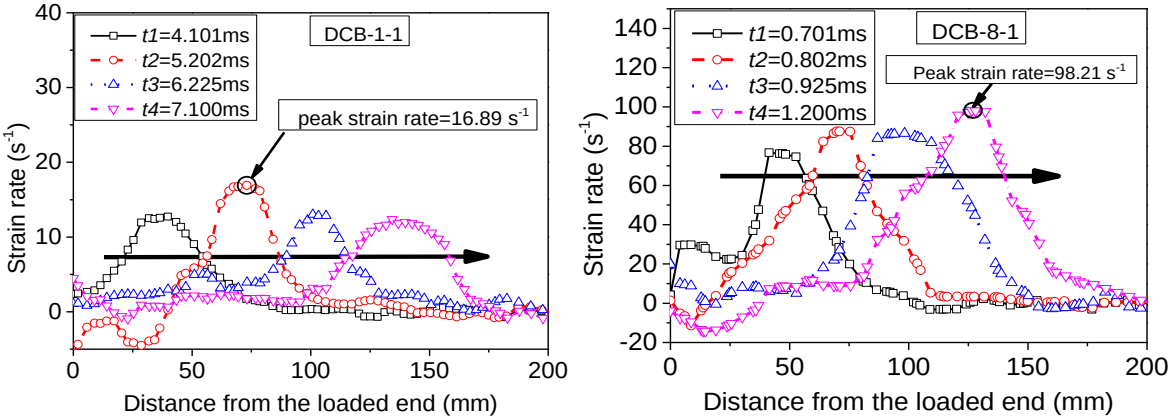

Figure 5-30. Strain rate of the tested specimens

5.2.2.3 Strain distributions

Figure 5-31 shows the strain profile along the centreline of FRP at different loading stages. It is found that the strain rate effect on the strain distributions is more prominent than the hybrid effect because the FRP debonding strain increased noticeably with strain rate. For the hybrid

composite-concrete interface, an additional layer of FRP sheet resulted in a lower ultimate debonding strain compared with the sole FRP-concrete interface at each loading rate. This is consistent with previous studies that the thicker FRP sheets cause the reduction of debonding strain (77). Additionally, the stacking sequence of FRP sheets gave rise to different ultimate debonding strains for hybrid FRP composites. The attachment of CFRP sheets (i.e., 1B1C) first to the concrete substrate caused a relatively higher initial debonding strain under quasi-static loads as compared to the attachment of BFRP sheet (i.e., 1C1B) first. However, the effect of stacking sequence on the ultimate strain was marginal with the increasing strain rate because a similar ultimate debonding strain of hybrid composites was observed under dynamic loads. The shear stress developed in the composite is proportional to the debonding strain and consequently, the higher debonding strain resulted in higher interfacial shear stress.

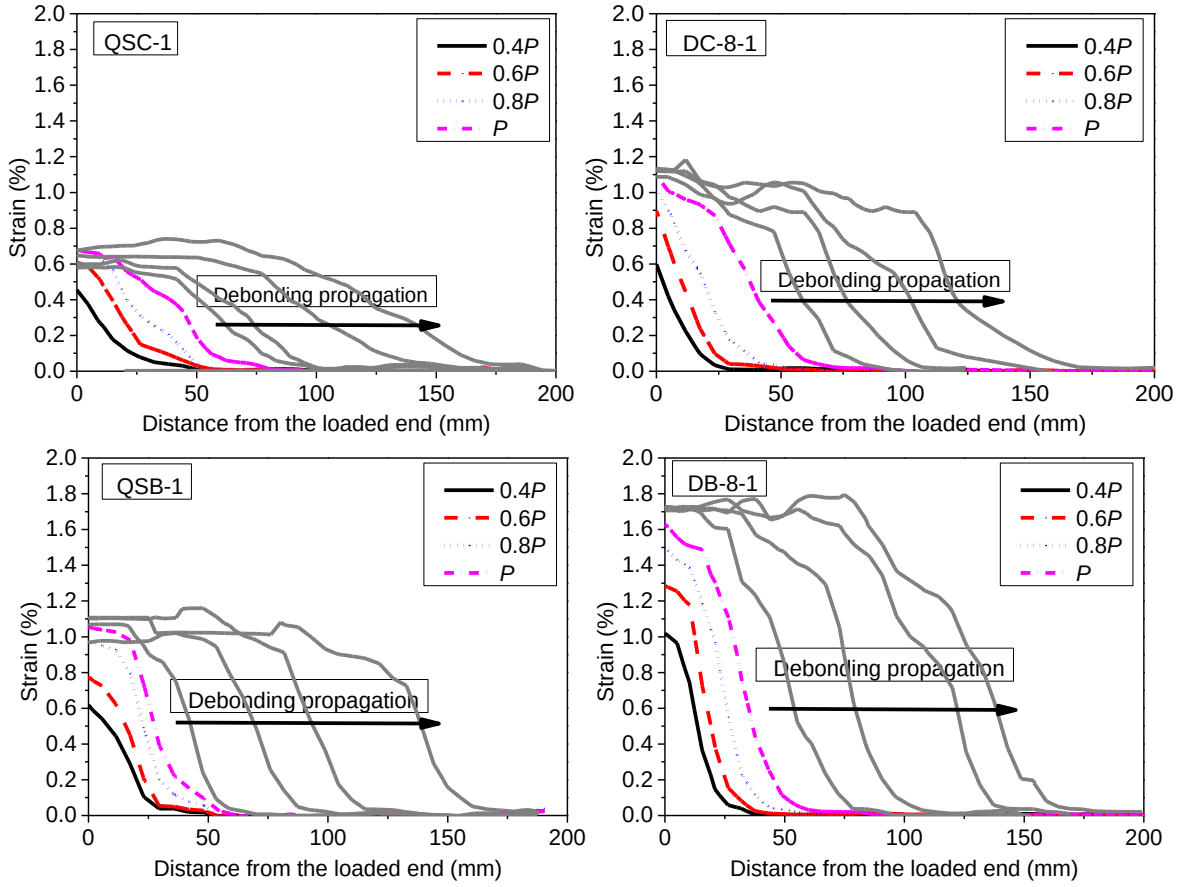

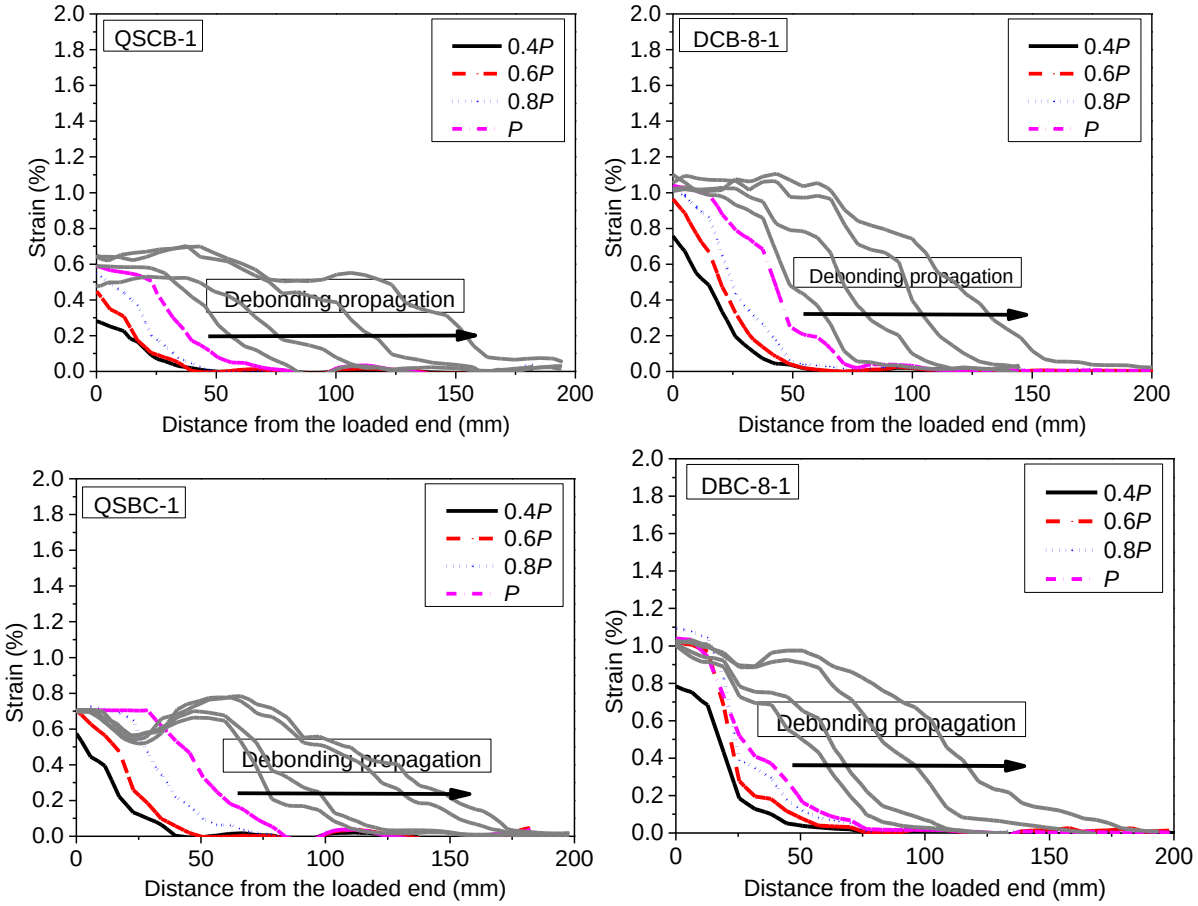

Figure 5-31. Typical strain distributions

The ultimate debonding strain at the initial debonding load *P* raised with strain rate while the range of stress transition zone reduced with the increasing strain rate. This is because the strain distribution gradient in the FRP was steeper than that under quasi-static loading, as shown in Figure 5-32. Equation (5-23) was used to fit the experimental strain profiles under different loading speeds and loading levels (145). The steeper strain distribution gradient means a shorter stress transition zone, which is also known as the effective bond length (EBL) (143, 144). It was observed that the EBL reduced with the rising strain rate. The decrease of the effective bond length was resulted from the increase of the interfacial shear stress with the increase of loading rate. The dynamic tensile strength of concrete increased with strain rate due to the dynamic increase factor (DIF) (76). As a result, the EBL decreased with the increasing loading rate, which is consistent with the previous study (77). The hybrid composites DCB-8-1 and DBC-8-1 showed an approximately similar EBL at the loading rate of 8 m/s as shown in Figure 5-32 (b), indicating that the stacking sequence has a marginal impact on the effective bond length under relatively higher loading rate. This is because there is not enough time for FRP

sheets to develop the relative slippage in the interlayers of hybrid composites at a relatively higher strain rate. The strain of FRP sheets can be estimated by the following equation:

$$\varepsilon(x) = \varepsilon_u + \frac{A}{1+e^{\left(\frac{x-x_o}{B}\right)}} \tag{5-23}$$

in which A and B are regression coefficients, x is the distance of the bonded BFRP sheet from 0 to 200 mm, x_o is the turning point of strain distribution as shown in Figure 5-32, and ε_u is the experimental ultimate debonding strain as listed in Table 5-3. The best fit coefficients A and B are summarized in Table 5-3.

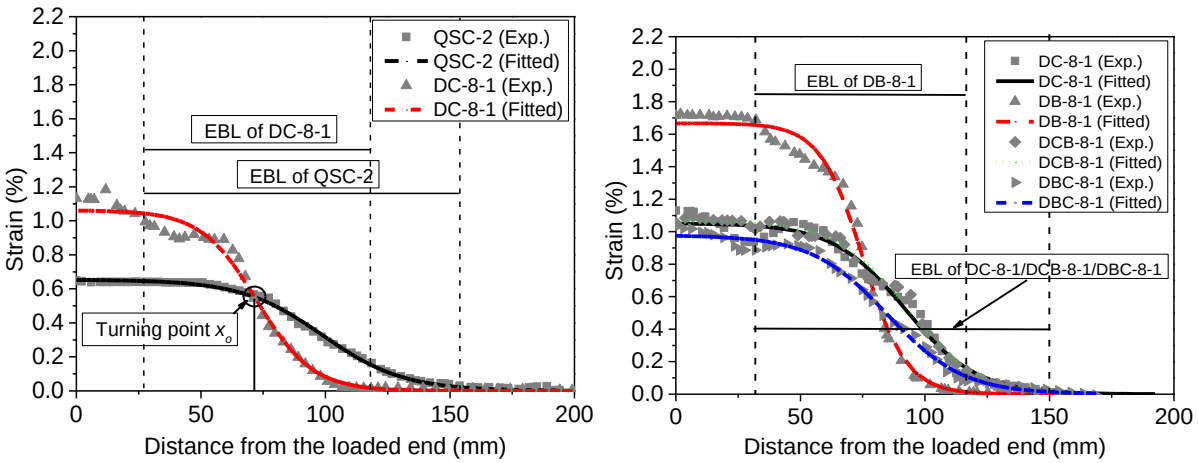

Figure 5-32. Effective bond length of the tested specimens

5.2.2.4 Bond-slip response

The relationship between the interfacial shear stress and the corresponding shear slip along the FRP sheets is discussed in this section. By assuming the zero relative slip between concrete and FRP at the free end before the final debonding as shown in Figure 5-22, the shear slip can be obtained by the integration of the measured strain profile along with the FRP sheets:

$$s(x) = \int \varepsilon dx \tag{5-24}$$

The axial FRP strain was measured by the DIC technique, thus, the interfacial shear stress can be obtained using the following equation:

$$\tau(x) = E_f t_f \frac{d\varepsilon}{dx} \tag{5-25}$$

in which $s(x)$ is the shear slip, $\tau(x)$ is the shear stress, ε is the BFRP strain, and $E_f t_f$ is the BFRP stiffness. Typical interfacial bond-slip curves of the tested specimens are shown in Figure 5-33. In order to obtain the mean shear stress and the slip, five different points after the initial debonding stage (i.e., P) are selected as shown in the legend, such as 65 mm and 185 mm. Both the ascending branch and the descending branch can be observed for all the specimens. The non-linear bond-slip response was resulted from the cracking of concrete. The general trend of the bond-slip response shows that the interfacial peak shear stress τ_m raised remarkably with strain rate. By comparing the testing results of the 1C-concrete and the 1B-concrete interface, it is found that the peak shear stress was significantly influenced by the FRP stiffness ($E_f t_f$).

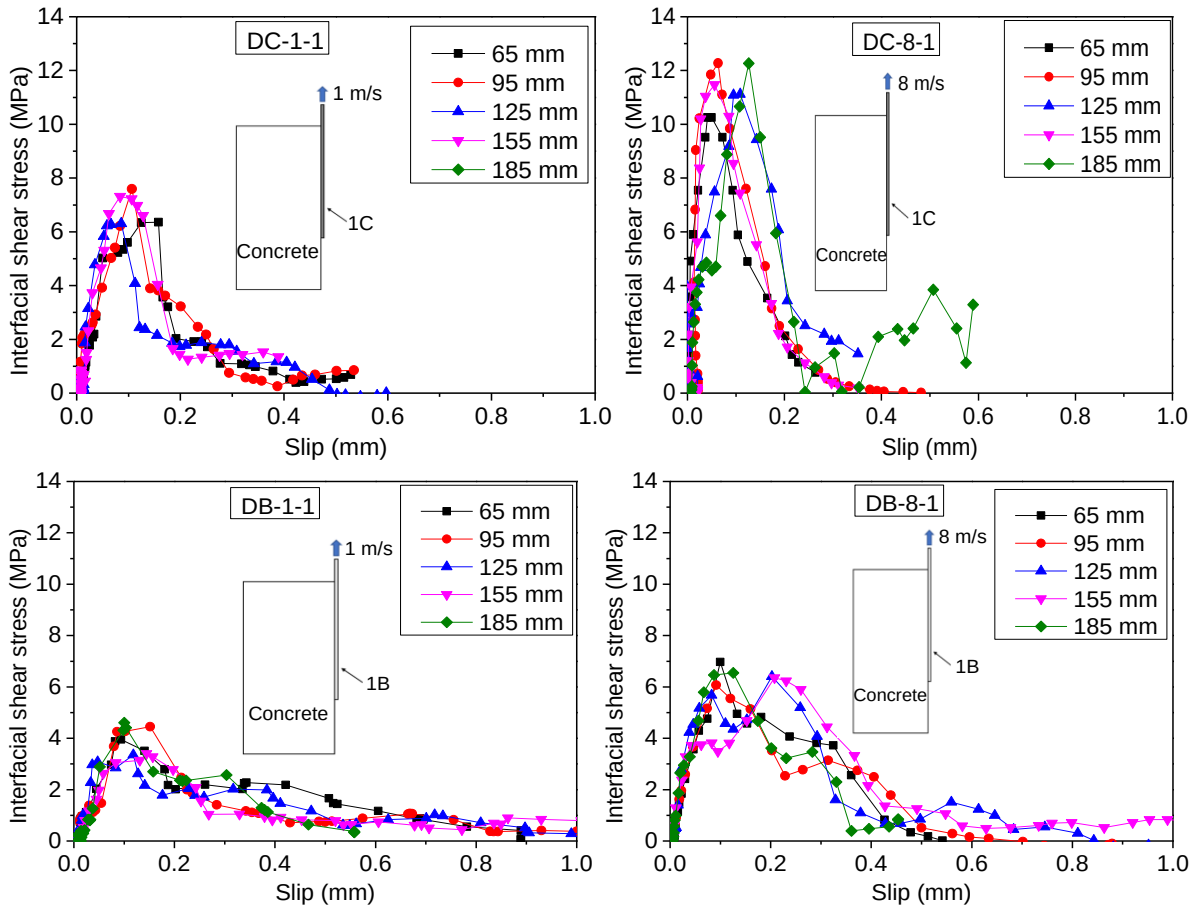

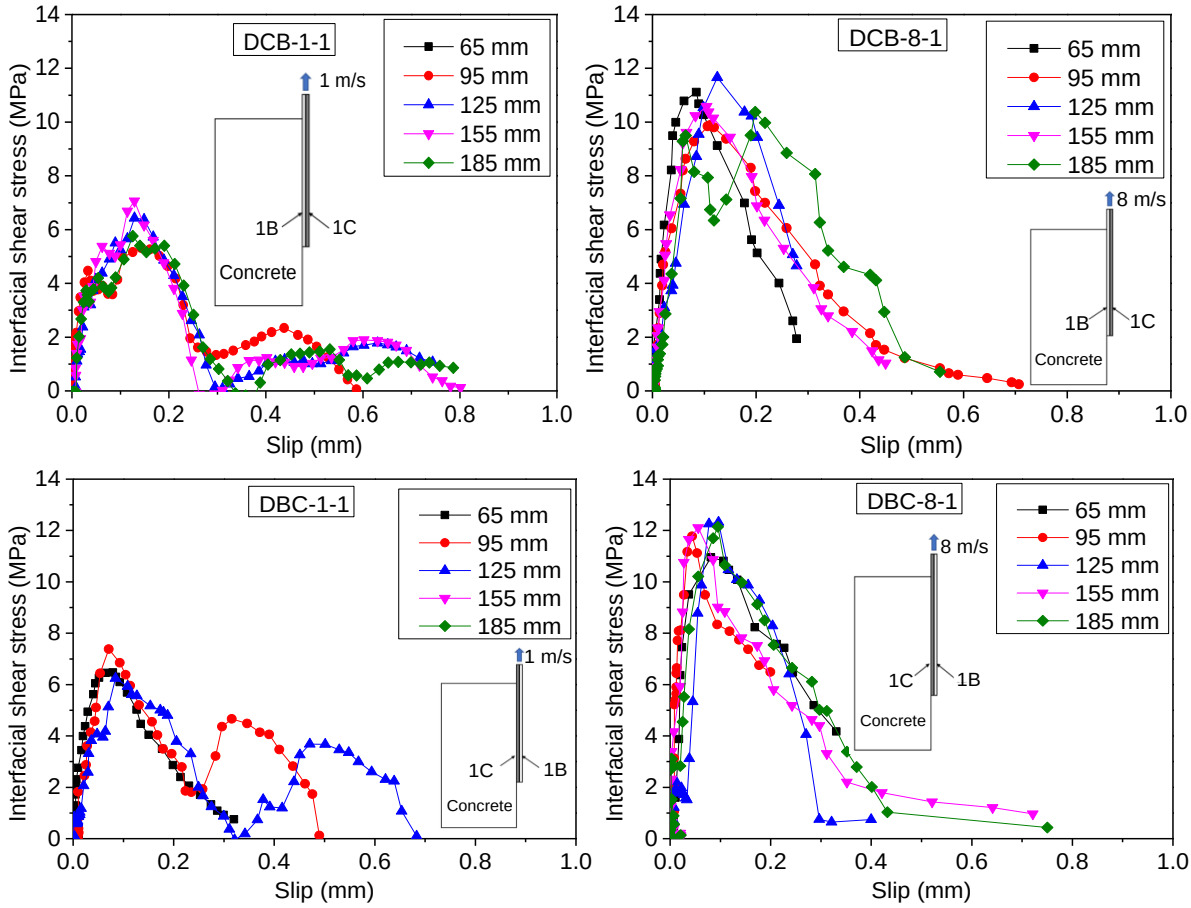

Figure 5-33. Typical bond-slip curves

Figure 5-34 illustrates the comparison of peak shear stress. It is found that the 1C-concrete interface showed higher interfacial shear stress than the 1B-concrete interface. The hybrid composites with the same FRP stiffness showed higher shear stress than sole FRP under the quasi-static load. This trend was also observed for the hybrid composites at which the peak shear stress of the 1B1C-concrete interface showed higher shear stress than its counterpart (i.e., 1C1B-concrete) under dynamic loadings from 1 m/s to 8 m/s. The increased interfacial shear stress was caused by the enhanced interfacial stiffness, which correlates well with the shear modulus of concrete and FRP sheets. An increment of 191%, 226%, 144%, and 157% in shear stress from quasi-static loading to 8 m/s dynamic loading was obtained for Specimen DC-8, DB-8, DCB-8, and DBC-8, respectively. The combination of CFRP and BFRP sheet not only made the hybrid composites sensitive to strain rate but also enhanced the shear resistance. The enhanced shear stress for hybrid composites should be resulted from the increased FRP stiffness and the enhanced concrete strength. At the largest loading speed, the peak shear stress between the 1C-concrete, 1C1B-concrete, and 1B1C-concrete interfaces was similar, indicating that the interfacial shear stress was more sensitive to strain rate than the hybrid effect

under dynamic loads. At the same loading rate, the 1B-concrete interface had a relatively low peak shear stress due to its low stiffness (i.e., 1B had the stiffness of 8.76 N/mm).

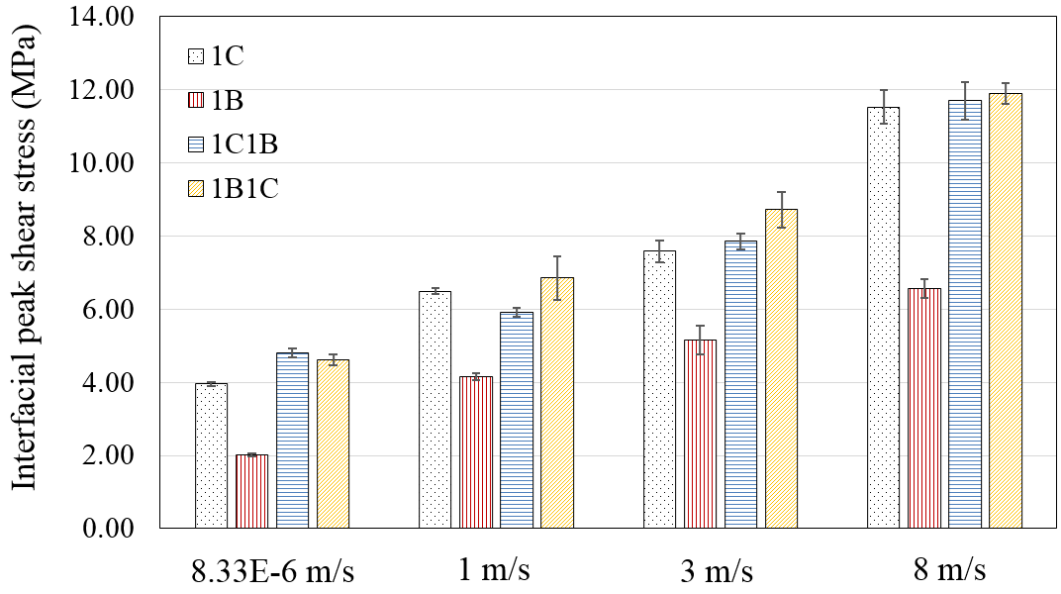

Figure 5-34. Interfacial peak shear stress at different loading rates

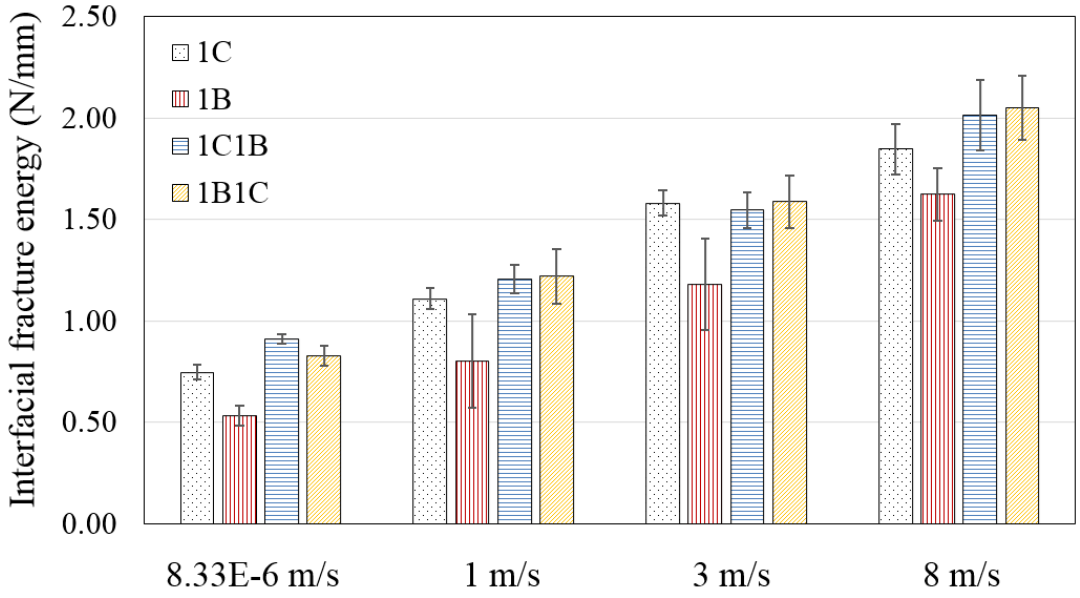

Figure 5-35. Comparison of interfacial fracture energy G_f

Figure 5-35 compares the interfacial fracture energy (G_f) of the FRP-to-concrete interface, which can be obtained from the enclosed area of the bond-slip curve (87). Due to the fluctuated bond-slip curves, the obtained G_f showed high dispersion, as indicated in the error bar of the experimental results in Figure 5-35. In general, the test results show that the G_f raised significantly with strain rate for all the specimens. This is due to the increased tensile strength

of concrete and previous studies have demonstrated that the G_f was proportional to the tensile strength of concrete and FRP stiffness (87). The specimen 1C1B-concrete interface had relatively higher fracture energy than that of the specimen 1B1C-concrete interface under the quasi-static loads, indicating that the attachment of BFRP sheet first to the concrete substrate caused relatively higher fracture energy. However, the hybrid effect on the fracture energy was marginal for hybrid composites under the dynamic loads from 1 m/s to 8 m/s as both the 1C1B-concrete and 1B1C-concrete interfaces showed a similar result. As the hybrid effect should be resulted from the stress redistributions within the internal layers between FRP sheets, there is not enough time for the shear stress to redistribute due to the increased strain rate. The G_f of hybrid composites is slightly higher than the sole FRP sheet in general.

5.2.3 Dynamic bond strength and shear stress

5.2.3.1 Strain rate effect on interfacial bond strength

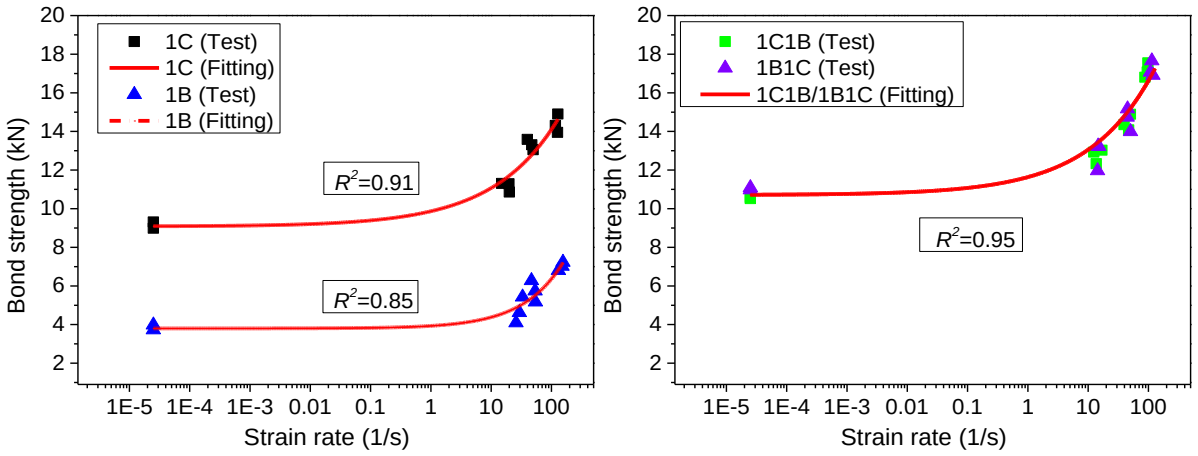

Figure 5-36. Interfacial bond strength vs. strain rate

Figure 5-36 plots the interfacial bond strength versus strain rate. The average quasi-static bond strength is 9.15 kN, 3.86 kN, 10.55 kN and 11.04 kN for 1C, 1B, 1C1B and 1B1C, respectively. The bond strength of all the specimens increases with the strain rate. The bond strength of specimen 1C at the strain rate of 127.97 s^{-1} is 14.90 kN, increased by 62.8% as compared to the quasi-static one. The bond strength of specimen 1C1B is 17.55 kN at the strain rate of 98.21 s^{-1}, increased by 66.4% as compared to the quasi-static one. For ease of comparison, the testing data and fitted curves of specimens 1C and 1B are grouped in Figure 5-36 (L). Figure 5-36 (R) shows the testing data and fitted curves of the specimens 1C1B and 1B1C. To predict the dynamic interfacial bond strength of the FRP-concrete interface, empirical formulae are proposed and expressed as follows. It should be noted that a single empirical formula is

proposed for the specimens 1C1B and 1B1C since they have a very similar strain rate effect on the bond strength.

For 1C,

$$P_{d,C} = P_{s,C}\left[0.086\left(\dot{\varepsilon}\right)^{0.402} + 0.992\right] \text{ when } 2.5\times10^{-5} \le \dot{\varepsilon} \le 128 \quad (5\text{-}26)$$

For 1B,

$$P_{d,B} = P_{s,B}\left[0.034\left(\dot{\varepsilon}\right)^{0.645} + 0.986\right] \text{ when } 2.5\times10^{-5} \le \dot{\varepsilon} \le 155 \quad (5\text{-}27)$$

For 1C1B and 1B1C,

$$P_{d,CB} = P_{s,CB}\left[0.039\left(\dot{\varepsilon}\right)^{0.577} + 0.998\right] \text{ when } 2.5\times10^{-5} \le \dot{\varepsilon} \le 119 \quad (5\text{-}28)$$

5.2.3.2 Strain rate effect on interfacial shear stress

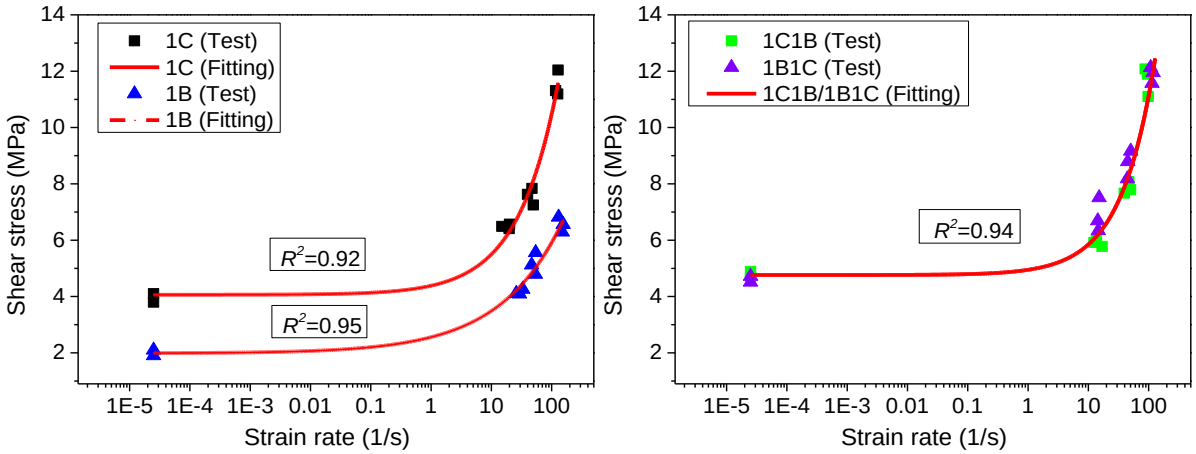

Figure 5-37. Interfacial shear stress vs. strain rate

Figure 5-37 illustrates the relationship of the interfacial shear stress versus strain rate. The average quasi-static shear stress is 3.95 MPa, 2.01 MPa, 4.80 MPa and 4.62 MPa for 1C, 1B, 1C1B and 1B1C, respectively. The shear stress of specimen 1C, 1B, 1C1B and 1B1C at the strain rate of 127.97 s^{-1}, 155.10 s^{-1}, 98.21 s^{-1} and 118.96 s^{-1} is 14.90 MPa, 7.23 MPa, 17.55 MPa and 16.91 MPa, with the increment of 277%, 226%, 144% and 157% as compared to the quasi-static one, respectively. Figure 5-37 (L) illustrates the testing data and fitted curves of the specimens 1C and 1B and Figure 5-37 (R) shows the experimental results and fitting curves of the specimens 1C1B and 1B1C. As the hybrid composites 1C1B and 1B1C exhibit similar

strain rate effects on shear stress, a single empirical formula is proposed for them. The empirical formulae to predict dynamic shear stress are given as follows.

For 1C,

$$\tau_{d,C} = \tau_{s,C}\left[0.081\left(\dot{\varepsilon}\right)^{0.649} + 1.028\right] \text{ when } 2.5\times10^{-5} \le \dot{\varepsilon} \le 128 \quad (5\text{-}29)$$

For 1B,

$$\tau_{d,B} = \tau_{s,B}\left[0.286\left(\dot{\varepsilon}\right)^{0.417} + 0.987\right] \text{ when } 2.5\times10^{-5} \le \dot{\varepsilon} \le 155 \quad (5\text{-}30)$$

For 1C1B and 1B1C,

$$\tau_{d,CB} = \tau_{s,CB}\left[0.041\left(\dot{\varepsilon}\right)^{0.772} + 1.014\right] \text{ when } 2.5\times10^{-5} \le \dot{\varepsilon} \le 119 \quad (5\text{-}31)$$

5.2.4 Section summary

In this section, to investigate the effect of hybrid FRPs, single-lap shear tests are conducted on the dynamic interfacial bond behaviour between hybrid carbon/basalt FRP sheet and concrete under the loading rates of 8.33E-6 m/s, 1 m/s, 3 m/s, and 8 m/s, corresponding to the strain rate between 2.50E-5 s^{-1} and 155.10 s^{-1}, the following conclusions can be drawn:

1. The debonding failure surface changes from concrete substrate to the interface between adhesive and concrete and a combined failure mode is observed with the rising strain rate for both sole and hybrid composites.
2. The debonding load increases remarkably with the strain rate for both the sole and hybrid composites. An additional layer of FRP sheet for hybrid composites enhances the bond strength. The stacking sequence of FRP sheets results in different bond strength under quasi-static loads while the effect of stacking sequence on bond strength is marginal when the loading rate is over 1 m/s. Empirical formulae are proposed to predict the dynamic interfacial bonding strength and shear stress.
3. The 1B-concrete interface shows higher strain rate sensitivity than that of the 1C-concrete interface due to the significant increment of ultimate debonding strain. An additional layer of FRP sheet for hybrid composites leads to the reduction of ultimate debonding strain due to the increased stiffness.
4. The stress transfer zone reduces with the increasing strain rate. The stacking sequence of the FRP sheet affects the stress transfer zone due to the shear stress redistribution in the

interlayers under static loads, while the stress transfer zone of hybrid composites shows similar results at the highest considered loading speed of 8 m/s.

5. The strain rate effect on the bond-slip response is more significant than the hybrid effect with the increasing loading rate because of the enhanced tensile strength of concrete. The interface between hybrid composites and concrete shows higher peak shear stress and interfacial fracture energy than that of sole FRP at the same loading rate.

5.3 Summary

This chapter investigates the effects of strain rate and FRP configurations on the dynamic interfacial bond performance with the consideration of strain rate in section 5.1 and hybrid FRPs (i.e. a mixture of CFRP and BFRP) in section 5.2. Although the effect of FRP stiffness and stacking sequence have influences on the bonding characteristics because an additional layer of FRP sheet for hybrid composites enhances the bond strength and the stacking sequence of FRP sheets results in different bond strength under quasi-static loads, the hybrid effect is marginal when the loading rate exceeds 1 m/s, indicating that the FRP-to-concrete interface is more sensitive to strain rate. Based on the test results, empirical dynamic increase factors (DIF) for the interface between FRP and concrete are proposed to estimate the dynamic interfacial bond strength and shear stress by incorporating the effects of strain rate and hybrid FRPs.

Chapter 6. Effect of concrete characteristics on dynamic bond behaviour

The effect of FRP configurations on the dynamic interfacial bond has been investigated in Chapter 5. In this chapter, the effects of concrete characteristics including aggregate size, concrete strength and adding short steel fibres on the dynamic bond behaviour are studied in section 6.1, 6.2, and 6.3, respectively.

6.1 Effect of aggregate size

To investigate the effect of aggregate size on dynamic interfacial bond behaviour between BFRP and concrete, the specimens with aggregate sizes (i.e. 5-10 mm, 10-15 mm, and 15-20 mm) are prepared and tested under various loading speeds (i.e. 8.33E-6, 0.1, 1.0, 3.0, 5.0, and 8.0 m/s). The testing results including the interfacial bond strength and bond-slip responses are evaluated and discussed.

The related work in this section has been published in Construction and Building Materials.

Yuan C, Chen W, Pham TM, Chen L, Cui J, Shi Y, Hao H. Effect of Aggregate Size on the Dynamic Interfacial Bond Behaviour between Basalt Fibre Reinforced Polymer Sheets and Concrete. Construction and Building Materials. 2019; 227:116584. 2018; 145:83-95. DOI: doi.org/10.1016/j.conbuildmat.2019.07.310

6.1.1 Experimental program

6.1.1.1 Material properties

Figure 6-1 illustrates the concrete substrates with different aggregate sizes at which three common sizes were selected for this test program, namely the small 5-10 mm, the medium 10-15 mm, and the large 15-20 mm. The concrete prisms with a length of 150 mm, the width of 150 mm and height of 300 mm were prepared in this test. The concrete mix design is given in Table 6-1. For the material properties, please refer to chapter 3.2.1.

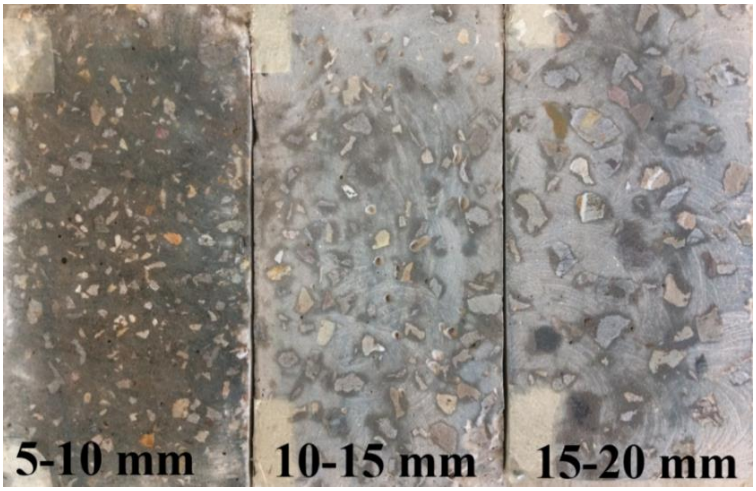

Figure 6-1. Concrete substrates with different aggregate sizes

Table 6-1. Concrete mix design and mechanical properties

Group ID	Water/Cement (%)	Sand/Aggregate (%)	Volume percentage of aggregate (%)	Aggregate size (mm)	Compressive strength (MPa)	Tensile strength (MPa)
G1	38	50.4	40	5-10	29.48 30.18 28.74	2.71 2.98 2.86
Mean					29.47 (COV=0.02)	2.85 (COV=0.05)
G2	38	50.4	40	10-15	32.70 33.04 30.09	2.68 2.72 2.62
Mean					31.94 (COV=0.05)	2.67 (COV=0.02)
G3	38	50.4	40	15-20	31.86 34.23 33.09	2.70 2.43 2.51
Mean					33.06 (COV=0.04)	2.55 (COV=0.05)

6.1.1.2 Dynamic testing procedure and specimen details

For static testing machine and test set-up, please refer to chapter 3.2.4. For dynamic test setup, please refer to chapter 5.1.1. The specimen details and the testing results are summarized in Table 6-2.

Table 6-2. Specimen details and testing results

Specimen ID	Aggregate size (mm)	Loading velocity (m/s)	Strain rate (s^{-1})	*Pu* (kN)	ε_m (%)	τ_m (MPa)	s_o (mm)	G_f (N/mm)	Failure mode
QS1-1	5-10	8.33E-6	2.50E-05	7.87	1.10	2.20	0.131	1.10	C
QS1-2	5-10	8.33E-6	2.50E-05	6.93	0.99	2.11	0.146	0.86	C
QS2-1	10-15	8.33E-6	2.50E-05	7.34	1.03	2.10	0.128	0.96	C
QS2-2	10-15	8.33E-6	2.50E-05	7.01	0.88	2.07	0.121	0.88	C
QS3-1	15-20	8.33E-6	2.50E-05	7.12	0.98	1.98	0.118	0.90	C
QS3-2	15-20	8.33E-6	2.50E-05	6.87	0.80	1.87	0.116	0.84	C
D1-1	5-10	0.1	4.51	8.07	1.18	3.25	0.130	1.16	C
D1-2	5-10	0.1	4.31	7.88	1.10	2.95	0.141	1.11	C
D1-3	5-10	0.1	4.21	7.67	1.09	2.68	0.135	1.05	C
D2-1	5-10	1.0	25.90	8.34	1.46	4.81	0.132	1.24	C
D2-2	5-10	1.0	33.31	9.86	1.50	4.85	0.140	1.73	C
D2-3	5-10	1.0	29.56	9.72	1.49	4.20	0.128	1.69	C
D3-1	5-10	3.0	65.12	10.51	1.65	5.34	0.124	1.97	C
D3-2	5-10	3.0	57.01	12.32	1.70	6.65	0.130	2.71	C
D3-3	5-10	3.0	60.75	12.08	1.70	6.31	0.121	2.60	C/CE
D4-1	5-10	5.0	110.21	12.23	1.66	7.25	0.108	2.67	C/CE
D4-2	5-10	5.0	104.8	11.78	1.68	7.03	0.118	2.48	C/CE
D4-3	5-10	5.0	110.45	12.21	1.66	6.85	0.120	2.66	C/CE
D5-1	5-10	8.0	173.55	12.01	1.83	9.44	0.107	2.57	C/CE
D5-2	5-10	8.0	155.55	11.89	1.79	9.05	0.098	2.52	C/CE
D5-3	5-10	8.0	150.75	13.50	1.84	9.82	0.112	3.25	C/CE
D6-1	10-15	0.1	5.12	7.53	1.10	3.02	0.122	1.01	C
D6-2	10-15	0.1	4.75	7.41	1.08	2.89	0.132	0.98	C
D6-3	10-15	0.1	5.06	7.27	1.07	2.78	0.135	0.94	C
D7-1	10-15	1.0	31.24	9.40	1.36	3.97	0.110	1.58	C
D7-2	10-15	1.0	29.82	8.87	1.30	4.32	0.131	1.40	C
D7-3	10-15	1.0	30.15	9.07	1.31	4.21	0.113	1.47	C
D8-1	10-15	3.0	73.78	10.23	1.52	5.11	0.138	1.87	C
D8-2	10-15	3.0	68.15	11.06	1.61	5.51	0.119	2.18	C
D8-3	10-15	3.0	59.78	10.77	1.60	4.98	0.115	2.07	C/CE
D9-1	10-15	5.0	121.05	11.78	1.64	7.10	0.114	2.48	C/CE
D9-2	10-15	5.0	117.23	11.17	1.62	7.02	0.103	2.23	C/CE
D9-3	10-15	5.0	110.78	12.21	1.71	6.59	0.101	2.66	C/CE
D10-1	10-15	8.0	144.9	13.02	1.71	8.64	0.104	3.02	C/CE
D10-2	10-15	8.0	150.35	12.19	1.70	8.49	0.110	2.65	C/CE
D10-3	10-15	8.0	155.51	11.19	1.62	8.34	0.098	2.23	C/CE
D11-1	15-20	0.1	5.17	7.19	1.05	2.82	0.118	0.92	C
D11-2	15-20	0.1	4.85	7.03	0.98	2.45	0.121	0.88	C
D11-3	15-20	0.1	5.05	7.34	1.00	2.41	0.115	0.96	C
D12-1	15-20	1.0	28.85	7.93	1.16	3.68	0.110	1.12	C
D12-2	15-20	1.0	30.75	8.13	1.22	4.11	0.120	1.18	C
D12-3	15-20	1.0	34.76	8.48	1.23	4.21	0.103	1.28	C
D13-1	15-20	3.0	78.78	9.38	1.51	5.02	0.138	1.57	C
D13-2	15-20	3.0	75.27	10.06	1.61	5.11	0.125	1.81	C/CE
D13-3	15-20	3.0	69.78	10.40	1.62	5.56	0.102	1.93	C
D14-1	15-20	5.0	120.5	10.78	1.63	7.03	0.114	2.07	C/CE
D14-2	15-20	5.0	121.45	11.68	1.69	7.02	0.112	2.43	C/CE
D14-3	15-20	5.0	118.21	11.09	1.65	6.78	0.104	2.19	C/CE
D15-1	15-20	8.0	179.30	11.93	1.70	8.20	0.118	2.54	C/CE
D15-2	15-20	8.0	155.78	12.89	1.80	8.69	0.102	2.96	C/CE
D15-3	15-20	8.0	158.36	11.73	1.70	8.17	0.101	2.45	C/CE

Note: *C* means debonding in the concrete; *CE* means debonding in the concrete-epoxy interface.

6.1.2 Testing results and discussions

Testing results of dynamic single-lap shear tests are valid only when stress equilibrium is achieved. In this section, the stress equilibrium of all the specimens was carefully checked and only those results which satisfy this condition were included. Details of the validation of stress equilibrium are presented in Section 6.3.2. The accuracy of the DIC technique was verified by matching the readings from strain gauges and those from the DIC technique. The results showed that these methods yielded almost the same measurements as also shown in the previous studies (127, 206).

6.1.2.1 Failure mode and debonding load

Table 6-2 summarizes failure modes of the tested specimens. For the specimens experienced low loading speeds (i.e. 8.33E-6 m/s, 0.1 m/s, and 1 m/s), a thin concrete layer beneath the epoxy layer was pulled off, as shown in Figure 6-2 (a). When the loading speed was over 3 m/s (i.e. 5 m/s and 8 m/s), the debonding pattern changed to a combined failure mode, in which the failure occurred at both the thin concrete layer and the concrete-epoxy interface, as shown in Figure 6-2 (b). The changed pattern of debonding failure mode indicates that the interfacial shear resistance of the FRP-concrete interface was enhanced with strain rate due to the increased tensile strength of the concrete substrate. As shown in Figure 6-2 (c), it was observed that a certain amount of aggregates was pulled out from the concrete matrix in the specimens with small aggregates (i.e. 5-10 mm) as also observed in a previous study (75). This might be due to the densely distributed small aggregates which caused a relatively higher area ratio of aggregate to mortar on the bond surface of concrete substrates. It was reported that the fracture path was prone to spread through the aggregates with a higher ratio of aggregate to mortar and the specimens with higher aggregate content were more sensitive to strain rate (75). In addition, the pull out of aggregates was not observed in the specimens with large aggregates (i.e. 15-20 mm). It might be because of the higher friction between large aggregates and matrix due to the effective embedment depth (52). Consequently, the fracture path only spreads through the mortar layer.

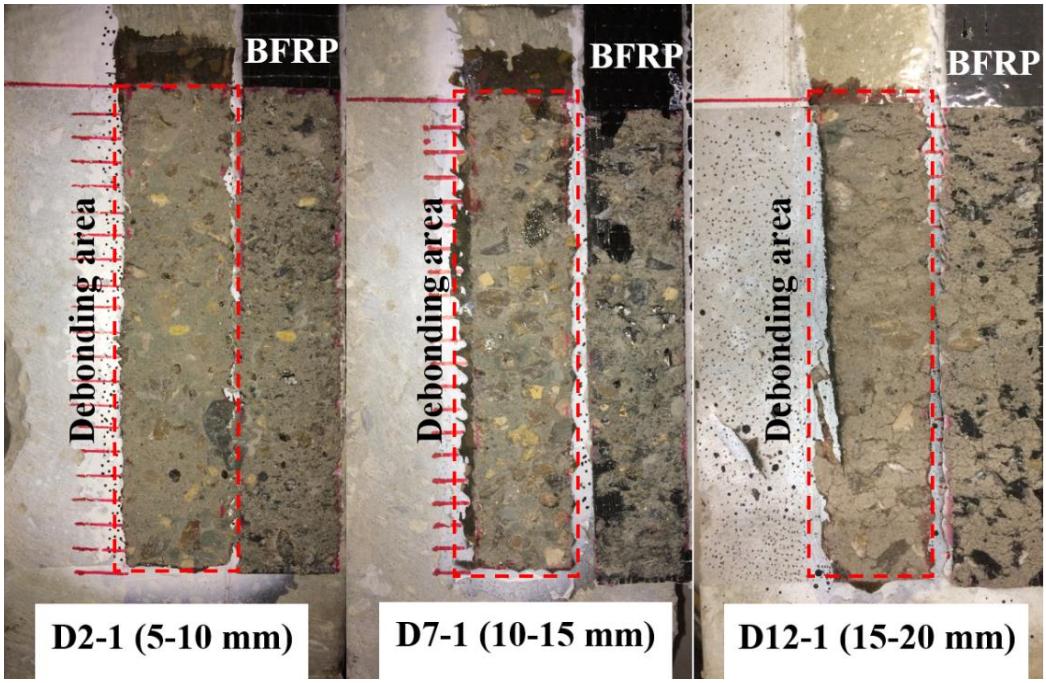

(a) Loading speed of 1 m/s

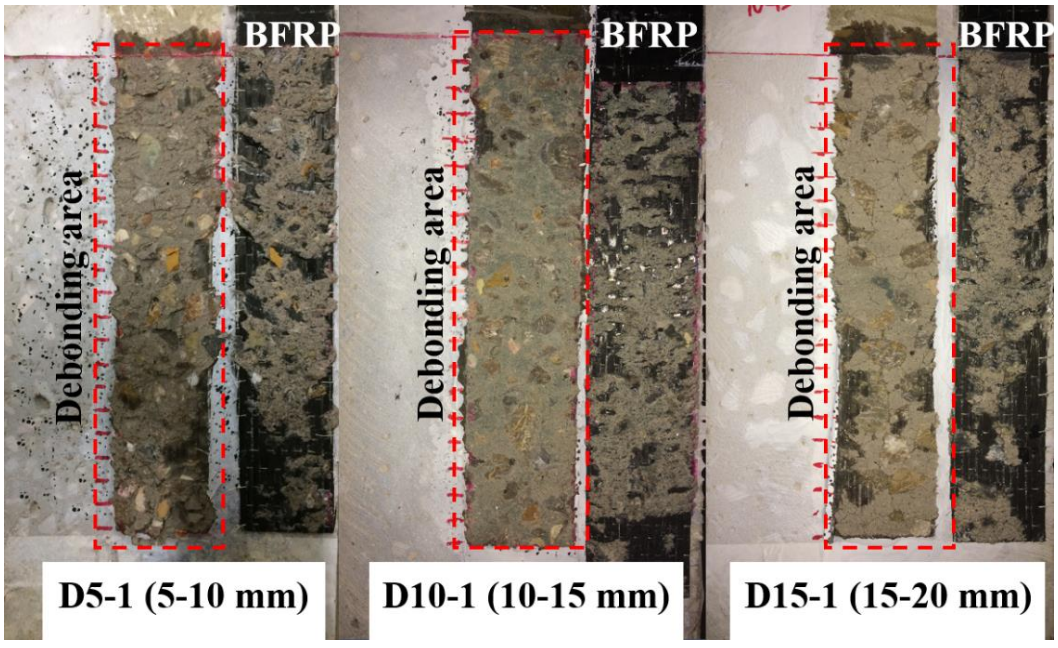

(b) Loading speed of 8 m/s

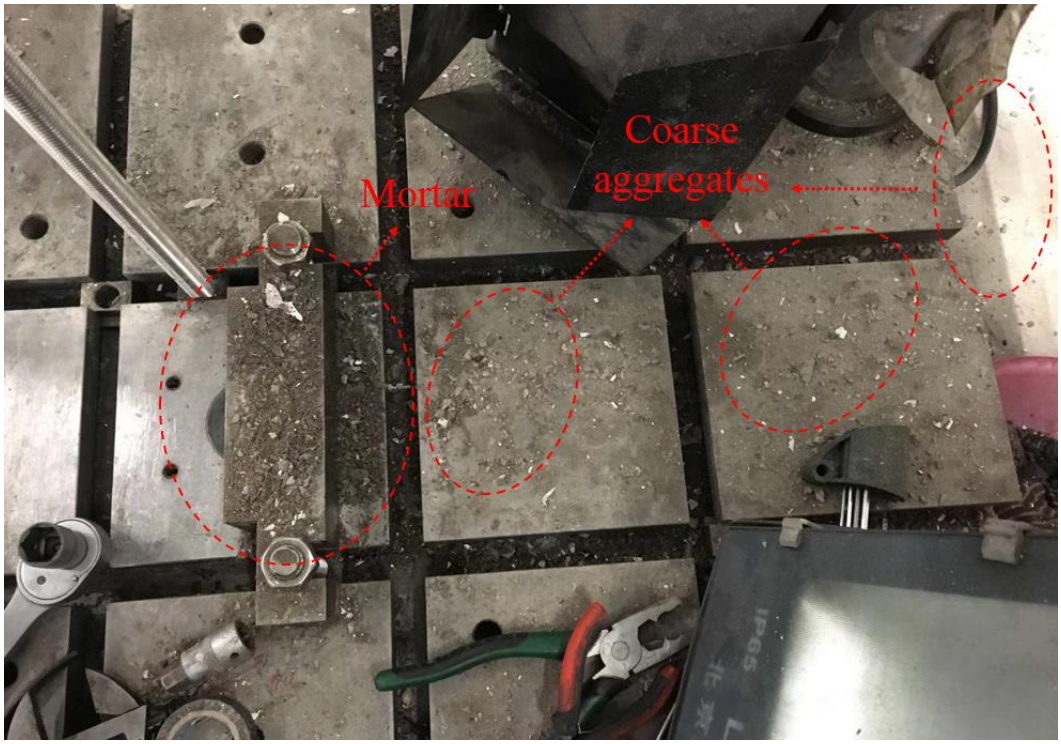

(c) Debris of D3-2 after testing at the loading speed of 3 m/s

Figure 6-2. Typical failure modes

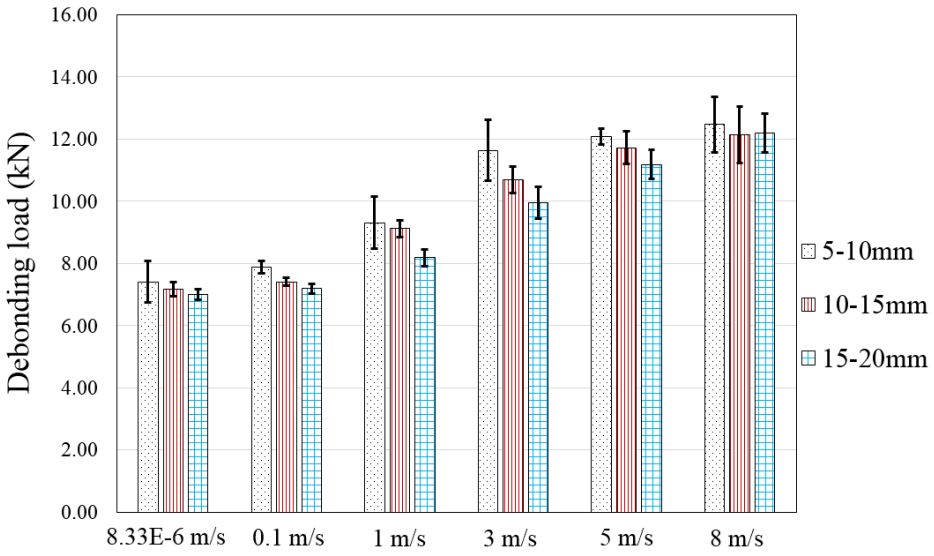

Figure 6-3. Average debonding load under different loading rates

Figure 6-3 illustrates the impact of different aggregate sizes on the debonding loads at different loading rates. It was found that the debonding load increased with the loading speed while the increment was marginal when the speed is higher than 3 m/s. Compared to the quasi-static tests, the increment of the debonding load for the specimen D5 (5-10mm), D10 (10-15 mm), and D15 (15-20mm) at the loading speed of 8 m/s was 68%, 69%, and 74%, respectively. The

significant increment of the bond strength indicates the enhanced interfacial shear resistance. For the specimens with different aggregate sizes under the same loading speed, the debonding load decreased with the increase of aggregate size, which was caused by the declined tensile strength of concrete with the increasing aggregate size. This phenomenon occurred at almost all the loading speeds. The declined tensile strength is due to the increased micro-cracks caused by stress concentration near the coarse aggregates (156).

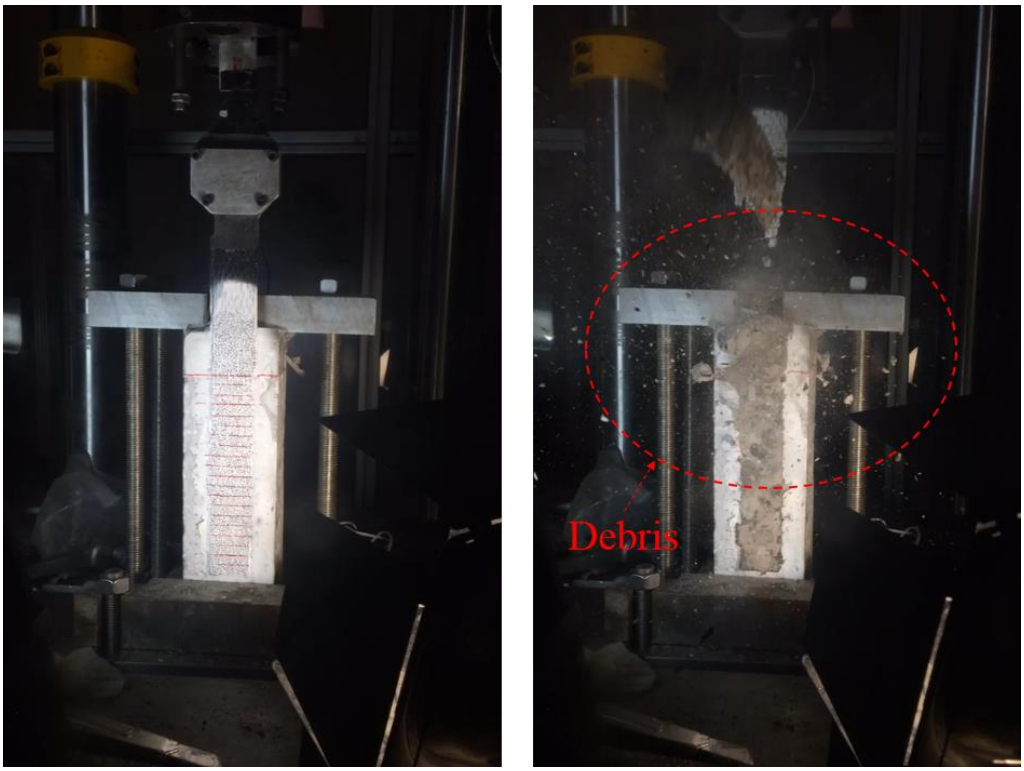

Figure 6-4. (L) Specimen D15-1 before test; (R) Debris after final debonding

Figure 6-4 shows the debris, mostly coarse aggregates, being pulled out from the concrete substrates under a dynamic loading speed of 8 m/s. The higher interfacial fracture energy caused by the pull-out of aggregates resulted in a higher debonding load under dynamic loadings. Figure 6-5 illustrates the effect of the aggregate size on the interlocking action. Small aggregates might result in stronger interlocking action due to their more uniform and dense distribution while large aggregates result in relatively weaker interaction due to the significant spacing between each other. This observation was also found in the effect of various aggregate sizes on the bond behaviour under static loads (128). Therefore, the stronger interlocking action enhanced the interfacial shear resistance and the consequently greater debonding load was resulted in the concrete specimens with small aggregates. Additionally, the interfacial bond strength between BFRP and concrete was proportional to the tensile strength of concrete while

the tensile strength would decrease with the rising aggregate size. Therefore, the interfacial bond strength of the BFRP-concrete interface declined with the increase of the aggregate size.

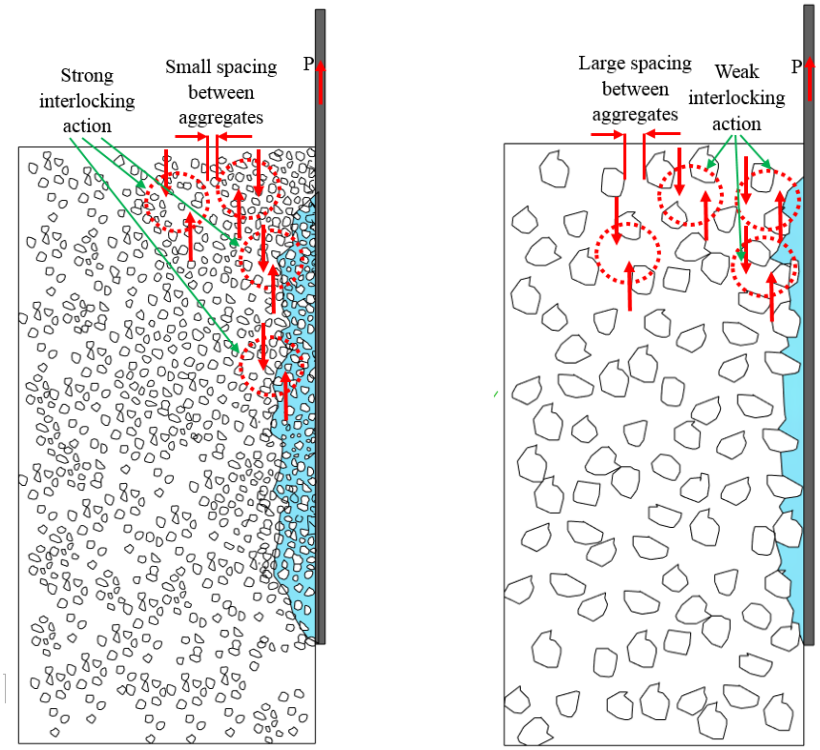

Figure 6-5. Illustrations of debonding failure process of concrete specimens with small (L) and large (R) aggregates

6.1.2.2 Strain rate and dynamic equilibrium

The typical strain contours at various loading stages and loading rates are shown in Figure 6-6. It is found that all the test specimens show a similar strain contour. The strain contours represented with red, yellow, green and blue colours are obtained from successive digital images. The region with the colors of yellow, red, green and light blue represents the shear stress transfer zone and the dark blue represents the non-stress zone. Meanwhile, the shear stress transfer zone propagated from the loaded end to the free end with the increase of the applied load. It is found that the strain rate and aggregate size have a marginal effect on the patterns of strain distributions since similar strain contours are observed for all the tested specimens. Additionally, the length of the stress transfer zone reaching the initial debonding load can be evaluated by the DIC technique, in which the distance of the shear stress distribution is defined as the effective bond length (EBL) (144, 157).

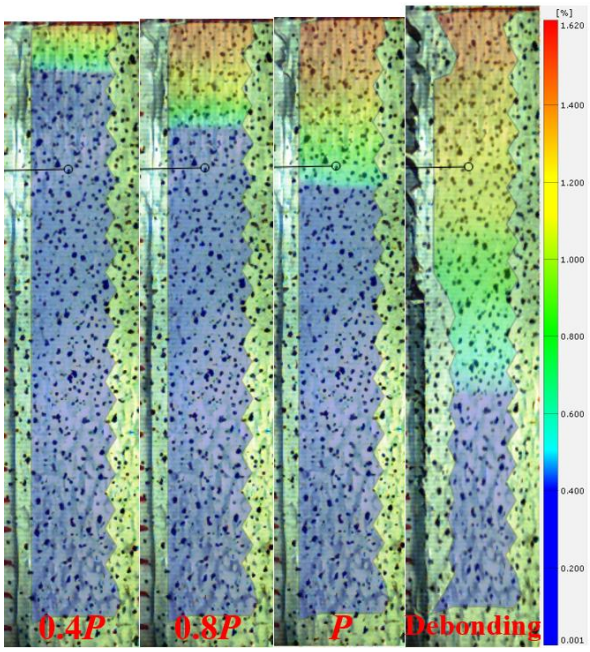

(a) D3-1 (5-10mm; 3 m/s)

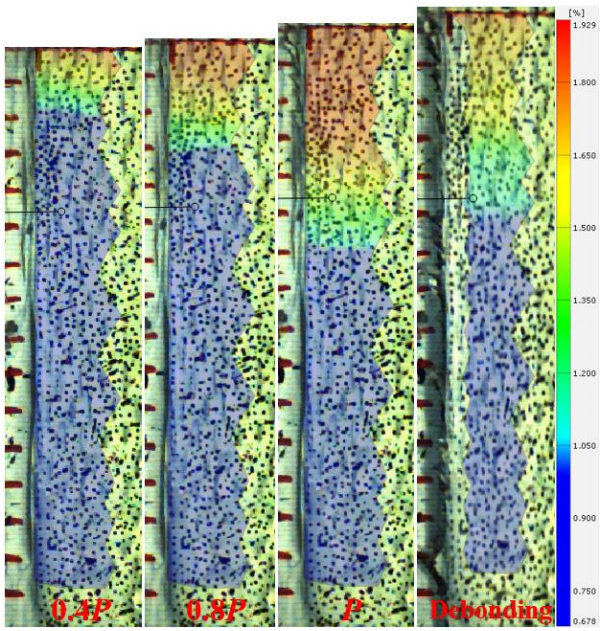

(b) D5-1 (5-10mm; 8 m/s)

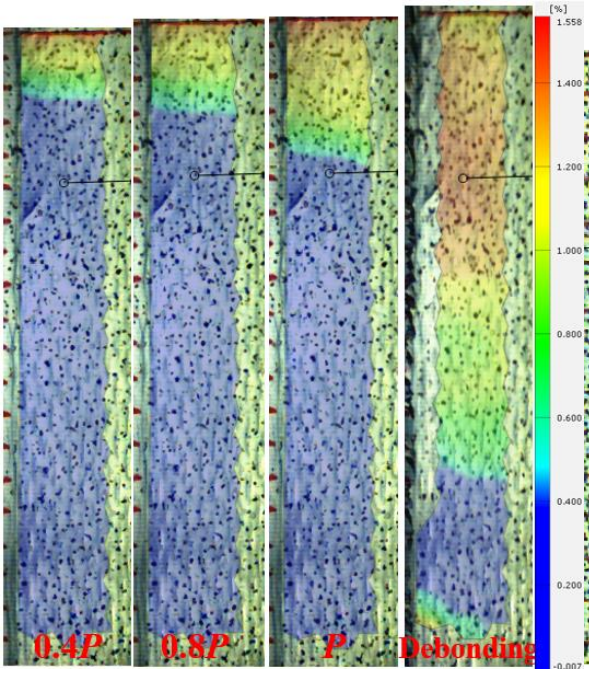

(c) D13-1 (15-20mm; 3 m/s)

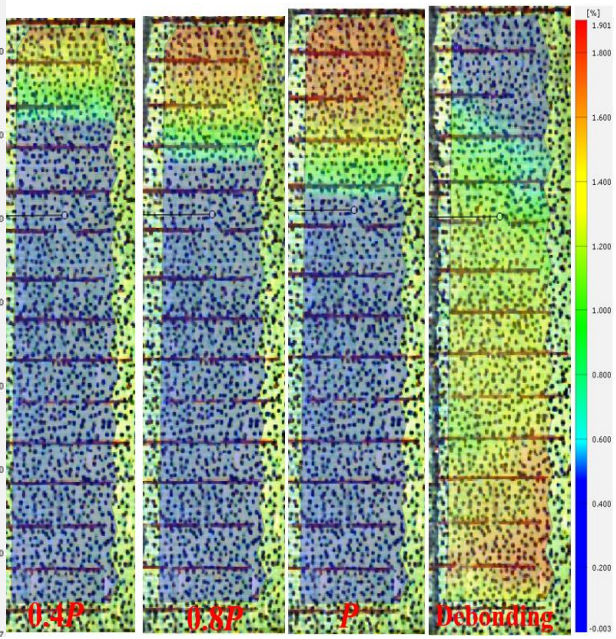

(d) D15-1 (15-20mm; 8 m/s)

Figure 6-6. Strain contours of the tested specimens

It was reported that at least three reverberations of stress waves in the specimen were required to achieve the dynamic stress equilibrium (192, 193). Please refer to Section 5.1.2.3 for the validation of dynamic stress equilibrium. The strain-time histories of Specimens D7-1 (1 m/s) and D10-1 (8 m/s) are plotted in Figure 6-7. The selected six points (Points 1 to 6) show a similar shape of strain distribution and the strain achieved an approximate plateau, indicating uniform stress distribution. It should be noted that the shape of Point 1 is somewhat different

from that at the other points since Point 1 is located at the boundary of the bonded and unbonded regions.

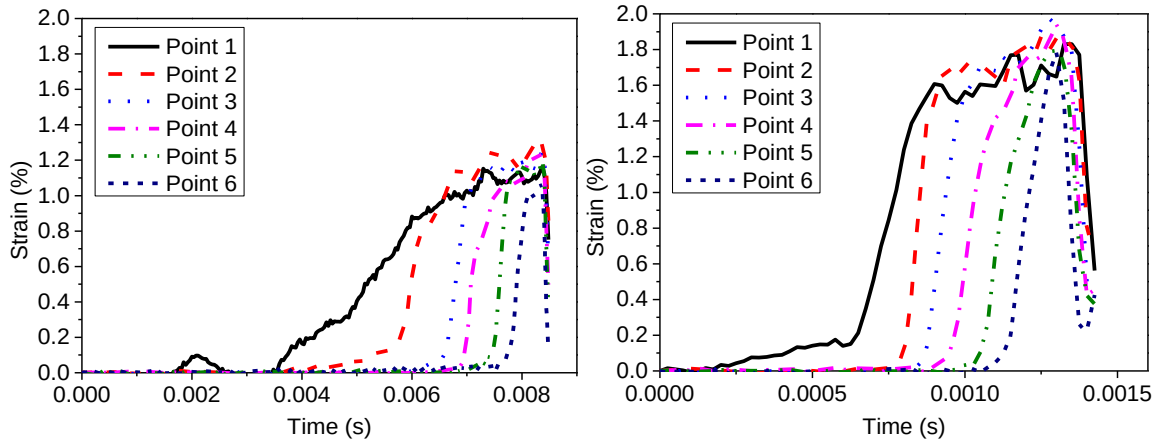

(a) D7-1 *(b) D10-1*

Figure 6-7. Strain-time histories

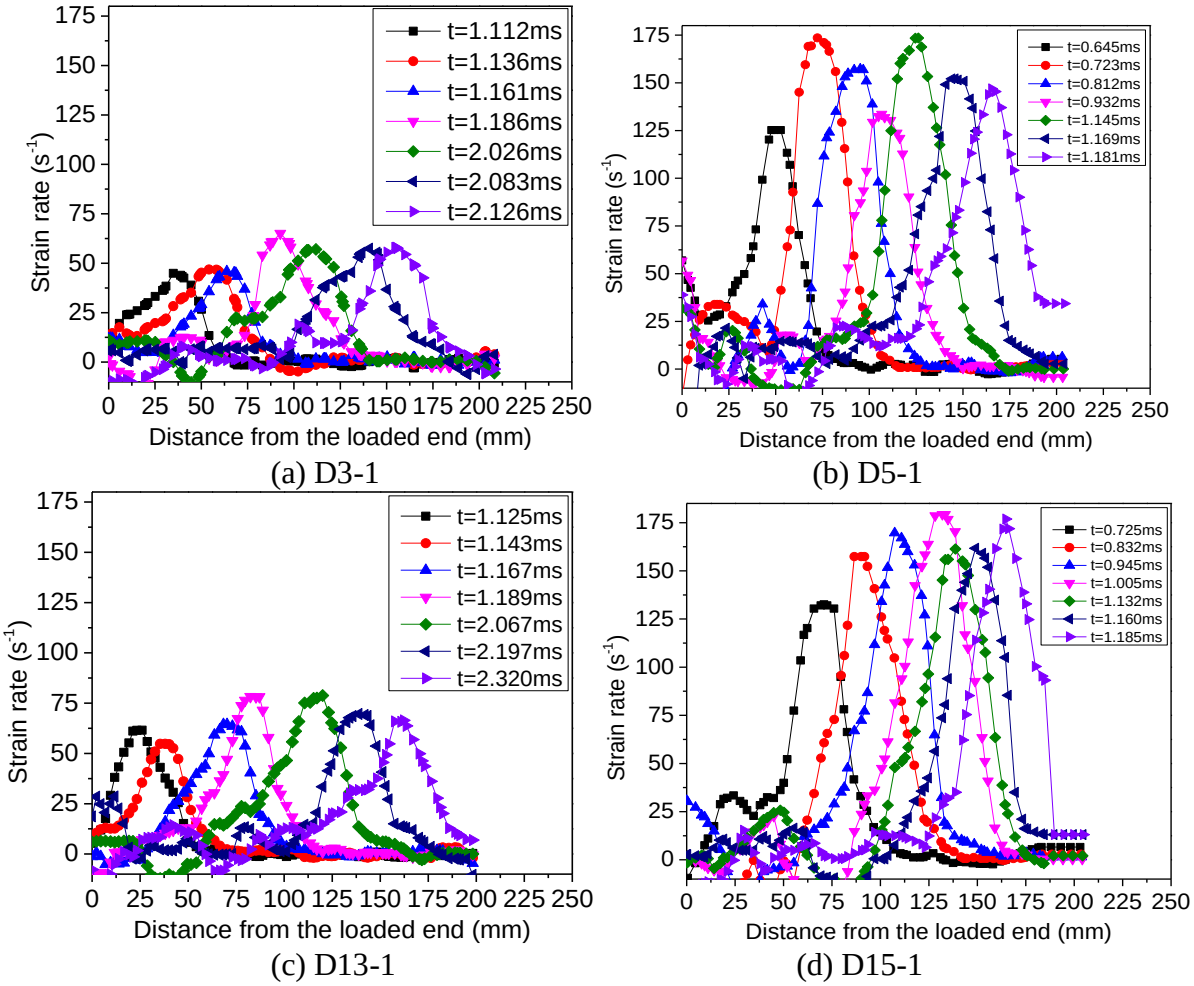

(a) D3-1 (b) D5-1

(c) D13-1 (d) D15-1

Figure 6-8. Strain rate distributions along the bond length

Figure 6-8 illustrates strain rate distributions along with the BFRP sheets at different time instants. The strain rate was obtained by differentiation of the strain time history. Table 6-2 summarizes the maximum strain rate of all the tested specimens. It is clear that the ultimate strain rate increased with loading rate while varied with loading time and maintained its bell shape to propagate along with the BFRP sheets.

6.1.2.3 Strain distribution

Figure 6-9 illustrates the strain distributions of the BFRP sheets at various loading levels and loading rates. The general trend of the testing results shows that the ultimate debonding strain increased with strain rate and the corresponding test results are summarized in Table 6-2. The maximum increment of the ultimate debonding strain for Specimen D5 (5-10mm), D10 (10-15mm), and D15 (15-20mm) was 74%, 76%, and 95% at the loading speed of 8 m/s, respectively, when compared to the quasi-static testing results. The increment indicates the enhanced shear resistance between BFRP and concrete. Increasing the size of aggregates resulted in a reduction of the ultimate debonding strain, which is shown in Figure 6-9 (a, c, and e). This is because of stronger interlocking action for smaller aggregates to resist micro-cracks in the concrete. For the specimens with large aggregates, only the weak layer of mortar was involved in debonding since no pull-out of large aggregates was observed from the tests. Additionally, there was no further increment of the ultimate strain after the initial debonding load P_u and the ultimate strain almost kept its "*S*" shape propagating until final detachment. It is observed that the strain profile along with the BFRP sheets under dynamic loading was steeper than that under static loading, indicating that the distance of the stress transfer zone decreased with the rising strain rate.

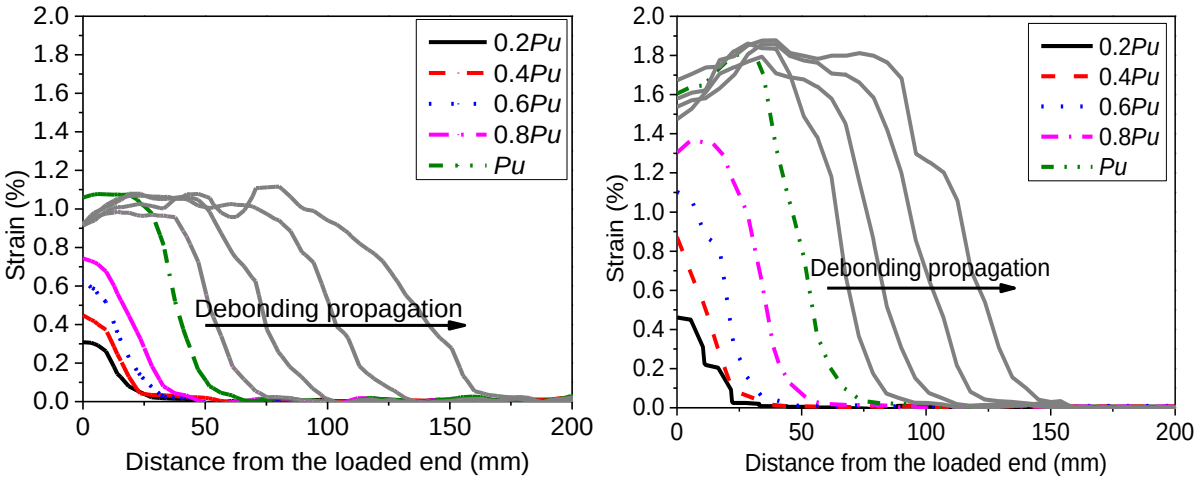

(a) QS1-1 (5-10mm) *(b) D5-1 (5-10mm)*

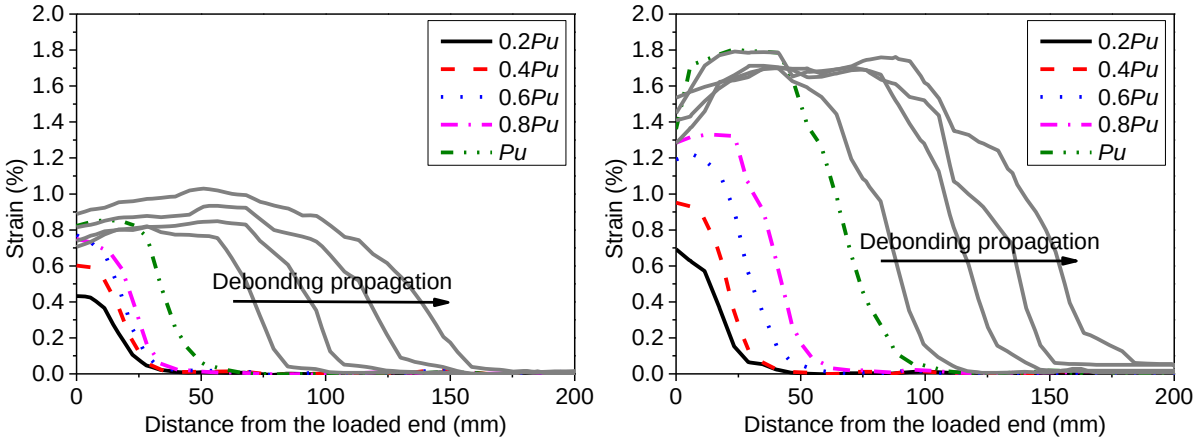

(c) QS2-1 (10-15mm) *(d) D10-1 (10-15mm)*

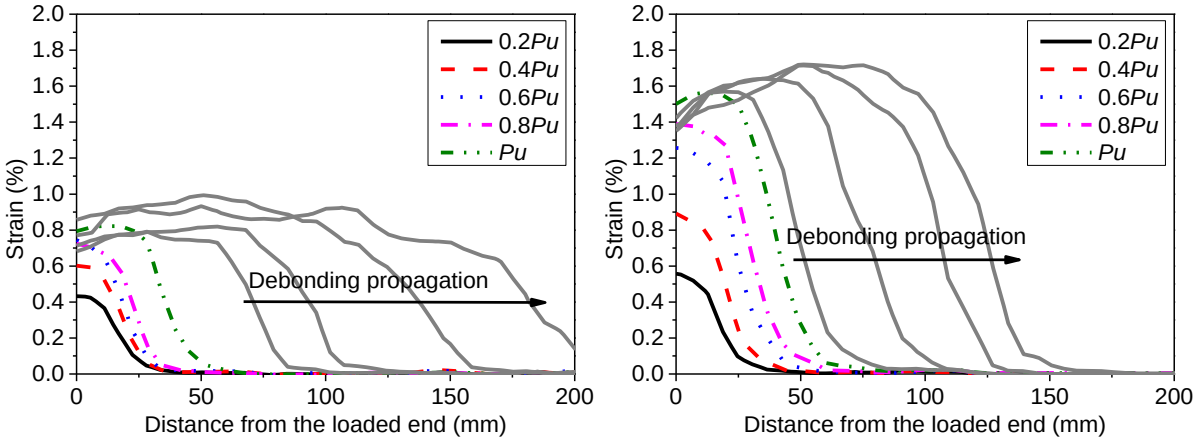

(e) QS3-1 (15-20mm) *(f) D15-1 (15-20mm)*

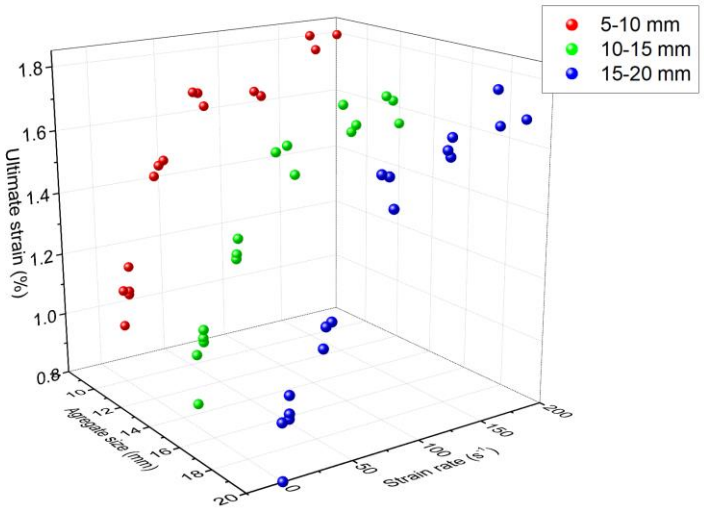

(g) Effect of aggregate size on the ultimate strain at various strain rates

Figure 6-9. Strain distributions of the tested specimens

6.1.2.4 Experimental curve of bond-slip

Figure 6-10 illustrates the relationship between shear stress and shear slip of the tested specimens. Four loading levels after the initial deboning stage were selected to form a

standardized bond-slip response. The distances of 85 mm, 115 mm, 145 mm, and 175 mm shown in the legend represent the range of strain distribution at the four loading stages after reaching an initial debonding load. The stress values at these four loading levels are averaged to obtain the peak shear stress. Because of the cracking of concrete, the local bond-slip curve of the BFRP-to-concrete interface shows a nonlinear relationship, i.e. nonlinear ascending and descending branches (197). It is found that the obtained bond-slip curves from tests are fluctuated, which affects the accuracy of data selection of the peak shear stress and the corresponding slip. Therefore, a widely used nonlinear formula $\tau(s)=\frac{E_f t_f \alpha}{\beta^2}\left(e^{-\frac{s}{\alpha}}-e^{-2\frac{s}{\alpha}}\right)$ for fitting the bond-slip relationship was used to average and smoothen the local bond-slip relationship (35, 87, 90, 208, 209). Similar bond-slip curves can be observed for all the tested specimens. The peak shear stress increased significantly with strain rate for the specimens with the same size of aggregates due to the increased ultimate debonding strain with the strain rate. The maximum increment of the peak shear stress for Specimens D5, D10, and D15 was 77%, 75%, and 74%, respectively, as compared to the corresponding quasi-static testing results. However, the peak shear stress reduced with the increase of aggregate size for the specimens at the same loading rate, as shown in Figure 6-11 (a). Additionally, the test results show that the interfacial fracture energy G_f, which is the enclosed area under the bond-slip curve, increased with the strain rate while decreased with the rising aggregate size, as shown in Figure 6-11 (b). However, the variation of interfacial fracture energy was marginal when the loading speed was over 5 m/s because of the shifted debonding surface from the concrete layer to the interface of concrete-epoxy.

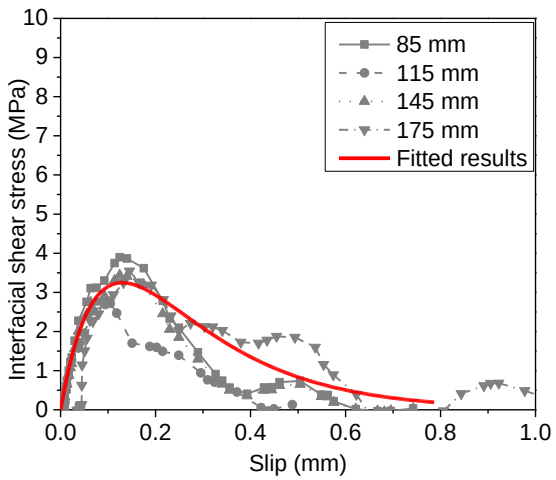

(a) QS1-1 (5-10mm)

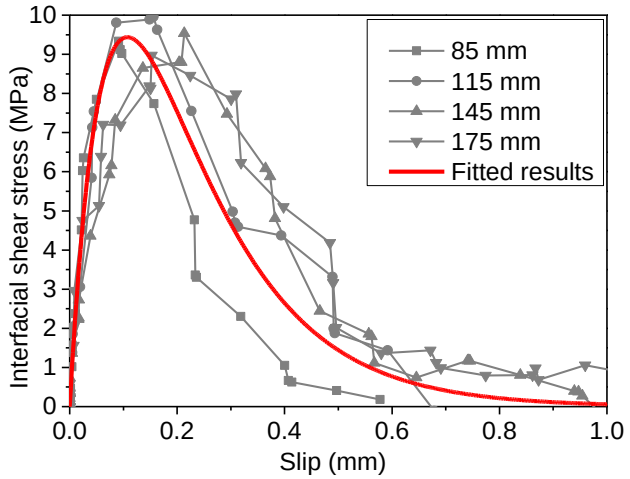

(b) D5-1 (5-10mm)

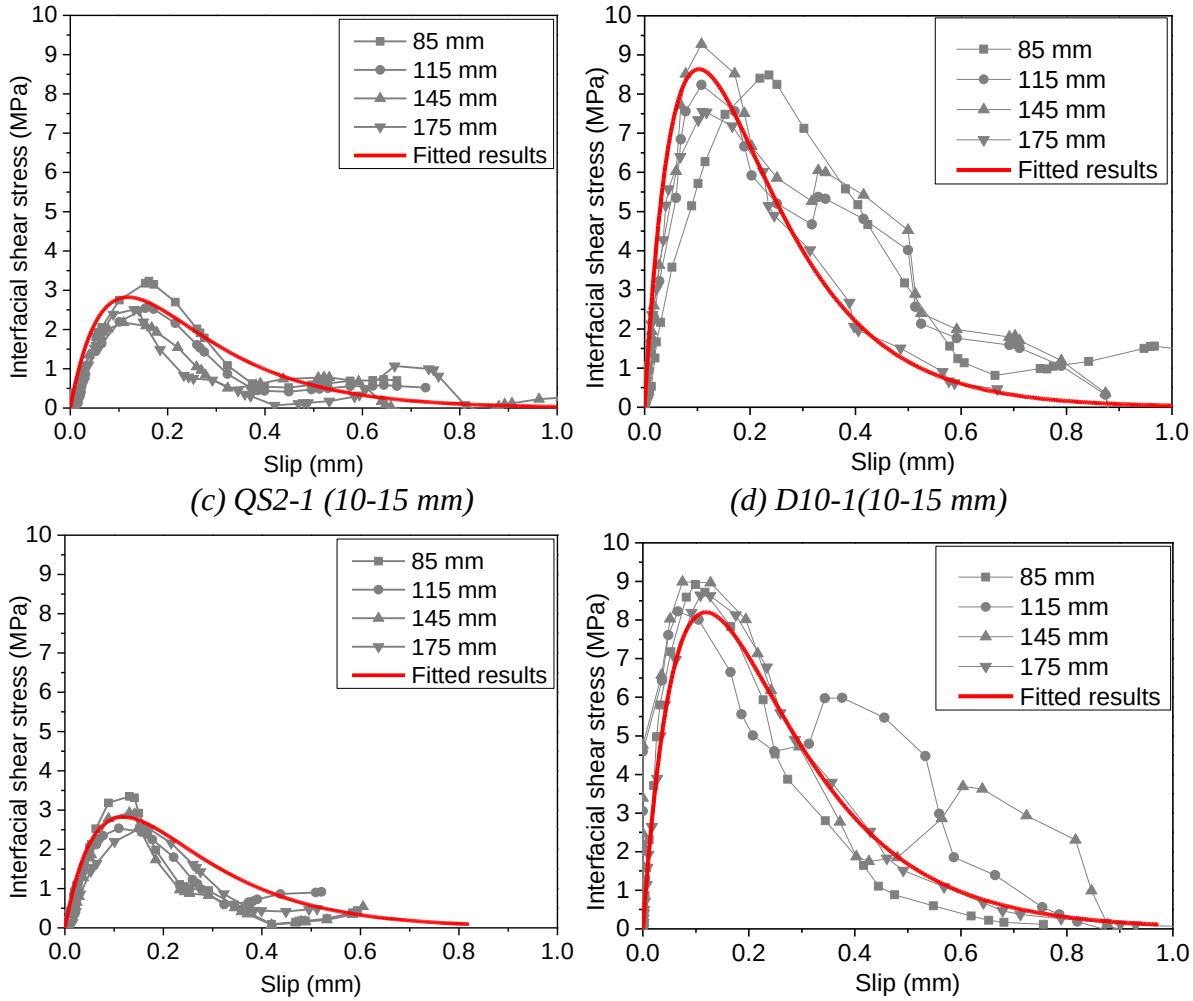

(c) QS2-1 (10-15 mm) *(d) D10-1(10-15 mm)*

(e) QS3-1 (15-20 mm) *(f) D15-1(15-20 mm)*

Figure 6-10. Typical bond-slip curves of the tested specimens at different loading speeds

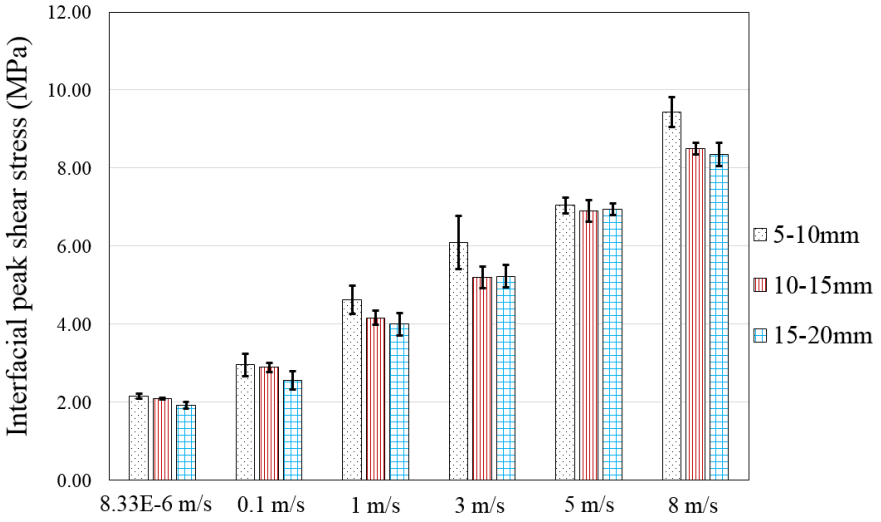

(a) Peak shear stress vs loading rate

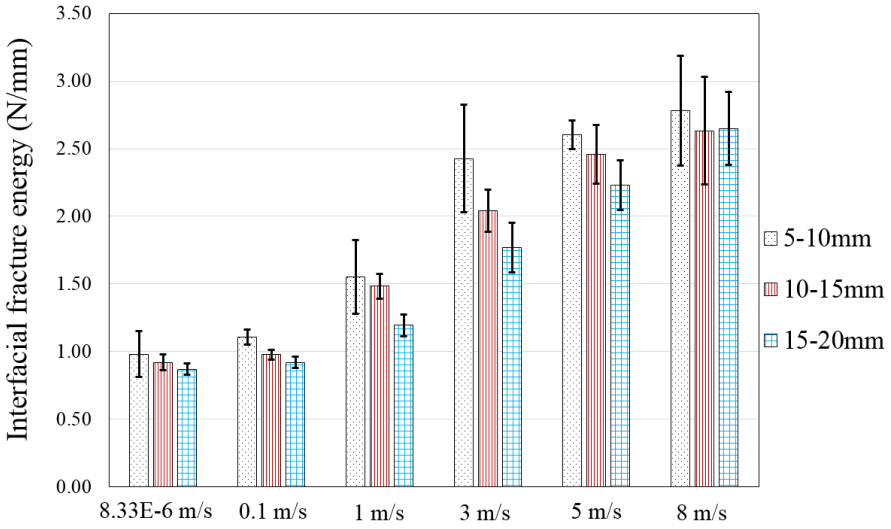

(b) Interfacial fracture energy vs loading rate

Figure 6-11. Effect of loading rate on the peak shear stress and interfacial fracture energy

6.1.3 Analytical investigation and proposed models

6.1.3.1 Effect of aggregate size on concrete properties

The general trend of the test results shows that the compressive strength increased while the tensile strength of concrete decreased with the increased aggregate size, as shown in Figure 6-12. This is because larger aggregates lead to a weak interfacial transition zone (ITZ) as well as the increased micro-cracks near the aggregates as reported in previous studies (51, 156). Therefore, Equations (6-1) and (6-2), proposed by the previous study (163), were adopted to obtain the compressive strength and tensile strength of concrete respectively:

$$f_c = 1.398 f_c^{'} - \frac{7.265 f_c^{'}}{\sqrt{1+\frac{d_{max}}{0.06263}(\frac{h}{d}-0.07717)}} \quad (6\text{-}1)$$

$$f_t = 28.2(f_c)^{-0.6817} \quad (6\text{-}2)$$

where f_t is the predicted tensile strength of concrete, f_c (MPa) is the predicted compressive strength of concrete, $f_c^{'}$ is the designed compressive strength which is 30 MPa in this section, d_{max} (mm) is the maximum aggregate size, and h and d are the height and diameter of the concrete cylinder, respectively.

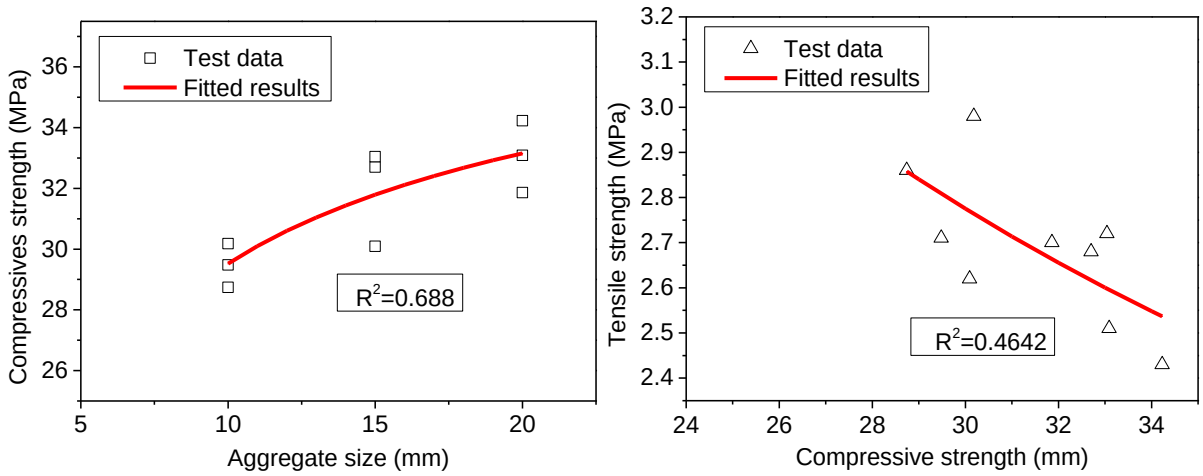

Figure 6-12. Fitted results of the compressive and tensile strength of concrete with different aggregate sizes

6.1.3.2 Modelling of interfacial fracture energy

The shear stress and slip response depend on the interfacial fracture energy (G_f). The interfacial fracture energy can be calculated by the enclosed area of bond-slip curves or derived from the debonding load. It is noted that interfacial fracture energy or bond-slip curves were not given in some previous studies but the debonding load was usually provided in most studies as listed in Table 6-3 and Table 6-5. Therefore, for easy comparison with the selected data, the interfacial fracture energy G_f of each specimen was calculated based on the debonding load in this section. A widely accepted and applied formula for the calculation of the interfacial fracture energy can be expressed as follows (35):

$$G_f = \frac{P_u^2}{2b_f^2 t_f E_f} \tag{6-3}$$

in which P_u is the debonding load, and E_f, t_f, and b_f are the elastic modulus, thickness, and width of BFRP sheets, respectively.

Table 6-2 summarizes the interfacial fracture energy of all the tested specimens. The general trend of the test results shows that the interfacial fracture energy decreased with the rising aggregate size under both static and dynamic loads, but the reduction became marginal for the loading velocity over 3 m/s. The threshold of 3 m/s is resulted from changing the debonding failure mode i.e. fracture surface shifted from concrete layer to the concrete-epoxy interface. For the specimens with the same aggregate size under different loading rates, the interfacial fracture energy increased with strain rate, as shown in Figure 6-13 (a). Due to the observed

fracture of the adhesive layer over the loading speed of 3 m/s, the model of interfacial fracture energy should take into account the contribution of the adhesive. Based on the study of Wang and Wu (210), the tensile strain energy of adhesive $\frac{f_a^{\,2}}{2E_a}$, which is the enclosed area of the uniaxial tensile stress-strain curves reflecting the strength and ductility of the adhesive, was incorporated into the proposed model. To expand the application of the proposed models, a total of 32 specimens collected from the previous studies were used to conduct the regression analysis (3, 41, 74, 83, 211). The details of the collected 32 tests are summarized in Table 6-3. Furthermore, the tensile strength of concrete in the form of $\sqrt{f_t}$, the width ratio of FRP to concrete in the form of $\beta_w^{\,2}$ are the factors determining the interfacial fracture energy. The static and dynamic interfacial fracture energies can be predicted by the following equations:

$$G_{f,s} = 0.55\beta_w^{\,2}\left(\frac{f_a^{\,2}}{2E_a}\right)^{0.42}\sqrt{f_t} \tag{6-4}$$

$$\frac{G_{f,d}}{G_{f,s}} = 1+1.096\times10^{-8}\left(\log\left(\frac{\dot{\varepsilon}_d}{\dot{\varepsilon}_s}\right)\right)^{9.09} \quad \text{when } 2.5\times10^{-5} \le \dot{\varepsilon} \le 179.30 \tag{6-5}$$

$$\beta_w = \sqrt{\frac{2.25 - b_f / b_c}{1.25 + b_f / b_c}} \tag{6-6}$$

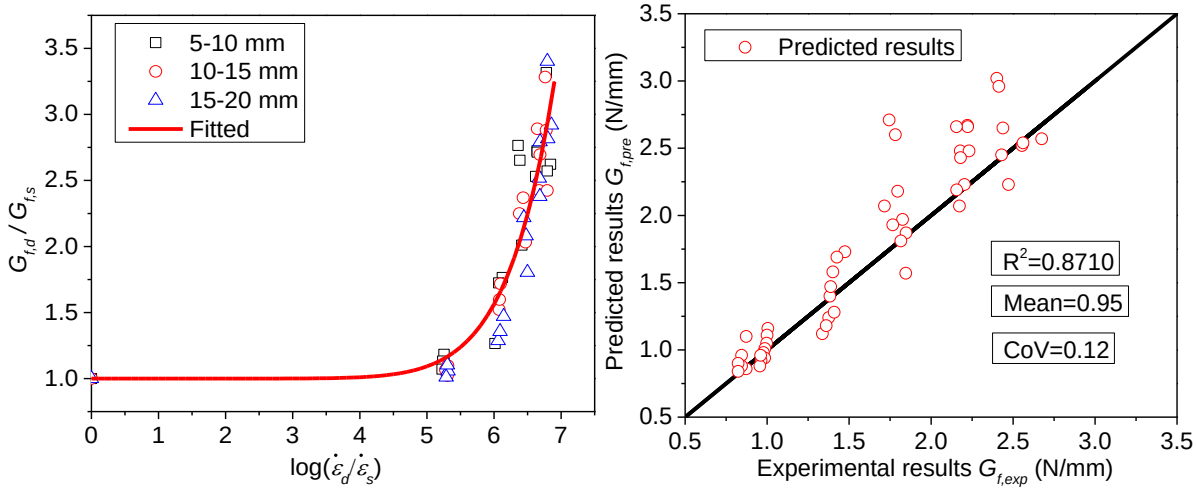

(a) (b)

Figure 6-13. (a) Interfacial fracture energy ratio vs. strain rate; (b) Comparison between experimental and predicted interfacial fracture energy

where f_a is the tensile strength of adhesive, E_a is the elastic modulus of adhesive, f_t is the tensile strength of concrete, $G_{f,s}$ is the static interfacial fracture energy, $G_{f,d}$ is the dynamic interfacial fracture energy, β_W is the width ratio of FRP to concrete, b_f is the width of BFRP, and b_c is the width of the concrete substrate. Figure 6-13 (b) compares the predicted results with the experimental results. The predicted results almost coincide with the test data as the mean value of the ratio of the predicted to experimental results is 0.95 and the corresponding coefficient of variation (COV) is 0.12.

Table 6-3. Data collected from previous studies for tensile strain energy of adhesive

Reference	Specimen ID	Test method	Adhesive			FRP			Concrete	$P_{u,exp}$ (kN)
			f_a (MPa)	E_a (GPa)	$f_a^2/2E_a$ (N/mm^2)	E_f (GPa)	t_f (mm)	b_f (mm)	f_t (MPa)	
Present section	QS1-1	Single shear	50.50	2.8	0.455	73	0.240	40	2.85	7.87
	QS1-2		50.50	2.8	0.455	73	0.240	40	2.85	6.93
	QS2-1		50.50	2.8	0.455	73	0.240	40	2.67	7.34
	QS2-2		50.50	2.8	0.455	73	0.240	40	2.67	7.01
	QS3-1		50.50	2.8	0.455	73	0.240	40	2.54	7.12
	QS3-2		50.50	2.8	0.455	73	0.240	40	2.54	6.87
Shen et al. (41)	L200-1	Double shear	45.80	2.6	0.403	105	0.121	50	2.62	11.40
	L200-2		45.80	2.6	0.403	105	0.121	50	2.62	10.80
	L200-3		45.80	2.6	0.403	105	0.121	50	2.62	13.60
Huo et al. (74)	C50-1-1	Beam	65.00	3.2	0.660	236	0.169	50	2.89	13.60
	C50-1-2		65.00	3.2	0.660	236	0.169	50	2.89	11.50
	C50-2-1		65.00	3.2	0.660	236	0.338	50	2.89	18.00
	C50-2-2		65.00	3.2	0.660	236	0.338	50	2.89	14.20
	C80-2-1		65.00	3.2	0.660	236	0.338	80	2.89	17.50
	C80-2-2		65.00	3.2	0.660	236	0.338	80	2.89	18.40
Toutanji et al. (211)	A-1	Single shear	23.60	4.1	0.068	110	0.495	50	2.73	7.56
	A-2		23.60	4.1	0.068	110	0.660	50	2.73	9.29
	A-3		23.60	4.1	0.068	110	0.825	50	2.73	11.64
	B-4		23.60	4.1	0.068	110	0.990	50	2.73	12.86
	B-1		23.60	4.1	0.068	110	0.495	50	2.73	12.55
	B-2		23.60	4.1	0.068	110	0.660	50	2.73	14.25
	B-3		23.60	4.1	0.068	110	0.825	50	2.73	17.72
	B-4		23.60	4.1	0.068	110	0.990	50	2.73	18.86
	C-1		23.60	4.1	0.068	110	0.495	50	2.73	13.24
	C-2		23.60	4.1	0.068	110	0.660	50	2.73	15.17
	C-3		23.60	4.1	0.068	110	0.825	50	2.73	18.86
	C-4		23.60	4.1	0.068	110	0.990	50	2.73	19.03
Yun et al. (3)	M-EB	Double shear	54.00	3.0	0.289	257	0.660	50	3.03	26.30
Yun and Wu (83)	N30-0-1	Single shear	45.00	3.5	0.289	235	0.167	50	2.81	23.70
	N30-0-2		45.00	3.5	0.289	235	0.167	50	2.81	24.40
	N45-0-1		45.00	3.5	0.289	235	0.167	50	3.22	27.70
	N45-0-2		45.00	3.5	0.289	235	0.167	50	3.22	27.40

Note: $f_t = 0.53\sqrt{f_c}$ (MPa) (89).

6.1.3.3 Modelling of dynamic bond-slip

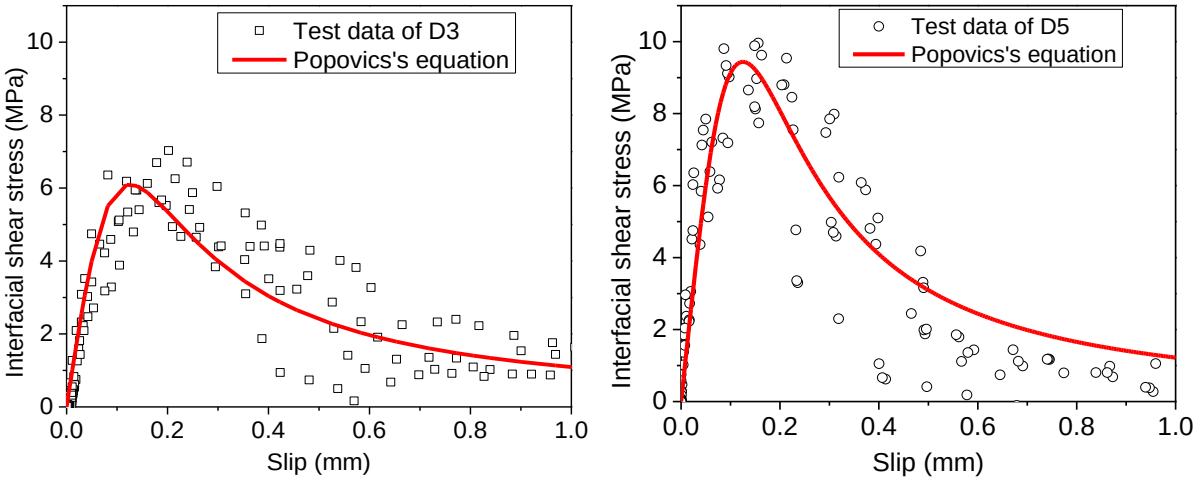

(a) D3 *(b) D5*

Figure 6-14. Fitted bond-slip curves

Popovics's equation (174) was used to describe the bond-slip relationship in this section as this equation has been widely used by numerous studies to predict the bond-slip response (91, 175). Two branches of the bond-slip curves including the ascending and descending obtained by the Popovics's equation match well with the experimental shear stress and slip curves, as shown in Figure 6-14. The formula of the Popovics's equation is shown in the following equation:

$$\tau(s) = \tau_m \left(\frac{s}{s_o} \frac{n}{(n-1)+(s/s_o)^n} \right) \tag{6-7}$$

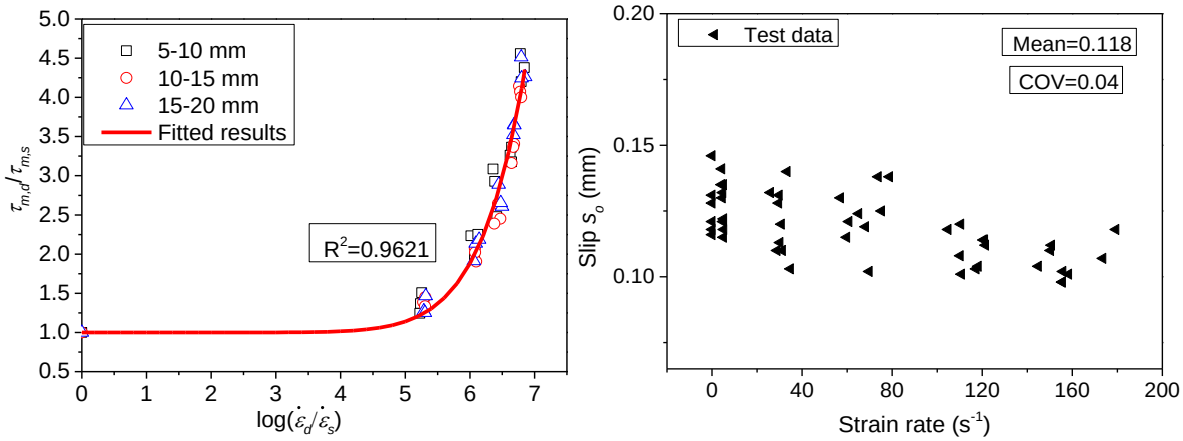

(a) Peak shear stress vs Strain rate *(b) Slip vs strain rate*

Figure 6-15. Relationship between strain rate with the peak shear stress and slip

in which τ_m is the peak shear stress, s_o is the maximum shear slip at the peak shear stress, and n is the coefficient determining the shape of bond-slip curves. The dynamic bond-slip curve can be obtained by replacing the static peak shear stress $\tau_{m,s}$ with the dynamic one $\tau_{m,d}$. The

regression coefficient n and the corresponding least square R^2 are summarized in Table 6-4. The predicted results of Popovics's equation are consistent with the testing results with the highest correlation coefficient given in Table 6-4.

Table 6-4. Experimental results and regression coefficients

Specimen ID	Loading speed (m/s)	Peak shear stress τ_m (MPa)	Slip s_o (mm)	Coefficient n	Correlation coefficient R^2
QS1	8.33E-6	2.16	0.125	2.221	0.8998
QS2	8.33E-6	2.09	0.117	2.109	0.9056
QS3	8.33E-6	1.93	0.114	2.021	0.8789
D1	0.1	2.96	0.125	2.264	0.8878
D2	1	4.62	0.125	2.444	0.8058
D3	3	6.10	0.125	2.512	0.8830
D4	5	7.04	0.125	2.507	0.8574
D5	8	9.44	0.125	3.602	0.8075
D6	0.1	2.90	0.117	2.098	0.8869
D7	1	4.17	0.117	2.724	0.8989
D8	3	5.20	0.117	3.278	0.8787
D9	5	6.90	0.117	3.307	0.8966
D10	8	8.49	0.117	2.687	0.8983
D11	0.1	2.56	0.114	2.002	0.8515
D12	1	4.00	0.114	2.708	0.7519
D13	3	5.23	0.114	3.167	0.8567
D14	5	6.94	0.114	3.385	0.8073
D15	8	8.35	0.114	2.275	0.8736
Mean			0.118	2.628	
COV			0.040	0.200	

The coefficient n slightly increases with the strain rate while the aggregate size has a rather marginal effect on the coefficient n. Given the scattered data, it is difficult to correlate the coefficient n with both strain rate and aggregate size due to the low correlation coefficient. As a result, the coefficient n was set as a constant of 2.628 in the proposed analytical model and the mean value and the corresponding coefficient of variation are summarized in Table 6-4. Based on the test results of the present section, the peak shear stress increased but the maximum slip s_o decreased with the increasing strain rate, as shown in Figure 6-15. However, the adopted maximum slip s_o was set as a constant of 0.118 mm which was the average of all the specimens due to the scattered data.

According to the previous peak shear stress models, the tensile strength of concrete (f_t) and the width ratio of FRP-to-concrete (β_w) are the factors determining the peak interfacial shear stress under static loads (99, 212). To expand the application of the proposed models, test results of 38 FRP-to-concrete joints were collected from the previous studies as summarized in Table 6-5

(41, 45, 74, 198, 213, 214). Equations (6-8) and (6-9) can be used to obtain the dynamic peak shear stress:

$$\tau_{m,s} = 0.056\beta_w f_t^4 \tag{6-8}$$

$$\frac{\tau_{m,d}}{\tau_{m,s}} = 1 + 1.216\times10^{-8}\left(\log\left(\frac{\dot{\varepsilon}_d}{\dot{\varepsilon}_s}\right)\right)^{10.1} \quad \text{when } 2.5\times10^{-5} \le \dot{\varepsilon} \le 179.30 \tag{6-9}$$

where f_t is the tensile strength of concrete, β_W is the width ratio of FRP-to-concrete, $\tau_{m,s}$ is the peak interfacial shear stress subjected to static loads, and $\tau_{m,d}$ is the dynamic peak interfacial shear stress.

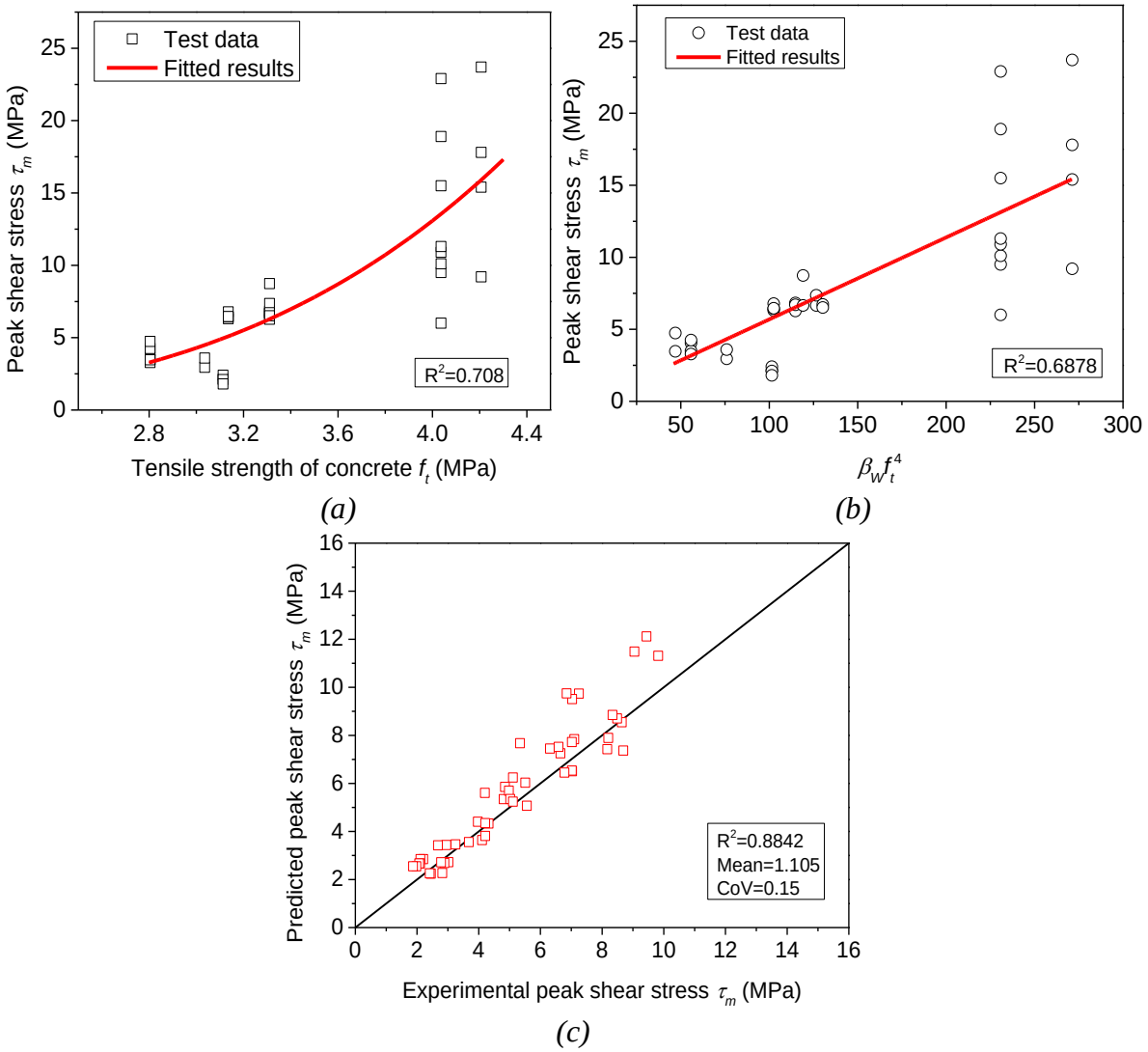

Figure 6-16. (a) Peak shear stress vs. tensile strength of concrete; (b) Peak shear stress τ_m vs. $\beta_w f_t^4$, (c) Comparison between experimental and predicted peak shear stress

Table 6-5. Data collection from previous studies for peak shear stress

Reference	Specimen ID	FRP			Concrete			τ_m (MPa)	S_o (mm)
		n	b_f (mm)	t_f (mm)	b_c (mm)	f_c (MPa)	f_t (MPa)		
Shen et al. (41)	L200-D0-1	2	50	0.121	100	32.8	3.04	2.95	0.1090
	L200-D0-2	2	50	0.121	100	32.8	3.04	3.59	0.1090
Huo et al. (74)	C50-1-S-1	1	50	0.165	100	28.0	2.80	4.05	0.0980
	C50-1-S-2	1	50	0.169	100	28.0	2.80	3.50	0.0920
	C50-2-S-1	2	50	0.169	100	28.0	2.80	3.28	0.0680
	C50-2-S-2	2	50	0.169	100	28.0	2.80	4.25	0.0780
	C80-2-S-1	2	80	0.169	100	28.0	2.80	4.74	0.0870
	C80-2-S-2	2	80	0.169	100	28.0	2.80	3.47	0.0740
Bizindavyi and Neale (213)	BN6	1	25.4	1.000	150	34.5	3.11	2.14	-
	BN20	2	25.4	2.000	150	34.5	3.11	2.40	-
	BN25	1	25.4	0.330	150	34.5	3.11	2.10	-
	BN32	2	25.4	0.660	150	34.5	3.11	1.80	-
Subramaniam et al. (198)	W-1	1	46	0.167	125	39.0	3.31	6.83	0.0412
	W-2	1	46	0.167	125	39.0	3.31	6.27	0.0319
	W-3	1	46	0.167	125	39.0	3.31	6.70	0.0297
	W-4	1	38	0.167	125	39.0	3.31	6.66	0.0361
	W-5	1	38	0.167	125	39.0	3.31	8.74	0.0283
	W-6	1	25	0.167	125	39.0	3.31	6.66	0.0286
	W-7	1	25	0.167	125	39.0	3.31	6.65	0.0263
	W-8	1	25	0.167	125	39.0	3.31	7.36	0.0333
	W-9	1	19	0.167	125	39.0	3.31	6.72	0.0331
	W-10	1	19	0.167	125	39.0	3.31	6.51	0.0282
Carloni et al. (214)	DS-S1	1	25	0.167	125	35.0	3.14	6.78	0.037
	DS-S2	1	25	0.167	125	35.0	3.14	6.31	0.040
	DS-S3	1	25	0.167	125	35.0	3.14	6.43	0.043
	DS-F4	1	25	0.167	125	35.0	3.14	6.46	0.035
Pellegrino et al. (45)	S1C1a	1	50	0.165	100	63.0	4.21	15.40	0.032
	S1C5c	1	50	0.165	100	58.0	4.04	15.50	0.036
	S1C5d	1	50	0.165	100	58.0	4.04	6.00	0.034
	S2C1a	2	50	0.165	100	63.0	4.21	17.80	0.027
	S2C1b	2	50	0.165	100	58.0	4.04	9.50	0.022
	S2C1c	2	50	0.165	100	58.0	4.04	18.90	0.031
	S3C1a	3	50	0.165	100	63.0	4.21	9.20	0.025
	S3C1b	3	50	0.165	100	58.0	4.04	10.10	0.022
	S3C1c	3	50	0.165	100	58.0	4.04	10.90	0.024
	S3C5a	3	50	0.165	100	63.0	4.21	23.70	0.019
	S3C5b	3	50	0.165	100	58.0	4.04	11.30	0.027
	S3C5c	3	50	0.165	100	58.0	4.04	22.90	0.030

Note: $f_t = 0.53\sqrt{f_c}$ (MPa) (89); "-" means unavailable data.

6.1.4.4 Validation of the proposed analytical model

Figure 6-17 illustrates the predicted shear stress and slip curves by using the Popovics's equation (174). Equations (6-8) and (6-9) are used to obtain the peak shear stress. As shown in Figure 6-16 (c), the predicted results match well with the experimental results with a mean ratio of 1.105 and a coefficient of variation (COV) of 0.15. The predicted bond-slip response is consistent with the experimental results, namely, the peak shear stress increases with strain rate while decreases with the rising aggregate size.

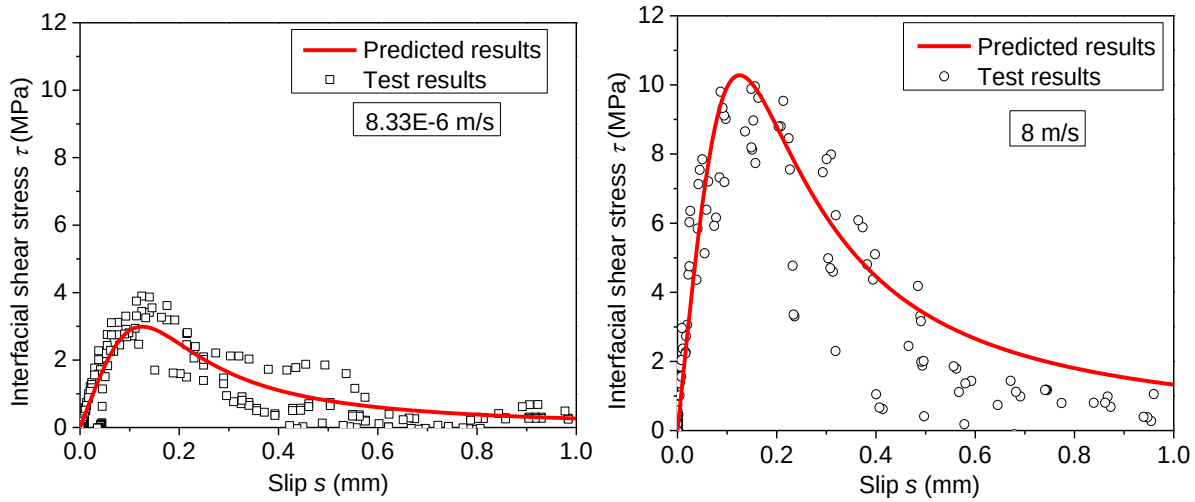

(a) QS1 (5-10 mm)

(b) D5 (10-15 mm)

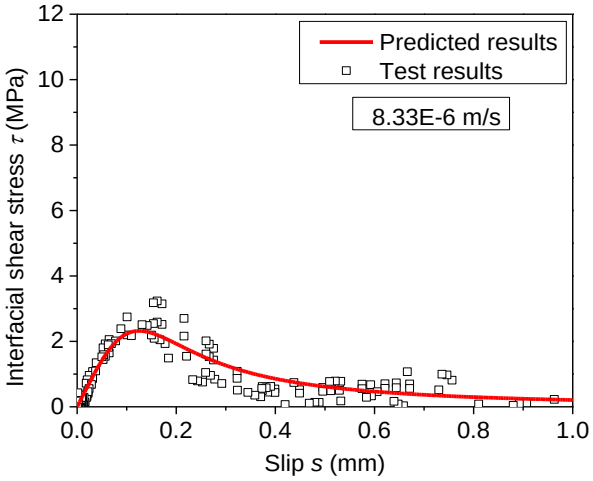

(c) QS2 (10-15 mm)

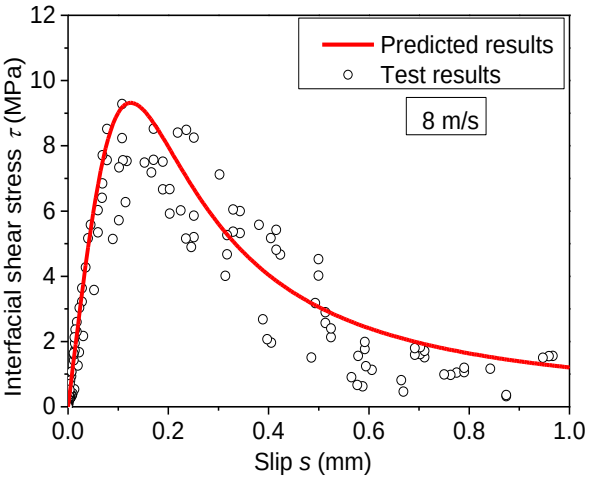

(d) D10 (10-15 mm)

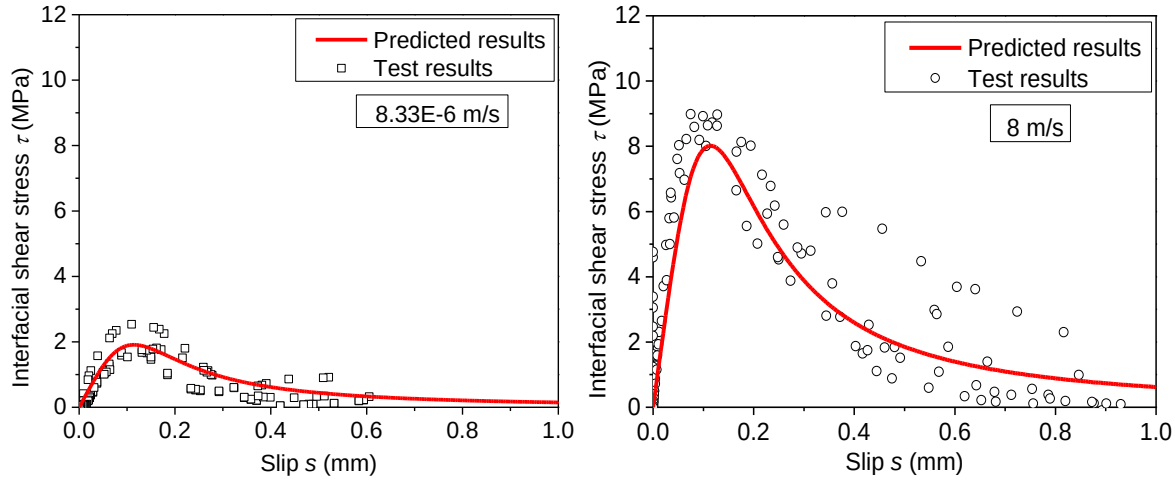

(e) QS3 (15-20 mm) *(f) D15 (15-20 mm)*

Figure 6-17. Comparison of predicted and test bond-slip curves

Previous studies have demonstrated that the debonding load, the peak bond stress, and BFRP strain distributions can be obtained by using the proposed bond-slip models in the previous studies (37, 142, 188). The debonding load and strain distribution can be directly obtained from the test data. Therefore, the validation of the proposed bond-slip models can be conducted regarding the debonding load and strain distribution. The debonding load can be obtained by incorporating the interfacial fracture energy under static loads. The proposed dynamic interfacial fracture energy $G_{f,d}$ can be used to replace the static one to obtain the dynamic results. The formula can be expressed as follows (35, 95, 154):

$$P_u = b_f \sqrt{2E_f t_f G_f} \tag{6-10}$$

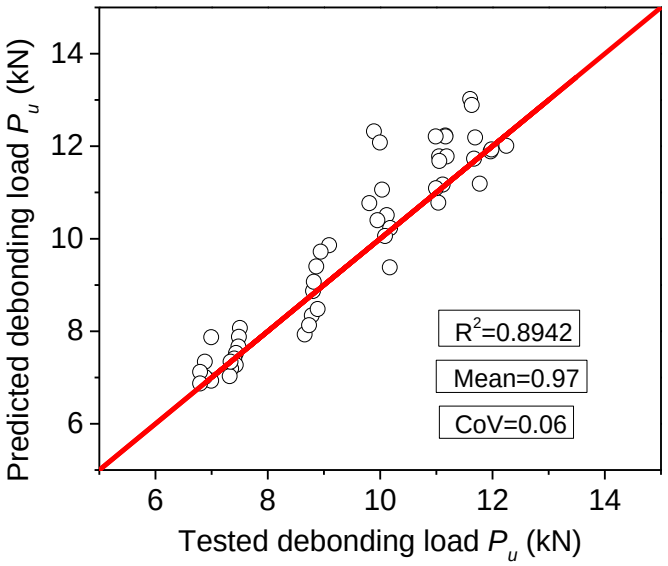

Figure 6-18. Comparison between the predicted and experimental debonding load

By substituting the dynamic interfacial fracture energy $G_{f,d}$ into Equation (6-10), the dynamic debonding load can be obtained accordingly. It is observed that the predicted debonding loads by incorporating the proposed interfacial energy match well with the experimental results. Figure 6-18 shows the mean value of 0.97 and the corresponding coefficient of variation (COV) of 0.06 between the predicted and experimental results.

6.1.4 Section summary

The section investigates the effect of aggregate size on the dynamic interfacial bond between BFRP sheets and concrete. The following observations and conclusions can be drawn:

1. Debonding failure mode changes with strain rate; the fracture surface shifts from the concrete substrate layer to the concrete-epoxy interface with the increase of strain rate.
2. The tested specimens under dynamic loads exhibit more ductile behaviour because of the improved debonding load and the ultimate slip. Compared to the static results, the maximum increments of the ultimate debonding load for Specimens with aggregate sizes of 5-10 mm, 10-15 mm and 15-20mm are 74%, 76%, and 95% at the loading speed of 8 m/s, respectively.
3. The strain distribution gradient under high dynamic loads is steeper than that under quasi-static loads, indicating the shorter shear stress transfer zone under dynamic loads.
4. The reduction of peak shear stress is observed for specimens with larger aggregates under the same loading rate. The maximum increments of peak shear stress at the loading speed of 8 m/s for Specimens with aggregates of 5 - 10 mm, 10 - 15 mm and 15 - 20 mm are 77%, 75%, and 74%, respectively, as compared to the static peak shear stress.
5. By validating the testing results, a dynamic bond-slip model by incorporating the coarse aggregate size and strain rate is proposed to predict the debonding load and shear stress and slip response of the BFRP-to-concrete interface under dynamic loads.

6.2 Effect of concrete strength

This section investigates the effect of concrete strength on the dynamic interfacial bond behaviour between basalt fibre reinforced polymer (BFRP) sheets and concrete under different loading speeds (i.e. 8.33E-6 m/s, 0.1 m/s, 1 m/s, 3 m/s, 5 m/s, and 8 m/s). Three concrete strengths (i.e. C20, C30, and C40) are considered to examine the influence of concrete strength

and strain rate on the interfacial bond-slip responses under dynamic loads. The test results including the strain distributions, interfacial fracture energy, and bond-slip response are evaluated and discussed.

The related work in this section has been published in Engineering Fracture Mechanics.

Yuan C, Chen W, Pham TM, Hao H, Cui J, Shi Y. Influence of Concrete Strength on Dynamic Interfacial Fracture Behaviour between Fibre Reinforced Polymer Sheets and Concrete. Engineering Fracture Mechanics. 2020:106934.
DOI: doi.org/10.1016/j.engfracmech.2020.106934.

6.2.1 Experimental program

6.2.1.1 Material properties

Concrete blocks with 150 x 150 x 300 mm in dimension were prepared for the tests. The compressive strengths of three series of concrete (C20, C30, and C40) were respectively 22.40 MPa, 30.14 MPa, and 42.34 MPa and the corresponding splitting tensile strengths were 2.11 MPa, 3.12 MPa, and 4.13 MPa, respectively. The coarse aggregate size of 5-20 mm was used in the test program. For the material properties of the BFRP sheet and epoxy resin, please refer to chapter 3.2.1.

6.2.1.2 Test setup

For static testing machine and test set-up, please refer to chapter 3.2.4. For dynamic test setup, please refer to chapter 5.1.1. The specimen details and tracking points are shown in Figure 6-19.

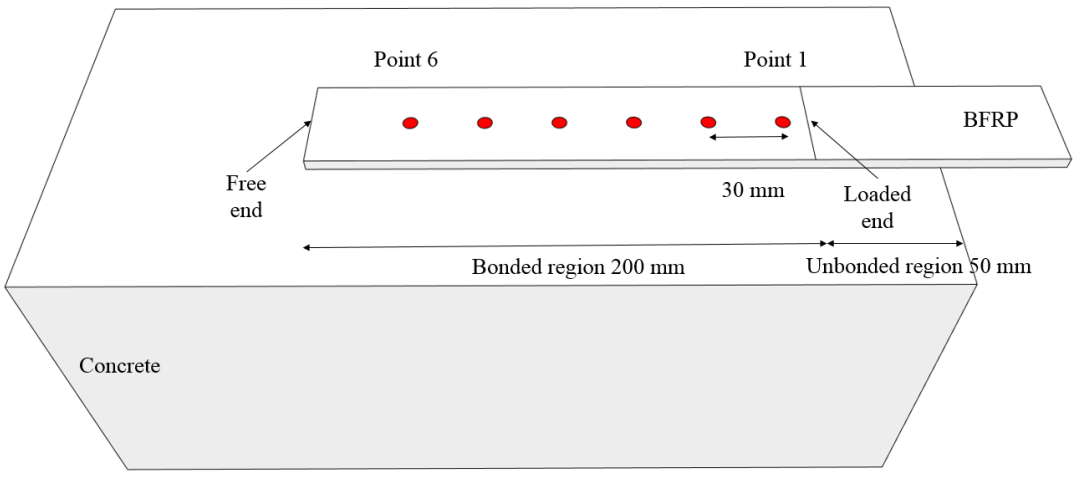

Figure 6-19. Specimen detail

6.2.2 Validation of dynamic stress equilibrium

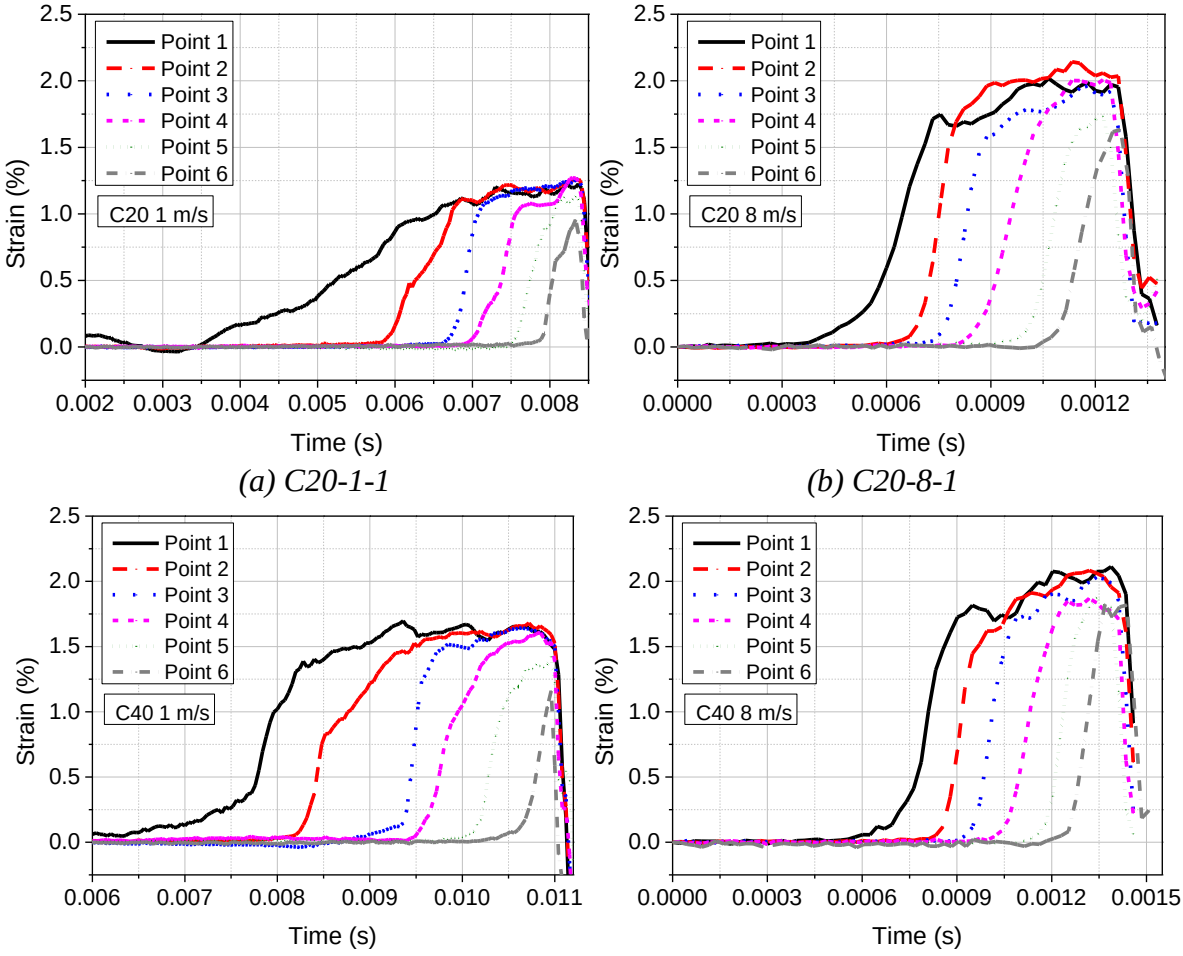

(a) C20-1-1 *(b) C20-8-1*

(c) C40-1-1 *(d) C40-8-1*

Figure 6-20. Strain time histories

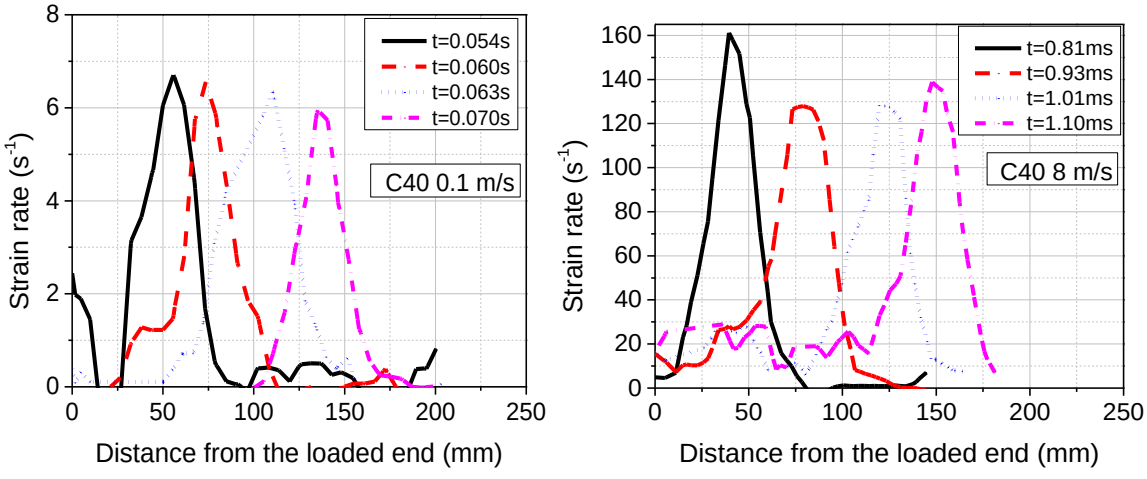

(a) C40-0.1-1 *(b) C40-8-1*

Figure 6-21. Strain rate distribution

As a non-contact measurement method, the accuracy of the DIC technique was carefully checked in the previous studies by the authors to obtain reliable test data (127, 128, 206). In addition, experimental results of dynamic debonding tests are valid only when stress equilibrium is achieved. Therefore, the strain-time histories of the tested specimens are plotted to prove the dynamic stress equilibrium, as shown in Figure 6-20. Six tracking points (Points 1 to 6) along the centreline of the FRP surface were selected to compare, as illustrated in Figure 6-19. Similar strain profiles were observed at different time instants and the strain developed a similar plateau, indicating uniform stress distribution. It is noted that the strain distributions of Point 1 and Point 6 are different from others since Point 1 is placed at the boundary of the bonded and unbonded region and Point 6 is located near the free end, which cannot develop the entire debonding process. It should be noted that specimen C20-1-2 refers to the specimen with compressive strength of 20 MPa subjected to the dynamic loading speed of 1 m/s and the last digit refers to the specimen number, i.e., the second specimen in the group of three identical specimens.

The strain rate can be derived from the differentiation of strain time history. Figure 6-21 illustrates the variation of the strain rate along the bonded length at different time instants. The peak strain rate was selected as the measured strain rate for each specimen. For instance, the peak strain rate for the specimen C40-8-1 was 161.18 s^{-1} and the maximum strain rate for the specimen C40-0.1-1 was 6.69 s^{-1}. The strain rate of each specimen is summarized in Table 6-6.

6.2.3 Test results and discussions

6.2.3.1 Debonding load and failure mode

Table 6-6 summarizes the test results of the debonding load and failure modes. The debonding load on average increased with the rising strain rate irrespective of the concrete strength, as shown in Figure 6-22. The specimens with the highest concrete strength (i.e. C40) showed the greatest bond strength at all the loading speeds. Previous studies have also reported that the debonding load enhanced with strain rate (40, 108). When subjected to the dynamic loads rate of 8 m/s, all the specimens experienced a minor difference in the debonding load. However, the specimens with the lowest concrete strength (i.e. C20) showed the highest increment on debonding load, which is shown in Figure 6-23. Compared to the quasi-static testing data, an increment of 129.14% is obtained for the specimen C20-8 at the dynamic testing of 8 m/s. Specimen C40-8 shows the lowest dynamic increment of 63.66% as compared to the specimens with lower concrete strength at the same speed. This indicates that the strain rate effect on the

bond strength of the specimens is concrete strength dependent. The specimens with the concrete strength of about 20 MPa are most strain rate sensitive. However, mixed observations for specimens with concrete strength of about 30 MPa and 40 MPa were obtained, i.e., the strain rate sensitivity of C30 specimens is not always higher than that of C40 specimens.

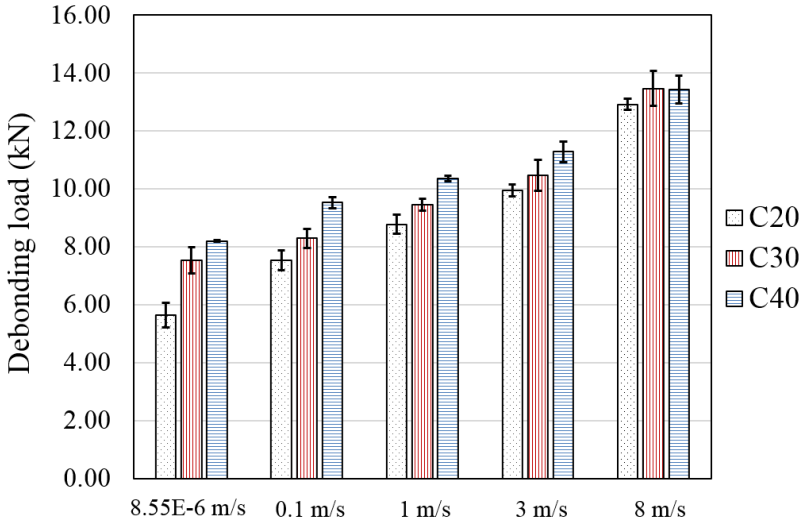

Figure 6-22. Debonding load of specimens

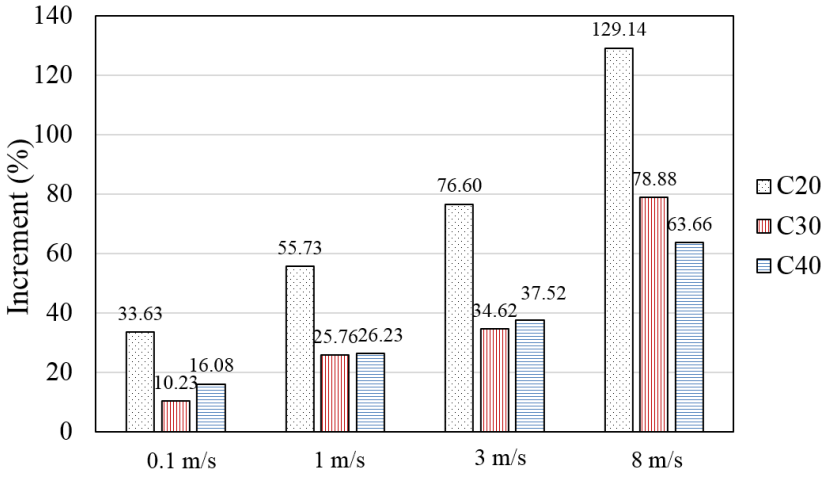

Figure 6-23. Increment ratio of debonding load

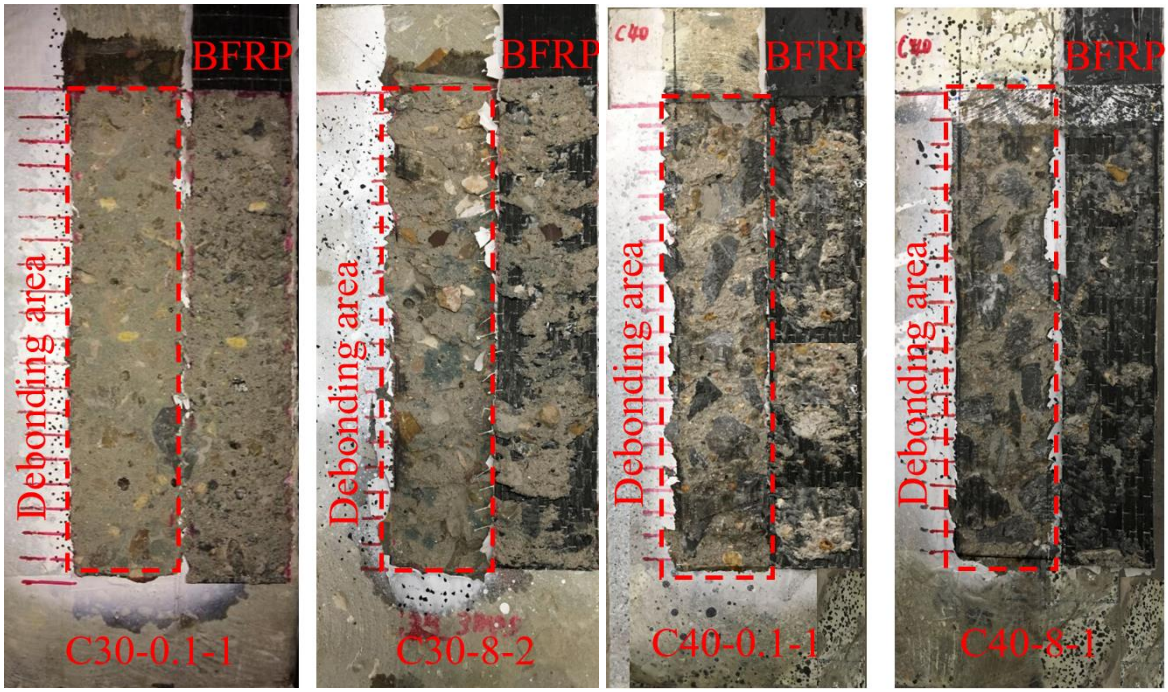

Figure 6-24. Typical failure modes

The enhanced dynamic interfacial bond strength is attributed to the enhanced concrete tensile strength with strain rate. Previous studies (76, 202) have demonstrated that both the compressive and tensile strength of concrete enhanced with strain rate and the corresponding enhancement of tensile strength varied from 10% to 170% when the strain rate increased from 10 s^{-1} to 100 s^{-1}. As the single-lap shear test method was employed in this test program, the interface between BFRP and concrete was subjected to shear stress through the adhesive layer or penetrated into the concrete layer (75). It is well-known that concrete is strong in compression but weak in tension. Therefore, the fracture of the concrete layer is normally governed by its tensile strength for single-lap shear tests. Under relatively low loading rates (less than 1 m/s), failure occurred inside the concrete layer as a thin layer of concrete beneath the BFRP sheets was observed after the final detachment, as shown in Figure 6-24. Therefore, the interfacial bond strength should be mainly determined by the tensile strength of concrete. The final detachment, as shown in Figure 6-24. Therefore, the interfacial bond strength should be mainly determined by the tensile strength of concrete.

Table 6-6. Specimen details and test results

Specimen ID	f_c (MPa)	f_t (MPa)	Loading speed (m/s)	Strain rate (s^{-1})	P_u (kN)	ε_u (%)	τ_m (MPa)	s_2 (mm)	G_f (N/mm)	$f_{t,d}$ (MPa)	$G_{f,pre.}$ (N/mm)	$\tau_{m,pre.}$ (MPa)	$\varepsilon_{u,pre.}$ (%)	$P_{u,pre.}$ (kN)	Failure mode
C20-QS-1	22.40	2.11	8.33E-6	2.50E-5	5.94	0.859	1.97	0.098	0.63	2.11	0.73	3.05	0.912	6.39	C
C20-QS-2	22.40	2.11	8.33E-6	2.50E-5	5.34	0.917	1.56	0.111	0.51	2.11	0.73	3.05	0.912	6.39	C
C20-0.1-1	22.40	2.11	0.1	4.57	7.19	1.040	4.16	0.131	0.92	6.71	1.30	5.45	1.218	8.54	C
C20-0.1-2	22.40	2.11	0.1	3.91	7.56	1.094	3.92	0.118	1.02	6.50	1.28	5.36	1.209	8.47	C
C20-0.1-3	22.40	2.11	0.1	3.76	7.86	1.137	4.08	0.102	1.10	6.45	1.27	5.34	1.206	8.45	C
C20-1-1	22.40	2.11	1	33.38	8.75	1.196	5.23	0.111	1.37	9.34	1.53	6.43	1.323	9.27	C
C20-1-2	22.40	2.11	1	29.79	9.12	1.319	4.54	0.124	1.48	9.19	1.52	6.37	1.318	9.23	C
C20-1-3	22.40	2.11	1	30.26	8.48	1.227	4.98	0.097	1.28	9.21	1.52	6.38	1.318	9.24	C
C20-3-1	22.40	2.11	3	52.36	9.91	1.434	7.19	0.111	1.75	9.94	2.04	6.63	1.524	10.68	C
C20-3-2	22.40	2.11	3	49.85	9.78	1.415	6.79	0.109	1.71	9.87	2.03	6.61	1.522	10.66	C
C20-3-3	22.40	2.11	3	45.23	10.19	1.474	7.41	0.101	1.85	9.74	2.02	6.56	1.517	10.63	C/CA
C20-8-1	22.40	2.11	8	147.37	12.84	1.858	10.12	0.112	2.94	11.30	2.17	7.07	1.574	11.03	C/CA
C20-8-2	22.40	2.11	8	151.74	12.79	1.850	9.31	0.104	2.92	11.34	2.17	7.08	1.575	11.04	C/CA
C20-8-3	22.40	2.11	8	124.60	13.14	1.901	9.47	0.103	3.08	11.08	2.15	7.00	1.566	10.98	C/CA
C30-QS-1	30.14	3.12	8.33E-6	2.50E-5	7.85	1.105	2.92	0.113	0.96	3.12	0.89	3.71	1.006	7.05	C
C30-QS-2	30.14	3.12	8.33E-6	2.50E-5	7.21	1.057	3.34	0.128	0.93	3.12	0.89	3.71	1.006	7.05	C
C30-0.1-1	30.14	3.12	0.1	4.91	8.38	1.153	5.19	0.119	1.25	10.06	1.59	6.67	1.348	9.45	C
C30-0.1-2	30.14	3.12	0.1	4.31	7.94	1.118	4.89	0.121	1.12	9.81	1.57	6.58	1.339	9.39	C
C30-0.1-3	30.14	3.12	0.1	4.21	8.58	1.208	5.41	0.118	1.31	9.76	1.57	6.57	1.338	9.37	C
C30-1-1	30.14	3.12	1	25.90	9.27	1.263	6.69	0.119	1.53	13.31	1.83	7.67	1.446	10.13	C
C30-1-2	30.14	3.12	1	33.31	9.46	1.332	6.83	0.117	1.60	13.81	1.86	7.81	1.459	10.22	C
C30-1-3	30.14	3.12	1	29.56	9.68	1.292	6.89	0.115	1.67	13.57	1.85	7.75	1.453	10.18	C
C30-3-1	30.14	3.12	3	65.12	10.11	1.423	8.32	0.101	1.82	15.12	2.51	8.17	1.693	11.86	C/CA
C30-3-2	30.14	3.12	3	57.01	11.09	1.387	7.85	0.121	2.19	14.86	2.49	8.10	1.686	11.81	C/CA
C30-3-3	30.14	3.12	3	60.75	10.21	1.437	8.19	0.103	1.86	14.98	2.50	8.14	1.689	11.84	C/CA
C30-8-1	30.14	3.12	8	155.55	14.07	1.981	10.21	0.111	3.53	16.82	2.65	8.62	1.739	12.18	C/CA
C30-8-2	30.14	3.12	8	175.65	13.47	1.896	9.82	0.106	3.24	17.06	2.67	8.68	1.745	12.23	C/CA
C30-8-3	30.14	3.12	8	150.76	12.87	1.812	9.39	0.102	2.95	16.76	2.64	8.61	1.737	12.17	C/CA
C40-QS-1	42.34	4.13	8.33E-6	2.50E-5	8.23	1.389	5.21	0.145	1.03	4.13	1.02	4.27	1.079	7.56	C
C40-QS-2	42.34	4.13	8.33E-6	2.50E-5	8.19	1.260	4.45	0.138	1.07	4.13	1.02	4.27	1.079	7.56	C
C40-0.1-1	42.34	4.13	0.1	6.69	9.55	1.552	6.28	0.129	1.46	13.58	1.85	7.75	1.453	10.18	C
C40-0.1-2	42.34	4.13	0.1	7.24	9.32	1.447	5.78	0.121	1.39	14.32	1.90	7.96	1.472	10.32	C
C40-0.1-3	42.34	4.13	0.1	4.03	9.72	1.491	6.54	0.124	1.52	12.81	1.80	7.52	1.432	10.03	C
C40-1-1	42.34	4.13	1	56.68	10.47	1.555	8.75	0.118	1.76	19.65	2.22	9.32	1.593	11.17	C
C40-1-2	42.34	4.13	1	33.45	10.26	1.709	9.05	0.117	1.69	18.29	2.15	8.99	1.565	10.97	C
C40-1-3	42.34	4.13	1	40.54	10.36	1.644	8.49	0.115	1.72	18.78	2.17	9.11	1.576	11.04	C/CA
C40-3-1	42.34	4.13	3	85.69	11.42	1.618	9.17	0.117	2.09	20.72	2.94	9.57	1.832	12.84	C/CA
C40-3-2	42.34	4.13	3	79.03	11.56	1.667	8.98	0.121	2.15	20.51	2.92	9.52	1.827	12.80	C/CA
C40-3-3	42.34	4.13	3	81.27	10.89	1.844	8.91	0.109	1.90	20.59	2.93	9.54	1.829	12.82	C/CA
C40-8-1	42.34	4.13	8	161.18	13.81	1.957	10.78	0.128	3.40	22.36	3.05	9.94	1.867	13.08	C/CA
C40-8-2	42.34	4.13	8	145.53	12.89	1.827	9.98	0.104	2.96	22.09	3.03	9.88	1.861	13.04	C/CA
C40-8-3	42.34	4.13	8	157.48	13.61	1.929	10.06	0.119	3.30	22.30	3.05	9.93	1.866	13.07	C/CA

Note: *C* refers to the debonding in the concrete layer, CA means the debonding in the concrete-adhesive layer, $f_{t,d}$ is the dynamic tensile strength of concrete, $G_{f,pre.}$ is the predicted interfacial fracture energy, $\tau_{m,pre.}$ is the predicted interfacial peak shear stress, $\varepsilon_{u,pre.}$ is the predicted ultimate debonding strain, $P_{u,pre.}$ is the predicted debonding load.

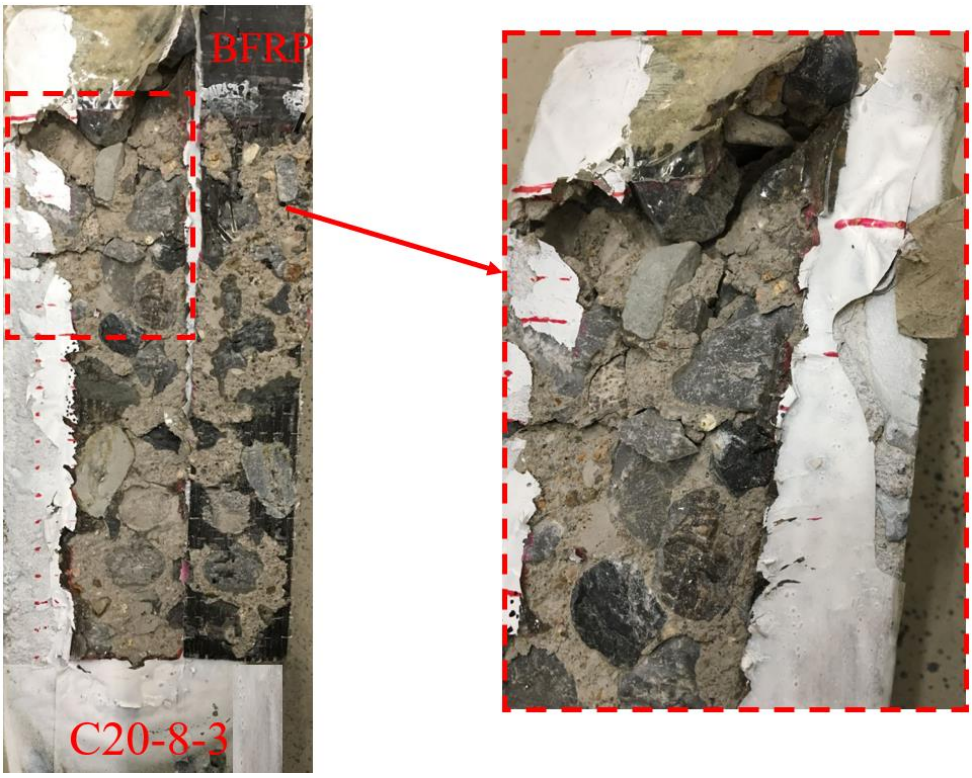

Figure 6-25. Fracture surface of C20-8-3

Meanwhile, a combined failure mode (i.e. C and CA) was observed when the testing velocity was over 3 m/s. The fracture interface shifted from a concrete layer to the interface of concrete-adhesive. This is because the dynamic increase factor (DIF) of concrete in tension increased faster than the epoxy resin and there was not enough time for the cracks to develop in the concrete under high loading rate. The fracture at the adhesive interface layer was also observed in some cases when the speed was over 3 m/s. As the tensile strength of the adhesive is stronger than other interfaces, fracture of the adhesive layer resulted in a greater debonding load. Compared with high strength concrete specimens, specimen C20 was more sensitive to strain rate due to the highest increment in bond strength and concrete damage after debonding. It is reasonable since the literature has shown that lower concrete strength is more sensitive to strain rate (75). As shown in Figure 6-25, specimen C20-8-3 experienced significant damage due to the pull-out of coarse aggregates and fracture of mortar. The observed fracture propagated along with the aggregate-to-mortar interface. This is due to the weakest interfacial transition zone (ITZ) caused by the high ratio of aggregates and a low ratio of cement used in the concrete mixture for C20. For the specimens with higher concrete strength, the damage of concrete was marginal at the dynamic testing of 8 m/s and only a flake of mortar fractured with the detachment of BFRP sheets, which is evidenced in Figure 6-24.

6.2.3.2 Strain distribution

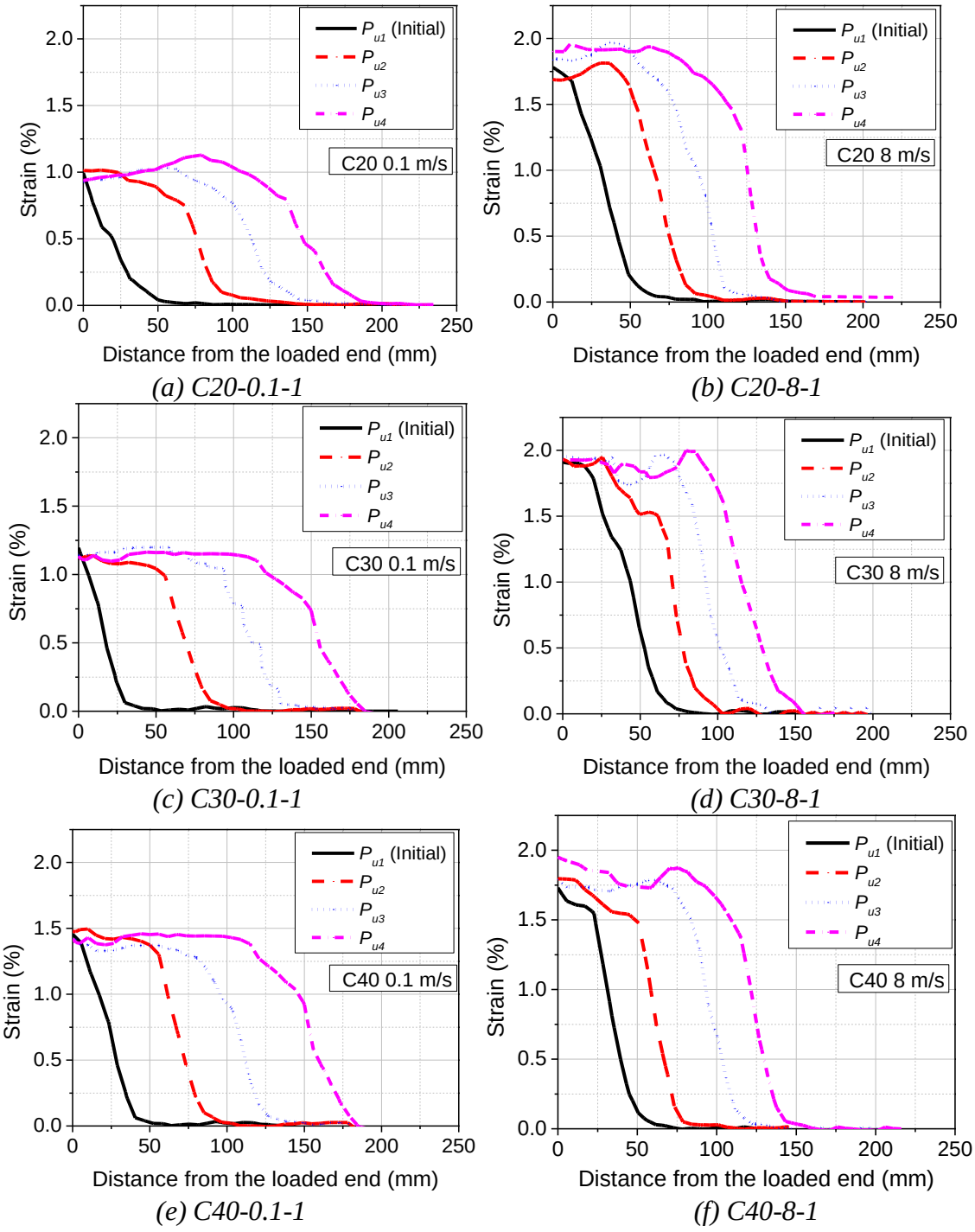

(a) C20-0.1-1 *(b) C20-8-1*

(c) C30-0.1-1 *(d) C30-8-1*

(e) C40-0.1-1 *(f) C40-8-1*

Figure 6-26. Typical strain profile

To quantify the dynamic interfacial bond-slip responses, the strain profiles along the centreline of the BFRP sheets at different loading levels are plotted in Figure 6-26. It is found that the debonding strain for all the tested specimens increased with strain rate irrespective of the concrete strength. After reaching the initial debonding load P_u, the ultimate strain was almost constant and maintained its "*Z*" shape when the debonding process propagated. To present the

strain distributions at different time instants, four loading stages after the initial debonding load P_u were selected and contrasted. Different from the specimens with a low concrete strength, specimen C40 showed the highest ultimate debonding strain when the testing speed was less than 3 m/s. This is because higher concrete strength resulted in the stronger interface and larger deformation of BFRP sheets to resist higher interfacial bond strength. However, when the testing velocity was over 3 m/s, the debonding strain showed an insignificant difference for specimens with different strengths. This is because the debonding strain was governed by the response of the interface rather than concrete. Therefore, the concrete strength did not considerably affect the debonding strain. Instead, the epoxy strength governed the fracture process and thus the debonding strain. All the specimens in this section used the same epoxy resin so that similar debonding strain was expected if the failure occurred at the interface.

6.2.3.3 Experimental bond-slip curves

The typical shear stress and slip curves are plotted in Figure 6-27. To obtain accurate and reliable results, five different loading stages within the plateau region of the load-slip curves after the initial debonding stage were selected to obtain the shear stress and slip curves, i.e., 60 mm, 90 mm, 120 mm, 150 mm and 180 mm, which refers to the available stress transfer length along the BFRP sheets. The obtained shear stress and the corresponding shear slip are the average values of five loading stages. All the tested specimens showed similar bond-slip profile with an ascending branch and a descending branch. The shear stress increased firstly with the applied load. After reaching the peak shear stress, the degradation of shear stress initiated until the final detachment. A relatively small shear slip developed in the ascending branch, which was caused by the elastic linear stage of the BFRP-to-concrete interface (87, 142). A larger shear slip was observed for the descending branch, which was resulted from the interfacial softening stage (197). The shear stress (τ) and shear slip (s) can be derived by using the equations as follows:

$$\tau(x) = E_f t_f \frac{d\varepsilon}{dx} \tag{6-11}$$

$$s(x) = \int \varepsilon dx \tag{6-12}$$

in which E_f is the elastic modulus of BFRP sheets, t_f is the thickness of a BFRP sheet, ε is the BFRP strain, $\tau(x)$ is the shear stress along the bonded area, and s(x) is the shear slip along the bonded area.

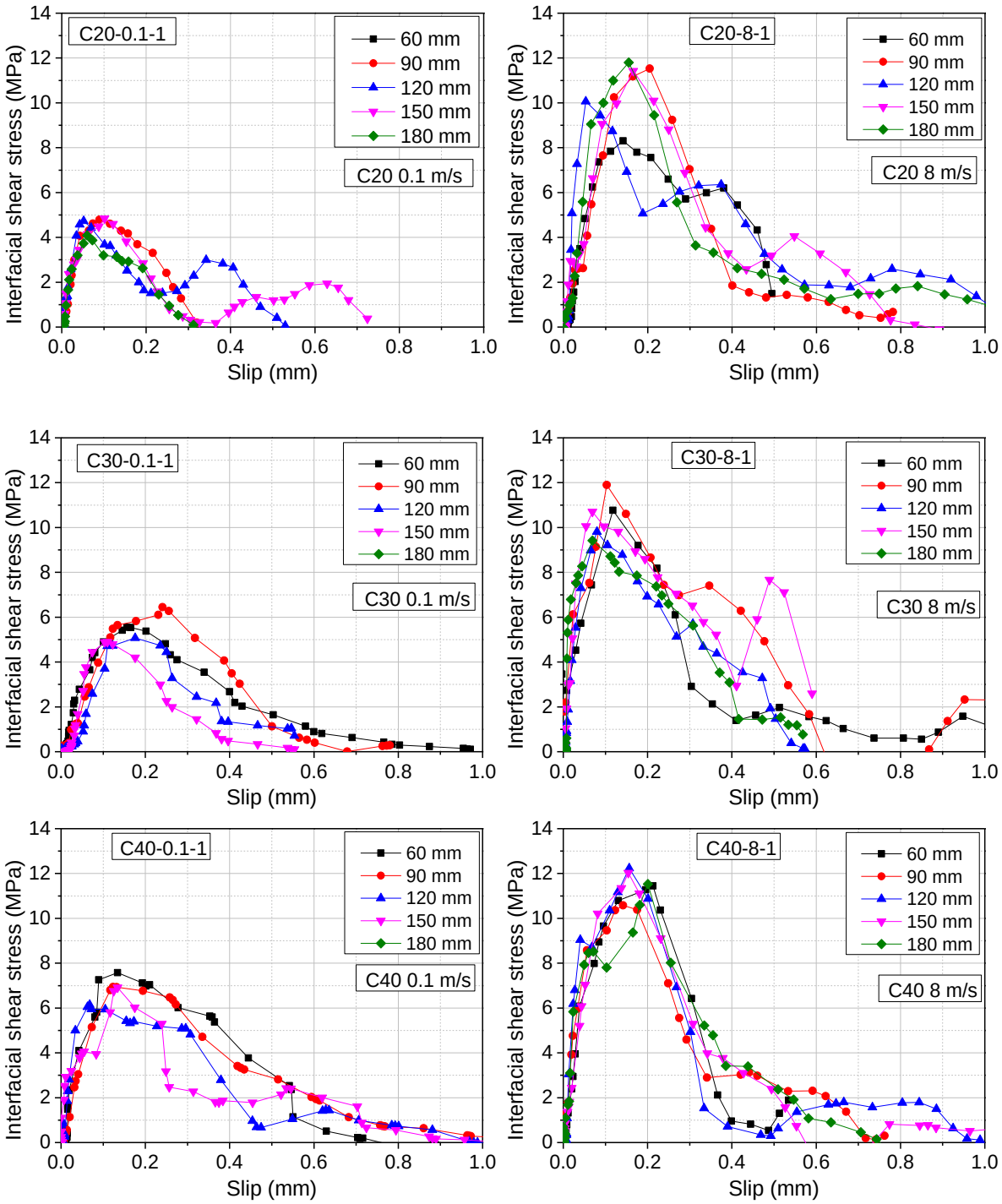

Figure 6-27. Typical shear stress and slip curves

It is observed that the peak shear stress increased significantly with strain rate, as shown in Figure 6-28. For the specimens with a lower concrete strength, specimen C20-QS showed the lowest interfacial shear stress, which was 1.77 MPa and the corresponding shear slip was 0.105

mm. The peak shear stress for specimen C30-QS and C40-QS was 3.13 MPa and 4.83 MPa and the corresponding slip was 0.121 mm and 0.142 mm, respectively, indicating that shear slip increased with the concrete strength. These observations are consistent with those reported in previous studies that the shear slip was proportional to the concrete strength (46, 142). The testing results show that the shear slip decreased with strain rate. The measured shear slips for specimens C20-8, C30-8, and C40-8 at the dynamic testing of 8 m/s were 0.106 mm, 0.106 mm, and 0.117 mm, respectively. Additionally, specimen C20 showed the highest increment in the peak shear stress, which increased by up to 453.35% at the dynamic testing of 8 m/s. However, specimen C40 only increased by up to 112.01% at the same testing speed. This indicates that the specimens with lower concrete strength showed greater strain rate sensitivity in interfacial shear stress while specimens with higher concrete strength exhibited less strain rate sensitivity and greater shear resistance. It is worth noting that the interfacial peak shear stress of specimens with different concrete strengths exhibited large variations but this variation became small at a high loading rate, i.e. 8 m/s. The reason for this phenomenon was due to the failure shifting from concrete-dominant to interface-dominant.

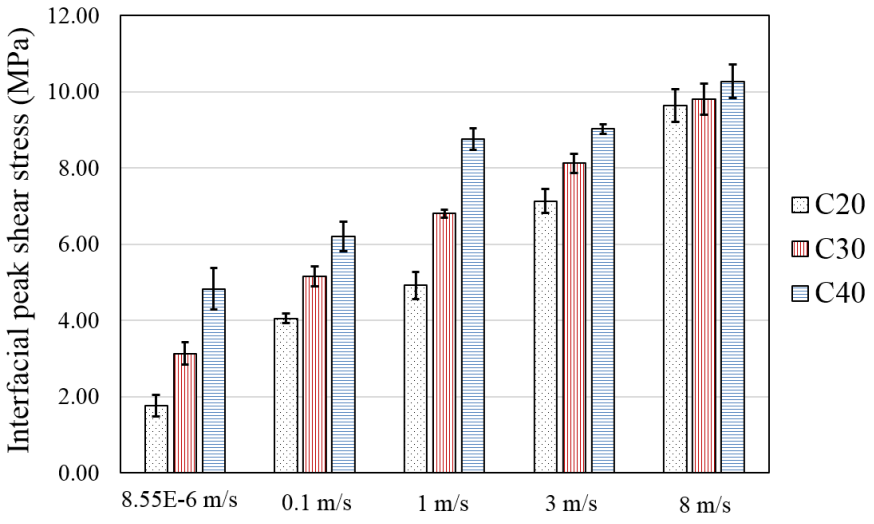

Figure 6-28. Comparison of interfacial shear stress

The enclosed area of the bond-slip curve represents the fracture energy G_f. It is observed that the interfacial fracture energy increased significantly with strain rate, especially for the specimens with low concrete strength. Figure 6-29 (a) plots the average result of each testing group. The interfacial fracture energy of specimen C20-QS was the lowest at 0.67 N/mm while the value for the specimen C40-QS was 1.59 N/mm, indicating that the specimens with higher concrete strength released greater energy during the debonding process. As the specimen with

the lowest concrete strength was more sensitive to strain rate, the interfacial fracture energy exhibited a higher increment. The interfacial fracture energy of specimen C20-8 raised by 423.63% when the loading speed was increased to 8 m/s. However, specimen C40-8 showed the lowest increment in fracture energy which was 206.96% at the highest loading speed, as shown in Figure 6-29 (b). Additionally, specimens C30 and C40 exhibited similar fracture energy under 8 m/s, indicating that the effect of strain rate on fracture energy was more significant than that of concrete strength when the loading speed was over 3 m/s. This is because of the shifted debonding failure from concrete to the concrete-epoxy interface at a relatively high strain rate due to the fact that the dynamic increase factor (DIF) of concrete in tension increased faster than the epoxy resin and there was insufficient time for the cracks to develop in concrete under high loading rate.

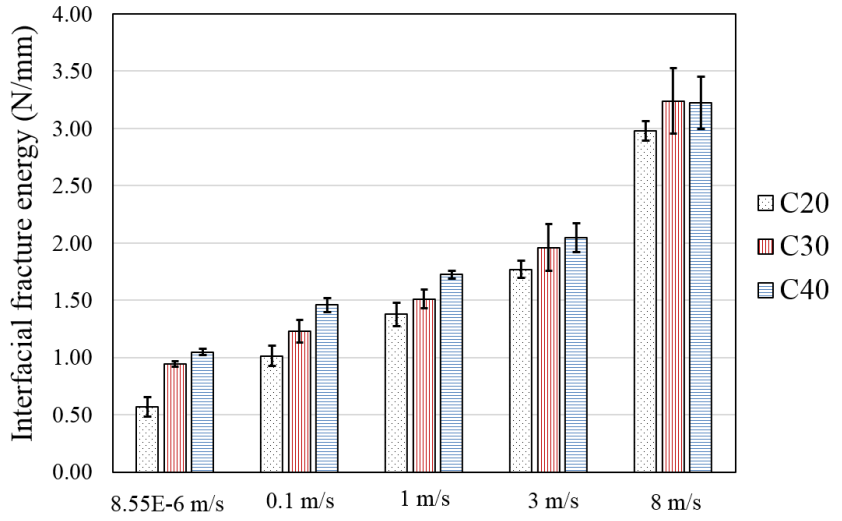

(a) Interfacial fracture energy vs. loading rate

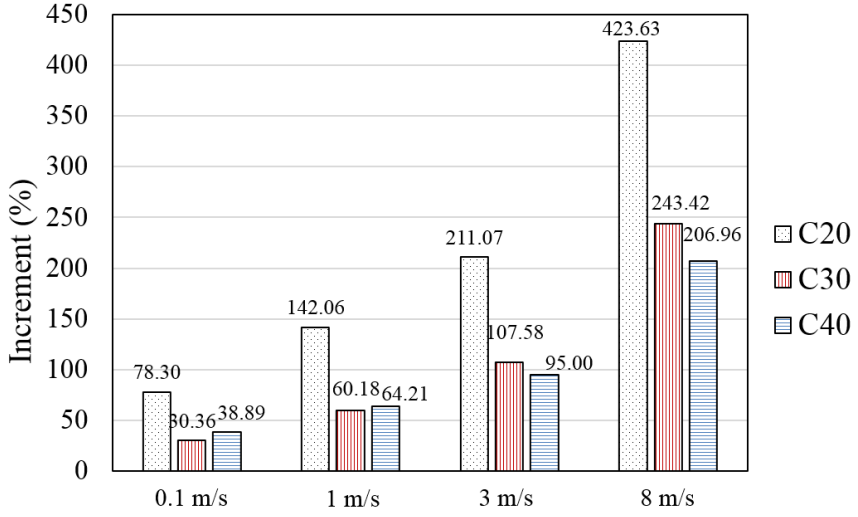

(b) Increment ratio of interfacial fracture energy

Figure 6-29. Test results of interfacial fracture energy

6.2.4 Analytical study of dynamic interfacial bond performance

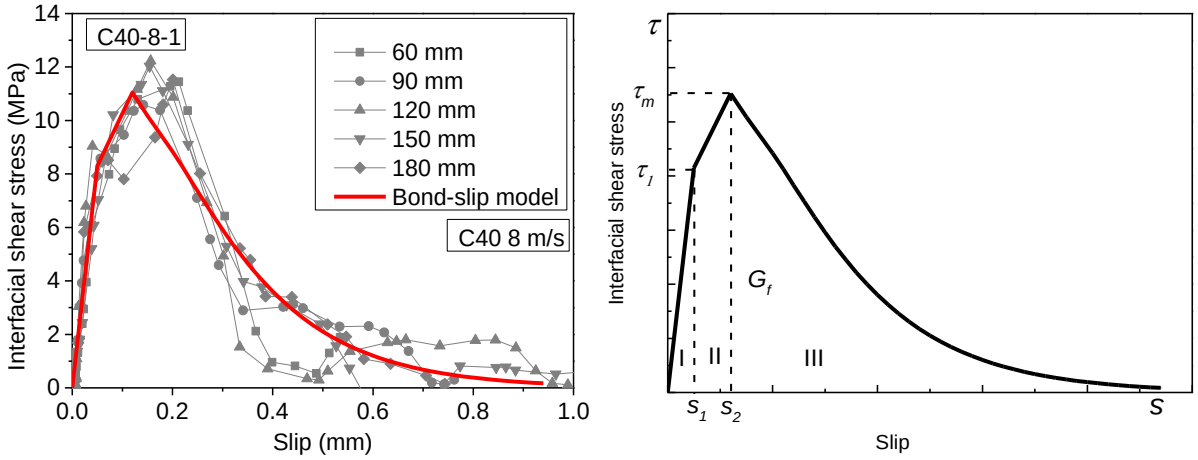

Figure 6-30. (L) Bond-slip curve of C40-8-1; (R) Simplified bond-slip law with hardening

Based on the shear stress-slip curves of the tested specimens under different loading speeds, an approximate triangle shape can be observed, as shown in Figure 6-27. For simplicity, a simplified bond-slip model is used to model the bond-slip relationship, as shown in Figure 6-30 (R). The simplified bond-slip law coincides with the experimental shear stress and slip curve. The difference from the previous bond-slip law is that the linear ascending stage is separated by a turning point, which represents the change of the slope of the bond-slip response and this stage is referred as the hardening stage (i.e. stage II) in the previous studies (85, 141).

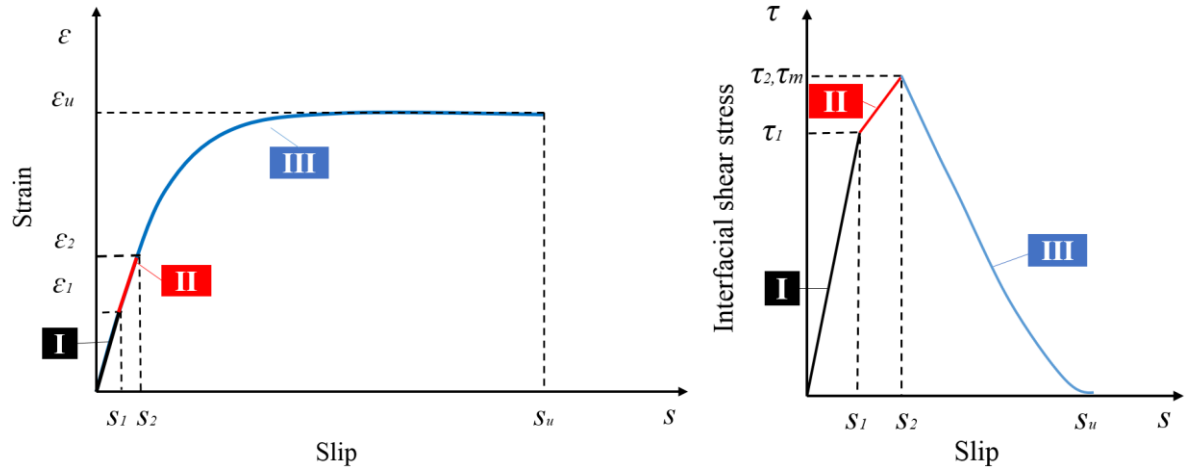

Figure 6-31. Determination of the bond-slip model

The simplified bond-slip law includes three stages (I, II, and III) including (I) linear-elastic stage when the shear slip increases to s_1; (II) linear hardening stage when the shear slip increased from s_1 to s_2 (85, 141); and (III) softening stage where the shear stress degrades

exponentially with the increased shear slip, as shown in Figure 6-31. The mathematical expressions for the simplified bond-slip model can be expressed as follows (85, 141):

$$\tau(s)=\begin{cases}\tau_1\left(\dfrac{s}{s_1}\right) & s\le s_1\\ \dfrac{\tau_2-\tau_1}{s_2-s_1}s+\dfrac{\tau_1 s_2}{s_2-s_1}-\dfrac{\tau_2 s_1}{s_2-s_1} & s_1<s\le s_2\\ \tau_m e^{-\omega(s-s_2)} & s_2<s\le s_u\end{cases} \tag{6-13}$$

in which τ is the interfacial shear stress, s is the shear slip, and ω is the factor determining the shape of the softening stage.

The bond-slip law is determined by some key parameters, i.e., τ_1, τ_2, τ_m, s_1, s_2, s_u, and ω. Meanwhile, the interfacial fracture energy G_f is the enclosed area of the bond-slip curve related to these parameters, which can be expressed by the following equation:

$$G_f=\int_0^{+\infty}\tau ds=\int_0^{s_1}\tau ds+\int_{s_1}^{s_2}\tau ds+\int_{s_u}^{+\infty}\tau ds \tag{6-14}$$

By integrating the shear stress and slip, G_f can be estimated as follows:

$$G_f=\frac{1}{2}\tau_1 s_1+\frac{1}{2}(\tau_1+\tau_2)(s_2-s_1)+\frac{\tau_m}{\omega} \tag{6-15}$$

in which, the coefficient ω can be expressed by:

$$\omega=\frac{\tau_m}{G_f-\dfrac{1}{2}\tau_1 s_1-\dfrac{1}{2}(\tau_1+\tau_2)(s_2-s_1)} \tag{6-16}$$

For the linear stage I in the strain-slip curve, strain ε_1 can be expressed as follows:

$$\varepsilon(s)=\frac{\varepsilon_1}{s_1}s \tag{6-17}$$

By considering $\varepsilon=\dfrac{ds}{dx}$ and $\tau(x)=E_f t_f\dfrac{d\varepsilon}{ds}\dfrac{ds}{dx}$, the function of the bond-slip in stage I can be expressed as follows (197):

$$\tau(s) = E_f t_f \left(\frac{\varepsilon_1}{s_1}\right)^2 s \tag{6-18}$$

By substituting $s=s_1$, the shear stress τ_1 in stage I can be calculated by:

$$\tau_1 = E_f t_f \frac{\varepsilon_1^{\,2}}{s_1} \tag{6-19}$$

The function of the bond-slip in stage II can be described by the following equation:

$$\tau(s) = \frac{\tau_2 - \tau_1}{s_2 - s_1} s + \frac{\tau_1 s_2}{s_2 - s_1} - \frac{\tau_2 s_1}{s_2 - s_1} \tag{6-20}$$

For the linear stage II in the strain-slip curve, the relationship between τ_1, τ_2, ε_1, and ε_2 can be obtained by the previous studies (85, 141):

$$s_1 = 0.5 s_2 \tag{6-21}$$

$$\tau_1 = 0.7 \tau_2 \tag{6-22}$$

Therefore, the coefficient ω can be written as:

$$\omega = \frac{\tau_m}{G_f - 0.55 \tau_2 s_2} \tag{6-23}$$

The elastic-hardening stage II and the nonlinear softening stage III in the strain-slip curve can be expressed by an exponential function to describe the relationship between strain and slip:

$$\varepsilon(s) = \varepsilon_u \left(1 - e^{-\omega s}\right) \tag{6-24}$$

in which $\varepsilon_u = \sqrt{\frac{2G_f}{E_f t_f}}$ (215).

All the parameters are determined by the interfacial fracture energy G_f. Therefore, an accurate analytical interfacial fracture energy prediction model is necessary.

6.2.4.1 Dynamic interfacial fracture energy

As fracture of concrete was observed varying with loading speeds, and the increased fracture energy is attributed to the increased concrete tensile strength. It has been demonstrated in the

previous studies that the interfacial fracture energy is correlated well with the width ratio β_w and tensile strength of concrete f_t (52, 96, 211). It is found that the interfacial shear stress not only exists in the bonded area of FRP-to-concrete interface but also in the surrounding unbonded concrete to resist the interfacial shear deformation, therefore the boundary effect should be taken into account in the bond-slip relationship (96). Compared with the results at the loading rate of 3 m/s, the results exceeding this loading rate showed different failure modes. Therefore, Equations (6-25) and (6-26) were proposed to obtain the dynamic interfacial fracture energy under different strain rates (56.68 s^{-1} corresponds to 1 m/s). It is noted that the fracture energy Gf proportional to $\sqrt{TDIF \cdot f_{t,s}}$ can give a better fit to test results and therefore this form was used in the following equations. To expand the scope of application of the proposed models, a total of 35 dynamic testing results of FRP-to-concrete joints were collected from the previous studies (41, 74). All the 35 collected data were used for model training and the parameter estimations were then tested on experimental results. Since the fracture of the adhesive layer was observed in some cases when the loading rate exceeded 3 m/s, the strain energy of the adhesive layer (i.e. $f_a^2/2E_a$) should be also incorporated into the proposed model.

$$G_{f,d} = \alpha_1 \beta_w^{\,2} \left(\frac{f_a^{\,2}}{2E_a} \right)^{\alpha_2} \sqrt{TDIF \cdot f_{t,s}} \quad \text{when} \quad 2.5\times10^{-5} s^{-1} < \dot{\varepsilon}_d \le 56.68 s^{-1} \qquad (6\text{-}25)$$

$$G_{f,d} = \alpha_3 \beta_w^{\,2} \left(\frac{f_a^{\,2}}{2E_a} \right)^{\alpha_2} \sqrt{TDIF \cdot f_{t,s}} \quad \text{when} \quad 56.68 s^{-1} < \dot{\varepsilon}_d \le 175.65 s^{-1} \qquad (6\text{-}26)$$

$$\beta_w = \sqrt{\frac{2 - b_f / b_c}{1 + b_f / b_c}} \qquad (6\text{-}27)$$

in which α_1, α_2 and α_3 are the coefficients to be obtained by the data collection, f_a is the tensile strength of adhesive, E_a refers to the elastic modulus of adhesive, b_c represents the width of the concrete substrate, and b_f refers to the width of BFRP sheet. The dynamic increase factor for concrete in tension (TDIF) (216) is adopted in the following equations:

$$TDIF = \begin{cases} f_{t,d} / f_{t,s} = 0.26\log(\dot{\varepsilon}) + 2.06 & \dot{\varepsilon}_d \le 1s^{-1} \\ f_{t,d} / f_{t,s} = 2\log(\dot{\varepsilon}) + 2.06 & \text{when } 1s^{-1} < \dot{\varepsilon}_d \le 2s^{-1} \\ f_{t,d} / f_{t,s} = 1.443\log(\dot{\varepsilon}) + 2.223 & 2s^{-1} < s \le 150s^{-1} \end{cases} \quad (6\text{-}28)$$

where $f_{t,d}$ is the dynamic tensile strength, $f_{t,s}$ is the static tensile strength and $\dot{\varepsilon}_d$ is the strain rate.

Table 6-7. Summary of data collection

Reference	Specimen ID	Adhesive			FRP			Strain rate (s^{-1})	*ft* (MPa)	$P_{u,exp}$ (kN)	τ_m (MPa)	G_f (N/mm)
		f_a (MPa)	E_a (GPa)	$f_a^2/2E_a$ (N/mm^2)	E_f (GPa)	t_f (mm)	b_f (mm)					
Shen et al. (41)	L200-D0-1	45.8	2.6	0.403	105	0.242	50	0.61E-3	2.62	11.40	2.95	1.02
	L200-D0-2	45.8	2.6	0.403	105	0.242	50	0.61E-3	2.62	10.80	3.59	0.92
	L200-D0-3	45.8	2.6	0.403	105	0.242	50	0.61E-3	2.62	13.60	-	1.45
	L200-D1-1	45.8	2.6	0.403	105	0.242	50	0.61E-2	3.89	15.00	4.64	1.39
	L200-D1-2	45.8	2.6	0.403	105	0.242	50	0.61E-2	3.89	13.30	5.00	1.23
	L200-D1-3	45.8	2.6	0.403	105	0.242	50	0.61E-2	3.89	12.50	3.89	1.02
	L200-D2-1	45.8	2.6	0.403	105	0.242	50	0.047	4.49	15.50	3.68	0.92
	L200-D2-2	45.8	2.6	0.403	105	0.242	50	0.047	4.49	14.50	5.37	1.46
	L200-D2-3	45.8	2.6	0.403	105	0.242	50	0.047	4.49	13.10	5.39	1.77
	L200-D3-1	45.8	2.6	0.403	105	0.242	50	0.63	5.26	16.20	5.95	1.39
	L200-D3-2	45.8	2.6	0.403	105	0.242	50	0.63	5.26	15.70	5.82	1.23
	L200-D3-3	45.8	2.6	0.403	105	0.242	50	0.63	5.26	15.60	5.49	1.89
Huo et al. (74)	C50-1-S-1	65.0	3.2	0.660	236	0.169	50	1E-5	2.85	13.60	4.05	0.64
	C50-1-S-2	65.0	3.2	0.660	236	0.169	50	1E-5	2.85	11.50	3.50	0.61
	C50-2-S-1	65.0	3.2	0.660	236	0.338	50	1E-5	2.85	18.00	3.28	0.64
	C50-2-S-2	65.0	3.2	0.660	236	0.338	50	1E-5	2.85	14.20	4.25	0.63
	C80-2-S-1	65.0	3.2	0.660	236	0.338	80	1E-5	2.85	17.50	4.74	0.70
	C80-2-S-2	65.0	3.2	0.660	236	0.338	80	1E-5	2.85	18.40	3.47	0.52
	C50-1-D200-1	65.0	3.2	0.660	236	0.169	50	3.12	8.38	15.10	5.40	1.43
	C50-1-D200-2	65.0	3.2	0.660	236	0.169	50	2.67	8.10	17.80	6.93	1.72
	C50-1-D200-3	65.0	3.2	0.660	236	0.169	50	4.56	9.06	16.90	6.02	1.71
	C50-1-D400-1	65.0	3.2	0.660	236	0.169	50	4.10	8.87	24.40	6.39	2.22
	C50-1-D400-2	65.0	3.2	0.660	236	0.169	50	4.90	9.19	18.00	5.47	1.39
	C50-1-D400-3	65.0	3.2	0.660	236	0.169	50	4.70	9.11	16.80	6.45	1.53
	C50-2-D200-1	65.0	3.2	0.660	236	0.169	50	2.09	7.66	20.00	5.58	1.20
	C50-2-D200-2	65.0	3.2	0.660	236	0.169	50	2.05	7.63	21.30	7.33	1.38
	C50-2-D200-3	65.0	3.2	0.660	236	0.169	50	2.62	8.07	27.20	5.22	0.81
	C50-2-D400-1	65.0	3.2	0.660	236	0.338	50	2.63	8.07	24.60	5.49	1.31
	C50-2-D400-2	65.0	3.2	0.660	236	0.338	50	3.13	8.39	33.10	6.21	1.94
	C50-2-D400-3	65.0	3.2	0.660	236	0.338	50	2.02	7.60	29.00	5.47	0.62
	C50-2-D600-2	65.0	3.2	0.660	236	0.338	50	3.59	8.63	24.90	6.56	1.79
	C50-2-D600-2	65.0	3.2	0.660	236	0.338	50	3.65	8.66	24.40	6.20	1.10
	C80-2-D400-1	65.0	3.2	0.660	236	0.338	80	2.55	8.02	27.20	6.48	1.80
	C80-2-D400-1	65.0	3.2	0.660	236	0.338	80	2.92	8.26	27.90	8.13	1.78
	C80-2-D400-1	65.0	3.2	0.660	236	0.338	80	2.10	7.67	21.10	5.68	0.96

Note: $f_t = 0.53\sqrt{f_c}$ (MPa) (89).

Figure 6-32 shows the relationship between the interfacial fracture energy (G_f) in the *Z* direction and concrete dynamic tensile strength ($f_{t,d}$) in the *Y* direction, adhesive strain energy ($f_a^2/2E_a$) in the *X* direction. After regression analyses, the best-fit coefficients of α_1, α_2 and α_3

are given as 0.53, 0.24 and 0.57 in Equations (6-29) and (6-30), respectively. The width β_w can be obtained by Equation (6-27). Therefore, the expression of the dynamic G_f can be expressed as follows:

$$G_{f,d} = 0.53\beta_w^{\,2}\left(\frac{f_a^{\,2}}{2E_a}\right)^{0.24}\sqrt{f_{t,d}} \quad \text{when} \quad 2.5\times10^{-5}s^{-1} < \dot{\varepsilon}_d \le 56.68s^{-1} \tag{6-29}$$

$$G_{f,d} = 0.57\beta_w^{\,2}\left(\frac{f_a^{\,2}}{2E_a}\right)^{0.24}\sqrt{f_{t,d}} \quad \text{when} \quad 56.68s^{-1} < \dot{\varepsilon}_d \le 175.65s^{-1} \tag{6-30}$$

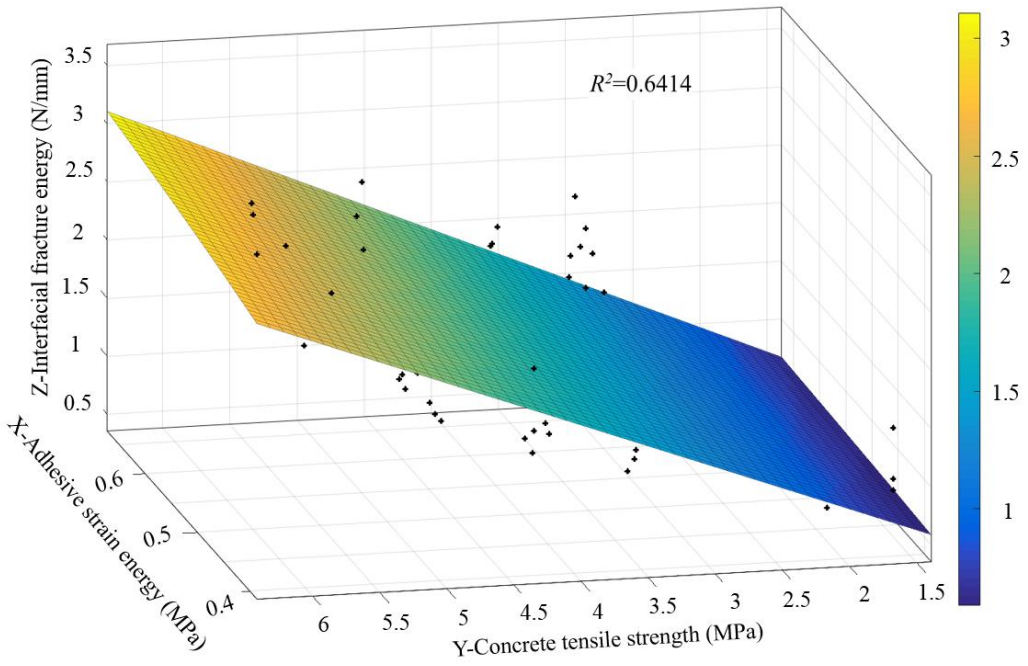

Figure 6-32. Best-fit coefficients for the interfacial fracture energy

Figure 6-33 illustrates the contrast between the predicted and experimental fracture energy. It can be seen that the analytical predictions are consistent with the experimental data. The mean ratio between the predicted and experimental results is 1.13 and the corresponding coefficient of variation (COV) is 0.19.

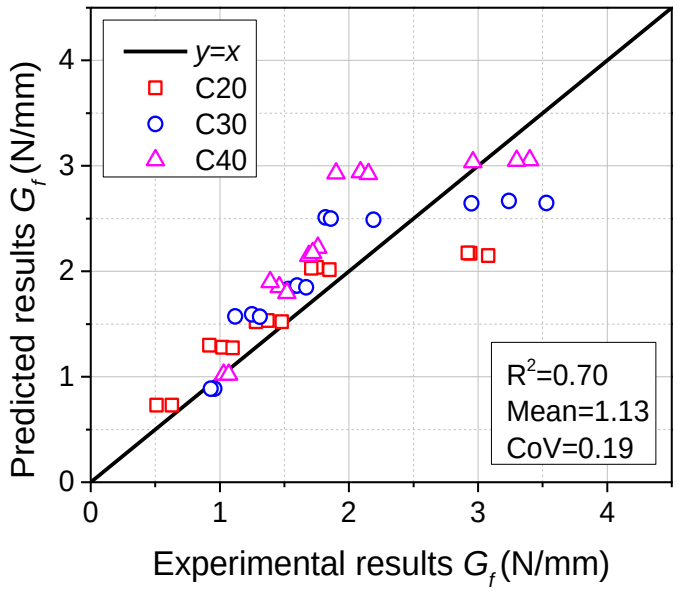

Figure 6-33. Experimental interfacial fracture energy vs predicted results

6.2.4.2 Dynamic ultimate debonding strain

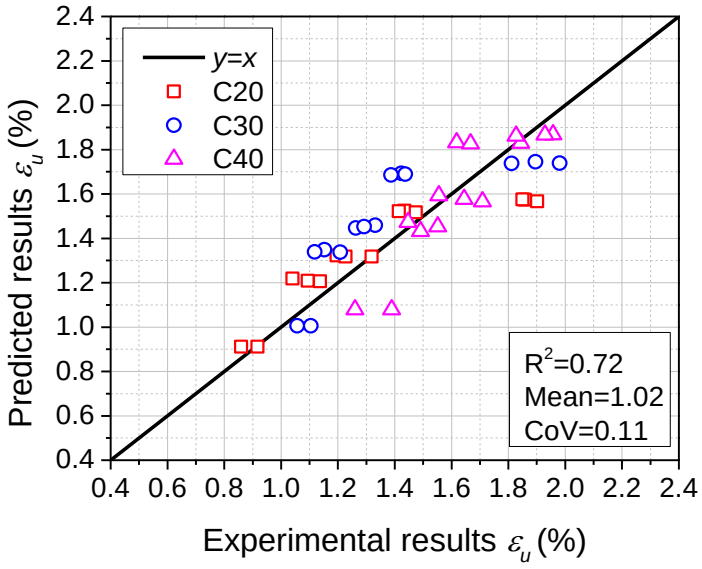

Figure 6-34. Experimental debonding strain vs predicted results

Previous studies (215, 217-219) have proposed some ultimate debonding strain models for structural design purpose based on quasi-static tests, which is used to simulate the FRP debonding caused by the intermediate crack (IC). However, a dynamic debonding strain model has not been proposed yet in the literature. Therefore, an empirical dynamic debonding strain model by incorporating the strain rate is proposed herein. A model proposed by Maruyama and Ueda (215) is adopted here to predict the dynamic debonding strain due to this model

incorporating both the FRP stiffness interfacial fracture energy and, which can be expressed as follows:

$$\varepsilon_u = \sqrt{\frac{2G_f}{E_f t_f}} \tag{6-31}$$

in which ε_u is the ultimate debonding strain, G_f is the interfacial fracture energy, and $E_f t_f$ is FRP stiffness. By substituting the dynamic fracture energy $G_{f,d}$ given in Equations (6-30) and (6-31) into Equation (6-32), the dynamic debonding strain $\varepsilon_{u,d}$ can be obtained and the comparison between the predicted and testing data is plotted in Figure 6-34. It is clear that the predicted results show good agreement with the testing data due to the mean value of 1.02 and the coefficient of variation (COV) of 0.11.

6.2.4.3 Dynamic bond stress and slip

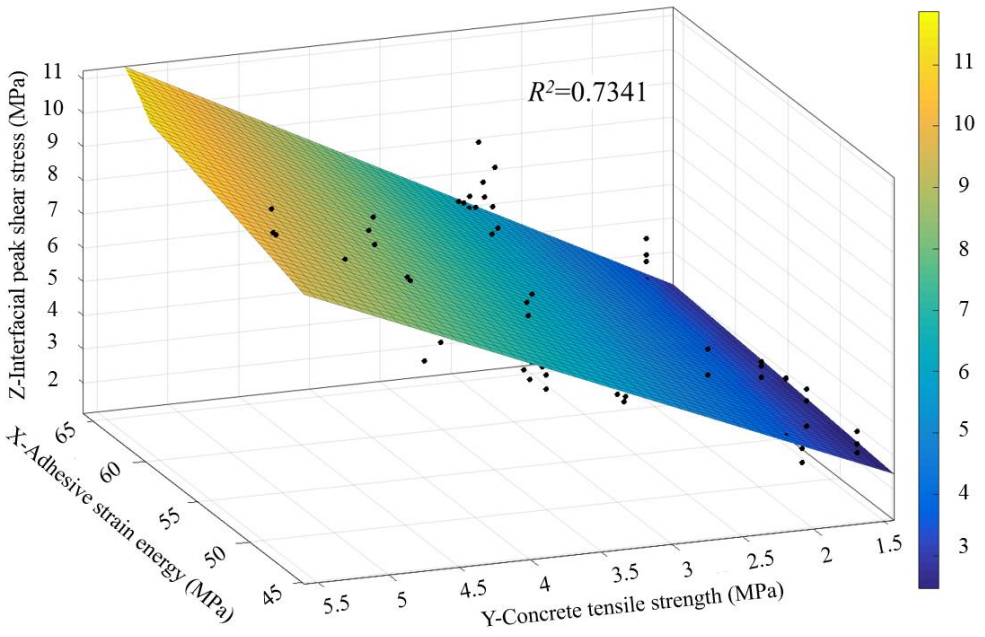

Figure 6-35. Best-fit coefficients for the peak shear stress

As the fracture of the adhesive layer was observed in some cases when the testing velocity was over 3 m/s, the tensile strength of adhesive (f_a) should be one of the factors determining dynamic shear stress of the BFRP-concrete interface. Previous studies (87) have demonstrated that the concrete tensile strength (f_t) width ratio (β_w) and are the key factors in determining the peak shear stress. To expand the scope of application of the proposed dynamic peak shear stress model, the previous test data listed in Table 6-7 are also selected to conduct the regression

analyses. Therefore, three parameters including f_a, β_w, and f_t are incorporated into the following equation to obtain the dynamic peak shear stress $\tau_{m,d}$:

$$\tau_{m,d} = \alpha_4 (f_a)^{\alpha_5} \beta_w \sqrt{TDIF \cdot f_{t,s}} \tag{6-32}$$

in which $\tau_{m,d}$ is the dynamic peak shear stress, *TDIF* is the dynamic increases factor for concrete in tension which can be obtained from Equation (6-28), and $f_{t,s}$ refers to the static concrete tensile strength. After regression analyses, the best-fit coefficients of α_4 and α_5 are 0.23 and 0.53, respectively. Figure 6-35 shows the relationship between the peak shear stress in the *Z* direction with the concrete tensile strength in the *Y* direction and the adhesive strain energy in the *X* direction. Therefore, the dynamic peak shear stress can be expressed by the following equation:

$$\tau_{m,d} = 0.23(f_a)^{0.53} \beta_w \sqrt{TDIF \cdot f_{t,s}} \tag{6-33}$$

Figure 6-36 illustrates the comparison between the predicted and experimental results. It is found that the analytical predictions are consistent with the testing results. The mean ratio between the analytical predictions and the testing data is 1.11, and the corresponding coefficient of variation (COV) is 0.22.

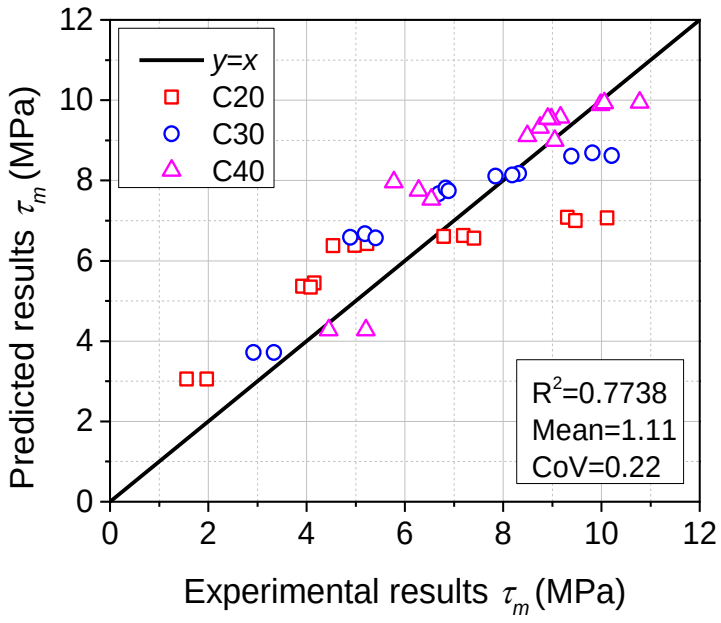

Figure 6-36. Experimental peak shear stress (τ_m) vs predicted results

According to the testing data, the peak shear slip s_2 at the peak shear stress τ_m decreases with strain rate. However, the adopted peak shear slip s_2 in this study is set as a constant of 0.115

mm which is the average of all the tested specimens (i.e., C20, C30 and C40) due to the scattered data, as shown in Figure 6-37.

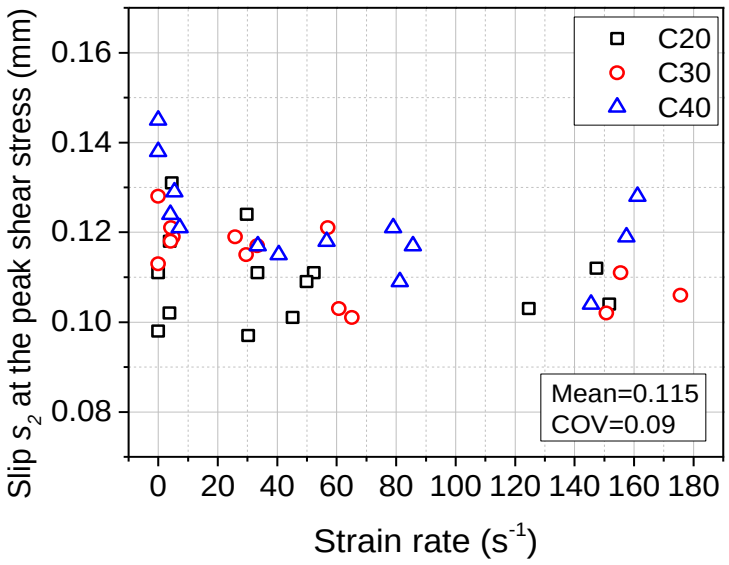

Figure 6-37. Shear slip s_2 vs strain rate

6.2.4.4 Validation of dynamic bond-slip model

Figure 6-38 illustrates the comparison between the predicted and experimental strain-slip and bond-slip curves. To demonstrate the reliability of the proposed model, at least four points along the bonded region were selected to track the strain and slip distributions. The distance of 60 mm, 90 mm, 120 mm, 150 mm, and 180 mm shown in the legend refers to the range of strain distribution at five loading stages after the initial debonding stage. The comparison shows that the proposed bond-slip model is in good agreement with the experimental data.

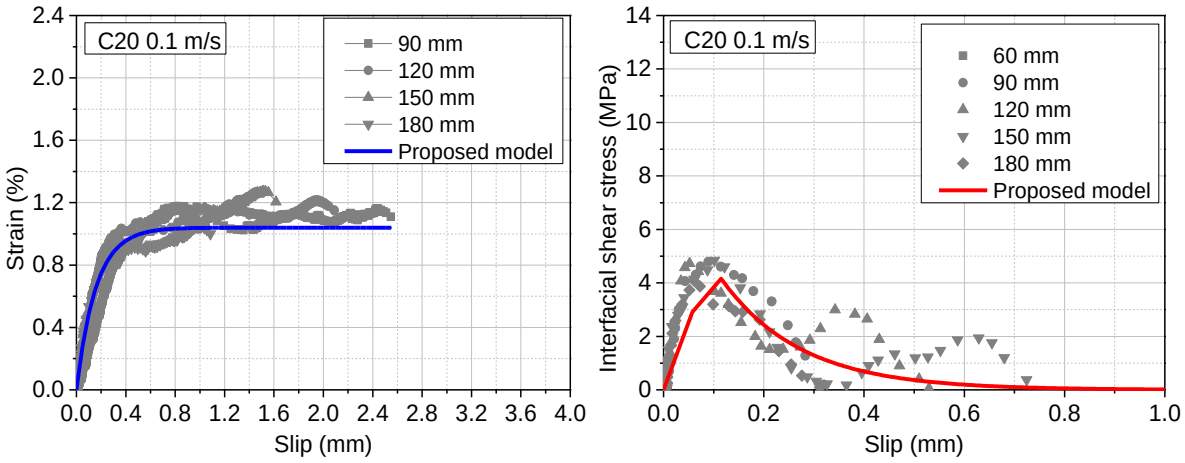

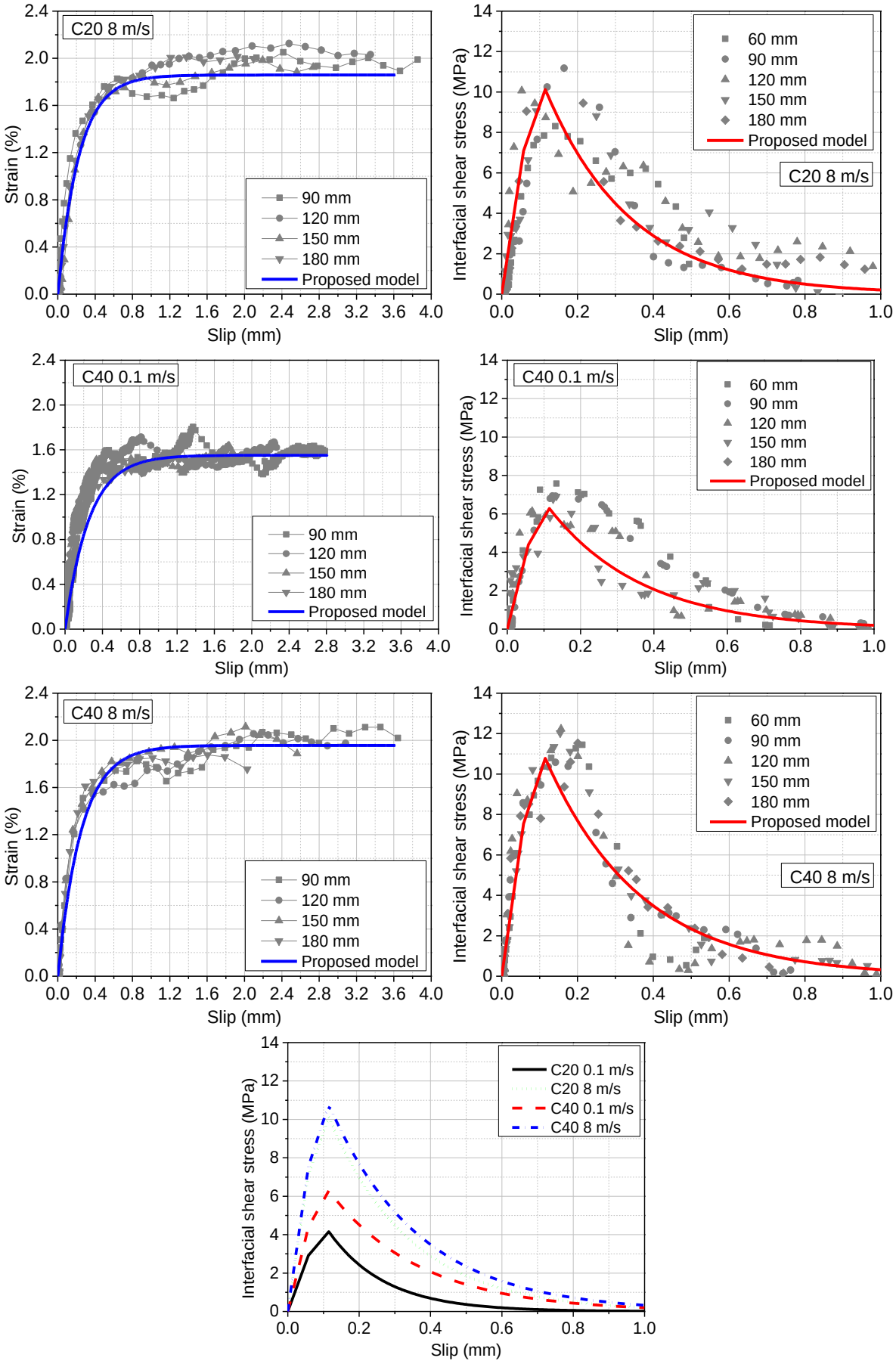

Figure 6-38. Analytical and experimental strain-slip curves and bond-slip curves

Numerous studies stated that some parameters (i.e. debonding load, shear stress or strain distribution) related to bond behaviour can be estimated by the proposed bond-slip models (45, 87, 95). Among these parameters, the debonding load and the strain distributions can be directly measured in the test program. Therefore, the validation of the analytical bond-slip model can be carried out via the debonding load and strain distribution. A widely accepted formula for calculating the debonding load can be expressed as follows (35, 46, 154, 220):

$$P_u = b_f \sqrt{2E_f t_f G_f} \tag{6-34}$$

By substituting the dynamic interfacial fracture energy $G_{f,d}$ into Equation (6-34), the dynamic debonding load can be obtained accordingly. Figure 6-39 shows the contrast between the predicted and experimental results. It is observed that the predicted debonding load matches well with the testing data. The mean ratio of the predicted and test results is 1.04 and the corresponding coefficient of variation (COV) is 0.10.

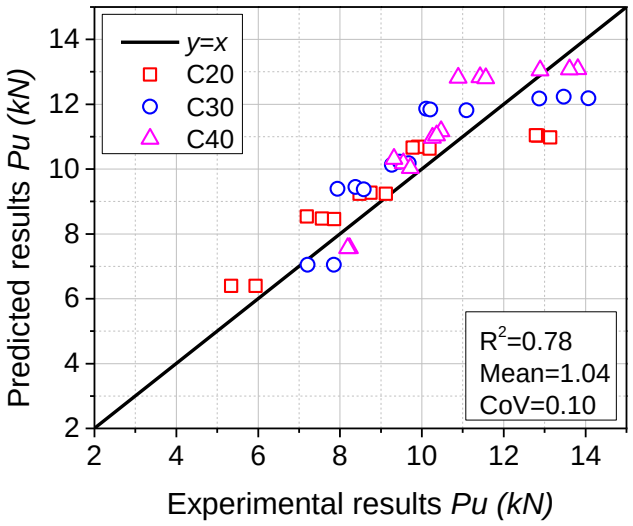

Figure 6-39. Experimental debonding load (P_u) vs predicted results

6.2.5 Section summary

This section investigates the effect of concrete strength on the dynamic interfacial bond performance between BFRP and concrete at various strain rates (from $2.50E^{-5}$ s^{-1} to 175.65 s^{-1}). The following conclusions can be drawn:

1. The quasi-static results show that the shear resistance increases with the concrete strength. The interfacial shear resistance increases with the loading rate, and the loading or strain

rate sensitivity is concrete strength dependent, specimens made of low-strength concrete is more sensitive to strain rate than those made of higher-strength concrete.

2. A mixed failure mode is observed in the dynamic tests. The interfacial fracture occurs mainly in the concrete layer when the loading rate is less than 3 m/s, but occurs in the concrete-adhesive interface when the loading rate is higher than 3 m/s. When failure occurs in the interface the concrete strength has an insignificant effect on the interlayer bonding performance.
3. Increased strain rate causes the enhancement on the dynamic bond strength. The specimen with the lowest concrete strength experiences the highest strain rate sensitivity with the largest increment ratio of the debonding load. Enhancement of up to 129.14% is observed for the specimens with concrete strength of about 20 MPa while the increment ratio of 63.66% is observed for the ones with concrete strength of about 40 MPa.
4. The interfacial fracture energy shows a remarkable increment with the strain rate, especially for the specimens with low concrete strength. Increment ratios of up to 423.63%, 243.42, and 206.96% are observed for specimens made of C20, C30, and C40 concrete, respectively.
5. The proposed bond-slip model by incorporating the dynamic increase factor of concrete in tension (TDIF) yields good predictions as compared with the testing data.

6.3 Effect of adding short steel fibres

The effect of adding steel fibres on the static interfacial bond between FRP and concrete has been investigated in chapter 4.2. This section is aimed to investigate the effect of adding short steel fibre on dynamic interfacial bond behaviour between basalt fibre (BFRP) sheets and SFRC. Concrete prisms are made of short steel fibres with three volumetric fractions (i.e. V_f = 0.5%, 1.0%, and 1.5%) to improve the tensile strengths. To achieve different strain rates, the loading velocities varies from 8.33E-6 m/s, 0.1 m/s, 1 m/s, 3 m/s, to 8 m/s. Based on the testing data, an empirical bond-slip model, incorporating the volumetric fraction of steel fibre and strain rate, is established for FRP-strengthened SFRC structures.

The related work in this section has been published in Composites Part B: Engineering.

Yuan C, Chen W, Pham TM, Hao H, Cui J, Shi Y. Strain Rate Effect on Interfacial Bond Behaviour between BFRP Sheets and Steel Fibre Reinforced Concrete. Composites Part B: Engineering. 2019:107032. DOI: doi.org/10.1016/j.compositesb.2019.107032

6.3.1 Experimental program

6.3.1.1 Material properties

Concrete prisms with a dimension of 150 x 150 x 300 mm were prepared for single-lap shear tests. The 28-day mechanical properties of concrete including compressive and tensile strengths are given in Table 6-8. Four volumetric fractions of steel fibres (i.e. 0%, 0.5%, 1.0% and 1.5%) were used for the concrete with the design grade of 30 MPa. The short steel fibres with the fibre-reinforcing index ($V_f L_f/\phi_f$) in the range of 0 to 1.25 were used in the experimental program. The Young's modulus, tensile strength, and density of steel fibres provided by the supplier are 200 GPa, 2.5 GPa, and 7,800 kg/m^3, respectively. For the material properties of BFRP sheet and epoxy resin, please refer to chapter 3.2.1.

Table 6-8. Mechanical properties of SFRC

Specimen ID	**Volume fraction V_f (%)**	**Fibre-reinforcing index ($V_f L_f / \phi_f$)**	**Compressive strength f_c' (MPa)**	**Splitting tensile strength f_t (MPa)**
PC-1	0	0	29.48	2.71
PC-2			30.18	2.98
PC-3			28.74	2.86
Mean			29.47 (COV=0.02)	2.85 (COV=0.05)
SFRC-0.5-1	0.50	0.417	31.33	2.97
SFRC-0.5-2			33.05	3.16
SFRC-0.5-3			32.90	3.21
Mean			32.43 (COV=0.03)	3.11 (COV=0.04)
SFRC-1.0-1	1.00	0.833	32.59	3.33
SFRC-1.0-2			34.09	3.58
SFRC-1.0-3			33.48	3.41
Mean			33.39 (COV=0.02)	3.44 (COV=0.04)
SFRC-1.5-1	1.50	1.250	33.72	3.93
SFRC-1.5-2			34.24	3.86
SFRC-1.5-3			32.39	3.57
Mean			33.45 (COV=0.03)	3.79 (COV=0.05)

6.3.1.2 Test matrix

For static testing machine, test set-up, and details of tracking points, please refer to Chapter 5.1.1. A total of 56 single-lap shear specimens were prepared for this section. Table 6-9 presents the specimen details and experimental results of the static and dynamic tests. The single-lap shear specimen ID was named as "*QSX-n"* and*" DX-m-n*". "*QSX* or *DX*" refers to the quasi-static (QS) or dynamic (D) single-lap shear tests with steel fibre volumetric fraction of *X*%. The letter "*m*" stands for the dynamic loading velocity. The letter "*n*" means the specimen number.

Table 6-9. Specimen details and experimental results

Specimen ID	Volume fraction V_f (%)	RI $(V_f L_f/\phi_f)$	Loading velocity (m/s)	Strain rate (s^{-1})	Pu (kN)	ε_m (%)	τ_m (MPa)	s_o (mm)	G_f (N/mm)	Failure mode
QS0-1	0	0	8.33E-6	2.50E-05	7.87	1.10	2.2	0.131	1.10	C
QS0-2	0	0	8.33E-6	2.50E-05	6.93	0.99	2.11	0.146	0.86	C
QS0.5-1	0.5	0.417	8.33E-6	2.50E-05	8.09	1.09	2.79	0.138	1.17	C
QS0.5-2	0.5	0.417	8.33E-6	2.50E-05	8.11	1.12	2.57	0.145	1.17	C
QS1-1	1.0	0.833	8.33E-6	2.50E-05	8.12	1.14	2.68	0.143	1.18	C
QS1-2	1.0	0.833	8.33E-6	2.50E-05	8.36	1.17	3.02	0.137	1.25	C
QS1.5-1	1.5	1.250	8.33E-6	2.50E-05	8.26	1.17	3.05	0.139	1.22	C
QS1.5-2	1.5	1.250	8.33E-6	2.50E-05	9.19	1.19	3.45	0.147	1.51	C
D0-0.1-1	0	0	0.1	4.51	8.07	1.18	3.25	0.13	1.16	C
D0-0.1-2	0	0	0.1	4.31	7.88	1.09	2.95	0.141	1.11	C
D0-0.1-3	0	0	0.1	4.21	7.67	1.08	2.68	0.135	1.05	C
D0-1-1	0	0	1.0	25.9	8.34	1.45	4.81	0.132	1.24	C
D0-1-2	0	0	1.0	-	-	-	-	-	-	-
D0-1-3	0	0	1.0	29.56	9.72	1.48	4.2	0.128	1.69	C
D0-3-1	0	0	3.0	65.12	10.51	1.65	5.34	0.124	1.97	C
D0-3-2	0	0	3.0	-	-	-	-	-	-	-
D0-3-3	0	0	3.0	60.75	11.18	1.69	6.31	0.121	2.23	C/CE
D0-8-1	0	0	8.0	173.55	12.01	1.82	9.44	0.107	2.57	C/CE
D0-8-2	0	0	8.0	155.55	11.89	1.78	9.05	0.098	2.52	C/CE
D0-8-3	0	0	8.0	150.75	13.5	1.83	9.82	0.112	3.25	C/CE
D0.5-0.1-1	0.5	0.417	0.1	2.11	9.14	1.44	4.67	0.135	1.49	C
D0.5-0.1-2	0.5	0.417	0.1	2.52	8.79	1.27	4.07	0.112	1.38	C
D0.5-0.1-3	0.5	0.417	0.1	1.62	8.34	1.20	4.16	0.153	1.24	C
D0.5-1-1	0.5	0.417	1.0	13.83	8.91	1.49	4.58	0.172	1.42	C
D0.5-1-2	0.5	0.417	1.0	16.06	9.53	1.51	5.73	0.111	1.62	C
D0.5-1-3	0.5	0.417	1.0	-	-	-	-	-	-	-
D0.5-3-1	0.5	0.417	3.0	76.55	11.34	1.70	7.75	0.167	2.29	C/CE
D0.5-3-2	0.5	0.417	3.0	64.93	10.42	1.71	8.49	0.166	1.94	C
D0.5-3-3	0.5	0.417	3.0	68.81	11.89	1.69	8.14	0.126	2.52	C/CE
D0.5-8-1	0.5	0.417	8.0	134.91	12.13	1.80	9.95	0.139	2.62	C/CE
D0.5-8-2	0.5	0.417	8.0	131.73	12.41	1.84	8.97	0.144	2.75	C/CE
D0.5-8-3	0.5	0.417	8.0	148.87	12.53	1.93	9.77	0.135	2.80	C/CE
D1-0.1-1	1.0	0.833	0.1	2.75	9.9	1.35	6.72	0.138	1.75	C
D1-0.1-2	1.0	0.833	0.1	2.07	9.12	1.34	5.47	0.129	1.48	C
D1-0.1-3	1.0	0.833	0.1	4.17	8.07	1.29	4.65	0.124	1.16	C
D1-1-1	1.0	0.833	1.0	28.09	9.32	1.46	6.35	0.125	1.55	C
D1-1-2	1.0	0.833	1.0	15.38	9.61	1.51	6.69	0.14	1.65	C
D1-1-3	1.0	0.833	1.0	27.93	9.87	1.53	7.23	0.146	1.74	C

D1-3-1	1.0	0.833	3.0	41.8	9.89	1.70	9.14	0.112	1.74	C
D1-3-2	1.0	0.833	3.0	43.95	12.25	1.72	8.16	0.126	2.68	C/CE
D1-3-3	1.0	0.833	3.0	61.49	11.69	1.71	8.84	0.13	2.44	C
D1-8-1	1.0	0.833	8.0	164.12	12.43	1.79	8.79	0.107	2.76	C/CE
D1-8-2	1.0	0.833	8.0	130.13	13.39	1.87	8.58	0.112	3.20	C/CE
D1-8-3	1.0	0.833	8.0	137.74	12.66	1.78	9.12	0.124	2.86	C/CE
D1.5-0.1-1	1.5	1.250	0.1	2.09	9.46	1.44	6.4	0.136	1.60	C
D1.5-0.1-2	1.5	1.250	0.1	2.16	9.49	1.45	5.98	0.12	1.61	C
D1.5-0.1-3	1.5	1.250	0.1	1.61	8.25	1.20	5.17	0.139	1.21	C
D1.5-1-1	1.5	1.250	1.0	29.44	12.01	1.63	8.85	0.141	2.57	C
D1.5-1-2	1.5	1.250	1.0	16.29	11.39	1.60	7.61	0.131	2.31	C
D1.5-1-3	1.5	1.250	1.0	23.03	11.25	1.51	8.09	0.132	2.26	C
D1.5-3-1	1.5	1.250	3.0	49.83	11.33	1.72	9.83	0.109	2.29	C
D1.5-3-2	1.5	1.250	3.0	38.21	11.66	1.73	9.78	0.11	2.43	C/CE
D1.5-3-3	1.5	1.250	3.0	42.28	12.86	1.78	9.98	0.117	2.95	C/CE
D1.5-8-1	1.5	1.250	8.0	167.54	13.3	1.97	8.58	0.102	3.16	C/CE
D1.5-8-2	1.5	1.250	8.0	129.46	12.97	1.87	8.76	0.112	3.00	C/CE
D1.5-8-3	1.5	1.250	8.0	160.61	12.32	1.80	9.34	0.108	2.71	C/CE

Note: RI represents the fibre-reinforcing index as indicated in Figure 1; *C* means debonding in the concrete layer; *CE* is the interface debonding between concrete and epoxy; and "-" means unavailable data.

6.3.2 Experimental results and discussions

6.3.2.1 Failure modes and debonding load

Debonding of BFRP sheets associated with concrete debris was observed in all the tested specimens under both quasi-static and dynamic loads. For all the test specimens, the debonding location changed from concrete layers to the interface of concrete-epoxy with the increase of loading rates. During the process of debonding, the debris of coarse aggregates, mortar and steel fibres with the detachment of FRP sheets can also be observed, as shown in Figure 6-40 (a), (b), and (c). Additionally, with the volumetric fraction of steel fibres increasing, more steel fibres were pulled out from the matrix. The typical debonding failure modes of the tested specimens are shown in Figure 6-40 (d) and (e). It is observed that the additional steel fibres had a marginal effect on the debonding mechanism for the BFRP-SFRC interface. However, the debonding mechanism changed with the debonding location from the concrete layer (*C*) to the interface between concrete and epoxy (*CE*) with the loading rate increasing, as shown in Figure 6-40 (d) and (e). This might be because the tensile strength of FRC concrete is enhanced significantly with the rising strain rate while the strain rate has a marginal effect on the strength of epoxy resin (221, 222). At a low loading rate, the specimen has enough time to initiate the internal defects and develop the cracks through the weak zone in the concrete substrate. However, at a high loading rate, the concrete strength is enhanced due to the strain rate effect, and at the same time, the specimen has no enough time to extend the cracks through the

concrete substrate. Therefore the failure extends along with the concrete-adhesive interface for the single-lap shear test.

(a) Plain concrete debris after testing (QS0-3-1) *(b) SFRC debris after testing (D1-3-1)*

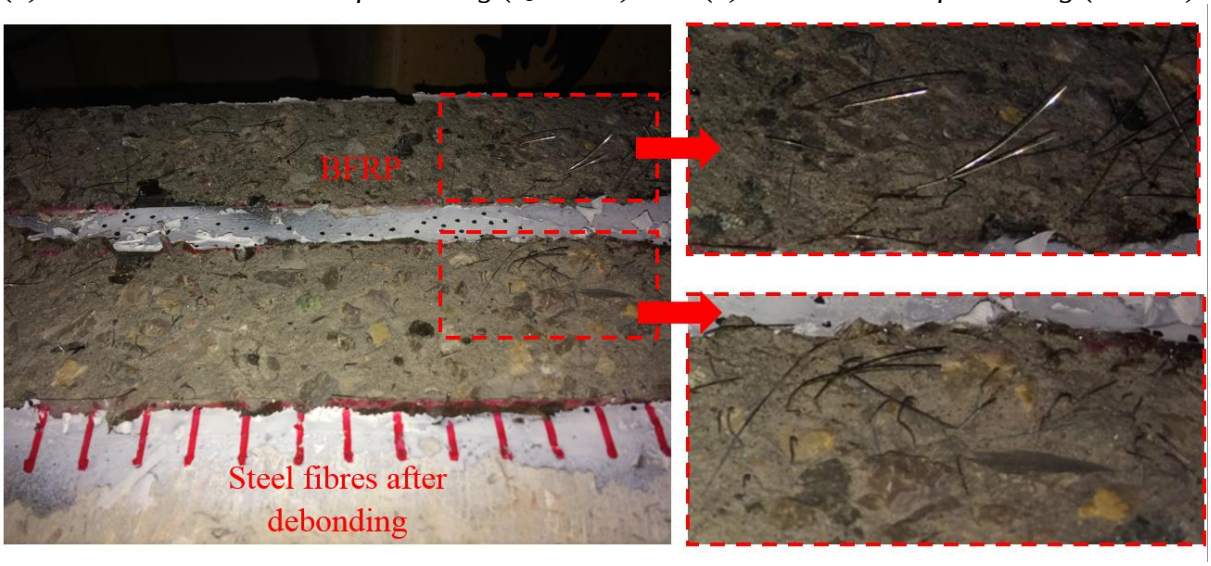

(c) Pull-out of steel fibres for D1-1-1 after testing

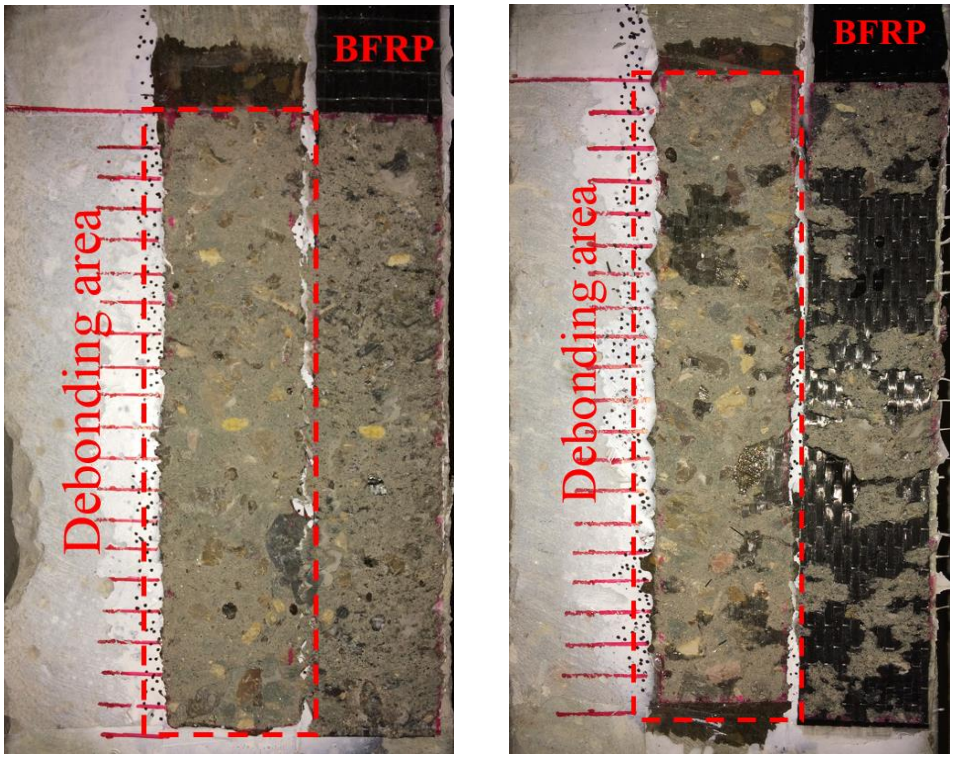

(d) Failure mode of (L) QS0-1 and (R) D0-8-1

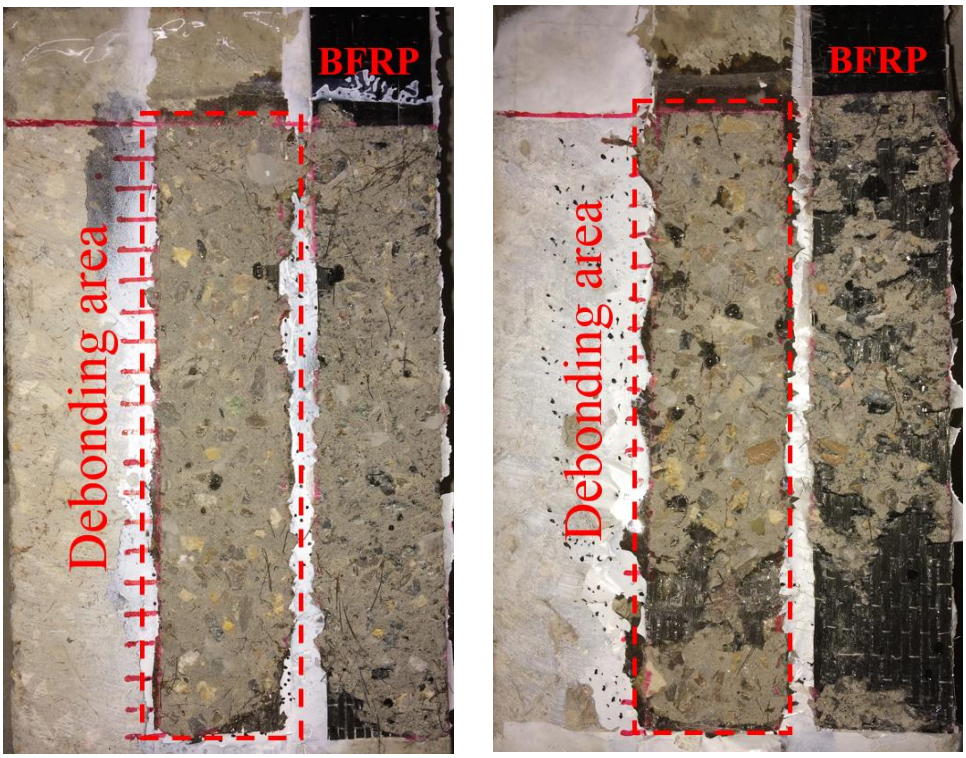

(e) Failure mode of (L) QS1-1 and (R) D1-8-1

Figure 6-40. Photograph of failure modes

Figure 6-41 shows the impact of steel fibre volume on the debonding loads under different loading rates. The general trend of the test results shows that the debonding load increased with fibre volume as well as the loading speed. The increased debonding load is caused by the

enhanced tensile strength of concrete with the fibre volume increasing. For example, as the volume increased from 0% to 1.5%, the debonding load increased by 15.2 % from 7.87 kN to 9.07 kN at the loading speed of 0.1 m/s.

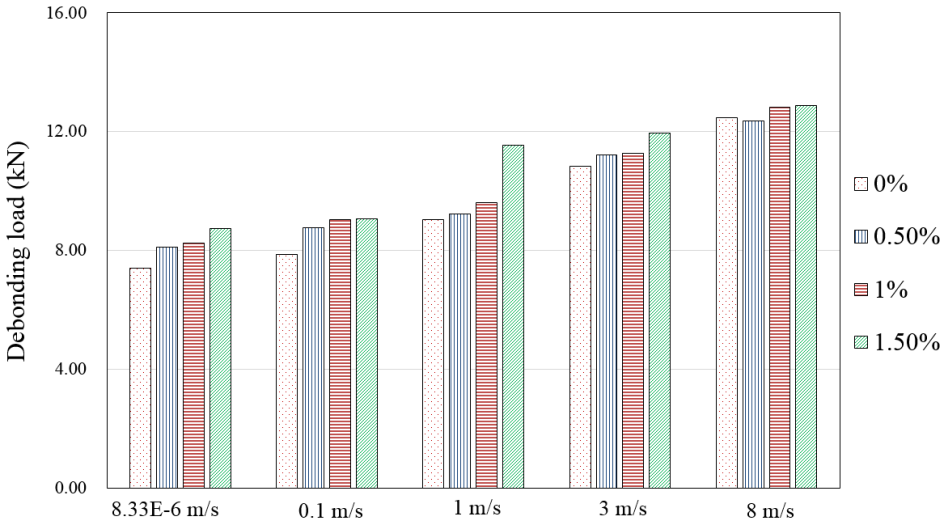

Figure 6-41. Debonding load under various loading rates

6.3.2.2 Strain time curves and stress equilibrium

Figure 6-42 plots the strain contours at different loading rates. The strain contour consists of different colours, red colour refers to the maximum strain while dark blue colour represents the minimum strain. The strain contours show the strain distributions at different loading stages under various loading velocities. At the initial stage of loading (i.e. 0.4*P*), a large local strain gradient in red colour was seen near the loaded end. With the tensile load increasing, the localized zone in red colour continued to develop and propagated along with the BFRP sheets and a transition zone in colours of yellow and green formed. The distance of the strain transition zone is known as the stress transfer zone, which increased slightly due to the added steel fibres but decreased with the loading rate increasing. The added steel fibres and strain rate had a marginal impact on the pattern of strain distribution.

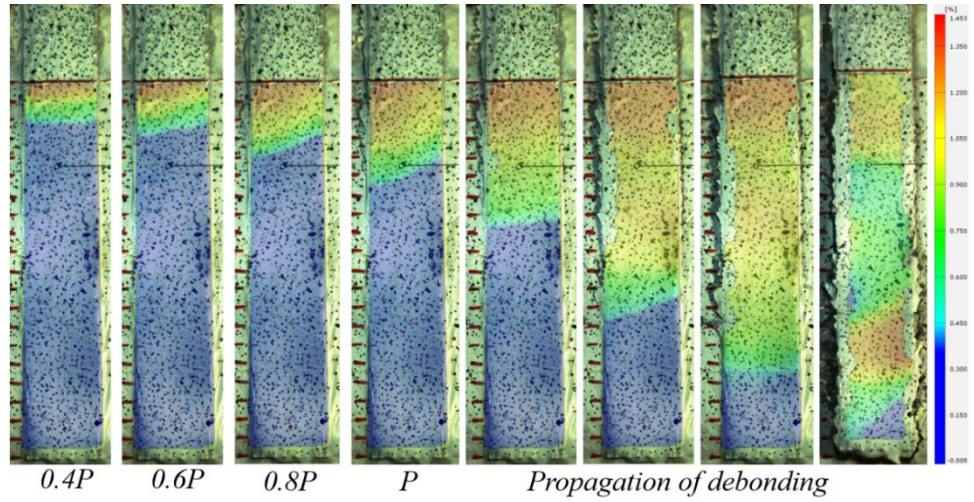

(a) D0.5-0.1-1

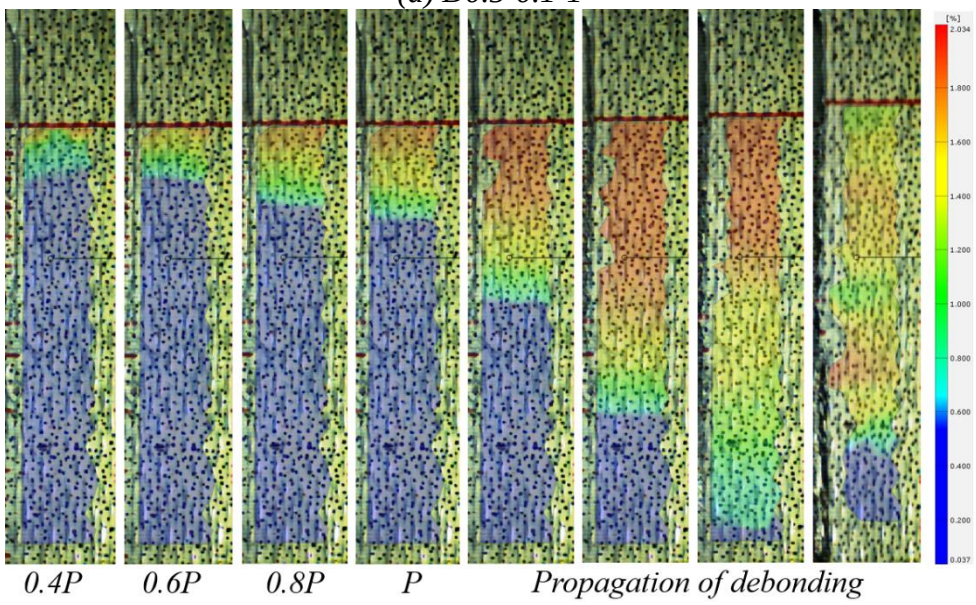

(b) D1.5-8-1

Figure 6-42. Strain contours at the loading velocities

Figure 6-43 illustrates the strain time histories of the tested specimens at the loading velocities of 0.1 m/s and 8 m/s. It is found that the strain vs. time curves are steeper under higher loading velocity than the case under lower loading velocity. Additionally, the ultimate debonding strain increased with the steel fibre volume under both the quasi-static and dynamic tests. The higher debonding strain of BFRP sheets resulted from the enhanced shear resistance of the BFRP-to-concrete interface.

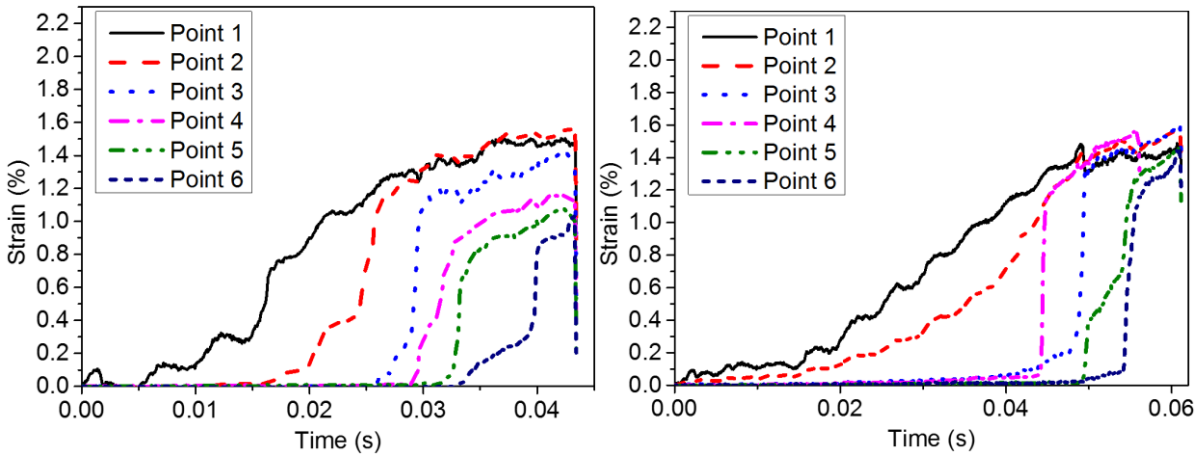

(a) D0.5-0.1-1 *(b) D1.5-0.1-1*

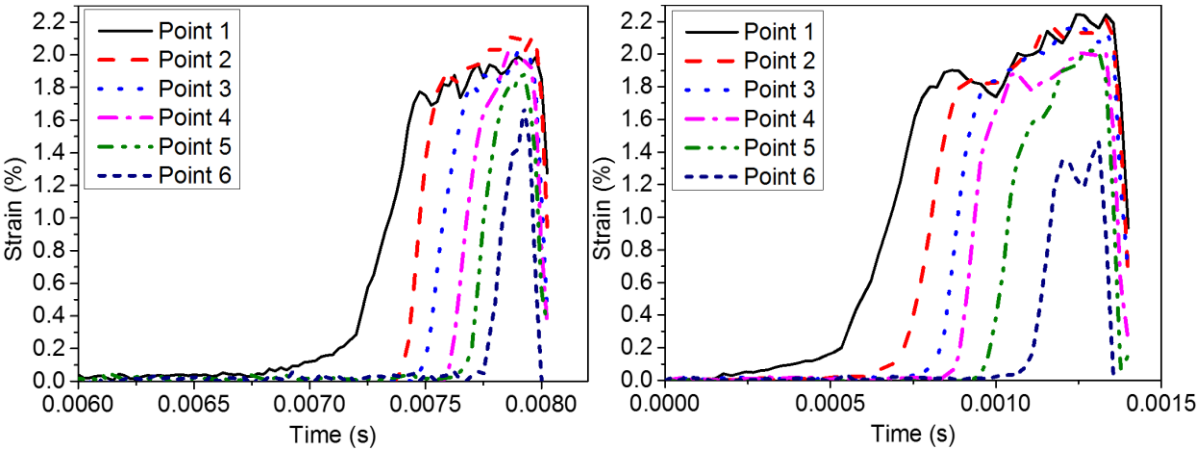

(c) D0.5-8-1 *(d) D1.5-8-1*

Figure 6-43. Strain-time histories

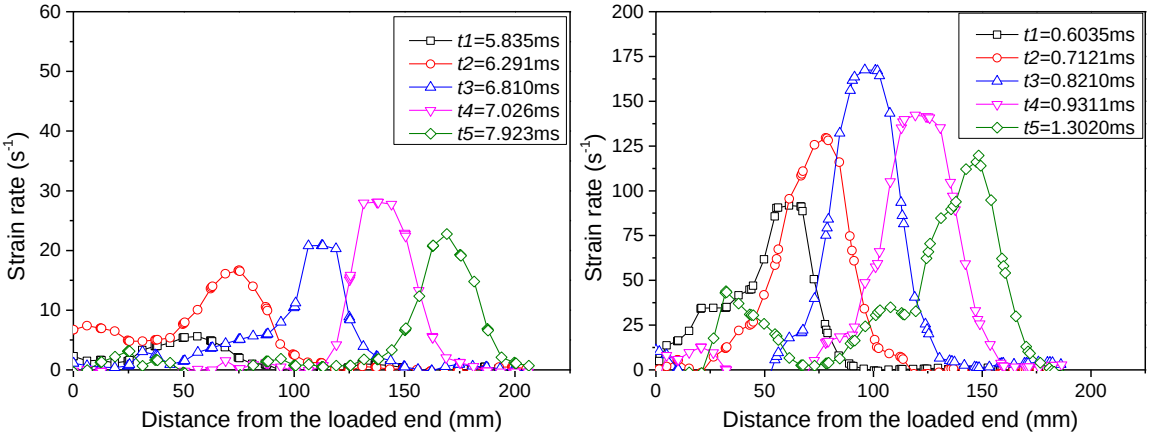

(a) D1-1-1 *(b) D1.5-8-1*

Figure 6-44. Strain rate distribution at different loading velocities

For the validation of the dynamic stress equilibrium, please refer to Section 6.2.2. Figure 6-44 illustrates the strain rate distributions along with the BFRP sheets at different time instants. The strain rate was obtained by the differentiation of strain time history using $\dot{\varepsilon} = \frac{d\varepsilon}{dt}$. A bell-

shape strain rate propagation along the BFRP sheets can be observed for all the test specimens. The strain rate increased with the loading speed and the strain rate for D1-1-1 was 28.09 s^{-1} at the loading velocity of 1 m/s and the strain rate for D1.5-8-1 was 167.54 s^{-1} at the loading velocity of 8 m/s. All the tested specimens show a similar strain rate distribution along the bonding length and the testing results are summarized in Table 6-9.

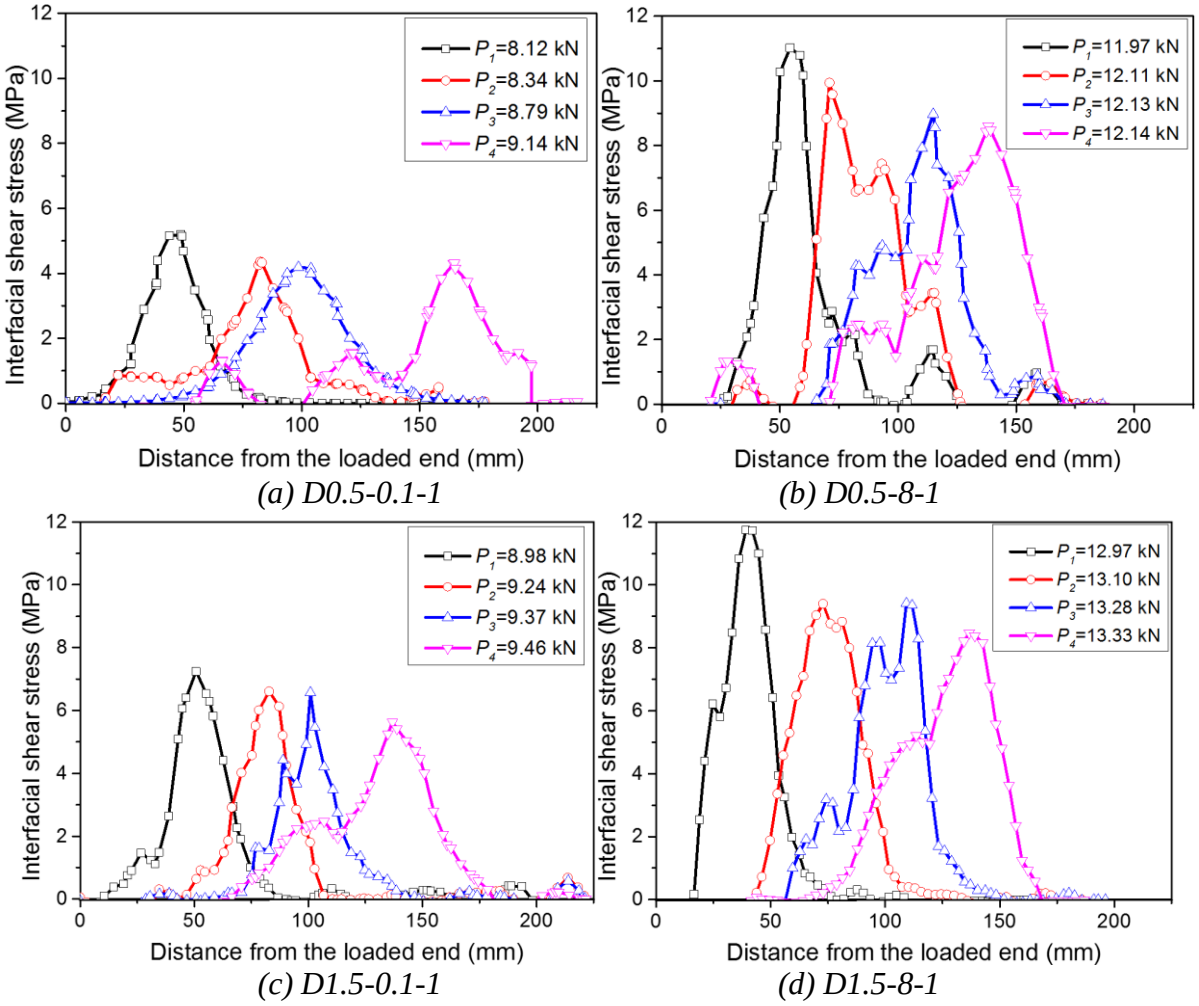

(a) D0.5-0.1-1 *(b) D0.5-8-1*

(c) D1.5-0.1-1 *(d) D1.5-8-1*

Figure 6-45. Local shear stress distribution

Figure 6-45 illustrates the local shear stress distribution. Four different loading levels after the initial debonding load were selected to obtain a robust shear stress distribution. With the applied load increases, the peak value of the shear stress gradually propagated to the free end. Due to the shear stress concentration near the loaded end, relatively higher shear stress was observed and then the shear stress maintained approximately constant with the debonding propagation. The shear stress increased significantly with the strain rate but increased slightly with the fibre volume. As compared to Specimen D0.5-0.1-1, the average PSS of Specimen D0.5-8-1 increased by 113% when the strain rate increased from 2.11 s^{-1} to 131.73 s^{-1}.

Compared to the strain rate effect, the effect of fibre volume on the PSS was relatively small. There was a 37% increment in the PSS at the same loading speed of 0.1 m/s when the fibre volume increased from 0.5% to 1.5%.

6.3.2.3 Experimental bond-slip curves

The DIC technique was used to measure the BFRP strain distributions and the relative slip, which can be used to obtain the interfacial bond-slip curves. The reliability of this technique as compared to readings from strain gauges was verified in the previous studies (127, 128). Figure 6-46 and Figure 6-47 illustrate the typical bond-slip curves with different steel fibre volumes under various loading rates. The following equations can be used to obtain the interfacial shear stress and shear slip based on the measured strain distributions (223):

$$\tau(x) = E_f t_f \frac{d\varepsilon}{dx} \tag{6-35}$$

$$s(x) = \int \varepsilon dx \tag{6-36}$$

where $\tau(x)$ is the interfacial shear stress, E_f is the elastic modulus, t_f is the thickness of BFRP sheet, $d\varepsilon/dx$ is the strain gradient, $s(x)$ is the shear slip along with the BFRP sheets, and ε is the strain measured by the DIC technique.

Figure 6-46 and Figure 6-47 illustrate the bond-slip relationships of each specimen under four loading levels and the peak shear stress (PSS) of each specimen is obtained from the mean value at four different loading levels after the initial debonding load. The distance of 85 mm, 115 mm, 145 mm, and 175 mm shown in the legend refer to the range of strain distributing at the four different loading levels after the initial debonding load. It is observed that the bond-slip curves for PCs and SFRCs under quasi-static and dynamic loadings exhibit a similar trend, i.e. non-linear ascending and descending branches (145). With the shear slip increasing, the reduction of shear stress was observed. Figure 6-46 illustrates the effect of steel fibre volume on the bond-slip response under quasi-static loading and the results show that the interfacial PSS increased with fibre volume. Figure 6-47 shows the effect of strain rate on the bond-slip response for Specimen D0.5 under different loading rates. It is clear that the PSS increased significantly with strain rate. Compared with the effect of fibre volume, the impact of the strain rate on the interfacial shear stress is more significant.

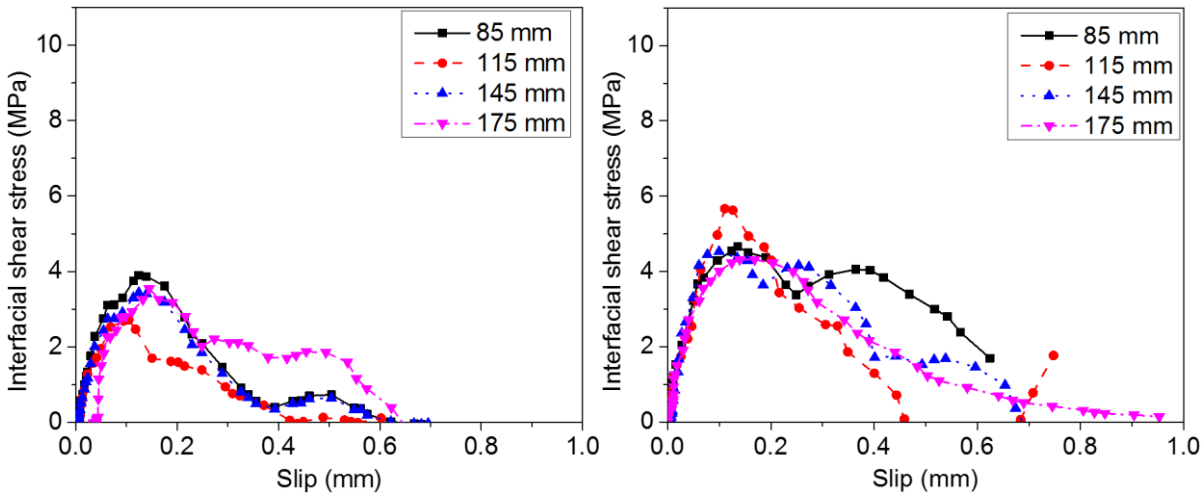

(a) QS0-1 *(b) QS0.5-1*

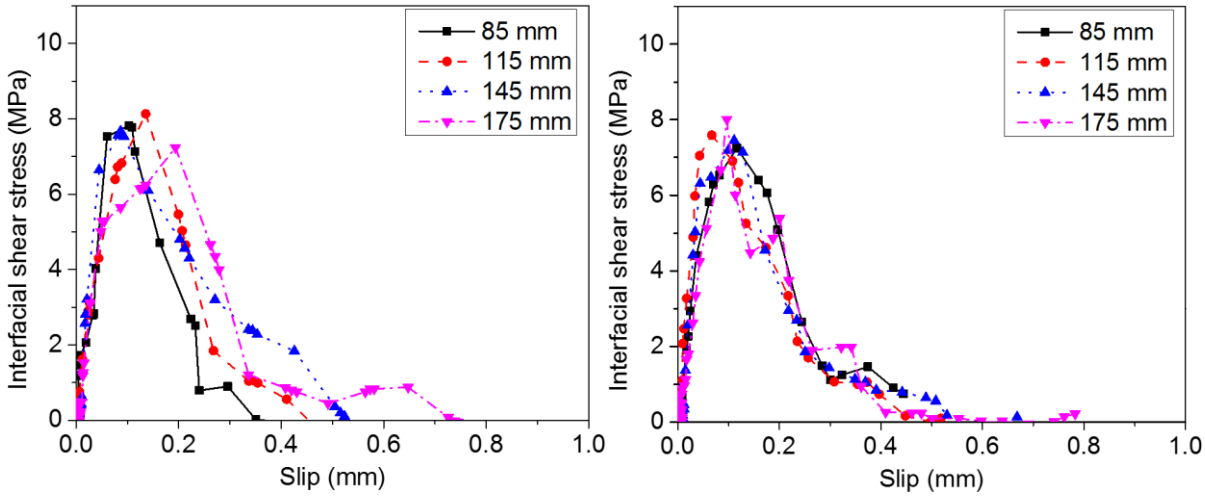

(c) QS1-1 *(d) QS1.5-1*

Figure 6-46. The relationship between peak shear stress and fibre volume under quasi-static loading

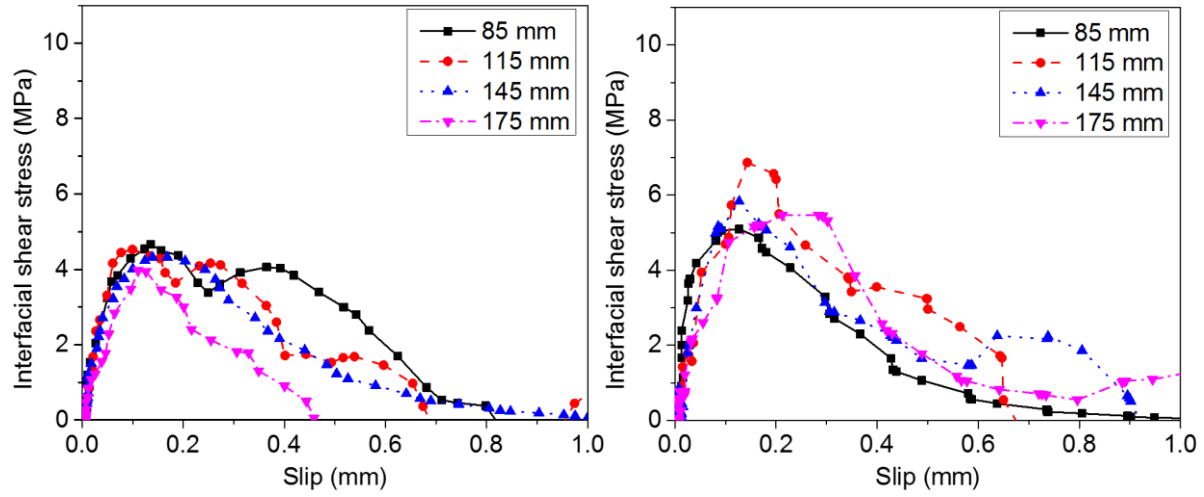

(a) D0.5-0.1-1 *(b) D0.5-1-1*

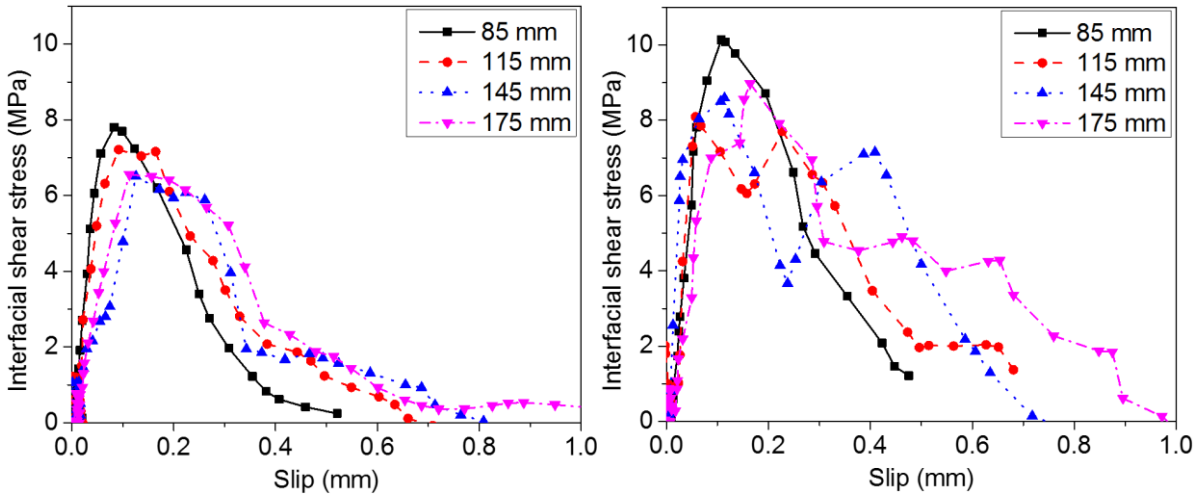

(c) D0.5-3-1 *(d) D0.5-8-1*

Figure 6-47. The relationship between peak shear stress and loading speed under different dynamic loadings

6.3.2.4 Effect of steel fibres on the interfacial bond

Figure 6-48 illustrates the influence of steel fibre volumetric fraction on the BFRP-concrete interface bond behaviour. It is found that the average debonding load, the interfacial fracture energy (IFE), the ultimate debonding strain, and the PSS increased with the steel fibre volume. As compared to the control group (PC), the average debonding loads of the specimens with volumetric fraction of 0.5%, 1%, and 1.5% increased by 9.46%, 11.35%, and 17.91% at quasi-static loads, and increased by 3.43%, 3.98%, and 10.19% at dynamic loading rate of 3 m/s, respectively. Due to the bridging action of fibres in the matrix, the fracture area of BFRP-to-SFRC is relatively larger than that of BFRP-to-PC. In this section, the tensile strength of concrete increased with the steel fibre volume, which is consistent with the previous study (185). The increased tensile strength of concrete leads to increased interfacial fracture energy. As compared to the quasi-static tests, the specimens with 0%, 0.5%, 1% and 1.5% fibre volume at the dynamic loading speed of 8 m/s experienced the increment of average PSS by 338%, 257%, 210%, and 174 % and the average IFE increased by 184%, 133%, 142%, and 117%, respectively. It should be noted that the interfacial PSS increased with the rising strain rate in general while the PSS stopped rising over the loading speed of 3 m/s for the case of 1.5% fibre volume. It might be due to the strain fluctuation caused by the system ringing under relatively high loading speed (i.e. 8 m/s) because the shear stress was derived from the strain profile. For instance, the obtained shear stress was averaged from the shear stress at four different locations (i.e. 85 mm, 115 mm, 145 mm and 175 mm), which show the variations of PSS as shown in Figure 6-47 (d).

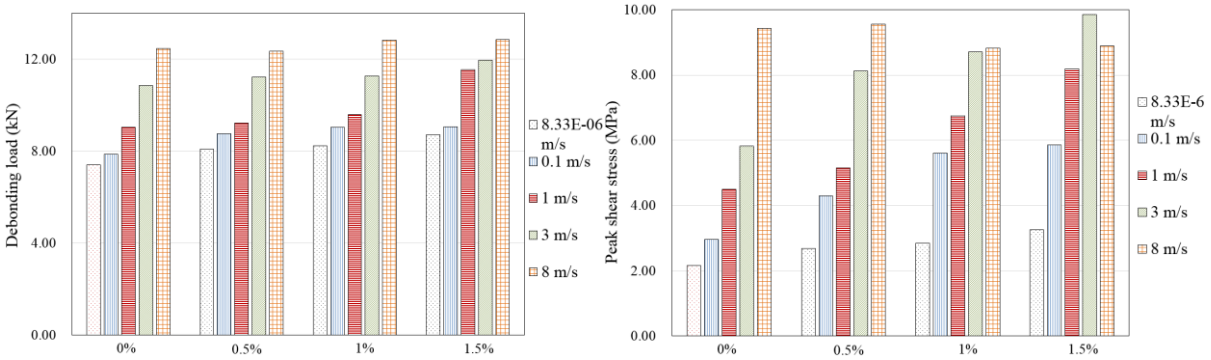

(a) Average debonding load

(b) Average peak shear stress

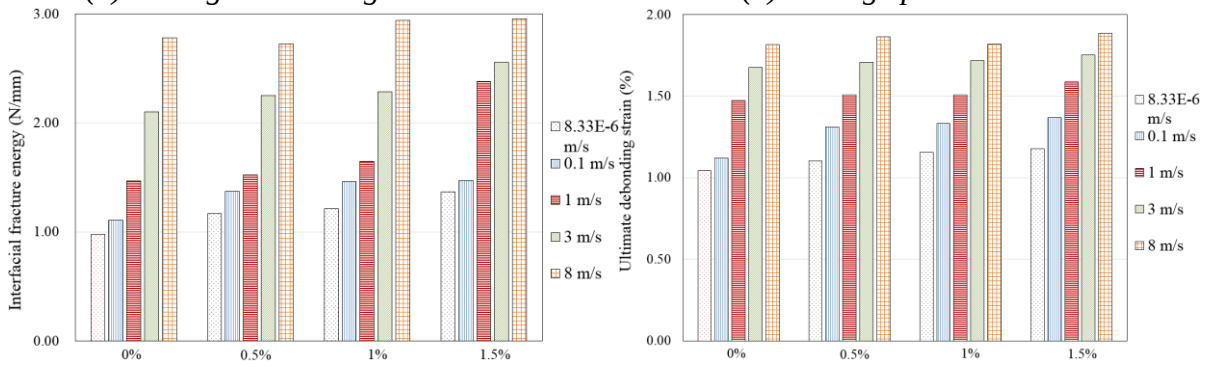

(c) Average interfacial fracture energy

(d) Average ultimate debonding strain

Figure 6-48. Effect of steel fibre volume under different loading rates

6.3.2.5 Effect of strain rate on the bond behaviour

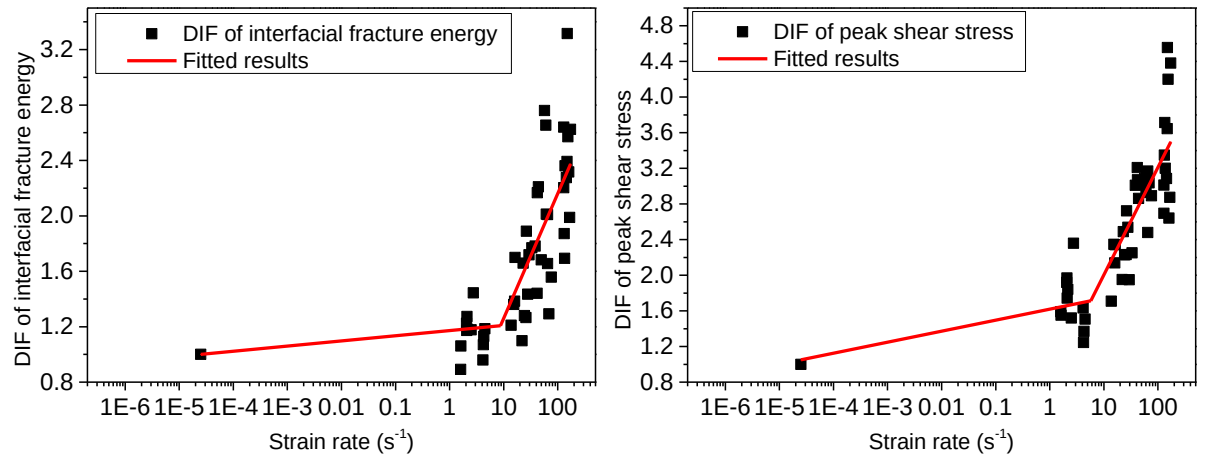

(a) Interfacial fracture energy *(b) Peak shear stress*

Figure 6-49. DIF vs. strain rate

As given in Table 6-9, the debonding load, the ultimate debonding strain, the IFE, and the PSS are strain rate dependent for both the BFRP-to-PC and BFRP-to-SFRC interfaces. For the modelling purpose in the following section, the dynamic increase factors (DIF) against the corresponding strain rate for the IFE (Gf) and PSS (τ_m) are proposed and plotted in Figure 6-49. A bilinear relationship between the obtained DIF and strain rate is presented in logarithmic functions. It is observed that the increments of IFE and PSS are not significant when the strain

rate is less than 3 s^{-1} while the increment becomes more apparent when the strain rate is great than 3 s^{-1}. This is because both the plain concrete (PC) and SFRC are strain rate dependent materials and the tensile strength increases with the strain rate, especially when the strain rate is higher than 3 s^{-1} (224, 225).

Based on the testing data, the following empirical equations are proposed for predicting the dynamic values by substituting the obtained DIF into the proposed model of IFE and PSS.

For dynamic interfacial fracture energy:

$$DIF_{G_f} = 0.0291\log(\dot{\varepsilon}) + 1.135, \text{ when } 2.5\times10^{-5}s^{-1} \le \dot{\varepsilon} \le 3s^{-1} \quad (6\text{-}37)$$

$$DIF_{G_f} = 0.9001\log(\dot{\varepsilon}) + 0.358, \text{ when } 3s^{-1} \le \dot{\varepsilon} \le 173.55s^{-1} \quad (6\text{-}38)$$

For dynamic interfacial PSS:

$$DIF_{\tau_m} = 0.1257\log(\dot{\varepsilon}) + 1.629, \text{ when } 2.5\times10^{-5}s^{-1} \le \dot{\varepsilon} \le 3s^{-1} \quad (6\text{-}39)$$

$$DIF_{\tau_m} = 1.2049\log(\dot{\varepsilon}) + 0.8, \text{ when } 3s^{-1} \le \dot{\varepsilon} \le 173.55s^{-1} \quad (6\text{-}40)$$

where DIF_{Gf} and $DIF_{\tau m}$ are respectively dynamic increase factor (*DIF*) of IFE G_f and PSS τ_m, and $\dot{\varepsilon}$ is strain rate.

6.3.3 Analytical investigation and the proposed model

6.3.3.1 Dynamic bond-slip relationship

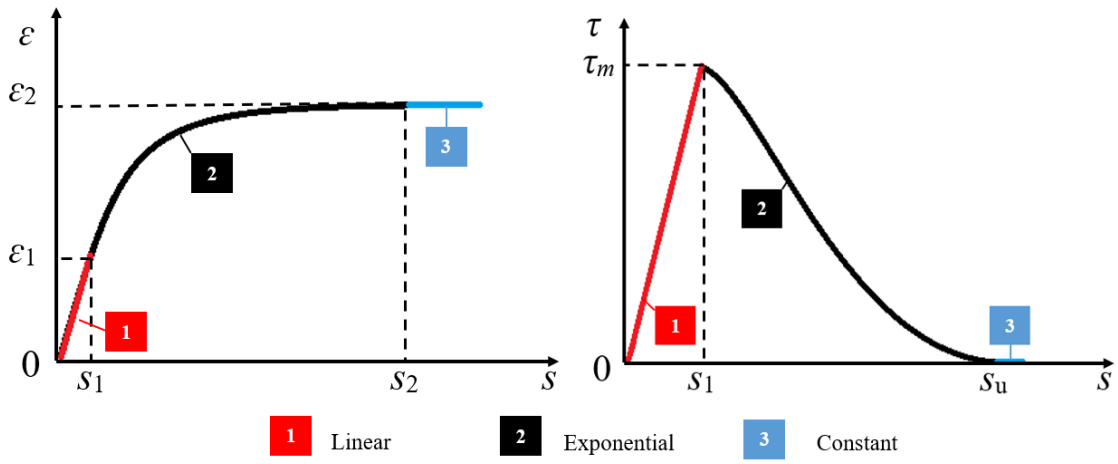

Figure 6-50. Determination of the bond-slip curve (L) Strain-slip curve; (R) Bond-slip curve

Figure 6-50 (R) illustrates the typical bond-slip curves for the tested specimens. It is observed that all the tested specimens exhibited an approximately triangular shape with a linear ascending stage before the PSS, and after that, a non-linear descending stage is observed until the final debonding (87, 167, 226). A linear equation can be used to depict the ascending stage, and an exponential function can be used to describe the descending stage. As shown in Figure 6-50 (L), three stages can be defined in the strain-slip curves: (a) linear; (b) nonlinear; and (c) constant (73, 227). These three stages from the strain-slip curves can derive the corresponding three parts in the local bond-slip curves as shown in Figure 6-50 (R).

Based on the determined shape of the bond-slip curve in Figure 6-50 (R), the shear stress can be expressed as follows (197):

$$\tau(s)=\begin{cases}\tau_m\left(\dfrac{s}{s_1}\right) & s\le s_1\\ \tau_m e^{-\omega(s-s_1)} & s_1\le s\le s_u\\ 0 & s_u\le s\end{cases} \tag{6-41}$$

where $\tau(s)$ is the shear stress, τ_m is the PSS, s_1 is the maximum elastic slip, and s is the shear slip.

The IFE G_f is defined as the enclosed area of the bond-slip curve for the FRP-to-concrete interface, the following expression can be used to calculate the interfacial fracture energy:

$$G_f=\int_0^{+\infty}\tau ds=\int_0^{s_1}\tau ds+\int_{s_1}^{+\infty}\tau ds \tag{6-42}$$

By integrating the shear stress and the slip, the IFE can be determined as follows:

$$G_f=\frac{1}{2}\tau_m s_1+\int_{s_1}^{+\infty}\tau_m e^{-\omega(s-s_1)}ds=\frac{1}{2}\tau_m s_1+\frac{\tau_m}{\omega} \tag{6-43}$$

The coefficient ω can be expressed by (228):

$$\omega=\frac{\tau_m}{G_f-\dfrac{1}{2}s_1\tau_m} \tag{6-44}$$

Therefore, the bond-slip model can be characterized by some key parameters (i.e. τ_m, s_1, s_u, and ω). It can be found that these key parameters can be determined by the interfacial fracture

energy (G_f). Once these key parameters are determined, the dynamic bond-slip relationship can be obtained.

6.3.3.2 Interfacial fracture energy

The IFE (G_f) is represented as the enclosed area of the bond-slip curve. However, due to the fluctuation of the obtained bond-slip curves, inaccurate interfacial fracture energy might be derived when using the bond-slip curves. Therefore, the IFE is obtained from the debonding load in this study, as follows (35, 37):

$$G_f = \frac{P_u^{\,2}}{2b_f^{\,2}t_f E_f} \tag{6-45}$$

The models to predict IFE have been proposed and adopted in numerous studies. It was reported that the interfacial fracture energy increases with the higher tensile strength of concrete. For SFRC, the splitting tensile strength increased with steel fibre volume, but the added steel fibres had slight effect on the compressive strength. Thus, the formula to calculate the tensile strength of SFRC by incorporating the fibre-reinforcing index (V_fL_f/ϕ_f) can be expressed as follows (186):

$$f_t = 0.516\left(f'_{cu}\right)^{0.5} + 0.101\left(f'_{cu}\right)^{0.5}\left(\frac{V_f L_f}{\phi_f}\right) + 0.199\left(\frac{V_f L_f}{\phi_f}\right) \tag{6-46}$$

For the BFRP-PC interface under quasi-static loading, it is found that the IFE correlates well with the FRP-to-concrete width ratio (β_w) and tensile strength of concrete (f_t) (95). In addition, the debonding failure shifted from concrete layer to epoxy-concrete interface and fracture of epoxy was also observed under high loading speed (i.e. 8 m/s). Thus, the contribution of epoxy on the IFE should be taken into account (210). The tensile strain energy of epoxy $\frac{f_a^{\,2}}{2E_a}$, which is represented as the area under the tensile stress-strain curves of the epoxy was incorporated into the proposed model. The testing data from the existing studies (3, 41, 74, 83, 211) and the testing data from this study were employed to conduct the regression analysis. Table 6-10 summarizes the specimen details and the test results. Therefore, the empirical model based on the best-fit coefficients can be obtained as follows:

$$G_{f,S}(PC) = 0.55\beta_w{}^2 \left(\frac{f_e{}^2}{2E_e}\right)^{0.42} \sqrt{f_t} \quad (6\text{-}47)$$

Table 6-10. Summary and comparison of testing data

Reference	Specimen ID	Test method	Adhesive			FRP			Concrete	$P_{u,exp}$ (kN)
			f_a (MPa)	E_a (GPa)	$f_a^2/2E_a$ (N/mm^2)	Ef (GPa)	tf (mm)	bf (mm)	f_t (MPa)	
Present study	QS1-1	Single shear	50.50	2.8	0.455	73	0.24	40	2.85	7.87
	QS1-2		50.50	2.8	0.455	73	0.24	40	2.85	6.93
Shen et al. (41)	1-1	Double shear	45.80	2.6	0.403	105	0.121	50	2.62	11.40
	1-2		45.80	2.6	0.403	105	0.121	50	2.62	10.80
	1-3		45.80	2.6	0.403	105	0.121	50	2.62	13.60
Huo et al. (74)	C50-1-1	Beam	65	3.2	0.660	236	0.169	50	2.89	13.60
	C50-1-2		65	3.2	0.660	236	0.169	50	2.89	11.50
	C50-2-1		65	3.2	0.660	236	0.338	50	2.89	18.00
	C50-2-2		65	3.2	0.660	236	0.338	50	2.89	14.20
	C80-2-1		65	3.2	0.660	236	0.338	80	2.89	17.50
	C80-2-2		65	3.2	0.660	236	0.338	80	2.89	18.40
Toutanji et al. (211)	AA-1	Single shear	23.6	4.1	0.068	110	0.495	50	2.73	7.56
	AA-2		23.6	4.1	0.068	110	0.66	50	2.73	9.29
	AA-3		23.6	4.1	0.068	110	0.825	50	2.73	11.64
	AA-4		23.6	4.1	0.068	110	0.99	50	2.73	12.86
	BB-1		23.6	4.1	0.068	110	0.495	50	2.73	12.55
	BB-2		23.6	4.1	0.068	110	0.66	50	2.73	14.25
	BB-3		23.6	4.1	0.068	110	0.825	50	2.73	17.72
	BB-4		23.6	4.1	0.068	110	0.99	50	2.73	18.86
	CC-1		23.6	4.1	0.068	110	0.495	50	2.73	13.24
	CC-2		23.6	4.1	0.068	110	0.66	50	2.73	15.17
	CC-3		23.6	4.1	0.068	110	0.825	50	2.73	18.86
	CC-4		23.6	4.1	0.068	110	0.99	50	2.73	19.03
Yun et al. (3)	M-EB	Double shear	54	3.0	0.289	257	0.66	50	3.03	26.30
Yun and Wu (83)	N30-0-1	Single shear	45	3.5	0.289	235	0.167	50	2.81	23.7
	N30-0-2		45	3.5	0.289	235	0.167	50	2.81	24.4
	N45-0-1		45	3.5	0.289	235	0.167	50	3.22	27.7
	N45-0-2		45	3.5	0.289	235	0.167	50	3.22	27.4

The IFE increased with the steel fibre volume. Therefore, the fibre-reinforcing index (V_fL_f/ϕ_f) was set as a factor to determine the IFE of the BFRP-SFRC interface. Based on the best-fitted coefficients through regression analysis, the relationship between the IFE and fibre-reinforcing index can be expressed as follows:

$$G_{f,S}(SFRC) = 1.321\left(\frac{V_f L_f}{\phi_f}\right)^{0.135} G_{f,S}(PC) \quad (6\text{-}48)$$

The IFE increased with the strain rate. Therefore, by substituting the DIF in Equations (6-37) and (6-38) into Equation (6-48), the dynamic IFE can be obtained in the following equation. Figure 6-51 shows the comparison between the predicted and experimental results. The predicted results are consistent with the experimental data and the mean ratio of the predicted results to the test results is 0.7407 with the corresponding coefficient of variation (COV) of 0.17.

$$G_{f,D}(SFRC) = DIF_{G_f} G_{f,S}(SFRC) \tag{6-49}$$

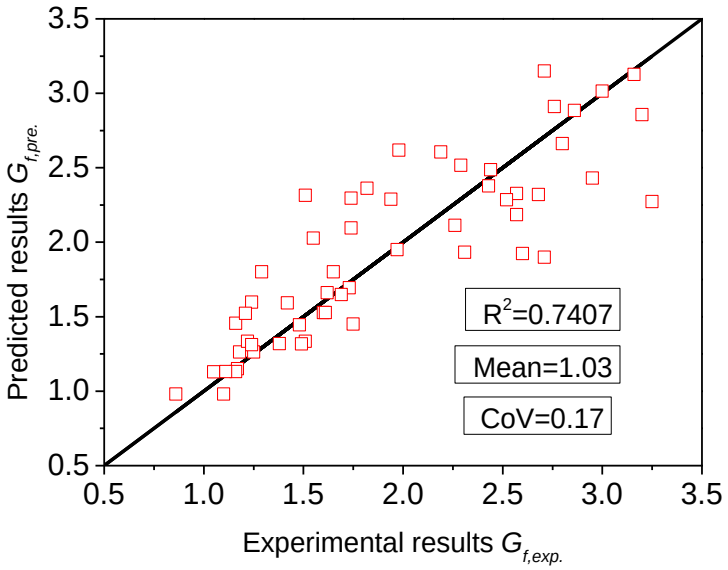

Figure 6-51. Experimental vs predicted interfacial fracture energy

6.3.3.3 Dynamic debonding strain

The single-lap shear test is used to simulate the intermediate crack (IC) induced interfacial debonding in the FRP-strengthened concrete structures. Due to the FRP debonding, only 30%-40% of FRP strength is utilized (34). Numerous debonding strain models have been proposed for design purpose (229). However, there is no debonding strain model available considering FRP-strengthened SFRC elements and strain rate effect. Therefore, an empirical debonding strain model by incorporating steel fibre volume and strain rate is proposed in this study. Using the model proposed by JSCE (215), the proposed IFE by incorporating the steel fibre volume and strain rate expressed in Equation (6-49) can be used to obtain the ultimate debonding strain in Equation (6-50). The predicted results are in good agreement with the experimental data, as shown in Figure 6-52. The mean ratio of the predicted results to the experimental results was 0.97, and the corresponding coefficient of variation (COV) was 0.059.

$$\varepsilon_{u,D} = \sqrt{\frac{2G_{f,D}}{E_f t_f}} \tag{6-50}$$

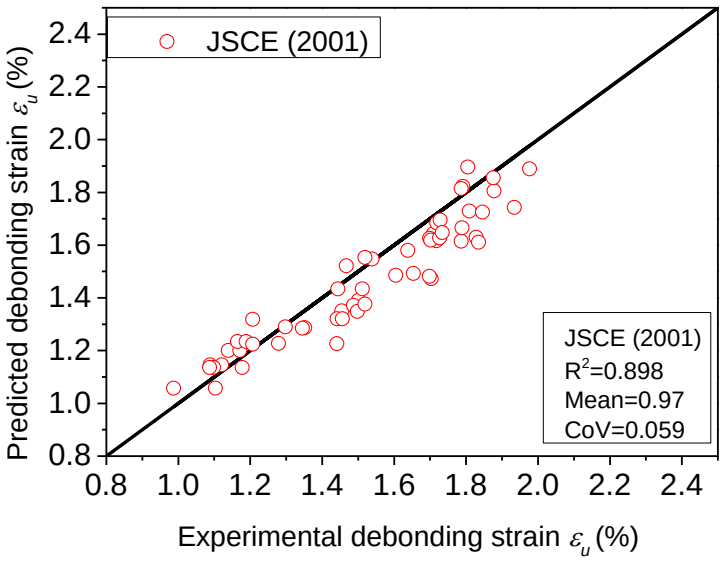

Figure 6-52. Experimental vs predicted debonding strain

6.3.3.4 Dynamic peak shear stress and slip

The interfacial PSS is obtained from the strain distributions. Based on the test results of the present study, the PSS increased slightly with steel fibre volume and increased significantly with strain rate. There is a consistent finding that the interfacial shear stress is determined by f_t and β_w (89, 182). Therefore, the formula to predict the static PSS can be expressed as follows:

$$\tau_{m,s}(PC) = 0.646\beta_w\sqrt{f_t} \tag{6-51}$$

The interfacial PSS increased with the steel fibre volume. Therefore, the fibre-reinforcing index ($V_f L_f/\phi_f$) should be a factor determining the PSS of the BFRP-SFRC interface. Based on the best-fit coefficients from regression analysis, the interfacial PSS can be expressed by the fibre-reinforcing index in the following way:

$$\tau_{m,s}(SFRC) = 1.421\left(\frac{V_f L_f}{\phi_f}\right)^{0.17}\tau_{m,s}(PC) \tag{6-52}$$

The interfacial PSS increased with the rising strain rate. Therefore, by substituting the DIF in Equations (6-39) and (6-40) into Equation (6-52), the dynamic interfacial PSS in Equation (6-53) can be obtained. Figure 6-53 shows the comparison between the predicted and experimental results. The predicted results are in good agreement with the test data as the ratio between the predicted and test results is 1.03 and the corresponding coefficient of variation (COV) is 0.14.

$$\tau_{m,D}\left(SFRC\right)=DIF_{\tau_{m,s}}\tau_{m,s}\left(SFRC\right) \tag{6-53}$$

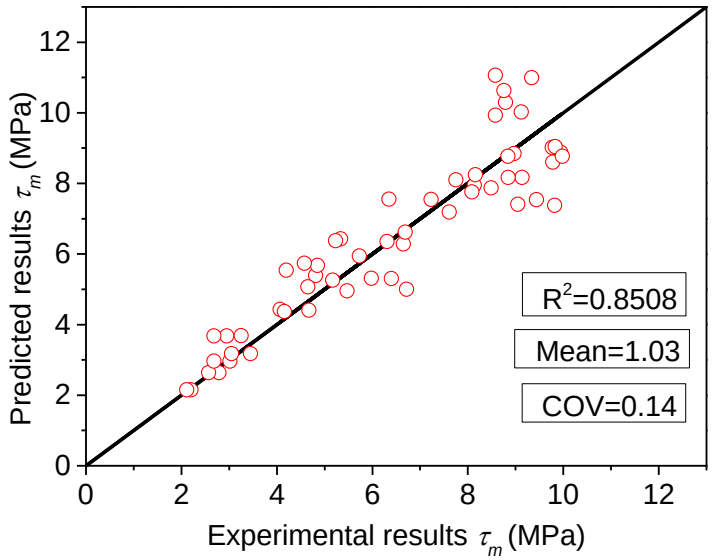

Figure 6-53. Experimental vs predicted interfacial peak shear stress

The maximum elastic slip s_1 is the maximum slip corresponding to the elastic stage of the bond-slip curves. The elastic slip mainly resulted from the shear deformation within the bonded region. The elastic slip slightly decreased with the increasing strain rate, but results were less consistent and presented higher scatter. As a result, the elastic shear slip was set as a constant of 0.13 mm for simplicity.

6.3.3.5 Analysis and validation of the dynamic bond-slip model

Figure 6-54 shows the comparisons between the model predictions based on Equations (6-41) to (6-53) and the directly measured experimental results for the strain-slip response and bond-slip response. Based on the obtained parameters τ_m, s_1, and ω, the predicted strain-slip and bond-slip relationships are in good agreement with the test data. This comparison demonstrates that the proposed bond-slip models can accurately predict the dynamic interfacial bond-slip of BFRP-to-SFRC interface. Figure 6-55 illustrates the comparison between the experimental and tested debonding load. The debonding load can be obtained by a widely accepted formula $P_u=b_f\sqrt{2E_f t_f G_f}$ (209) with the strain rate effect included in the corresponding dynamic interfacial fracture energy. As shown the predictions agree well with the test data, with a mean value of 1.013 and a *COV* of 0.08.

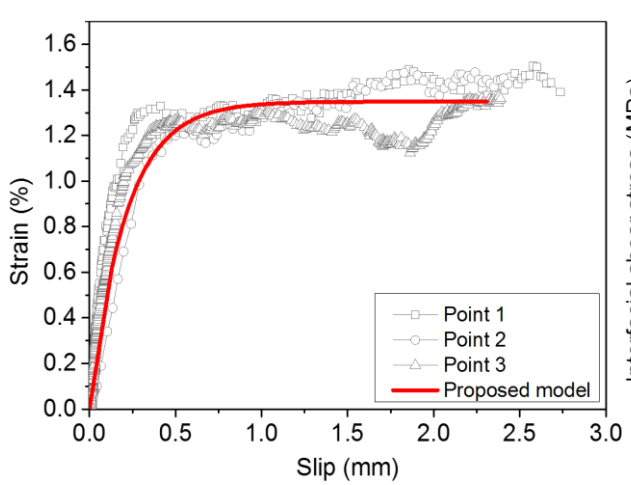

(a) Strain-slip response of D0.5-1-1

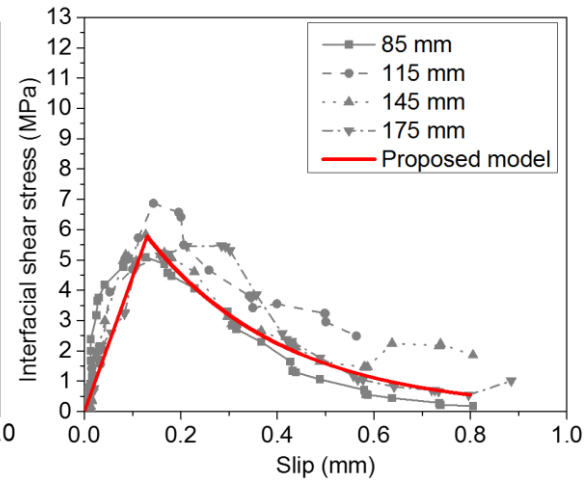

(b) Bond-slip response of D0.5-1-1

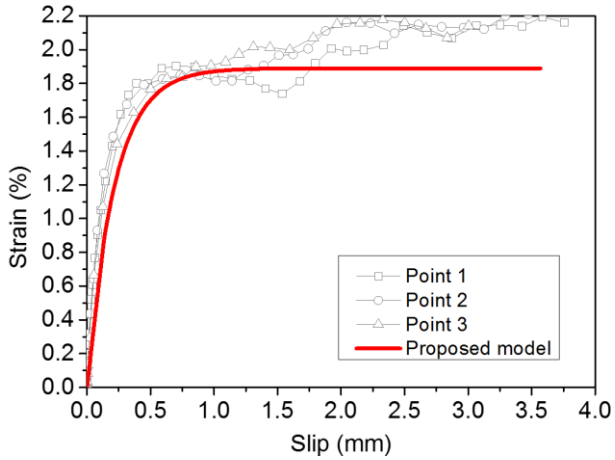

(c) Strain-slip response of D1.5-8-1

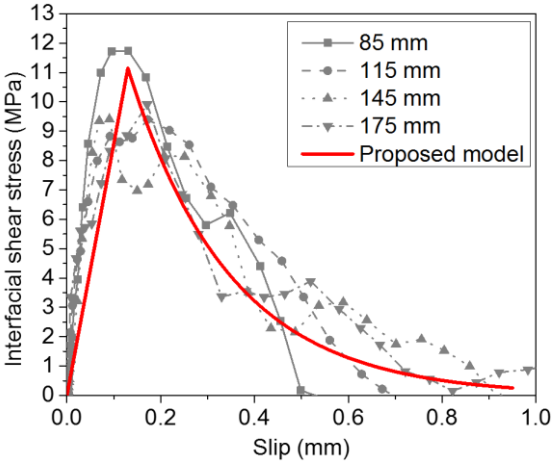

(d) Bond-slip response of D1.5-8-1

Figure 6-54. Comparisons of analytical predictions and tests data of strain-slip curve and bond-slip curve

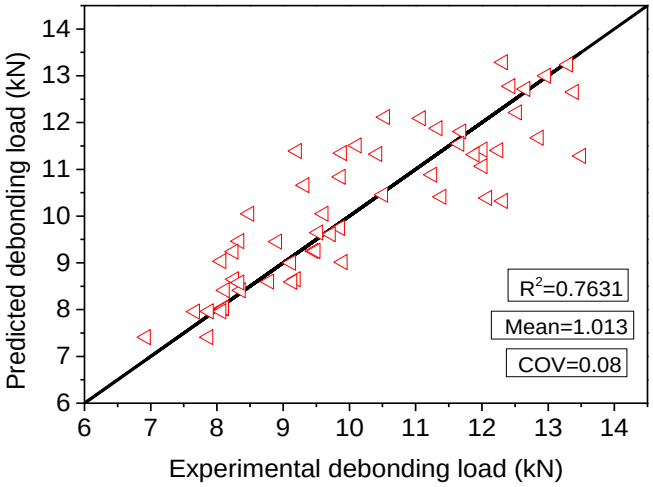

Figure 6-55. Experimental vs predicted debonding load

6.3.4 Section summary

This section investigates the effect of adding short steel fibre on the dynamic interfacial bond behaviour of BFRP-to-SFRC interface. The following conclusions can be drawn:

1. Strain rate has a significant effect on the debonding failure modes. With the increasing strain rate, the damage mode shifts the debonding area from concrete layer to the concrete-epoxy interface. When the damage mode changes to the concrete-epoxy interface, adding steel fibres has only limited improvement on the debonding load.
2. The addition of steel fibres increase the debonding load due to the improved microcracking resistant capacity of SFRC substrate. Additionally, the strain rate has a more significant effect on the debonding load than the enhanced tensile strength of SFRC by adding steel fibre.
3. The addition of steel fibres result in higher interfacial fracture energy as the large fracture area dissipates more fracture energy. In addition, the interfacial fracture energy increases with strain rate as the shear resistance is enhanced under high loading rate.
4. The addition of steel fibres result in higher interfacial shear stress due to the enhanced bond strength. In addition, the strain rate has a significant effect on the peak shear stress as the ultimate debonding strain of BFRP increases with the strain rate.
5. The empirical bond-slip model is proposed by incorporating the strain rate effect. The proposed model gives great predictions of the experimental results.

6.4 Summary

This chapter investigates the effects of concrete substrate characteristics on dynamic bond behaviour with the consideration of the effect coarse aggregate sizes (i.e. 5-10 mm, 10-15 mm, and 15-20 mm) in section 6.1, various concrete strength (i.e. C20, C30, and C40) in section 6.2, and micro steel fibre volume (i.e. V_f = 0.5%, 1.0%, and 1.5%) in section 6.3, respectively. The effect of aggregate size, concrete strength and fibre volume on the bonding performance is significant under low loading rates, while the effect is marginal when the loading rate exceeds 3 m/s, indicating that the effect of strain rate is remarkable under relatively high strain rate as compared with other parameters.

Chapter 7. Numerical study of static and dynamic interfacial bond behaviours

7.1 Introduction

Experimental and analytical investigations on the static and dynamic interfacial bond behaviour have been evaluated and discussed in Chapters 3 to 6, a numerical study on the dynamic interfacial bond between FRP and concrete is deemed necessary. In this chapter, dynamic debonding behaviour between fibre-reinforced polymer (FRP) and concrete is numerically investigated by using finite element code LS-DYNA. A three-dimensional (3D) finite element (FE) model is built and a bond-slip model is incorporated into the simulation of the interfacial bond between FRP and concrete. To validate the accuracy of the numerical model, experimental results from 42 dynamic single shear tests on FRP-concrete joints are employed. The debonding load and shear slip responses, FRP strain distributions, and interfacial bond-slip responses are compared between the numerical and experimental results.

The related work in this chapter has been published in Construction and Building Materials.

Yuan C, Chen W, Pham TM, Hao H. Finite Element Modelling of Dynamic Bonding Behaviours between Fibre Reinforced Polymer Sheet and Concrete. Construction and Building Materials. 2020; 255:118939.

7.1.1 Numerical models

A three-dimensional (3D) finite-element model is built by using LS-DYNA and shown in Figure 7-1. After conducting a mesh convergence test, the minimum element size is determined as 0.75 mm around the interface. The determination of minimum element size is also based on the results of the previous studies on existing FE models of FRP-to-concrete joints (230, 231). The strain rate sensitivity of the interface is incorporated in the bond-slip responses since the interfacial peak shear stress and interfacial fracture energy increased with strain rate (41, 74, 232). The loading velocities varies from 0.01 m/s, 0.1 m/s, 1.0 m/s, 3.0 m/s to 8.0 m/s in this chapter. In order to reduce the computational cost, the quasi-static debonding process is simulated at the loading speed of 0.01 m/s based on results from the previous study (233). Chen et al. (233) used the dynamic approach with the loading speed of 0.01 m/s to simulate quasi-static debonding of FRP-strengthened concrete beam and the numerical results showed accurate predictions of the experimental results under quasi-static loads. Shi et al. (64) also

proposed a dynamic approach with a ramp loading scheme to simulate the interfacial bond capacity affected by the thickness of adhesive and the numerical results were in good agreement with the tests. Therefore, the loading rate of 0.01 m/s without consideration of DIF of concrete is used in the FEM to simulate the quasi-static debonding and the obtained FEM results match well with the quasi-static experimental results.

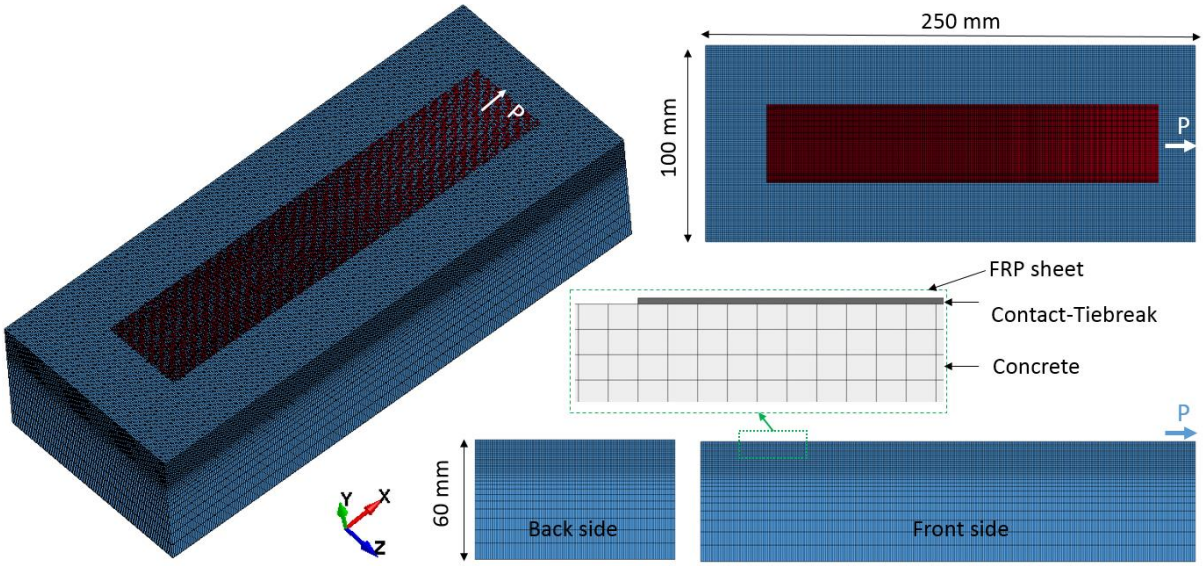

Figure 7-1. Numerical model of a single shear test specimen

7.1.2 Bond behaviour between FRP and concrete

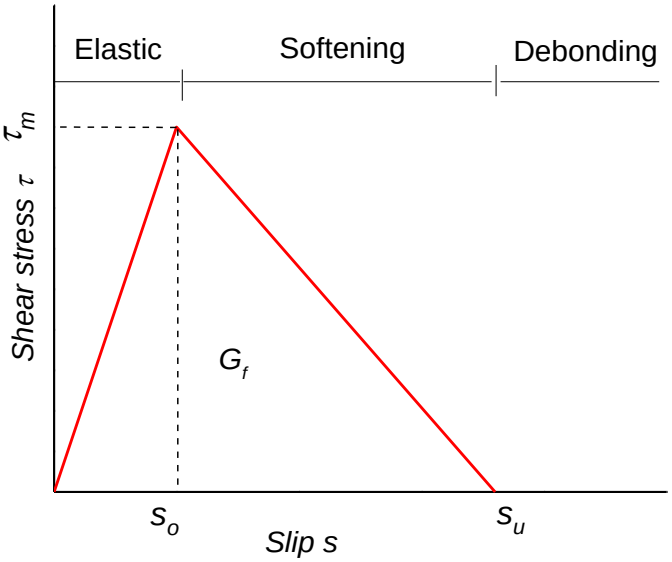

Figure 7-2. Bilinear bond-slip model (84, 86, 234)

The bond behaviour between BFRP sheets and concrete is simulated by using tie-break function (*Contact_Automatic_Surface_to_Surface_Tiebreak) that considers both shear stress and fracture energy criteria in LS-DYNA. Option 9 is selected as the failure criterion for the

delamination modelling, which has Benzeggagh–Kenane (BK) mode interaction law (235) to account for Mode I and Mode II interaction and allows for a better definition of the constitutive laws (236-238). The traction-separation relation between the contact pair is used to model the tangential separation. As a user-defined contact, shear failure stress σ_s (i.e. the peak shear stress) and the corresponding shear energy release rate G_f (i.e. the interfacial fracture energy) can be defined based on the dynamic testing results summarized in Table 6-6. The tensile strength of concrete is set as the normal failure stress (σ_n) based on a previous study (84). The debonding failure criterion based on shear and normal stresses at the interface is defined as follows (239):

$$\left(\frac{|\sigma_n|}{R_n}\right)^2+\left(\frac{|\sigma_s|}{R_s}\right)^2 \geq 1 \tag{7-1}$$

where R_n and R_s refer to the normal failure stress and shear stress failure at the contact surface, respectively; σ_n and σ_s represent the normal stress and shear stress, respectively.

The bond-slip model of FRP-to-concrete interface is defined as a bi-linear elastic-softening curve as shown in Figure 7-2. The bilinear curves are defined by three parameters: the peak shear stress (τ_m), the corresponding separation or shear slip (s_o), and the debonding separation or the ultimate shear slip (s_u) (237). The peak shear stress demonstrates the strain rate effect as the interfacial peak shear stress and interfacial fracture energy increase with the rising strain rate (41, 74, 232). The relationship between the shear stress and the shear slip is defined as follows (84, 86, 234):

$$\tau(s)=\begin{cases}\dfrac{\tau_m}{s_o}s & 0\leq s\leq s_o\\ \dfrac{\tau_m}{s_u-s_o}\left(s-s_o\right) & s_o\leq s\leq s_u\\ 0 & s\geq s_u\end{cases} \tag{7-2}$$

where $\tau(s)$ is the relationship between shear stress and shear slip (s), τ_m refers to the peak shear stress, s_o is the corresponding shear slip, and s_u is the ultimate shear slip between FRP and concrete. The interfacial energy released rate G_f is represented by the area under the bilinear curve.

7.1.3 Material models

The concrete material is modelled by using the K&C concrete damage model (*MAT_72R3 in LS-DYNA) (240). To avoid computational overflow, the erosion feature *MAT_ADD_EROSION is used and the maximum principal strain at failure as a criterion is defined as 0.4 in this chapter, which yields a good prediction of the cracking pattern of concrete in FE modelling. Three grades of concrete strength are considered (i.e., C20, C30, and C40) and the parameters are summarized in Table 6-6. The strain rate effect of concrete is considered by applying CDIF (compressive dynamic increase factor) in compression and TDIF (tensile dynamic increase factor) in tension for concrete as given below (216):

$$CDIF = \frac{f_{c,d}}{f_{c,s}} = \begin{cases} 0.0419\left(\log \dot{\varepsilon}_d\right) + 1.2165 & \left(\dot{\varepsilon}_d \le 30s^{-1}\right) \\ 0.8988\left(\log \dot{\varepsilon}_d\right)^2 - 2.8255\left(\log \dot{\varepsilon}_d\right) + 3.4907 & \left(\dot{\varepsilon}_d > 30s^{-1}\right) \end{cases} \tag{7-3}$$

$$TDIF = \frac{f_{t,d}}{f_{t,s}} = \begin{cases} 0.26\left(\log \dot{\varepsilon}_d\right) + 2.06 & \left(\dot{\varepsilon}_d \le 1s^{-1}\right) \\ 2\left(\log \dot{\varepsilon}_d\right) + 2.06 & \left(1s^{-1} < \dot{\varepsilon}_d \le 2s^{-1}\right) \\ 1.44331\left(\log \dot{\varepsilon}_d\right) + 2.2276 & \left(2s^{-1} < \dot{\varepsilon}_d \le 150s^{-1}\right) \end{cases} \tag{7-4}$$

where $f_{c,s}$ and $f_{t,s}$ are the static compressive and tensile strengths, respectively; and $f_{c,d}$ and $f_{t,d}$ are the dynamic compressive and tensile strengths, respectively.

The BFRP sheet is modelled by an enhanced version of composite model *MAT_55 in LS-DYNA, which can accurately detect damage initiation in FRP composites. The Tsai-Wu (241) failure model is employed as the FRP failure criterion. The material properties are summarized in Table 7-1.

Table 7-1. Material properties of concrete and FRP

Material	LS-DYNA model	Input parameter	Magnitude
Concrete	*MAT_CONCRETE_DAMAGE_REL3 (MAT_72R3)	Poisson's ratio	0.2
		Mass density	2400 kg/m^3
		Unconfined strength	20/30/40 MPa
		Erosion failure strain	0.4
FRP sheet	*MAT_ENHANCED_COMPOSITE_DAMAGE (MAT_55)	Poisson's ratio	0.2
		Mass density	1600 kg/m^3
		Young's modulus	78 GPa
		Tensile strength	1600 MPa
		Failure strain	0.02

7.2 Numerical results

To verify the FE model, the experimental results from the previous study by the authors (242) are used to compare with the numerical results. A total of 42 experimental results (C20, C30, and C40) are summarized in Table 6-6. The load-slip curves, FRP strain distributions, and interfacial bond-slip responses between FRP and concrete are evaluated and discussed by comparing the numerical and experimental results. For the sake of brevity, the testing results and numerical results of the specimens with C40 are discussed in the following sections.

7.2.1 Load-slip curves

Figure 7-3 shows the numerical and experimental results of the load-slip curves from various loading velocities applied at the loaded end of FRP sheets. In general, the proposed FE model can well capture the general trend of the testing results. Both the bond strength and the ultimate shear slip between FRP and concrete increase with the rising strain rate, which was observed in the testing and numerical results. It should be noted that a reduction of the debonding load (i.e. circled in blue) is observed during the debonding process in numerical results for the static loads only as shown in Figure 7-3 (a). This phenomenon is not seen in the case of high loading rate because the failure surface is relatively shallower and smoother than that under static loading. The uneven fracture depth of concrete layer during the debonding process and the cracking pattern of concrete are discussed in the flowing section. Figure 7-3 (f) shows the comparisons of the experimental and FEM results of debonding loads and ultimate shear slip. The mean ratio of FEM-to-test and the corresponding coefficient of variation of debonding loads is 1.09 and 5.57%, respectively. The enhanced bond strength indicates that the interface is strain rate dependent and the enhancement of the bond strength should be mainly caused by the improved cracking-resistance of concrete. Accordingly, the analysis of the cracking pattern in concrete is discussed in the following section.

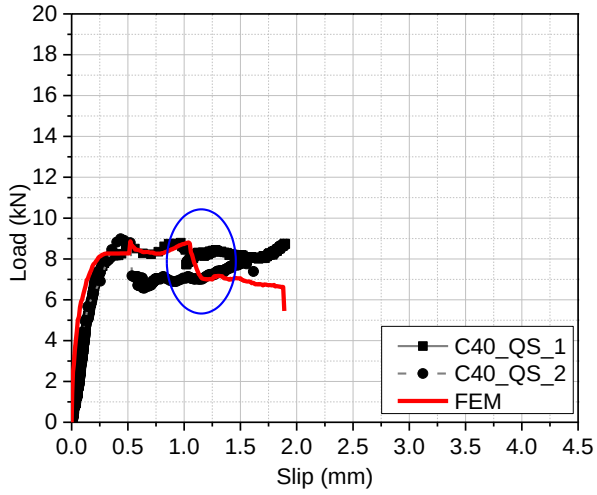

(a) QS

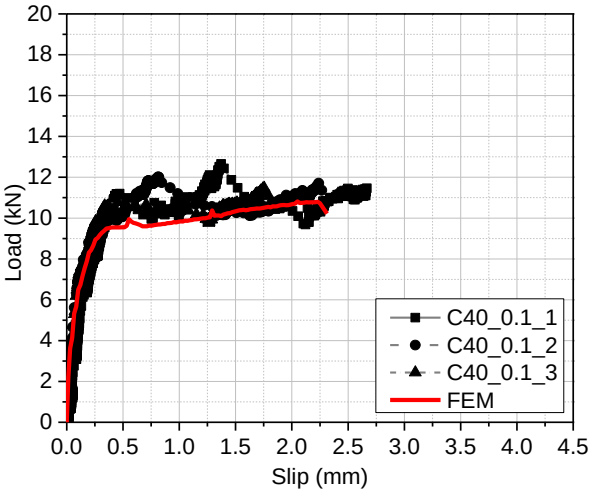

(b) 0.1 m/s

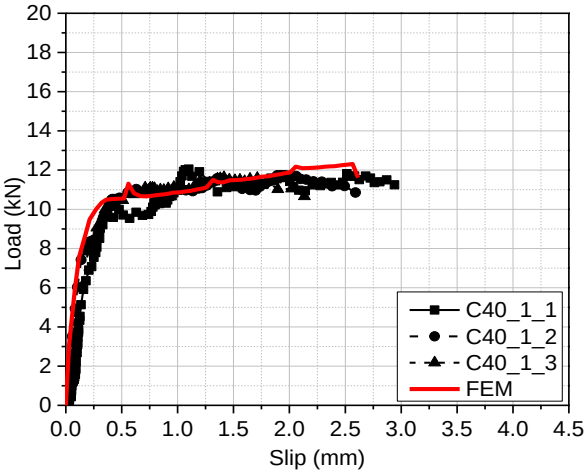

(c) 1.0 m/s

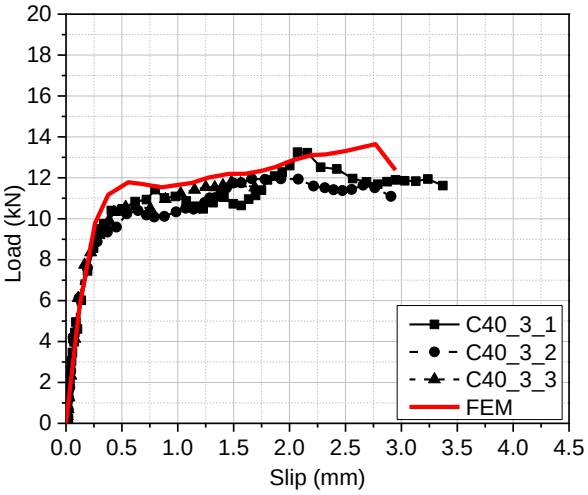

(d) 3.0 m/s

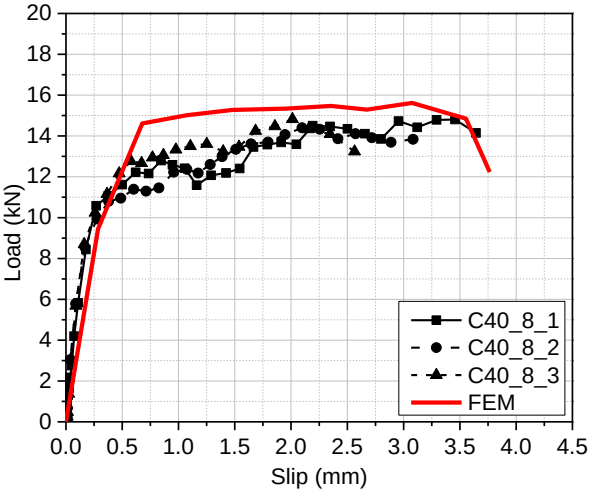

(e) 8.0 m/s

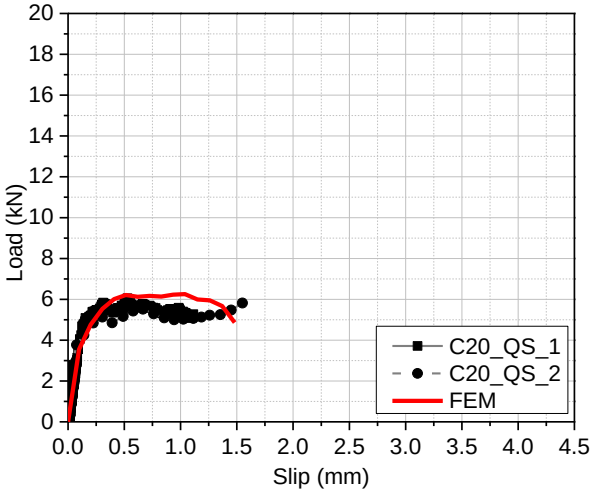

(f) QS

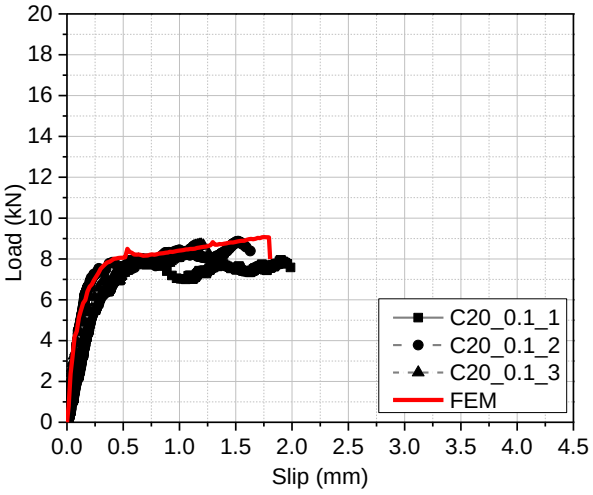

(g) 0.1 m/s

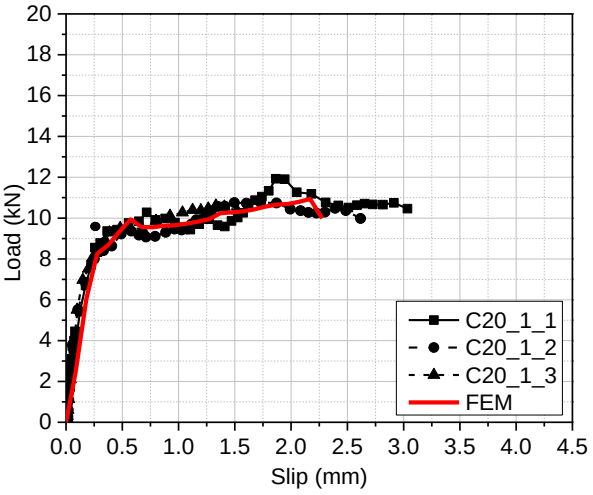

(h) 1.0 m/s

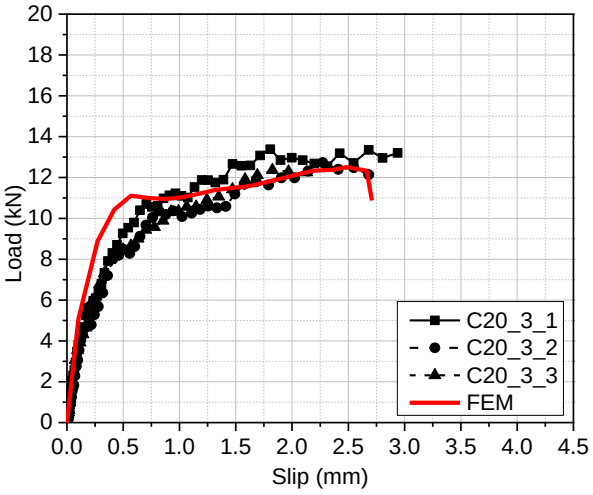

(i) 3.0 m/s

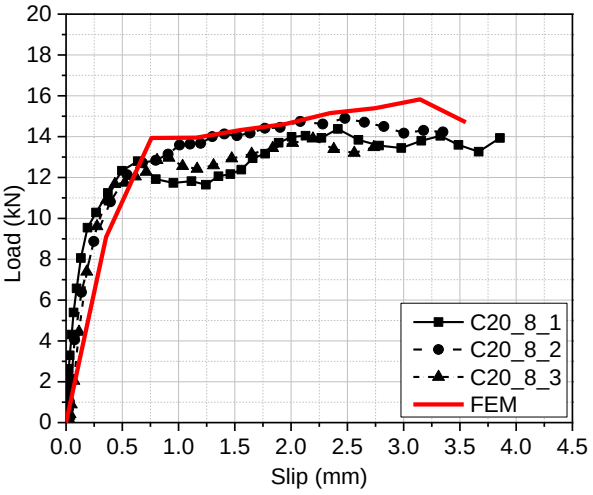

(j) 8.0 m/s

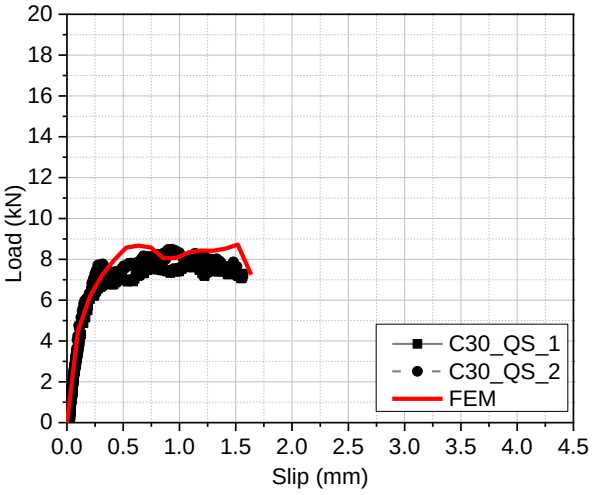

(k) QS

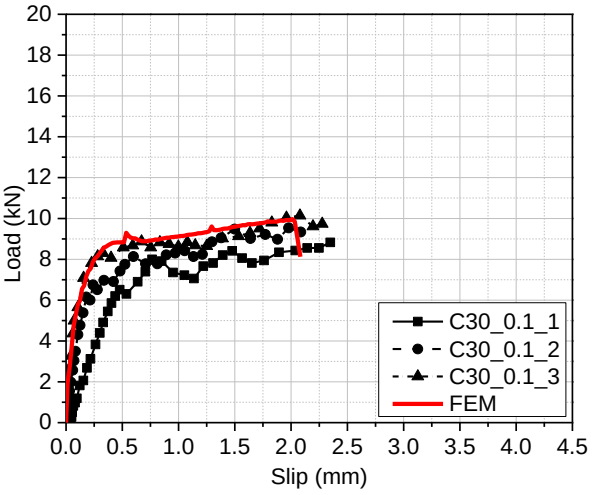

(l) 0.1 m/s

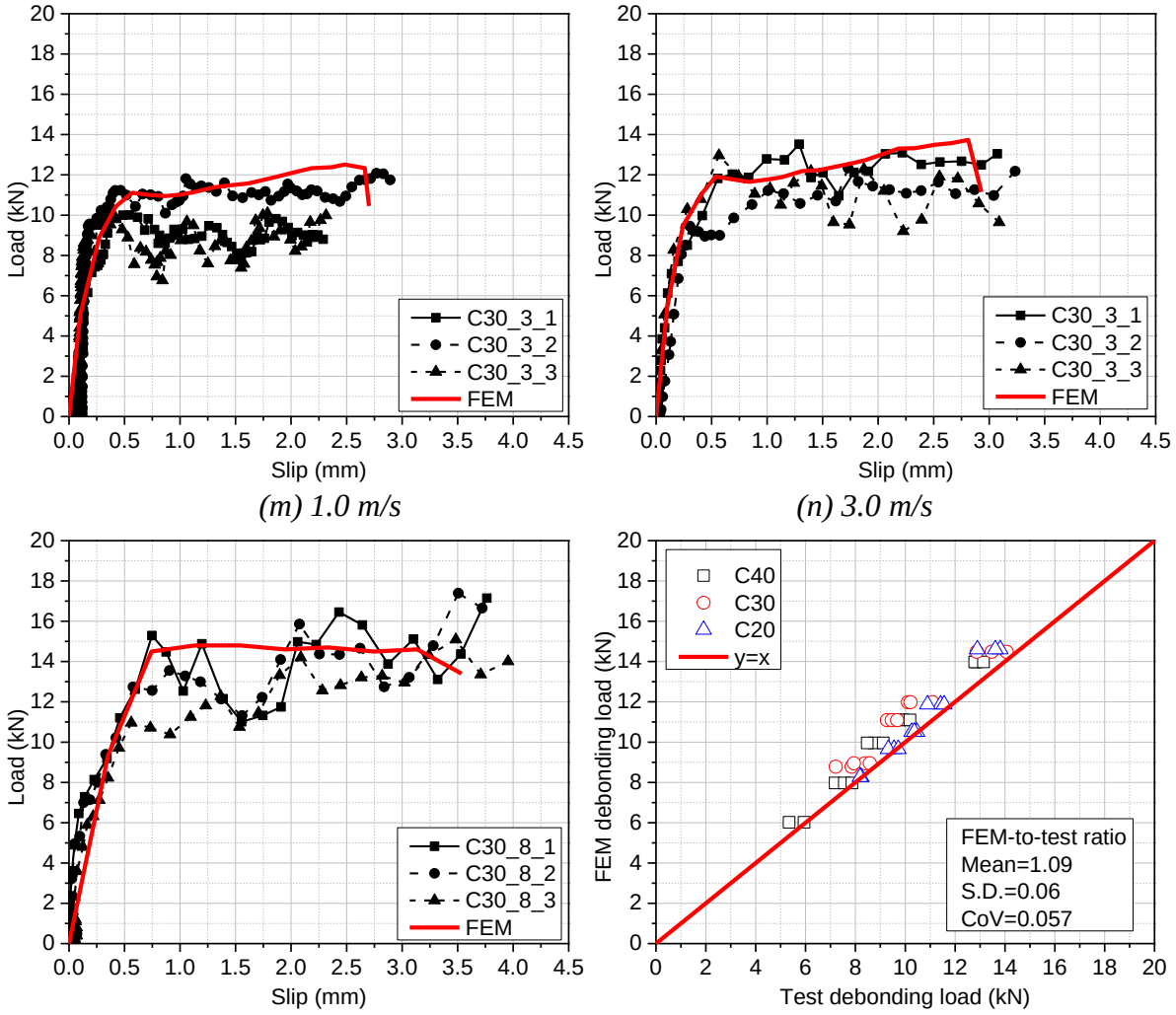

(m) 1.0 m/s *(n) 3.0 m/s*

(o) 8.0 m/s *(p) Comparison between FEM and test*

Figure 7-3. Load-slip curves of specimens (Test (242) vs. FEM)

The experimental results of Specimens C40_QS_1, C40_8_1 and C20_8_1 in Yuan et al. (242) and the corresponding FEM results are selected as the references to compare the cracking patterns in concrete. Four loading stages (i=1,2,3,4) of the load-slip curves (i.e. *Ai*, *Bi* and *Ci*) of Specimens C40_QS_1, C40_8_1 and C20_8_1 are selected for comparison as shown in Figure 7-4 and the corresponding tensile damage contours are plotted in Figure 7-5. Yu and Chen (230) stated that the tensile damage in concrete can be represented by the cracking plastic strain and consequently the crack pattern in concrete can be characterized by these contours. The progressive damage of concrete also represents the propagation of debonding. Previous studies found that the cracking in concrete has an angle of approximate 45^{o} to the horizontal direction to propagate debonding failure at the static loading condition (230, 233). It is observed that the cracking pattern under dynamic loads is similar to that under static loads because inclined cracks (i.e. circled in white) are also observed and shown in Figure 7-5, especially near the loaded end and free end. The red regions in the contours refer to the tensile

damage of concrete elements. After the initial debonding stage, obvious micro-cracks (i.e. the red regions) in the concrete are observed.

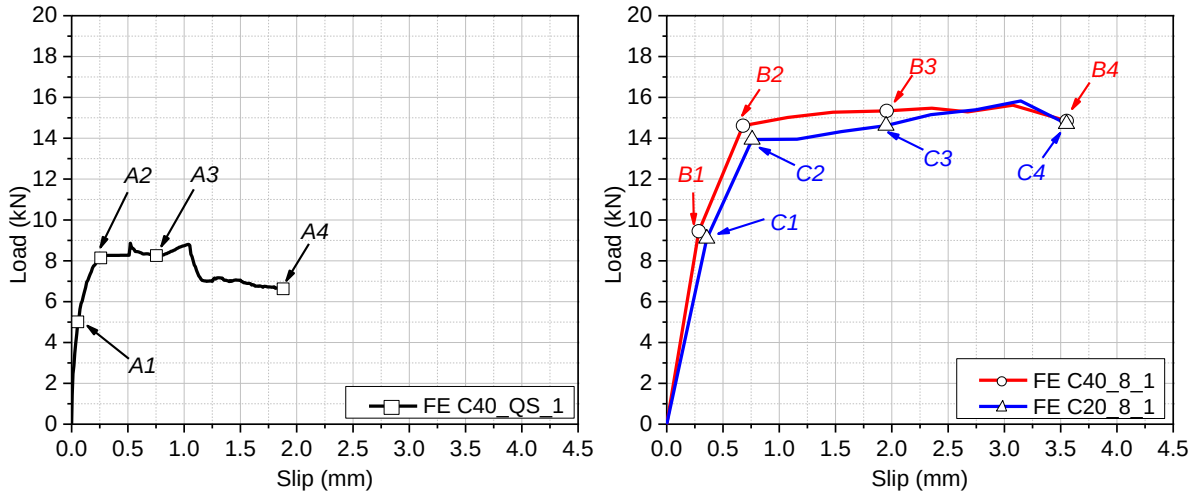

(a) Quasi-static *(b) Dynamic*

Figure 7-4. Four loading stages (i=1, 2, 3, 4) of C40_QS_1, C40_8_1 and C20_8_1

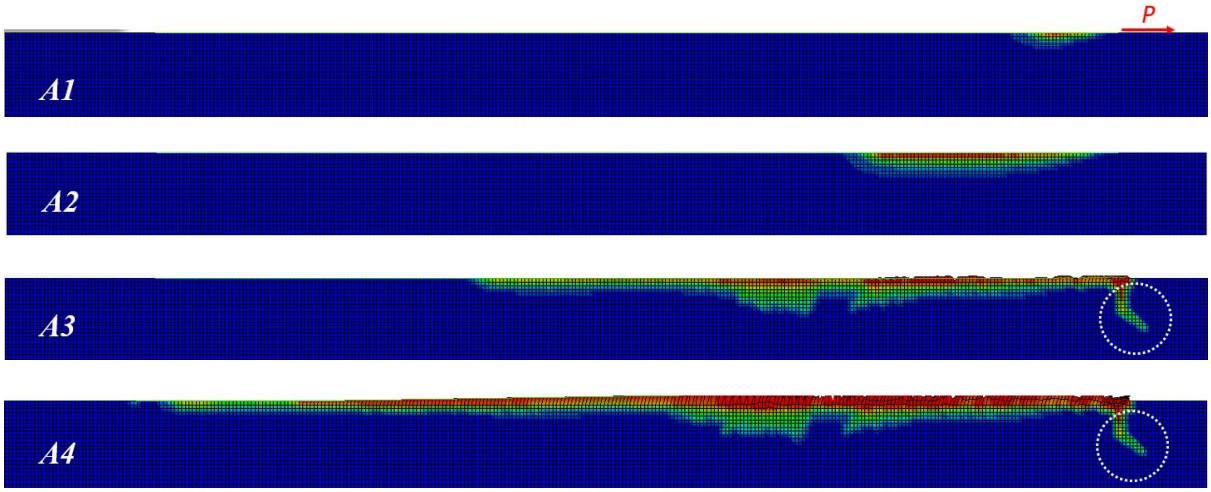

(a) C40_QS

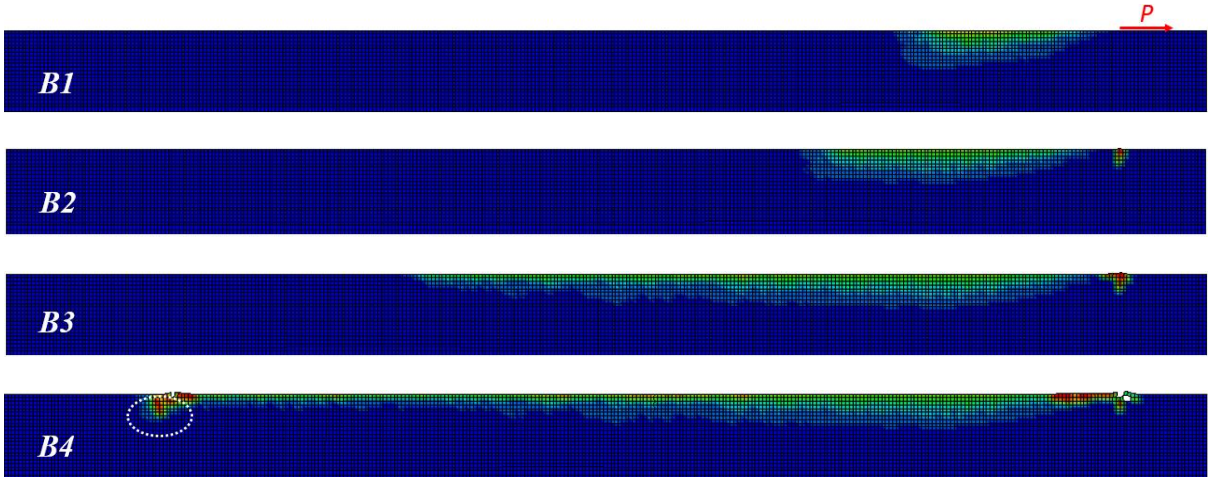

(b) C40_8.0 m/s

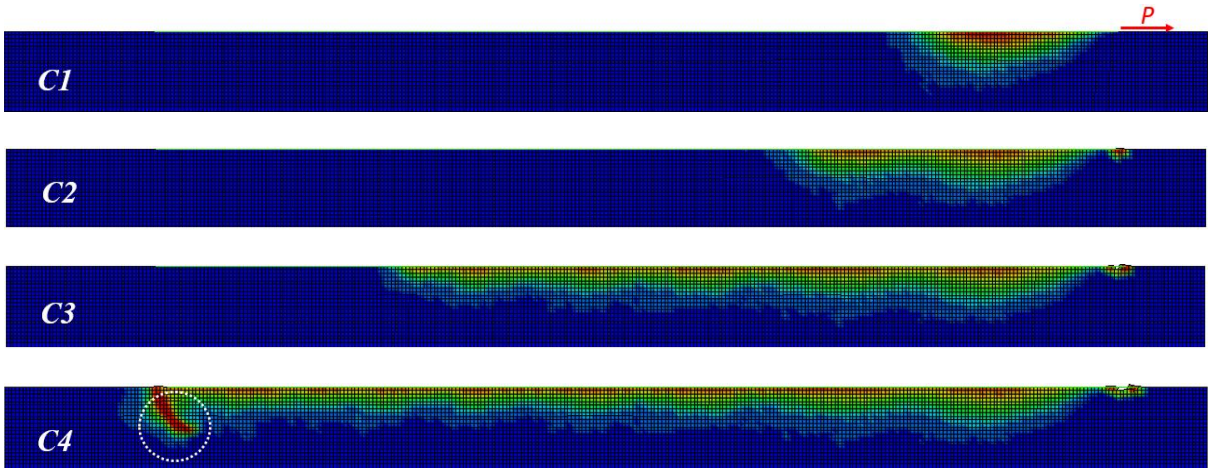

(c) C20_8.0 m/s

Figure 7-5. Cracking patterns of concrete under different loading rates

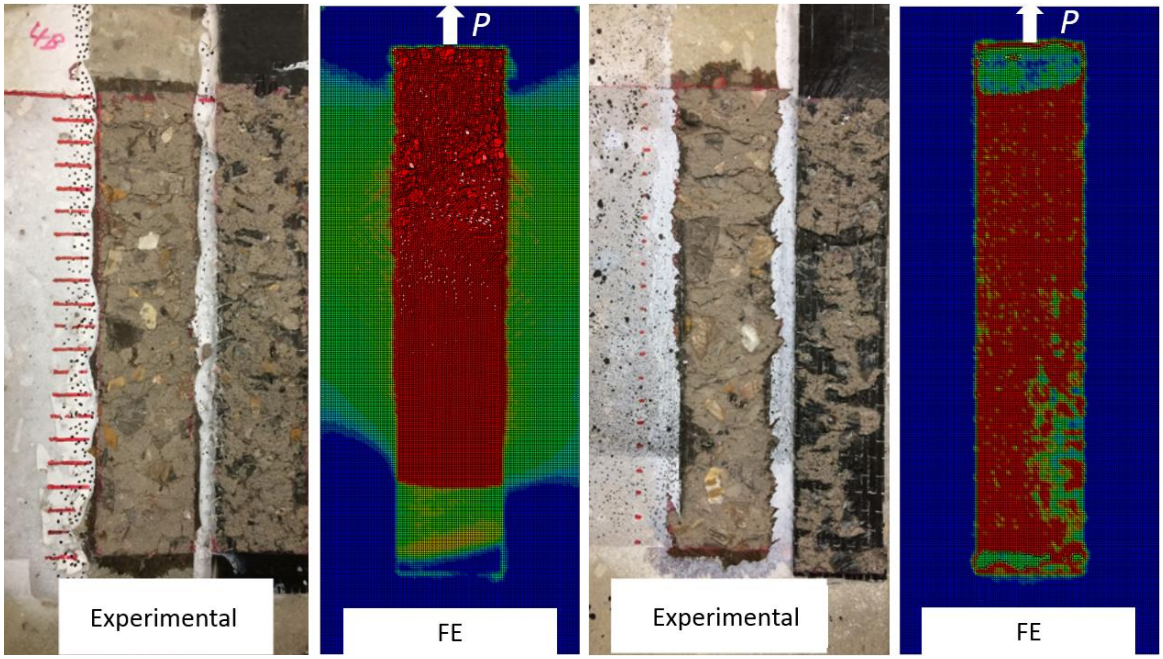

(a) *(b)*

Figure 7-6. Typical failure modes of FRP-to-concrete with C40 derived from tests (242) and FEM: (a) Quasi-static; (b) Dynamic loading rate of 8.0 m/s

As compared with the cracking pattern of Specimen C40_QS-1 under the loading rate of 0.01 m/s, Specimen C40_8_1 has lower cracking depth (i.e. the propagation depth of plastic strain), especially at the loading stages of *A4* and *B4*, indicating that the tensile strength of concrete is enhanced under high strain rate and the fracture surface shifts to the interface as also observed in the experimental tests (232, 242). This is because there is not enough time for the cracks to develop inside the concrete under high loading rate (71, 232). The concrete elements under static loading experience more fracture failure while less concrete elements fail with the

increase of loading rate. As observed in the experimental tests, the combined failure modes including debonding in concrete and debonding in the adhesive-concrete interface can be shown in Figure 7-6. Additionally, the concrete strength (i.e. C40 vs. C20) also has a significant effect on the cracking pattern of concrete and the depth of concrete fracture failure. As shown in the loading stages of *B4* and *C4* in Figure 7-5, the lower strength concrete (i.e. C20) experience the deeper concrete fracture failure. In general, the damage contours derived from FEM are in agreement with the testing results due to the similar failure modes as shown in Figure 7-6.

7.2.2 Distribution of FRP strain

Figure 7-7 shows the axial strain of the FRP sheets obtained from the FEM with those from the experimental results. Four different loading stages as shown in Figure 7-7, i.e. P_{u1}, P_{u2}, P_{u3} and P_{u4} shown in the legend after the initial debonding stage are selected for comparison. Generally, the predicted FRP strain by FEM is close to the testing results. The strain profiles at different loading stages exhibit a similar shape during the debonding process. The ultimate debonding strain increases remarkably with the rising loading rates, indicating that the debonding strain is sensitive to strain rate. Figure 7-7 (f) shows the comparisons between the FEM and testing results of FRP ultimate debonding strain. The FEM results agree well with the testing data with the low standard deviation of 0.07 and coefficient of variation of 7.47%. It is also observed that the axial strain distributions in FRP during the entire debonding process are non-uniform (i.e. discrete distributions of strain) for the testing results while the FEM gives predictions with smoother curves in general.

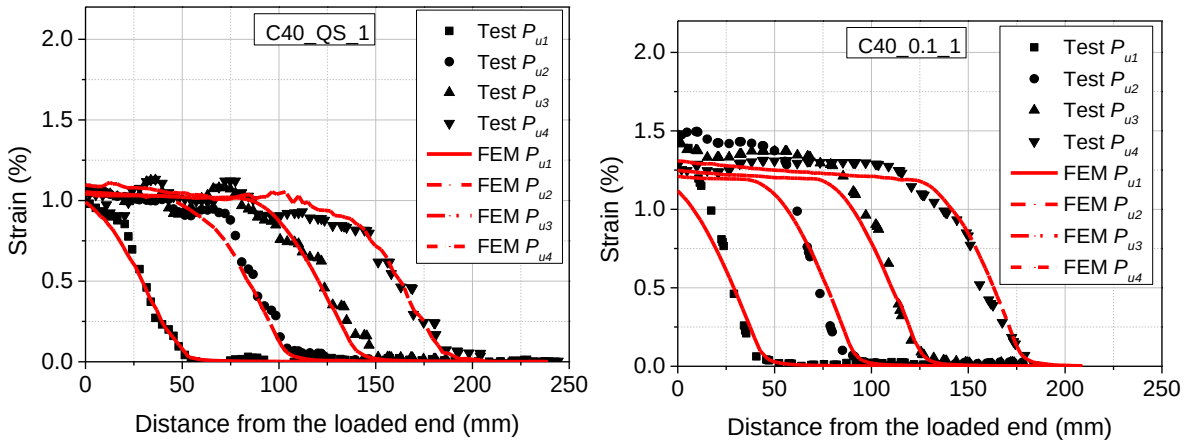

(a) QS *(b) 0.1 m/s*

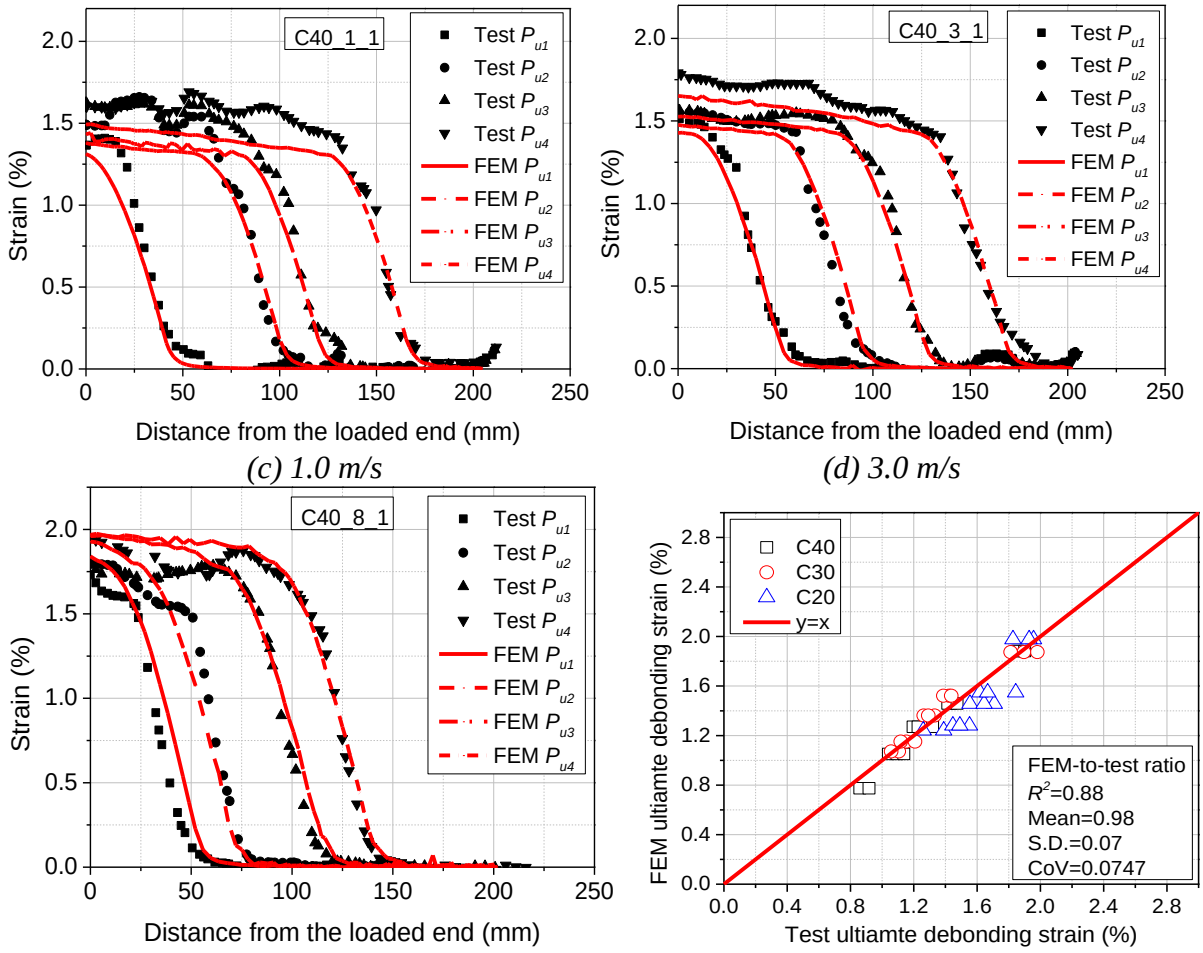

(c) 1.0 m/s *(d) 3.0 m/s*

(e) 8.0 m/s *(f) Comparison between FEM and test*

Figure 7-7. Comparisons between FRP strain distributions obtained from experimental results (242) and FE results on Specimen C40

In addition, the strain contours of the debonding process are obtained from the FE model and compared with the testing results, as shown in Figure 7-8. As digital image correlation (DIC) technique was employed to measure the FRP strain in the experimental tests, five loading stages of FRP strain contours are selected from the experimental tests and FEM for comparison. It is observed that the mean strain contours include four colours, i.e. red, yellow, green and blue. The red and blue colours refer to the maximum and minimum strain, respectively. The area in the red color represents the region where the debonding has occurred and FRP has reached the ultimate debonding strain. The colors of yellow and green refer to the stress transition zone while the blue region represents the approximate non-stress transfer zone.

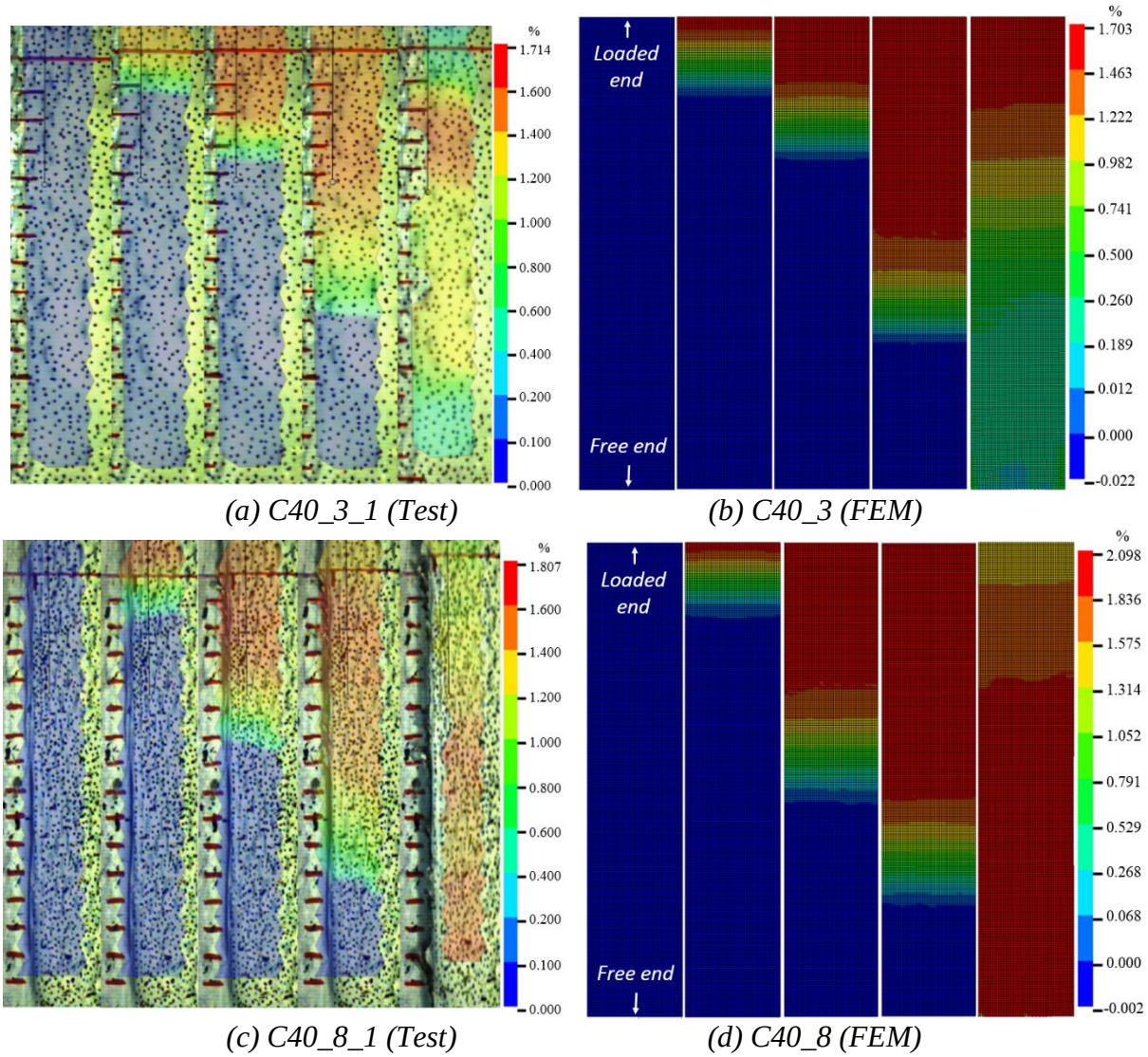

(a) C40_3_1 (Test) *(b) C40_3 (FEM)*

(c) C40_8_1 (Test) *(d) C40_8 (FEM)*

Figure 7-8. FRP mean strain contours from tests (242) and FEM

Figure 7-9 shows the failure modes of concrete under different loading rates. Four loading stages (i.e. A_i and B_i) are selected as the reference for comparison. For the static loading as shown in Figure 7-9 (a), the shear strain develops to the unbonded area on the left and right sides (i.e. circled in white) with the increase of applied load and the destruction of a wide range of concrete elements (i.e. the red region) in the bonded area is observed. On the other hand, under dynamic loads, the strain distribution in the unbonded region (i.e. the green region) is not observed, indicating that the failure of FRP-to-concrete interface is more localized under dynamic loads than that under static loads. The induced interfacial shear stress seeks weaker and longer stress paths under static loads but it usually propagates in straighter paths under dynamic loads. Meanwhile, the width ratio factor (β_w) between FRP and concrete was considered for the stress redistribution under static loads. There is a consistent finding that the interfacial shear deformation causes stresses not only on the concrete within the bonded area

but also the surrounding concrete (i.e. the green region as shown in Figure 7-9) outside the bonded area (96, 198) under static loads. However, it is observed that the effect of width ratio has barely effect on the dynamic results due to more significant stress localization. It can be concluded that the effects of the width ratio between FRP and concrete on bonding behaviour under static and dynamic loads are different and the effect of width ratio under dynamic loads can be neglected based on the FEM results.

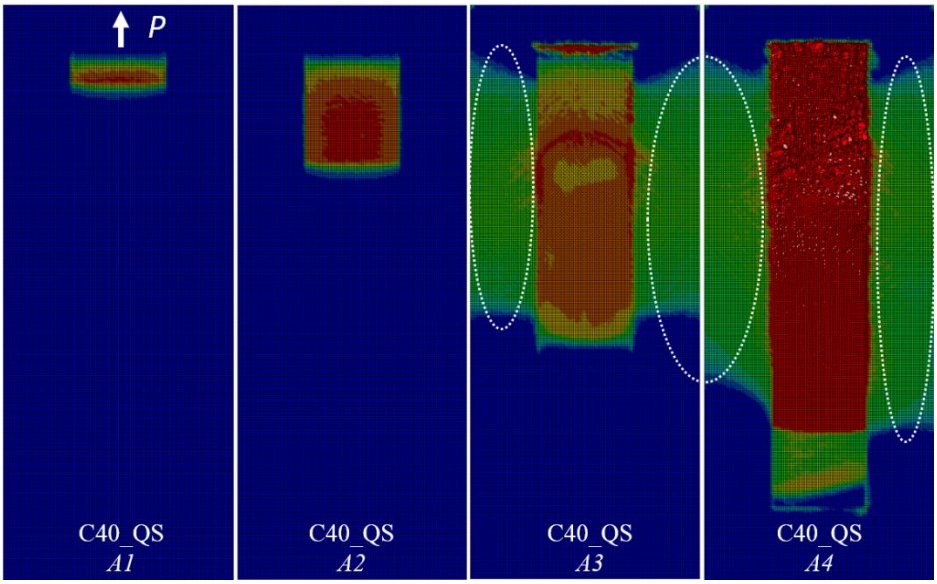

(a) C40 QS

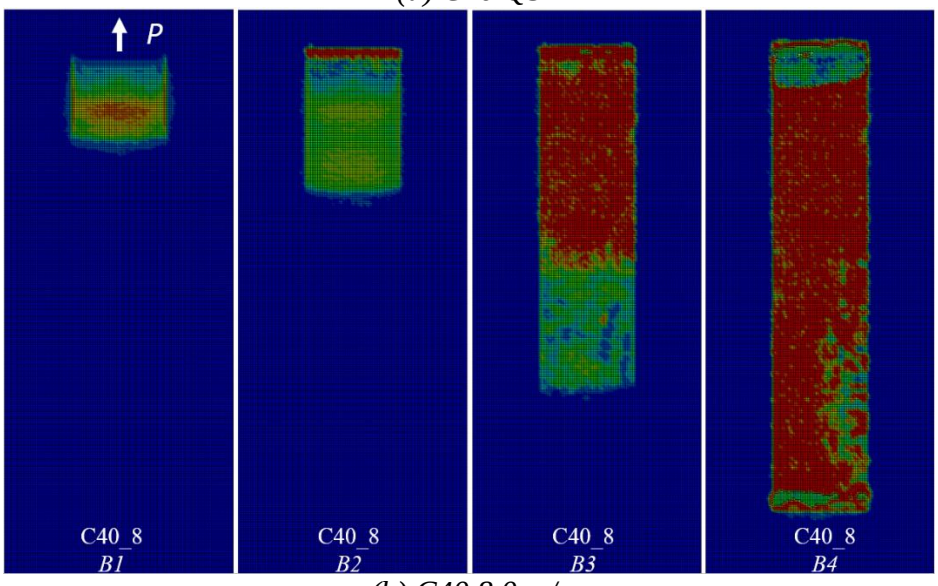

(b) C40 8.0 m/s

Figure 7-9. Plastic strain contours in concrete from FEM results

7.2.3 Shear stress distributions

Figure 7-10 shows the interfacial shear stress distributions along the bonded area obtained from the FEM and experimental results. The general tendency of the interfacial shear stress

distribution obtained from the FEM is in good agreement with the experimental results due to the low standard deviation of 0.07 and coefficient of variation of 7.56% as shown in Figure 7-10 (f). It is found that the peak shear stress is maintained at an approximately constant value during the course of debonding propagation. Both the testing and FEM results found that the interfacial peak shear stress is sensitive to strain rate and the peak shear stress increases remarkably under dynamic loading. The enhancement of the interfacial shear stress should be caused by the enhanced shear resistance due to the improved tensile strength of concrete under dynamic loads. As shown in Figure 7-5 and Figure 7-9, the cracking pattern of concrete under the dynamic loading speed of 8.0 m/s shows a relatively shallow cracking depth as compared to the static results, which is also due to the enhanced tensile strength of concrete under dynamic loads.

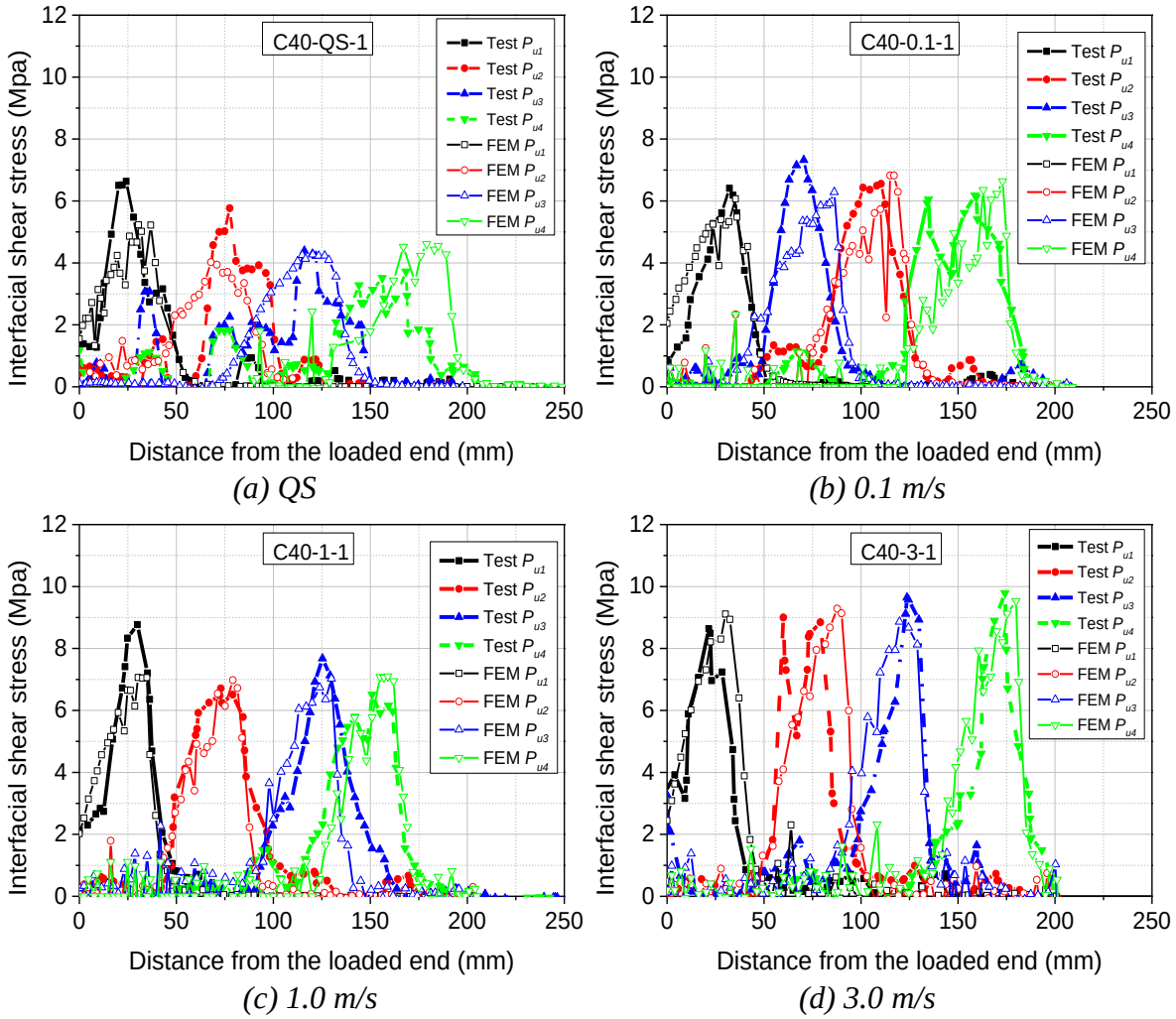

(a) QS *(b) 0.1 m/s*

(c) 1.0 m/s *(d) 3.0 m/s*

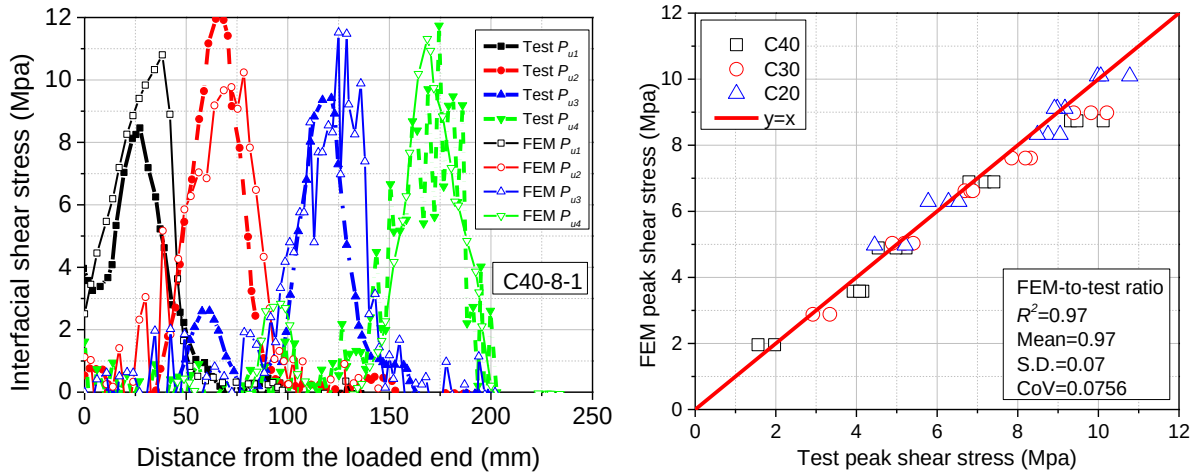

(e) 8.0 m/s *(f) Comparison between FEM and test*

Figure 7-10. Comparisons of interfacial shear stress distributions between experimental results (242) and FEM results

7.2.4 Bond-slip response

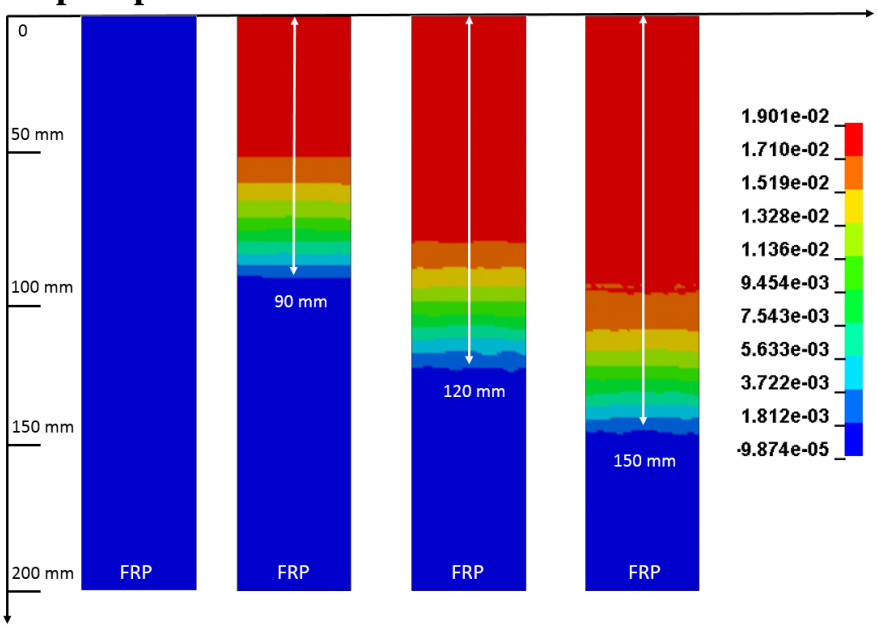

Figure 7-11. Strain distributions at 90 mm, 120 mm and 150 mm of Specimen C40 8.0 m/s

The distance of 90 mm, 120 mm and 150 mm refers to the strain distribution over the entire bonding length as shown in Figure 7-11. These strain distributions at the distance, i.e. 90 mm, 120 mm and 150 mm from the load end are selected to derive the bond-slip relationship by using the formulae of $\tau(x) = E_f t_f \frac{d\varepsilon}{dx}$ and $s(x) = \int \varepsilon dx$ (35, 126, 197, 223), where ε is the axial strain of FRP sheets and $d\varepsilon/dx$ is the strain gradient. Figure 7-12 shows the comparisons between the numerical and experimental results of the bond-slip curves. As can be seen that the FEM results match well with the testing results and both the results show that the peak

shear stress increases with loading rate, indicating that the bond-slip responses are strain-rate dependent.

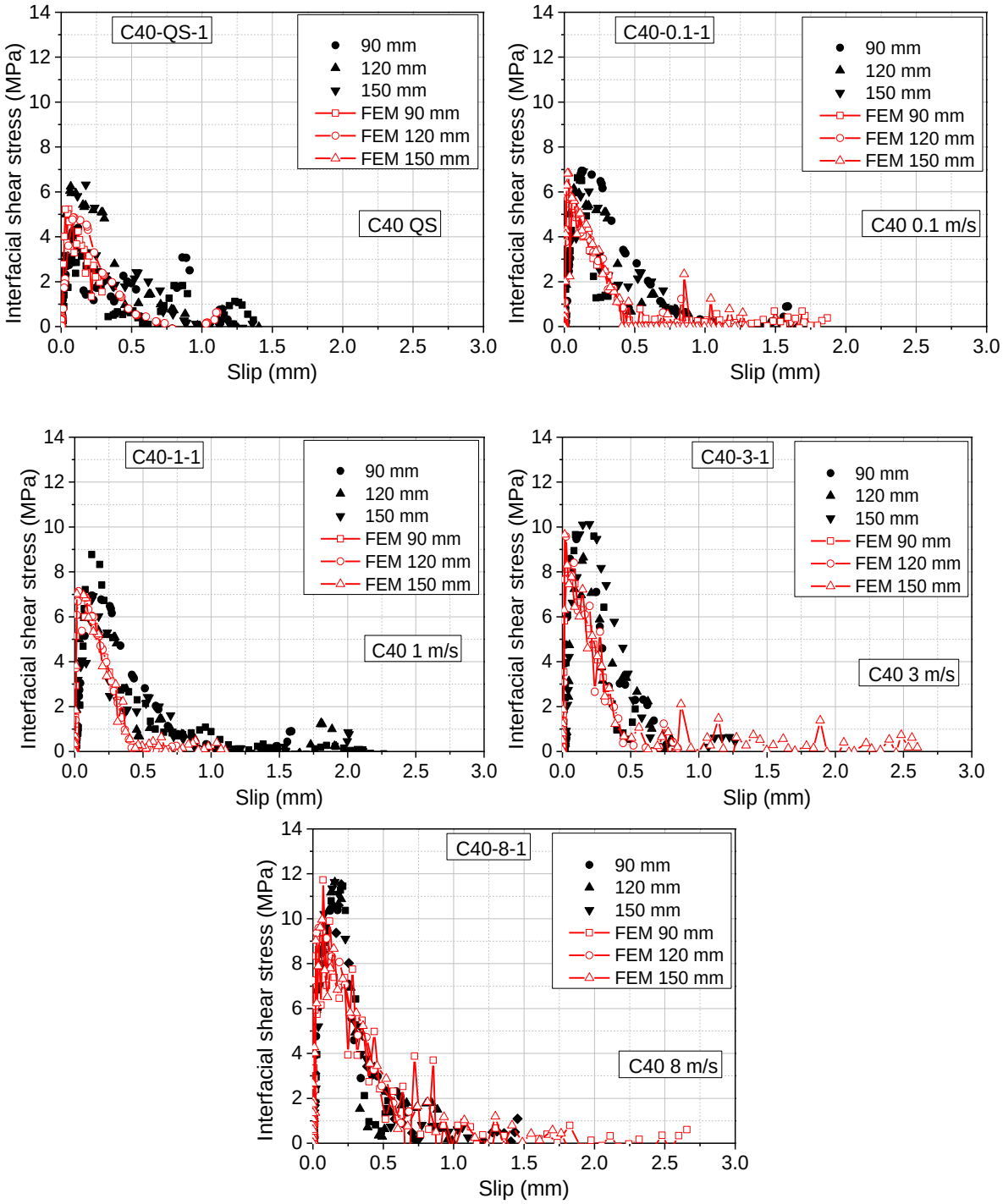

Figure 7-12. Experimental (242) and FEM bond-slip curves

7.3 Analytical study

7.3.1 Dynamic bond strength model

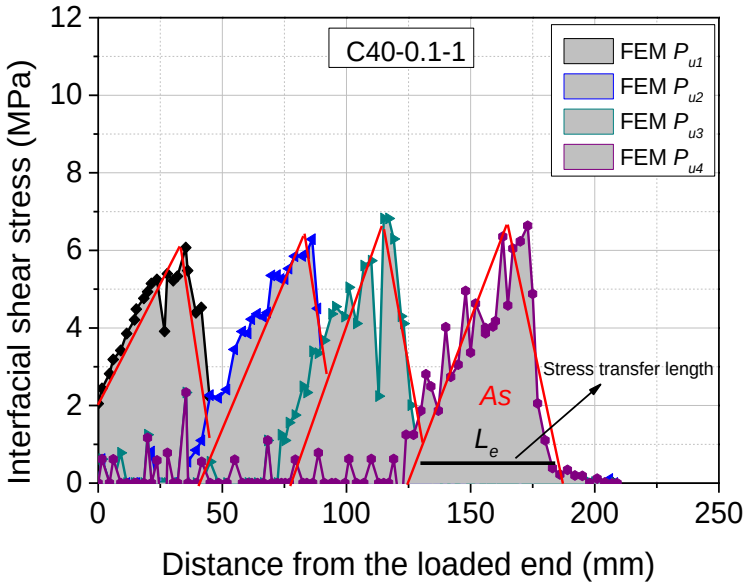

Figure 7-13. Shear stress block A_s *and active stress transfer length*

A semi-empirical model of bond strength has been proposed by the authors (242) based on the interfacial fracture energy. It should be noted that the estimation of the interfacial fracture energy is based on the filtered testing strain profiles, which requires more calculation and might sacrifice the accuracy of the prediction of the bond strength. Additionally, the new finding from the FEM results of this section has shown that the width ratio effect is marginal under dynamic loads. Furthermore, the analytical model incorporating the strain rate effect can be barely found in the literature. Therefore, to avoid possible errors induced by data processing, the dynamic bond strength is derived based on the ultimate debonding strain without curve filtering. The ultimate debonding strain can be obtained by using a newly proposed model based on more uniform and consistent shear stress block from the FEM, which has incorporated the dynamic increase factor and strain rate. It should be noted that since the strain of concrete cannot be directly measured and debonding always initiates inside the concrete substrate beneath the FRP sheet, the strain rate experienced by concrete is derived from the measured FRP strain rate. Therefore, the prediction of the dynamic strength of concrete is based on the strain rate derived from FRP sheets and the strain rate for all the following formulae ranges from $2.5E^{-5}$ s^{-1} to 175 s^{-1}.

The debonding load P_u can be obtained by the following equation:

$$P_u = E_f t_f b_f \varepsilon_{f,d} \tag{7-5}$$

The FRP axial strain can be determined by Equation (7-6) as follows:

$$\varepsilon_{f,d} = \frac{b_f \int_0^{L_e} \tau ds}{E_f t_f b_f} = \frac{A_s}{E_f t_f} \tag{7-6}$$

where $\varepsilon_{f,d}$ is the FRP axial strain, τ is the interfacial shear stress, A_s is the net area of shear stress transfer zone and L_e is the shear stress transfer length which is also known as the effective bond length (EBL) as shown in Figure 7-13, and E_f, t_f, and b_f are the elastic modulus, thickness, and width of FRP sheets, respectively. EBL can be obtained from the distance between two points belonging to the ascending and descending branches, at which shear stress is 10% of the peak shear stress (91, 243). The net area of the active shear stress transfer zone can be obtained by integrating the shear stress block (grey area). For simplification, the shear stress block is fitted to a triangle (red curves). The height of the stress block is the peak shear stress τ_m and the length is defined as the EBL (L_e). Therefore, the net area can be expressed as:

$$A_s \approx \frac{1}{2} L_e \tau_m \tag{7-7}$$

Based on the experimental and FE results, the effective bond length L_e decreases with the increasing strain rate, which is consistent with the previous studies (41, 74). A widely accepted effective bond length model is adopted (4) and the effect of strain rate is also incorporated into this model to obtain more accurate results. The EBL (L_e) can be expressed as follows:

$$L_e = \sqrt{\frac{E_f t_f}{0.41\sqrt{CDIF \cdot f_{c,s}}}} \tag{7-8}$$

The static peak shear stress ($\tau_{m,s}$) and dynamic peak shear stress ($\tau_{m,d}$) can be obtained by using bond-slip models proposed by the author (242). Width ratio effect is not considered under dynamic loads due to its marginal effect on the interfacial bond and the expressions can be expressed as follows:

$$\tau_{m,s} = 0.23(f_a)^{0.53} \beta_w \sqrt{f_{t,s}} \tag{7-9}$$

$$\tau_{m,d} = 0.23(f_a)^{0.53} \sqrt{TDIF \cdot f_{t,s}} \tag{7-10}$$

in which $\tau_{m,s}$ and $\tau_{m,d}$ is the peak shear stress under static and dynamic loads, respectively, f_a is the rupture strength of adhesive, β_w is the width ratio between FRP and concrete, $f_{t,s}$ is the static tensile strength of concrete, and *CDIF* and *TDIF* are the dynamic increase factor in compression and tension, respectively, which can be expressed by Equations (7-3) and (7-4).

The width ratio between FRP and concrete is an important factor determining the interfacial bond under static loads. A comprehensive model proposed by Wu and He (96) is employed in this chapter to determine the width ratio β_w as follows:

$$\beta_w = 1 + \left(f_{c,s}\right)^{0.385}\left[8\left(E_f t_f\right)^{-0.25} + 0.001\right]\left(1 - b_f / b_c\right)^{0.61} / \left(1 + 0.01 b_f^{1.5}\right) \quad (7\text{-}11)$$

By substituting Equations (7-9) and (7-10) into Equation (7-6), the proposed ultimate debonding strain equation of the FRP-to-concrete interface by incorporating the effect of strain rate can be given as follows:

$$\varepsilon_{f,s} = 0.18 f_a^{0.53} \beta_w \sqrt{\frac{f_{t,s}}{E_f t_f \sqrt{f_{c,s}}}} \quad (7\text{-}12)$$

$$\varepsilon_{f,d} = 0.18 f_a^{0.53} \sqrt{\frac{TDIF \cdot f_{t,s}}{E_f t_f \sqrt{CDIF \cdot f_{c,s}}}} \quad (7\text{-}13)$$

By substituting Equations (7-12) and (7-13) into Equation (7-5), the debonding load under static and dynamic loads can be obtained by the following equations:

$$P_{u,s} = 0.18 f_a^{0.53} b_f \beta_w \sqrt{\frac{E_f t_f f_{t,s}}{\sqrt{f_{c,s}}}} \quad (7\text{-}14)$$

$$P_{u,d} = 0.12 f_a^{0.53} b_f \sqrt{\frac{E_f t_f \cdot TDIF \cdot f_{t,s}}{\sqrt{CDIF \cdot f_{c,s}}}} \quad (7\text{-}15)$$

where $\varepsilon_{f,s}$ and $\varepsilon_{f,d}$ refer to the static and dynamic ultimate debonding strain, respectively, and $P_{u,s}$ and $P_{u,d}$ represent the static and dynamic debonding loads, respectively.

7.3.2 Model validation

To validate the accuracy of the proposed model, a total of 77 FRP-to-concrete joints with varied values including the strain rates, concrete strength, FRP stiffness ($E_f t_f$) and rupture strength of adhesive (f_a) are collected from the previous studies (41, 74), as summarized in Table 7-2. Figure 7-14 shows the comparisons between analytical results and testing results. It is observed that the results obtained from the proposed model are in agreement with those of tests by demonstrating a mean ratio (FEM-to-test) of 1.09 and a low coefficient of variation of 18%.

Overall, these results indicate that the proposed semi-empirical model can well predict the ultimate debonding strain and debonding load under both static and dynamic loading conditions.

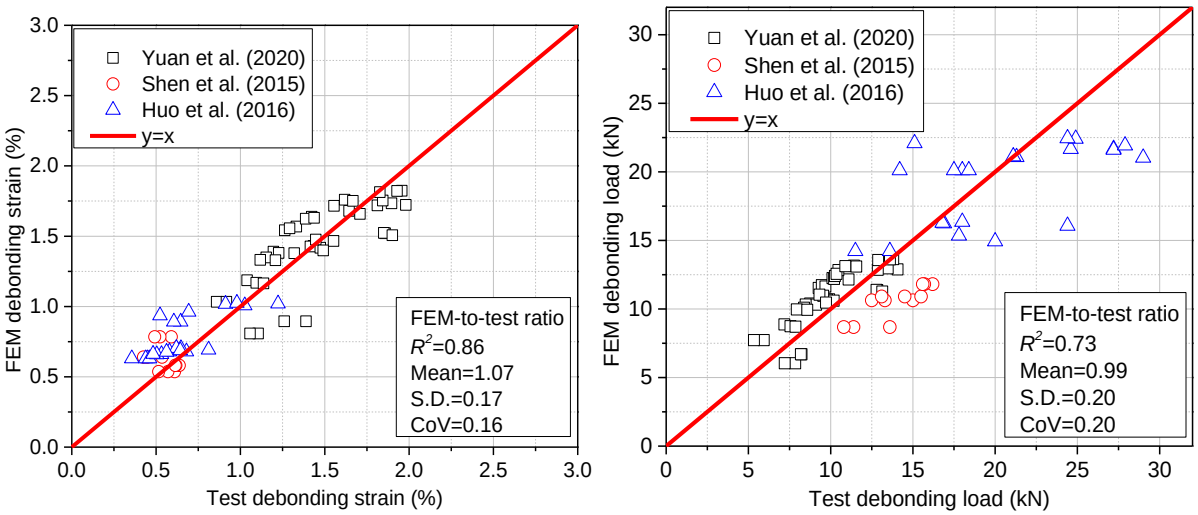

(a) *(b)*

Figure 7-14. Comparisons between analytical and experimental results: (a) Debonding strain; (b) Debonding load

Table 7-2. Comparison of results from tests and FEM.

Data source	Specimen ID	Strain rate (s^{-1})	E_f (GPa)	t_f (mm)	b_f (mm)	f_c (MPa)	f_t (MPa)	Test		Semi-empirical model	
								$P_{u,e}$ (kN)	$\varepsilon_{u,e}$ (%)	$P_{u,a}$ (kN)	$\varepsilon_{u,a}$ (%)
Shen et al. (41)	L200-D0-1	6.10E-04	105	0.484	50	32.8	2.62	11.4	0.449	8.68	0.427
	L200-D0-2	6.10E-04	105	0.484	50	32.8	2.62	10.8	0.425	8.68	0.427
	L200-D0-3	6.10E-04	105	0.484	50	32.8	2.62	13.6	0.535	8.68	0.427
	L200-D1-1	6.10E-03	105	0.484	50	32.8	3.89	15.0	0.590	10.63	0.523
	L200-D1-2	6.10E-03	105	0.484	50	32.8	3.89	13.3	0.523	10.63	0.523
	L200-D1-3	6.10E-03	105	0.484	50	32.8	3.89	12.5	0.492	10.63	0.523
	L200-D2-1	0.047	105	0.484	50	32.8	4.49	15.5	0.610	10.91	0.537
	L200-D2-2	0.047	105	0.484	50	32.8	4.49	14.5	0.571	10.91	0.537
	L200-D2-3	0.047	105	0.484	50	32.8	4.49	13.1	0.516	10.91	0.537
	L200-D3-1	0.63	105	0.484	50	32.8	5.26	16.2	0.638	11.81	0.581
	L200-D3-2	0.63	105	0.484	50	32.8	5.26	15.7	0.618	11.81	0.581
	L200-D3-3	0.63	105	0.484	50	32.8	5.26	15.6	0.614	11.81	0.581
Huo et al. (74)	C50-1-S-1	1.00E-05	236	0.169	50	35.2	2.85	13.6	0.646	14.22	0.891
	C50-1-S-2	1.00E-05	236	0.169	50	35.2	2.85	11.5	0.605	14.22	0.891
	C50-2-S-1	1.00E-05	236	0.338	50	35.2	2.85	18.0	0.449	20.11	0.630
	C50-2-S-2	1.00E-05	236	0.338	50	35.2	2.85	14.2	0.356	20.11	0.630
	C80-2-S-1	1.00E-05	236	0.338	80	35.2	2.85	17.5	0.438	20.11	0.630
	C80-2-S-2	1.00E-05	236	0.338	80	35.2	2.85	18.4	0.461	20.11	0.630
	C50-1-D200-1	3.12	236	0.338	50	35.2	8.38	15.1	0.811	22.08	0.692
	C50-1-D200-2	2.67	236	0.169	50	35.2	8.1	17.8	0.693	15.35	0.962
	C50-1-D200-3	4.56	236	0.169	50	35.2	9.06	16.9	0.912	16.24	1.018
	C50-1-D400-1	4.10	236	0.169	50	35.2	8.87	24.4	1.026	16.07	1.007
	C50-1-D400-2	4.90	236	0.169	50	35.2	9.19	18.0	0.979	16.35	1.025
	C50-1-D400-3	4.70	236	0.169	50	35.2	9.11	16.8	1.223	16.28	1.021
	C50-2-D200-1	2.09	236	0.169	50	35.2	7.66	20.0	0.523	14.93	0.936
	C50-2-D200-2	2.05	236	0.338	50	35.2	7.63	21.3	0.532	21.07	0.660
	C50-2-D200-3	2.62	236	0.338	50	35.2	8.07	27.2	0.680	21.67	0.679
	C50-2-D400-1	2.63	236	0.338	50	35.2	8.07	24.6	0.579	21.67	0.679
	C50-2-D400-2	3.13	236	0.338	50	35.2	8.39	33.1	0.626	22.10	0.693
	C50-2-D400-3	2.02	236	0.338	50	35.2	7.6	29.0	0.504	21.03	0.659
	C50-2-D600-2	3.59	236	0.338	50	35.2	8.63	24.9	0.647	22.41	0.702
	C50-2-D600-2	3.65	236	0.338	50	35.2	8.66	24.4	0.620	22.45	0.704
	C80-2-D400-1	2.55	236	0.338	80	35.2	8.02	27.2	0.562	21.60	0.677
	C80-2-D400-1	2.92	236	0.338	80	35.2	8.26	27.9	0.643	21.93	0.687
	C80-2-D400-1	2.10	236	0.338	80	35.2	7.67	21.1	0.482	21.13	0.662

7.4 Summary

In this chapter, the 3D FE model of a single shear test is built for simulating dynamic bond behaviour of the FRP-to-concrete interface by using LS-DYNA. A bond-slip model is incorporated into the modelling of the interfacial bond between FRP and concrete. To validate the accuracy of the numerical model, the experimental results from 42 dynamic single shear tests on FRP-concrete joints are employed. The numerical debonding load and shear slip responses, FRP strain distributions, and interfacial bond-slip responses are compared with the experimental results. Additionally, a semi-empirical model for predicting ultimate debonding strain and bond strength is also proposed based on the shear stress obtained from the numerical results and a total of 119 tests are collected from the database for model validation. The findings can be summarized as follows:

1. The damage modes under static and dynamic loads are different in terms of the cracking patterns of concrete. The numerical model can well predict the damage mode of FRP-concrete joints and describe the progressive debonding process and the stress/strain distributions.
2. The load-slip curves, FRP strain distributions, and bond-slip curves of FRP-concrete joints under various loading rates can be well predicted by the proposed FE model.
3. The numerical model of interfacial bonding between FRP and concrete under various strain rates has been well verified with the testing data. The verified numerical model of interfacial bonding can be used to predict the behaviors of structural components strengthened by the FRP sheet under dynamic loads.
4. A semi-empirical model of dynamic debonding strength based on FRP debonding strain is proposed to predict the debonding loads by incorporating dynamic increase factor of concrete. By comparing the predicted results and testing results, the proposed model can give sound predictions on the ultimate debonding strain and debonding loads.

Chapter 8. Enhanced bond performance by using new epoxy anchor

8.1 Introduction

To enhance the interfacial bond strength between basalt fibre reinforced polymer (BFRP) sheets and concrete, a new epoxy anchor is proposed in this chapter. Epoxy anchors are formed by drilling holes into the concrete substrate before applying epoxy resin. The depth and diameter of epoxy anchors are designed to enhance the cohesive strength of the interface. A bond strength model by incorporating the effects of strain energy and bonding area of epoxy resin is proposed to analyse the effect of anchorage.

The related work in this chapter has been published in Construction and Building Materials.

Yuan C, Chen W, Pham TM, Hao H, Chen L, Zhang M. New Epoxy Anchor for Better Bonding between FRP Sheets and Concrete. Construction and Building Materials. 2020; 248:118628.

8.2 Epoxy anchor

Figure 8-1 (a) illustrates the sketch of the proposed epoxy anchors. Epoxy anchors are cured as hardened epoxy resin in the concrete pre-drilled holes. The interfacial bond strength can be enhanced by the epoxy bonding and interlocking action between epoxy and concrete. The preparation of the epoxy anchors included drilling the designed holes on the concrete block by using a hammer drill as shown in Figure 8-1 (b), then filling the holes with epoxy resin as shown in Figure 8-1 (c), and finally bonding BFRP sheets. Prior to preparing epoxy anchor, the concrete substrates were roughened by a needle scaler to remove the weak layer of mortar. The epoxy anchors used in this chapter had various diameters (d_i) of 6 mm, 10 mm, and 15 mm. The embedment depth (d_e) of the anchor was kept unchanged and set as 20 mm, which was less than the thickness of the concrete cover. The distance between anchors (L_e) was set as 40 mm, which was less than the effective bond length (i.e. 50 mm in this chapter). The FRP composite was formed by three layers of BFRP sheets to avoid FRP rupture upon loading. This epoxy anchorage system was proposed to (a) enhance the cracking-resistance of the concrete substrate; (b) eliminate or delay the interfacial cracking; and (c) increase the effective interfacial shear stress transfer length.

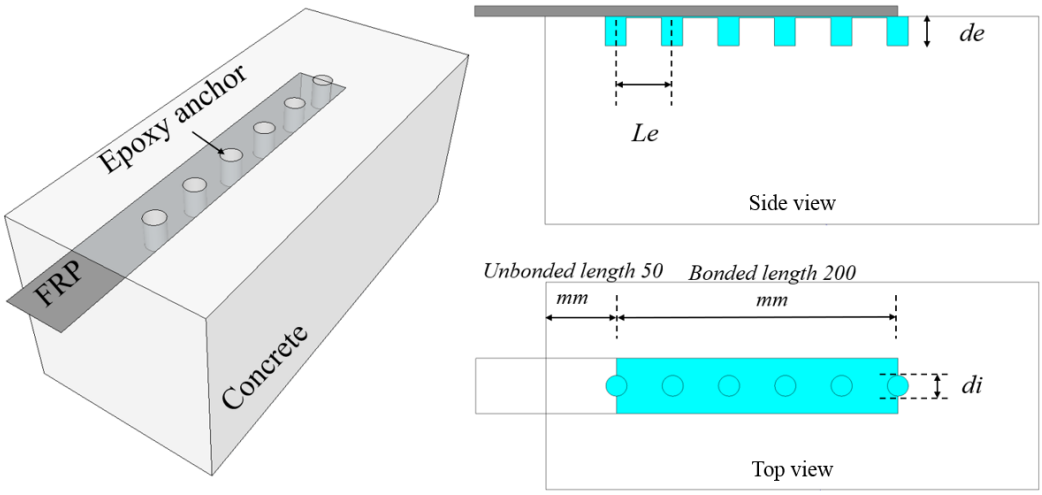

(a) Epoxy anchor: (L) 3D view; (R) 2D view

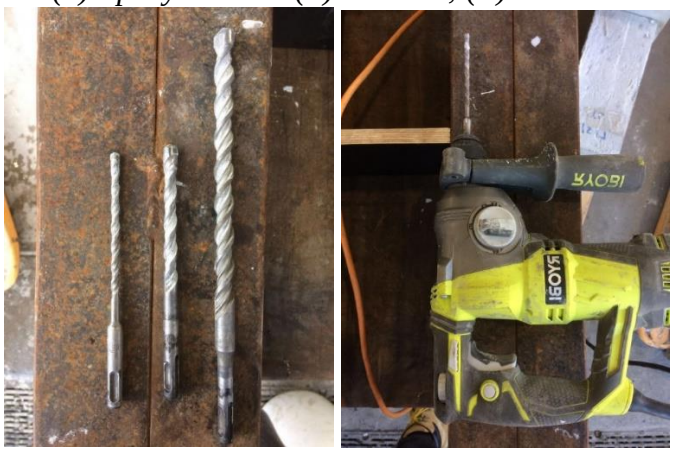

(b) Hammer drill

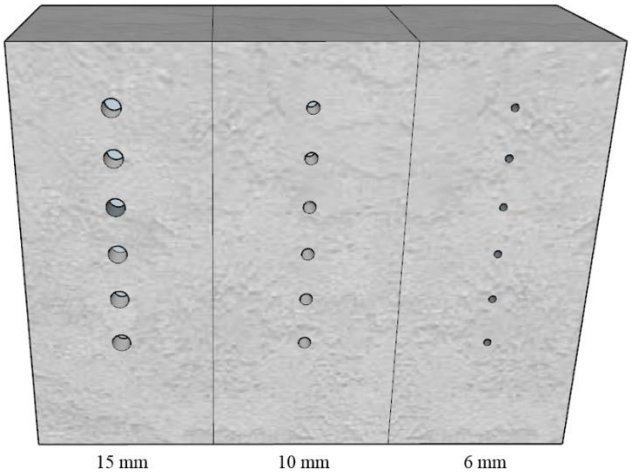

(c) Preparation of concrete surface and holes

Figure 8-1. Epoxy anchor

8.3 Material properties

A total of 21 single-lap shear specimens were prepared in this chapter. Concrete blocks with 150 x 150 x 350 mm^3 in dimensions were prepared as substrates. The maximum coarse

aggregate size was 20 mm in the concrete mix. The compressive strength and split tensile strength of the concrete substrates was 40 MPa and 3.90 MPa, respectively. Please refer to chapter 3.2.1 for material properties. The specimen details and testing schemes are summarized in Table 8-1. Figure 8-2 plots the sketch of the tested specimens, which consider various sizes and numbers of epoxy anchors. The specimen with epoxy anchors was labelled as "*DX-Y-n*". The letter, *DX*, represents the diameter of the anchor (i.e. 6 mm, 10 mm, and 15 mm). The letter, *Y*, represents the number of epoxy anchors (i.e. 1, 2, 3, and 6). The letter, *n*, refers to the number of identical specimens (i.e. 1, 2, and 3).

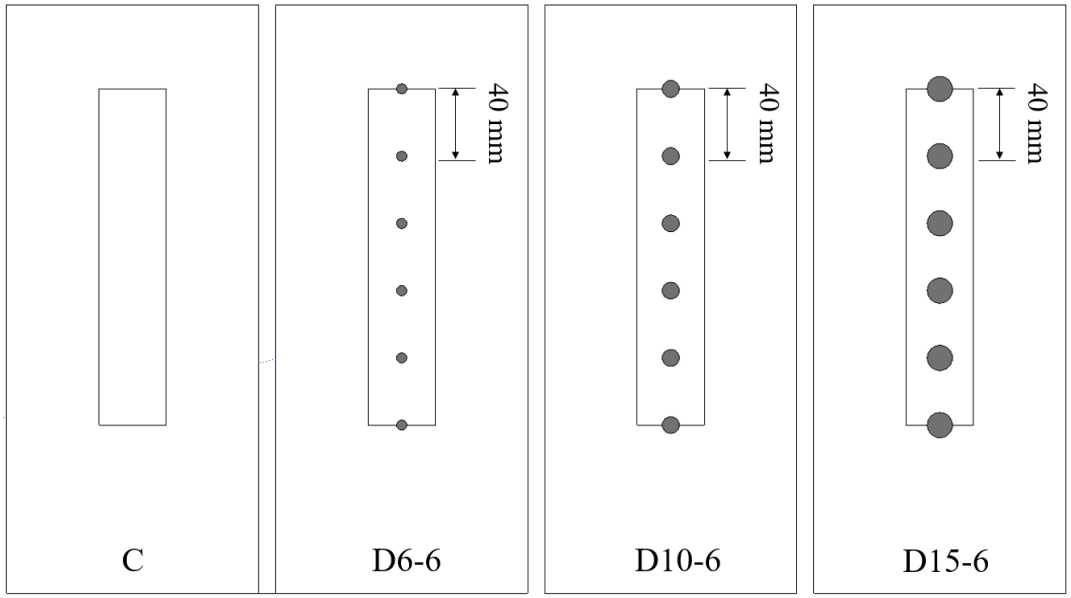

(a) The effect of epoxy anchor size

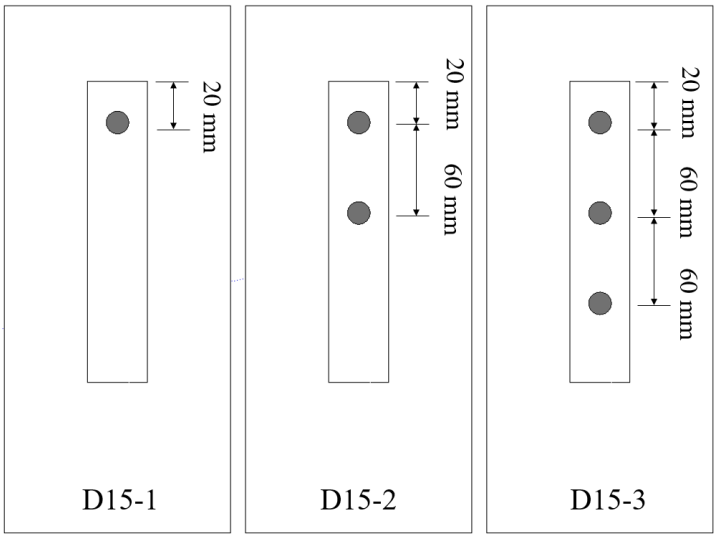

(b) The effect of epoxy anchor number

Figure 8-2. Schematic diagram of epoxy anchor layout

Table 8-1. Specimen details and test results

Specimen ID	d_i (mm)	d_e (mm)	L_d (mm)	P_1 (kN)	P_2 (kN)	P_u (kN)	ε_u (%)	τ_m (MPa)	s_o (mm)	G_f (N/mm)	EC (J)	α (mm)	β (mm)	Failure mode
C-1	/	/	/	11.16	11.16	10.84	0.957	4.21	1.62	1.48	7.24	0.20	17.57	C
C-2	/	/	/	9.08	9.08	10.13	0.981	4.19	1.58	1.31	5.87	0.29	21.31	C
C-3	/	/	/	9.11	9.11	11.02	1.012	4.79	1.35	1.64	7.04	0.28	19.59	C
D6-6-1	6	20	40	9.78	10.62	11.86	1.307	4.50	1.79	1.83	7.82	0.15	14.72	C
D6-6-2	6	20	40	9.02	11.56	11.82	1.287	5.74	1.93	1.78	8.70	0.35	20.00	C
D6-6-3	6	20	40	9.71	13.20	14.46	1.298	4.63	1.97	1.47	7.25	0.17	15.49	C
D10-6-1	10	20	40	10.01	13.50	15.63	1.500	5.60	2.22	2.89	10.06	0.19	14.87	C/CE
D10-6-2	10	20	40	9.92	12.29	13.57	1.675	4.35	2.29	2.32	11.32	0.22	18.21	C/CE
D10-6-3	10	20	40	10.53	13.37	13.63	1.569	6.19	2.35	2.51	12.62	0.34	19.00	C/CE
D15-6-1	15	20	40	10.56	18.50	18.61	1.865	8.21	2.34	4.50	17.63	0.24	13.84	C/CE
D15-6-2	15	20	40	12.80	18.25	19.44	1.843	7.47	2.50	4.76	16.97	0.23	14.21	C/CE
D15-6-3	15	20	40	10.76	17.06	18.73	1.800	7.81	2.48	4.19	14.42	0.25	14.47	C/CE
D15-1-1	15	20	40	8.72	15.24	11.89	1.450	5.34	2.25	/	13.28	/	/	C/CE
D15-1-2	15	20	40	11.37	16.58	11.62	1.571	4.89	2.24	/	13.31	/	/	C/CE
D15-1-3	15	20	40	10.20	15.37	11.17	1.462	5.21	1.89	/	11.75	/	/	C/CE
D15-2-1	15	20	40	10.42	15.08	12.32	1.534	5.19	2.49	/	15.03	/	/	C/CE
D15-2-2	15	20	40	8.74	16.15	10.84	1.549	5.46	2.32	/	15.30	/	/	C/CE
D15-2-3	15	20	40	8.81	15.12	12.11	1.671	5.17	2.27	/	15.11	/	/	C/CE
D15-3-1	15	20	40	8.05	15.20	17.30	1.578	6.11	2.71	/	17.45	/	/	C/CE
D15-3-2	15	20	40	8.89	15.42	14.31	1.645	5.52	2.34	/	14.94	/	/	C/CE
D15-3-3	15	20	40	10.31	15.24	11.90	1.649	6.21	2.26	/	14.75	/	/	C/CE

Note: d_i refers to the diameter of epoxy anchor; d_e represents the embedment depth of epoxy anchor; L_d refers to the spacing of epoxy anchors; P_1 is the load of elastic stage; P_2 represents the load of interfacial hardening stage; P_u is the ultimate debonding load; ε_u is the ultimate debonding strain of BFRP sheet; τ_m is the peak shear stress; s_o refers to the peak slip; G_f is the interfacial fracture energy; EC refers to the energy consumption of the debonding process; α and β refer to the fitting coefficients, and "/" means data not available.

8.4 Experimental program

Please refer to Section 3.2.4 for testing setup details.

8.4.1 Load and slip response

The load-slip curves at the loaded end are plotted in Figure 8-3. It is found that the ultimate debonding load and the ultimate slip increased in general with the diameter of epoxy anchors, indicating that using epoxy anchors enhanced the interfacial bond strength and delayed the debonding process. It can be observed that the load-slip curves of all the specimens changed slightly at approximately 4 kN, indicating that the micro-cracking initiated at the interface. Due to the existence of epoxy anchors, the difference of bonding behaviour was remarkable between the control specimen and the specimen with epoxy anchors. For the control specimens, the

ultimate slip was around 1.60 mm on average. As shown in Figure 8-3 (b-g), the specimens with epoxy anchors experienced hardening behaviour before debonding which showed significantly enhanced ultimate debonding load and shear slip. The epoxy anchors enhanced the load-bearing capacity and ductility of the interface and thus increased the effective utilization of BFRP sheets. The specimens with 15 mm diameter epoxy anchors showed the highest increment in both the bond strength and the ultimate shear slip. For the specimens D-15-3 with three anchors, the debonding load should be constant in the un-anchored area, but one of the test results shows a significant growth trend, which was caused by the thicker layer of adhesive near the last hole. Further, the rupture of epoxy anchors was observed after testing, as shown in Figure 8-4.

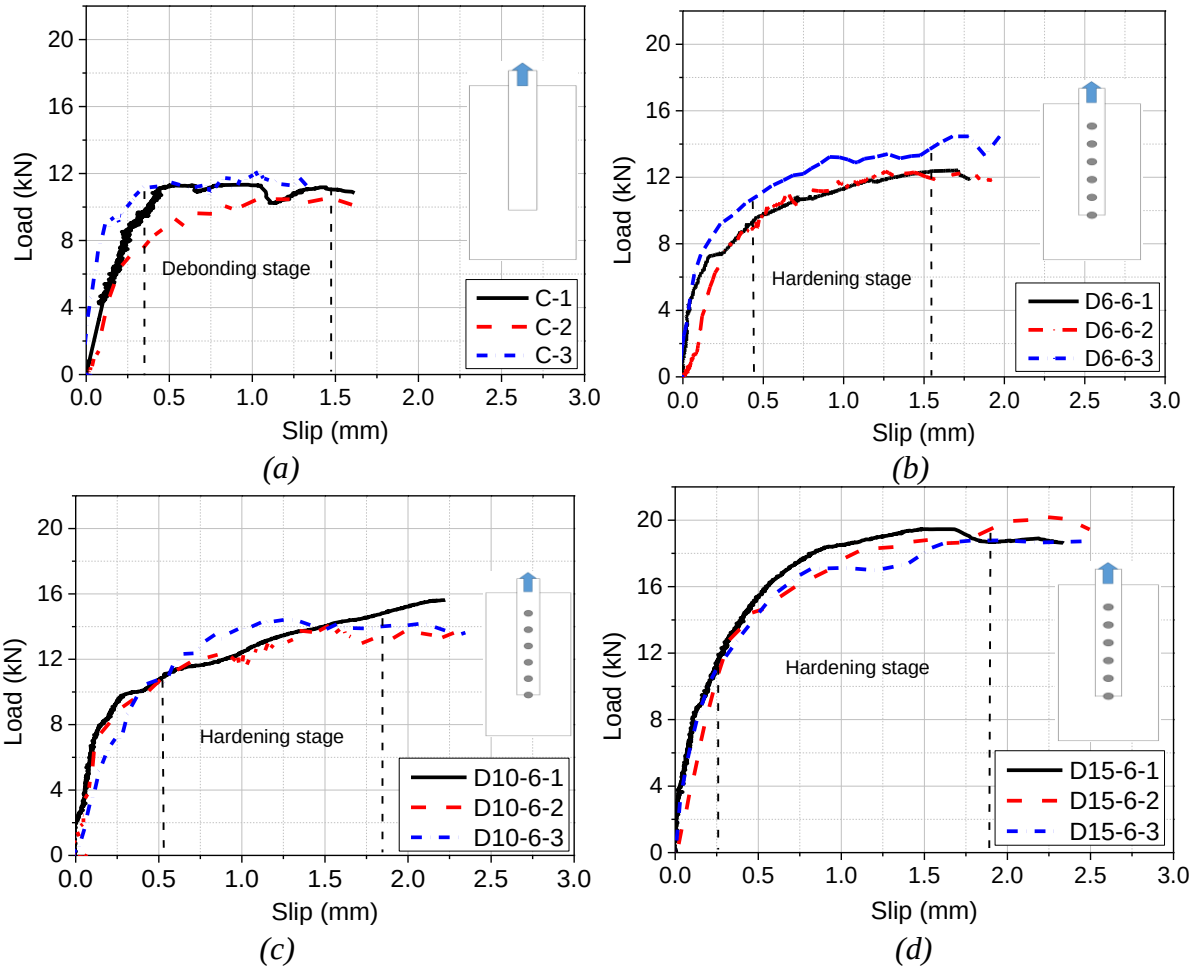

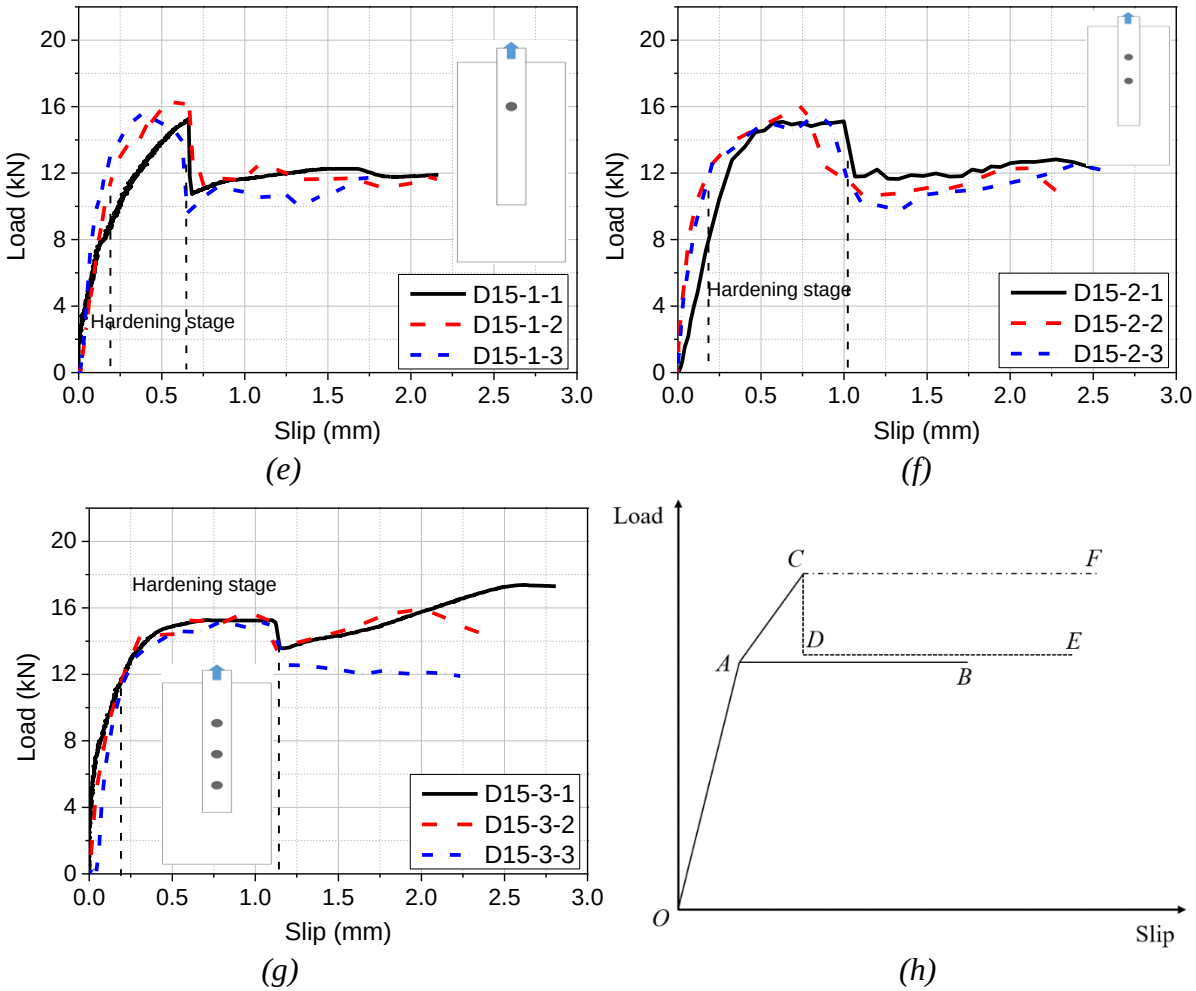

Figure 8-3. Load and slip curves

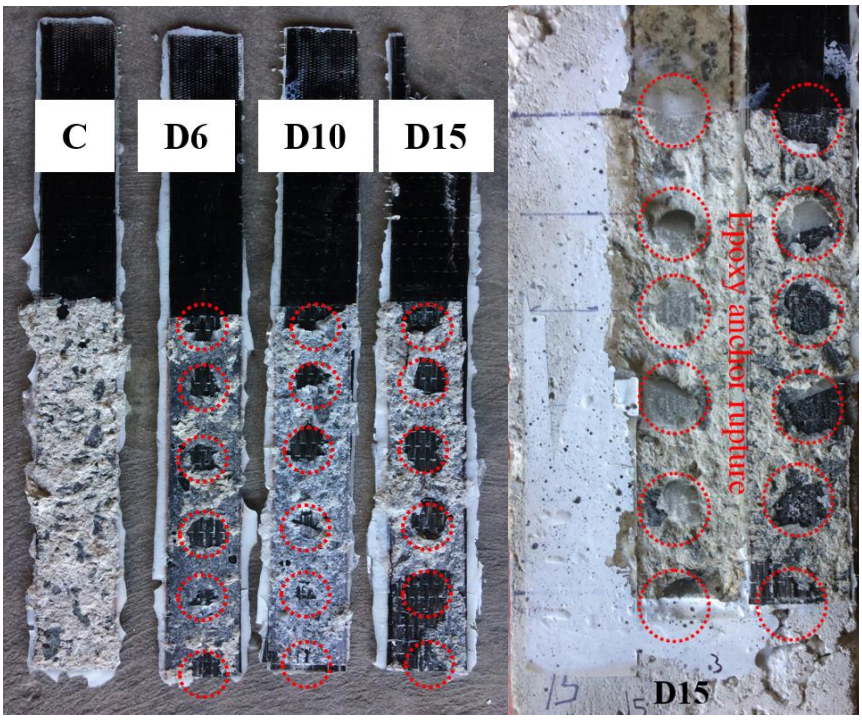

Figure 8-4. Fracture of epoxy anchors

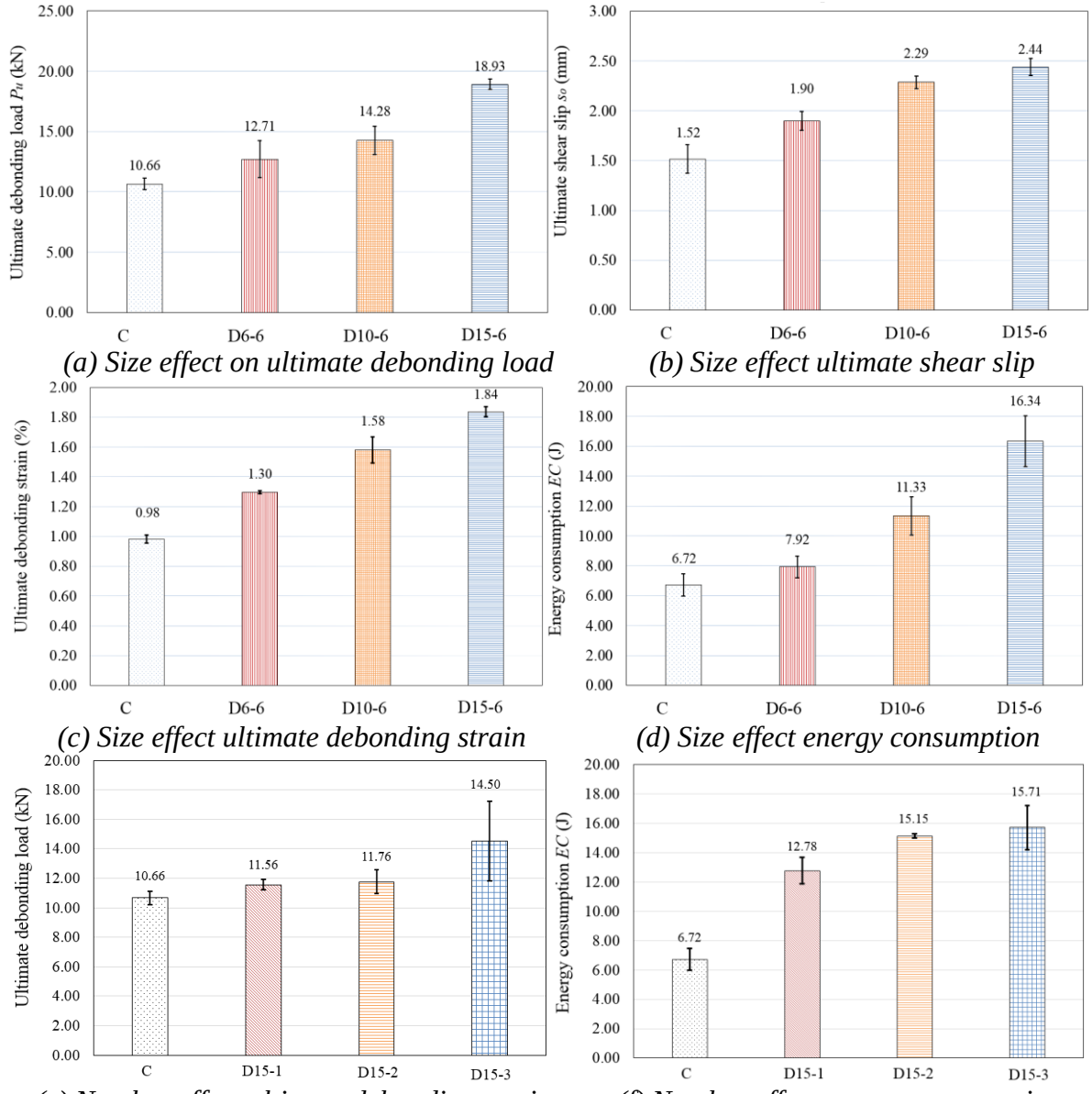

(a) Size effect on ultimate debonding load *(b) Size effect ultimate shear slip*

(c) Size effect ultimate debonding strain *(d) Size effect energy consumption*

(e) Number effect ultimate debonding strain *(f) Number effect energy consumption*

Figure 8-5. Effect of size and number of epoxy anchor on bonding behaviour

To study the effect of the number of epoxy anchors on the bond performance, specimens D15-1 with one epoxy anchor, D15-2 with two epoxy anchors, D15-3 with three epoxy anchors, and D15-6 with six epoxy anchors were tested, the results are shown in Figure 8-3 (e-g), respectively. It can be observed that the specimens with one, two, or three anchors exhibited different load-slip shapes as compared to the specimens with six anchors. The specimens with one, two, or three anchors showed a drop of the debonding load to a level similar to the debonding load of the reference specimen without anchor after the peak load, while the debonding load drop was not observed in specimens D15-6, in which the peak load was maintained up to a slip reaching about 2.5 mm in the test, indicating the greatly improved strength and slip due to sufficient anchors. Figure 8-3 (h) shows the simplified bond and slip

curves proposed in the section based on the observations of test data. A generic load-slip curve for the control group (unanchored) can be expressed by the path O-A-B. The path O-A-C-F represents the generic behaviour of the specimens with sufficient anchors, i.e. six anchors, while the path O-A-C-D-E refers to the generic behaviour of the specimens with insufficient anchors or less than six anchors in this chapter (i.e. D15-1, D15-2 and D15-3). Stage OA refers to the load linearly increase up to the initial debonding load. After Point A, the debonding load of unanchored specimen is a constant determined by the bonding strength of concrete and FRP interface until FRP is fully detached from the concrete prism at Point B. The anchored specimen, however, has an increased debond load-carrying capacity after Point A, with the ultimate debonding load at Point C as shown in the figure. If the specimen has a sufficient number of anchors, the debond load-carrying capacity after Point C remains constant until the final detachment at Point F owing to the total failure of anchors. For the specimen with insufficient number of anchors, the load-carrying capacity drops to Point D and remains constant until the final detachment at Point E. The load level of Point D depends on the number of anchors. If there is only one anchor, the anchor failure makes the interface the same as the case without anchor, the load level then is the same as the reference case. If there is more than one anchor, the load level of Point D is slightly higher than that of the reference specimen. To quantify the enhancement of shear resistance of the anchored BFRP-to-concrete joints, the energy consumption (*EC*) of the BFRP-concrete interface which refers to the enclosed area of the load-slip curve is compared herein. The obtained *EC* is summarized in Table 8-1.

Figure 8-5 shows the effect of using epoxy anchors on the bonding behaviour of the BFRP-to-concrete interface. The general trend of the testing results shows that the average ultimate load, the ultimate shear slip, the ultimate debonding strain and the energy consumption increased remarkably with the diameter of epoxy anchor increasing from 6 mm to 15 mm. As compared to the control group, the increment of 19.23%, 33.89%, and 77.49% was obtained for the ultimate debonding load for specimens D6, D10, and D15, respectively. The ultimate slip increased by 25.05%, 50.77%, and 60.88%, respectively, while the ultimate debonding strain increased by 31.93%, 60.81%, and 86.71% for specimens with anchors of D6, D10, and D15, respectively. By virtue of epoxy anchors, more energy can be absorbed during the debonding process. The maximum energy consumption was 16.34 J and an increment of 143.28% was achieved for the specimens with 15 mm epoxy anchors as compared with the control group. Figure 8-5 (e) and (f) show the effect of the number of anchors on the ultimate debonding load and energy consumption. As shown in the load-slip curves in Figure 8-3, the specimens with

insufficient anchors (i.e. D15-1, D15-2 and D15-3) and sufficient anchors showed similar ultimate debonding load and ultimate debonding strain, implying each anchor acts independently in resisting the debonding. This is because debonding initiates at the loaded end and propagates along with the interface, before debonding reaches the particular anchor, its contribution to resisting debonding is minimum. In general, the testing results showed that the embedded part of epoxy anchors led to a stronger bonding strength on the interface, which means higher strength efficiency of BFRP sheets was utilized.

Figure 8-6 illustrates the typical debonding failure modes after the detachment. The debonding failure initiated in the concrete layer with a flake of concrete pulling out from the concrete substrate. It was found that the thickness of damaged concrete for the specimens with epoxy anchors (e.g. D15-1) was thinner than the control group. The decreased concrete damage thickness was caused by the shifted debonding failure mode. For the control group without any anchors, the shear stress penetrated through the weakest concrete layer and consequently damaged the concrete layer, where the shear stress changed into tensile stress in an angle of 45^{o} (75). Therefore, the debonding initiated on the tensile side of the concrete element. However, for the specimens with epoxy anchors, the cracking resistance of concrete near the epoxy anchors was enhanced and consequently, the debonding failure shifted to the interface between adhesive and concrete. Meanwhile, the fracture of epoxy anchors was observed at the interface between adhesive and concrete, indicating that the embedment depth of 20 mm was sufficient for the epoxy anchors and consequently a strong dowel action was achieved.

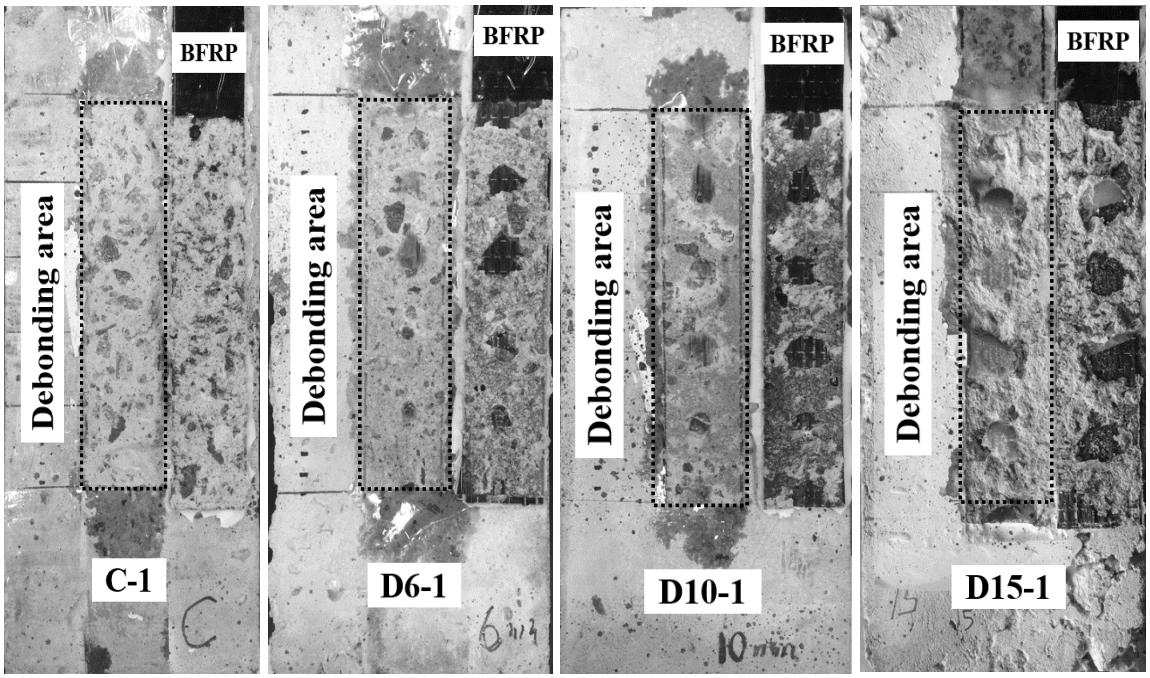

Figure 8-6. Typical debonding failure modes

Figure 8-7 illustrates the enhancement mechanism of using epoxy anchors. For the control specimens without anchors, the cracks penetrated through the concrete tensile side as the tensile strength of concrete (i.e. 3.9 MPa) was much lower than that of epoxy resin (i.e. 50 MPa). However, for the specimens with epoxy anchors, the interlocking action between epoxy anchors and concrete enhanced due to the effective embedment depth of epoxy anchors and consequently the epoxy anchors failed at the interface of the BFRP and epoxy resin. As epoxy anchors were arranged within the effective bond length (i.e. 40 mm), the consistent improvement in the shear stress transfer was achieved which can be verified in the load-slip response.

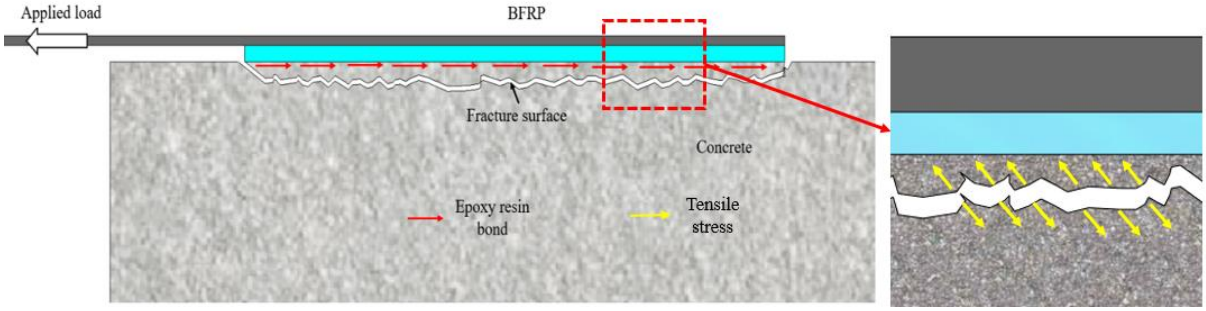

(a) Unanchored specimen

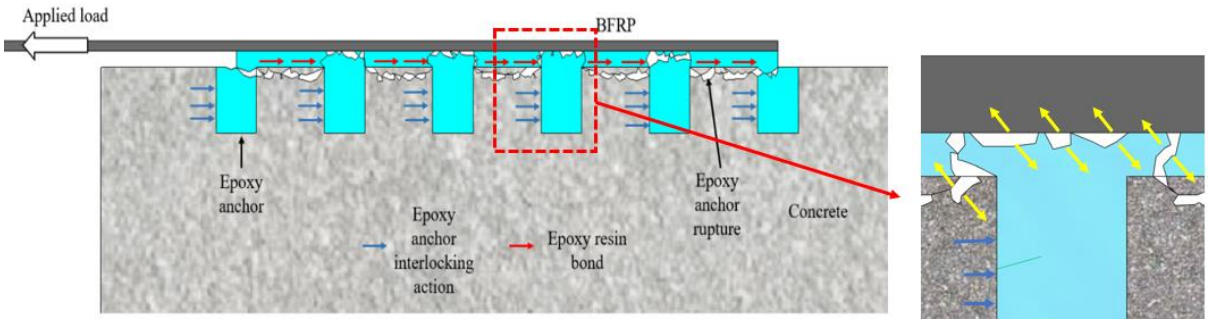

(b) Multiple-anchored specimen

Figure 8-7. Debonding mechanism with and without epoxy anchor

8.4.2 Strain distributions

The DIC technique was used to measure the BFRP strain and the accuracy of this non-contact technique was carefully validated in the previous studies by the authors to achieve reliable test data (128, 206). The typical strain distributions along the BFRP sheets are plotted in Figure 8-8 (a-d). Four different loading levels (P_2, P_3, P_4 and P_5) after the initial debonding stage (P_1) were selected to present the strain distributions in the debonding process. The difference between the anchored and un-anchored specimens is the initial debonding stage and final debonding stage, which are marked as red circles in Figure 8-9. For the control specimens, the debonding strain at the initial debonding stage (0.79%) was close to that at the final debonding

stage (0.98%). For the anchored specimens (i.e., D6-6, D10-6 and D15-6), the debonding strain increased more significantly from the initial debonding stage to final debonding stage as compared to the un-anchored specimens. For instance, the debonding strain increased from 1.19% at the initial debonding stage to 1.74% at the final debonding stage for specimen D15-6 owing to the existence of the interfacial hardening stage.

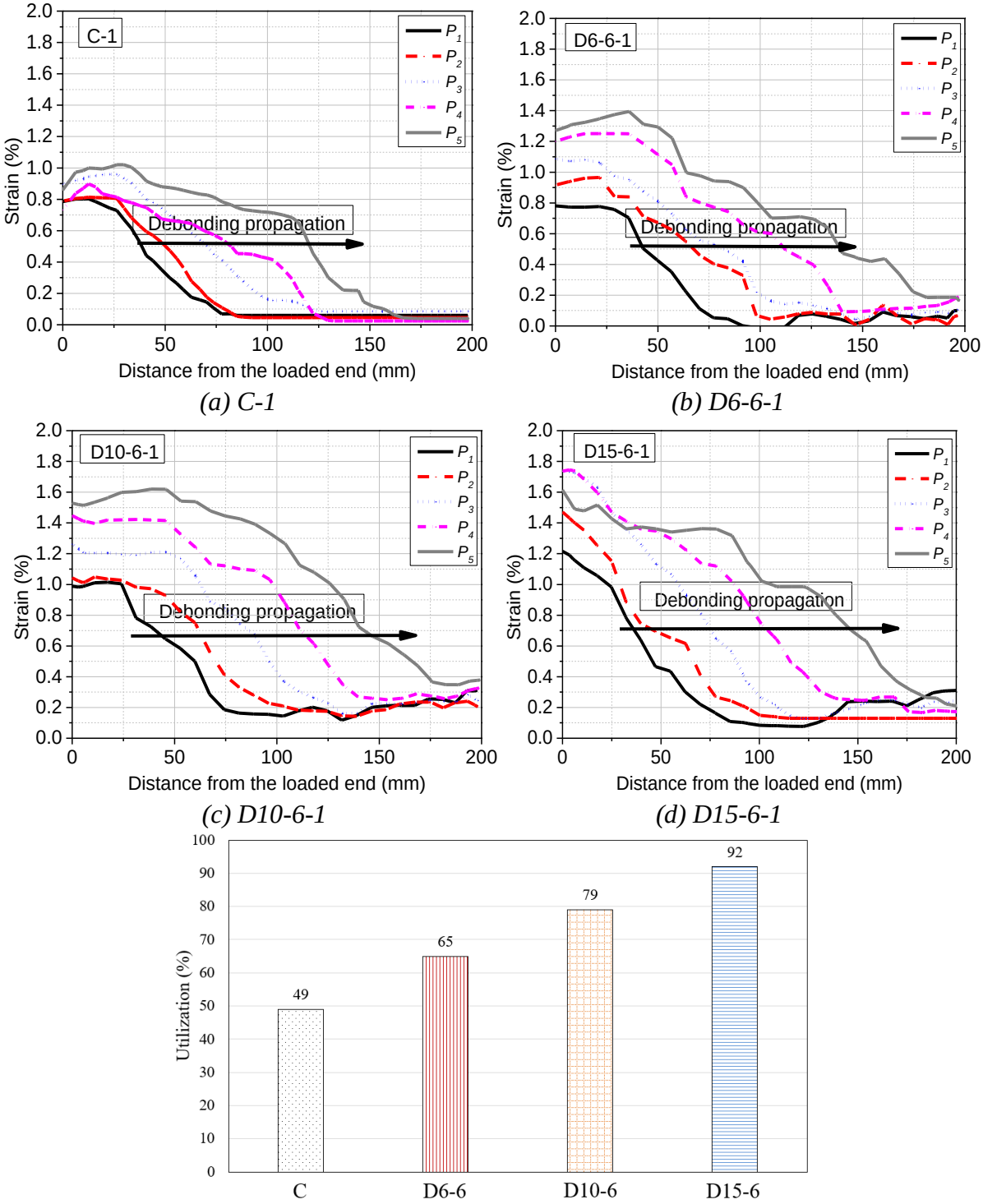

(a) C-1 *(b) D6-6-1*

(c) D10-6-1 *(d) D15-6-1*

(e) Utilization of rupture strain capacity of BFRP sheet

Figure 8-8. BFRP strain distribution and utilization rate

Figure 8-8 (e) illustrates the utilization of rupture strain capacity of BFRP sheets (i.e. strain utilization), which is defined as the ratio of its maximum debonding strain and ultimate rupture strain. The ultimate rupture strain of BFRP sheets was obtained from the coupon tensile tests. The maximum debonding strain increased from 0.98% to 1.80% on average as compared to the control specimen. The strain utilization of BFRP sheets on average increased from 49% to 92% as compared to the control specimen. This enhancement was dependent on the increased size of epoxy anchors, i.e., the increase of the anchorage area. It should be noted that this enhancement can only be achieved by continuously increasing the anchor size within the effective bond length. Therefore, the epoxy anchors can improve the utilization efficacy of the strengthening materials.

8.4.3 Effective shear stress transfer length

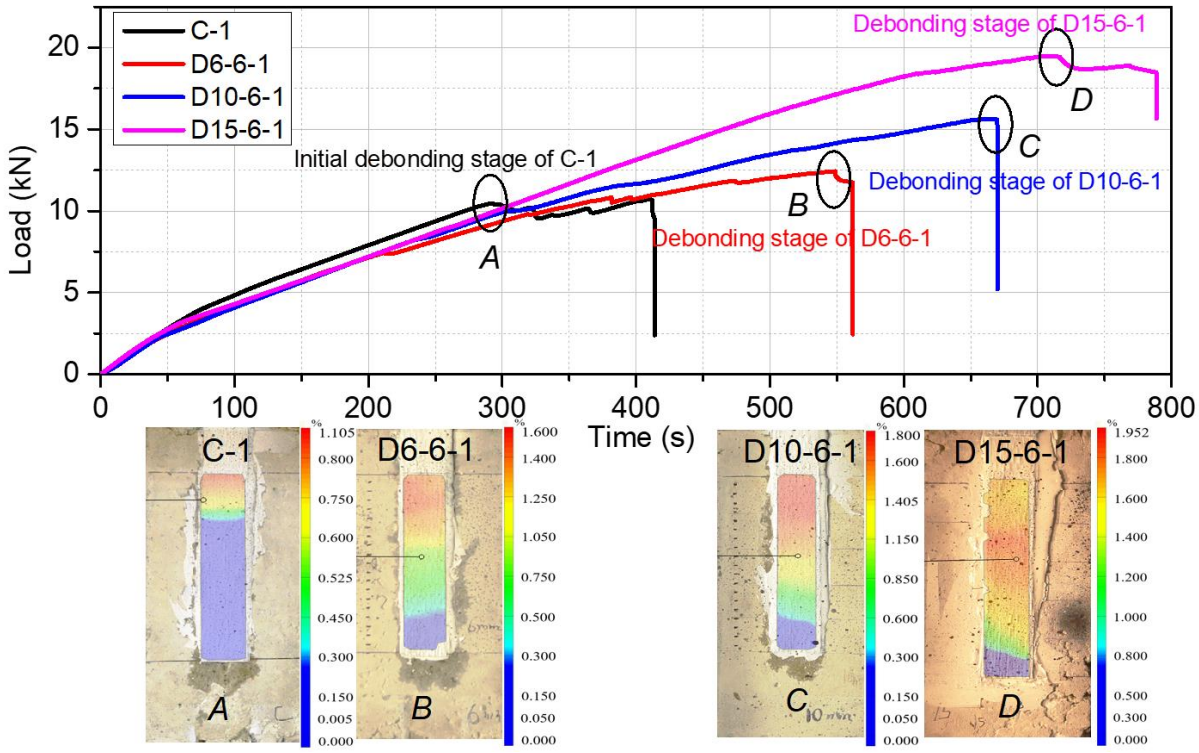

Figure 8-9. Debonding load and effective bond length (EBL)

Figure 8-9 illustrates the initial debonding stage of the tested specimens. The specimens with epoxy anchors did not show a significant initial debonding stage as compared to the control specimen C-1. After the initial debonding stage at approximately 290 s, the control specimen C-1 showed a significant loading plateau before the final detachment. At the initial debonding stage, the shear stress transfer length of specimen C-1was around 50 mm, as shown in the strain contour graph in Figure 8-9, which can be also defined as the effective bond length (EBL).

Previous studies (4, 45) have reported that the EBL is the active bond zone, over which the extension of bond length has no effect on debonding capacity. As shown in Figure 8-9, the strain contours consisting of red, yellow, green, light blue and dark blue colours refer to the shear stress transfer length at the initial debonding stage. Since the initial debonding stage coincided with the final detachment of the specimens with epoxy anchors due to the hardening behaviour, it is collectively named as the debonding stage for all the specimens with epoxy anchors. According to the strain contours, the EBL increased remarkably due to the anchorage effect. For the specimens with sufficient anchors, the EBL was approximately 200 mm which was close to the entire bonding length, indicating that the existence of epoxy anchors not only extended the stress transfer length but also prolonged the duration of debonding.

8.4.4 Shear stress and slip response

Figure 8-10 shows the relationship between shear stress and slip of the tested specimens. The shear stress and slip were obtained using Equations (8-1) and (8-2) (35, 90), as below

$$s(x) = \int_0^{\infty} \varepsilon dx \tag{8-1}$$

$$\tau(x) = \frac{d\varepsilon}{dx} E_f t_f \tag{8-2}$$

in which E_f is the elastic modulus of BFRP sheets, t_f is the nominal thickness of BFRP sheets, and ε is the strain along with BFRP sheets. The general trend shows that the peak shear stress increased with the addition of epoxy anchors. To obtain more accurate and consistent bond-slip responses, at least four loading stages (i.e. P_1, P_2, P_3 and P_4) were selected. The experimental bond-slip curves showed fluctuations due to the non-uniformity of the concrete surface. To eliminate the impact of data fluctuations and obtain the average shear stress, an analytical regression equation proposed by the previous studies (37, 87, 244) was also adopted in this chapter, which can be expressed as $\tau(s) = \frac{E_f t_f \alpha}{\beta^2} e^{-\frac{s}{\alpha}} \left(1 - e^{-\frac{s}{\alpha}}\right)$, where α and β are the fitting coefficients given in Table 8-1. It should be noted that the bond-slip response of specimen D15-6-1 shows a different profile after the softening stage as compared to the other specimens, which is due to the residual stress caused by the rupture of epoxy resin. The residual stress increased with the anchor size.

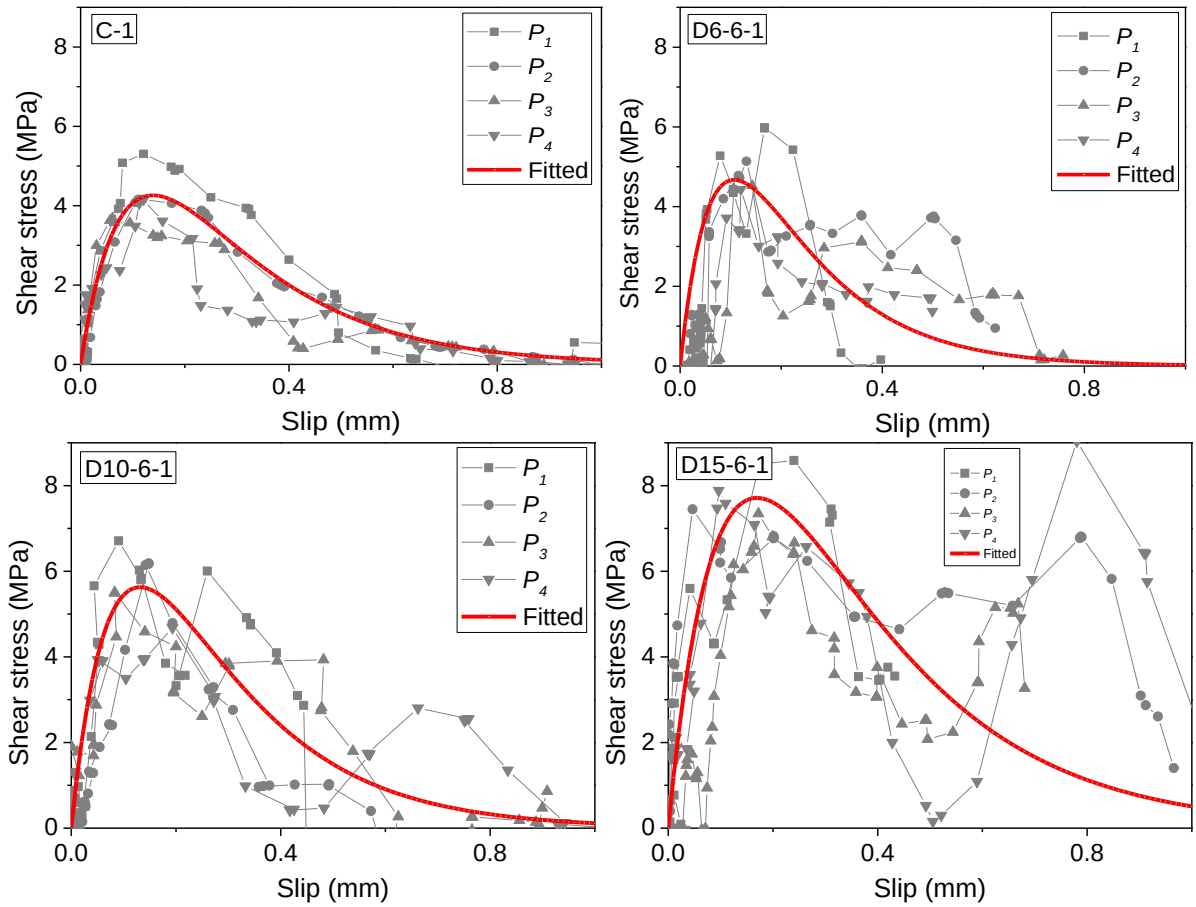

Figure 8-10. Bond-slip response

8.5 Analytical study on the effect of epoxy anchors

8.5.1 Simplified load-strain response

To quantify the contribution of epoxy anchors on the interfacial bond strength, the debonding load at different loading stages can be predicted using strain of BFRP sheets. Based on the derived load-strain relationships, a simplified model is suggested for the specimens with or without sufficient epoxy anchors. It should be noted that the micro-cracking stage induced by concrete cracking was neglected for ease of comparison. As shown in Figure 8-11 (e), two main stages (i.e. elastic stage and debonding stage) were observed for the control group, and three main stages (i.e. elastic stage, hardening stage and debonding stage) were observed for the specimens with epoxy anchors. The power function of $P = \lambda_1 \varepsilon^{\lambda_2}$ was used to describe the non-linear stage (i.e. hardening stage), in which P is the debonding load, ε is the FRP strain and the parameters $\lambda_1 = 11.25$ and $\lambda_2 = 0.20$ are fitting coefficients derived from the experimental results. Compared with the control group, the specimens with epoxy anchors exhibited the hardening stage, which greatly enhanced both the interfacial bond strength and

ductility. Due to different cross-sectional areas of epoxy resin anchors, the level of enhancement varied with the sizes of epoxy anchors.

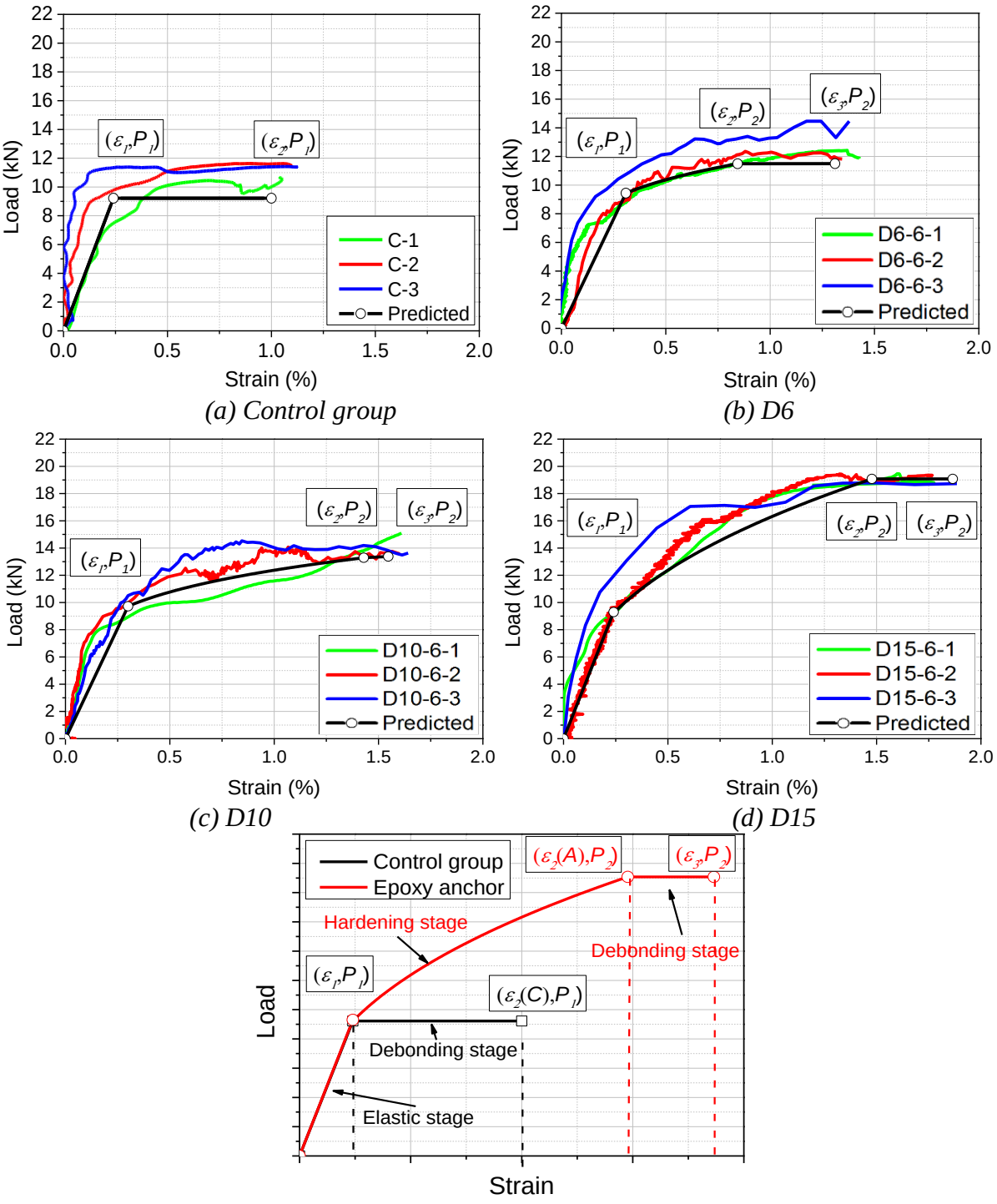

(a) Control group *(b) D6*

(c) D10 *(d) D15*

(e) Comparison between control group and anchorage group

Figure 8-11. Load-strain responses

8.5.2 Shear stress distribution

Figure 8-12 shows the shear stress distributions along the bond area. Compared with the control group, the specimens with epoxy anchors exhibited a higher bond strength due to the dowel action from the embedded epoxy resin anchors. Based on the predicted debonding loads at different loading stages, the corresponding strain can be obtained. By integrating the strain along the bond length, the shear slip can be obtained accordingly. The strain distribution of BFRP sheets within the effective bond length can be expressed as follows:

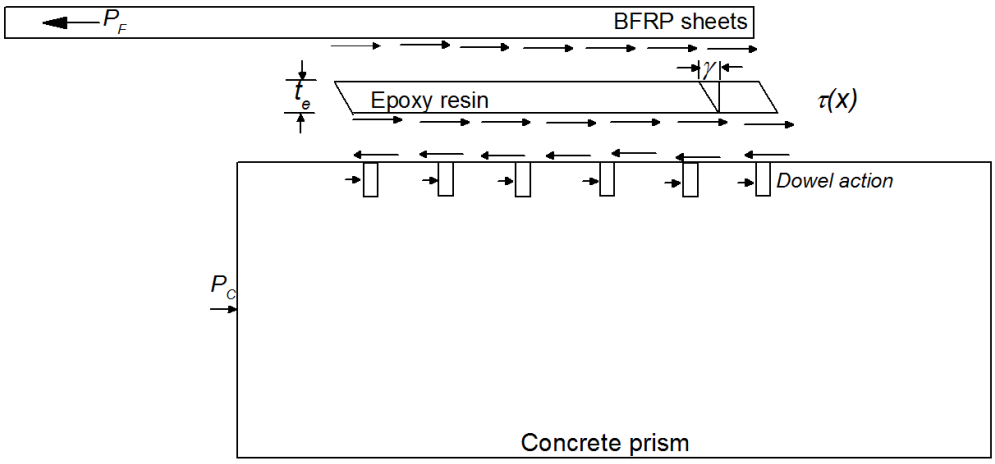

Figure 8-12. Shear stress distributions

$$\varepsilon_F(x) = \frac{Pi}{bE_F t_F} \frac{\sinh\left[\phi(L_e - x)\right]}{\sinh(\phi L_e)} \tag{8-3}$$

with $\phi^2 = \left(\frac{G_A}{t_A} \frac{1}{E_F t_F} \left(1 + \frac{E_F A_F}{E_C A_C} \right) \right)$.

The interfacial fracture energy G_f can be defined as the enclosed area under the bond-slip curve, which can be expressed as follows:

$$G_f = \int_0^{Le} \tau(x) ds \tag{8-4}$$

with $ds = \frac{t_A}{G_A} d\tau(x)$

$$G_f = \frac{1}{2} \frac{Pi^2}{b^2 E_F t_F} \left(1 + \frac{E_F A_F}{E_C A_C} \right) \tag{8-5}$$

in which *Pi* is the load at different stages, ε_F refers to BFRP strain at different loading stages, *b* is the bonding width of BFRP sheet, $E_f t_f$ is the BFRP stiffness, G_A is the shear modulus of epoxy resin, and t_A is the thickness of epoxy resin. The debonding loads of the two stages need to be determined first, followed by the corresponding strain. The bond strength model proposed by Chen and Teng (13) was used to predict the bonding load *P* as the accuracy of this model has been verified in the previous studies (96, 206). Therefore, the bonding load P_1 at the elastic stage can be determined by Equation (8-6).

$$P_1 = 0.427 k_w b_f L_e \sqrt{f_c} \tag{8-6}$$

in which $k_w = \sqrt{\frac{2 - b_f / b_c}{1 + b_f / b_c}}$ and $L_e = \sqrt{\frac{E_f t_f}{\sqrt{f_c}}}$.

For the specimens with epoxy anchors, the initial debonding load increased with the size of epoxy anchors (d_e). As fracture of epoxy anchors was observed for all the specimens with anchors, the strain energy ($\frac{f_e^{\,2}}{2E_e}$) and bonding area (A_e) of epoxy anchors should be also the factors for determining the interfacial bond strength. Therefore, the initial debonding load P_2 at the hardening stage can be determined by the following equation:

$$P_2 = P_1 + \alpha_1 d_e \left(\frac{f_e^{\,2}}{2E_e} A_e \right)^{\alpha_2} \tag{8-7}$$

in which P_1 is the bonding strength of the elastic stage, P_2 is the bonding strength of the hardening stage and α_1 and α_2 are the fitting coefficients. The best-fitted results are plotted in Figure 8-13. The derived bonding strength P_1 from Equation (8-6) was 9.22 kN and the regressed coefficients α_1 and α_2 were 0.59 and 0.18, respectively. Therefore, the following equation can be obtained by substituting these coefficients into Equation (8-7):

$$P_2 = P_1 + 0.59 d_e \left(\frac{f_e^{\,2}}{2E_e} A_e \right)^{0.18} \tag{8-8}$$

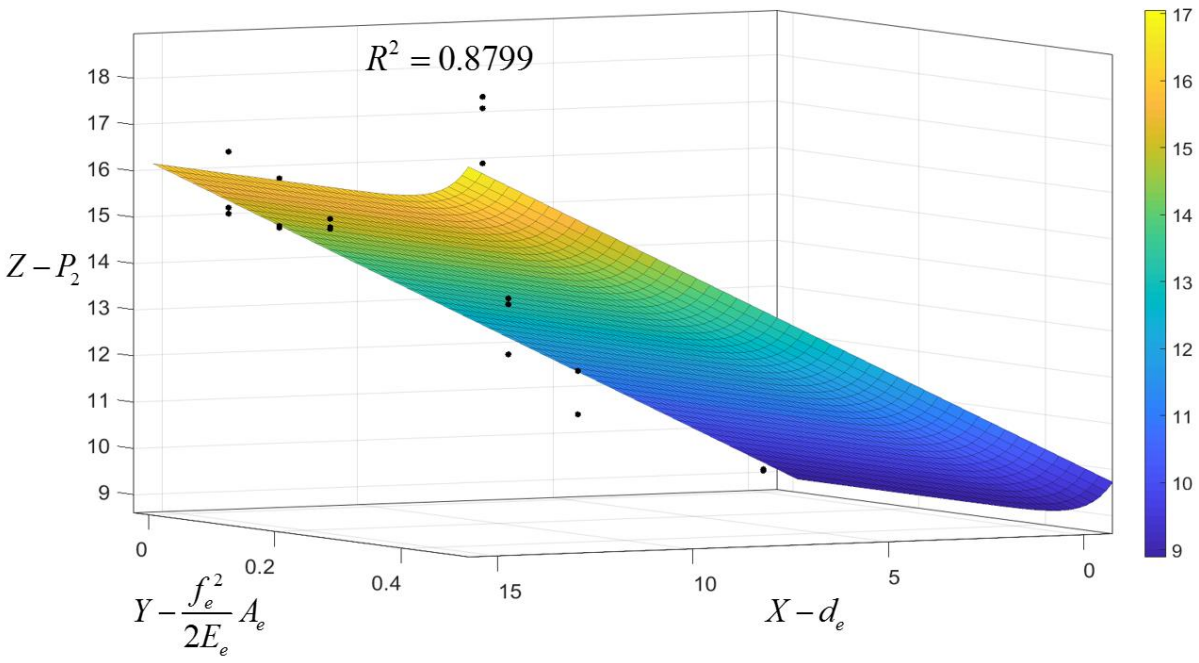

Figure 8-13. Regression analysis of bond strength P_2

Figure 8-14 shows the comparison between the predicted and tested bond strength of P_1 and P_2. It is observed that the analytical results match well with the experimental data with a high correlation coefficient R^2=0.87, indicating that the proposed analytical bond strength model by incorporating the effect of epoxy anchors yields good prediction.

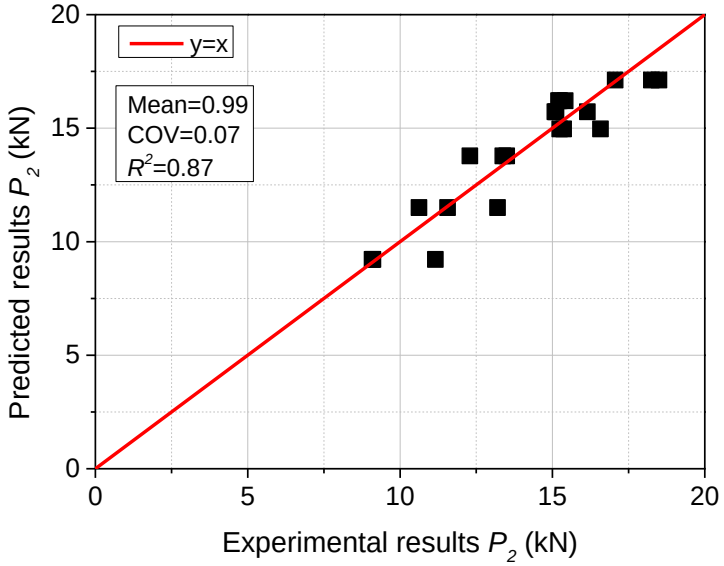

Figure 8-14. Comparison between the predicted and experimental results P_2

8.5.3 Debonding load

Based on the typical simplified load-strain curves, the bond strength P_1 can be obtained for all the tested specimens based on the analytical models proposed in this chapter. Based on the derived bond strength P_1 from Equation (8-6), the elastic debonding strain ε_1 can be expressed as:

$$\varepsilon_1 = \frac{P_1}{bE_F t_F} \frac{\sinh\left[\phi\left(L_e - x\right)\right]}{\sinh\left(\phi L_e\right)} \tag{8-9}$$

For the specimens without epoxy anchors, after the initial debonding stage the BFRP-to-concrete interface maintained the same debonding load P_1 until the final detachment. The tensile strain ε_2 can be determined by the derived bond strength P_1, as shown in the following equation:

$$\varepsilon_{2(C)} = \frac{P_1}{b_f E_F t_F} \tag{8-10}$$

in which P_1 is the bond strength at the elastic stage, $\varepsilon_{2(C)}$ is the ultimate debonding strain of the control group, L_e is the effective bond length and x is the distance from the loaded end.

For the specimens with epoxy anchors, the interface continued to carry higher loads after the elastic stage due to the existence of epoxy anchors. The BFRP sheets continued to be subjected to the interfacial bond strength provided by the epoxy anchors and the corresponding strain ε_2 can be predicted by the bond strength P_2 at the hardening stage, as shown in the following equation:

$$\varepsilon_{2(A)} = \frac{P_2}{bE_F t_F} \frac{\sinh\left[\phi\left(L_e - x\right)\right]}{\sinh\left(\phi L_e\right)} \tag{8-11}$$

in which P_2 is the initial debonding load for the specimens with epoxy anchors and $\varepsilon_{2(A)}$ is the initial debonding strain for the specimens with epoxy anchors. Once the debonding initiated, the BFRP sheets are only subjected to tensile force without any bonding after the epoxy resin hardening. The elongation of BFRP at the debonding plateau ε_3 can be determined by the sum of the elastic debonding strain ε_1 and the initial debonding strain $\varepsilon_{2(A)}$, as shown in the following equation:

$$\varepsilon_3 = \varepsilon_{2(A)} + \varepsilon_1 \tag{8-12}$$

The predicted bond strength P_1 and P_2 and the corresponding strain ε_1, $\varepsilon_{2(C)}$, $\varepsilon_{2(A)}$ and ε_3 are summarized in Table 8-2. It should be noted that x is the position of the selected point from the loaded end. The predicted results are plotted in Figure 8-15. It is observed that the bond strength and the ultimate debonding strain increased with the rising anchorage area, which is consistent with the experimental results.

Table 8-2. Comparison of predicted results and experimental results

Specimen ID	$P_{1,exp.}$ (kN)	$P_{1,pre.}$ (kN)	$P_{2,exp.}$ (kN)	$P_{2,pre.}$ (kN)	$\varepsilon_{1,pre.}$ (%)	$\varepsilon_{2,exp.}$ (%)	$\varepsilon_{2,pre.}$ (%)	$\varepsilon_{3,pre.}$ (%)
C	9.78	9.22	9.78	9.22	0.236	0.983	0.877	/
D6	9.50	9.22	11.79	11.50	0.236	1.297	1.094	1.330
D10	10.15	9.22	13.05	13.78	0.236	1.581	1.311	1.547
D15	11.37	9.22	17.94	17.12	0.236	1.836	1.629	1.865

Note: $P_{i,exp}$ and $\varepsilon_{i,exp}$ refer to the average experimental results and $P_{i,pre}$ and $\varepsilon_{i,pre}$ refer to the predicted results.

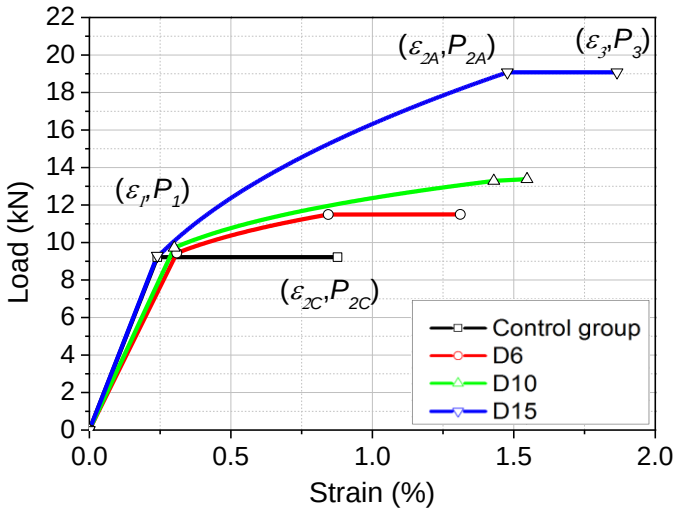

Figure 8-15. Predicted debonding load and strain

8.6 Summary

In this chapter, a new epoxy anchor system is developed to enhance the interfacial bond performance between BFRP sheets and concrete. As compared to the existing anchors, the newly proposed epoxy anchor system is easy to implement for engineering practice and required less workmanship. The embedded part of the epoxy anchor in the concrete formed self-anchorage to enhance the interfacial shear resistance. The experimental results show 77.49%

increment in bond strength, 86.71% increment in the utilization of BFRP sheet, and 78.10% increase in the peak shear stress on average. The size of epoxy anchors significantly affects the shear resistance. Increasing the diameter of epoxy anchor greatly enhanced the shear resistance while the peak bond strength and peak shear stress are not affected by the number of epoxy anchors in general. In addition, an analytical bond strength model is proposed by incorporating the bonding area and strain energy of epoxy resin and it shows a good agreement with the testing results. With the analytical bond strength model, the FRP strain at different loading stages can be also predicted.

Chapter 9. Interfacial debonding damage detection by using SA sensors

9.1 Introduction

Interfacial bond behaviours under static and dynamic loadings with the consideration of FRP configurations and concrete characteristics have been investigated experimentally, analytically and numerically in Chapter 3-7. It is also essential to monitor the debonding and quantify the interfacial damage caused by debonding. In this chapter, a stress wave-based sensing approach to quantitatively monitor the debonding process by using surface mounted piezoceramic-based transducers (also called as smart aggregates SAs) is adopted. The scanning wave signals in swept-frequency mode and single frequency mode are utilized in experimental and numerical methods, respectively. To quantify the debonding level and provide an assessment of the interface condition, a wavelet packet-based debonding index is established and its validity is verified by the data retrieved from digital image correlation (DIC) measurement.

The related work in this chapter is published in Smart Materials and Structures.

Yuan C, Kong Q, Chen W, Jiang J, Hao H. Interfacial Debonding Detection in Externally Bonded BFRP Reinforced Concrete Using Stress Wave-based Sensing Approach. Smart Materials and Structures. 2020; 29: 035039.

9.2 Methodology

9.2.1 Stress wave scanning using smart aggregates

Piezoelectric Lead Zirconate Titanate (PZT) transducers have emerged as one of the most popular devices for wave signal generation and detection due to their low cost, quick installation, wide frequency range, and high sensitivity (245, 246). To ensure the survivability of fragile PZT material, smart aggregate (SA) transducer was used in this chapter. The SA was designed as a sandwiched structure by protecting the PZT patch with two marble blocks, as shown in Figure 9-1(a, b). The reliability, functionality, and feasibility of using SAs for SHM projects have been proven in the past ten years (247).

In this chapter, two pairs of SAs were used to detect the interfacial debonding at two locations along with the BFRP sheet. The schematic diagram of the sensing approach using SA enabled stress wave for the debonding detection of the externally bonded BFRP reinforced concrete is

given in Figure 9-1 (c, d). For each pair of SAs, the one marked with red colour functions as a generator to emit a designed stress wave signal from the concrete side to the BFRP side. The other one on the BFRP side functions as a receiver to detect the propagated stress wave. When debonding damage occurs, the existence of the gap which acts as an additional interface will cause amplified wave reflection. Therefore, the stress wave attenuation from the concrete side to the BFRP side increases correspondingly as debonding intensifies.

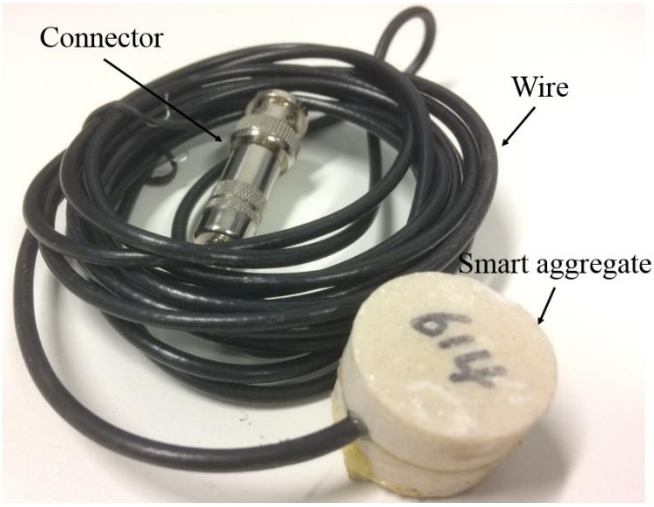

(a) The photo of smart aggregate

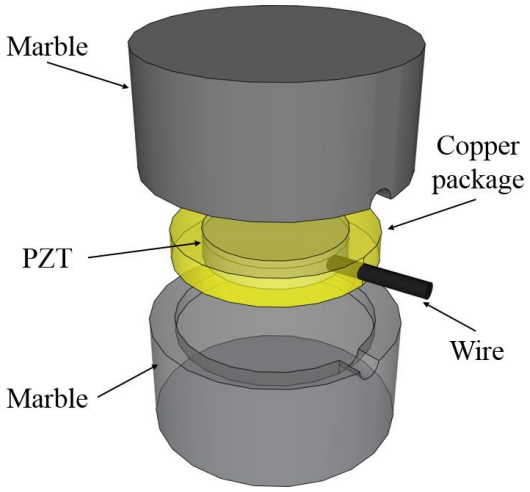

(b) The sketch of smart aggregate

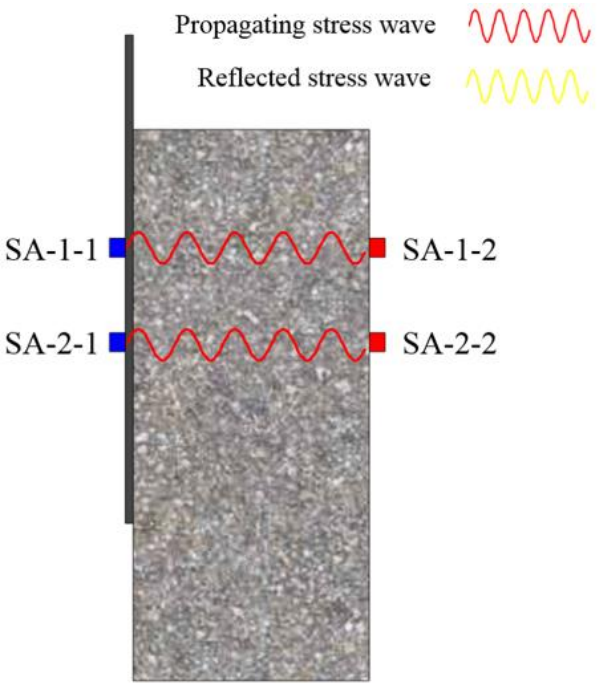

(c) Pre-debonding

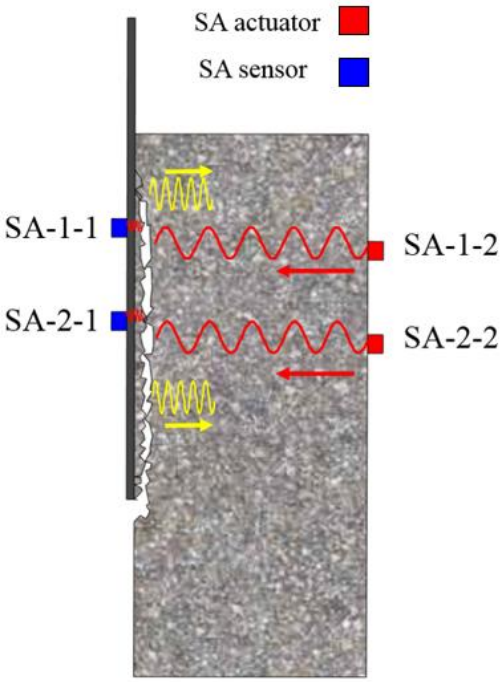

(d) Post-debonding

Figure 9-1. The diagrams of smart aggregate (SA) and debonding detection using stress wave scanning

9.2.2 Debonding damage index

To define the debonding induced stress wave energy loss and quantify the debonding condition of the BFRP-to-concrete interface, a wavelet packet-based debonding damage index was adopted in this chapter. Wavelet analysis has been widely used as an effective signal processing tool in the field of structural health monitoring (247, 248). In this chapter, wavelet packet decomposition divides the sensor signal Y into 2^n signal sets $\{Y_1, Y_2, \cdots, Y_j, \cdots, Y_{2^n}\}$, in which j is the frequency of band at the n-level decomposition ($j = 1, \cdots, 2^n$), and Y_j can be represented by Equation (9-1):

$$Y_j = \left[y_{j,1}, y_{j,2}, \cdots, y_{j,m} \right] \tag{9-1}$$

where m is the data samplings. The energy E_j of the decomposed signal Y_j is defined by Equation (9-2):

$$E_j = \left\| Y_j \right\|^2 = y_{j,1}^2 + y_{j,2}^2 + \cdots + y_{j,m}^2 \tag{9-2}$$

The energy vector $E_{i,j}$ of the sensor signal Y_i, where i refers to the i^{th} measurement is defined by Equation (9-3):

$$E_{i,j} = \left[E_{i,1}, E_{i,2}, \cdots, E_{i,2^n} \right] \tag{9-3}$$

The energy vector $E_{0,j}$, as a baseline, is retrieved from the measurement on the healthy state of the BFRP-to-concrete interface. The debonding damage index I is defined by Equation (9-4):

$$I = \sqrt{\frac{\sum_{j=1}^{2^n} (E_{i,j} - E_{o,j})^2}{\sum_{j=1}^{2^n} E_{o,j}^{\ 2}}} \tag{9-4}$$

The debonding damage index (I) refers to the energy attenuation caused by the debonding between the BFRP sheet and concrete. When the bonding condition is in a healthy state, the values of $E_{0,j}$ and $E_{i,j}$ are very close to each other, therefore the damage index value remains zero. The increase of the debonding index value corresponds to the increase of the stress wave

attenuation ratio at the BFRP-concrete interface. If the BFRP sheet is entirely debonded from concrete at the sensor location, the sensor will not detect any stress wave energy from the actuator. Therefore, the debonding damage index value is one as $E_{i,j}$ in this state is close to zero.

9.3 Experimental setup

9.3.1 Test specimen and SA location

In this chapter, a concrete block with a compressive strength of 40 MPa was prepared for the single-lap shear test. The dimensions of the prepared concrete block were 150 x 150 x 350 mm. Two layers of BFRP sheets with a density of 300 g/m^2 were bonded onto the surface of the concrete prism. Please refer to chapter 3.2.1 for material properties.

Figure 9-2 shows the details of the single-lap specimen and the location of SAs. SA-1-1 and SA-2-1 were used as receivers while SA-1-2 and SA-2-2 were set to be actuators, respectively. The SA-1-1 and SA-1-2 pairs were placed near the loaded end to detect the early debonding. The SA-2-1 and SA-2-2 pairs were placed 40 mm away from the SA-1-1 and SA-1-2 to detect the debonding within the effective bond length (EBL). EBL refers to the bond length of BFRP sheet over which there is no debonding resistance. By means of two pairs of SAs, debonding failure at two SAs' locations can be monitored in real-time.

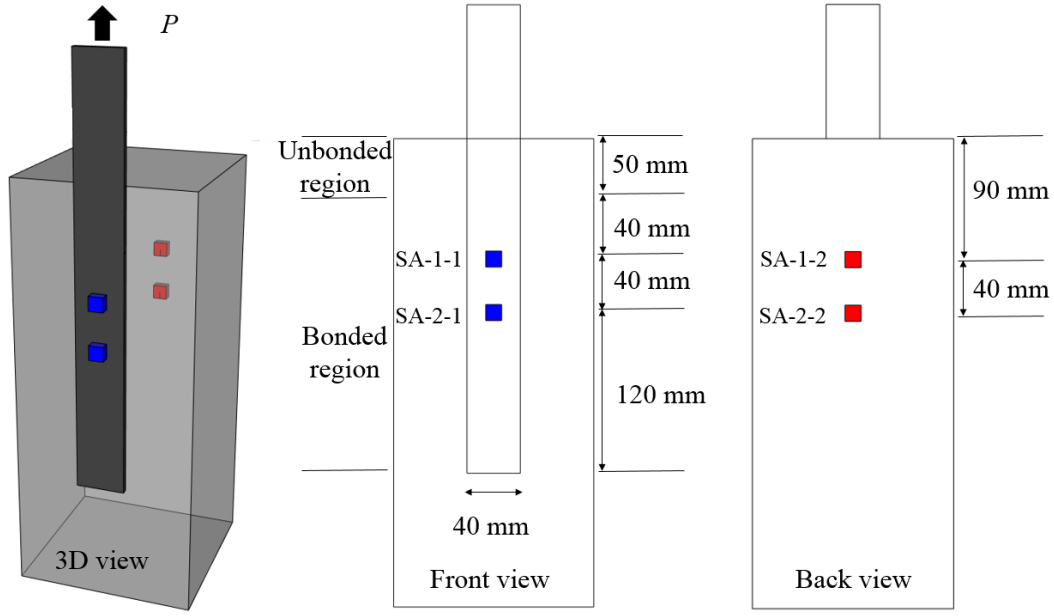

Figure 9-2. Specimen details

9.3.2 Testing facilities

In the test, the concrete block was fixed by a designed steel fixture on the workbench and tensile loading was applied on the loading end of BFRP. The debonding load was measured by a built-in load cell of the universal testing machine. The testing facilities are shown in Figure 9-3, which include two pairs of SAs (i.e., four SAs), data acquisition system (NI-USB6366), laptop, testing machine and DIC camera. During the tensile loading, both SA actuators on the concrete side periodically generated the designed stress wave signal in swept-frequency mode, which propagated through the BFRP-concrete interface and was detected by the paired SA sensors. The amplitude, start frequency, stop frequency and the sweeping period of the swept sine wave signal was 10 V, 1 kHz, 300 kHz, and 1 s, respectively. The sampling rate of the data acquisition system for each channel was 2 MHz.

2D Digital image correlation (2D-DIC) technique was used to measure the full-field displacement and strain of the BFRP sheet. The measured surface strain was used to obtain the interfacial shear stress and the local bond-slip was consequently obtained. The shear slip of the BFRP sheet was measured by the DIC technique and the relationship between debonding damage index and the shear slip was established accordingly.

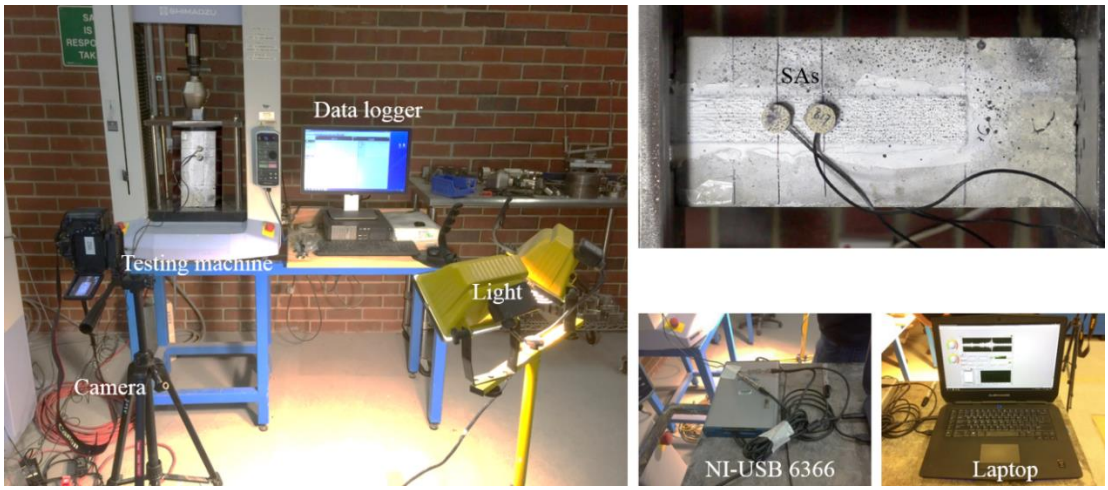

Figure 9-3. Test setup

9.4 Experimental results

9.4.1 Debonding load and shear slip

Figure 9-4 illustrates the load-slip response and load-time history, respectively. It was observed that the debonding load of the tested specimen was around 12 kN. Three regions can be observed for the interfacial load-slip curves, as shown in Figure 9-4. At the initial stage OA,

the shear slip between BFRP sheet and concrete was small and this stage was defined as the elastic region. With the increase of the applied load, the shear slip increased gradually in stage AB, which was resulted from the microcracking of concrete. As shown in Figure 9-4 (b), the initial debonding initiated at the instant of 450 s, i.e. point B. After reaching the initial debonding point B, the shear slip increased sharply while the applied load almost remained constant during the debonding process of the stage BC as shown in Figure 9-4 (a). After reaching Point C, the final detachment of BFRP sheet was observed. The entire debonding process completed at around 600 s.

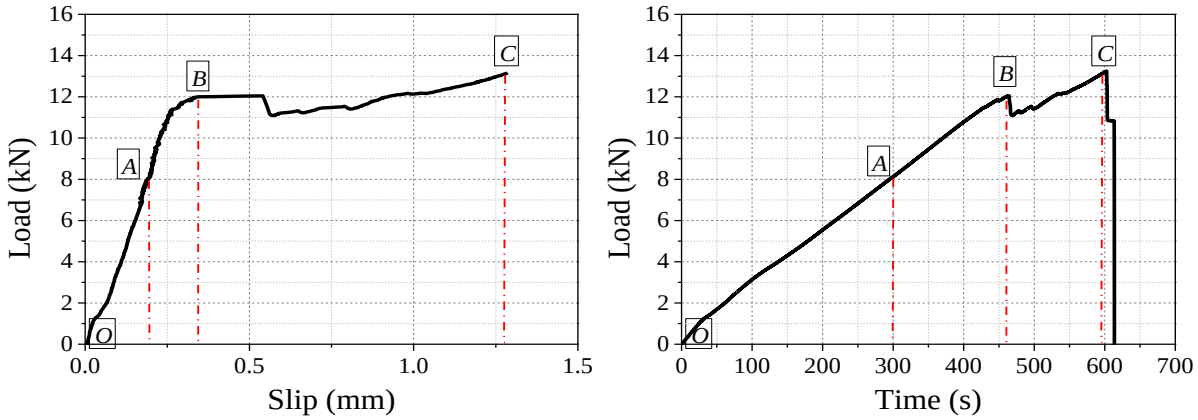

Figure 9-4. (a) Load-slip curve; and (b) Load-time curve

9.4.2 Interfacial damage identification

Figure 9-5. Failure mode of the tested specimen

The tested specimen experienced a sudden failure with a flake of concrete generated beneath the BFRP sheet. Figure 9-5 shows the typical failure mode after the final detachment. It was observed that all the debonding failures initiated and propagated inside the concrete substrate layer. As the single-lap shear testing method was employed in this testing program, the effect

of normal stress on the debonding was marginal. The debonding of BFRP-concrete interface initiated from the adhesive layer and penetrated into the concrete layer upon tensile loading. The shear stress at the interface was transformed into tensile stress and compressive stress along 45^{o} plane (75). As tensile strength of concrete was much weaker than its compressive strength, debonding damage always initiated from the tensile side of the strengthened concrete element. Therefore, the detected local bond-slip by the SAs was actually caused by the fracture of concrete for BFRP-strengthened concrete structures.

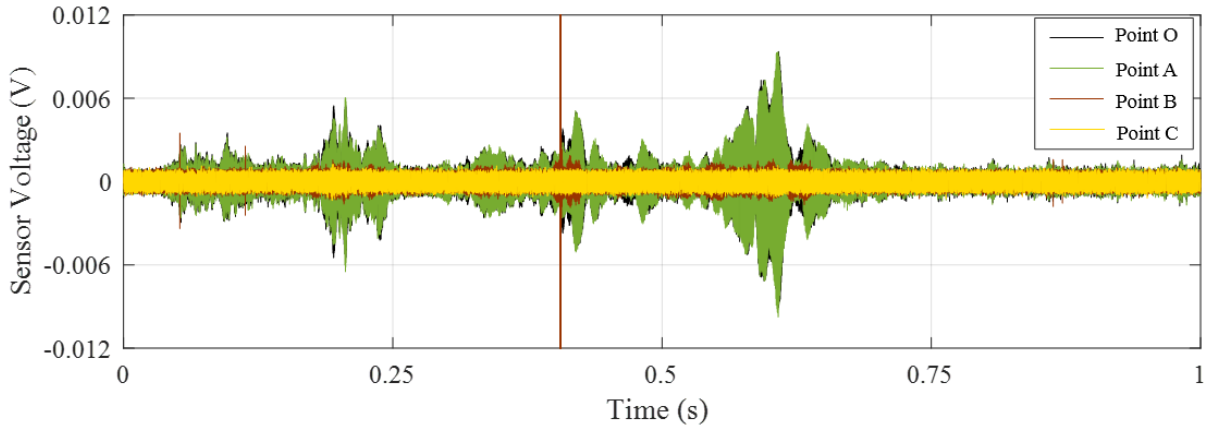

(a) SA-1-1

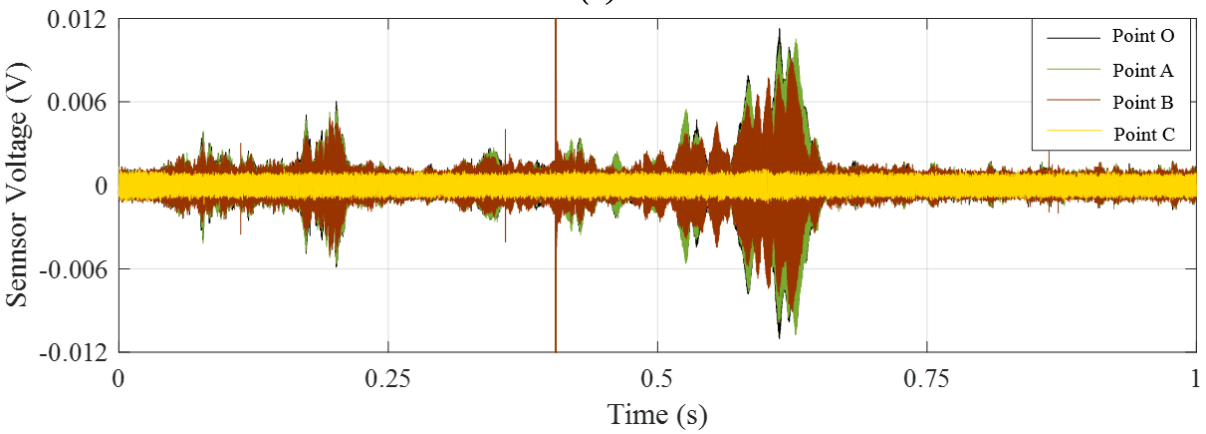

(b) SA-2-1

Figure 9-6. Received signals of SA sensors at different debonding stages (note: Points O/A/B/C refer to Figure 9-4)

Figure 9-6 illustrates the wave signals detected by SA-1-1 and SA-2-1, respectively. The curves with different colours represent the received signals at different bond-slip stages. The black curve refers to the healthy state of the interface at the initial loading stage (i.e. Point O in Figure 9-4). At the instant of debonding initiation, i.e., Point B in Figure 9-4, interfacial debonding occurred at the SA-1-1 location, resulting in a significant decrease of the signal amplitude (i.e. the brown curves). However, there was no obvious decrease in the signal detected by SA-2-1 sensor at the free end at this moment as debonding initiated from the loaded end and has yet

propagated to the free end. SA-2-1 sensor only showed a slight reduction of signal amplitude at the instant corresponding to Point B as compared to the instant of Point A due to the microcracking damage. After initiation, the debonding propagated and passed the location of SA-2-1. Both SA sensors measured noise signal (i.e. the yellow curves) due to the full debonding. In the subsequent section, the amplitude attenuation is quantified through wavelet packet-based debonding damage index.

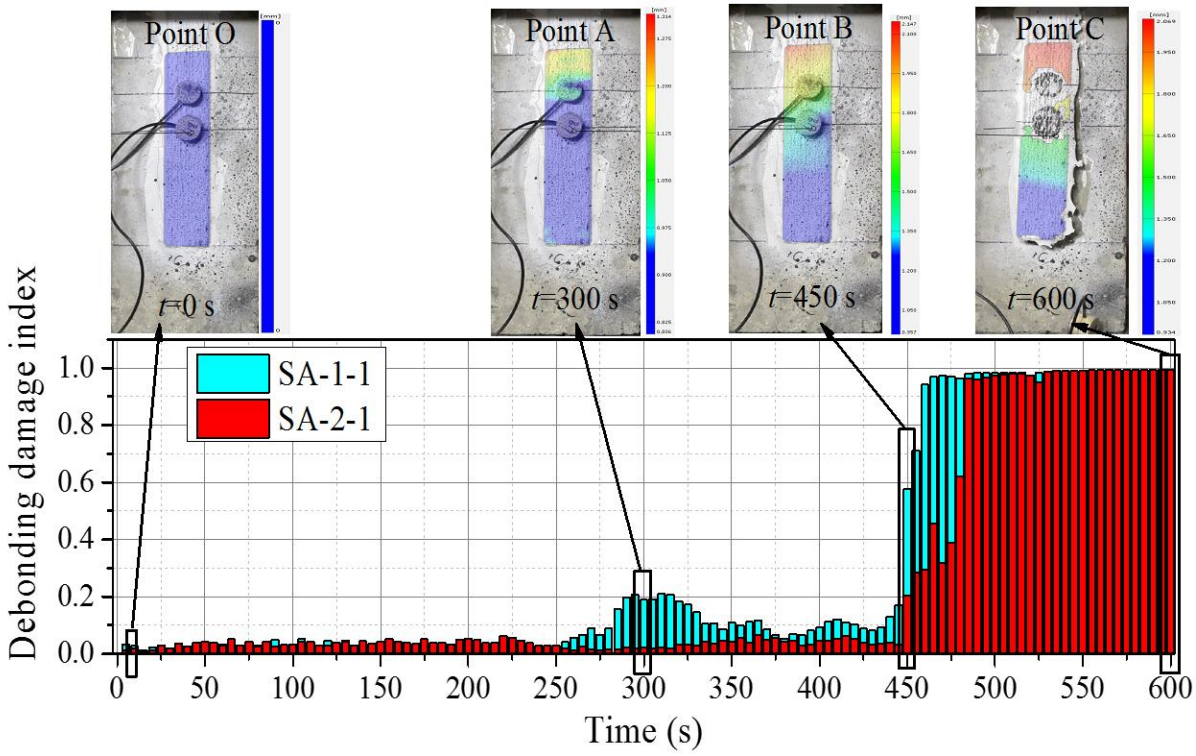

Figure 9-7. Shear slip and debonding damage index

Figure 9-7 illustrates the computed debonding damage indices for SA-1-1 and SA-2-1, as well as the shear slip contours of the BFRP sheet at four important instants of the debonding process. At the very beginning of the test, there was no debonding, so that he debonding index values for both SA-1-1 and SA-2-1 were close to zero. As shown in the shear slip contours from the DIC analysis, SA-1-1 firstly experienced the local bond-slip damage at Point A because the shear slip contours consisting of yellow and green colours covered the SA-1-1. However, no stress was transmitted to the SA-2-1 yet as shown in the colour of dark blue, which represents the zero slippage. The debonding damage index for SA-1-1 increased up to 0.2, while the value for SA-2-1 was still close to zero. With the increase of the applied tensile load, the interface experienced more damage and the debonding continued to propagate along with the interface. The shear slip contours consisting of red, yellow and green colours covered both SAs at Point B, indicating that the debonding has passed the location of SA-2-1. It can be seen from the

damage indices of SA-2-1 that the index value increased up to 0.2 at Point B, indicating the initial debonding occurred at the location of SA-2-1. After that, the damage index of both SAs increased sharply to the peak value, indicating that the BFRP-to-concrete interface was fully debonded.

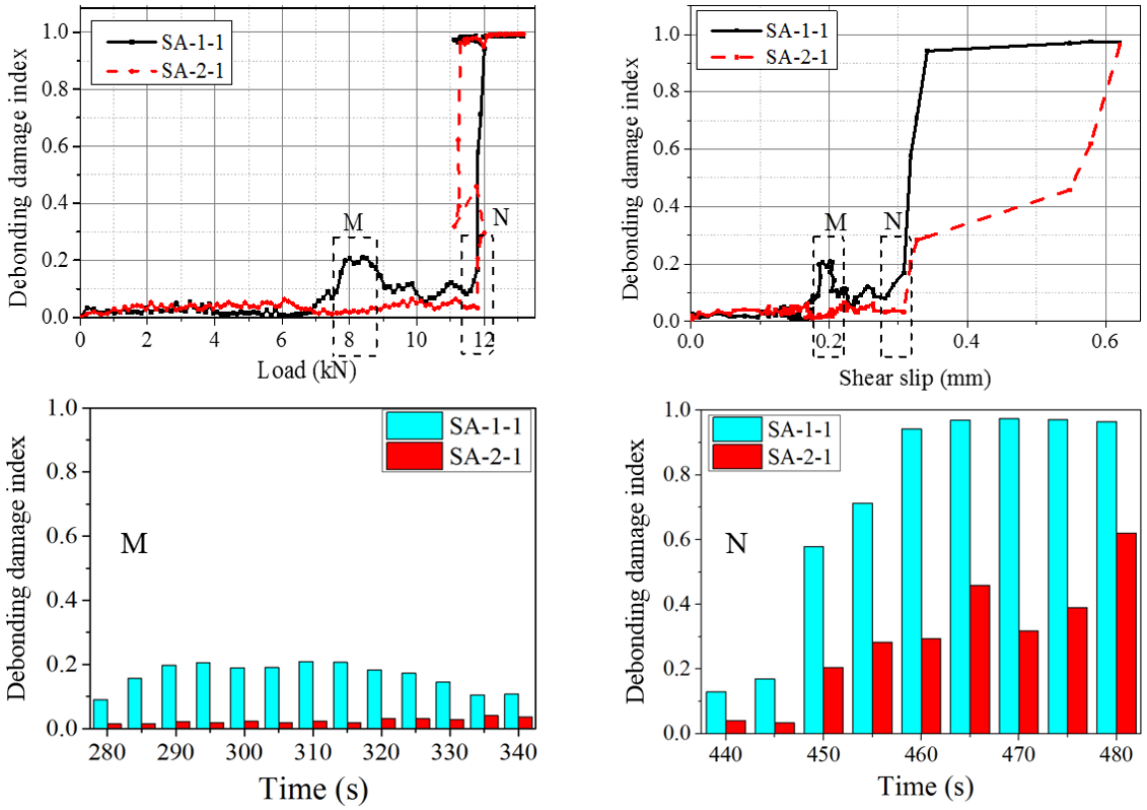

Figure 9-8. (a) The relationship between damage index and load; and (b) The relationship between damage index and shear slip at different time instants

Figure 9-8 (a, b) shows the relationship between debonding damage index and debonding load as well as shear slip of SA-1-1 and SA-2-1, respectively. It is observed that the debonding of BFRP-strengthened concrete elements is very brittle due to the sharp increment of the damage index after initial debonding stage (i.e. 450 s). As shown in Figure 9-8 (a), the damage index of SA-1-1 and SA-2-1 is close to zero before reaching the microcracking stage, indicating that the BFRP sheet and concrete interface is still well bonded and consequently the state of wave propagation is the same as those in the healthy state. The SA-1-1 first detected the initial damage at the loading force of 6.5 kN, indicating that the interface between BFRP and concrete experienced concrete microcracking with local bond-slip damage, which resulted in the attenuation of wave propagation. With the increase in the applied load, the damage index of SA-1-1 increased to the range from 0.1 to 0.2 after the moment of 250 s. However, the damage

index of SA-1-1 slightly reduced after the loading of 8.2 kN. This is because the microcracks in the concrete were suppressed by the applied load along the in-plane direction. The SA-2-1 is still in the healthy state before the moment of 450 s, indicating that there is marginal local bond-slip damage in its vicinity. However, the damage index of SA-2-1 increases up to 0.2 at the moment of 450 s and continues to increase until the final debonding. Figure 9-8 (b) illustrates the relationship between the damage index and shear slip, which is similar to the relationship between the damage index and debonding load. It can be found that the debonding detection of the SA-2-1 is always delayed than that of the SA-1-1. The SA-1-1 first detected the initiation of local damage and the damage index increased sharply after the initial debonding stage (i.e. 450 s), where the shear slip was around 0.31 mm. Meanwhile, the SA-2-1 quickly sensed the brittle interfacial debonding with the attenuation of the wave propagation and the corresponding damage index increased gradually with the increasing shear slip. After the development of the local bond-slip damage within effective bond length (EBL), the debonding damage process repeated in the next EBL until the final detachment of BFRP sheet. It should be noted the detected debonding by the SAs is the local damage rather than the global damage.

9.4.3 Interfacial bond-slip response

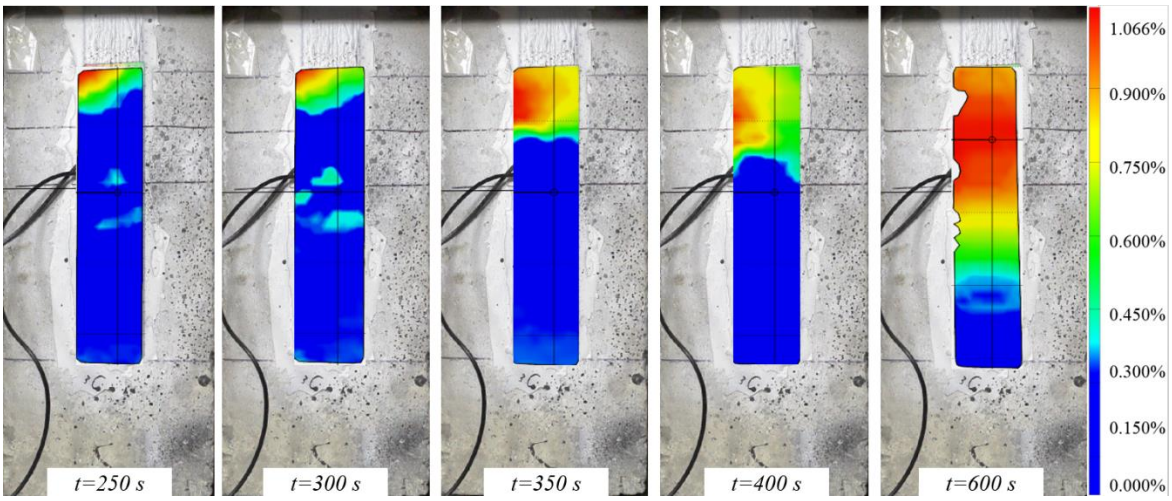

Figure 9-9. Strain contours at different time instants

Figure 9-9 illustrates the strain contours from the DIC technique. The obtained strain contours at different damage stages consist of different colours. Red and blue colours refer to the maximum and minimum strain. At the initial debonding stage, the distance of strain transfer is known as the active stress transfer zone, which is also defined as the effective bond length (EBL). Figure 9-10 shows the shear slip and strain distributions of the tested specimen at

different time instants, which provides a global insight into the pre-debonding and post-debonding process. The obtained shear slip is derived from the DIC analysis. The shear slip maintains a similar shape for debonding propagation. With the increase of the applied load, the shear slip increases until the final detachment. At the moments of 300 s and 450 s, the maximum shear slip is around 0.2 mm and 0.31 mm, respectively, which match well with the results provided in Figure 9-8 (b). To better understand the shear stress transfer mechanism from the BFRP sheet to the concrete element, the strain profile is obtained for the shear stress propagation. It is observed that the strain maintains a similar shape for the debonding propagation after the initial debonding stage (i.e. 450 s), this is consistent with the previous studies (96). The discontinued parts of the curves are shown in Figure 9-10 (a) and (b) as the areas covered by two SAs cannot be captured by the DIC technique.

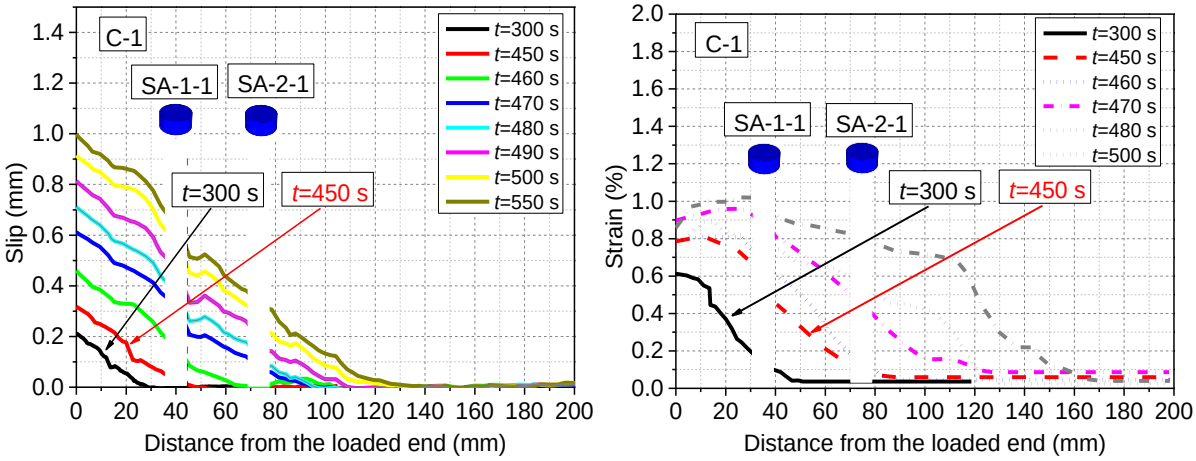

(a) Slip distribution *(b) Strain distribution*

Figure 9-10. Shear slip and strain distributions

To quantify the local bond-slip response of the interface, the shear stress can be derived using the measured strain by the following formula (90, 96):

$$\tau(x) = \frac{\varepsilon_{k+1} - \varepsilon_k}{dx} E_f t_f \tag{9-5}$$

in which E_f and t_f are the elastic modulus and thickness of the BFRP sheet, respectively, $\varepsilon_{k+1} - \varepsilon_k$ refers to the strain difference between two sets (k+1 and k) on the BFRP sheet, and dx is the distance between the set $k+1$ and the set k. Figure 9-11 illustrates the bond-slip response of the tested specimen at different time instants. It is observed that the bond-slip responses show an ascending branch before the peak shear stress, and a descending branch is observed after the peak value. The average peak shear stress is around 5.6 MPa for the tested specimen. Three regions can be identified for the local bond-slip response, i.e. the interfacial

elastic stage of the ascending branch (OA), the interfacial softening stage caused by the microcracking of concrete (AB) and the debonding stage (BC). Using the obtained debonding damage index, the SA-based active sensing process can well quantify the damage level of the elastic, microcracking and debonding stages. The quantified damage index for the microcracking stage is around 0.2, which is reasonable due to the fact that the microcracking of concrete results in a slight attenuation of stress wave energy.

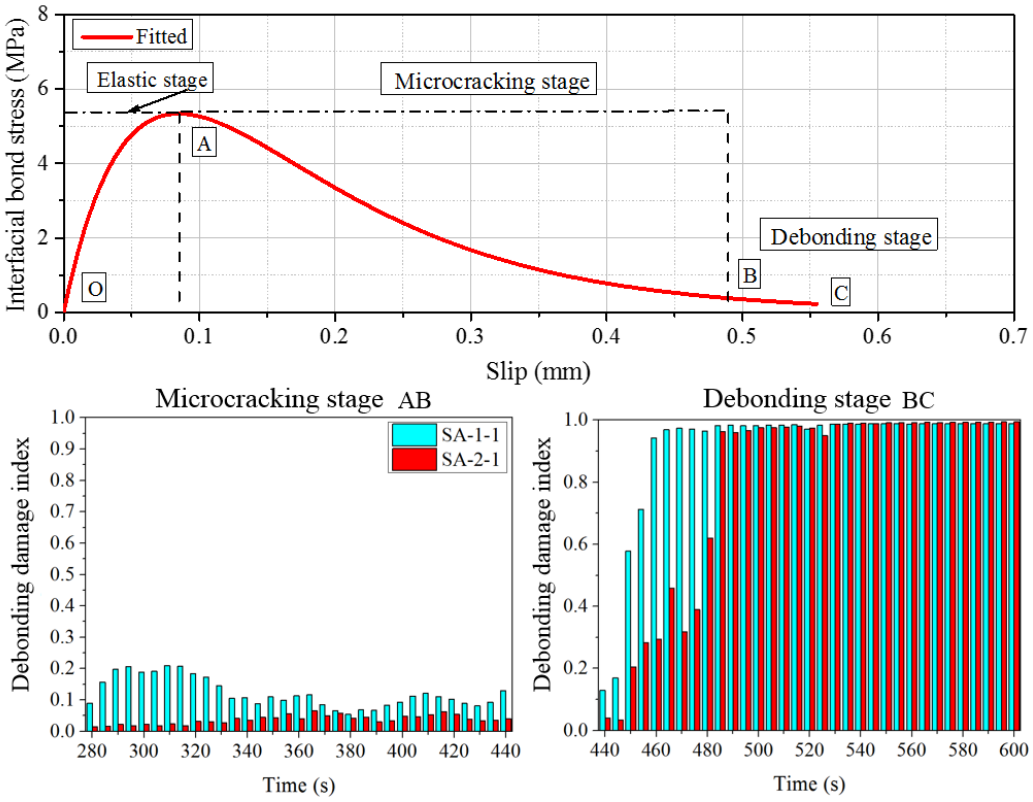

Figure 9-11. Bond-slip response and debonding damage index

9.5 Numerical validation

To further investigate the effect of BFRP debonding on the stress wave energy attenuation at the BFRP-to-concrete interface, a 3D finite element model of BFRP-to-concrete interface was built by using Abaqus commercial package. Figure 9-12 (a) shows the sketch of the numerical model. The BFRP sheet was tied to the concrete surface since the debonding always initiated from concrete with local bond-slip. One damaged condition of the BFRP-to-concrete interface was considered to investigate the effect of debonding cracking on the attenuation of the stress wave energy by notching the concrete beneath the BFRP sheet. Healthy condition without concrete damage was designed to simulate the healthy state of the interface and damaged condition with 40 (length) x 40 (width) x 5 (depth) mm notch of concrete was designed to

simulate the initial debonding damage, as shown in Figure 9-12 (b). The corresponding material properties of BFRP sheet and concrete are summarized in Table 9-1.

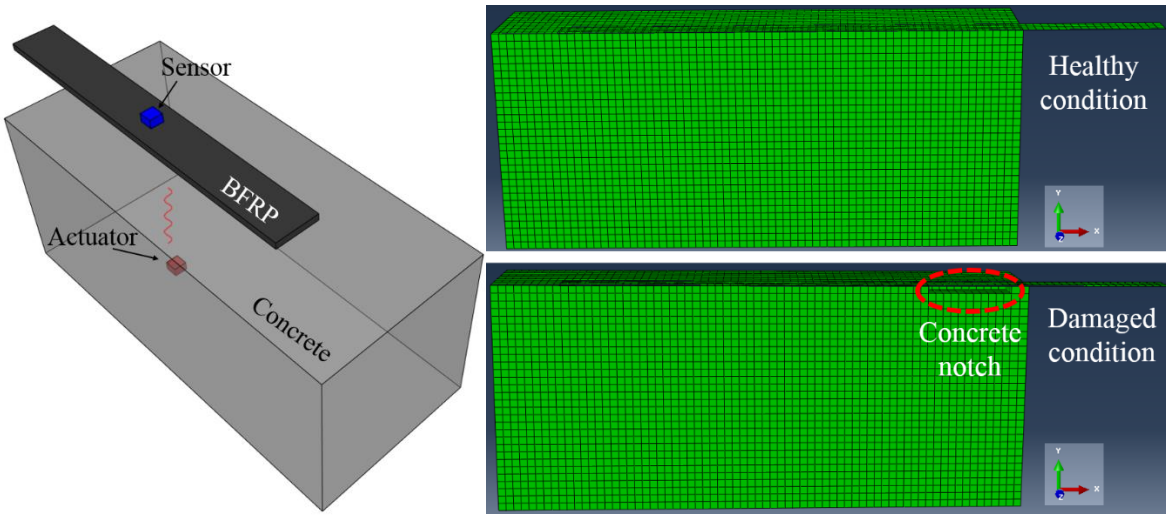

(a) Sketch of the model *(b) Two conditions*

Figure 9-12. Schematic diagram and numerical models

Table 9-1. Material properties.

Material	Properties	Values
BFRP	Density	1700 kg/m^3
	Poisson ratio	0.36
	Elastic modulus	73 GPa
Concrete	Density	2400 kg/m^3
	Poisson ratio	0.20
	Compressive strength	40 MPa

Harmonic sinusoidal input signal with the frequency of 100 kHz (two cycles) was used for the numerical study, instead of the swept sine wave input signal which was used in the experimental study. Song et al. (249) investigated the effect of actuation frequency from 10 to 180 kHz on the sensor response and found that the range of 90-110 kHz resulted in the strongest sensor response. Therefore, 100 kHz was selected as the actuating frequency in the numerical simulation. The wave propagation derived from the numerical model at the same moment is shown in Figure 9-13 (a) and (b). It is observed that the propagation of stress wave at the damaged interface is different from that in the healthy interface. For the damaged interface, the stress wave cannot propagate through the crack (i.e. notch) due to the presence of the air gap and thus form a reflected wave, which is different from the transmission of the stress wave at the healthy interface. This can be verified by the stress wave colour map as shown in Figure

9-13 (a) and (b), e.g. the red colour region at the edge of the notch of the damaged interface. The travelling wave signal passing two different debonding states can be obtained and the amplitudes of the received signal in different debonding states are plotted in Figure 9-14. The general trend of the testing results shows that the received signal is sensitive to the interfacial debonding condition. The stress wave propagation across the BFRP-to-concrete interface is weakened by the interfacial debonding. The increased debonding damage level leads to the reduction of the amplitude of the received signal.

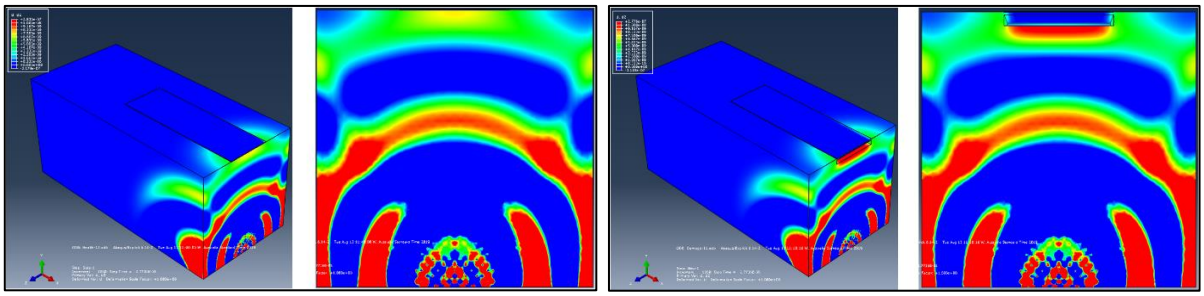

(a) *(b)*

Figure 9-13. Stress wave propagation: (a) Stress wave propagation through healthy BFRP-concrete interface; and (b) Stress wave propagation through debonded BFRP-concrete interface

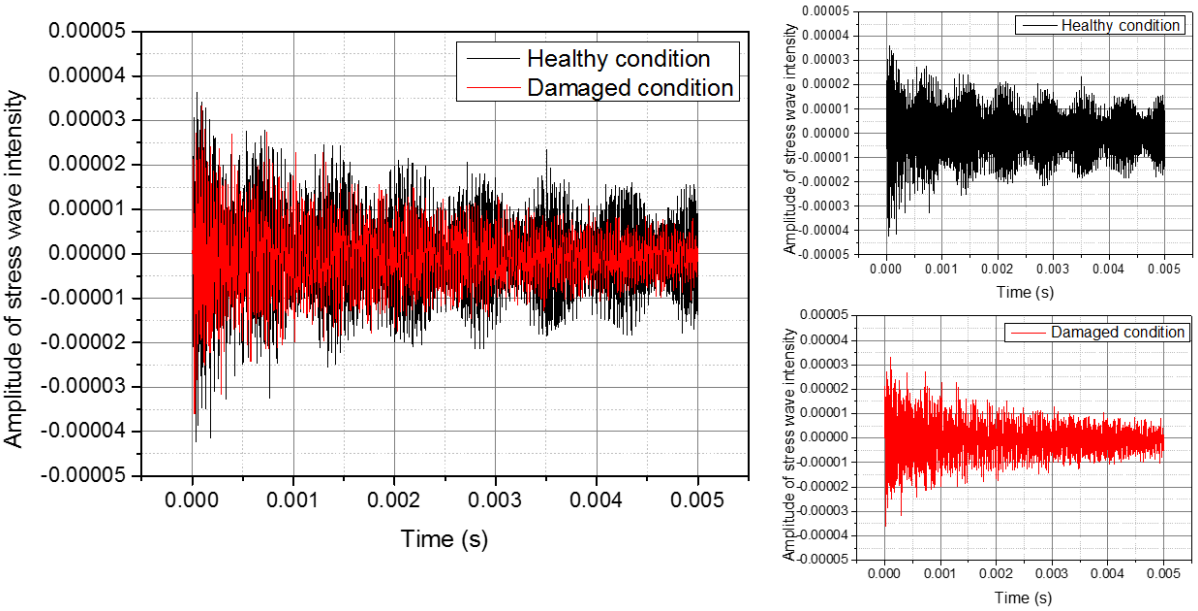

Figure 9-14. Comparison of amplitude of the stress wave intensity (100 kHz) under healthy and damaged conditions

9.6 Summary

In this chapter, the single-lap shear test is carried out to simulate the BFRP debonding from the concrete element. The SA-based active sensing approach is developed to monitor the interfacial debonding of the FRP-concrete interface. The wavelet packet-based debonding damage index can successfully quantify the interfacial debonding damage level and its validity is verified by the digital image correlation (DIC) measurement. In addition, as validated by the numerical results, the obtained debonding damage index can represent the interfacial damage level. As single SA pair can only detect the local damage, multiple SA pairs are suggested to be used for extending the detected range from local to global. The developed method in this chapter provides an alternative solution for fast detection and real-time monitoring of FRP-concrete interfacial debonding in engineering practice.

Chapter 10. Conclusions and future work

10.1 Main findings

In this study, the interfacial bond performance between FRP and concrete with the consideration of FRP configurations (sole BFRP, sole CFRP and BFRP/CFRP hybrid FRPs), concrete substrate characteristics (coarse aggregate sizes, concrete strength and steel fibre characteristics in fibre reinforced concrete) and strain rate effect under dynamic loading conditions are experimentally, analytically and numerically investigated. Semi empirical formulae were proposed to predict bonding performance of FRP layer from strengthened concrete with consideration of these parameters. A new anchorage system is also proposed to enhance the interfacial bond and an SA-based active sensing approach is used to quantify the interfacial damage caused by FRP debonding.

Chapter 3 and Chapter 4 present the static bond performance affected by FRP configurations (sole BFRP, sole CFRP and BFRP/CFRP hybrid FRPs) and concrete substrate characteristics (coarse aggregate sizes, concrete strength and adding steel fibres). In Chapter 3, experimental and analytical investigations on the bond behaviour between hybrid FRPs and concrete are conducted. It is found that the FRP stacking order has obvious influences on the debonding load and the bond-slip relationship. The maximum shear stress reduces if the contacting layer is stuck with a stiffer FRP plate. However, the ultimate slip improves when a stiffer FRP sheet is used. For the effect of concrete substrate characteristics in Chapter 4, it is found that the interfacial bond is sensitive to coarse aggregate size and volume of short steel fibres. Findings from the present tests show that the specimens with the aggregate size of 10–15 mm and 15–20 mm experience a significant decrease in the peak shear stress up to 18.46% and 33.71% as compared to the specimens with the size of 5–10 mm. An increase of 11.61% and 21.43% for the specimens with the aggregate size of 10–15 mm and 15–20 mm is found as compared to the specimens with the aggregate size of 5–10 mm. In addition, for the specimens with additional micro steel fibers, it is found that the specimens with 0.25%, 0.50% and 1.0% volume percentage steel fiber reinforcement experience a significant increase in the peak interfacial shear stress up to 31%, 53%, and 76% as compared to the referenced specimen without steel fibers, respectively.

Chapter 5, Chapter 6 and Chapter 7 present the dynamic interfacial bond behaviour with the consideration of FRP configurations and concrete substrate characteristics. It is found that the

primary contribution to the strain rate effect on bond performance comes from the strain rate sensitivity of the concrete substrate. Increased strain rate causes the enhancement on the dynamic concrete strength, hence on the bond strength of between FRP and concrete. It is also found that the specimen with the lowest concrete strength shows the highest strain rate sensitivity with the largest increment ratio of debonding load. An enhancement of up to 129.14% is observed for the specimens with concrete strength of about 20 MPa while the increment ratio of 63.66% is observed for the ones with concrete strength of about 40 MPa.

Chapter 8 presents a new proposed epoxy anchor to enhance the interfacial bond strength between FRP sheets and concrete. The experimental results show a 77.49% increment in bond strength, 86.71% increment in the utilization of BFRP sheet, and 78.10% increase in the peak shear stress on average. The size of epoxy anchors significantly affects the shear resistance. Increasing the diameter of the epoxy anchor greatly enhances the shear resistance while the peak bond strength and peak shear stress are not affected by the number of epoxy anchors in general.

Chapter 9 presents an approach for quantifying interfacial damage between FRP and concrete caused by debonding. The wavelet packet-based debonding damage index can successfully quantify the interfacial debonding damage level and its validity is verified by the digital image correlation (DIC) measurement. In addition, as validated by the numerical results, the obtained debonding damage index can represent the interfacial damage level.

10.2 Recommendations for future work

In Chapter 5 and 6, strain rate effect on the interfacial bond has been experimentally and analytically investigated. It should be noted that the strain rate effect on the dynamic tensile properties of epoxy resin on the bonding behaviour was not considered in this study, which is deemed necessary for further investigations.

In Chapter 7, the 3D FE model of a single shear test has been built for simulating dynamic bond behaviour of the FRP-to-concrete interface by using LS-DYNA. To extend the study, dynamic response of FRP-strengthened RC structural components under impact or blast loads can be further investigated by incorporating dynamic bond-slip model.

In Chapter 8, the new epoxy anchor has been proposed for enhancing the interfacial bond performance. The performance of FRP-strengthened RC structures with new epoxy anchors could be investigated in future work.

It should be noted that debonding failure under direct tensile force is another common failure mode, and proper models to estimate the tensile bond strength is also needed for predicting debonding failure. Very limited studies on direct tensile bond strength under static loading have been reported, no such study on dynamic tensile bond strength is available yet. This is deemed an important topic for future study.

Reference

1. Smith ST, Teng J. FRP-strengthened RC beams. I: review of debonding strength models. Eng Struct. 2002;24(4):385-95.
2. Fernando D, Yu T, Teng J-G, Zhao XL. CFRP strengthening of rectangular steel tubes subjected to end bearing loads: Effect of adhesive properties and finite element modelling. Thin-Walled Structures. 2009;47(10):1020-8.
3. Yun Y, Wu Y-F, Tang WC. Performance of FRP bonding systems under fatigue loading. Eng Struct. 2008;30(11):3129-40.
4. Chen JF, Teng J. Anchorage strength models for FRP and steel plates bonded to concrete. J Struct Eng. 2001;127(7):784-91.
5. Teng J, Chen J-F, Smith ST, Lam L. FRP: strengthened RC structures. AIP Conf Proc. 2002:266.
6. Chen WH, Hong; Jong, Michael; Cui, Jian; Shi, Yanchao; Chen, Li; Pham, Thong M. . Quasi-static and dynamic tensile properties of basalt fibre reinforced polymer. Composites Part B: Engineering. 2017;125:123-33.
7. Yao M, Zhu D, Yao Y, Zhang H, Mobasher B. Experimental study on basalt FRP/steel single-lap joints under different loading rates and temperatures. Compos Struct. 2016;145:68-79.
8. Pan J, Leung CK. Effect of concrete composition on interfacial parameters governing FRP debonding from the concrete substrate. Adv Struct Eng. 2009;12(5):627-37.
9. Franco A, Royer-Carfagni G. Effective bond length of FRP stiffeners. Int J Nonlin Mech. 2014;60:46-57.
10. Wu Z-M, Hu C-H, Wu Y-F, Zheng J-J. Application of improved hybrid bonded FRP technique to FRP debonding prevention. Constr Build Mater. 2011;25(6):2898-905.
11. Zhang H, Smith ST, Gravina RJ, Wang Z. Modelling of FRP-concrete bonded interfaces containing FRP anchors. Constr Build Mater. 2017;139:394-402.
12. Mostofinejad D, Shameli SM. Externally bonded reinforcement in grooves (EBRIG) technique to postpone debonding of FRP sheets in strengthened concrete beams. Constr Build Mater. 2013;38:751-8.
13. Chen J, Teng J. Shear capacity of FRP-strengthened RC beams: FRP debonding. Constr Build Mater. 2003;17(1):27-41.
14. Chen W, Pham TM, Sichembe H, Chen L, Hao H. Experimental study of flexural behaviour of RC beams strengthened by longitudinal and U-shaped basalt FRP sheet. Compos B Eng. 2018;134:114-26.
15. Spadea G, Bencardino F, Sorrenti F, Swamy RN. Structural effectiveness of FRP materials in strengthening RC beams. Eng Struct. 2015;99:631-41.
16. Bonacci J, Maalej M. Behavioral trends of RC beams strengthened with externally bonded FRP. J Compos Constr. 2001;5(2):102-13.
17. Yao J, Teng J, Lam L. Experimental study on intermediate crack debonding in FRP-strengthened RC flexural members. Adv Struct Eng. 2005;8(4):365-96.
18. Teng J, Smith ST, Yao J, Chen J-F. Intermediate crack-induced debonding in RC beams and slabs. Constr Build Mater. 2003;17(6-7):447-62.
19. Pham TM, Hao H. Impact behavior of FRP-strengthened RC beams without stirrups. J Compos Constr. 2016;20(4):04016011.
20. Razaqpur AG, Contestabile E, Tolba A. Experimental study of the strength and deformations of carbon fibre reinforced polymer (CFRP) retrofitted reinforced concrete slabs under blast load. Canadian Journal of Civil Engineering. 2009;36(8):1366-77.

21. ACI, editor Building code requirements for structural concrete (ACI 318-08) and commentary2008; Committee American Concrete Institute International Organization for Standardization: American Concrete Institute.
22. Pham TM, Hao H, editors. Review of concrete structures strengthened with FRP against impact loading. Structures; 2016: Elsevier.
23. Soleimani SM, Banthia N, Mindess S. Sprayed GFRP shear-strengthened reinforced concrete Beams under Impact Loading. Advances in Construction Materials 2007: Springer; 2007. p. 279-86.
24. Pham TM, Hao H. Behavior of fiber-reinforced polymer-strengthened reinforced concrete beams under static and impact loads. International Journal of Protective Structures. 2017;8(1):3-24.
25. Jerome D, Ross C. Simulation of the dynamic response of concrete beams externally reinforced with carbon-fiber reinforced plastic. Computers & structures. 1997;64(5-6):1129-53.
26. Erki M, Meier U. Impact loading of concrete beams externally strengthened with CFRP laminates. J Compos Constr. 1999;3(3):117-24.
27. Tang T, Saadatmanesh H. Analytical and experimental studies of fiber-reinforced polymer-strengthened concrete beams under impact loading. ACI Struct J. 2005;102(1):139.
28. R-08 AA. Guide for the design and construction of externally bonded FRP systems for strengthening concrete structures ACI Committee.440. 2008:519.
29. Hamed E, Rabinovitch O. Dynamic behavior of reinforced concrete beams strengthened with composite materials. J Compos Constr. 2005;9(5):429-40.
30. Beckmann B, Hummeltenberg A, Weber T, Curbach M. Concrete under high strain rates: Local material and global structure response to impact loading. International Journal of Protective Structures. 2011;2(3):283-93.
31. Zhou X, Kuznetsov V, Hao H, Waschl J. Numerical prediction of concrete slab response to blast loading. International Journal of Impact Engineering. 2008;35(10):1186-200.
32. Hao H, Li Z-X, Shi Y. Reliability analysis of RC columns and frame with FRP strengthening subjected to explosive loads. Journal of Performance of constructed Facilities. 2015;30(2):04015017.
33. Buchan P, Chen J. Blast resistance of FRP composites and polymer strengthened concrete and masonry structures–A state-of-the-art review. Compos B Eng. 2007;38(5-6):509-22.
34. Mukhtar FM, Faysal RM. A review of test methods for studying the FRP-concrete interfacial bond behavior. Constr Build Mater. 2018;169:877-87.
35. Wu Y-F, Jiang C. Quantification of bond-slip relationship for externally bonded FRP-to-concrete joints. J Compos Constr. 2013;17(5):673-86.
36. Wu Y-F, He L, Bank L. Bond-test protocol for plate-to-concrete interface involving all mechanisms. J Compos Constr. 2015;20(1):04015022.
37. Zhou Y-W, Wu Y-F, Yun Y. Analytical modeling of the bond–slip relationship at FRP-concrete interfaces for adhesively-bonded joints. Compos B Eng. 2010;41(6):423-33.
38. Serbescu A, Guadagnini M, Pilakoutas K. Standardised double-shear test for determining bond of FRP to concrete and corresponding model development. Compos B Eng. 2013;55:277-97.
39. Yao J, Teng J, Chen JF. Experimental study on FRP-to-concrete bonded joints. Compos B Eng. 2005;36(2):99-113.
40. Shen D, Ji Y, Yin F, Zhang J. Dynamic bond stress-slip relationship between basalt FRP sheet and concrete under initial static loading. J Compos Constr. 2015;19(6):04015012.
41. Shen D, Shi H, Ji Y, Yin F. Strain rate effect on effective bond length of basalt FRP sheet bonded to concrete. Constr Build Mater. 2015;82:206-18.

42. Shen D, Shi X, Ji Y, Yin F. Strain rate effect on bond stress–slip relationship between basalt fiber-reinforced polymer sheet and concrete. J Reinf Plast Comp. 2015;34(7):547-63.
43. Gartner A, Douglas EP, Dolan CW, Hamilton H. Small beam bond test method for CFRP composites applied to concrete. J Compos Constr. 2011;15(1):52-61.
44. Silva MA, Biscaia H. Degradation of bond between FRP and RC beams. Compos Struct. 2008;85(2):164-74.
45. Pellegrino C, Tinazzi D, Modena C. Experimental study on bond behavior between concrete and FRP reinforcement. J Compos Constr. 2008;12(2):180-9.
46. Laura De Lorenzis B, Antonio N. Bond of fiber-reinforced polymer laminates to concrete. Mater J. 2001;98:256-64.
47. Iovinella I, Prota A, Mazzotti C. Influence of surface roughness on the bond of FRP laminates to concrete. Constr Build Mater. 2013;40:533-42.
48. López-González JC, Fernández-Gómez J, González-Valle E. Effect of adhesive thickness and concrete strength on FRP-concrete bonds. J Compos Constr. 2012;16(6):705-11.
49. Shrestha J, Ueda T, Zhang D. Durability of FRP concrete bonds and its constituent properties under the influence of moisture conditions. J Mater Civil Eng. 2015;27(2):A4014009.
50. Carloni C, Subramaniam KV, Savoia M, Mazzotti C. Experimental determination of FRP–concrete cohesive interface properties under fatigue loading. Compos Struct. 2012;94(4):1288-96.
51. Jiang C, Wu Y-F, Jiang J-F. Effect of aggregate size on stress-strain behavior of concrete confined by fiber composites. Compos Struct. 2017;168:851-62.
52. Pan J, Leung CK. Effect of concrete composition on FRP/concrete bond capacity. J Compos Constr. 2007;11(6):611-8.
53. Nabil F. Grace GA-S, and Wael F. Ragheb. Strengthening of concrete beams using innovative ductile fiber-reinforced polymer fabric. 2002.
54. Li L-j, Guo Y-c, Huang P-y, Liu F, Deng J, Zhu J. Interfacial stress analysis of RC beams strengthened with hybrid CFS and GFS. Construction and building materials. 2009;23(6):2394-401.
55. Choi E, Utui N, Kim HS. Experimental and analytical investigations on debonding of hybrid FRPs for flexural strengthening of RC beams. Compos B Eng. 2013;45(1):248-56.
56. Hawileh RA, Rasheed HA, Abdalla JA, Al-Tamimi AK. Behavior of reinforced concrete beams strengthened with externally bonded hybrid fiber reinforced polymer systems. Materials & Design. 2014;53:972-82.
57. Hao Y, Hao H, Chen G. Experimental investigation of the behaviour of spiral steel fibre reinforced concrete beams subjected to drop-weight impact loads. Materials and Structures. 2016;49(1-2):353-70.
58. Wang Z, Wu J, Wang J. Experimental and numerical analysis on effect of fibre aspect ratio on mechanical properties of SRFC. Constr Build Mater. 2010;24(4):559-65.
59. Chen W, Pham TM, Sichembe H, Chen L, Hao H. Experimental study of flexural behaviour of RC beams strengthened by longitudinal and U-shaped basalt FRP sheet. Compos B Eng. 2017.
60. Fu B, Teng JG, Chen JF, Chen GM, Guo YC. Concrete Cover Separation in FRP-Plated RC Beams: Mitigation Using FRP U-Jackets. J Compos Constr. 2016;21(2):04016077.
61. Ibrahim SS, Eswari S, Sundararajan T. Experimental Investigation on FRC Beams Strengthened with GFRP Laminates. Electronic Journal of Structural Engineering. 2015;15:1.
62. Li L, Guo Y, Liu F. Test analysis for FRC beams strengthened with externally bonded FRP sheets. Constr Build Mater. 2008;22(3):315-23.
63. Yin J, Wu ZS. Structural performances of short steel-fiber reinforced concrete beams with externally bonded FRP sheets. Constr Build Mater. 2003;17(6-7):463-70.

64. Shi J-W, Cao W-H, Wu Z-S. Effect of adhesive properties on the bond behaviour of externally bonded FRP-to-concrete joints. Compos B Eng. 2019;177:107365.
65. Harries KA, Reeve B, Zorn A. Experimental evaluation of factors affecting monotonic and fatigue behavior of fiber-reinforced polymer-to-concrete bond in reinforced concrete beams. ACI Struct J. 2007;104(6):667.
66. Hosseini A, Ghafoori E, Al-Mahaidi R, Zhao X-L, Motavalli M. Strengthening of a 19th-century roadway metallic bridge using nonprestressed bonded and prestressed unbonded CFRP plates. Constr Build Mater. 2019;209:240-59.
67. Shi J-W, Zhu H, Dai J-G, Wang X, Wu Z-S. Effect of rubber toughening modification on the tensile behavior of FRP composites in concrete-based alkaline environment. J Mater Civil Eng. 2015;27(12):04015054.
68. Oehlers D, Seracino R, Smith S. Design handbook for RC structures retrofitted with FRP and metal plates: Beams and slabs. Standards Publishing Department (of Standards Australia); 2008.
69. Triantafillou T, Matthys S, Audenaert K, Balázs G, Blaschko M, Blontrock H, et al. Externally bonded FRP reinforcement for RC structures. International Federation for Structural Concrete (fib); 2001.
70. Council NR. Guide for the design and construction of externally bonded FRP systems for strengthening existing structures. CNR-DT200. 2004.
71. Yuan C, Chen W, Pham TM, Hao H, Cui J, Shi Y. Strain rate effect on interfacial bond behaviour between BFRP sheets and steel fibre reinforced concrete. Compos B Eng. 2019d:107032.
72. Shi JW, Zhu H, Wu ZS, Wu G. Experimental study of the strain rate effect of FRP sheet-concrete interface. China Civil Eng J. 2012;45(12):99-107.
73. Caggiano A, Martinelli E, Schicchi DS, Etse G. A modified Duvaut-Lions zero-thickness interface model for simulating the rate-dependent bond behavior of FRP-concrete joints. Compos B Eng. 2018;149:260-7.
74. Huo J, Liu J, Dai X, Yang J, Lu Y, Xiao Y, et al. Experimental study on dynamic behavior of CFRP-to-concrete interface. J Compos Constr. 2016;20(5):04016026.
75. Salimian MS, Mostofinejad D. Experimental Evaluation of CFRP-Concrete Bond Behavior under High Loading Rates Using Particle Image Velocimetry Method. J Compos Constr. 2019;23(3):04019010.
76. Cui J, Hao H, Shi Y. Discussion on the suitability of concrete constitutive models for high-rate response predictions of RC structures. International Journal of Impact Engineering. 2017;106:202-16.
77. Huo J, Liu J, Lu Y, Yang J, Xiao Y. Experimental study on dynamic behavior of GFRP-to-concrete interface. Eng Struct. 2016;118:371-82.
78. Teng J, Yuan H, Chen J. FRP-to-concrete interfaces between two adjacent cracks: Theoretical model for debonding failure. Int J Solids Struct. 2006;43(18-19):5750-78.
79. Yan D, Lin G. Dynamic properties of concrete in direct tension. Cement Concrete Res. 2006;36(7):1371-8.
80. Silva MA, Biscaia HC, Marreiros R. Bond–slip on CFRP/GFRP-to-concrete joints subjected to moisture, salt fog and temperature cycles. Compos B Eng. 2013;55:374-85.
81. Pan Y, Xian G, Silva MA. Effects of water immersion on the bond behavior between CFRP plates and concrete substrate. Constr Build Mater. 2015;101:326-37.
82. Al-Mahmoud F, Mechling J-M, Shaban M. Bond strength of different strengthening systems–Concrete elements under freeze–thaw cycles and salt water immersion exposure. Constr Build Mater. 2014;70:399-409.
83. Yun Y, Wu Y-F. Durability of CFRP–concrete joints under freeze–thaw cycling. Cold Regions Science and Technology. 2011;65(3):401-12.

84. Muñoz-Reja M, Cornetti P, Távara L, Mantič V. Interface crack model using finite fracture mechanics applied to the double pull-push shear test. Int J Solids Struct. 2019.
85. Yuan H, Lu X, Hui D, Feo L. Studies on FRP-concrete interface with hardening and softening bond-slip law. Compos Struct. 2012;94(12):3781-92.
86. Yuan H, Teng J, Seracino R, Wu Z, Yao J. Full-range behavior of FRP-to-concrete bonded joints. Eng Struct. 2004;26(5):553-65.
87. Wu Y-F, Xu X-S, Sun J-B, Jiang C. Analytical solution for the bond strength of externally bonded reinforcement. Compos Struct. 2012;94(11):3232-9.
88. Wu Z, Islam S, Said H. A three-parameter bond strength model for frp—concrete interface. J Reinf Plast Comp. 2009;28(19):2309-23.
89. Lu XZ, Teng JG, Ye LP, Jiang JJ. Bond–slip models for FRP sheets/plates bonded to concrete. Eng Struct. 2005;27(6):920-37.
90. Dai JG, Ueda T, Sato Y. Development of the nonlinear bond stress–slip model of fiber reinforced plastics sheet–concrete interfaces with a simple method. J Compos Constr. 2005;9(1):52-62.
91. Nakaba K, Kanakubo T, Furuta T, Yoshizawa H. Bond behavior between fiber-reinforced polymer laminates and concrete. Structural Journal. 2001;98(3):359-67.
92. Távara L, Reinoso J, Blázquez A, Mantič V. On the 3D extension of failure models for adhesive joints under mixed-mode fracture conditions: LEBIM and CZM. Theoretical and Applied Fracture Mechanics. 2019;100:362-76.
93. Hillerborg A, Modéer M, Petersson P-E. Analysis of crack formation and crack growth in concrete by means of fracture mechanics and finite elements. Cement Concrete Res. 1976;6(6):773-81.
94. Carrara P, Ferretti D. A finite-difference model with mixed interface laws for shear tests of FRP plates bonded to concrete. Compos B Eng. 2013;54:329-42.
95. Dai J, Ueda T, Sato Y. Bonding characteristics of fiber-reinforced polymer sheet-concrete interfaces under dowel load. J Compos Constr. 2007;11(2):138-48.
96. Wu Y-F, He L. Width effect of interfacial bond characteristics. Constr Build Mater. 2019;220:712-26.
97. Bilotta A, Di Ludovico M, Nigro E. FRP-to-concrete interface debonding: Experimental calibration of a capacity model. Compos B Eng. 2011;42(6):1539-53.
98. Pham HB, Al-Mahaidi R, Saouma V. Modelling of CFRP–concrete bond using smeared and discrete cracks. Compos Struct. 2006;75(1-4):145-50.
99. Pham HB, Al-Mahaidi R. Modelling of CFRP-concrete shear-lap tests. Constr Build Mater. 2007;21(4):727-35.
100. Diab H, Wu Z. Nonlinear constitutive model for time-dependent behavior of FRP-concrete interface. Composites science and technology. 2007;67(11-12):2323-33.
101. Salomoni V, Mazzucco G, Pellegrino C, Majorana C. Three-dimensional modelling of bond behaviour between concrete and FRP reinforcement. Engineering Computations. 2011.
102. Lu X, Jiang J, Teng J, Ye L. Finite element simulation of debonding in FRP-to-concrete bonded joints. Constr Build Mater. 2006;20(6):412-24.
103. Coronado CA, Lopez MM. Experimental characterization of concrete-epoxy interfaces. J Mater Civil Eng. 2008;20(4):303-12.
104. Coronado CA, Lopez MM. Damage approach for the prediction of debonding failure on concrete elements strengthened with FRP. J Compos Constr. 2007;11(4):391-400.
105. Bažant ZP, Oh BH. Crack band theory for fracture of concrete. Matériaux et construction. 1983;16(3):155-77.
106. Yang Z, Chen J, Proverbs D. Finite element modelling of concrete cover separation failure in FRP plated RC beams. Constr Build Mater. 2003;17(1):3-13.

107. Su X, Yang Z, Liu G. Monte Carlo simulation of complex cohesive fracture in random heterogeneous quasi-brittle materials: A 3D study. Int J Solids Struct. 2010;47(17):2336-45.
108. Li X, Chen J-F, Lu Y, Yang Z. Modelling static and dynamic FRP-concrete bond behaviour using a local concrete damage model. Adv Struct Eng. 2015;18(1):45-58.
109. Cicekli U, Voyiadjis GZ, Al-Rub RKA. A plasticity and anisotropic damage model for plain concrete. International Journal of plasticity. 2007;23(10-11):1874-900.
110. Zhang H, Smith ST. Influence of plate length and anchor position on FRP-to-concrete joints anchored with FRP anchors. Compos Struct. 2017;159:615-24.
111. Ozbakkaloglu T, Saatcioglu M. Tensile behavior of FRP anchors in concrete. J Compos Constr. 2009;13(2):82-92.
112. Kalfat R, Al-Mahaidi R, Smith ST. Anchorage devices used to improve the performance of reinforced concrete beams retrofitted with FRP composites: State-of-the-art review. J Compos Constr. 2011;17(1):14-33.
113. Wu Y-F, Huang Y. Hybrid bonding of FRP to reinforced concrete structures. J Compos Constr. 2008;12(3):266-73.
114. Carozzi FG, Colombi P, Fava G, Poggi C. Mechanical and bond properties of FRP anchor spikes in concrete and masonry blocks. Compos Struct. 2018;183:185-98.
115. Toutanji H, Ortiz G. The effect of surface preparation on the bond interface between FRP sheets and concrete members. Compos Struct. 2001;53(4):457-62.
116. Mohammadi M, Mostofinejad D, Barghian M. Effects of surface preparation method on FRP-concrete bond strength under alkaline conditions. J Compos Constr. 2017;21(4):04017010.
117. Hosseini A, Mostofinejad D. Effect of groove characteristics on CFRP-to-concrete bond behavior of EBROG joints: experimental study using particle image velocimetry (PIV). Constr Build Mater. 2013;49:364-73.
118. Hosseini A, Mostofinejad D. Experimental investigation into bond behavior of CFRP sheets attached to concrete using EBR and EBROG techniques. Compos B Eng. 2013;51:130-9.
119. De Lorenzis L, Teng J. Near-surface mounted FRP reinforcement: An emerging technique for strengthening structures. Compos B Eng. 2007;38(2):119-43.
120. Zhang S, Teng J, Yu T. Bond–slip model for CFRP strips near-surface mounted to concrete. Eng Struct. 2013;56:945-53.
121. Zhang S, Teng J. End cover separation in RC beams strengthened in flexure with bonded FRP reinforcement: simplified finite element approach. Materials and Structures. 2016;49(6):2223-36.
122. Committee A. Guide for the design and construction of externally bonded FRP systems for strengthening concrete structures (ACI 440.2 R-17). Farmington Hills, MI: Author. 2008.
123. Mostofinejad D, Mofrad MH, Hosseini A, Mofrad HH. Investigating the effects of concrete compressive strength, CFRP thickness and groove depth on CFRP-concrete bond strength of EBROG joints. Constr Build Mater. 2018;189:323-37.
124. Mostofinejad D, Torabian A. Experimental study of circular RC columns strengthened with longitudinal CFRP composites under eccentric loading: comparative evaluation of EBR and EBROG methods. J Compos Constr. 2016;20(2):04015055.
125. Mostofinejad D, Kashani AT. Experimental study on effect of EBR and EBROG methods on debonding of FRP sheets used for shear strengthening of RC beams. Compos B Eng. 2013;45(1):1704-13.
126. Jiang C, Wan B, Wu Y-F, Omboko J. Epoxy interlocking: A novel approach to enhance FRP-to-concrete bond behavior. Constr Build Mater. 2018;193:643-53.
127. Yuan C, Chen W, Pham TM, Hao H. Bond behavior between basalt fibres reinforced polymer sheets and steel fibres reinforced concrete. Eng Struct. 2018;176:812-24.

128. Yuan C, Chen W, Pham TM, Hao H. Effect of aggregate size on bond behaviour between basalt fibre reinforced polymer sheets and concrete. Compos B Eng. 2019c;158:459-74.
129. Jiang J, Luo J, Yu J, Wang Z. Performance Improvement of a Fiber-Reinforced Polymer Bar for a Reinforced Sea Sand and Seawater Concrete Beam in the Serviceability Limit State. Sensors. 2019;19(3):654.
130. Giri P, Kharkovsky S, Zhu X, Clark SM, Taheri S, Samali B. Characterization of carbon fiber reinforced polymer strengthened concrete and gap detection with a piezoelectric-based sensory technique. Structural Health Monitoring. 2019;18(1):172-9.
131. He J, Yuan F-G. Lamb wave-based subwavelength damage imaging using the DORT-MUSIC technique in metallic plates. Structural Health Monitoring. 2016;15(1):65-80.
132. Ong WH, Rajic N, Chiu WK, Rosalie C. Lamb wave–based detection of a controlled disbond in a lap joint. Structural Health Monitoring. 2018;17(3):668-83.
133. Beale C, Willis DJ, Niezrecki C, Inalpolat M. Passive acoustic damage detection of structural cavities using flow-induced acoustic excitations. Structural Health Monitoring. 2019:1475921719860389.
134. Arora V, Wijnant YH, de Boer A. Acoustic-based damage detection method. Applied acoustics. 2014;80:23-7.
135. Poozesh P, Aizawa K, Niezrecki C, Baqersad J, Inalpolat M, Heilmann G. Structural health monitoring of wind turbine blades using acoustic microphone array. Structural Health Monitoring. 2017;16(4):471-85.
136. West System. Epoxy resins and hardeners—Physical properties. (http://www.westsystem.com/ss/typical-physical-properties) (Jan. 31, 2015).
137. ASTM. Standard test method for tensile properties of polymer matrix composite materials. ASTM D3039. 2008; West Conshohocken, PA.
138. Fawzia S, Al-Mahaidi R, Zhao X-L. Experimental and finite element analysis of a double strap joint between steel plates and normal modulus CFRP. Compos Struct. 2006;75(1-4):156-62.
139. Manders PW, Bader M. The strength of hybrid glass/carbon fibre composites. J Mater Sci. 1981;16(8):2233-45.
140. Aveston J, Sillwood J. Synergistic fibre strengthening in hybrid composites. J Mater Sci. 1976;11(10):1877-83.
141. Woo S-K, Lee Y. Experimental study on interfacial behavior of CFRP-bonded concrete. KSCE Journal of Civil Engineering. 2010;14(3):385-93.
142. Sun W, Peng X, Liu HF, Qi HP. Numerical studies on the entire debonding propagation process of FRP strips externally bonded to the concrete substrate. Constr Build Mater. 2017;149:218-35.
143. Hosseini A, Mostofinejad D. Effective bond length of FRP-to-concrete adhesively-bonded joints: Experimental evaluation of existing models. Int J Adhes Adhes. 2014;48:150-8.
144. Ouezdou MB, Belarbi A, Bae S-W. Effective bond length of FRP sheets externally bonded to concrete. Int J Concr Struct M. 2009;3(2):127-31.
145. Ali-Ahmad M, Subramaniam K, Ghosn M. Experimental investigation and fracture analysis of debonding between concrete and FRP sheets. J Eng Mech. 2006;132(9):914-23.
146. Baldoni J, Lionello G, Zama F, Cristofolini L. Comparison of different filtering strategies to reduce noise in strain measurement with digital image correlation. The Journal of Strain Analysis for Engineering Design. 2016;51(6):416-30.
147. Ferracuti B, Savoia M, Mazzotti C. Interface law for FRP–concrete delamination. Compos Struct. 2007;80(4):523-31.
148. Ali-Ahmad M, Subramaniam K, Ghosn M, editors. Fracture analysis of the debonding between FRP and concrete using digital image correlation. Proceedings of FRAMCOS-5

international conference on fracture of concrete and concrete structures/Vail, Colorado; 2004 2004.
149. Gravina RJ, Aydin H, Visintin P. Extraction and Analysis of Bond-Slip Characteristics in Deteriorated FRP-to-Concrete Joints Using a Mechanics-Based Approach. J Mater Civil Eng. 2017;29(6):04017013.
150. Instructions for the design, execution and control of strengthening measures through fiber-reinforced composites. Italian Society Research Society 2004; CNR-DT 200/04.
151. Lu X. Study on FRP-concrete interface. PhD thesis, PRC: Tsinghua Univ; 2004 (in Chinese). 2004.
152. ASTM, C39. Standard test method for compressive strength of cylindrical concrete specimens. ASTM International. 2001.
153. ASTM C496/C496M-11. Standard test method for splitting tensile strength of cylindrical concrete specimens. West Conshohocken; 2004.
154. Wan B, Jiang C, Wu Y-F. Effect of defects in externally bonded FRP reinforced concrete. Constr Build Mater. 2018;172:63-76.
155. Neubauer U RF. Design aspects of concrete structures strengthened with externally bonded CFRP-plates. Proceedings of the seventh international conference on structural faults and repair, 8 July 1997 Volume 2: Concrete and Composites 1997.
156. Akçaoğlu T, Tokyay M, Çelik T. Effect of coarse aggregate size on interfacial cracking under uniaxial compression. Mater Lett. 2002;57(4):828-33.
157. Ghiassi B, Xavier J, Oliveira DV, Lourenço PB. Application of digital image correlation in investigating the bond between FRP and masonry. Compos Struct. 2013;106:340-9.
158. Czaderski C, Soudki K, Motavalli M. Front and side view image correlation measurements on FRP to concrete pull-off bond tests. J Compos Constr. 2010;14(4):451-63.
159. Täljsten B. Defining anchor lengths of steel and CFRP plates bonded to concrete. International Journal of Adhesion and Adhesives. 1997;17(4):319-27.
160. Kang TH-K, Howell J, Kim S, Lee DJ. A state-of-the-art review on debonding failures of FRP laminates externally adhered to concrete. Int J Concr Struct M. 2012;6(2):123-34.
161. Ueda T, Dai J, editors. New shear bond model for FRP–concrete interface–from modeling to application. FRP Composites in Civil Engineering-CICE 2004: Proceedings of the 2nd International Conference on FRP Composites in Civil Engineering-CICE 2004, 8-10 December 2004, Adelaide, Australia; 2004: Taylor & Francis.
162. Hu J, Wang K. Effect of coarse aggregate characteristics on concrete rheology. Constr Build Mater. 2011;25(3):1196-204.
163. Bažant ZP, Yu Q. Universal size effect law and effect of crack depth on quasi-brittle structure strength. J Eng Mech. 2009;135(2):78-84.
164. Kim J-K, Yi S-T, Park C-K, Eo S-H. Size effect on compressive strength of plain and spirally reinforced concrete cylinders. ACI Struct J. 1999;96:88-94.
165. structures. C-Fmcfc. Evaluation of the time dependent behavior of concrete. Bulletin d' information No. 199. Lausanne: Comite Europe du Béton/Fédération Internationale de Precontrainte; 1991.
166. Wu Y-F, Zhou Y-W. Unified strength model based on Hoek-Brown failure criterion for circular and square concrete columns confined by FRP. Journal of Composites for Construction. 2010;14(2):175-84.
167. Ko H, Matthys S, Palmieri A, Sato Y. Development of a simplified bond stress–slip model for bonded FRP–concrete interfaces. Constr Build Mater. 2014;68:142-57.
168. Sato Y, Kimura K and Kobatake Y. Bond behavior between CFRP sheet and concrete (part 1). J Struct Constr Eng AIJ 1997; 500: 75–82. (in Japanese).

169. Tanaka T. Shear resisting mechanism of reinforced concrete beams with CFS as shear reinforcement. Japan: Hokkaido University, 1996.
170. Neubauer U, Rostasy F, editors. Design aspects of concrete structures strengthened with externally bonded CFRP-plates. Proceedings of the seventh international conference on structural faults and repair, 8 July 1997 Volume 2: Concrete and Composites; 1997.
171. Yang Y, Yue Q, Hu Y. Experimental study on bond performance between carbon fiber sheets and concrete. J Build Struct 2001; 22: 36–42. (in Chinese).
172. Chajes MJ, Finch WW, Thomson TA. Bond and force transfer of composite-material plates bonded to concrete. Structural Journal. 1996;93(2):209-17.
173. Mazzotti C, Savoia M, Ferracuti B. An experimental study on delamination of FRP plates bonded to concrete. Constr Build Mater. 2008;22(7):1409-21.
174. Popovics S. A numerical approach to the complete stress-strain curve of concrete. Cement Concrete Res. 1973;3(5):583-99.
175. Sato Y, Vecchio FJ. Tension stiffening and crack formation in reinforced concrete members with fiber-reinforced polymer sheets. J Struct Eng. 2003;129(6):717-24.
176. Dai J, Ueda T. Local bond stress slip relations for FRP sheets-concrete interfaces. Fibre-Reinforced Polymer Reinforcement for Concrete Structures: (In 2 Volumes): World Scientific; 2003. p. 143-52.
177. C39 A. Standard test method for compressive strength of cylindrical concrete specimens. ASTM International. 2001.
178. C496 AS. Standard test method for splitting tensile strength of cylindrical concrete specimens. 2004.
179. Van Chanh N, editor Steel fiber reinforced concrete. Faculty of Civil Engineering Ho chi minh City university of Technology Seminar Material; 2004.
180. İnan G, Tabak V. Effect of aspect ratio and volume fraction of steel fiber on the mechanical properties of SFRC. Constr Build Mater. 2007;21(6):1250-3.
181. Rossi P, Daviau Desnoyers DT, Jean Louis. Analysis of cracking in steel fibre reinforced concrete (SFRC) structures in bending using probabilistic modelling. Structural Concrete. 2015;16(3):381-8.
182. Ko H, Sato Y. Bond stress–slip relationship between FRP sheet and concrete under cyclic load. J Compos Constr. 2007;11(4):419-26.
183. Wang HT, Wu G, Dai YT, He XY. Experimental study on bond behavior between CFRP plates and steel substrates using digital image correlation. J Compos Constr. 2016;20(6):04016054.
184. Gao J, Sun W, Morino K. Mechanical properties of steel fiber-reinforced, high-strength, lightweight concrete. Cement Concrete Comp. 1997;19(4):307-13.
185. Olivito R, Zuccarello F. An experimental study on the tensile strength of steel fiber reinforced concrete. Compos B Eng. 2010;41(3):246-55.
186. Thomas J, Ramaswamy A. Mechanical properties of steel fiber-reinforced concrete. J Mater Civil Eng. 2007;19(5):385-92.
187. Mansur M, Islam M. Interpretation of concrete strength for nonstandard specimens. J Mater Civil Eng. 2002;14(2):151-5.
188. Dai JG, Ueda T, Sato Y. Bonding characteristics of fiber-reinforced polymer sheet-concrete interfaces under dowel load. J Compos Constr. 2007;11(2):138-48.
189. Xia Y, Zhu J, Wang K, Zhou Q. Design and verification of a strain gauge based load sensor for medium-speed dynamic tests with a hydraulic test machine. International Journal of Impact Engineering. 2016;88:139-52.
190. Li J, Fang X. Stress wave analysis and optical force measurement of servo-hydraulic machine for high strain rate testing. Experimental Mechanics. 2014;54(8):1497-501.

191. Baky HA, Ebead U, Neale K. Nonlinear micromechanics-based bond–slip model for FRP/concrete interfaces. Eng Struct. 2012;39:11-23.
192. Xiao X. Dynamic tensile testing of plastic materials. Polymer Testing. 2008;27(2):164-78.
193. Chen W, Hao H, Hughes D, Shi Y, Cui J, Li Z-X. Static and dynamic mechanical properties of expanded polystyrene. Materials & Design. 2015;69:170-80.
194. Fitoussi J, Meraghni F, Jendli Z, Hug G, Baptiste D. Experimental methodology for high strain-rates tensile behaviour analysis of polymer matrix composites. Composites Science and Technology. 2005;65(14):2174-88.
195. Boyce BL, Dilmore MF. The dynamic tensile behavior of tough, ultrahigh-strength steels at strain-rates from 0.0002 s− 1 to 200 s− 1. International Journal of Impact Engineering. 2009;36(2):263-71.
196. Hao H, Tang EK. Numerical simulation of a cable-stayed bridge response to blast loads, Part II: Damage prediction and FRP strengthening. Eng Struct. 2010;32(10):3193-205.
197. Biscaia HC, Chastre C, Borba IS, Silva C, Cruz D. Experimental evaluation of bonding between CFRP laminates and different structural materials. J Compos Constr. 2015;20(3):04015070.
198. Subramaniam KV, Carloni C, Nobile L. Width effect in the interface fracture during shear debonding of FRP sheets from concrete. Eng Struct. 2007;74(4):578-94.
199. Council NR. Guide for the design and construction of externally bonded FRP systems for strengthening existing structures. CNR-DT200. 2013.
200. Pan Y, Xian G, Li H. Effects of Freeze-Thaw Cycles on the Behavior of the Bond between CFRP Plates and Concrete Substrates. J Compos Constr. 2018;22(3):04018011.
201. Liao L, Kobayashi T, Sawa T, Goda Y. 3-D FEM stress analysis and strength evaluation of single-lap adhesive joints subjected to impact tensile loads. Int J Adhes Adhes. 2011;31(7):612-9.
202. Hao Y, Hao H. Dynamic compressive behaviour of spiral steel fibre reinforced concrete in split Hopkinson pressure bar tests. Constr Build Mater. 2013;48:521-32.
203. Chen W, Hao H, Jong M, Cui J, Shi Y, Chen L, et al. Quasi-static and dynamic tensile properties of basalt fibre reinforced polymer. Compos B Eng. 2017;125:123-33.
204. Hao Y, Hao H, Zhang X. Numerical analysis of concrete material properties at high strain rate under direct tension. International Journal of Impact Engineering. 2012;39(1):51-62.
205. Yen CF, Caiazzo A. Innovative processing of multifunctional composite armor for ground vehicles. ARL Technical Report ARL-CR-484. US Army Research Laboratory, Aberdeen Proving Ground, MD, 2000.
206. Yuan C, Chen W, Pham TM, Hao H. Bond behaviour between hybrid fiber reinforced polymer sheets and concrete. Constr Build Mater. 2019b;210:93-110.
207. Bunsell A, Harris B. Hybrid carbon and glass fibre composites. Composites. 1974;5(4):157-64.
208. Liu K, Wu Y-F. Analytical identification of bond–slip relationship of EB-FRP joints. Compos B Eng. 2012;43(4):1955-63.
209. Jiang C, Wan B, Omboko J. Enhancing FRP-to-concrete Bond Behavior by Epoxy Ribs. Special Publication. 2018;327:25.1-.14.
210. Wang H-T, Wu G. Bond-slip models for CFRP plates externally bonded to steel substrates. Compos Struct. 2018;184:1204-14.
211. Toutanji H, Saxena P, Zhao L, Ooi T. Prediction of interfacial bond failure of FRP–concrete surface. J Compos Constr. 2007;11(4):427-36.
212. Sun W, Peng X, Yu Y. Development of a simplified bond model used for simulating FRP strips bonded to concrete. Compos Struct. 2017;171:462-72.

213. Bizindavyi L, Neale K. Transfer lengths and bond strengths for composites bonded to concrete. J Compos Constr. 1999;3(4):153-60.
214. Carloni C, Subramaniam KV. Investigation of sub-critical fatigue crack growth in FRP/concrete cohesive interface using digital image analysis. Compos B Eng. 2013;51:35-43.
215. Maruyama K, Ueda T, editors. JSCE recommendations for upgrading of concrete structures with use of continuous fiber sheets. FRP Composites in Civil Engineering Proceedings of the International Conference on FRP composites in Civil EngineeringHong Kong Institution of Engineers, Hong Kong Institution of Steel Construction; 2001.
216. Hao Y, Hao H. Influence of the concrete DIF model on the numerical predictions of RC wall responses to blast loadings. Eng Struct. 2014;73:24-38.
217. Teng J, Smith ST, Yao J, Chen JF. Intermediate crack-induced debonding in RC beams and slabs. Constr Build Mater. 2003;17(6):447-62.
218. Said H, Wu Z. Evaluating and proposing models of predicting IC debonding failure. J Compos Constr. 2008;12(3):284-99.
219. Elsanadedy H, Abbas H, Al-Salloum Y, Almusallam T. Prediction of intermediate crack debonding strain of externally bonded FRP laminates in RC beams and one-way slabs. J Compos Constr. 2014;18(5):04014008.
220. Biscaia HC, Chastre C, Silva MA. Linear and nonlinear analysis of bond-slip models for interfaces between FRP composites and concrete. Compos B Eng. 2013;45(1):1554-68.
221. Taniguchi N, Nishiwaki T, Hirayama N, Nishida H, Kawada H. Dynamic tensile properties of carbon fiber composite based on thermoplastic epoxy resin loaded in matrix-dominant directions. Composites Science and Technology. 2009;69(2):207-13.
222. Chen W, Lu F, Cheng M. Tension and compression tests of two polymers under quasi-static and dynamic loading. Polymer testing. 2002;21(2):113-21.
223. Zhang D, Gu X-L, Yu Q-Q, Huang H, Wan B, Jiang C. Fully probabilistic analysis of FRP-to-concrete bonded joints considering model uncertainty. Compos Struct. 2018;185:786-806.
224. Zhou X, Hao H. Modelling of compressive behaviour of concrete-like materials at high strain rate. Int J Solids Struct. 2008;45(17):4648-61.
225. Hao Y, Hao H, Jiang G, Zhou Y. Experimental confirmation of some factors influencing dynamic concrete compressive strengths in high-speed impact tests. Cement Concrete Res. 2013;52:63-70.
226. Perrella M, Berardi V, Cricrì G. A novel methodology for shear cohesive law identification of bonded reinforcements. Compos B Eng. 2018;144:126-33.
227. Liu S, Yuan H, Wu J. Full-range mechanical behavior study of FRP-to-concrete interface for pull-pull bonded joints. Compos B Eng. 2019;164:333-44.
228. He J, Xian G. Bond-slip behavior of fiber reinforced polymer strips-steel interface. Constr Build Mater. 2017;155:250-8.
229. Huang X, Sui L, Xing F, Zhou Y, Wu Y. Reliability assessment for flexural FRP-Strengthened reinforced concrete beams based on Importance Sampling. Compos B Eng. 2019;156:378-98.
230. Tao Y, Chen J-F. Concrete damage plasticity model for modeling FRP-to-concrete bond behavior. J Compos Constr. 2014;19(1):04014026.
231. Qiu C, Bai Y, Zhang L, Jin L. Bending Performance of Splice Connections for Assembly of Tubular Section FRP Members: Experimental and Numerical Study. J Compos Constr. 2019;23(5):04019040.
232. Yuan C, Chen W, Pham TM, Chen L, Cui J, Shi Y, et al. Effect of aggregate size on the dynamic interfacial bond behaviour between basalt fiber reinforced polymer sheets and concrete. Constr Build Mater. 2019a;227:116584.

233. Chen G, Teng J, Chen J, Xiao Q. Finite element modeling of debonding failures in FRP-strengthened RC beams: A dynamic approach. Computers & structures. 2015;158:167-83.
234. Teng J, Yuan H, Chen J. FRP-to-concrete interfaces between two adjacent cracks: theoretical model for debonding failure. International Journal of Solids and Structures. 2006;43(18):5750-78.
235. Benzeggagh ML, Kenane M. Measurement of mixed-mode delamination fracture toughness of unidirectional glass/epoxy composites with mixed-mode bending apparatus. Composites science and technology. 1996;56(4):439-49.
236. De Lorenzis L, Fernando D, Teng J-G. Coupled mixed-mode cohesive zone modeling of interfacial debonding in simply supported plated beams. Int J Solids Struct. 2013;50(14-15):2477-94.
237. Leung CK, Tung W. Three-parameter model for debonding of FRP plate from concrete substrate. J Eng Mech. 2006;132(5):509-18.
238. Hutchinson JW, Suo Z. Mixed mode cracking in layered materials. Advances in applied mechanics. 29: Elsevier; 1991. p. 63-191.
239. Tsai SW. Strength Characteristics of Composite Materials. Philco Corp Newport Beach CA, 1965.
240. Malvar LJ, Crawford JE, Wesevich JW, Simons D. A plasticity concrete material model for DYNA3D. International journal of impact engineering. 1997;19(9-10):847-73.
241. Tsai SW, Wu EM. A general theory of strength for anisotropic materials. Journal of composite materials. 1971;5(1):58-80.
242. Yuan C, Chen W, Pham TM, Hao H, Cui J, Shi Y. Influence of Concrete Strength on Dynamic Interfacial Fracture Behaviour between Fibre Reinforced Polymer Sheets and Concrete. Eng Struct. 2020:106934.
243. Chen G, Teng J, Chen J. Process of debonding in RC beams shear-strengthened with FRP U-strips or side strips. Int J Solids Struct. 2012;49(10):1266-82.
244. Vaculik J, Sturm AB, Visintin P, Griffith MC. Modelling FRP-to-substrate joints using the bilinear bond-slip rule with allowance for friction—Full-range analytical solutions for long and short bonded lengths. Int J Solids Struct. 2018;135:245-60.
245. Zhu J, Ren L, Ho S-C, Jia Z, Song G. Gas pipeline leakage detection based on PZT sensors. Smart Materials and Structures. 2017;26(2):025022.
246. Yao P, Kong Q, Xu K, Jiang T, Huo L-s, Song G. Structural health monitoring of multi-spot welded joints using a lead zirconate titanate based active sensing approach. Smart Materials and Structures. 2015;25(1):015031.
247. Kong Q, Song G. A comparative study of the very early age cement hydration monitoring using compressive and shear mode smart aggregates. IEEE Sensors Journal. 2016;17(2):256-60.
248. Xu B, Li B, Song G. Active debonding detection for large rectangular CFSTs based on wavelet packet energy spectrum with piezoceramics. J Struct Eng. 2012;139(9):1435-43.
249. Song F, Huang G, Kim J, Haran S. On the study of surface wave propagation in concrete structures using a piezoelectric actuator/sensor system. Smart materials and Structures. 2008;17(5):055024.

Appendix I

STATEMENTS OF CONTRIBUTION OF CO-AUTHORS

To whom it may concern,

I, Cheng Yuan, conducted experimental, analytical and numerical investigations, data processing & analysis and wrote manuscripts of the papers titled as follows, which were revised and edited by the co-authors. They also provided insights on experimental preparation, data processing and data analysis.

1. Bond Behaviour between Hybrid Fibres Reinforced Polymer Sheets and Concrete

2. Effect of Aggregate Size on Bond Behaviour between Basalt Fibre Reinforced Polymer Sheets and Concrete

3. Bond Behaviour between Basalt Fibres Reinforced Polymer Sheets and Steel Fibres Reinforced Concrete

4. Dynamic Interfacial Bond Behaviour between Basalt Fibre Reinforced Polymer Sheets and Concrete

5. Dynamic Interfacial Bond Behaviour between Hybrid Fibre Reinforced Polymer Sheets and Concrete

6. Effect of Aggregate Size on the Dynamic Interfacial Bond Behaviour between Basalt Fibre Reinforced Polymer Sheets and Concrete

7. Influence of Concrete Strength on Dynamic Interfacial Fracture Behaviour between Fibre Reinforced Polymer Sheets and Concrete

8. Strain Rate Effect on Interfacial Bond Behaviour between BFRP Sheets and Steel Fibre Reinforced Concrete

9. Finite Element Modelling of Dynamic Bonding Behaviours between Fibre Reinforced Polymer Sheet and Concrete

10. New Epoxy Anchor for Better Bonding between FRP Sheets and Concrete

11. Interfacial Debonding Detection in Externally Bonded BFRP Reinforced Concrete Using Stress Wave-based Sensing Approach

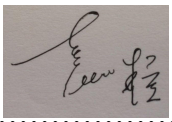

(……)

I, as a co-author, endorse that this level of contribution by the candidate indicated above is appropriate.

(Dr. Wensu Chen)

(Prof. Hong Hao)

(Dr. Thong M. Pham)

(Prof. Li Chen)

(Dr. Jian Cui)

(Prof. Yanchao Shi)

(Dr. Qingzhao Kong)

(Dr. Jiafei Jiang)

(Ms. Mi Zhang)

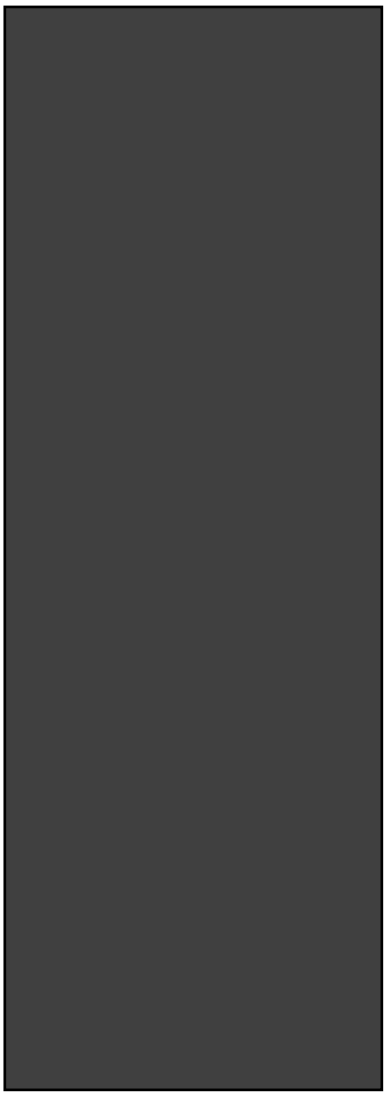

Appendix II

Copyright Clearance

The proof of the rights, granted by publisher for the publication that form the chapters of this thesis are attached below.

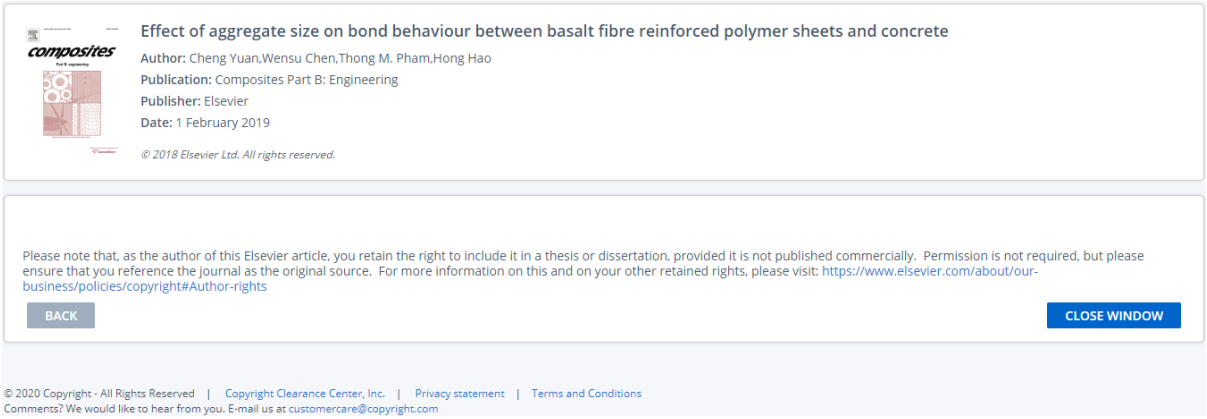

Yuan C, Chen W, Pham TM, Hao H. Effect of aggregate size on bond behaviour between basalt fibre reinforced polymer sheets and concrete. Composites Part B: Engineering. 2019c; 158:459-74.

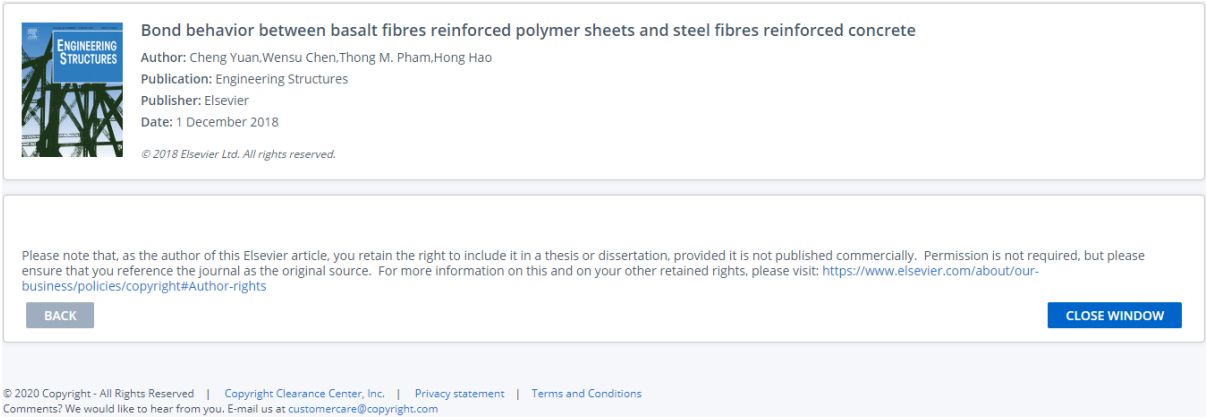

Yuan C, Chen W, Pham TM, Hao H. Bond behaviour between basalt fibres reinforced polymer sheets and steel fibres reinforced concrete. Engineering structures. 2018; 176:812-24.

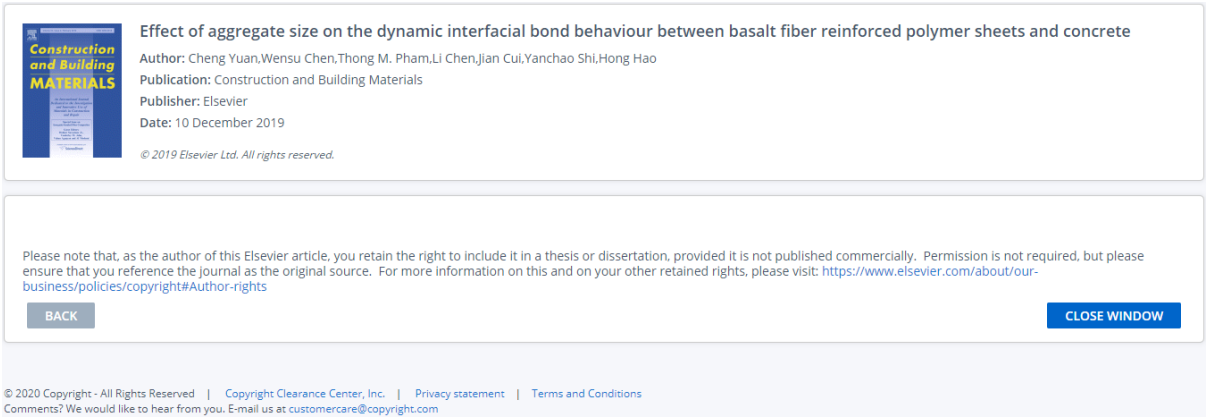

Yuan C, Chen W, Pham TM, Chen L, Cui J, Shi Y, Hao H. Effect of aggregate size on the dynamic interfacial bond behaviour between basalt fibre reinforced polymer sheets and concrete. Construction and Building Materials. 2019a; 227:116584.

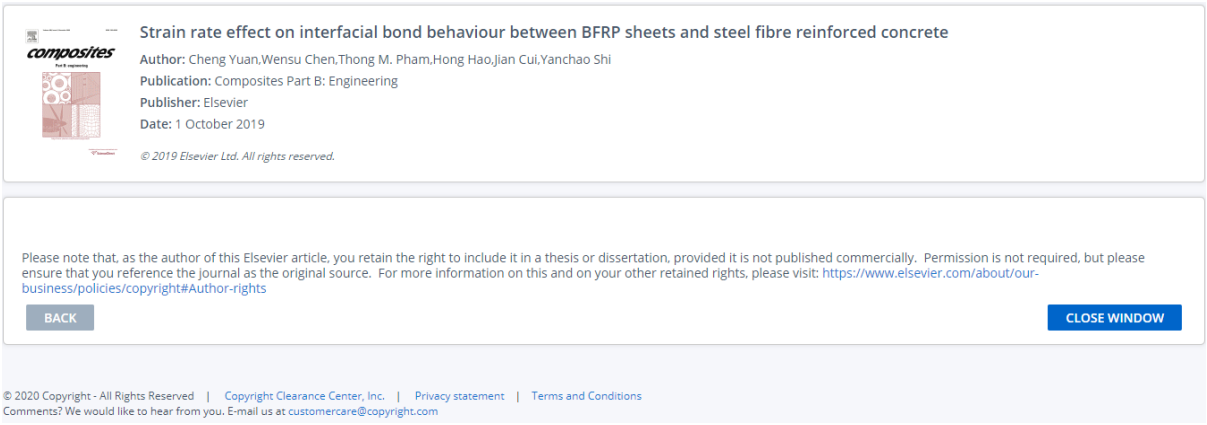

Yuan C, Chen W, Pham TM, Hao H, Cui J, Shi Y. Strain rate effect on interfacial bond behaviour between BFRP sheets and steel fibre reinforced concrete. Composites Part B: Engineering. 2019d: 107032.

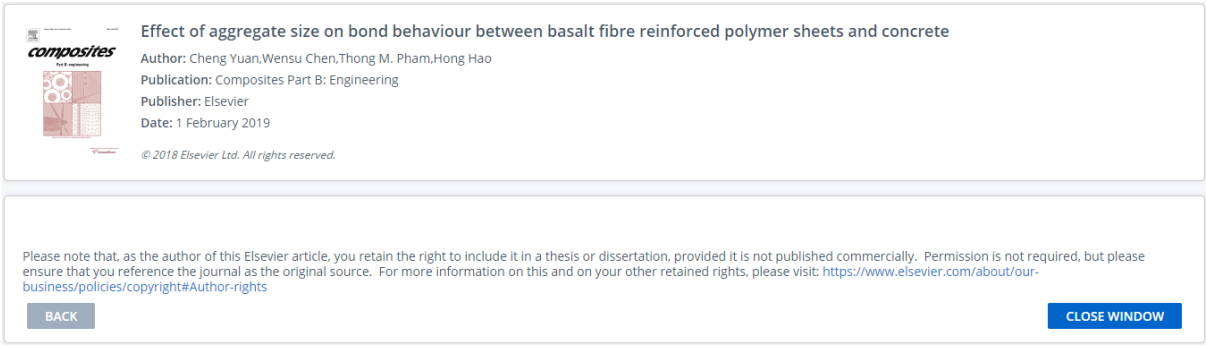

Yuan C, Chen W, Pham TM, Hao H. Effect of aggregate size on bond behaviour between basalt fibres reinforced polymer sheets and concrete. Composites Part B: Engineering. 2019c; 158:459-74.

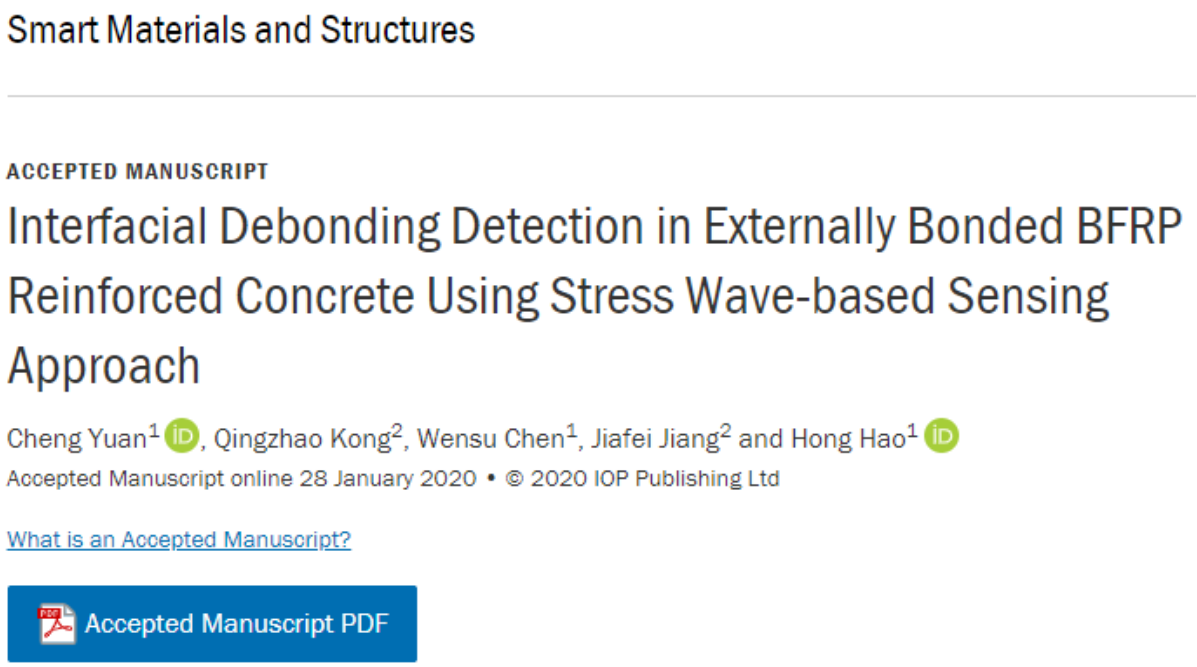

Yuan C, Kong Q, Chen W, Jiang J, Hao H. Interfacial Debonding Detection in Externally Bonded BFRP Reinforced Concrete Using Stress Wave-based Sensing Approach. Smart Materials and Structures. 2020; 29:035039.

Influence of concrete strength on dynamic interfacial fracture behaviour between fibre reinforced polymer sheets and concrete

Author: Cheng Yuan,Wensu Chen,Thong M. Pham,Hong Hao,Jian Cui,Yanchao Shi
Publication: Engineering Fracture Mechanics
Publisher: Elsevier
Date: 15 April 2020

© 2020 Elsevier Ltd. All rights reserved.

Please note that, as the author of this Elsevier article, you retain the right to include it in a thesis or dissertation, provided it is not published commercially. Permission is not required, but please ensure that you reference the journal as the original source. For more information on this and on your other retained rights, please visit: https://www.elsevier.com/about/our-business/policies/copyright#Author-rights

BACK CLOSE WINDOW

Yuan C, Chen W, Pham TM, Hao H, Cui J, Shi Y. Influence of Concrete Strength on Dynamic Interfacial Fracture Behaviour between Fibre Reinforced Polymer Sheets and Concrete. Engineering Fracture Mechanics. 2020:106934.

Interfacial bond behaviour between hybrid carbon/basalt fibre composites and concrete under dynamic loading

Author: Cheng Yuan,Wensu Chen,Thong M. Pham,Hong Hao,Jian Cui,Yanchao Shi
Publication: International Journal of Adhesion and Adhesives
Publisher: Elsevier
Date: June 2020

© 2020 Elsevier Ltd. All rights reserved.

Please note that, as the author of this Elsevier article, you retain the right to include it in a thesis or dissertation, provided it is not published commercially. Permission is not required, but please ensure that you reference the journal as the original source. For more information on this and on your other retained rights, please visit: https://www.elsevier.com/about/our-business/policies/copyright#Author-rights

BACK CLOSE WINDOW

Yuan C, Chen W, Pham TM, Hao H, Jian C, Shi Y. Interfacial Bond Behaviour between Hybrid Carbon/Basalt Fibre Composites and Concrete under Dynamic Loading. International Journal of Adhesion and Adhesives. 2020:102569.

New epoxy anchor for better bonding between FRP sheets and concrete

Author: Cheng Yuan,Wensu Chen,Thong M. Pham,Hong Hao,Li Chen,Mi Zhang
Publication: Construction and Building Materials
Publisher: Elsevier
Date: 10 July 2020

© 2020 Elsevier Ltd. All rights reserved.

Please note that, as the author of this Elsevier article, you retain the right to include it in a thesis or dissertation, provided it is not published commercially. Permission is not required, but please ensure that you reference the journal as the original source. For more information on this and on your other retained rights, please visit: https://www.elsevier.com/about/our-business/policies/copyright#Author-rights

BACK CLOSE WINDOW

Yuan C, Chen W, Pham TM, Hao H, Chen L, Zhang M. New epoxy anchor for better bonding between FRP sheets and concrete. Construction and Building Materials. 2020; 248:118628.

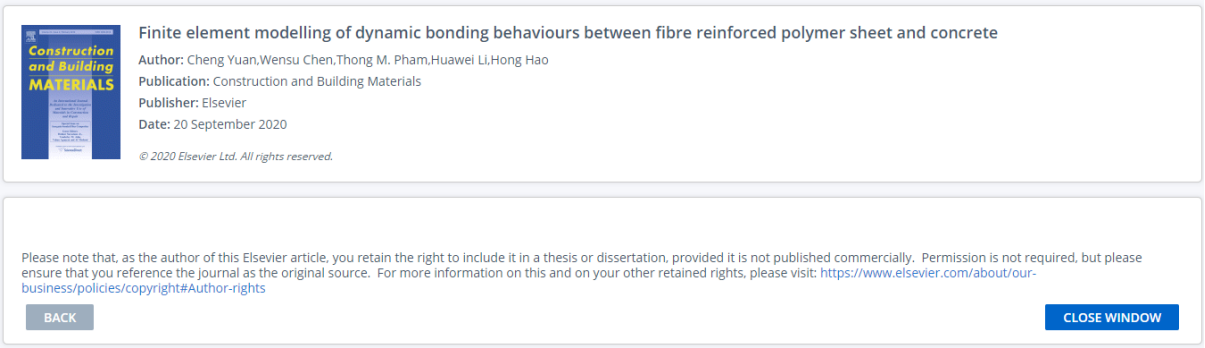

Yuan C, Chen W, Pham TM, Li H, Hao H. Finite element modelling of dynamic bonding behaviours between fibre reinforced polymer sheet and concrete. Construction and Building Materials. 2020; 255:118939.